



## **Blast Loading on Glass in Facades**

### Flexural Strength of Monolithic Flat Glass at High Strain Rates

**Meyland, Martin Jensen**

*Link to article, DOI:*  
[10.11581/DTU.00000229](https://doi.org/10.11581/DTU.00000229)

*Publication date:*  
2022

*Document Version*  
Publisher's PDF, also known as Version of record

[Link back to DTU Orbit](#)

*Citation (APA):*  
Meyland, M. J. (2022). *Blast Loading on Glass in Facades: Flexural Strength of Monolithic Flat Glass at High Strain Rates*. Department of Civil and Mechanical Engineering, Technical University of Denmark.  
<https://doi.org/10.11581/DTU.00000229>

---

#### **General rights**

Copyright and moral rights for the publications made accessible in the public portal are retained by the authors and/or other copyright owners and it is a condition of accessing publications that users recognise and abide by the legal requirements associated with these rights.

- Users may download and print one copy of any publication from the public portal for the purpose of private study or research.
- You may not further distribute the material or use it for any profit-making activity or commercial gain
- You may freely distribute the URL identifying the publication in the public portal

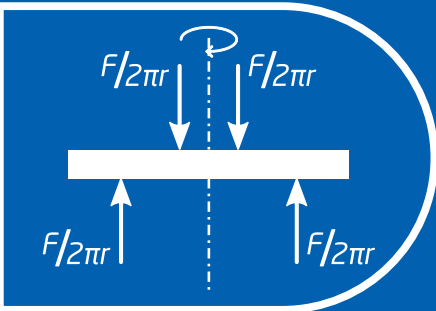
If you believe that this document breaches copyright please contact us providing details, and we will remove access to the work immediately and investigate your claim.

# Blast Loading on Glass in Facades

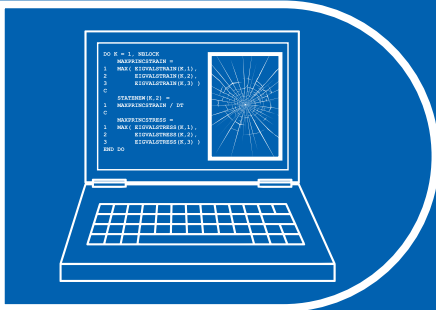
## Flexural Strength of Monolithic Flat Glass at High Strain Rates

Martin Jensen Meyland

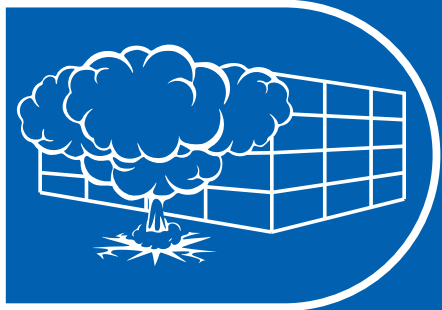
PHASE 1



PHASE 2



PHASE 3





TECHNICAL UNIVERSITY OF DENMARK  
**DEPARTMENT OF CIVIL AND MECHANICAL ENGINEERING**

REPORT R-466 | ISBN 978-87-7877-569-6  
DOI 10.11581/DTU.00000229  
Ph.D. THESIS

# **BLAST LOADING ON GLASS IN FACADES**

Flexural Strength of Monolithic Flat  
Glass at High Strain Rates

MARTIN JENSEN MEYLAND, M.Sc.

Copyright © 2022 by Martin Jensen Meyland  
All rights reserved.

Printed by STEP  
Typeset in L<sup>A</sup>T<sub>E</sub>X

Project period: January 2019 – March 2022  
Date of public defence: 8 June 2022

**For information, address:**

Technical University of Denmark, Department of Civil and Mechanical Engineering,  
Brovej, Building 118, 2800 Kgs. Lyngby, Denmark

Homepage: [www.byg.dtu.dk](http://www.byg.dtu.dk)

**Principal Supervisor:**

Jens Henrik Nielsen, M.Sc., Ph.D., Associate Professor  
*Section for Structures and Safety, Department of Civil and Mechanical Engineering  
Technical University of Denmark, Kgs. Lyngby, Denmark*

**Co-supervisors:**

Søren Peter Kristensen, B.A., Chief Specialist  
*Structures & Facade Engineering, Buildings, Specialised Engineering  
Ramboll Denmark A/S, Copenhagen, Denmark*

Hans Exner, M.Sc., Ph.D., Senior Chief Consultant  
*Structures & Facade Engineering, Buildings, Specialised Engineering  
Ramboll Denmark A/S, Copenhagen, Denmark*

Rasmus N. W. Eriksen, M.Sc., Ph.D., Head of Engineering & Partner  
*IDTCE ApS, Copenhagen, Denmark*

**Assessment Committee:**

Henrik Stang, M.Sc., Ph.D., Professor  
*Section for Structures and Safety, Department of Civil and Mechanical Engineering  
Technical University of Denmark, Kgs. Lyngby, Denmark*

Mauro Overend, M.Sc., Ph.D., Professor  
*Department of Architectural Engineering & Technology, Faculty of Architecture and the Built  
Environment  
Delft University of Technology, Delft, The Netherlands*

Weinong Wayne Chen, M.S., Ph.D., Professor  
*School of Aeronautics and Astronautics/School of Materials Engineering  
Purdue University, West Lafayette, Indiana, USA*

**Sources of Project Finance:**

Innovation Fund Denmark (IFD), Grant No. 8053-00088B  
Rambøll Fonden, Grant No. 2018-51  
Ramboll Denmark A/S

**How to cite:** Meyland, M. J. (2022). *Blast Loading on Glass in Facades – Flexural Strength of Monolithic Flat Glass at High Strain Rates*. Ph.D. Thesis, Technical University of Denmark, Department of Civil and Mechanical Engineering. <https://doi.org/10.11581/DTU.00000229>



*To the loving memory of my grandfathers  
Martin & Hans Uve*

An excellent craftsman and a passionate engineer.



# Preface

This thesis is submitted in partial fulfilment of the requirements for the Danish Ph.D. degree. The research was undertaken at the former Department of Civil Engineering (the Department of Civil and Mechanical Engineering as of the 1<sup>st</sup> of March 2022) at the Technical University of Denmark (DTU) and the engineering consultancy Ramboll Denmark A/S, Structures & Facade Engineering, Buildings, Specialised Engineering (place of employment), between January 2019 and March 2022. The COVID-19 pandemic and the resulting lockdown of the society, including the Danish universities, caused a project extension of three months. The project was supervised at DTU by Associate Professor Jens Henrik Nielsen. Chief Specialist Søren Peter Kristensen and Senior Chief Consultant Hans Exner were the supervisors from Ramboll Denmark A/S, together with Rasmus N. W. Eriksen from the engineering consultancy IDTCE ApS. Part of the work was carried out during an external research stay, from February to April 2021, at the Technical University of Darmstadt in Germany, Institute of Structural Mechanics and Design (ISM+D), under the supervision of Professor Dr.-Ing. Jens Schneider.

The industrial Ph.D. project was jointly funded by the Innovation Fund Denmark (IFD) [grant No. 8053-00088B], Rambøll Fonden [grant No. 2018-51], and Ramboll Denmark A/S. For the construction of the experimental setup employed in the project, additional funding was given by Rambøll Fonden [grant No. 2019-090], the laboratories at DTU Civil Engineering, and the manufacturer of the setup AVOS A/S by Anders Vølund.

The thesis by publication at hand is divided into two parts. The first part introduces the research field, highlights the significant findings, and provides an overview of the work along with a discussion. The second part is a collection of three scientific papers, which constitute the basis of this work and present the research in greater detail.

Kgs. Lyngby, 31 March 2022

*Martin Jensen Meyland*



# Acknowledgements

I gratefully acknowledge Innovation Fund Denmark (IFD), Rambøll Fonden and the Structures & Facade Engineering department at Ramboll Denmark A/S for jointly funding this Ph.D. project, and the former Department of Civil Engineering at the Technical University of Denmark (DTU) for offering the facilities needed for this research. Acknowledgement is also given to the additional funding for the realisation of a new experimental setup by Rambøll Fonden, the laboratories at DTU Civil Engineering, and the manufacturer of the setup AVOS A/S by Anders Vølund, who furthermore provided great help with the design.

I want to express my sincere gratitude to my principal supervisor, Associate Professor Jens Henrik Nielsen, who introduced me to the fascinating world of glass as a structural material and the challenges that come with it. His dedication to the realisation and execution of this project was outstanding. Thanks for your support and guidance and for always having time for discussions. Furthermore, I would like to thank my co-supervisors, Søren Peter Kristensen and Hans Exner from Ramboll Denmark A/S and Rasmus N. W. Eriksen from IDTCE ApS, for their support, interest and assistance throughout the project. I would also like to thank my colleagues at Ramboll Denmark A/S for their support and interest in the Ph.D. project. Additional acknowledgements go to the technical personnel at DTU for their assistance in several technical tasks to be solved regarding the project's experimental work.

A big thank you to Professor Dr.-Ing. Jens Schneider and the Institute of Structural Mechanics and Design (ISM+D) at the Technical University of Darmstadt in Germany for hosting my three-month external research stay. I felt very welcomed and enjoyed experiencing your academic and social environment despite the challenges due to the COVID-19 pandemic. Also, I want to thank Dr.-Ing. Philipp Rosendahl for his guidance during my stay and for taking me out on mountain bike trips, showing me around in the gorgeous surroundings of Darmstadt.

Sincere thanks to my academic colleagues and my Ph.D. fellows at the Section for Structures and Safety for a great working environment at DTU. Especially, I want to thank Pablo Alberdi-Pagola, with whom I could share the daily struggles and successes in conducting experiments. Furthermore, Jesper H. Sørensen, Sebastian Andersen and Sajeel Hussain are acknowledged for their assistance in proofreading the thesis.

Last but not least, I want to thank my family and friends for always supporting and motivating me throughout this time and reminding me that there also exist other than conducting experiments and writing papers. A special thanks go to my parents Bente & Jens, my sister Janne, and my partner Stavroula for outstanding care and support — Thank you!

## Acknowledgements

# Abstract

Glass has been known to humanity for thousands of years and is considered one of the most important materials that have enabled the development of modern society. Widely used in construction, it often constitutes a significant part of buildings' facade, where it allows for daylight and views while protecting the occupants against the weather. In extreme events, such as blast loading, the exterior glazing can also offer the first line of defence if the design is accordingly, e.g. using a laminated glass design. Although bombings in urban areas are rare, it has been shown that the consequences can be disastrous if the glazing design is not resistant to blast loading. However, it is challenging for engineers to quantify this resistance at such high loading rates. An essential parameter to assess in this regard is glass strength.

Glass is a linear elastic, brittle material that fails suddenly and rapidly once its resistance is exceeded. The glass strength depends on the load duration and rate of loading due to sub-critical crack growth. The present thesis investigates the tensile strength and stiffness (Young's modulus) of glass at loading rates relevant to blast loading. Furthermore, and application of these mechanical material properties in the simulation of glass fracture under blast loading using the explicit Finite Element Method (FEM) is presented.

State-of-the-art knowledge about the dynamic fatigue behaviour of soda-lime-silica glass has been obtained through a comprehensive literature review. The review revealed that the tensile strength significantly increases with increasing strain rate, while a very limited amount of data characterise the glass at the extremes of strain rates. Furthermore, a good agreement between the experimental data and most load duration factors defined by various national and international Standards for glass was observed.

To investigate glass at high strain rates, a novel experimental setup was designed and built, which is a modification of the well-known Split-Hopkinson Pressure Bar (SHPB). The modifications enabled high-speed cameras for fracture assessment and non-contact optical full-field deflection measurements using the Stereo Digital Image Correlation (Stereo-DIC) technique in a ring-on-ring bend test configuration. The high strain rate material characterisation at  $48 \text{ s}^{-1}$  ( $\approx 4.3 \cdot 10^6 \text{ MPa s}^{-1}$ ) included annealed float glass and also thermally tempered glass to study the effect of residual stresses. A significant strength enhancement was ascertained compared to a quasi-static strain rate, while the residual stresses did not affect the glass' strain rate sensitivity. Also, the glass strength showed an expected increase with increasing residual compressive surface stress. The performed Stereo-DIC deflection measurements did not find a strain rate sensitivity in the glass' Young's modulus.

The gained mechanical properties of the glass at high strain rates formed the basis to de-

## Abstract

velop a rate-dependent progressive material damage model for explicit FEM. The focus was on a simple implementation, practicable for general engineering practice, using the element deletion technique to simulate the dynamic fracture of large-sized, thin-walled monolithic glass panes under blast loading. Global quantities such as a glass pane's load-bearing capacity and post-fracture response were predicted and compared to results from blast tests found in the literature.

**Keywords** Structural glass, Material characterisation, Dynamic fatigue, High strain rates, Split-Hopkinson Pressure Bar, Blast loading, Numerical modelling

# Resumé

Glas har været kendt af menneskeheden i tusindvis af år og anses for at være et af de vigtigste materialer, der har muliggjort udviklingen af det moderne samfund. Det bruges i vid udstrækning i byggeriet og udgør oftest en væsentlig del af bygningers facader, hvor det muliggør indtrængen af dagslys og udsigt til omgivelserne, samtidig med at det beskytter brugerne mod vejret. Ved ekstreme hændelser, såsom eksplosionsbelastninger, kan udvendige ruder også udgøre den første forsvarslinje, hvis designet er tilsvarende, f.eks. ved brug af en lamineret glasopbygning. Selvom bombeangreb i byområder er sjældne, har det vist sig, at konsekvenserne kan være katastrofale, hvis glasdesignet ikke er modstandsdygtigt over for eksplosionsbelastningen. Det er dog en udfordring for ingeniører at kvantificere denne modstandsdygtighed ved så høj en belastningshastighed. En vigtig parameter at vurdere i denne sammenhæng er glassets styrke.

Glas er et lineært elastisk og sprødt materiale, der svigter pludseligt og hurtigt, når dets styrke er overskredet. Glassets styrke afhænger af belastningens varighed og belastningshastigheden på grund af subkritisk revnevækst. I denne afhandling undersøges glassets trækstyrke og stivhed (elasticitetsmodul) ved belastningshastigheder, der er relevante for eksplosionsbelastninger. Ydermere præsenteres anvendelsen af disse mekaniske materialeegenskaber til simulering af glasbrud ved eksplosionsbelastning under anvendelse af den eksplicite elementmetode (FEM).

State-of-the-art viden om glassets dynamiske udmattelsesadfærd er blevet opnået ved hjælp af en omfattende litteraturgennemgang. Gennemgangen viste, at trækstyrken stiger betydeligt med stigende tøjningshastighed, mens meget begrænsede mængder data er tilgængelige ved de ekstreme tøjningshastigheder. Desuden er der vist en god overensstemmelse mellem de eksperimentelle data og de fleste koefficienter for belastningsvarigheden, der er defineret i forskellige nationale og internationale glasnormer.

Til undersøgelse af glas ved høje tøjningshastigheder blev der designet og bygget en ny eksperimentel opstilling, der er en modificering af den velkendte Split-Hopkinson-Pressure-Bar (SHPB). Modifikationerne muliggjorde anvendelsen af højhastighedskameraer til vurdering af brud og kontaktfri optiske deformationsmålinger ved hjælp af Stereo-Digital-Image-Correlation (Stereo-DIC) teknikken i en dobbeltring-testkonfiguration. Materialekarakteriseringen med høj tøjningshastighed ved  $48 \text{ s}^{-1}$  ( $\approx 4.3 \cdot 10^6 \text{ MPa s}^{-1}$ ) omfattede både udglødet floatglas og termisk hærdet glas for også at undersøge virkningen af egenspændinger. Der blev konstateret en betydelig styrkeforøgelse sammenlignet med en kvasi-statisk tøjningshastighed, mens egenspændingerne ikke påvirkede glassets følsomhed overfor tøjningshastigheden. Glasstyrken viste også en forventet stigning som følge af

## Resumé

stigende trykegenspændinger i overfladen. De gennemførte Stereo-DIC-deformationsmålinger fandt ikke en sensitivitet over for tøjningshastighed i glassets elasticitetsmodul.

De opnåede mekaniske egenskaber af glasset ved høje tøjningshastigheder dannede grundlag for udviklingen af en hastighedsafhængig progressiv materialeskademodel til eksplicit FEM. Fokuset var på en simpel, i almindelig ingeniørpraksis gennemførlig implementering ved hjælp af “element deletion” teknikken til simulering af dynamisk brud af store, tyndvæggede monolitiske glasruder udsat for eksplosionsbelastning. Globale størrelser såsom glasrudens bæreevne og respons efter brud blev forudsagt og sammenlignet med resultater fra eksplosionsforsøg fundet i litteraturen.

**Nøgleord** Strukturel glas, Materialekarakterisering, Dynamisk udmattelse, Høje tøjningshastigheder, Split-Hopkinson Pressure Bar, Eksplosionsbelastning, Numerisk modellering

# Kurzfassung

Glas ist der Menschheit seit Tausenden von Jahren bekannt und gilt als eines der wichtigsten Materialien, die die Entwicklung der modernen Gesellschaft ermöglicht haben. Im Bauwesen weit verbreitet, stellt es oft einen wesentlichen Teil der Gebäudefassade dar, wo es Tageslicht und Ausblicke ermöglicht und gleichzeitig die Nutzer vor Witterungseinflüssen schützt. Bei extremen Ereignissen, wie einer Explosionsbelastung, kann die Außenverglasung auch die erste Verteidigungslinie bilden, sofern die Konstruktion entsprechend ausgelegt ist, z. B. durch Verwendung eines Verbundglasaufbaus. Obwohl Bombenanschläge in städtischen Gebieten selten sind, hat sich gezeigt, dass die Folgen verheerend sein können, wenn die Verglasung nicht beständig gegen Explosionsbelastungen ist. Für Ingenieure ist es jedoch eine Herausforderung, diese Widerstandsfähigkeit bei derart hohen Belastungsraten zu quantifizieren. Ein wesentlicher Parameter, der in dieser Hinsicht zu bewerten ist, ist die Glasfestigkeit.

Glas ist ein linear elastisches, sprödes Material, das plötzlich und schnell versagt, sobald seine Festigkeit überschritten wird. Die Glasfestigkeit ist aufgrund des unterkritischen Risswachstums von der Belastungsdauer und der Belastungsgeschwindigkeit abhängig. In der vorliegenden Arbeit werden die Zugfestigkeit und die Steifigkeit (Elastizitätsmodul) von Glas bei den für die Explosionsbeanspruchung relevanten Belastungsraten untersucht. Darüber hinaus wird die Anwendung dieser mechanischen Materialeigenschaften bei der Simulation von Glasbruch unter Explosionsbeanspruchung mit der expliziten Finite-Elemente-Methode (FEM) vorgestellt.

Der aktuelle Stand des Wissens über das dynamische Ermüdungsverhalten von Kalk-Natron-Silikatglas (KNS) wurde durch eine umfassende Literaturrecherche zusammengetragen. Die Recherche ergab, dass die Zugfestigkeit mit zunehmender Dehnungsrate deutlich ansteigt, während nur sehr wenige Daten das Glas bei den extremen Dehnungsraten charakterisieren. Darüber hinaus wurde eine gute Übereinstimmung zwischen den experimentellen Daten und den meisten in verschiedenen nationalen und internationalen Bemessungsnormen für Glas festgelegten Belastungsdauerfaktoren festgestellt.

Um Glas bei hohen Dehnungsraten zu untersuchen, wurde ein neuartiger Versuchsaufbau entworfen und gebaut, der eine Abwandlung des bekannten Split-Hopkinson-Pressure-Bar (SHPB) ist. Die Modifikationen ermöglichten Hochgeschwindigkeitskameras für die Bruchbeurteilung und berührungslose optische Vollfeld-Durchbiegungsmessungen mit der Stereo-Digital-Image-Correlation (Stereo-DIC) Technik in einer Ring-auf-Ring-Biegeversuchsanordnung. Die Materialcharakterisierung mit hoher Dehnungsrate bei  $48 \text{ s}^{-1}$  ( $\approx 4.3 \cdot 10^6 \text{ MPa s}^{-1}$ ) umfasste sowohl entspanntes Floatglas als auch thermisch vorgespanntes Glas, um die Auswirkungen von Eigenspannungen zu untersuchen. Im Vergleich zu ei-

ner quasistatischen Dehnrate wurde eine wesentliche Erhöhung der Festigkeit festgestellt, während die Eigenspannungen die Dehnratenempfindlichkeit des Glases nicht beeinflussten. Außerdem zeigte die Festigkeit des Glases einen erwarteten Anstieg mit zunehmender Druckeigenspannung an der Oberfläche. Die durchgeführten Stereo-DIC-Durchbiegungsmessungen ergaben keine Dehnratenempfindlichkeit des Elastizitätsmoduls des Glases.

Die gewonnenen mechanischen Eigenschaften des Glases bei hohen Dehnungsraten bildeten die Grundlage für die Entwicklung eines ratenabhängigen progressiven Materialschädigungsmodells für die explizite FEM. Der Schwerpunkt lag auf einer möglichst simplen, für die allgemeine Ingenieurpraxis praktikablen Implementierung unter der Verwendung der Elementlöschtechnik zur Simulation des dynamischen Bruchs von großformatigen, dünnwandigen monolithischen Glasscheiben unter Explosionsbeanspruchung. Globale Größen wie die Tragfähigkeit einer Glasscheibe und das Verhalten nach dem Bruch wurden vorhergesagt und mit Ergebnissen aus Explosionsversuchen aus der Literatur verglichen.

**Schlagwörter** Konstruktiver Glasbau, Materialcharakterisierung, Dynamische Ermüdung, Hohe Dehnungsraten, Split-Hopkinson Pressure Bar, Explosionsbeanspruchung, Numerische Modellierung

# Table of Contents

<b>Preface</b>	<b>i</b>
<b>Acknowledgements</b>	<b>iii</b>
<b>Abstract</b>	<b>v</b>
<b>Resumé</b>	<b>vii</b>
<b>Kurzfassung</b>	<b>ix</b>
<b>Additional Work</b>	<b>xv</b>
<b>Nomenclature</b>	<b>xvii</b>
<b>Part I Introduction and Summary</b>	<b>1</b>
<b>1 Introduction</b>	<b>3</b>
1.1 Glass and its Application in Buildings . . . . .	4
1.1.1 Glass Products . . . . .	8
1.2 Extreme Loading . . . . .	10
1.2.1 Blast Effects on Buildings . . . . .	11
1.3 Current Research on Blast Resilient Glazing . . . . .	16
1.4 Research Objectives of the Thesis . . . . .	17
1.5 Thesis Structure . . . . .	18
<b>2 Fracture Strength of Glass and the Significance of Load Duration</b>	<b>21</b>
2.1 Fundamental Theory of Glass Fracture . . . . .	21
2.1.1 Sub-critical Crack Growth . . . . .	22
2.1.2 Stress Intensity Factor . . . . .	24
2.1.3 Energy Release Rate . . . . .	25
2.1.4 Resistance of a Single Crack (or Flaw) . . . . .	26
2.2 Literature Review on Experimental Strength Data . . . . .	30
2.3 Normative Glass Strength Design . . . . .	37
<b>3 Experimental Methodology for High Strain Rate Testing</b>	<b>41</b>
3.1 Background . . . . .	41
3.2 A Modified Split-Hopkinson Pressure Bar . . . . .	44

Table of Contents

3.2.1	Testing Conditions . . . . .	45
3.2.2	Alignment of the Bar/Tube System . . . . .	48
3.3	Experimental Procedures and Techniques . . . . .	49
3.3.1	Data Acquisition System . . . . .	49
3.3.2	Setup Calibration . . . . .	50
3.3.3	Pulse Shaping . . . . .	51
3.3.4	Wave Dispersion Analysis . . . . .	56
3.4	High-speed Cameras and Stereo Digital Image Correlation . . . . .	58
<b>4</b>	<b>High Strain Rate Characterisation of Glass Mechanical Properties</b>	<b>63</b>
4.1	Introduction to the Material Testing . . . . .	63
4.2	Glass Samples . . . . .	64
4.2.1	Measurement of the Compressive Surface Stress . . . . .	65
4.2.2	Edge Quality Enhancement by Etching . . . . .	66
4.3	Equibiaxial Flexural Strength . . . . .	66
4.3.1	Fracture Assessment . . . . .	68
4.3.2	Strength Evaluation . . . . .	69
4.4	Deflection Measurements with Stereo-DIC . . . . .	74
4.5	Material Stiffness (Young's Modulus) . . . . .	77
<b>5</b>	<b>Simulation of Monolithic Glass Fracture Under Blast Loading</b>	<b>81</b>
5.1	Numerical Modelling . . . . .	81
5.1.1	Explicit Finite Element Method . . . . .	81
5.1.2	Modelling Techniques for Brittle Failure . . . . .	82
5.2	Rate-dependent Progressive Damage Model for Dynamic Glass Fracture . . . . .	84
5.2.1	User Subroutine Implementation . . . . .	86
5.2.2	Unit Element Test . . . . .	91
5.3	Damage Model Validation on Full-scale Blast Test Data . . . . .	95
5.3.1	Pre-fracture Response (Test A) . . . . .	97
5.3.2	Post-fracture Response (Test B) . . . . .	100
5.3.3	Concluding Remarks . . . . .	105
<b>6</b>	<b>Conclusions and Future Work</b>	<b>107</b>
6.1	Conclusions . . . . .	107
6.2	Future Work . . . . .	109
	<b>Bibliography</b>	<b>111</b>
<b>A</b>	<b>Additional Experimental Details</b>	<b>127</b>
<b>B</b>	<b>Stereo-DIC Results</b>	<b>143</b>
<b>C</b>	<b>User Subroutine for ABAQUS/Explicit</b>	<b>153</b>
<b>D</b>	<b>Mesh Convergence Analysis</b>	<b>165</b>

## Part II Scientific Papers 169

### Paper I

Tensile behaviour of soda-lime-silica glass and the significance of load duration –  
A literature review

MEYLAND, M. J., NIELSEN, J. H., and KOCER, C.

Published in: *Journal of Building Engineering* (2021) . . . . . 171

### Paper II

A modified split-Hopkinson pressure bar setup enabling stereo digital image correlation measurements for flexural testing

MEYLAND, M. J., ERIKSEN, R. N. W., and NIELSEN, J. H.

Submitted to: *International Journal of Impact Engineering* (2021) . . . . . 201

### Paper III

High strain rate characterisation of soda-lime-silica glass and the effect of residual stresses

MEYLAND, M. J., and NIELSEN, J. H.

Accepted for publication in: *Glass Structures & Engineering* (2022) . . . . . 217

## Table of Contents

## Additional Work

The following is a list of other work that was prepared during the course of the Ph.D. project and is related to it but not included in the present thesis:

- [1] MEYLAND, M. J. (2019). Failure characterisation of glass at high strain-rates. Extended abstract presented at: *Glass Fracture Symposium, Technical University of Darmstadt, Germany*.
- [2] MEYLAND, M. J., ERIKSEN, R. N. W., and NIELSEN, J. H. (2019). A novel full-view split Hopkinson pressure bar technique for flexural testing. In proceedings: *13<sup>th</sup> International Conference on Shock & Impact Loads on Structures, Guangzhou, China*.
- [3] MEYLAND, M. J., and NIELSEN, J. H. (2020). Ongoing Research into the Failure of Glass at High Strain-Rates. In proceedings: *Challenging Glass 7 (Webinar), Conference on Architectural and Structural Applications of Glass, Ghent University, Belgium*. DOI: 10.7480/cgc.7.4428.
- [4] NIELSEN, J. H., THIELE, K., SCHNEIDER, J., and MEYLAND, M. J. (2021). Compressive zone depth of thermally tempered glass. Published in: *Construction and Building Materials*. DOI: 10.1016/j.conbuildmat.2021.125238.

## Published Datasets

The following is a list of published datasets that were compiled during the course of the Ph.D. project:

- [A] MEYLAND, M. J., NIELSEN, J. H., and KOCER, C. (2021). Datasets: Tensile behaviour of soda-lime-silica glass and the significance of load duration – A literature review. Published online: *DTU Data, Technical University of Denmark*. DOI: 10.11583/DTU.13655525.
- [B] MEYLAND, M. J., and NIELSEN, J. H. (2022). Datasets: High strain rate characterisation of soda-lime-silica glass and the effect of residual stresses. Published online: *DTU Data, Technical University of Denmark*. DOI: 10.11583/DTU.17694692.

Additional Work

# Nomenclature

## Abbreviations

CFD	Computational Fluid Dynamics
CMOD	Crack Mouth Opening Displacement
Cu-DHP	Deoxidized High Phosphorus Copper
DEM	Discrete Element Method
DIC	Digital Image Correlation
EDS	Energy-dispersive X-ray Spectroscopy
FEM	Finite Element Method
FEM/DEM	Combined Finite-Discrete Element Method
LEFM	Linear Elastic Fracture Mechanics
SDG	Sustainable Development Goal
SDOF	Single Degree Of Freedom
SEM	Scanning Electron Microscope
SHPB	Split-Hopkinson Pressure Bar
Stereo-DIC	Stereo Digital Image Correlation
TSL	Traction-Separation Law
WLS	Weighted Least Squares
XFEM	Extended Finite Element Method

## Latin Symbols

$A$	Cross-sectional area
$a$	Crack depth <i>or</i> half the crack length
$a_0$	Initial cross-sectional area of pulse shaper
$a_f$	Critical crack (or flaw) depth causing failure
$t_f$	Time to failure <i>or</i> lifetime of a crack (or flaw)
$a_i$	Initial crack (or flaw) depth
$A_{IB}$	Cross-sectional area of the incident bar
$a(t)$	Current cross-sectional area of pulse shaper
$a_{th}$	Threshold crack (or flaw) depth
$A_{TT}$	Cross-sectional area of the transmission tube
$C$	Photoelastic constant

## Nomenclature

$C_0$	Elastic wave speed
$C_{0,st}$	Elastic wave speed of striker bar material
$C_\ell$	Longitudinal wave speed
$C_p$	Phase velocity
$D$	Sample diameter
$D$	Damage scalar
$d_0$	Initial diameter of pulse shaper
$D_L$	Load ring diameter
$D_S$	Support ring diameter
$E$	Young's modulus
$E'$	Element stiffness in principal direction (normal to crack)
$E_b$	Young's modulus of the bar material
$\dot{F}$	Loading rate
$F$	Force
$\Delta F$	Force difference
$f$	Frequency
$f_{b,k}$	Normative characteristic bending strength of glass after a strengthening treatment
$f_{g,k}$	Normative characteristic bending strength of annealed glass
$F_{LR}$	Force on the load ring side
$F_m$	Force mean
$F_{max}$	Peak force <i>or</i> failure load
$F_{SR}$	Force on the support ring side
$G$	Energy release rate
$g(\epsilon_p)$	A function of the pulse shaper axial engineering strain
$G_c$	Critical energy release rate <i>or</i> fracture energy
$G_{Ic}$	Critical energy release rate <i>or</i> fracture energy for a Mode I crack
$h$	Glass thickness
$h_0$	Initial thickness of pulse shaper
$h(t)$	Current thickness of pulse shaper
$\mathbf{I}$	Internal element force vector
$\mathbf{I}$	Second-order identity tensor
$K$	Initial stiffness in Traction-Separation Law (TSL)
$K_I$	Stress intensity factor
$K_{Ic}$	Critical stress intensity factor <i>or</i> fracture toughness for a Mode I crack
$k_{mod}$	Load duration factor as defined by Standards
$K_{th}$	Crack growth threshold

$L_{\min}$	Smallest element dimension in a mesh
$L_e$	Characteristic element length
$L_{\text{st}}$	Length of striker bar
$\mathbf{M}$	Mass matrix
$N$	Sample size
$n$	Sub-critical crack growth parameter
$N_{\text{el}}$	Number of elements
$\mathbf{P}$	Externally applied force vector
$p_o$	Atmospheric pressure
$p_r^-$	Peak negative reflected pressure
$p_r$	Peak positive reflected pressure
$p_{\text{so}}^-$	Peak negative incident pressure
$p_{\text{so}}$	Peak positive incident pressure
$R$	Distance to explosive <i>or</i> stand-off distance
$r$	Cylindrical bar radius
$s$	Crack area
$\Delta t$	Time increment
$t_{\text{nom}}$	Nominal glass thickness
$\Delta t_{\text{stable}}$	Stability limit for the explicit time integration in FEM
$t_a$	Arrival time of blast wave front
$t_{f,d}$	Load duration for a constant applied stress rate
$t_{f,s}$	Load duration for a constant applied stress
$\Delta u$	Relative nodal displacement
$\ddot{\mathbf{u}}$	Nodal acceleration vector
$\Delta u_0$	Relative nodal displacement at crack growth initiation
$\Delta u_f$	Relative nodal displacement at which a crack is considered fully developed
$v$	Crack velocity
$v_0$	Linear crack velocity parameter defining the sub-critical crack growth
$v_{\text{ps},1}$	Particle velocity at the striker bar/pulse shaper interface
$v_{\text{ps},2}$	Particle velocity at the pulse shaper/incident bar interface
$v_{\text{st}}$	Striker bar velocity
$W$	Mass of spherical or hemispherical TNT explosive
$\Delta w_{\text{cf}}$	Relative crack opening displacement for fully developed crack
$\Delta w_c$	Relative crack opening displacement
$x_{\text{sg,IB}}$	Position of strain gauges on the incident bar
$x_{\text{sg,TT}}$	Position of strain gauges on the transmission tube
$Y$	Dimensionless geometry (correction) factor governing $K_{\text{I}}$ (cf. Eq. (2.4))

## Nomenclature

Z Scaled distance

## Greek Symbols

$\gamma$	Specific surface energy
$\delta$	Plate bending deflection
$\delta_{ij}$	Kronecker delta
$\dot{\epsilon}$	Strain rate
$\boldsymbol{\epsilon}$	Symmetric strain tensor (tensor notation)
$\epsilon_0$	Strain at crack growth initiation
$\dot{\epsilon}_0$	Quasi-static strain rate
$\epsilon_1$	Maximum principal strain (principal tensile strain)
$\epsilon_{ij}$	Symmetric strain tensor (index notation)
$\epsilon_f$	Strain at which a crack is considered fully developed
$\epsilon_i$	Incident pulse strain
$\dot{\epsilon}_{in}$	Limiting strain rate for the inert strength limit
$\epsilon_p$	Axial engineering strain in pulse shaper
$\epsilon_r$	Reflected pulse strain
$\epsilon_t$	Transmitted pulse strain
$\dot{\epsilon}_{th}$	Limiting strain rate for the sub-critical crack growth threshold
$\Lambda$	Wavelength
$\lambda$	Lamé's first parameter
$\mu$	Lamé's second parameter
$\nu$	Poisson's ratio
$\Pi$	Potential energy
$\rho$	Density
$\rho_b$	Density of the bar material
$\rho_{st}$	Density of striker bar material
$\dot{\sigma}$	Stress rate
$\boldsymbol{\sigma}$	Symmetric stress tensor (tensor notation)
$\sigma_{\perp}$	Crack opening stress (perpendicular to crack surface)
$\sigma$	Crack opening stress
$\sigma^*$	Stress constant defined in Eq. (3.8)
$\sigma_0$	Apparent tensile strength at quasi-static loading rate
$\sigma_1$	Maximum principal stress (principal tensile stress)
$\tilde{\sigma}_{ij}$	Symmetric stress tensor in the undamaged state (index notation)
$\sigma_c$	Residual compressive surface stress
$\sigma_f$	Apparent tensile strength
$\sigma_{f,d}$	A crack's resistance to constant stress rate loading

$\sigma_{f,s}$	A crack's resistance to constant stress loading
$\sigma_i$	Intrinsic glass strength
$\sigma_i$	Incident pulse stress
$\sigma_m$	Residual tensile mid-plane stress
$\sigma_p$	True axial stress in pulse shaper
$\sigma_r$	Reflected pulse stress
$\sigma_t$	Transmitted pulse stress
$\sigma_x$	Residual compressive surface stress in the $x$ -direction
$\sigma_y$	Residual compressive surface stress in the $y$ -direction
$\tau$	Time for two wave transits in the striker bar

## Nomenclature

# Part I

## Introduction and Summary



## Introduction

Glass as an independent material has been known to humanity for thousands of years. The earliest developments in glass production can be dated back to ~2500 BCE, having originated in Mesopotamia and Syria (RASMUSSEN 2012). The discovery of the glassblowing pipe around 200 BCE in Syria revolutionised glass production and was the first step to making flat glass out of blown cylindrical glass bodies that were cut up and 'ironed' flat (PFAENDER 1996). Further significant developments in the flat glass production were made by the Roman glass-makers in the first half of the 1<sup>st</sup> century CE, who cast molten glass on a flat slab of stone and spread it as much as possible (CHOPINET 2019). Flat glass production has undergone a long process of development ever since, leading to the float process, which was commercially introduced by the Pilkington Brothers in 1959 and is the most popular primary manufacturing process today (HALDIMANN et al. 2008). Every year in Europe, 10 million tonnes of flat glass are produced, of which 80 % are used in the building industry (GLASS FOR EUROPE 2022).

Glass has proven to be one of the most important materials that enabled the development of modern society. Therefore, in 2022, the material is internationally celebrated through the United Nations Year of Glass to face the challenges of building a sustainable society (IYoG 2022). Due to glass' manifold applications, it is a significant contributor, and within the building industry, three of the seventeen Sustainable Development Goals (SDG) of the United Nations can be addressed substantially (see Fig. 1.1).



**Fig. 1.1** The three UN Sustainable Development Goals that are addressed substantially by glass applications in the building industry.

Towards sustainable cities and communities (SDG 11), the flat glass industry is actively developing new energy efficiency technologies for buildings, such as glass and glazing units that can significantly reduce the need for heating and cooling, thereby reducing energy consumption and emission of carbon dioxide (IYoG 2022). Also, glass is one of the few materials that can be recycled infinitely, thus contributing to responsible consumption and production (SDG 12). Throughout its life-cycle, it carries a minimal impact on the environment because the manufacturing process uses a low quantity of water and produces little waste or other pollutants (GLASS FOR EUROPE 2022). However, glass requires

## 1. Introduction

energy to be produced but helps save a vast amount of energy in its main application, i.e. in windows and buildings, again addressing the SDG 11. Lastly, glass plays a major role in combating climate change due to its energy saving functions in buildings, therefore further contributing to climate action (SDG 13).

Widely used in architecture for its practical application and appealing aesthetics, glass is often included in the outer building envelope (the facade), bringing daylight into homes and offices while at the same time protecting the occupants from weather, such as heat, cold, snow, ice, wind and rain. In the future, climate change can cause weather events to become more extreme (IPCC 2022). Apart from extreme weather events such as tornados and hurricanes, other loads of an even more extreme character, such as blast loading, accidental or man-made, can also be a hazard to buildings. In either case, the glass is subjected to loads beyond the usual static load assumptions.

Unfortunately, during the last two decades, society worldwide has been faced increasingly with terror-related bombings (START 2019). In Europe and nationally in Denmark, the terrorist threat has recently been classified as significant (EUROPOL 2021; CTA 2021). Although explosion events in urban areas are rare, they can have disastrous consequences when the load scenario is not accounted for in the glass design, e.g. typical for urban houses where monolithic annealed glass constitutes a significant part of the installed windows. Usually, the blast loading shatters the annealed glass into angular, jagged, irregular fragments, resulting in a sudden and immediately high hazard to building occupants (see Fig. 1.2). Historically, it has been shown that up to 80 % of injuries from bomb explosions were caused by flying glass shards (SMITH 2001). Therefore, mitigating an explosion's effect is crucial, which demands detailed knowledge about the material response at the rapid loading. Every window comes with some degree of resistance to blast loading, even though it may be relatively small. The challenge for engineers lies in quantifying that resistance and the loading that might be applied.

A fundamental parameter to assess in the prediction of glass failure is strength. The thesis aims to provide an understanding of the mechanical properties of glass at loading rates relevant to blast loading and give insights into the experimental high strain rate material characterisation that has been developed and carried out to expand on the current level of knowledge. In extension, to support computer-aided engineering, the further application of the material characteristics to simulate glass fracture under blast loading is addressed. The following three sections introduce the material glass and its application in buildings (Sec. 1.1), deliver an understanding of extreme loading and blast effects on buildings (Sec. 1.2), and summarise current research on blast resilient glazing and its importance (Sec. 1.3). With a state-of-the-art understanding of the research challenges addressed, the main research objectives of the thesis are defined (Sec. 1.4), and finally, the structure of the thesis is outlined to provide a guide for the reader (Sec. 1.5).

### 1.1 Glass and its Application in Buildings

Glass has a widespread application in buildings. Usually considered an architectural feature included in building facades, it now also attracts increased attention from structural



(a) Brussels Airport, 22 March 2016.



(b) Danish Tax Agency in Copenhagen, 6 August 2019.

**Fig. 1.2** Examples of recent bombings in Europe where fractured annealed float glass in the facades constituted a significant part of the damage seen to the attacked buildings.

## 1. Introduction

engineers to use it for the load-bearing elements, such as beams and columns (see e.g. SNIJDER 2004; SCHITTICH et al. 2007; STEIN et al. 2019).

In everyday language, the word ‘glass’ has various meanings depending on its use: thus, the term can refer to beverage containers or characterise the component of a window. However, considering the glass as a material, it may be characterised as an inorganic product of fusion that has solidified without crystallisation. Most of the glass used for buildings is soda-lime-silica glass (SLSG)<sup>1</sup>, whose main components are quartz sand, lime and soda (see Table 1.1). In production, the raw materials are melted in a furnace, poured on to a shallow pool of molten tin (the float process), and further on to rollers into an annealing lehr, securing slow cooling of the glass to prevent the formation of residual stresses. The thickness of the glass is controlled by the speed of the rollers. The end product is termed *annealed float glass*.

**Table 1.1** The chemical elemental composition (in oxide wt%) of soda-lime-silica glass according to the European Standard EN 572-1:2012.

Silicon dioxide (quartz)	SiO <sub>2</sub>	69-74 %
Calcium oxide (lime)	CaO	5-14 %
Sodium oxide (soda)	Na <sub>2</sub> O	10-16 %
Magnesium oxide	MgO	0-6 %
Aluminium oxide	Al <sub>2</sub> O <sub>3</sub>	0-3 %
Others		0-5 %

During the transition from the melt to the solid, there is no specific solidification point but a glass transition region, which for SLSG is about 530 °C (HALDIMANN et al. 2008). As a solid, glass is characterised as a perfectly isotropic linear elastic material, where the relationship between stresses ( $\sigma$ ) and deformations ( $\epsilon$ ), i.e. the stiffness ( $E$ ), up to failure, may entirely be described by Hooke’s law ( $\sigma = \epsilon \cdot E$ ). In structural applications, the stiffness is usually not associated with a time and temperature dependency (SCHNEIDER et al. 2016), and also, at increased loading rates, Young’s modulus seems not to be significantly affected, as evident from the few studies reviewed in MEYLAND et al. (2021a). A summary of the physical properties of soda-lime-silica glass, as defined by the European Standard EN 572-1:2012, is provided in Table 1.2. Compared to other materials used in construction, glass has a stiffness and density similar to aluminium and is around three times less stiff than steel.

Glass cannot redistribute stresses (yielding), as is the case for, e.g. steel, causing sensitivity to stress concentrations. Therefore it is characterised as a brittle material that fails suddenly and rapidly once its resistance is exceeded. Theoretically, the tensile strength of glass can reach values as high as 14 GPa based on molecular forces (PAVELCHEK and DOREMUS 1974). However, it is irrelevant for structural applications. Due to its brittleness, the tensile strength is governed by surface flaws (or surface cracks), causing much lower strength. A glass element will fail when the stress intensity at the tip of one surface flaw, due to tensile stresses, reaches its critical value. When the glass is loaded below its momentary strength, it has the unique characteristic where flaws grow with time, causing

<sup>1</sup>Throughout the thesis, the term *glass* is primarily used, thus referring to soda-lime-silica glass.

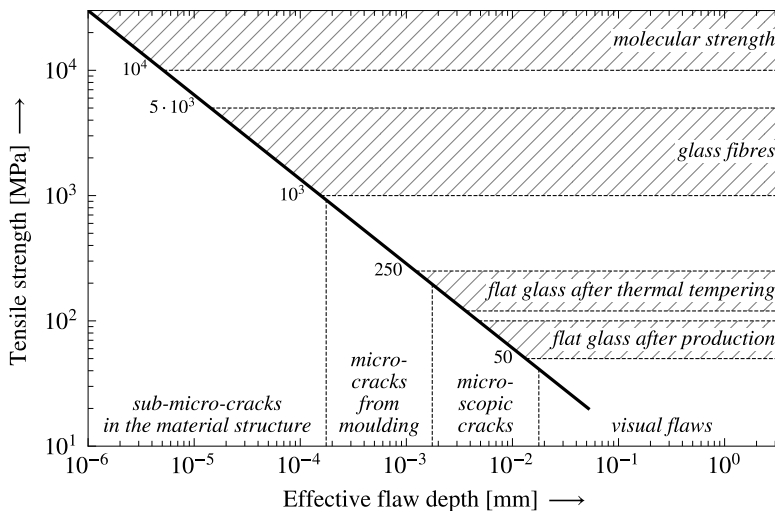
**Table 1.2** Physical properties of soda-lime-silica glass according to the European Standard EN 572-1:2012.

Characteristic	Symbol	Value and unit
Density	$\rho$	2500 kg m <sup>-3</sup>
Knoop hardness	HK <sub>0,1/20</sub>	6 GPa
Young's modulus	$E$	70 GPa
Poisson's ratio	$\nu$	0.23*
Coefficient of thermal expansion <sup>†</sup>	$\alpha_T$	$9 \cdot 10^{-6} \text{ K}^{-1}$
Specific thermal capacity	$c_p$	720 J kg <sup>-1</sup> K <sup>-1</sup>
Thermal conductivity	$\lambda$	1 W m <sup>-1</sup> K <sup>-1</sup>
Mean refractive index to visible radiation (at 589.3 nm)	$n$	1.50
Emissivity (corrected)	$\epsilon$	0.837

\* EN 572-1:2012 gives 0.2. In research and application, values between 0.22 and 0.24 are commonly used (HALDIMANN et al. 2008), and in the European glass code CEN/TS 19100-1:2021 the value 0.23 is given.

<sup>†</sup> Mean between 20 °C and 300 °C.

the strength to degrade. Contrary, higher strengths can be determined for short-duration loads. These phenomena are discussed in detail in Chapter 2. Because of the typical characteristic differences in surface flaws, the tensile strength of glass cannot be considered a material constant, therefore often treated statistically (see e.g. OVEREND et al. 2007a). A rough overview of short-term strengths that can be expected for different flaw depths is given in Fig. 1.3. Additionally, the size of the glass element, the load history (intensity and duration), the residual stress, and the environmental conditions significantly alter the

**Fig. 1.3** Typical short-term tensile strengths as a function of the effective flaw depth. (adapted from PETZOLD et al. 1990)

tensile strength.

For structural applications, short-term tensile strengths between 30 MPa and 80 MPa can be expected for glass (PETZOLD et al. 1990), and in the European glass code CEN/TS 19100-1:2021, a characteristic value of 45 MPa is given. As surface flaws are not affected by compression loading, the compressive strength is much higher, around 400 MPa to 900 MPa (PETZOLD et al. 1990). However, it rarely becomes relevant for structural design because the glass' tensile strength is typically exceeded first due to, e.g. stability problems (buckling) or locally arising tensile stresses. Therefore, the tensile strength is only addressed from now on.

### 1.1.1 Glass Products

The glass industry commands a large portfolio of glass products for buildings. Depending on the particular needs in shape, performance and appearance, the monolithic annealed float glass is often processed further. After cutting, edge working, possible hole drilling and coating applications, the prevailing post-processing procedures include thermal tempering, lamination and the insulating glass unit assembly.

The thermal tempering, which is a process of heating and subsequently quenching, strengthens the annealed float glass by introducing a residual stress field with compressive stresses near the surface, balanced by tensile stresses in the core. Far from the edges, the stress distribution can be approximated by a symmetric parabolic function, as shown in Fig. 1.4. The depth of the compressive zone is both analytically and experimentally found to be reasonably approximated by 21 % of the glass thickness (NIELSEN et al. 2021).

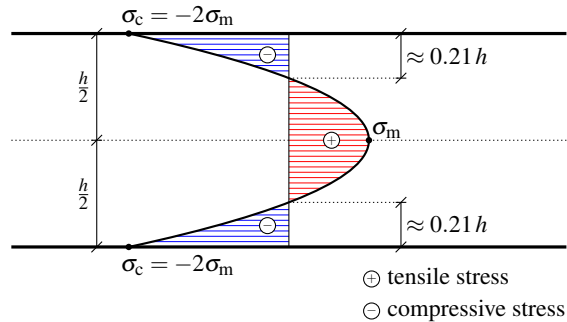


**Fig. 1.4** Symmetric parabolic distribution of residual stresses across the thickness of thermally tempered glass ( $\sigma_c$  is the surface stress;  $\sigma_m$  is the mid-plane stress;  $h$  is the glass thickness). (from Paper III)

The growth of surface flaws is prevented as long as compressive surface stresses are present. However, once these are overcome by tensile stresses, e.g. due to bending loading, flaws will start to grow until the equilibrated residual stress state is disturbed sufficiently, causing catastrophic failure of the glass. By varying the cooling rate in the thermal tempering process, glass with different levels of residual stresses can be achieved (POURMOGHADDAM and SCHNEIDER 2019). In the glass industry, two are common: heat-strengthened glass (HSG) and fully tempered glass (FTG). These can be distinguished

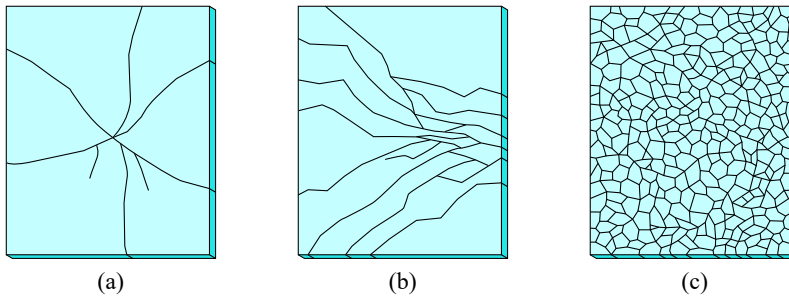


**Fig. 1.5** Fracture pattern (not in scale) of (a) annealed glass, (b) heat-strengthened glass, and (c) fully tempered glass. (after SCHITTICH et al. 2007)

by the way they fracture, as illustrated in Fig. 1.5. The fracture pattern is a function of stored energy in the glass (residual stress and stress from loading). Usually, it is seen that fragments decrease in size with increasing energy levels (see e.g. NIELSEN and BJARRUM 2017; POURMOGHADDAM et al. 2018). Because fully tempered glass has the highest residual stress level, it breaks into small dice, therefore sometimes referred to as 'safety glass'. While having the highest resistance to external loads with a characteristic bending strength of 120 MPa (EN12150-1:2015), its post-failure performance is poor due to the tiny fragments. The heat-strengthened glass with less residual stresses and a characteristic bending strength of 70 MPa (EN 1863-1:2012) shows a larger fragmentation, providing improved post-failure performance. The largest fragments are typically seen when annealed glass breaks. Although thermally tempered glass has an enhanced resistance to external loading, when used as monolithic glazing, it poses a high hazard to building occupants independent of the residual stress level if it breaks under a blast load (CORMIE et al. 2019).

Improved post-failure performance can be achieved by lamination, where two or more monolithic glass panes are bonded together by some transparent plastic interlayer (usually polyvinyl butyral – PVB). The glass panes may be annealed, thermally tempered or a combination of both with equal or unequal thicknesses, depending on the required structural performance. While glass alone is brittle, the plastic film between the panes adds ductility to the sandwich structure. In a blast event, glass fragments will adhere to the film after breakage, reducing glass-related injuries. Also, the plastic interlayer can deform further in the fractured state of the laminated glass, thereby absorbing additional blast energy in membrane action if the framing is sufficiently designed (see Fig. 1.6). This makes the laminated glass the preferred choice in the design of blast resilient glazing.

To comply with the energy performance requirements of buildings, all types of monolithic and laminated glass (or a combination of them) can be assembled to an insulating glass unit (IGU) to reduce thermal losses. The structure consists of two or more panes connected by spacers enclosing a hermetically sealed air space filled with air or a noble gas, such as argon. Also, a vacuum can be introduced into the air space, making it a vacuum insulated glazing (VIG), which, compared to IGUs, can have an improved, reduced heat transfer coefficient (U-value) (see e.g. MCSPORRAN 2014; RIEDEL et al. 2022). When utilising

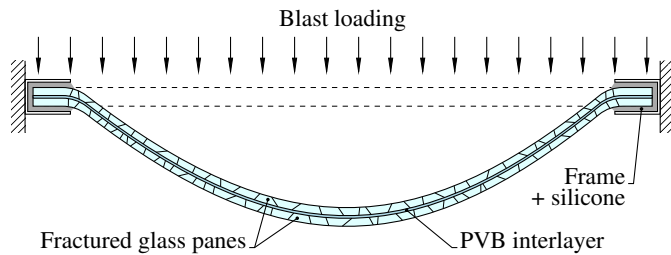


**Fig. 1.6** Example of the post-failure deformation of laminated glass due to blast loading.

IGUs in a blast resilient glazing design, the inner pane, i.e. the pane facing the building's interior, should be laminated and the outer pane heat-strengthened or fully tempered monolithic glass (see e.g. DAS ADHIKARY 2016; CORMIE et al. 2019).

## 1.2 Extreme Loading

Loading conditions may be considered extreme when an event is unforeseen, the loading by far exceeds its original design, or the requirements become very demanding such that standard approaches do not cover them anymore. In general, the more extreme the load, the rarer it is to occur. However, if a risk is known, protective measures are crucial and should be taken to reduce or even prevent the loss of human life and property.

In buildings, glass often constitutes a significant part of the outer envelope, thus being the first part of a structure loaded by externally imposed loads. At extreme loading events, it also can offer the first line of defence, protecting the building's occupants if designed accordingly. Weather-related loads such as moderate wind and snow are reasonably predictable, therefore not considered extreme and thus generally covered by normative design guidelines. The more unforeseen events, and therefore more demanding to design for, may include accidental loads, earthquakes (seismic loads), tornados and hurricanes with resulting debris impacts, ballistic (hail and bullets) impacts and blast loading – all considerably shorter in load duration than the usual static load assumptions. Inherently, the impact and impulse loading events cause the glass material to deform more rapidly, significantly altering its mechanical properties (MEYLAND et al. 2021a). Other materials used in civil engineering structures, like steel, concrete, rock, and wood, also show a sensitivity to the rate-of-loading (see e.g. ARMSTRONG and WALLEY 2008; BISCHOFF and PERRY 1991; ZHANG and ZHAO 2014; POLOÇOŞER et al. 2017).

The scientific understanding of a material's deformation and failure at impact and impulse loading is usually associated with a strain rate ( $\dot{\epsilon}$ ) or stress rate ( $\dot{\sigma}$ ) (see e.g. SHUKLA et al. 2010), which is the change in strain or stress with respect to time, i.e.  $\dot{\epsilon} = d\epsilon/dt$  or  $\dot{\sigma} = d\sigma/dt$ . To accurately design structures against extreme loading events and mitigate their effects, it is essential that detailed knowledge of a material's behaviour has been discovered over a wide range of strain rates. Fig. 1.7 provides an overview of strain rates associated with different laboratory experiments and structural loads. One of the harshest loading events (in terms of strain rate) building components can be exposed to is blast loading, which furthermore shows a broad range of associated strain rates. This is because several factors determine an explosion's effect: the type, the size of the explosive and

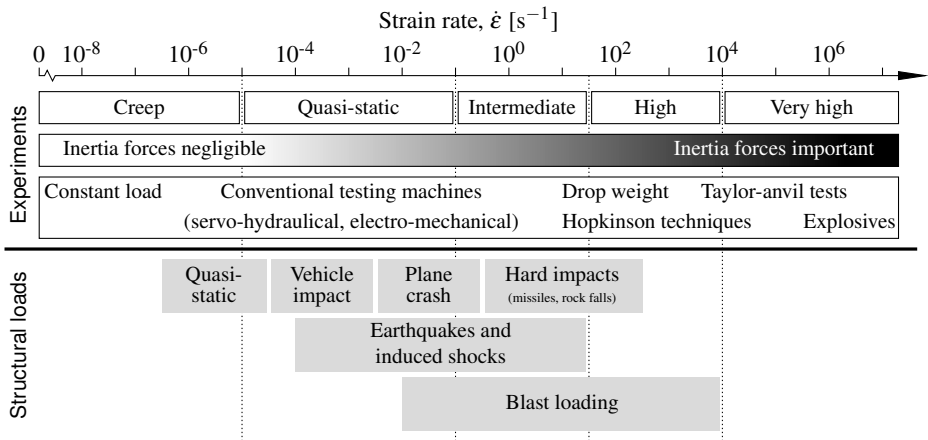


**Fig. 1.7** Ranges of strain rates associated with different laboratory experiments and structural loads (compiled from NEMAT-NASSER (2000) and HENTZ et al. (2004)).

the location of the attack. Undoubtedly, any combination is conceivable, so defining a typical explosion scenario for a design is difficult. In the literature for instance, mean strain rates ranging from  $7.6 \text{ s}^{-1}$  to  $17.5 \text{ s}^{-1}$  were recorded by MORISON (2007), and from  $10 \text{ s}^{-1}$  to  $40 \text{ s}^{-1}$  by HOOPER et al. (2012), both during full-scale high-explosive blast tests on laminated glass panes.

Many reported extreme loading events have a terrorist background. Looking at data registered in the Global Terrorism Database (GTD) for Europe dating back to 1970 (START 2019), half relate to bombings and explosions, as evident from Fig. 1.8, which also shows a distribution of the attacked targets. Fig. 1.9(a) is a map of Europe marking the locations of the bombings and explosions together with a histogram in Fig. 1.9(b) of the annual registered numbers of incidents worldwide and in Europe. Although the numbers of bombings/explosions in Europe are relatively small compared to the ones registered worldwide, a significant terrorist threat remains in Europe (EUROPOL 2021) and historically seen, there is a 50/50 chance that a bomb/explosion will be used again, leaving a possible hazard against buildings. Thus, in Norway, after the Oslo bombing in 2011, and now also in Denmark, there exist guidelines on how to consider counter-terrorism measures for buildings and urban spaces (FORSVARSBYGG 2016; DBI 2021).

### 1.2.1 Blast Effects on Buildings

Blast waves and their effect on buildings are introduced in the following based on CORMIE et al. (2019), to better understand the load case addressed in the thesis. Sources of blast waves are typically explosions that are categorised as physical (e.g. volcanic eruptions or bursts of pressure vessels), nuclear or chemical events. However, most man-made explosions are chemical and therefore the focus of the following.

At the reaction of an explosive compound, such as trinitrotoluene (TNT), heat evolves

1. Introduction

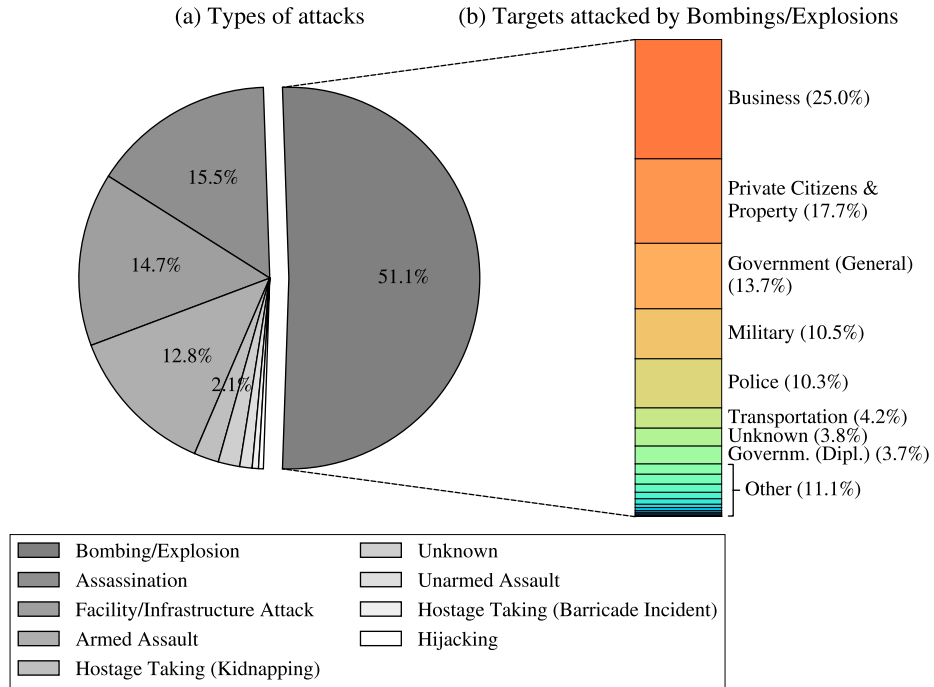


**Fig. 1.8** Types of terror-related attacks in Europe from 1970 to 2019 (a), and the distribution of targets attacked by bombings/explosions (b). The data were retrieved from START (2019) (data for 1993 are missing).

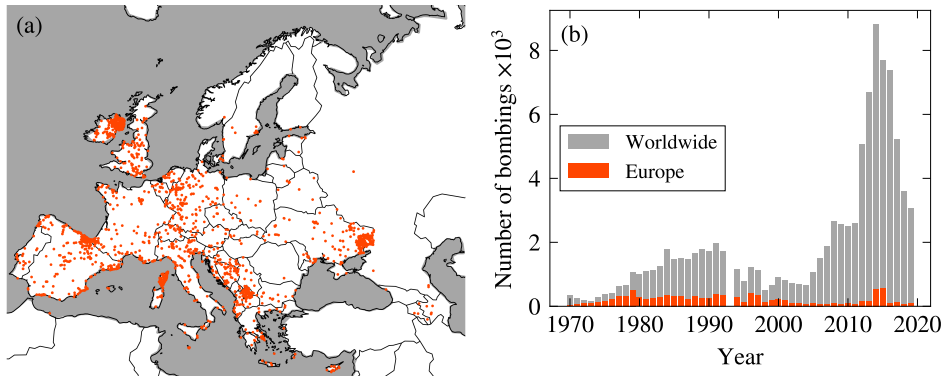


**Fig. 1.9** Registered incidents of terror-related bombings/explosions between 1970 and 2019 (data for 1993 are missing): (a) a map of Europe marking the locations of incidents, and (b) a plot of the annual registered number of bombings worldwide and in Europe. The data were retrieved from START (2019).

(around 3000–4000 °C), and gas expands rapidly at a pressure of 10–30 GPa (CORMIE et al. 2019). The rapid expansion of the gas in the air produces the so-called blast wave, which is a layer of compressed air surrounding the gaseous product. Due to a disequilibrium between the highly compressed air in the blast wave front and the undisturbed air in front of it, the blast wave travels spherically outwards from the centre of the explosion. The gas also over-expands due to its momentum, leading to a negative phase where the pressure at the blast wave’s tail falls below normal atmospheric pressure, resulting in suction. Typically, the peak pressure of the negative phase is smaller than the peak pressure of the positive phase.

The energy in a blast wave is transferred to a structure through pressure energy. If the encountered object is infinitely small, the blast wave will pass it undisturbed with a pressure-time history as shown in Fig. 1.10, referred to as the *incident pressure*, where the peaks of the positive and negative phases are denoted  $p_{so}$  and  $p_{so}^-$ , respectively. Contrary, if a blast wave encounters a solid surface (or other media denser than air), it will reflect and diffract around it depending on its geometry and size. For instance, a simple case is a facade of an infinitely large building exposed to a surface explosion on which the blast wave encounters normally. When the incident blast wave reflects from the building, a region of further air compression is produced locally to the structure. Consequently, an increased pressure arises compared to the incident pressure, called the *reflected pressure*

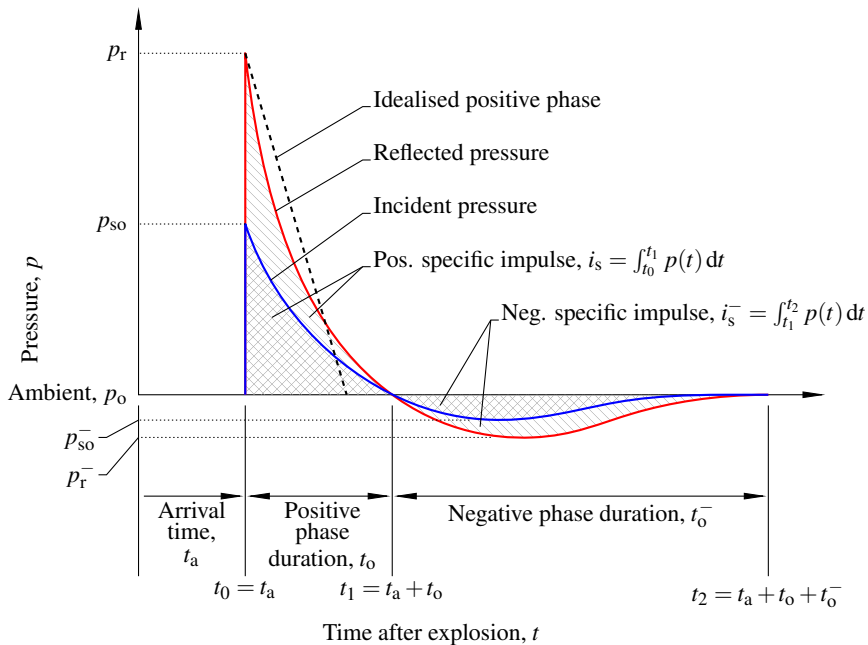


**Fig. 1.10** A typical pressure-time profile for a blast wave shown as the incident pressure and reflected pressure curve. (adapted from UFC 3-340-02 (2008))

## 1. Introduction

with  $p_r$  and  $p_r^-$  defining the peaks of the positive and negative phase, respectively. Thus, the reflected pressure is to be used in the design of building components exposed to blast loading. The pressure-time history of a blast wave relative to the atmospheric pressure,  $p_o$ , and its arrival time,  $t_a$ , may be analytically approximated by the exponential modified Friedlander equation (see e.g. DEWEY 2018):

$$p(t) = p_o + p_{\max} \left( 1 - \frac{t}{t_o} \right) \exp \left\{ -\frac{\alpha t}{t_o} \right\} \quad (1.1)$$

where  $p_{\max}$  is the peak pressure in the positive phase that can be taken as  $p_{so}$  or  $p_r$ , depending on the pressure curve to be described, and  $\alpha$  is a wave form parameter (or a decay coefficient) that can take values between 0 and 4 according to the European Standard EN 13123-1:2001.

When an explosive is ignited in the air, it produces a spherical blast wave. However, this ignition place is not the most obvious choice, and therefore a placement on or close to the ground is more frequently seen in attacks. The interaction with the ground significantly impacts the propagating blast wave that changes to a hemispherical development. Assuming the ground is a perfect reflector, i.e. no energy dissipates in producing a crater, the produced blast wave will be enhanced by a factor of 2 compared to a free air blast. As this usually is not the case, a factor of 1.8 is more reasonable (BAKER et al. 1983). Blast wave parameters, as in Fig. 1.10, for hemispherical TNT surface explosions are made graphically available by UFC 3-340-02 (2008) and are shown in Fig. 1.11. The data curves were determined using a scaled distance,  $Z$ , which stems from the Hopkinson-Cranz scaling approach and is defined as follows (CORMIE et al. 2019):

$$Z = \frac{R}{W^{1/3}} \quad (1.2)$$

where  $R$  denotes the distance in metres to the explosive's centre and  $W$  is the mass of the explosive expressed in kilograms of TNT. Using such scale enables the direct comparison of blast waves originating from different combinations of  $R$  and  $W$ .

Using the mass of TNT as a reference has become standard practice. However, if the blast wave source is other than TNT, then the actual mass of the charge can be converted into a TNT equivalent mass by means of a conversion factor taking into account its specific mass energy and that of TNT. Conversion factors for a number of explosives are given in Table 1.3. For example, from the table, it is seen that 100 kg of ANFO is equivalent to 87 kg of TNT.

The determination of blast wave properties is not always a straightforward task, as it could appear here. Often explosions happen in urban areas where multiple buildings with various geometries and shapes account for complex interactions with blast waves. Therefore, at times, more advanced numerical tools are needed such as Computational Fluid Dynamics (CFD) (see e.g. SMITH and ROSE 2006). Suppose the blast scenario is less complex, but computer tools are still essential for the design, then also within the Finite Element

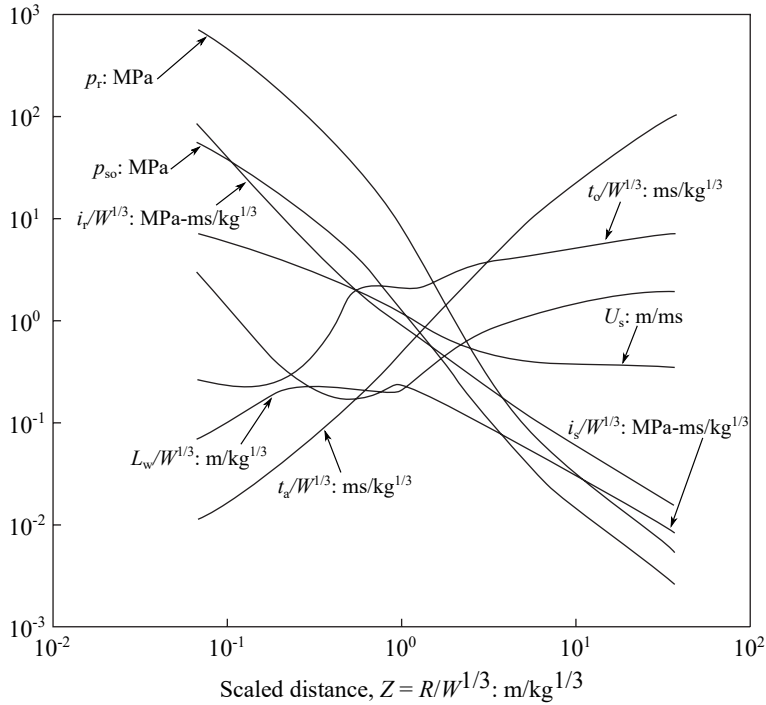


**Fig. 1.11** Incident and reflected positive phase blast wave parameters for a hemispherical TNT explosion on the surface at sea level. (adapted from UFC 3-340-02 (2008))

**Table 1.3** TNT equivalents for a number of explosive compounds. (after CORMIE et al. 2019)

Explosive	Mass specific energy $Q_x$ [ $\text{kJ kg}^{-1}$ ]	TNT equivalent ( $Q_x/Q_{\text{TNT}}$ )
Nitroglycerine (liquid)	6700	1.481
C4 (91 % RDX)	–	1.19-1.37
HMX	5680	1.256
Semtex	5660	1.250
RDX (cyclonite)	5360	1.185
Compound B (60 % RDX, 40 % TNT)	5190	1.148
TNT	4520	1.000
Blasting gelatin	4520	1.000
ANFO (94 % ammonium nitrate, 6 % fuel oil)	3932	0.870
60 % nitroglycerine dynamite	2710	0.600

## 1. Introduction

Method (FEM) framework, several options exist to simulate structures under blast loading more simply without the need to model the fluid medium (BØRVIK et al. 2009). Finally, if blast wave characteristics are already known, the design of building components can be based on dynamic calculations, e.g. using Single Degree Of Freedom (SDOF) systems or the explicit Finite Element Method. A typically used simplification in this regard is the linearisation of the Friedlander equation maintaining the positive specific impulse (indicated by the dashed line in Fig. 1.10 for the reflected pressure), which is tantamount to setting  $\alpha = 0$  in Eq. (1.1). In the present thesis (see Chapter 5), the shock load formulation implemented in the FEM software ABAQUS/Explicit 2021 is employed together with the CONWEP<sup>2</sup> air/surface blast model.

### 1.3 Current Research on Blast Resilient Glazing

The importance of considering blast resilience in the glazing design becomes evident from a number of cases. A study of the bombing of the Alfred P. Murrah Federal Building in Oklahoma City in 1995 (USA) revealed that 39% (200/508) of injured persons within a radius of 970 m (excluding persons inside the attacked building) suffered glass-related injuries (NORVILLE et al. 1999; RUDICK and NORVILLE 2000). In 2011, a car bomb attacked an official government building in Oslo (Norway), generating a shock wave that blew out windows in the targeted building as well as the neighbouring buildings (WIKIPEDIA 2022). On August 4, 2020, a devastating accidental explosion happened in the port of Beirut (Lebanon) where approximately 2750 tonnes of ammonium nitrate stored in a warehouse detonated, causing windows to be blown out as far away as 3.2 km from the port with hundreds of glass-related injuries (KIRK et al. 2020; SUKKARIEH et al. 2021).

The primary purpose of blast resilient glazing is thus to minimise the number of injuries caused by sharp-edged glass fragments detached and propelled from glazed building openings due to blast loading. The secondary is to protect property and minimise damage to it. As discussed in Sec. 1.1.1, a blast resilient performance can be achieved with laminated glass panels. Hence, numerous experimental, numerical and analytical studies on the blast performance of laminated glass can be found in the scientific literature. An overview of some of the current research is given here.

The experimental characterisation of laminated glass to blast loading is necessary to understand the complex panel response. Reported experiments relate to different size scales and load application methods. Blast tests on full-sized panels with explosives and shock tubes (ZHANG et al. 2015b; BERMBACH et al. 2016), as well as tests in controlled laboratory environments on smaller specimens with pre-defined crack configurations to study high strain rate effects on the process of delamination and the post-fracture capacity (KUNTSCHKE 2015; DEL LINZ et al. 2017; ANGELIDES et al. 2021; ANGELIDES et al. 2022), can be found in the literature. Several other studies also report on the response of laminated glass panes to blast loading, both before and after fracture, and additionally compare to numerical simulations using the Finite Element Method (HOOPER et al. 2012; DEL LINZ et al. 2015;

---

<sup>2</sup>A collection of conventional weapons effects calculations including an assortment of air blast routines, fragment and projectile penetrations, breach, cratering, and ground shock (HYDE 1991).

KUNTSCHKE 2015; ZHANG and HAO 2015; PELFRENE 2016; PELFRENE et al. 2016; OSNES et al. 2019). Some publications are exclusively dedicated to numerical investigations, studying the replication of experiments conducted by other researchers (LARCHER et al. 2012; ZHANG et al. 2013; HIDALLANA-GAMAGE et al. 2014). Analytical solutions have also been derived to describe the response of laminated glass panes to high strain rates both during the elastic deformation of the pane and in the post-fracture state (DEL LINZ et al. 2016; YUAN et al. 2017; ANGELIDES et al. 2019). Different analysis methods to support the design of laminated glass panels exposed to blast loading are discussed in a review paper by ANGELIDES and TALBOT (2021). These are essential to reduce the need for expensive testing, often required to develop a design that complies with Standards for explosion-resistant windows (e.g. EN 13541:2001; EN 13123-1:2001; EN 13123-2:2004; EN 13124-1:2001; EN 13124-2:2004; ISO 16933:2007; ISO 16934:2007).

However, much of the effort to better understand the response of laminated glass to blast loading focuses on the interlayer material (the PVB) and the composite interactions in the post-fracture state. Less considered are the glass' mechanical properties at these extreme loading conditions, such as failure criteria. These must be considered necessary to estimate a glass pane's resistance. This highlights that glass remains a relatively under-researched material at high strain rates, as some recent review papers also emphasise (LARCHER et al. 2016; ZHANG and HAO 2016; ZHANG and BEDON 2017; FORQUIN 2017).

## 1.4 Research Objectives of the Thesis

Throughout the previous sections, an overview of the research field has been given by introducing the material glass as a construction material, its application in buildings and facades, the understanding of extreme loading, and glass' performance to it, specifically blast loading, in the context of the threats facing our society, among others, terror. Bombings in the past have revealed that the ability to design blast resilient glazing is crucial. In this regard, the research community has already put forward extensive effort. Still, some gaps for further investigations remain, including the understanding of the glass' mechanical properties at high strain rates, which must be considered essential in the blast design of facade glazing. The research objectives of the present thesis are thus:

- ↔ to pursue a comprehensive, state-of-the-art understanding of the mechanical properties of glass, focusing on tensile strength and stiffness over a broad range of strain rates,
- ↔ to develop an experimental framework for the high strain rate material characterisation, as this is not a standard laboratory discipline at DTU,
- ↔ to investigate and characterise the tensile strength and stiffness of glass at high strain rates relevant to blast loading, thereby expanding on the existing knowledge, and
- ↔ to develop and validate a rate-dependent material damage model for the numerical simulation of monolithic glass panes subjected to blast loading by adopting simple approaches that are practicable in general engineering practice.

To achieve the research objectives, the project was divided into three phases, which increased in scale and set the project’s milestones: (1) material characterisation, (2) development of a material model, and (3) validation and application of the material model.

### 1.5 Thesis Structure

The thesis is divided into two parts. *Part I* is an introduction to the research field and a summary of the conducted research with a discussion of the main findings, organised into six chapters and four appendices, and *Part II* is a collection of three scientific papers that present the research output in greater detail. An overview of the thesis structure is provided in Fig. 1.12 as a flowchart of the main chapters and the related publications, covering the research objectives stated in Sec. 1.4.

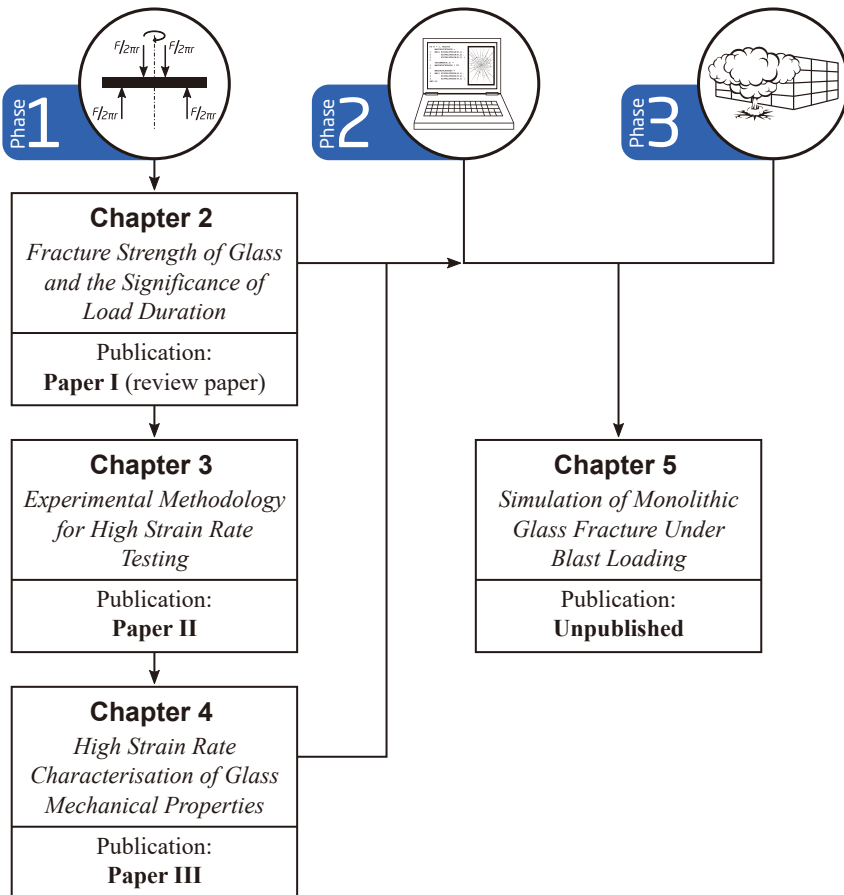


**Fig. 1.12** Based on the project’s three phases, a flowchart of the thesis structure with the main chapters in Part I and the related publications appended in Part II.

**Chapter 2** provides the fundamental theory essential to determine glass failure and emphasises the time-dependency of the glass strength, a vital parameter to consider in the blast design of facade glazing. The theoretical framework is substantiated by a comprehensive literature review (**Paper I**, MEYLAND et al. 2021a) on experimental studies on the dynamic fatigue behaviour of glass, and the normative glass strength design is discussed.

**Chapter 3** presents the experimental methodology reported in **Paper II**, developed to characterise glass at high strain rates, which was considered necessary based on the finding of Paper I. First, an introduction to the material testing at high strain rates is given, followed by a presentation and discussion of a modified design of the well-known Split-Hopkinson Pressure Bar (SHPB), which enables high-speed cameras for fracture assessment and Stereo Digital Image Correlation (Stereo-DIC) deflection measurements in a ring-on-ring bend test configuration. The related experimental procedures and techniques are also outlined.

**Chapter 4** investigates the mechanical properties, such as tensile strength and stiffness (Young's modulus), of glass at high strain rates, as reported in **Paper III**, using the experimental methodology from Chapter 3. Both annealed float glass and also thermally tempered glass was studied to include the effect of residual stresses.

**Chapter 5** introduces the numerical modelling and related failure formulations practicable for brittle materials. With a state-of-the-art understanding of the mechanical properties of glass at high strain rates gained through Chapter 2 and Chapter 4, a rate-dependent material damage model for the simulation of monolithic glass panes subjected to blast loading is presented. The focus is on a simple formulation that is feasible for general engineering practice. Experimental data from two full-scale blast tests found in the scientific literature are used to validate the developed material model through full-scale simulations.

**Chapter 6** concludes the conducted research and gives recommendations for future work.

**Appendix A** includes additional experimental details that relate to Chapter 3, such as technical drawings and different calibration data.

**Appendix B** provides additional results for Chapter 4 from the deflection measurements performed with high-speed cameras and the Stereo-DIC technique.

**Appendix C** contains details for the developed rate-dependent progressive damage model for dynamic glass fracture in Chapter 5. That is, additional information for the use of shell elements, a flow chart of the material model (implemented as an ABAQUS VUMAT user subroutine) and the associated source code written in FORTRAN.

**Appendix D** provides mesh convergence analyses related to the performed full-scale simulations of monolithic glazing under blast loading reported in Chapter 5.

## 1. Introduction

## Fracture Strength of Glass and the Significance of Load Duration

The aim of this chapter is to provide an understanding of the fracture strength of glass and highlight the significance of the load duration and loading rate. First, the fundamental theory of the unique mechanisms of glass fracture is presented, outlining why a dependency on the load duration and rate-of-loading exists (Sec. 2.1). With a focus on the loading rate, the theoretical framework is further substantiated by a summary and discussion of a comprehensive literature review on experimental studies that report on the glass strength's time-dependency (Sec. 2.2), which can be found detailed in Paper I (MEYLAND et al. 2021a). In closing, this chapter addresses the normative glass strength design according to current Standards, and discusses their definition of the load duration dependency compared to the data collected in the literature review (Sec. 2.3).

This chapter addresses the findings reported in Paper I on page 171.

### 2.1 Fundamental Theory of Glass Fracture

When designing structural glass members, it has become general engineering practice to use a deterministic approach, often given by the Rankine criterion (or sometimes known as the maximum normal stress theory). It states that failure due to fracture occurs in a multi-axial stress state when the maximum principal stress,  $\sigma_1$ , at any point exceeds the apparent<sup>1</sup> tensile strength,  $\sigma_f$  (SAMUEL and WEIR 1999):

$$\sigma_1 \geq \sigma_f \quad (2.1)$$

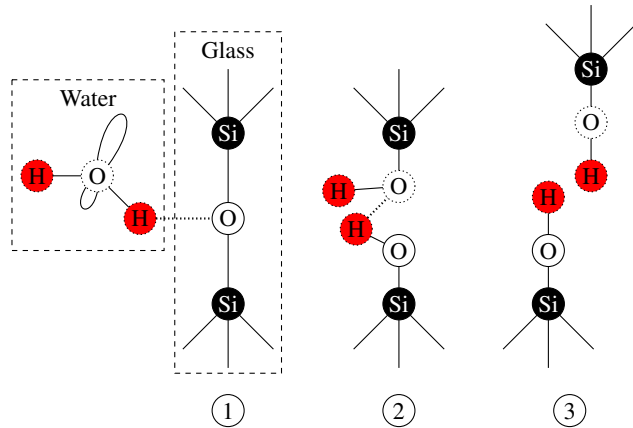
Thus, in a design case, maximum principal stresses occurring under a design load are compared to a bending strength resistance, which is either defined normative (e.g. CEN/TS 19100-1:2021) or determined experimentally (e.g. EN 1288-1:2001; EN 1288-2:2001; EN 1288-3:2001; EN 1288-5:2001). However, this is a very practical approach. In fact, the fracture strength of glass is determined by stress concentrations in surface defects, which are well-described by the theory of Linear Elastic Fracture Mechanics (LEFM). To understand the mechanisms that govern glass fracture, a closer look into stress corrosion, a phenomenon that causes existing surface flaws to grow slowly in size under tensile loading before failure, often referred to as 'sub-critical crack growth', is required. The following subsections introduce the fundamental theory necessary to determine glass fracture.

<sup>1</sup>The term 'apparent' refers to the strength that originates from the intrinsic glass strength and eventual superimposed residual stresses, i.e. the strength measured directly by testing.

### 2.1.1 Sub-critical Crack Growth

The strength of glass is time-dependent; however, in a vacuum, the dependency is almost negated (GURNEY and PEARSON 1949). Under normal environmental conditions where a level of humidity is present, water molecules react with the glass' atomic structure, causing flaws to grow slowly when exposed to a crack opening stress. This chemical reaction is termed *stress corrosion* and an illustration of it is given in Fig. 2.1. The consequence of the stress corrosion, i.e. the growth of surface flaws, is known as *sub-critical crack growth*. For a glass element that is loaded below its momentary strength, the stress corrosion will cause it to fail after the time necessary for the most critical flaw to grow to its critical size at that particular load level. Therefore, the momentary strength of a loaded glass element will decrease with time, even if the load is applied statically. First observations to this phenomenon were made by the French scientist GRENET in 1899, who also explained the unexpected fracture of filled champagne bottles by the delayed failure of glass.

**Fig. 2.1** The chemical reaction at the crack tip defining the stress corrosion: (1) adsorption of water to Si-O bond, (2) concerted reaction involving simultaneous proton and electron transfer, and (3) formation of surface hydroxyl groups. (after MICHALSKE and FREIMAN 1983)



In the theory of stress corrosion initiated by CHARLES and HILLIG (1962) and further developed by MICHALSKE and FREIMAN (1983), the crack velocity modifies with the kinetics of the chemical reaction, in which the activation energy depends on the local stress and the radius of curvature at the crack tip. Therefore, a relationship exists between the crack velocity,  $v$ , and the stress intensity factor,  $K_I$ , at the crack tip (cf. Sec. 2.1.2). A schematic of this relationship is shown in Fig. 2.2 with four essential regions highlighted:

- 0:** Below the crack growth threshold,  $K_{th}$ , no measurable sub-critical crack growth occurs. For soda-lime-silica glass this value can range from 0.14 to 0.28 MPa m<sup>1/2</sup> in water (WIEDERHORN and BOLZ 1970; SIMMONS and FREIMAN 1981; GEHRKE et al. 1990; WAN et al. 1990; SGLAVO and GREEN 1996; KOCER and COLLINS 2001; SGLAVO and BERTOLDI 2006; GHOSH et al. 2010) and from 0.37 to 0.39 MPa m<sup>1/2</sup> in air (50 % RH) (WAN et al. 1990; KOCER and COLLINS 2001), at crack velocities as low as 10<sup>-14</sup> m s<sup>-1</sup>. For most applications  $K_{th} = 0.25$  MPa m<sup>1/2</sup> may be representative (see e.g. OVEREND and ZAMMIT 2012).

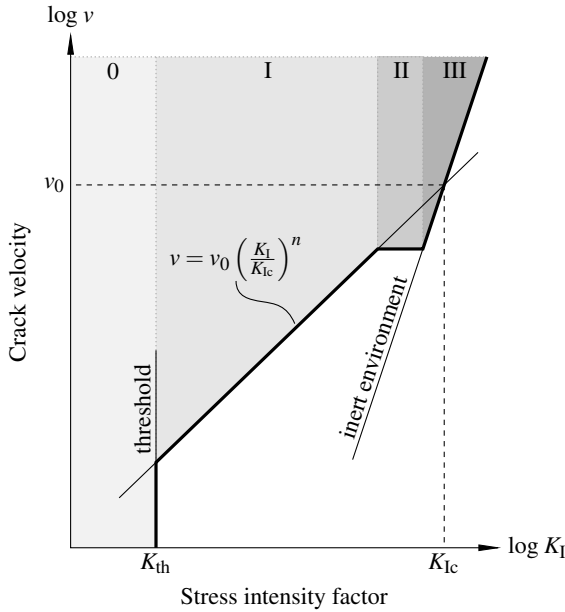


**Fig. 2.2** Schematic representation of a typical  $v(K_I)$ -curve seen for soda-lime-silica glass. (from Paper I, MEYLAND et al. 2021a)

**I:** This is the actual region that relates to the sub-critical crack growth. Here, the crack velocity is essentially governed by the stress corrosion's molecular mechanisms at the crack tip. Thus, there is a dependence on the applied stress intensity and the relative humidity in the environment. A good approximation of the  $v(K_I)$ -relationship in this region is given by the following empirical power law originally proposed by EVANS and WIEDERHORN (1974):

$$v = A \cdot K_I^n \quad (2.2)$$

which, by using  $A = v_0 \cdot K_{Ic}^{-n}$ , may also be expressed as (MUNZ and FETT 1999):

$$v = v_0 \left( \frac{K_I}{K_{Ic}} \right)^n \quad \text{for } K_I \leq K_{Ic} \quad (2.3)$$

Here,  $v_0$ , on a logarithmic scale, represents the ordinate of the critical stress intensity factor (see description of region III),  $K_{Ic}$ , and the exponent  $n$  defines the slope of the curve, which is a measure of how reactive water molecules are within the glass lattice. When the value of the sub-critical crack growth parameter  $n$  is high, it indicates that the chemical reactivity at the crack tip is reduced due to a lower level of humidity, implying a slow crack growth. The opposite is true when  $n$  is low. For the design of structural glass, a constant value of  $n = 16$  is a reasonable assumption together with  $v_0 = 6 \text{ mm s}^{-1}$  being a conservative choice for general applications, while  $v_0 = 30 \text{ mm s}^{-1}$  is more representative for glass immersed in water (HALDIMANN et al. 2008).

## 2. Fracture Strength of Glass and the Significance of Load Duration

- II:** A plateau is formed as the crack velocity is restricted by a reduced supply rate of water to the crack tip. Hence, the crack velocity in this region is essentially independent of  $K_I$  but depends on the amount of humidity in the environment. The range of constant crack velocity narrows as relative humidity increases, which emerges from the findings of WIEDERHORN (1967).
- III:** In region III, the stress corrosion mechanisms can no longer follow the crack tip. At this point  $v$  increase rapidly, between  $10^{-3} \text{ m s}^{-1}$  and  $1 \text{ m s}^{-1}$ , approaching the limit for an inert environment. After reaching the critical stress intensity factor,  $K_{Ic}$ , crack growth becomes unstable reaching speeds of  $1500 \text{ m s}^{-1}$  to  $2500 \text{ m s}^{-1}$  (OVEREND et al. 2007b).  $K_{Ic}$  is considered a material constant and for soda-lime-silica glass it is found to range from 0.72 to 0.82  $\text{MPa m}^{1/2}$  at room temperature (MENČÍK 1992). A value of  $K_{Ic} = 0.75 \text{ MPa m}^{1/2}$  is suitable for most practical purposes (HALDIMANN et al. 2008).

In addition to humidity, the sub-critical crack growth may also be affected by the temperature, the pH value of the surrounding medium, the chemical composition of the glass, and the loading rate (GY 2003; HALDIMANN et al. 2008). Typically, it is sufficient only to consider region I when predicting a glass element's design lifetime. The contributions of regions II and III are only minor because of the high crack velocities that emerge. Thus, a conservative estimate is provided when neglecting them.

### 2.1.2 Stress Intensity Factor

The concept of the stress intensity factor is anchored in the theory of Linear Elastic Fracture Mechanics, which provides a quantitative description of the mechanical behaviour of bodies containing one or multiple cracks. The following is a short introduction to the formulation of stress concentrations at a crack tip, which for the later lifetime prediction of a glass element is combined with the previously discussed sub-critical crack growth effects. In general, a crack or flaw in a piece of material can be subjected to complex stress fields, which may be decomposed into three crack opening modes as illustrated in Fig. 2.3: tensile opening (Mode I), in-plane shear (Mode II), and out-of-plane shear (Mode III). However, as surface flaws in structural glass members are predominantly loaded with normal tensile stresses due to, e.g. bending, a description based entirely on Mode I is sufficient. Depending on the crack opening stress,  $\sigma$ , the stress intensity factor,  $K_I$ , as introduced by

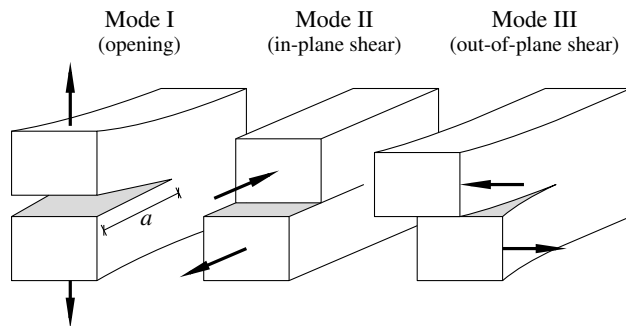


**Fig. 2.3** The three modes of loading that can be applied to a crack.

IRWIN (1957), at the crack tip for Mode I opening may be expressed as follows (see e.g. ANDERSON 2017):

$$K_I = \sigma Y \sqrt{\pi a} \quad (2.4)$$

where  $a$  is the crack (or flaw) depth or half the crack's length depending on the configuration, and  $Y$  is a dimensionless geometry (correction) factor, which equals  $0.637 (= 2/\pi)$  for half penny shaped cracks and 1.12 for edge cracks in semi-infinite plates. Instantaneous failure of a glass element will occur when  $K_I$  for one crack equals or exceeds the *critical stress intensity factor* (or *fracture toughness*),  $K_{Ic}$ :

$$K_I \geq K_{Ic} \quad (2.5)$$

This criterion is known as *Irwin's fracture criterion* for pure Mode I fracture of a crack.

### 2.1.3 Energy Release Rate

There are other concepts in Linear Elastic Fracture Mechanics, which can describe glass fracture analytically. One of these concepts is formulated considering an energy approach. In 1956, IRWIN defined the *energy release rate*,  $G$ , which is essentially equivalent to the Griffith energy balance (GRIFFITH 1920). It is a measure of the instantaneous loss of total potential energy,  $\Pi$ , per unit crack growth area,  $s$ :

$$G \equiv -\frac{d\Pi}{ds} \quad [\text{J m}^{-2}] \quad (2.6)$$

In the simple case of a wide plate in plane stress with a stationary crack of length  $2a$  perpendicular to the load, i.e. the Griffith crack shown in Fig. 2.4, the energy release rate is given by the following expression (ANDERSON 2017):

$$G = \frac{\pi \sigma^2 a}{E} \quad (2.7)$$

Similar to the critical stress intensity factor, there is a *critical energy release rate* (or *fracture energy*),  $G_c$ .

Since during crack extension two crack surfaces are created,  $G_c$  is by definition equal to  $2\gamma$ , where  $\gamma$  denotes the specific surface energy. Thus, unstable crack extension occurs when the energy release rate exceeds  $G_c$ :

$$G \geq G_c = 2\gamma \quad (2.8)$$

This criterion is known as the *Griffith's fracture criterion*. There also exists a direct relationship between  $G_{Ic}$  (the fracture energy for a Mode I crack) and  $K_{Ic}$ , because the stress

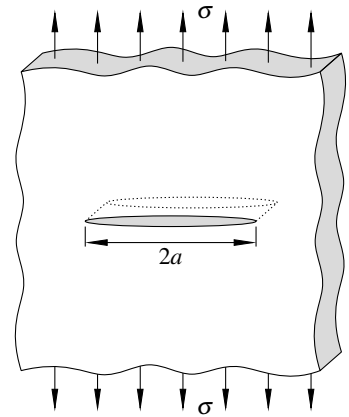


**Fig. 2.4** A through-thickness crack in an infinitely wide plate subjected to remote tensile stresses. (after ANDERSON 2017)

## 2. Fracture Strength of Glass and the Significance of Load Duration

**Table 2.1** The Mode I fracture energy for soda-lime-silica glass determined experimentally in air, at room temperature, by different authors.

Reference	Test method	$G_{Ic}$ [ $J m^{-2}$ ]
CULF (1957)	Cone crack	7.4-8.6
WIEDERHORN (1966)	Double-cantilever cleavage	5.2-5.3
LINGER and HOLLOWAY (1968)	Double-cantilever cleavage	6.6-7.8
WIEDERHORN (1969)	Double-cantilever cleavage	7.6-7.8
MECHOLSKY et al. (1974)	Double-cantilever cleavage	7.0
INAGAKI et al. (1985)	Chevron notch test	8.8
SMITH et al. (2009)	Chevron notch test	7.0

intensity factor for the crack shown in Fig. 2.4 is given by Eq. (2.4) for  $Y = 1$ . Combining Eqs. (2.4) and (2.7), and considering the fracture criteria given by Eqs. (2.5) and (2.8), the following relationship between  $G_{Ic}$  and  $K_{Ic}$  for plane stress can be derived:

$$G_{Ic} = \frac{K_{Ic}^2}{E} \quad (2.9)$$

For plane strain conditions,  $E$  must be replaced by  $E / (1 - \nu^2)$ . IRWIN (1957) performed a crack closure analysis, which proved that Eq. (2.9) is a general relationship valid for all Mode I crack configurations and not only for the one given in Fig. 2.4. For glass,  $G_{Ic}$  is considered a material constant, which different standard tests can measure. A selection of experimentally determined values for soda-lime-silica glass tested in air, at room temperature, is provided in Table 2.1. With  $K_{Ic} = 0.75 \text{ MPa m}^{1/2}$  and  $E = 70 \text{ GPa}$ , Eq. (2.9) determines  $G_{Ic} = 8.0 \text{ J m}^{-2}$  for plane stress conditions, which complies with the values in Table 2.1. Higher values for fracture energy are also found in the literature. For example, SHARON and FINEBERG (1999) measured values between 30 and 40  $\text{J m}^{-2}$  by a notched sheet tensile test. However, the measurements were performed on a dynamically propagating crack. The fracture energies in Table 2.1 relate to a stationary crack.

### 2.1.4 Resistance of a Single Crack (or Flaw)

The lifetime or resistance of a single crack (or flaw) on a glass surface is determined by combining the sub-critical crack growth (c.f. Sec. 2.1.1) with the theory of stress concentrations at a crack tip (c.f. Sec. 2.1.2). The following outlines the derivation of equations to predict a crack's resistance to two commonly assumed load cases, constant stress and constant stress rate, which is an approximation to the load induced by explosion blast waves (see e.g. KUNTSCHKE 2015).

For the prediction of a single crack's resistance to a given tensile stress history normal to the crack,  $\sigma(t)$ , only the course of region I (cf. Fig. 2.2) is considered, meaning that the extension of the crack growth into regions II and III is approximated by Eq. (2.3) as well. This simplification can be found in MENČÍK (1992), MUNZ and FETT (1999), and WACHTMAN et al. (2009) for lifetime predictions of ceramics, and HALDIMANN (2006) applied it to predict the lifetime of structural glass. OVEREND and ZAMMIT (2012) extended the

simplified crack growth to also account for strength limits governed by the crack growth threshold,  $K_{th}$ , for very long duration and the fracture toughness,  $K_{Ic}$ , for very short duration. Based on Eq. (2.4) these limits may be expressed as:

$$\frac{K_{th}}{Y\sqrt{\pi a_{th}}} \leq \sigma_f \leq \frac{K_{Ic}}{Y\sqrt{\pi a_f}} \quad (2.10)$$

where  $a_{th}$  and  $a_f$  are the threshold crack depth and the critical crack depth, respectively. The limits are also known as the *threshold strength* and the *inert strength*. Their formulation was further elaborated by ALTER et al. (2017) to account for loading rate. Neglecting the actual contributions from regions II and III results in a slight underestimation of the time-to-failure, therefore providing a conservative estimate. For instance, at a constant stress rate of  $10^4 \text{ MPa s}^{-1}$ , KUNTSCHE (2015) showed in his pendulum impact tests that this simplification reduced the predicted resistance with 6%, as a direct consequence of an underestimated failure time.

The simplified sub-critical crack growth can be described by the following ordinary differential equation, which is obtained by substituting Eq. (2.4) into Eq. (2.3), and defining the crack velocity,  $v$ , as a change in crack depth with time, i.e.  $v = da/dt$ :

$$\frac{da}{dt} = v = v_0 \left( \frac{\sigma(t)Y\sqrt{\pi a}}{K_{Ic}} \right)^n \quad (2.11)$$

Assuming that Eq. (2.11) is valid for  $K_I \leq K_{Ic}$  (i.e. neglecting the crack growth threshold) and that  $n$  is constant over the full range of  $K_I$ , the method of variable separation yields:

$$\int_{a_i}^{a_f} a^{-n/2} da = v_0 (Y\sqrt{\pi})^n K_{Ic}^{-n} \int_0^{t_f} \sigma^n(t) dt \quad (2.12)$$

where  $a_i$  is the initial crack depth (at time  $t = 0$ ) and  $a_f$  is the critical crack depth at  $t_f$ , defining the time to failure or lifetime of the crack in question. By integrating the left-hand side of Eq. (2.12) and rearranging, the following fundamental relationship between stress, time and crack depth is obtained:

$$\int_0^{t_f} \sigma^n(t) dt = \frac{2 K_{Ic}^n}{(n-2) a_i^{(n-2)/2} \cdot v_0 (Y\sqrt{\pi})^n} \left[ 1 - \left( \frac{a_i}{a_f} \right)^{(n-2)/2} \right] \quad (2.13)$$

For  $a_i \ll a_f$ ,  $(a_i/a_f)^{(n-2)/2} \rightarrow 0$ , therefore Eq. (2.13) can be simplified to:

$$\int_0^{t_f} \sigma^n(t) dt = \frac{2 K_{Ic}^n}{(n-2) a_i^{(n-2)/2} \cdot v_0 (Y\sqrt{\pi})^n} \quad (2.14)$$

With a given stress history,  $\sigma(t)$ , Eq. (2.14) enables the calculation of a crack's lifetime or its resistance after a given load duration; both provided that the initial crack depth,  $a_i$ , is known.

## 2. Fracture Strength of Glass and the Significance of Load Duration

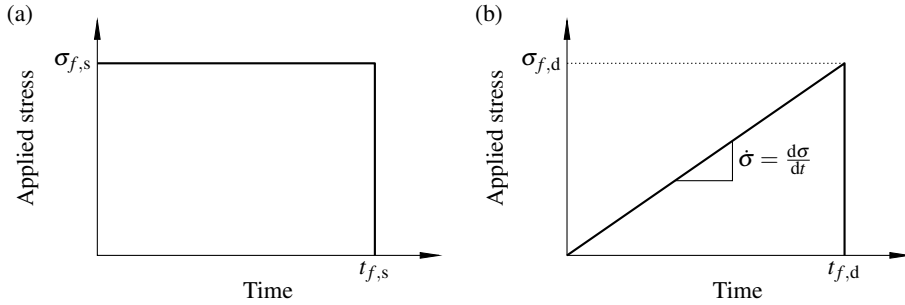


**Fig. 2.5** Stress-time history for constant applied stress in (a) and constant stress rate loading in (b). ( $t_{f,s}$  and  $t_{f,d}$  are the time to failure or load duration;  $\sigma_{f,s}$  is a statically applied stress;  $\sigma_{f,d}$  is a dynamic fracture strength;  $\dot{\sigma}$  is a stress rate)

### A Crack's Resistance to Constant Stress

For a constant applied stress (static loading), i.e.  $\sigma(t) = \sigma_{f,s}$ , as shown in Fig. 2.5(a) and typically applied when static fatigue testing glass, a crack's resistance after a given load duration,  $t_{f,s}$ , can be determined by inserting the stress history into the left-hand side of Eq. (2.14). Performing the integration and isolating  $\sigma_{f,s}$  yields the following expression:

$$\sigma_{f,s} = \alpha \cdot t_{f,s}^{-1/n} \quad (2.15)$$

where

$$\alpha = \left[ \frac{(n-2) a_i^{(n-2)/2} \cdot v_0 (Y\sqrt{\pi})^n}{2K_{Ic}^n} \right]^{-1/n} \quad (2.16)$$

It follows from Eq. (2.15) that when  $\alpha$  is identical for two cracks found on two glass elements, index 1 and 2, the interrelationship between the constant applied stresses and the related times-to-failure can be expressed as:

$$\frac{\sigma_{f,s,2}}{\sigma_{f,s,1}} = \left( \frac{t_{f,s,1}}{t_{f,s,2}} \right)^{1/n} \quad \text{or} \quad \frac{t_{f,s,1}}{t_{f,s,2}} = \left( \frac{\sigma_{f,s,2}}{\sigma_{f,s,1}} \right)^n \quad (2.17)$$

Since Eq. (2.17) is independent of  $v_0$  it can be used to determine  $n$  from experiments, given that the strength limits determined by  $K_{th}$  and  $K_{Ic}$  are not reached.

### A Crack's Resistance to Constant Stress Rate

For a constant stress rate (dynamic loading),  $\dot{\sigma}$ , which is commonly used for strength testing glass or dynamic fatigue tests, the applied stress increases linearly with time as shown in Fig. 2.5(b), providing the following stress history:

$$\dot{\sigma} = \frac{d\sigma}{dt} = \text{const.} \quad \Rightarrow \quad \sigma(t) = \dot{\sigma} \cdot t \quad (2.18)$$

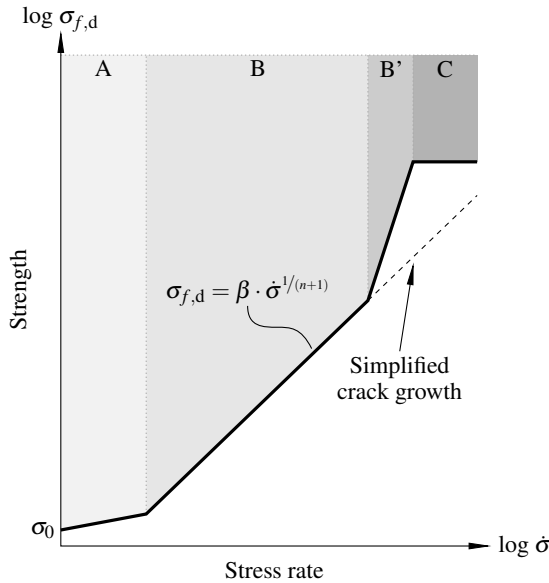


**Fig. 2.6** An illustration of the stress rate dependency of the glass strength, predicted from the 4-region sub-critical crack growth curve in Fig. 2.2. (adapted from Paper I, MEYLAND et al. 2021a; after EVANS 1974, EVANS and JOHNSON 1975 and CHANDAN et al. 1978)

A crack's resistance to a given stress rate, i.e.  $\dot{\sigma} = \sigma_{f,d}/t_{f,d}$ , is thus found by introducing Eq. (2.18) into the integral on the left-hand side of Eq. (2.14). Performing the integration and isolating  $\sigma_{f,d}$  gives:

$$\sigma_{f,d} = \beta \cdot \dot{\sigma}^{1/(n+1)} \quad (2.19)$$

where

$$\beta = \left[ \frac{2(n+1)K_{Ic}^n}{(n-2)a_i^{(n-2)/2} \cdot v_0 (Y\sqrt{\pi})^n} \right]^{1/(n+1)} = [\alpha^n \cdot (n+1)]^{1/(n+1)} \quad (2.20)$$

The constant  $\alpha$  (cf. Eq. (2.16)) is retrieved in  $\beta$ , such that  $\beta$  is also formulated with a dependence on  $\alpha$ . This enables the description of crack growth at constant stress rate loading using data from tests with constant applied stress. The reverse approach is also possible when data from constant stress rate tests are available. However, both approaches imply that crack sizes and conditions ( $a_i$ ,  $Y$ ,  $v_0$ ,  $n$ ,  $K_{Ic}$ ) can be assumed identical between the two testing conditions to be able to perform the conversion.

The double-logarithmic linear relationship between stress and stress rate given by Eq. (2.19) was first suggested by CHARLES (1958) based on an exponential Arrhenius approach. In the 1970s, this relationship was revisited by EVANS (1974), EVANS and JOHNSON (1975), and CHANDAN et al. (1978), who furthermore expanded on the  $v(K_I)$ -curve (cf. Fig. 2.2) by suggesting to integrate over the 4-regions of sub-critical crack growth, thereby obtaining a new curve where fracture strength is a function of stress rate. With four regions now denoted A, B, B' and C, the new curve is depicted in Fig. 2.6. At low stress rates, region

## 2. Fracture Strength of Glass and the Significance of Load Duration

A, strength begins to increase slowly from a minimum value,  $\sigma_0$ . For further increasing stress rates, traversing region B, there exists a simple logarithmic relationship between  $\sigma$  and  $\sigma_{f,d}$  given by Eq. (2.19). At still higher stress rates, region B', strength varies in a non-trivial manner, and in region C, the strength levels out due to the absence of sub-critical crack growth effects. From Fig. 2.6 it is evident that the simplification to only consider the course of region I (here region B), conservatively predicts a crack's resistance to high stress rates that fall within region B' and C (the dashed-line extension). The strength data reported by EVANS and JOHNSON (1975) and CHANDAN et al. (1978) for soda-lime-silica glass tested at stress rates up to  $2 \cdot 10^6$  MPa s<sup>-1</sup>, however, did not provide any conclusive evidence of distinctly different regions.

Again, it follows from Eq. (2.19) that when  $\beta$  (cf. Eq. (2.20)) is identical for two cracks found on two glass elements, index 1 and 2, the interrelationship between the failure stresses and the related constant applied stress rates can be expressed as follows:

$$\frac{\sigma_{f,d,2}}{\sigma_{f,d,1}} = \left( \frac{\dot{\sigma}_2}{\dot{\sigma}_1} \right)^{1/(n+1)} \quad (2.21)$$

Since Eq. (2.21) is also independent of  $v_0$ , it is commonly used to determine  $n$  from constant stress rate experiments by plotting the failure stress as a function of the stress rate on a logarithmic scale, resulting in a slope of  $1/(n+1)$ . However, it has to be ensured that the limits of the strength given by Eq. (2.10) are not reached, while at the same time, caution should be given as  $v_0$  may show some rate dependency according to HALDIMANN et al. (2008).

## 2.2 Literature Review on Experimental Strength Data

A comprehensive literature review on experimental strength data for soda-lime-silica glass emphasises the analytical discussion regarding the load duration and loading rate dependency. In total, 92 publications dating back to 1899 were reviewed in detail to compile a summary of the current state-of-the-art understanding of the time-dependent tensile strength of glass. All details can be found in Paper I (MEYLAND et al. 2021a), which also includes an Appendix A with additional experimental information to each publication reviewed. In the following, the glass strength's dependence on the loading rate, also termed the dynamic fatigue behaviour, is exclusively addressed based on 57 publications because of the relevance for the later Chapters 3, 4, and 5.

Glass' tensile strength is governed by surface defects and their characteristics, as it emerges from the fundamentals of fracture mechanics outlined previously. Because of the characteristic differences in surface flaws, the tensile strength cannot be considered a material constant. Therefore, different strength data are found in the literature that characterise glass and its dependence on various factors (also in combination) such as loading rate, temperature, humidity, surface quality, and the surrounding medium. Since the strength of glass also relates to the size of the stressed area, commonly referred to as the size effect (see e.g. HALDIMANN et al. 2008), additional variations are caused by the different inves-

tigated specimen sizes and employed test configurations, typically seen as a three-point and four-point bend test, or axisymmetric bending (coaxial double ring test or ring-on-ring test).

In the literature, the dynamic fatigue behaviour of the glass was studied using different experimental techniques that applied loads at various constant strain rates, typically expected in practice (see Fig. 1.7). With techniques ranging from the universal testing machine to more advanced setups (in terms of execution), such as the Split-Hopkinson Pressure Bar (SHPB), strain rates between  $3.5 \cdot 10^{-11} \text{ s}^{-1}$  (JOHAR 1982) and  $9.9 \cdot 10^2 \text{ s}^{-1}$  (ZHANG et al. 2012) are reported. A detailed summary of the range of strain rates achieved in the reviewed literature is given in Fig. 2.7. Most investigations before 2010 are located at quasi-static strain rates between  $10^{-7} \text{ s}^{-1}$  and  $10^{-3} \text{ s}^{-1}$ , which highlights the fact that most of the published data rely on experiments with universal testing machines. Only recently, increased interest is seen, where experiments on glass have been designed to approach strain rates above  $1 \text{ s}^{-1}$  ( $\approx 7 \cdot 10^4 \text{ MPa s}^{-1}$ ), which are relevant to extreme events, such as blast loading. This identified trend is believed to be a direct consequence of an increased terrorist threat in society (cf. Sec. 1.2), demanding this kind of knowledge. These experiments were performed by PERONI et al. (2011), KÖNIG (2012), ZHANG et al. (2012), and MEYLAND et al. (2019), employing high-speed servo-hydraulic testing machines and SHPB setups.

All the reviewed dynamic fatigue data<sup>2</sup> for soda-lime-silica glass, normalised as outlined in Paper I, are presented in Fig. 2.8 as a plot of the relative failure stress as a function of strain rate. Through the normalisation, crack properties (as defined by  $\beta$ , cf. Eq. (2.20)) and specimen size effects were made dimensionless, which means that only the rate dependency of the glass strength dominates and other effects were removed. It is clearly seen that strength increases with increasing strain rate, and that the majority of data are in good agreement within the range of quasi-static loading, i.e. from  $10^{-7} \text{ s}^{-1}$  to  $10^{-3} \text{ s}^{-1}$ . At the outermost values, a strength reduction of about 60 % and an increase of about 175 % with respect to  $\sigma_{f,d}/\sigma_0 = 1.0$  can be read. When looking at the extremes of strain rates (low and high), there are fewer data points because the experimental execution is more involved. Also, these data points exhibit a strong divergence from the general trend of the dynamic fatigue curve. However, most of them should not be treated as a scatter. Since no distinction has been made between tests conducted under different conditions, such as varying temperature and humidity, the shown deviations can be explained by the sub-critical crack growth, which is sensitive to changes in the surrounding environment (cf. Sec. 2.1.1). This sensitivity results in a variation of the log-log linear slope. However, some of the divergences in the data may also be attributed to the fact that strength limits as given in Eq. (2.10) possibly were approached. Also, the complexity in the execution and analysis of high strain rate experiments may explain some of the seen deviations.

The results relevant to high strain rate loading by blast waves from explosions are now considered in more detail. For the other data shown in Fig. 2.8, the reader is referred to Paper

<sup>2</sup>The datasets are openly available (© licensed under CC0 1.0, <https://creativecommons.org/publicdomain/zero/1.0/>) in the data repository *DTU Data*, a figshare platform, at <https://doi.org/10.11583/DTU.13655525>.

## 2. Fracture Strength of Glass and the Significance of Load Duration

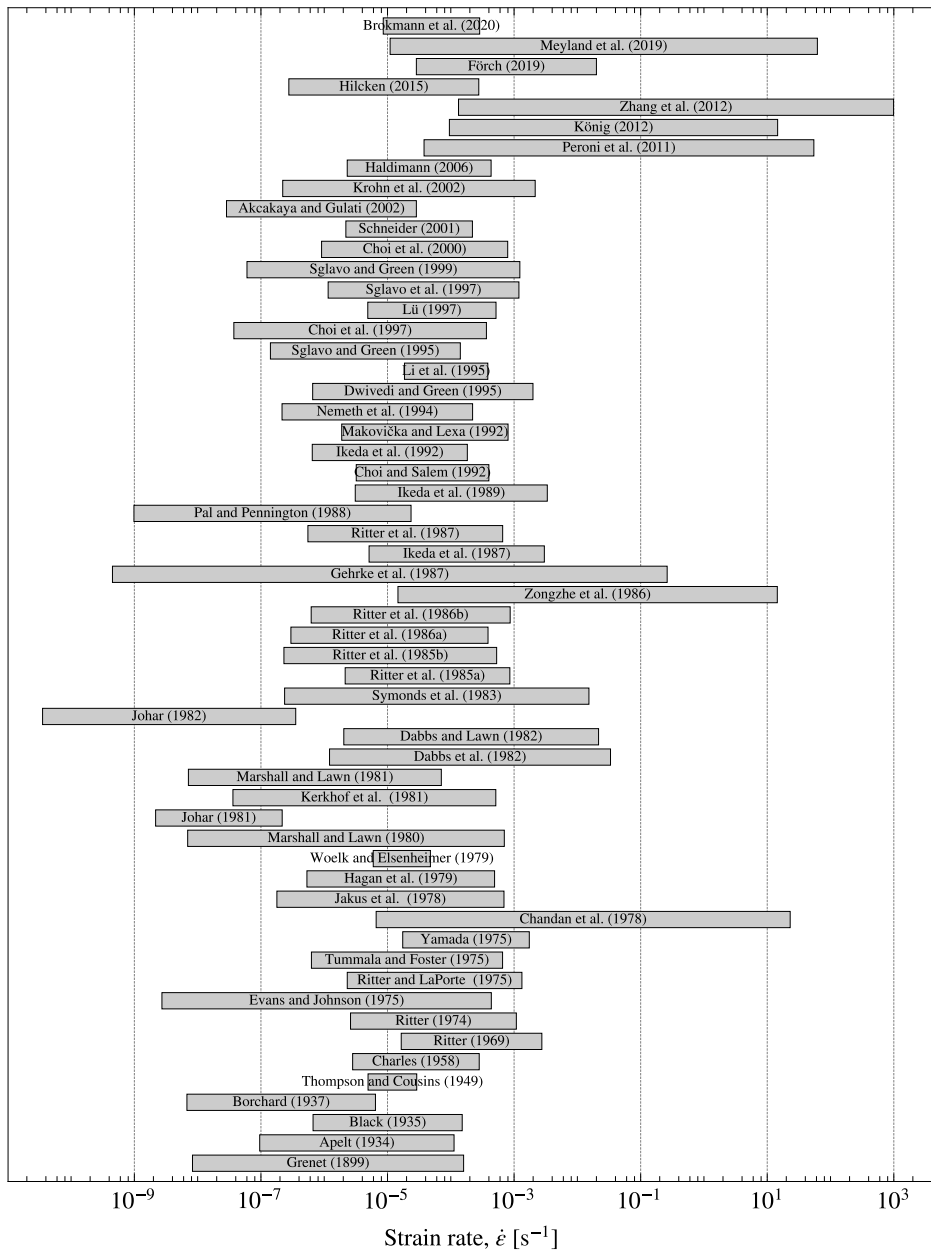


**Fig. 2.7** Range of experimental strain rates reported in the published dynamic fatigue tests on soda-lime-silica glass. (from Paper I, MEYLAND et al. 2021a)

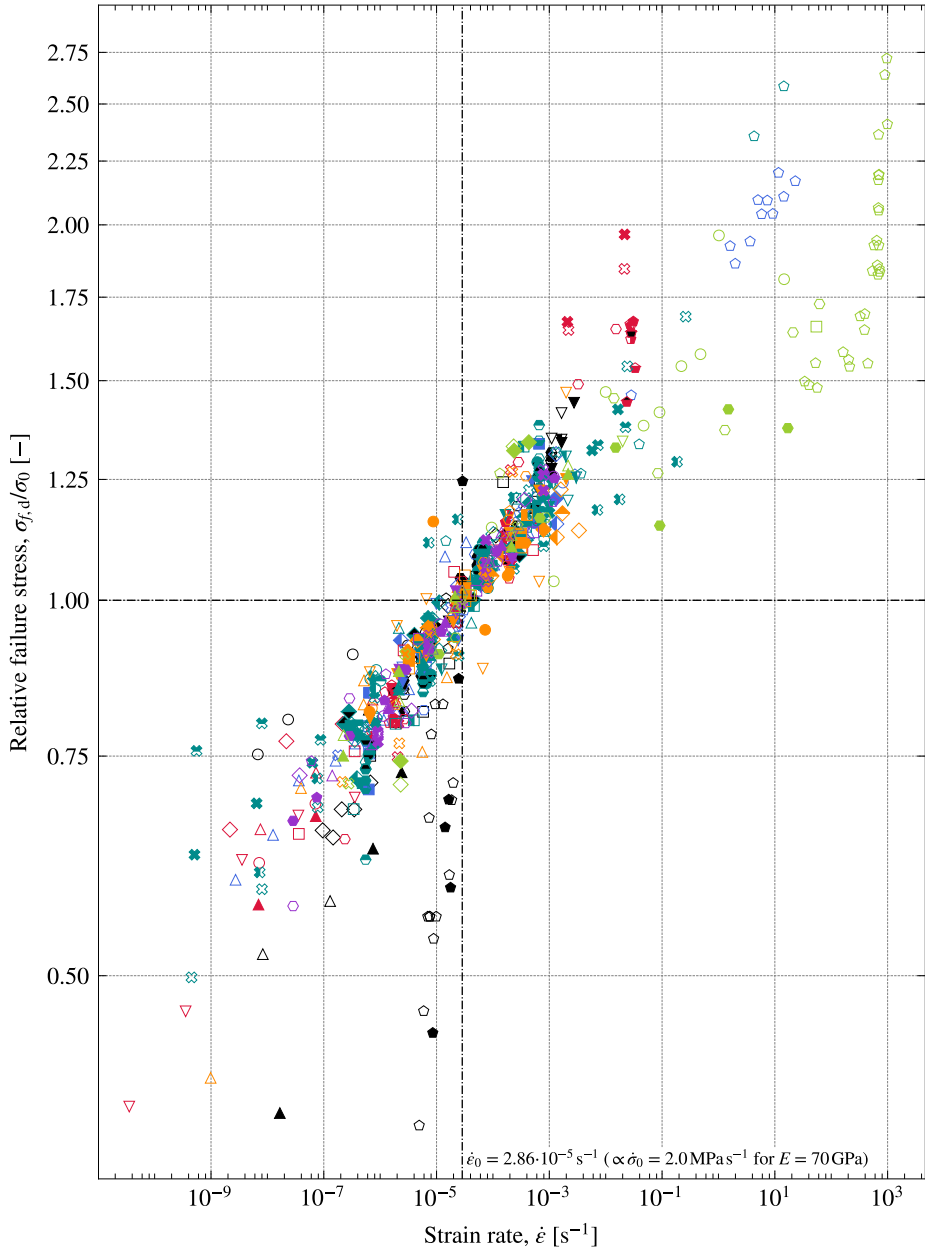


**Fig. 2.8** A re-plot of the reviewed dynamic fatigue data of soda-lime-silica glass, as the relative failure stress as a function of strain rate. (from Paper I, MEYLAND et al. 2021a) (*Continued on the next page with the figure legend*)

## 2. Fracture Strength of Glass and the Significance of Load Duration

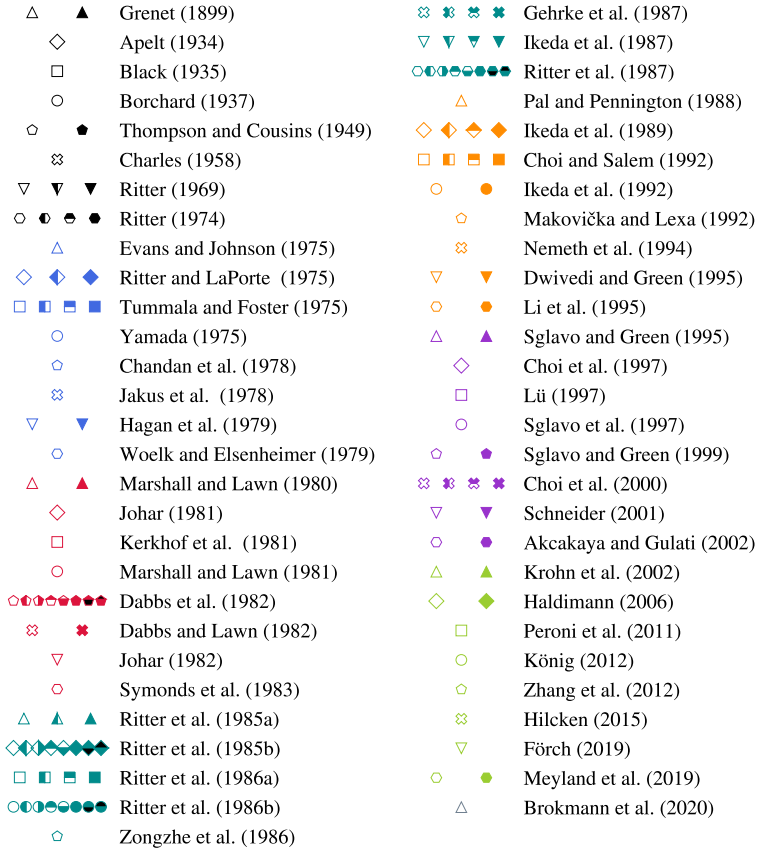


**Fig. 2.8** A re-plot of the reviewed dynamic fatigue data of soda-lime-silica glass, as the relative failure stress as a function of strain rate. (from Paper I, MEYLAND et al. 2021a)

I (MEYLAND et al. 2021a). Only a few high strain rate publications investigating soda-lime-silica glass above  $1 \text{ s}^{-1}$  were found. The data published by CHANDAN et al. (1978), ZONGZHE et al. (1986), and KÖNIG (2012) all show an almost linear dynamic fatigue behaviour, which continue the trend of the other data at the lower strain rates. The other studies in the high strain rate regime (PERONI et al. 2011; ZHANG et al. 2012; MEYLAND et al. 2019), tend to deflect from the general trend. From all publications reviewed, ZHANG et al. reached the highest strain rates in the investigation of cylindrical glass samples loaded in diametral compression using a Split-Hopkinson Pressure Bar setup. They propose two linear dynamic increase functions (DIF) within the ranges (1)  $10^{-5} \text{ s}^{-1} \leq \dot{\epsilon} \leq 3.5 \cdot 10^2 \text{ s}^{-1}$  and (2)  $3.5 \cdot 10^2 \text{ s}^{-1} < \dot{\epsilon}$ , which were fitted to individual measurements (not mean values). It is the only study found where a sudden increase in strength is seen. However, the related strain rates are also higher than what was reported by other researchers. Similar experi-

ments were performed by PERONI et al. at two strain rates,  $3.8 \cdot 10^{-5} \text{ s}^{-1}$  and  $5.5 \cdot 10^1 \text{ s}^{-1}$ , also confirming a strain rate sensitivity, but with a lower slope, i.e. a higher value for  $n$  (cf. Appendix A, Table A.4 in Paper I), compared to the other data, which might indicate an approaching limit. This trend can be seen again for the dynamic fatigue data provided by MEYLAND et al. (2019), who investigated circular flat glass samples with two surface treatments, as-received and pre-damaged, in axisymmetric bending at 6-7 different strain rates. Furthermore, the data for the as-received glass samples are found to comply with the investigations conducted by NIE et al. (2010) on as-polished borosilicate<sup>3</sup> glass samples, as can be seen in MEYLAND and NIELSEN (2020). A general explanation for the observed strength enhancement with increasing strain rate is the decrease (or even absence) of the sub-critical crack growth effect. Since it takes time for water molecules to reach a crack tip, which is significantly reduced or not given by the rapid loading, the occurrence of crack growth is delayed or inhibited, causing higher crack resistance.

No special attention is given to the test environment for the data shown in Fig. 2.8. While an evident strain rate sensitivity is seen for the tensile strength of the glass, the effect of water in the surrounding medium, which is a controlling parameter in the sub-critical crack growth, is less prevailing. To highlight these environmental effects, Fig. 2.9 are two plots, which divide the relevant data from Fig. 2.8 into test environments that can be assumed decisive for the construction industry (around room temperature): (a) air (25-67 % RH) and (b) water (liquid or 100 % RH). In the estimation of the sub-critical crack growth parameter,  $n$ , the extreme data points were excluded by only considering values within the interval from the 2.5<sup>th</sup> to the 97.5<sup>th</sup> percentile, i.e. the interval of values containing the central 95 % of the data. Since the majority of these data points are mean values that are based on different sample sizes, the method of Weighted Least Squares (WLS) was used for the linear regression with  $\sqrt{N}$  as the weight factor, where  $N$  is the sample size that relates to each data point (provided in MEYLAND et al. 2021b). For instance, a single measurement is represented by  $N = 1$ . The resulting slopes of the linear regressions in Fig. 2.9, i.e.  $1/(n + 1)$ , determine  $n = 18.1$  for the glass tested in air and a slightly lower value of  $n = 16.5$  for the glass tested in water, which is due to an increase in the chemical reactivity (increased water content). These values are in accordance with the recommended conservative estimate  $n = 16$ , typically applied for the design of glass members for building (see e.g. HALDIMANN et al. 2008).

According to Eq. (2.10), it is unlikely to think of the glass strength decreasing or increasing continuously for strain rates approaching zero or infinity, respectively. A lower limit could be shown by GEHRKE et al. (1987), whereas an upper limit, as suggested by EVANS (1974), EVANS and JOHNSON (1975), and CHANDAN et al. (1978) (see Fig. 2.6), has not been well validated, although a small indication of it seems to be present in Fig. 2.9(a). Based on the aforementioned percentiles, estimates for these limits are given in Fig. 2.9. Both test environments result in identical lower limits with a value of  $\sigma_{f,d}/\sigma_0 = 0.65$ . The

<sup>3</sup>Borosilicate glass (BSG) has a different chemical composition than soda-lime-silica glass, offering very high resistance to temperature changes as well as very high acid resistance. Thus, it is used for special applications such as fire protection glazing and heat-resistant glazing or laboratory equipment.

2. Fracture Strength of Glass and the Significance of Load Duration

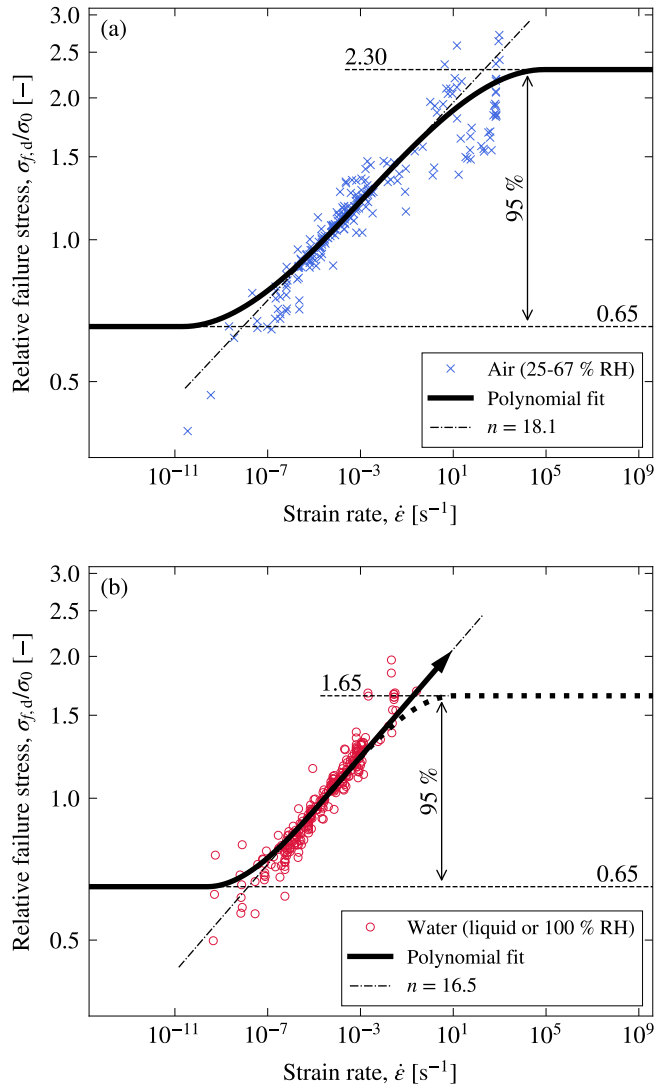


**Fig. 2.9** Cubic function fitted to the dynamic fatigue data from Fig. 2.8, divided into the test environments (a) air (25-67 % RH) and (b) water (liquid or 100 % RH). Due to an observed lack of data at high strain rates in (b), the arrow and dotted line indicate that a limit possibly is not reached. (from Paper I, MEYLAND et al. 2021a)

upper limit for the glass tested in air is 2.30, meaning that the strength increases by up to 130 % for  $\dot{\epsilon} \rightarrow 2.1 \cdot 10^2 \text{ s}^{-1}$  (following the linear regression), as compared to the reference tensile strength,  $\sigma_0$ . In comparison, the value of 1.65 for the glass tested in water seems relatively low. However, there is also no indication of asymptotic dynamic fatigue behaviour, therefore showing the dotted line in Fig. 2.9(b) together with an arrow indicating a possible further strength increase at higher strain rates. The data needed to determine the upper limit are lacking because it can be difficult to execute high strain rate experiments in a controlled water environment.

It is obvious from the reviewed dynamic fatigue data for soda-lime-silica glass that for both test environments highlighted, more tests are needed in the high strain rate regime; first, in air to rule out the disagreement in the dynamic fatigue curves, and then, in water to measure well-defined data. The low strain rate range needs further attention to obtain a more conclusive threshold strength limit. However, the focus of this work is high strain rate loading, as thus it is covered exclusively in the following chapters.

## 2.3 Normative Glass Strength Design

Structural engineers are usually bound by normative design guidelines (Standards), which maintain the required safety in the design of building structures. For the design of load-bearing glass members, there are numerous Standards, both embedded national and international. They all define the interrelationship between the load duration and the glass strength differently. A review of these different definitions is provided in this section for the most current Standards available. First, the concept of normative glass strength design is shortly introduced.

The analytical glass strength determination considering a single crack is not suitable for Standards because of the characteristic differences in surface flaws on glass products. Therefore, a characteristic bending strength is typically defined based on a deterministic approach, for example, as given by Eq. (2.1). In the framework of the Eurocode, the characteristic strength usually relates to a 5% probability of failure at the lower limit of the 95% confidence interval. For soda-lime-silica glass (annealed float glass), this value equals 45 MPa according to EN 572-1:2012. The characteristic strength is then modified based upon usage, load duration and other factors that relate to modifications to the basic glass product, e.g. edge/hole finish, surface profile, and pre-stress, to obtain a design bending strength. An example of a design formula for the bending strength of glass is given on the basis of the new European glass code, currently available as the Technical Specification CEN/TS 19100-1:2021:

$$f_{g,d} = \underbrace{k_e \cdot k_{sp} \cdot \lambda_A \cdot \lambda_1 \cdot k_{mod} \cdot \frac{f_{g,k}}{\gamma_M}}_{\text{Intrinsic glass strength}} + \underbrace{k_p \cdot k_{e,p} \cdot \frac{f_{b,k} - f_{g,k}}{\gamma_p}}_{\text{Surface pre-stress}} \quad (2.22)$$

Here, the total design bending strength is a sum of the intrinsic glass strength and eventual pre-stress (a compressive surface stress) from thermal or chemical strengthening. The characteristic bending strengths are denoted  $f_{g,k}$  and  $f_{b,k}$  for the basic glass product and the pre-stressed glass, respectively, and the related partial factors are  $\gamma_M$  and  $\gamma_p$ , respectively. The factors,  $k_e$ ,  $k_{sp}$ ,  $k_p$ , and  $k_{e,p}$ , account for the variations in strength due to modifications to the basic glass product, while  $\lambda_A$  and  $\lambda_1$  are factors related to size effects in strength (only applicable if a glass pane exceeds 18 m<sup>2</sup>). These strength modifying factors may be defined differently in other Standards. However, one they all have in common is a factor accounting for the load duration dependence. This strength reducing/enhancing load duration factor, denoted  $k_{mod}$ , is the normative representation of sub-critical crack growth effects in annealed float glass. It is expressed as the glass strength relative to a strength

## 2. Fracture Strength of Glass and the Significance of Load Duration

at a given reference load duration  $t_0$ , i.e.  $k_{\text{mod}}(t) = \sigma_f(t) / \sigma_{f0}$  (equals one when  $t = t_0$ ), a relationship that is compliant with Eq. (2.17). For pre-stressed glass,  $k_{\text{mod}}$  typically takes the value one because, at long-term quasi-static loads, no sub-critical crack growth occurs due to the presence of compressive surface stresses, which prevent cracks from opening. However, in case of extreme loads with very short duration, e.g. blast loading, where the compressive surface stress probably is exceeded, it would be appropriate to take into account a  $k_{\text{mod}}$  that is larger than one, as will be shown in Chapter 4.

A summary of the load duration factors for annealed float glass, as defined by the various Standards reviewed, is given in Fig. 2.10, where  $k_{\text{mod}}$  is plotted as a function of load duration in hours. For comparison, the static and dynamic fatigue data from Figs. 11 and 14 in Paper I (MEYLAND et al. 2021a) are included as well, which are supported additionally by an analytical relationship given by Eq. (2.17) with  $n = 16$ . The strain rates in the dynamic fatigue data are converted to load duration by assuming a constant loading rate as depicted in Fig. 2.5(b). Both experimental data and the analytical solution are normalised with a ‘60-second’ strength, which is shown to be a less conservative normalisation compared to the Standards.

The experimental data show to be well represented by Eq. (2.17), again confirming that  $n = 16$  is a reasonable choice for the design of structural glass members. When further examining the normative definitions of the glass strength’s load duration dependency, two approaches become evident:

- (1) A continuous function or a set of values that relate to such a function, which is based on the interrelationship between crack growth and stress intensity as derived by the empirical power law in Eq. (2.3) (EN 16612:2019; NEN 2608:2014; CEN/TS 19100-1:2021; ASTM E1300-16; AS 1288-2006; CNR-DT 210/2013), and
- (2) A more conservative approach (especially at the very short load duration,  $< 1$  s), where fixed values for given types of load configurations (e.g. long-term, medium-term, and short-term load duration) are defined, resulting in a step function (AS 1288-2006; DIN 18008-1:2010; DIN 18008-4:2013; ÖNORM B 3716-1:2016).

The Standards using the continuous function approach agree on the sub-critical crack growth parameter  $n = 16$ , while the choice of  $t_0$  is different, causing the seen deviations. The smaller the reference load duration is, the more conservative the estimate of the glass strength. In CNR-DT 210,  $t_0 = 0.67$  s is the reference, whereas AS 1288 and ASTM E1300-16 use 3 s. The longest reference load duration of 5 s is found in EN 16612 and NEN 2608. Overall, the Standards’ definition of the load duration dependency agrees with the experimental data (better matches can be obtained using a different reference load duration for the experimental data). However, no data are found to support the extrapolations provided for long-term lifetime predictions ( $> 1$  yr), often seen up to 50 years. In the dynamic range of load duration ( $20 \text{ ms} \leq t < 1$  s), EN 16612 and CEN/TS 19100-1 define an upper limit for  $k_{\text{mod}}$ , although the experimental data support an extrapolation into even shorter load duration. This could become relevant for the design of blast resilient glazing against small to large charges, e.g. person-borne or vehicle-borne explosives (DEL-

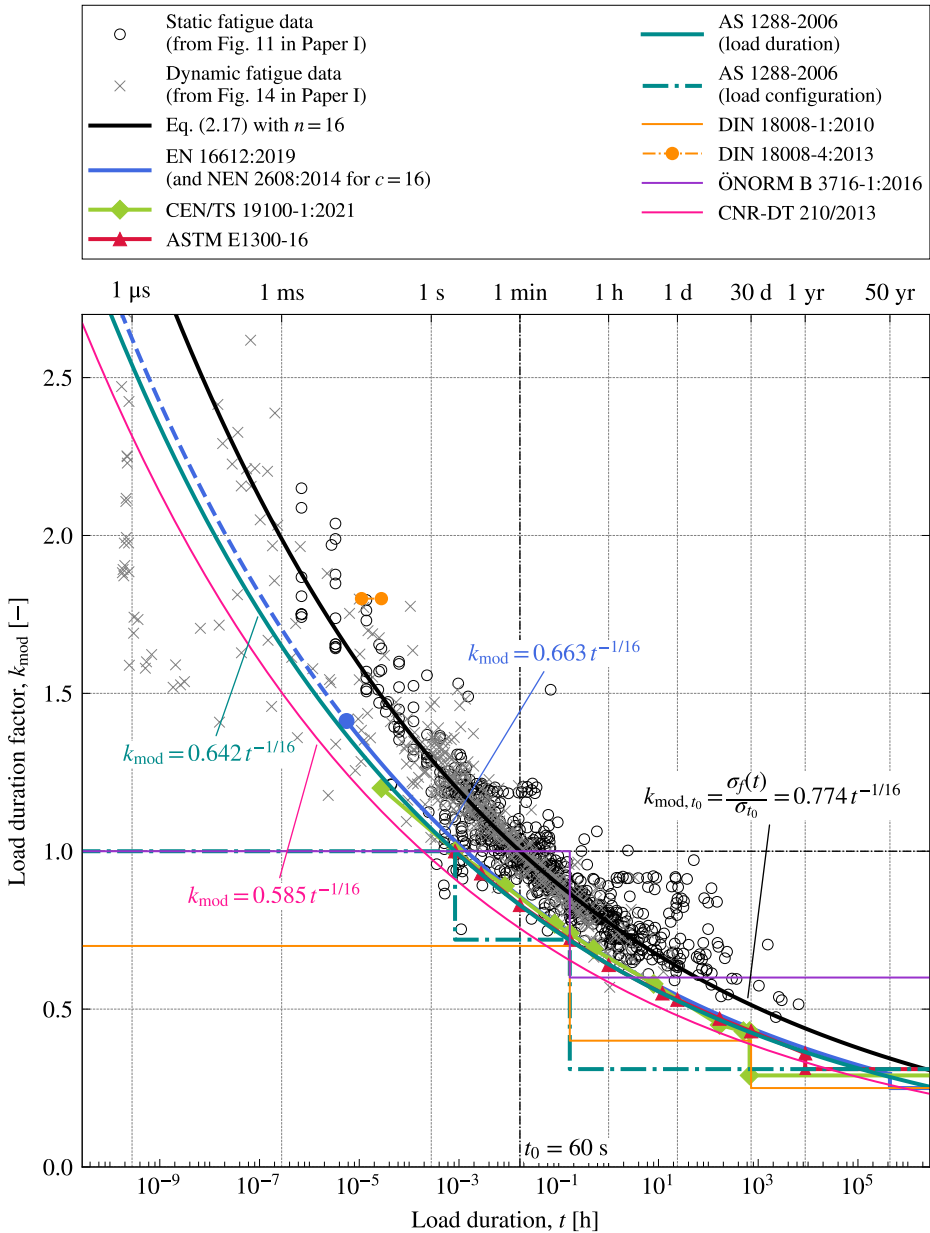


**Fig. 2.10** The load duration factor,  $k_{mod}$ , as defined by different Standards for annealed float glass compared to static and dynamic fatigue data from Paper I (MEYLAND et al. 2021a) as well as an analytical solution based on the relationship in Eq. (2.17).

## 2. Fracture Strength of Glass and the Significance of Load Duration

LIEU et al. 2018). The possibility of using higher values for  $k_{\text{mod}}$  for dynamic loading is provided in CEN/TS 19100-1, requiring that these are taken from a transparent and reproducible assessment that complies with the requirements of EN 1990:2002. Within the ASTM Standards, short-duration loads relevant for blast loading are covered by ASTM F2248-19, which defines an equivalent 3-second duration (the shortest duration in ASTM E1300-16, resulting in  $k_{\text{mod}} = 1$ ) design load; however, only valid for laminated glass.

The step function approach used by some of the Standards to express the glass strength's load duration dependency is much more conservative. While the points of step-changes coincide with both the experimental data and the continuous functions, the steps (the plateaus) are located conservatively apart from these. The most significant deviation to the values obtained from experiments is seen in the range of load duration below 1 s, meaning that the glass strength is determined with greater certainty there. For longer load duration, the step functions provide a better description of the glass strength. The impact of the presented variations in the load duration factor,  $k_{\text{mod}}$ , on the design of glass members is further emphasised in Paper I (MEYLAND et al. 2021a) in the example of a load duration of 100 ms.

## Experimental Methodology for High Strain Rate Testing

A literature review, subject of the previous Chapter 2, on experimentally obtained tensile strength data for soda-lime-silica glass showed a significant lack of data in the high strain rate regime, relevant to blast loading, and some disagreements among the studies reviewed. This chapter addresses Paper II, which covers the experimental methodology for high strain rate testing developed in this project to accommodate the identified needs. That is, to obtain a reliable understanding of the glass' mechanical properties, such as strength and stiffness, when subjected to high strain rate loading. First, some background on the high strain rate characterisation of materials is given with a focus on glass (Sec. 3.1). With an identified need for a new experimental test rig, the design of a modified version of the traditional Split-Hopkinson Pressure Bar (SHPB) setup and the related testing conditions are presented and discussed (Sec. 3.2). Finally, all experimental procedures and techniques established for the SHPB experiments on glass are outlined (Sec. 3.3) and the application of high-speed cameras is presented (Sec. 3.4).

This chapter addresses the findings reported in Paper II on page 201.

### 3.1 Background

The characterisation of engineering materials for structural applications usually takes place at quasi-static strain rates below  $10^{-1} \text{ s}^{-1}$  using conventional testing machines (see Fig. 1.7). If the load to design for is more extreme, higher strain rates up to  $10^2 \text{ s}^{-1}$  can be achieved using fast valves and gas reservoirs to pressurise an oil reservoir (a pneumatic-hydraulic system). Such a design often differs from the conventional by not having a closed-loop feedback control system of the loading conditions, which is difficult to include for short-duration loading. Thus, inherently making the strain rate more dependable on the relationship between machine and specimen stiffness (BISCHOFF and PERRY 1991). However, since the importance of inertia forces increases with the speed of loading, these special hydraulic testing machines reach a limit at some point, which is not directly related to the machine design but the sensors measuring the load application. Typically, conventional load cells are included, which start to vibrate severely when the load application is too rapid, making reliable measurements difficult. For instance, this is reported by KÖNIG (2012) and MEYLAND et al. (2019) in their dynamic glass strength investigations at strain rates up to  $10^1 \text{ s}^{-1}$ . Going higher in strain rate, these challenges can be overcome using a Split-Hopkinson Pressure Bar (SHPB), which is well-known and frequently applied for high strain rate testing of materials between  $50 \text{ s}^{-1}$  and  $10^4 \text{ s}^{-1}$ , depending on the sample size (NEMAT-NASSER 2000; CHEN and SONG 2011).

### 3. Experimental Methodology for High Strain Rate Testing

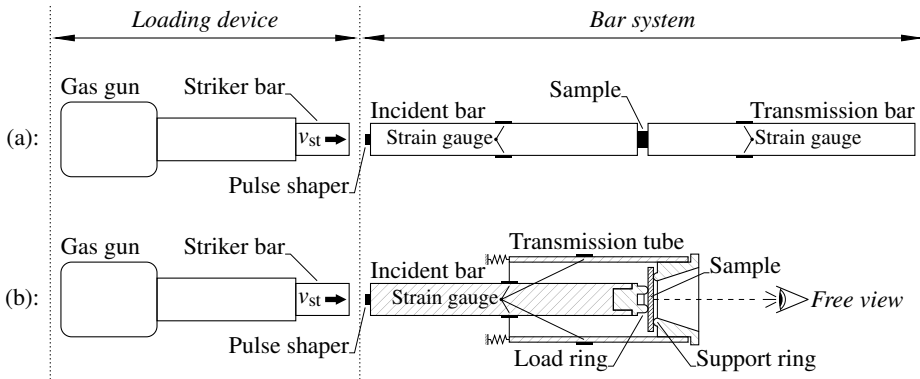


**Fig. 3.1** The traditional Split-Hopkinson Pressure Bar design in (a) compared to a modified design in (b), developed and employed in the present study.

The first steps into such material testing technique were pioneered by JOHN HOPKINSON (1872) and his son, BERTRAM HOPKINSON (1914), the inventor of the pressure-bar method. Further important contributions were made by ROBERTSON (1921), LANDON and QUINNEY (1923), and DAVIES (1948), leading to the design of today's known Split-Hopkinson Pressure Bar, devised originally by KOLSKY (1949); therefore, also named 'Kolsky bar'. The basic concept involves a material sample that is placed between two elastic bars, denoted incident bar and transmission bar, as schematically shown in Fig. 3.1(a). An external load is then exerted on the incident bar, typically with a gas gun that launches a striker bar. The impact generates a compressive stress wave that travels towards the sample, loading it at high strain rates. Part of the wave reflects at the interface between the incident bar and the sample, whereas the rest transmits through the sample into the transmission bar. A measurement of the material's stress/strain response is provided by analysing the recorded strains in the bars. For different strain rates, the impact velocity and the specimen size may be varied.

The Split-Hopkinson Pressure Bar also does not have a closed-loop feedback control system, making real-time adjustments of the loading conditions applied to the sample impossible. Usually, the stiffness ratio between the used bars and the sample is low, making the sample stiffness critical to consider in the experiment design. Due to the missing feedback control, the desired testing conditions can only be achieved iteratively. However, the material sample response is initially unknown. Therefore, the design of an SHPB experiment can become rather complex.

Several techniques have been employed within the glass and ceramics research community using the Split-Hopkinson Pressure Bar to investigate the material's strain rate sensitivity to tensile stresses. PERONI et al. (2011) and ZHANG et al. (2012) tested cylindrical soda-lime-silica glass samples in diametral compression (split tensile test or Brazilian test) with the original SHPB design, similar to what is shown in Fig. 3.1(a). However, a different stress state is expected in thin-walled glass panes subjected to transient loading from ex-

plosion shock waves that instead relate to bending induced stresses. A convenient setup introducing such a stress state was developed by CHENG et al. (2002), who employed a modified piston-on-three-ball test configuration to study thin ceramic substrates dynamically in flexure. Borosilicate glass became the subject of a series of investigations, in which rectangular samples were tested in a four-point bending fixture and circular samples in a ring-on-ring test configuration (NIE et al. 2009; NIE et al. 2010; NIE and CHEN 2012). Based on the findings reported, the ring-on-ring test configuration showed to be the preferred choice. This is because the axisymmetric bending minimises stressing of a sample's edge (see stress distribution in Fig. 3.2) where typically more severe defects are located due to cutting, causing an unwanted strength reduction. With maximum constant stresses in the sample centre within the load ring, edge failures are thus less likely to occur, providing a more reliable measure of the surface strength.

Testing materials at high strain rates typically happens in the range of microseconds. In such a short time frame, many processes become impossible to assess with standard laboratory equipment. Therefore, the application of high-speed cameras and the Digital Image Correlation (DIC) technique for non-contact optical measurements have been established as a general practice within the field of dynamic material characterisation (TSUJI 2018). These techniques enable the study of failure/fracture processes and displacement/strain fields in length scales ranging from microns to meters (SUTTON et al. 2009), thereby adding information to the material other than strength, e.g. determined from SHPB experiments. However, their application to a bend test configuration arranged in a traditional SHPB design is challenging because the sample surfaces are hidden by the bars, making them not visible for cameras.

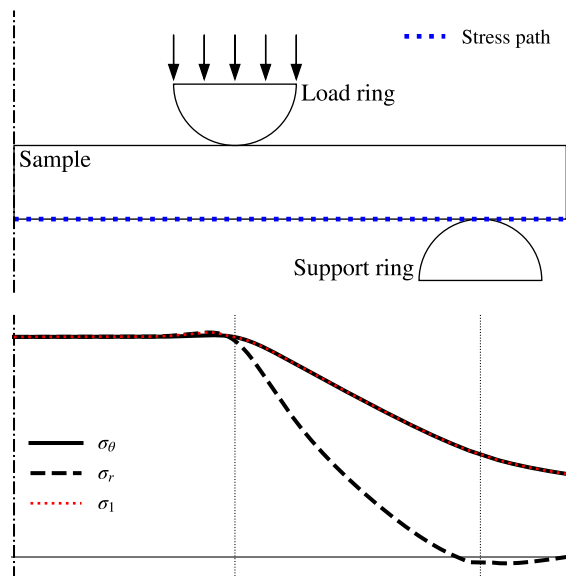


**Fig. 3.2** The equibiaxial stress state for small deflections in a circular sample loaded in a ring-on-ring test configuration ( $\sigma_\theta$  is the tangential stress;  $\sigma_r$  is the radial stress;  $\sigma_1$  is the first principal stress).

The present study intends to investigate the flexural behaviour of flat, circular soda-lime-silica glass samples at high strain rates ( $> 10^1 \text{ s}^{-1}$ ); see more in Chapter 4. Therefore, the following sections introduces a novel design of an experimental setup, as illustrated in Fig. 3.1(b), that encompasses the aforementioned needs and challenges by a modification of the well-known SHPB design.

### 3.2 A Modified Split-Hopkinson Pressure Bar

In an SHPB setup, three main parts are crucial to the design: (i) a loading device, (ii) a bar system, and (iii) a data acquisition system. Very little has changed in this regard in the modified version, as evident in the comparison provided in Fig. 3.1. Since the new experimental setup requirement is to enable the application of high-speed cameras to detail the glass' behaviour in an axisymmetric bending fixture, only a reinvention of the bar system is performed. An unobstructed view of the sample's centre is established by replacing the traditional transmission bar with a tube having the incident bar going through. The interchangeable ring-on-ring test configuration is placed at the end furthest away from the loading device with the smaller load ring mounted to the 1.99 m-long incident bar and the larger support ring to the 1.35 m-long transmission tube, as shown in Fig. 3.3 together with bar and tube diameters. The highlighted ring dimensions are determined according to ASTM C1499-15 for a sample with dimensions  $\varnothing 45 \text{ mm} \times 3 \text{ mm} \pm 1 \text{ mm}$ . A conical through-going hole in the support ring exposes approximately 54 % of the sample's tensile surface, which corresponds to an area of  $855 \text{ mm}^2$ . All setup parts making up the complete bar/tube system are fabricated from a high-strength aluminium alloy (Alumec 89<sup>®</sup> – a 7000 series alloy) with a stiffness similar to glass. The striker bars, in lengths 250 mm and 500 mm, have the same cross-section as the incident bar. The whole setup is constructed on top of a 4 m-long HEB steel beam, as shown in Fig. 3.4. Further details to the setup construction can be found in Paper II and a selection of technical drawings is provided in Appendix A, Sec. A.1.

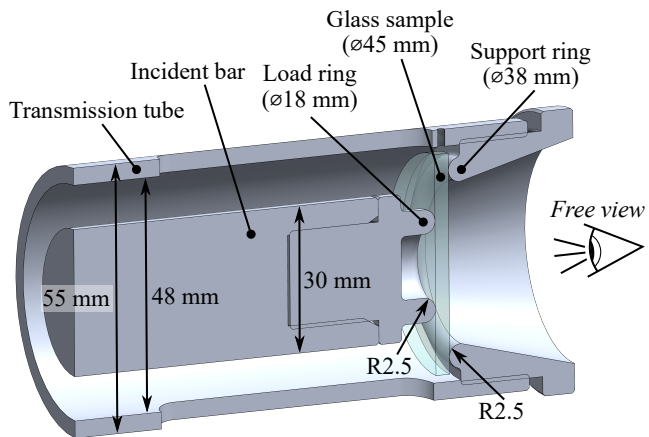


**Fig. 3.3** Detailed view, section through the centre, of the ring-on-ring test configuration located at the furthest end of the setup away from the loading device and mounted to the bar/tube system. (adapted from Paper II)

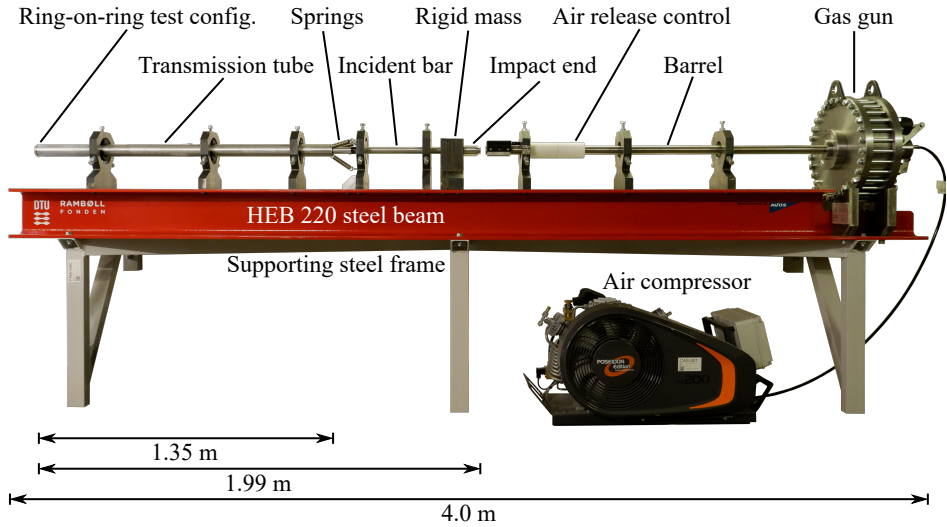


**Fig. 3.4** A photo of the modified SHPB setup with the main parts highlighted. (from Paper II)

### 3.2.1 Testing Conditions

In an experiment with the modified SHPB, a fast opening gas gun pressurised with air (details to the valve mechanism can be seen in Appendix A, Sec. A.1) launches a 500 mm-long striker bar on the incident bar with a pulse shaper placed on its impact end (elaborated in Sec. 3.3.3). The impact generates a shaped compressive stress wave<sup>1</sup>, the incident pulse, that travels towards the ring-on-ring test configuration with a loading duration proportional to the striker bar length and a speed corresponding to the elastic wave speed of the bar/tube material,  $C_0$ . Assuming one-dimensional elastic wave propagation,  $C_0$  is determined from the Young's modulus,  $E_b$ , and density,  $\rho_b$ , of the bar/tube material (see e.g. MEYERS 1994):

$$C_0 = \sqrt{\frac{E_b}{\rho_b}} \quad (3.1)$$

When the incident pulse encounters the glass sample, part of the wave reflects at the load ring/sample interface due to a wave impedance mismatch. The rest transmits through the glass, on the support ring and into the transmission tube until the sample fails. Consequently, three pulses in the propagating strains/stresses in the bar/tube system can be identified as highlighted in Fig. 3.5, showing a typical record by strain gauges on the bar and tube surface (see Sec. 3.3.1):

1. the incident pulse,  $\varepsilon_i$  or  $\sigma_i$ ,

<sup>1</sup>Without a pulse shaper, the stress wave generated by the impact is analytically predictable. However, due to the limited application in the present experiments, it will not be discussed further here; for details, the reader is referred to, e.g. CHEN and SONG (2011).

### 3. Experimental Methodology for High Strain Rate Testing

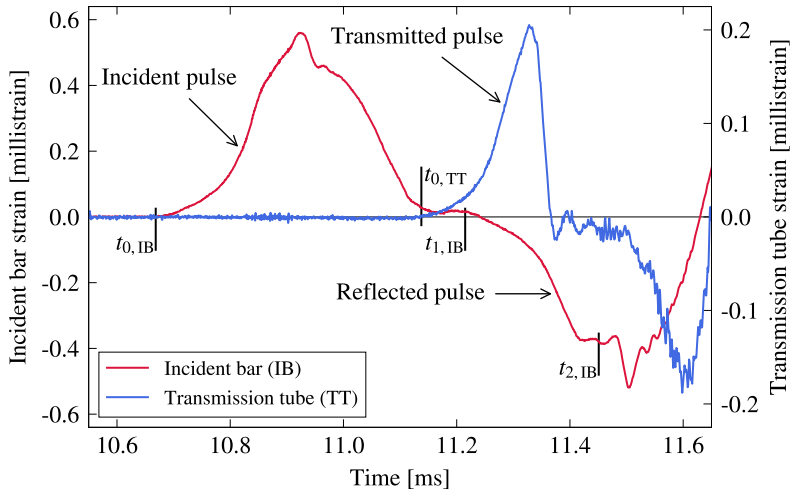


**Fig. 3.5** A representative example of recorded strain signals in the incident bar and the transmission tube from an experiment on an annealed float glass sample with the 500 mm-long striker bar launched at  $v_{st} \approx 6 \text{ m s}^{-1}$ . The experiment used a pulse shaper as described in Sec. 3.3.3. The times indicated are the arrival times of the stress waves at the strain gauges.

2. the reflected pulse,  $\varepsilon_r$  or  $\sigma_r$ , and
3. the transmitted pulse,  $\varepsilon_t$  or  $\sigma_t$ .

These three pulses determine the material response to high strain rate loading. However, they were recorded before and after the sample deformation took place, due to the strain gauges distance to the sample, as illustrated in Fig. 3.1(b). Therefore, proper time synchronisation is necessary for the data post-processing, which turns out to be a critical part of SHPB experiments, as it more or less relies on the experimenter's judgement of the incident pulse's starting point (CHEN and SONG 2011). Since the complex geometry of the ring-on-ring test configuration makes the determination of the time difference between the starting points of the incident and transmitted pulse difficult, both have to be estimated. These are denoted  $t_{0,IB}$  and  $t_{0,TT}$ , respectively, as shown in Fig. 3.5. Based on the starting point of the incident pulse, the corresponding starting point of the reflected pulse,  $t_{1,IB}$ , can be estimated by:

$$t_{1,IB} = t_{0,IB} + \frac{2(L_{IB} - x_{sg,IB})}{C_0} \quad (3.2)$$

where  $L_{IB}$  is the total length of the incident bar measured from the impact end to the tip of the load ring, and  $x_{sg,IB}$  is the position of the strain gauge (details in Sec. 3.3.1) also measured from the impact end. However, in the time synchronisation of the experiments, it has become apparent that Eq. (3.2) causes a slight overestimation of up to  $10 \mu\text{s}$ , which is taken into account in the post-processing. This can be related to the fact that the incident

bar is not purely cylindrical, as assumed in Eq. (3.2). Furthermore, due to the relatively short incident bar chosen for the setup ( $L_{IB} = 1.99\text{m}$ ), a signal overlap in the rear portion of the reflected pulse might become critical, depending on the pulse duration. Therefore, an additional assessment of the incident pulse after its second reflection at the impact end is vital in these experiments. Based on the starting point of the reflected pulse, the time for its third arrival at the strain gauge,  $t_{2,IB}$ , can be estimated by the following expression:

$$t_{2,IB} = t_{1,IB} + \frac{2x_{sg,IB}}{C_0} \quad (3.3)$$

From the example shown in Fig. 3.5, which is representative for the experiments conducted in this study, the starting point of the signal overlap in the reflected pulse is located slightly after glass fracture took place, i.e. the duration  $t_{2,IB} - t_{1,IB}$  is longer than the duration of the transmitted pulse. An overlap could have been prevented by using a longer incident bar. However, in its current application, the identified signal overlap is shown not to be critical in the determination of the glass' response to high strain rate loading.

Once proper time synchronisation is established between the three pulses, the resulting forces at the loading and supporting side of the glass sample,  $F_{LR}$  and  $F_{SR}$ , can be determined as follows:

$$F_{LR} = E_b A_{IB} (\varepsilon_i + \varepsilon_r) \quad (3.4)$$

$$F_{SR} = E_b A_{TT} \varepsilon_t \quad (3.5)$$

where  $A_{IB}$  and  $A_{TT}$  are the cross-sectional areas of the incident bar and the transmission tube, respectively. The determination of a glass sample's failure load using Eqs. (3.4) and (3.5) requires that a dynamic force equilibrium has been established across the sample, i.e.  $F_{LR} \cong F_{SR}$ . However, since the sample is initially at rest, it takes time to build up nearly equilibrated forces, which is not directly given at the rapid loading. A typical dynamic force equilibrium check is exemplified in Fig. 3.6(a), where the shown force histories are determined from the signals in Fig. 3.5 using Eqs. (3.4) and (3.5).

An overall good agreement is seen between the two force histories during the entire loading period. However, some oscillations are present on the load ring side, which do not appear on the support ring side. They were most likely caused by stress wave reflections in the load ring section, modifying the reflected pulse on the way back to the impact end, not affecting the loading of the glass sample. Looking further at the signal amplitudes of the incident and reflected pulse in Fig. 3.5, only a minor difference can be noticed. This indicates a sample with a low force amplitude relative to the incident pulse, making it a "weak" sample. Since the force history on the load ring side is determined by adding together the incident and reflected pulse (with opposite signs), possible noise in the signal caused by the geometrical modifications in the incident bar may have been amplified due to the weak sample response, further explaining the emerging oscillations.

In a quantitative manner, the dynamic force equilibrium can be checked using the follow-

### 3. Experimental Methodology for High Strain Rate Testing

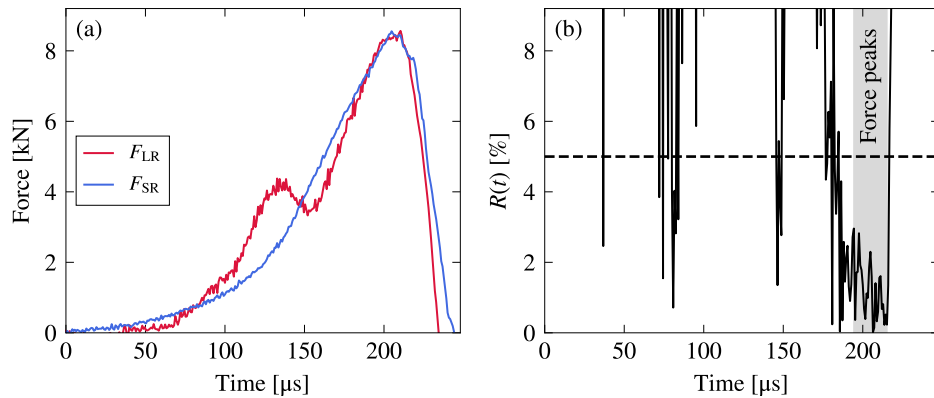


**Fig. 3.6** Example of a dynamic force equilibrium check based on the signals shown in Fig. 3.5: (a) comparison of the force histories  $F_{LR}$  and  $F_{SR}$ , and (b) the equilibrium check using Eq. (3.6).

ing equation (RAVICHANDRAN and SUBHASH 1994):

$$R(t) = \left| \frac{\Delta F(t)}{F_m(t)} \right| = 2 \left| \frac{F_{LR} - F_{SR}}{F_{LR} + F_{SR}} \right| \quad (3.6)$$

which determines the ratio of the force difference between the sample's surfaces,  $\Delta F$ , to the mean force within the sample,  $F_m$ . The forces can be considered equilibrated when  $R(t) \leq 5\%$  (RAVICHANDRAN and SUBHASH 1994). This check is performed in Fig. 3.6(b) for the force histories in Fig. 3.6(a). The limit of 5% cannot be met around the observed oscillations in  $F_{LR}$ , which is also not considered critical because it is believed that the loading of the glass sample is not affected by the fluctuations, as shown later in Sec. 3.4. However, considering the time range  $\pm 10\mu s$  around the force peaks (highlighted in grey), the equilibrium check yields satisfactory results. This leaves the conclusion that the forces acting on the glass sample are in equilibrium at failure, allowing the calculation of a sample's failure load with Eqs. (3.4) and (3.5).

When the dynamic force equilibrium in the sample is achieved, the further characterisation of the glass is, however, entirely based on the force history from the support ring side, i.e. Eq. (3.5). This is straightforward and more accurate than the load ring side, where signals need to be added and contain oscillations.

#### 3.2.2 Alignment of the Bar/Tube System

Reliable and precise measurements with the modified SHPB require a good bar/tube system alignment. Along the steel beam on which the entire setup is built, the incident bar and the transmission tube are held in place by supports, as shown in Appendix A, Sec. A.1. Linear bearings are included for the bar and 3D-printed brackets with ball bearing for the tube, both securing minimal friction in horizontal movements. To make the necessary adjustments, each support holds the bar/tube with three bolts that can modify its posi-

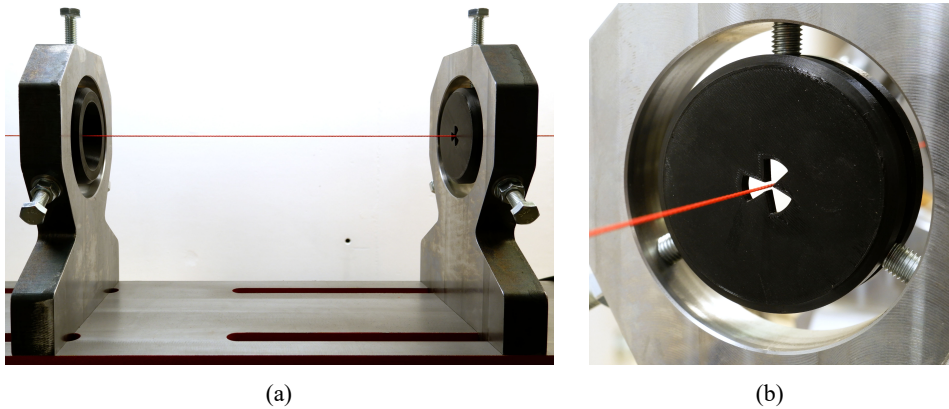


**Fig. 3.7** Photos of the alignment procedure used for the bar/tube system: (a) a side view showing the cord passing two bar/tube supports, and (b) a close-up of one of the 3D-printed crosshairs.

tion. Inside the tube, the incident bar is supported by in-house fabricated, low friction PTFE (polytetrafluoroethylene) bearings, also shown in Appendix A, Sec. A.1. Before the placement of the bar/tube system, the alignment of the supports was performed using a cord, which was tensioned from the gas gun, through the barrel and each support, to the last support furthest away. At each support, a 3D-printed crosshairs with the same outer geometry as the actual bearings/brackets was placed, helping to align the supports centred around the cord. Some photos detailing the procedure are given in Fig. 3.7. Paper II concludes that this procedure resulted in a good alignment, which was checked through an unshaped incident pulse and a FEM simulation being a measure for the perfect alignment.

### 3.3 Experimental Procedures and Techniques

Several experimental procedures and techniques are necessary to consider for the high strain rate characterisation of the soda-lime-silica glass using the modified SHPB. These are outlined in the following; some in more detail than the others as Paper II does not provide all details.

#### 3.3.1 Data Acquisition System

All the data measured in the experiments were acquired with a multifunction I/O device (National Instruments USB-6356 (BNC)) controlled via LabVIEW NXG 5.0. That is, the exit velocity of the striker bar and the strains in the incident bar and the transmission tube.

#### Striker Bar Exit Velocity Measurement

An in-house fabricated velocity measurer with two photogates was mounted to the barrel's muzzle. The striker bar's exit velocity was determined by the time it took to pass the two photogates with a mutual distance of 50 mm. A high-speed camera placed perpendicular to the barrel's muzzle verified the velocity measurer. The exit velocity was controlled

### 3. Experimental Methodology for High Strain Rate Testing

by changing the striker bar's position inside the barrel and/or the gas gun's air pressure. In the present study, the 500 mm-long striker bar was placed 10 cm inside the barrel, and the pressure was set between 3 bar and 3.5 bar to measure a striker bar velocity,  $v_{st}$ , of approximately  $6 \text{ m s}^{-1}$ . Also, the photogates of the velocity measurer triggered the data acquisition system.

#### Strain Measurements

The core measurements in the experiments with the modified SHPB are the strains in the incident bar and the transmission tube because they provide the necessary information to characterise the glass strength at high strain rates. However, the geometrical complexities introduced, as presented in Sec. 3.2, can influence their propagation and thus the decision of where to place the strain gauges used to measure them. Therefore, Paper II presents a FEM model of the experiment with a 500 mm-long striker bar, which simulates the characteristics of the propagating strains. Based on the numerically determined peak strains in the incident, reflected, and transmitted pulse, no significant changes in the strains are reported between 0.4 m and 1.3 m on the incident bar (measured from the impact end), and between 0.2 m and 0.75 m on the transmission tube (measured from the sample's tensile surface). Within these ranges, the strain gauges can be positioned reliably.

Diagonal Wheatstone half-bridge circuits were chosen for the strain measurements, with two  $120 \Omega$  strain gauges each on the rod and the tube attached on the surface towards each other; see Fig. 3.1(b). On the bar they were placed at  $x_{sg,IB} = 60.0 \text{ cm}$  and on the tube at  $x_{sg,TT} = 62.3 \text{ cm}$ . The off-centred position on the incident bar was chosen to maximise the time between the incident and reflected pulse. Since the voltage output from the Wheatstone bridges is of small amplitude, a high-speed transducer amplifier (FYLDE FE-H379-TA) was used to condition the signals for accurate data acquisition. Before the execution of the experiments, the amplifier was shunt calibrated<sup>2</sup> following the procedure outlined in Appendix A, Sec. A.2. The experiments used a sampling rate of 1.25 MHz, which was the limit of the multifunction I/O device.

#### 3.3.2 Setup Calibration

The post-processing of the strains acquired from the experiments with the modified SHPB depends on the material properties of the bar/tube system. That is, the Young's modulus ( $E_b$ ), the density ( $\rho_b$ ), and the elastic wave speed ( $C_0$ ), whose relationship is given by Eq. (3.1). These quantities need to be calibrated carefully from experiments, as any error that might evolve is directly found in the determined stress/strain response of the tested material sample (see e.g. LIFSHITZ and LEBER 1994). The calibration is reported in Paper II and the resulting material properties are given in Table 3.1. A summary of data related to the experimental determination of  $C_0$  can be found in Appendix A, Sec. A.3. Compared to the datasheet values provided for the high-strength aluminium alloy (Alumec 89<sup>®</sup>), the calibrated values of the density and the Young's modulus deviate with  $-0.2\%$  and  $2.2\%$ , respectively.

---

<sup>2</sup>Simulation of a bridge output signal by shunting one arm of a bridge by a resistor of known size.

$\rho_b$	$C_0$	$E_b$
2823.6 kg m <sup>-3</sup>	5086.4 m s <sup>-1</sup>	73.051 GPa

**Table 3.1** Calibrated material properties of the high-strength aluminium alloy used for the modified SHPB.

### 3.3.3 Pulse Shaping

In an SHPB experiment, when the striker bar directly impacts the incident bar, a trapezoidal-shaped incident pulse with high-frequency oscillations in the plateau is created (shown later in Fig. 3.14(a)). Depending on the material response, such loading can become inappropriate for achieving stress equilibrium and constant strain rate deformation in the sample. For example, brittle materials such as glass fracture at small elastic strains (without subsequent plastic deformation), resulting in very short loading times, in which dynamic stress equilibrium is difficult to achieve. The desired equilibrium and constant loading rate in the characterisation of the glass can thus be facilitated by having an incident pulse with increased rising time (a ramp history), preferably matching the material response (SUBHASH and RAVICHANDRAN 2000; FREW et al. 2001; FREW et al. 2002; CHEN and SONG 2011; NAGHDABADI et al. 2012).

The research community has developed several pulse shaping techniques, summarised in detail by CHEN and SONG (2011). However, one that became dominant over the years is the use of a thin, ductile metal disc, named *pulse shaper*, which is placed on the impact end of the incident bar, as shown in Fig. 3.1. Such disc can be varied in thickness, diameter, and material to obtain the desired pulse shape. First developments in the analytical description of the deformation process of the pulse shaper were made by NEMAT-NASSER et al. (1991), and that work was later on extended and improved by FREW et al. (2001) and FREW et al. (2002). The use of copper for the pulse shaper is a commonly seen practice (FREW et al. 2001; FREW et al. 2002; NIE et al. 2007; NIE et al. 2009; NIE et al. 2010; NIE and CHEN 2012; ZHANG et al. 2012; NIE and CHEN 2013; ERIKSEN 2014). Since the material has been shown to perform well, it is also employed in the present work to shape the incident pulse. The following presents the application of this pulse shaping technique.

#### Pulse Shaper Model

The model described is based on the work from NEMAT-NASSER et al. (1991) and FREW et al. (2002). Fig. 3.8(a) is a schematic illustration of the loading end of an SHPB setup with a pulse shaper attached to the incident bar. The initial geometry of the pulse shaper is defined by the cross-sectional area,  $a_0$ , and the thickness,  $h_0$ . The striker bar ( $\rho_{st}$ ,  $C_{0,st}$ ,  $A$ ) impacts the pulse shaper with the velocity  $v_{st}$ , and compressive forces are gradually transferred to the incident bar ( $\rho_b$ ,  $C_0$ ,  $A$ ,  $E_b$ ). While the pulse shaper deforms, its load-carrying capacity increases due to the increasing cross-sectional area and the strain hardening of the material. The increase in load-carrying capacity extends the duration of the incident pulse.

In the plastic deformation of the pulse shaper, the resulting axial engineering strain,  $\varepsilon_p(t)$ , is given by:

$$\varepsilon_p(t) = \frac{h_0 - h(t)}{h_0} = 1 - \frac{h(t)}{h_0} \quad (3.7)$$

### 3. Experimental Methodology for High Strain Rate Testing

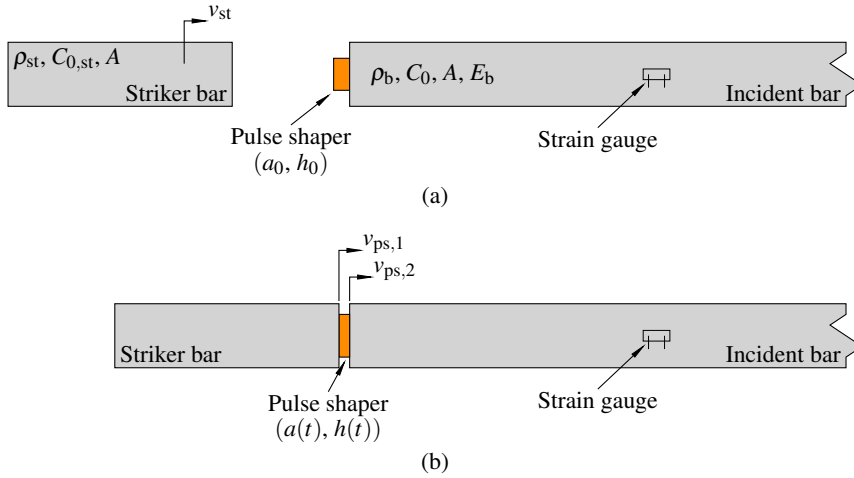


**Fig. 3.8** A schematic of the loading end of an SHPB setup with a pulse shaper: (a) before loading the pulse shaper, and (b) during loading of the pulse shaper. (after FREW et al. 2002)

with  $h(t)$  being the current thickness of the pulse shaper. Further, the related true axial stress,  $\sigma_p$ , is assumed to follow a one-dimensional stress-strain relationship of the form:

$$\sigma_p = \sigma^* \cdot g(\varepsilon_p) = \sigma^* \cdot \frac{\varepsilon_p^n}{1 - \varepsilon_p^m} \quad (3.8)$$

where  $\sigma^*$  is a stress constant and  $g(\varepsilon_p)$  is a function of the pulse shaper axial engineering strain. The impact on the pulse shaper generates a reverse-travelling compressive wave in the striker bar. Based on the first wave reflection in the striker bar, the loading strain in the pulse shaper,  $\varepsilon_p(t)$ , can be calculated from:

$$t = \frac{h_0}{v_{st}} \int_0^{\varepsilon_p} \left[ 1 - K \left( \frac{1}{\rho_b C_0} + \frac{1}{\rho_{st} C_{0,st}} \right) \frac{g(x)}{1-x} \right]^{-1} dx, \quad (3.9a)$$

$$\text{for } 0 \leq t < \tau$$

with

$$K = \frac{\sigma^* a_0}{A v_{st}} \quad \text{and} \quad \tau = \frac{2L_{st}}{C_{0,st}} \quad (3.9b)$$

where  $A$  is the cross-sectional area of both the striker bar and the incident bar,  $\tau$  is the time for two wave transits in the striker bar,  $L_{st}$  is the length of the striker bar, and  $C_{0,st}$  is the elastic wave speed of the striker bar material. Eq. (3.9a) is only valid as long as the pulse shaper does not deform plastically beyond the bar surfaces, i.e.  $a(t) \leq A$ .

The deformation of the pulse shaper may continue for multiple wave transits in the striker

bar. Therefore, the total strain as a function of time is defined as follows:

$$t = n\tau + \frac{h_0}{v_{st}} \int_{\varepsilon_p^n}^{\varepsilon_p} \left[ 1 - K \left( \frac{1}{\rho_b C_0} + \frac{1}{\rho_{st} C_{0,st}} \right) \frac{g(x)}{1-x} - \frac{2K}{\rho_{st} C_{0,st}} \sum_{k=1}^n \frac{g(\varepsilon_p(t-k\tau))}{1-\varepsilon_p(t-k\tau)} \right]^{-1} dx, \quad \text{for } n\tau \leq t < (n+1)\tau \quad (3.10)$$

where  $\varepsilon_p^n$  is the strain in the pulse shaper at  $t = n\tau$ , and  $n$  is the number of wave transits in the striker bar (back and forth counts as one). Again, the pulse shaper is not allowed to expand beyond the bar surfaces. In addition, Eq. (3.10) is only applicable as long as the pulse shaper deforms in compression. In terms of the particle velocities at the pulse shaper/bar interfaces shown in Fig. 3.8(b) (defined by Eqs. (24a) and (24b) in FREW et al. (2002)), this means  $(v_{ps,1} - v_{ps,2}) \geq 0$ . When  $v_{ps,1} < v_{ps,2}$ , the pulse shaper is assumed to unload elastically, and thus another set of equations is to be applied. Since only the compressive deformation of the pulse shaper is focused on in the following, further details to the unloading model can be found in FREW et al. (2002).

Eqs. (3.9a) and (3.10) require that the pulse shaper material response defined by Eq. (3.8) is known. For that, a series of pulse shaping experiments using different combinations of pulse shaper dimensions, striker bar lengths, and striking velocities, must be conducted. Using an end-point method<sup>3</sup>, the final axial engineering strain in the tested pulse shaper is determined from Eq. (3.7). The peak strain or stress from the measured incident pulse,  $\max(\varepsilon_i)$  or  $\max(\sigma_i)$ , is then extracted to determine the true axial stress,  $\sigma_p$ , using Eq. (3.11):

$$\sigma_p = \frac{E_b A}{a_0} (1 - \varepsilon_p) \max(\varepsilon_i) = \frac{A}{a_0} (1 - \varepsilon_p) \max(\sigma_i) \quad (3.11)$$

Once data points are obtained over a broad range of  $\varepsilon_p$ , Eq. (3.8) is fitted with the least squares method to obtain the parameters  $\sigma^*$ ,  $n$ , and  $m$ .

Since the pulse shaper model aims to predict a stress-time curve in the incident bar, the true axial strain in the pulse shaper,  $\varepsilon_p(t)$ , calculated from Eqs. (3.9a) and (3.10) needs to be converted into axial stresses in the bar as follows:

$$\sigma_i(t) = \sigma_{st}(t) = \frac{\sigma^* a_0}{A} \frac{g(\varepsilon_p)}{1 - \varepsilon_p} \quad (3.12)$$

By knowing the response of the material chosen for shaping the incident pulse, one can now design a pulse shaper that meets the desired experimental conditions by varying the disc dimensions, the striker bar length and the striking velocity.

<sup>3</sup>A method that determines the pulse shaper response from its final deformed state after test.

**Pulse Shaper Material Response**

The following determines the response of annealed Cu-DHP (CW024A – R240, cf. EN 1652:1998) copper, the material chosen for the pulse shapers employed in the high strain rate material characterisation of flat glass samples outlined in Chapter 4.

Pulse shapers in diameter,  $d_0$ , from 2 mm to 15 mm were punched and laser cut from copper sheets of thicknesses 1, 2, 3, 4, and 5 mm, resulting in thickness-to-diameter ratios from 0.07 to 1.00. The as-received copper discs were heated for approx. 2 h at 500 °C to obtain the annealed condition. In total, 44 tests were conducted to calibrate the resistance function given by Eq. (3.8). The various pulse shaper geometries were tested with varying striker bar lengths and striking velocities to obtain data over a broad range of  $\epsilon_p$ . The final pulse shaper data are plotted in Fig. 3.9 together with the fitted resistance function with  $\sigma^* = 553.0\text{MPa}$ ,  $n = 0.3008$ , and  $m = 4.815$ . A detailed summary of the pulse shaper experiments can be found in Appendix A, Table A.2.

The applicability of the pulse shaper model using the calibrated resistance function of the annealed Cu-DHP copper is examined by comparison with experimentally obtained incident pulses. In Fig. 3.10, results from two different pulse shaper experiments are shown together with the model predictions. Since it is vital to properly shape the rise of the incident pulse when testing brittle materials, only the compressive loading of the pulse shaper is considered in the predictions.

Overall, the shown data agree satisfactory with the model, verifying the applicability of the fitted resistance function to design a pulse shaper of the annealed Cu-DHP copper. However, the very beginning in both incident stress-time predictions does not follow the

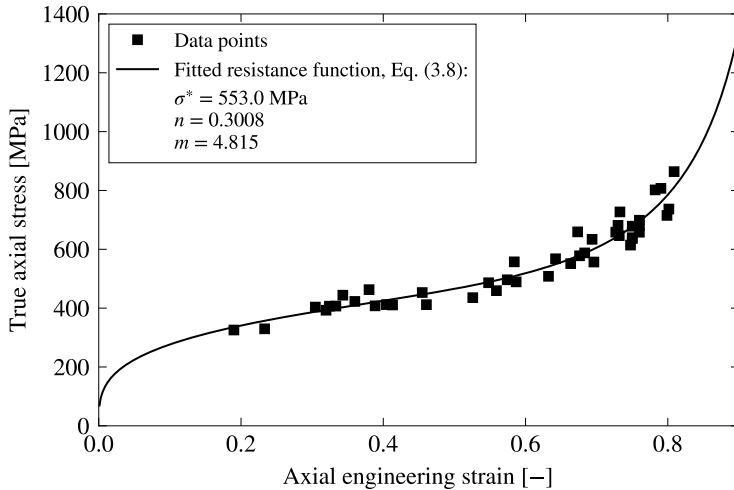


**Fig. 3.9** Pulse shaper data and resistance function for the annealed Cu-DHP (CW024A – R240, cf. EN 1652:1998) copper. See also Appendix A, Table A.2.

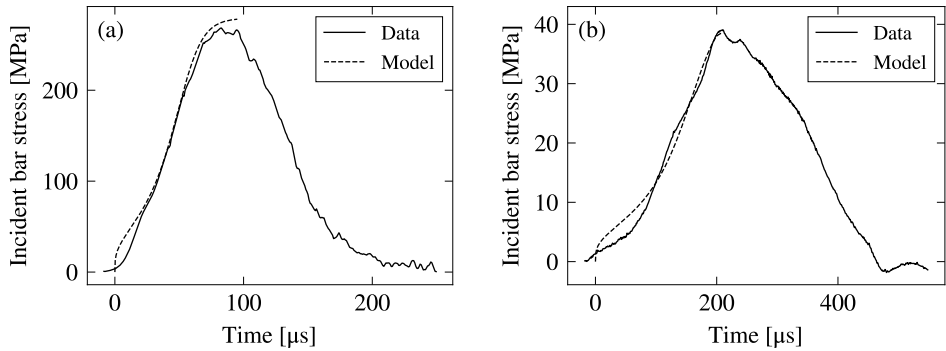


**Fig. 3.10** Incident bar stress data and model predictions (unloading excluded) using the resistance function for the annealed Cu-DHP copper: (a)  $h_0 = 2.06$  mm,  $d_0 = 10.07$  mm,  $L_{st} = 250$  mm,  $v_{st} = 38.95$  m/s, and (b)  $h_0 = 1.00$  mm,  $d_0 = 3.60$  mm,  $L_{st} = 500$  mm,  $v_{st} = 6.02$  m/s.

incident pulse's actual rise because the model determines a sudden steep stress build-up. Similar can be seen in the curves provided by FREW et al. (2002), but no explanation is given in the reference for this model behaviour.

### Final Pulse Shaper Dimensions

The pulse shaper model with the resistance function for the annealed Cu-DHP copper was applied to determine the final pulse shaper dimensions. The aim was to sufficiently extend the rise time of the incident pulse to facilitate dynamic force equilibrium and constant strain rate loading in the SHPB experiments on the flat glass samples. Four essential parameters can be varied to modify the shape of the incident pulse: the pulse shaper diameter ( $d_0$ ) and thickness ( $h_0$ ), the striking velocity ( $v_{st}$ ), and the striker bar length ( $L_{st}$ ). A parametric study of their impact on the pulse shape using the pulse shaper model is shown in Fig. 3.11, in which the basic parameters were chosen as  $d_0 = 3.0$  mm,  $h_0 = 1.0$  mm,  $v_{st} = 6.0$  m s<sup>-1</sup>, and  $L_{st} = 500$  mm. Each parameter was varied individually, while the remaining three were kept constant with the primary value.

Starting with the diameter (Fig. 3.11(a)), it is seen that the increase causes the initial elastic response to increase because the pulse shaper exerts higher forces on the incident bar before the pulse shaper starts yielding. Also, increasing the diameter helps to reduce the amount of plastic strain in the pulse shaper, increasing the incident bar response. Increasing the thickness (Fig. 3.11(b)) lowers the incident pulse amplitude while extending the pulse duration. The increase in striking velocity (Fig. 3.11(c)) causes an increase in the incident pulse amplitude while the loading duration decreases. Lastly, elongating the striker bar (Fig. 3.11(d)) causes an increase in both the incident pulse amplitude and the loading duration.

Since the shape of the incident pulse is a function of the four parameters, various combinations exist that can fulfil the experimental needs. Therefore, the final pulse shaper design was not entirely based on the parametric study presented. With a good starting point in

### 3. Experimental Methodology for High Strain Rate Testing

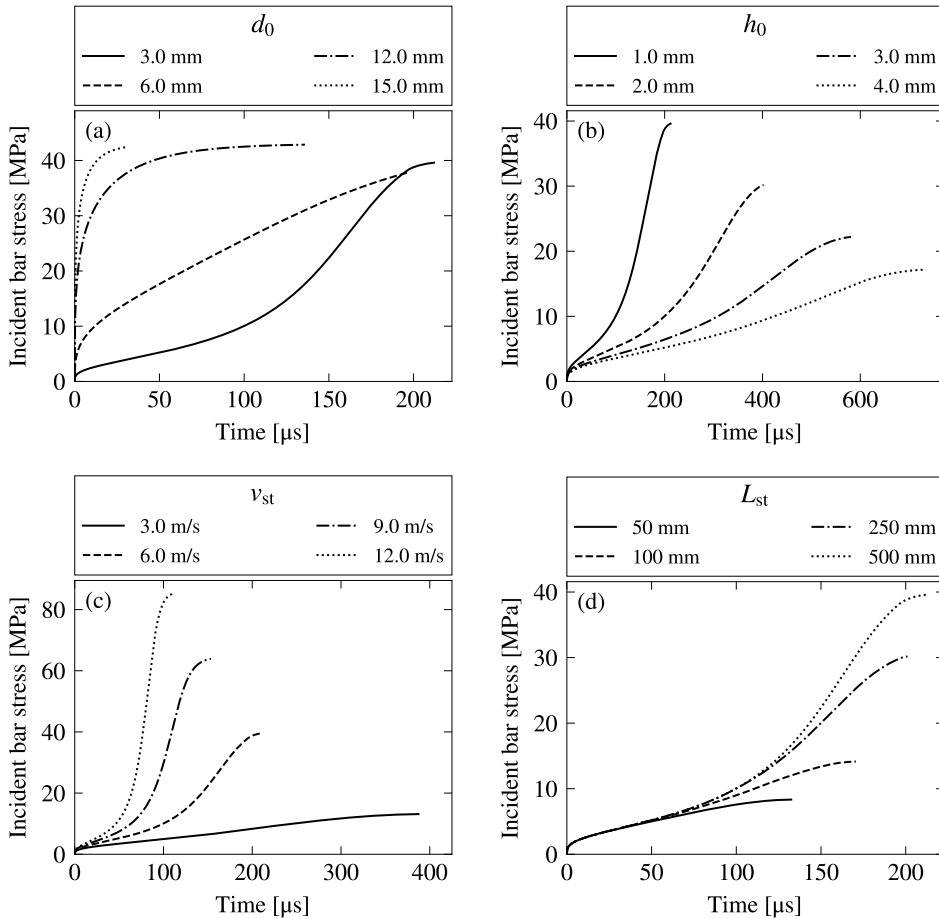


**Fig. 3.11** Parametric study with the pulse shaper model varying the four essential parameters: (a) pulse shaper diameter, (b) pulse shaper thickness, (c) striking velocity, and (d) striker bar length.

Fig. 3.11 and some additional experiments, a pulse shaper made of the annealed Cu-DHP copper with the dimensions  $\varnothing 3.6 \text{ mm} \times 1.0 \text{ mm}$  was found applicable for the 500 mm-long striker bar with a striking velocity of around  $6 \text{ m s}^{-1}$ . This design extended the rise time of the incident pulse sufficiently while ensuring that its amplitude did not entirely drop out the comparatively low force amplitude of the glass samples tested in bending. An example of the resulting incident pulse is already given in Fig. 3.10(b) where it is compared to the model prediction.

#### 3.3.4 Wave Dispersion Analysis

The material characterisation with a Split-Hopkinson Pressure Bar assumes one-dimensional elastic wave propagation in the bars by Eq. (3.1). Since the bar material is free to

move in the radial direction, the actual wave propagation is of two-dimensional nature governed by the lateral material motion, Poisson's effects and resulting inertia-induced stresses. Combined, these effects result in wave dispersion, accumulating when propagating along the bars. For increasing bar diameter, the effects of wave dispersion become more significant and need to be corrected for in the recorded bar signals (see e.g. TYAS and WATSON 2001). However, if the bar is slender enough, wave dispersion is negligible, and thus, wave propagation may be considered to be approximately one-dimensional for the determination of axial quantities.

POCHHAMMER (1876) and CHREE (1889) independently solved the equation of motion for a sinusoidal wave propagating in an infinitely long, homogeneous, isotropic cylinder of uniform cross-section. The Pochhammer-Chree equation can be solved for different vibration modes. For the Split-Hopkinson Pressure Bar, the first mode governs the determination of wave dispersion in the bars (DAVIES 1948). Its solution is graphically shown in Fig. 3.12. Here, the wave dispersion is plotted as the phase velocity,  $C_p$ , as a function of the ratio between the cylindrical bar radius,  $r$ , and the wavelength,  $\Lambda$  (inversely proportional to the frequency by  $C_p = \Lambda f$ ), for material with  $\nu = 0.29$ . In comparison, the longitudinal, the one-dimensional (Eq. (3.1)), the shear and the Rayleigh wave velocities are shown. It is seen that the phase velocity of a propagating stress wave decreases with decreasing wavelength (or increasing frequency), approaching the Rayleigh wave velocity. The same holds for an increasing bar radius if the wavelength is fixed. However, one-dimensional wave propagation theory applies if all the energy of a stress wave signal contains frequency components of long wavelength in the range  $r/\Lambda \leq 0.05-0.10$  (TYAS and WATSON 2001). An upper limit for the frequency content in a stress wave signal can thus be found for which a wave dispersion correction is negligible.

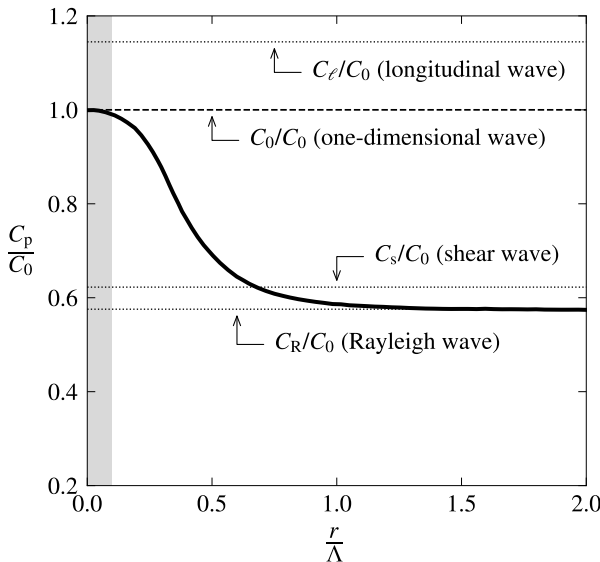


**Fig. 3.12** The phase velocity,  $C_p$ , of the first vibration mode of a bar as calculated by DAVIES (1948) from the Pochhammer-Chree equation for  $\nu = 0.29$  plotted as a function of the ratio  $r/\Lambda$ . The other velocities shown for comparison are the longitudinal, the one-dimensional, the shear, and the Rayleigh (or surface) wave (see e.g. MEYERS 1994).

### 3. Experimental Methodology for High Strain Rate Testing

An estimate of the maximum allowable frequency content in a propagating stress wave as a function of the cylindrical bar diameter ( $= 2r$ ) is given in Fig. 3.13, determined for the limit  $r/\Lambda = 0.1$ , which is the grey highlighted range in Fig. 3.12. Assuming that the curve represents the high-strength aluminium alloy with a Poisson's ratio of 0.33 (slightly larger than the 0.29) used for the modified SHPB, an upper frequency limit of 33.6 kHz is found for the incident bar with a diameter of 30 mm. The frequencies contained in a shaped incident pulse from an experiment with the  $\varnothing 3.6 \text{ mm} \times 1.0 \text{ mm}$  pulse shaper are determined in Fig. 3.14. The pulse exhibits no significant frequencies above 20 kHz, thus confirming that the assumption of one-dimensional wave propagation in the incident bar is reasonable. Furthermore, Fig. 3.14 demonstrates that the applied pulse shaping technique minimises wave dispersion effects, as higher frequencies seen in the unshaped pulse are filtered out.

### 3.4 High-speed Cameras and Stereo Digital Image Correlation

The modifications in the SHPB design presented in Sec. 3.2 enable the application of high-speed cameras due to an unobstructed view of the flat glass sample. Two high-speed cameras (Phantom v2512) with a maximum frame rate of 1,000,000 fps at the lowest resolution are accessible at the Villum Center for Advanced Structural and Material Testing (CASMaT), a laboratory facility at DTU. These, equipped with 100 mm macro lenses, were placed in a stereo setup using a master-slave configuration with two different views of the glass sample, as shown in Fig. 3.15. The resulting mutual angle between the cameras was approximately  $20^\circ$ , and the distance to the sample was 70 cm. The experiments used an image resolution of  $256 \times 256 \text{ pixels}^2$  with a  $35 \times 35 \text{ mm}^2$  field-of-view, with which sufficient details could be captured at 200,000 fps.

The application of the high-speed cameras served two purposes:

- (1) to assess the fracture and its origin, as the fractured glass samples could not be retained after the dynamic loading, and
- (2) to conduct non-contact optical full-field deflection measurements with the technique of Stereo Digital Image Correlation (Stereo-DIC) (see e.g. SUTTON et al. 2009), which provided an investigation of the material stiffness.

Time synchronisation between the two cameras was not necessary for the fracture assessment, therefore the frame rate was doubled using an alternating image acquisition, as described and exemplified by a recorded image series in Paper II. However, series of image pairs needed to be captured for the Stereo-DIC measurements, which require a proper time synchronisation of the exposure. This was ensured using an oscilloscope to which the strobe signals of the cameras were connected. Thereby, the exposure signals from the master and slave cameras could be read and matched. The Stereo-DIC further requires that the surface to measure is provided with a random pattern of dark and light features, which allows finding the best match between corresponding points in the two images. Such a surface was created using chalk spray paint in white for the ground and black for the speckles,

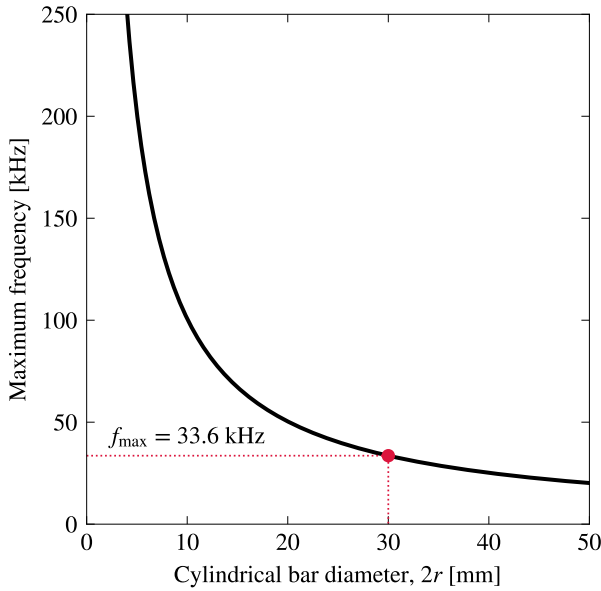


**Fig. 3.13** An estimate of the maximum allowable frequency that may be included in the frequency spectrum of the incident bar signal as a function of the cylindrical bar diameter. Determined from Fig. 3.12 for the limit  $r/\Lambda = 0.1$ .

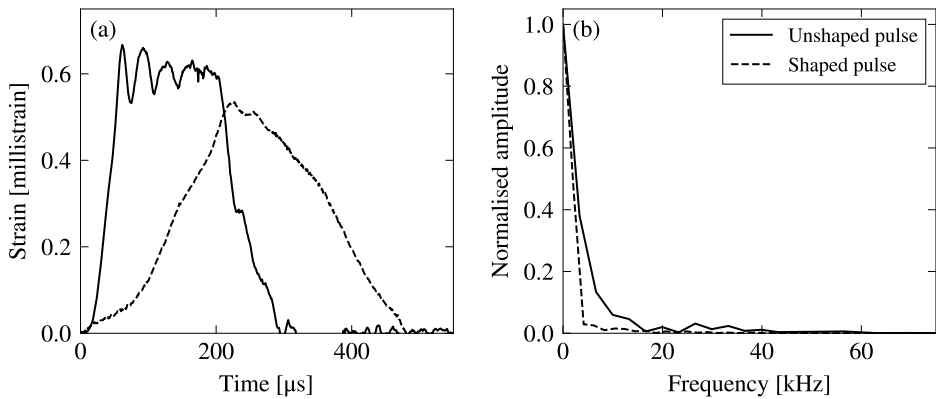
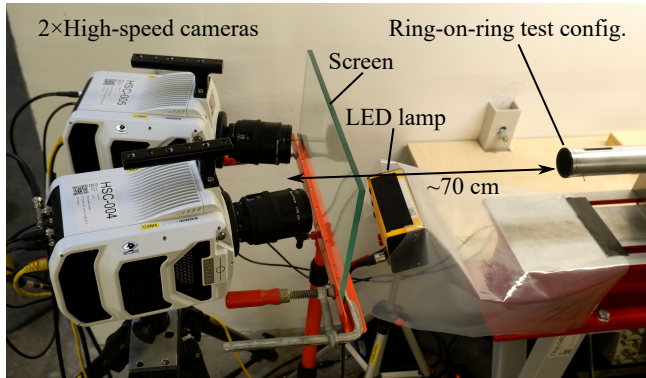


**Fig. 3.14** An unshaped and a shaped incident pulse from an experiment with the  $\varnothing 3.6$  mm  $\times$  1.0 mm annealed copper pulse shaper in (a), and the associated frequency content from a Fourier transformation in (b).

### 3. Experimental Methodology for High Strain Rate Testing

**Fig. 3.15** The two Phantom v2512 high-speed cameras in a stereo setup facing the ring-on-ring test configuration in the modified SHPB setup. (from Paper III)



resulting in a pattern feature size of approximately 3 to 4 pixels. An example of a speckle-patterned glass sample placed in the ring-on-ring test configuration is given in Fig. 3.16(a). The photo also shows that the support ring was spray-painted black, which was done to remove light reflections from the LED lamp shown in Fig. 3.15. However, before an image series could be captured for a Stereo-DIC measurement, a camera setup calibration was required to ensure a dimensional consistency of the measuring system. Since the image correlation was performed with the software GOM Correlate Professional 2019, an associated coded calibration cube (GOM / CP 20 / MV  $30 \times 24 \text{ mm}^2$ ) was used following the software manual. This resulted in a measuring volume of  $35 \times 35 \times 20 \text{ mm}^3$ , enclosing the visible sample surface. Additional Stereo-DIC analysis parameters are given along with the results presented in Chapter 4.



**Fig. 3.16** Photos showing the measuring techniques directly applied to a glass sample's tensile surface in the ring-on-ring test configuration: (a) a spray-painted speckle pattern for non-contact optical full-field deflection measurements with Stereo-DIC, and (b) a strain gauge glued to the centre of the tensile surface.

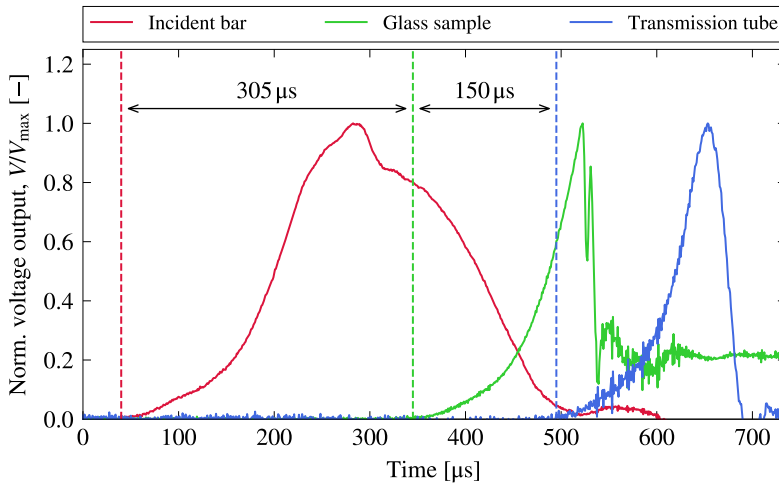


**Fig. 3.17** Recorded strain signals from an experiment in which a glass sample was equipped with a strain gauge to determine the time difference between the camera recordings and the incident and transmitted pulse, respectively.

A reliable relation between the dynamically applied load and the measured deflections was established by synchronising the image acquisition with the acquisition of strain signals using the master camera's built-in clock. However, a time difference was present between the resulting force histories and the acquired image series because strains in the bar/tube system were measured before and after the sample has deformed (the SHPB design principle). Therefore, an experiment was conducted in which a glass sample was equipped with a centrally placed strain gauge, as shown in Fig. 3.16(b). This could determine when the glass was loaded relative to the starting points of the incident and transmitted pulse with high precision. The three recorded strain gauge signals are provided in Fig. 3.17 as a plot of the normalised voltage output as a function of time. The starting point of each pulse is marked with a vertical dashed line. As specified, a time difference to the glass sample response of  $305 \mu\text{s}$  is found for the incident pulse and  $150 \mu\text{s}$  for the transmitted pulse. Since in the experimental execution, a tiny gap might be present between a sample and the rings of the load configuration, the time between the incident pulse and the glass response modifies with the time it takes to establish full contact during loading. Thus, the most correct measure is the time difference between the glass response and the transmitted pulse, which is owed to the fact that the sample needs to contact the rings to transmit forces. Therefore, the post-processed Stereo-DIC measurements, further discussed in Chapter 4, relate to the force history on the support ring side, cf. Eq. (3.5). Additionally, Fig. 3.17 reveals that the loading of the glass sample corresponds to the transmitted pulse, confirming that the oscillations observed in Fig. 3.6 for the load ring forces did not interact with the sample.

### 3. Experimental Methodology for High Strain Rate Testing

# High Strain Rate Characterisation of Glass Mechanical Properties

The need for a more detailed level of knowledge of glass' mechanical properties at high strain rates was identified in Chapter 2. The experimental methodology to obtain such was discussed in Chapter 3. This chapter addresses Paper III, which covers the experimental investigation of flat, circular soda-lime-silica glass samples subjected to high strain rate loading using the modified SHPB setup. First, an introduction to the material testing is given (Sec. 4.1), followed by a description and analysis of the glass samples under investigation (Sec. 4.2). Finally, results<sup>1</sup> related to the glass' flexural strength (Sec. 4.3), the samples measured deflections (Sec. 4.4), and the glass' stiffness (Sec. 4.5) are presented and discussed.

This chapter addresses the findings reported in Paper III on page 217.

## 4.1 Introduction to the Material Testing

The material testing aimed to characterise the strain rate sensitivity of the flexural mechanical properties of annealed float glass, such as surface tensile strength and stiffness (Young's modulus), at rates above  $10^1 \text{ s}^{-1}$ . A range that can be expected for facade glass panels exposed to blast loading (cf. Sec. 1.2) but is sparingly covered in the literature (cf. Sec. 2.2). Also, data is limited to show how the residual stress state in thermally tempered glass (see Sec. 1.1.1) affects the tensile strength at high strain rates. From the publications reviewed in Sec. 2.2, only a few included such investigations for strain rates up to  $1 \text{ s}^{-1}$  (KÖNIG 2012; KUNTSCHKE 2015; FÖRCH 2019). For this reason, thermally tempered glass with different residual compressive surface stresses was also included in the investigation covered by this chapter.

The equibiaxial flexural tests were performed at two different strain rates to enable the determination of a strength enhancement: a quasi-static in average at  $2.2 \cdot 10^{-5} \text{ s}^{-1}$  ( $\approx 2.0 \text{ MPa s}^{-1}$ ), which is a loading rate as prescribed in the European Standards for the determination of the bending strength of glass (EN 1288-1:2001; EN 1288-2:2001; EN 1288-3:2001; EN 1288-5:2001), and a dynamic in average at  $48 \text{ s}^{-1}$  ( $\approx 4.3 \cdot 10^6 \text{ MPa s}^{-1}$ ). A universal testing machine (Instron 8872,  $\pm 25 \text{ kN}$ ; see e.g. EIS (2022)) was used for the quasi-static tests with a fixture that could hold the same ring-on-ring test configuration as used in the modified SHPB setup for the dynamic tests (see Fig. 4.1). Furthermore, in the quasi-static tests, all samples were equipped with an adhesive foil on the compressive

<sup>1</sup>The datasets are openly available (©) licensed under CC BY-SA 4.0, <https://creativecommons.org/licenses/by-sa/4.0/>) in the data repository *DTU Data*, a figshare platform, at <https://doi.org/10.11583/DTU.17694692>.



**Fig. 4.1** A photo of the loading fixture in the universal testing machine holding the same ring-on-ring test configuration as included in the modified SHPB.

surface (the surface the load ring contacts) not modifying the tensile strength, to retain the fractured glass for later assessment. In the dynamic tests, the assessment was done with recordings from the high-speed cameras, as described in Sec. 3.4. The experiments were performed in an environment with an average temperature of  $23.4^{\circ}\text{C}$  ( $\pm 0.4^{\circ}\text{C}$ ) and an average relative humidity of  $43.4\%$  ( $\pm 5.2\%$ ).

## 4.2 Glass Samples

For the investigations, circular glass samples with a diameter of  $45\text{ mm} \pm 0.5\text{ mm}$  were cut out of annealed soda-lime-silica glass sheets with a nominal thickness of  $3\text{ mm} \pm 0.2\text{ mm}$ . The actual thicknesses were measured with a digital vernier calliper, ranging from  $3.08\text{ mm}$  to  $3.14\text{ mm}$  with a mean of  $3.11\text{ mm}$  ( $\pm 0.01\text{ mm}$ ). Afterwards, edges were seamed to remove sharp burrs, securing safe handling. The surfaces remained unmachined not to modify the actual glass strength, therefore termed *as-received* in the following. However, due to the float glass production process, the glass came with two surface conditions: an air-side and a tin-side that contacted the transport rollers in the cooling area of the production line. Typically, they have different strengths, with the tin-side being weaker, as surface flaws are larger than on the air-side due to roller contact (KROHN et al. 2004; HALDIMANN et al. 2008; SWAB et al. 2014). Therefore, a UV-light was used to identify and mark the samples air-side to secure that the strength tests relate to identical surface conditions, i.e. the air-side. Furthermore, the chemical elemental composition of the glass samples was measured using a Scanning Electron Microscope (SEM) together with Energy-dispersive X-ray Spectroscopy (EDS), which confirmed conformity to the European Standard EN 572-1:2012 (cf. Table 1 in Paper III). Some of the glass samples were further post-processed with a thermal tempering to include the effect of residual stresses in the high strain rate characterisation. In this process, the tin-sides were in contact with the transport rollers again, ensuring less damage to the air-side. POURMOGHADDAM and SCHNEIDER (2019) conducted a study that determined a linear relationship between the mid-plane tensile stress of the tempered glass and the cooling rate in the quenching (engine power in %). Therefore, the glass samples were ordered in four different quench

levels, evenly spaced, to increase the variability in the study: 25 %, 50 %, 75 % and 100 %.

#### 4.2.1 Measurement of the Compressive Surface Stress

The residual compressive surface stresses,  $\sigma_c$ , in the thermally tempered glass samples were measured using a SCALP-05, a Scattered Light Polariscopes from GlasStress Ltd., Tallinn, Estonia. For the measurement of the surface stress, a photoelastic constant  $C = 3.01 \text{ TPa}^{-1}$  was used as found by NIELSEN et al. (2010). Details of this measuring technique are given in Paper III. For additional references, the reader is referred to ABEN and GUILLEMET (1993) and ANTON (2015). Since it was presumed that the thermal tempering process did not result in a perfect equibiaxial stress state, measurements were performed in two orthogonal directions on each sample's air-side, originating from the sample centre. The orientation of the samples was chosen arbitrarily due to the circular geometry. Each measurement was repeated five times to determine a mean for both directions. A mathematical correction of the measured stresses was performed using a so-called stress separation as outlined in Paper III, resulting in the two residual compressive surface stresses  $\sigma_x$  and  $\sigma_y$ . The results of the measurements on 720 samples in total are shown as box-plots in Fig. 4.2, together with the data distribution.

Overall, the residual compressive surface stresses across the quench levels range from 30 MPa to 60 MPa. This range is lower than what is typically expected for fully tempered glass, which according to ISO 20657:2017, should be a minimum of 80 MPa to obtain a bending strength of 120 MPa. Considering heat-strengthened glass, the surface pre-stress should according to ISO 22509:2020 be between 25 MPa and 52 MPa, a range that covers most of the measured residual compressive surface stresses. Furthermore, the results for

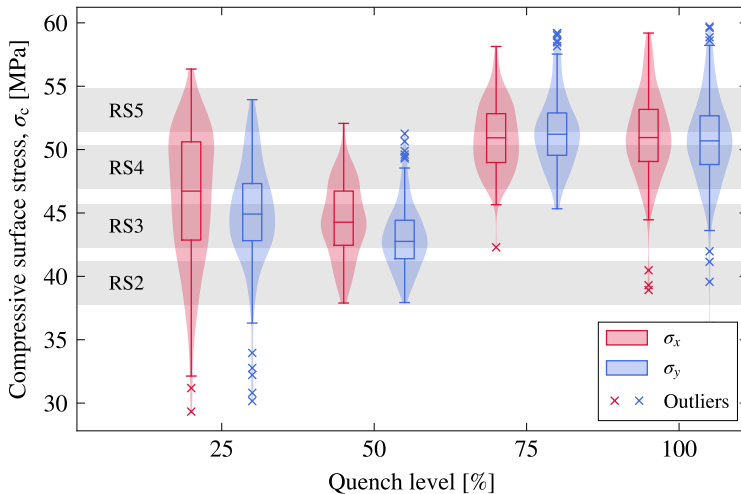


**Fig. 4.2** The measured residual compressive surface stresses after stress separation of the thermally tempered glass samples in the four quench levels shown as box-plot together with the distribution of the data. Additionally, the chosen grouping (RS2 to RS5) of the samples is grey highlighted.

#### 4. High Strain Rate Characterisation of Glass Mechanical Properties

each quench level show a large scatter. However, the reason is difficult to outline because details of the thermal tempering process are unknown. Looking at the quench levels, the samples were ordered with a linear variation, which expectedly should have resulted in a linear variation in the residual compressive surface stresses. Although some increase was measured, this linear variation is not evident in Fig. 4.2, presumably caused by the small sample geometry, challenging a uniform thermal tempering. Also, the measurements show that the variation within a sample, i.e. between  $\sigma_x$  and  $\sigma_y$ , is minor, indicating that shear stresses in the residual stresses are negligible.

The large scatter observed in the measurements demanded another grouping than the quench levels to more reliably investigate the effect of residual stresses on the glass strength's strain rate sensitivity. Therefore, the thermally tempered glass samples were divided into four residual stress (RS) groups, RS2 to RS5, with a span of  $\sigma_c \pm 1.7$  MPa across the four quench levels, which allowed for smaller variations. The group intervals were evenly spaced (a linear variation), as highlighted with grey in Fig. 4.2, and the sample selection was based on the minimum measured compressive surface stress, i.e.  $\min(\sigma_x, \sigma_y)$ . The annealed float glass samples were placed in the residual stress group RS1. A statistical evaluation of the residual compressive surface stresses contained in each residual stress group is tabulated in Paper III, Table 2. The maximum determined standard deviation equals  $\pm 1.0$  MPa, which demonstrates that the grouping resulted in a smaller variation suitable for the characterisation of the glass.

##### 4.2.2 Edge Quality Enhancement by Etching

A partial aim of the glass characterisation was to determine a surface strength. However, the high strain rate tests challenged the determination, as a more significant number of samples failed at the edge (a cause for rejection, as will be discussed in Sec. 4.3), where more severe flaws were present compared to the surface. This observed behaviour may be explained by the rate-induced strength enhancement, which resulted in higher loads. At the increased load level, the failure mechanisms began to compete between surface and edge flaws, with edge flaws increasingly being the governing ones. Shifting the failure towards the sample surface thus required an enhanced edge quality, i.e. a reduction of sharp-edged flaws being a cause for stress concentrations. This was achieved by etching using a 15-wt%  $\text{NH}_4\text{HF}_2$  aqueous acid solution (ammonium hydrogen fluoride). A technique, which was developed to modify the edge only while maintaining the as-received surface condition, is presented in Paper III. As a result, the rate of edge failures could be reduced from 57% to 26%. Since the challenge of edge failure was observed during the experimental execution, not all samples included in the glass characterisation campaign were subjected to the etching. This could presumably have been avoided if the glass samples had a polished edge instead of a seamed edge.

#### 4.3 Equibiaxial Flexural Strength

In Paper III, 315 glass samples, divided into the five residual stress groups, were subjected to equibiaxial flexural strength tests at a quasi-static and a dynamic loading rate using the ring-on-ring test configuration presented in Chapter 3. Representative examples of force

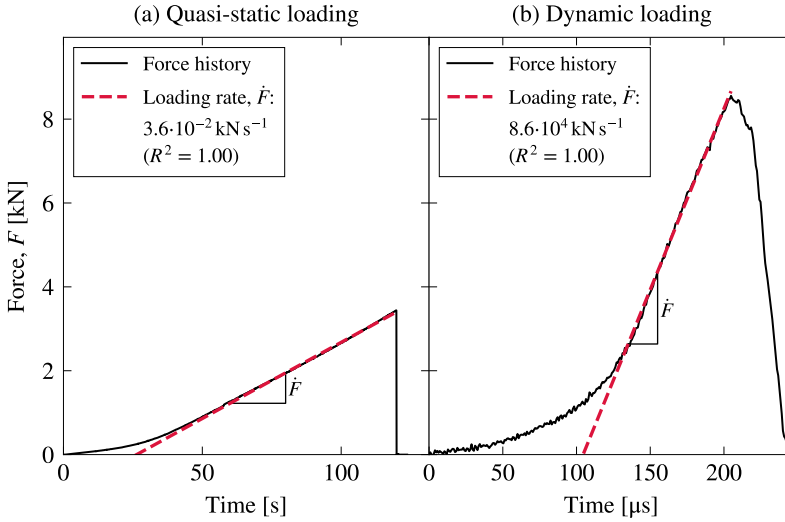


**Fig. 4.3** Examples of force histories from strength tests on annealed float glass samples (RS1) and the loading rate estimation: (a) quasi-static loading and (b) dynamic loading.

histories acquired from tests on as-received annealed float glass samples (RS1) are given in Fig. 4.3. Here, the quasi-static load was measured with a load cell using a sampling rate of 25 Hz, and the dynamic load was determined from the transmitted pulse, i.e. the support ring side, in the modified SHPB (cf. Sec. 3.2.1). From the force histories,  $F(t)$ , the achieved loading rates were determined from a linear regression using the method of least squares for data between  $0.4 \cdot \max(F)$  and  $\max(F)$  to exclude the slow loading at the beginning. In the quasi-static tests it was caused by the adhesive foil and in the dynamic by the shape of the incident pulse. The slope of the regression then directly provides the loading rate  $\dot{F}$ , as shown in Fig. 4.3. The R-squared values of both regressions in Fig. 4.3 reveal that the data are well-represented by a straight line, indicating that a constant loading rate could be established in a significant part of the loading up to fracture.

Once a sample's failure load was found from the peak in the force history,  $F_{\max}$ , the maximum normal stress theory, as defined by Eq. (2.1), was used to predict the surface tensile strength from maximum principal stresses. For small sample deflections, i.e. approximately less than half the glass thickness (EN 1288-1:2001), the stress state within the load ring can be considered rotationally symmetrical, resulting in constant maximum principal stresses (see Fig. 3.2). These can be determined analytically from linear elastic plate bending theory (TIMOSHENKO and WOINOWSKY-KRIEGER 1959):

$$\sigma_1 = \frac{3F}{2\pi h^2} \left[ (1-\nu) \frac{D_S^2 - D_L^2}{2D^2} + (1+\nu) \ln \frac{D_S}{D_L} \right] \quad (4.1)$$

where  $h$  is the sample thickness,  $D$  is the sample diameter,  $D_L$  is the load ring diameter,

#### 4. High Strain Rate Characterisation of Glass Mechanical Properties

and  $D_S$  is the support ring diameter. Inserting  $F_{\max}$  for  $F$  gives the glass' apparent tensile strength,  $\sigma_f$ , according to the failure criterion in Eq. (2.1), and by inserting  $\dot{F}$ , Eq. (4.1) determines a stress rate,  $\dot{\sigma}$ . Furthermore, maximum principal strains,  $\varepsilon_1$ , within the load ring can be determined from the following relationship, which also relates to a rotationally symmetrical stress distribution:

$$\varepsilon_1 = \frac{\sigma_1}{E} (1 - \nu) \quad (4.2)$$

Eq. (4.2) also determines a strain rate,  $\dot{\varepsilon}$ , for  $\dot{\sigma}$  instead of  $\sigma_1$ .

##### 4.3.1 Fracture Assessment

Eqs. (4.1) and (4.2) imply that failure must originate within the load ring. Since surface defects govern glass failure, the failure origin can usually be traced back to a single point, which relates to the critical flaw. This eased the assessment of the fractured glass samples, performed either by looking at the quasi-statically tested samples or at the high-speed recordings taken in the dynamic tests (cf. Sec. 3.4). From the experiments, three locations of failure origin could be observed categorised as follows:

- (1) within the loading ring
- (2) outside the load ring on the surface, and
- (3) edge.

Examples of the three locations are shown in Fig. 4.4(a)-(c) on samples tested quasi-statically and in Fig. 4.4(d)-(f) on samples tested dynamically. From (a)+(d), a radial fracture pattern is clearly seen that originates within the load ring. The black dot/shadow in (d) around the point of failure origin, may be referred to as *caustics* (see e.g. ROSSMANITH 1982; KALTHOFF 2000). In (b)+(e), a similar radial fracture pattern is observed, however, originating outside the load ring, and in (c)+(f), the fracture develops into a non-radial pattern starting from an edge flaw, which is outside the visible glass area in (f). The high-speed recordings, especially (d) and (e), indicate that pure bending induced failures were achieved in the SHPB experiments (more details in Sec. 4.4), which can rule out the concern of punching failure raised by KUNTSCHKE (2015) for the results reported by NIE et al. (2010), who investigated a similar sample geometry in a similar ring-on-ring test configuration.

Usually, Standards for the equibiaxial flexural glass strength determination, such as ASTM C1499-15 or EN 1288-5:2001, require that failure occur within the diameter of the load ring and to exclude samples from the evaluation, which do not comply. However, in the present study, it was decided to include the samples that failed between the load and support ring, as they could determine the aimed surface strength by knowing the exact point of failure origin, thereby extending the sample size. The location of failure origin could be measured with a precision of roughly  $\pm 0.5$  mm.

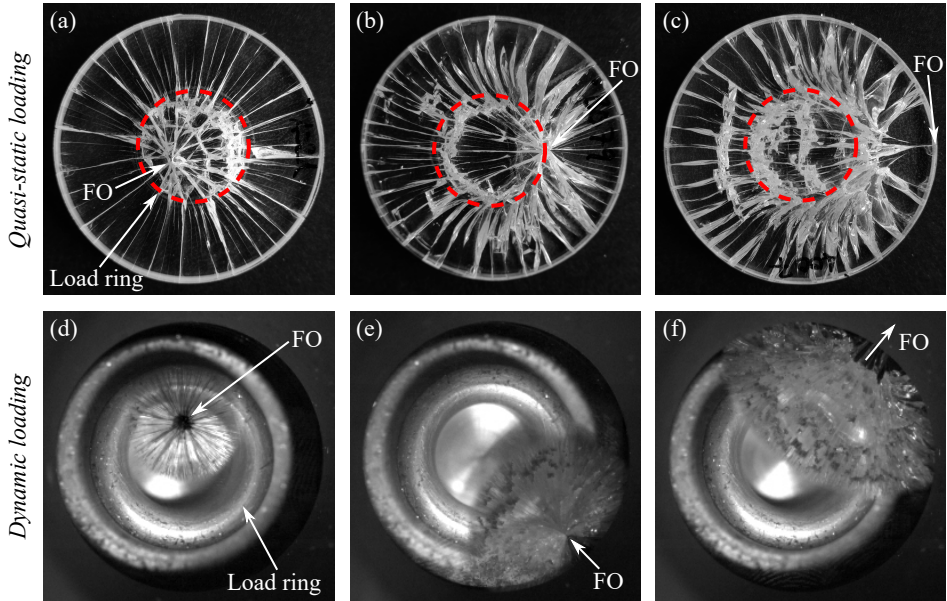


**Fig. 4.4** Examples of the observed locations of failure origin (FO) achieved in the quasi-static (upper row) and dynamic tests (lower row): (a)+(d) within the load ring, (b)+(e) outside the load ring on the surface, and (c)+(f) edge (outside the visible glass area in (f)).

### 4.3.2 Strength Evaluation

The strength evaluation was initially based on 30 samples for each loading rate within each residual stress group. A minimum of 15 valid samples, i.e. no edge failure, was the aim to estimate a mean flexural surface strength (e.g. ASTM C1499-15 defines a minimum of 10 valid samples). Another two samples were added to each residual stress group tested dynamically, which relate to the performed Stereo-DIC measurements reported in Sec. 4.5. Furthermore, five extra samples were included in RS4 for the dynamic tests, as the minimum number of valid samples was not reached during the experiments. Each sample's apparent tensile strength,  $\sigma_f$ , was determined from Eq. (4.1) using the applied peak force, and the associated strain rate was found from Eq. (4.2), assuming a rate-independent Young's modulus of 70 GPa (see Sec. 4.5). For the samples that failed outside the load ring,  $\sigma_f$  and  $\dot{\epsilon}$  were reduced according to the rotationally symmetric maximum principal stress/strain distribution shown in Fig. 4.5 using the exact location of the failure origin. The distributions were determined numerically from an axisymmetric FEM model in ABAQUS/Standard 2021 using 3-node quadratic shell elements (SAX2 in ABAQUS) for the discretisation of the glass sample. The observed difference between the maximum principal stress and strain is due to the glass' Poisson's ratio. With the previously mentioned precision in measuring the failure origin location, the reduced tensile strengths and strain rates were determined with a precision of  $\pm 2-3\%$  of their maximum, directly given by Eqs. (4.1) and (4.2).

#### 4. High Strain Rate Characterisation of Glass Mechanical Properties

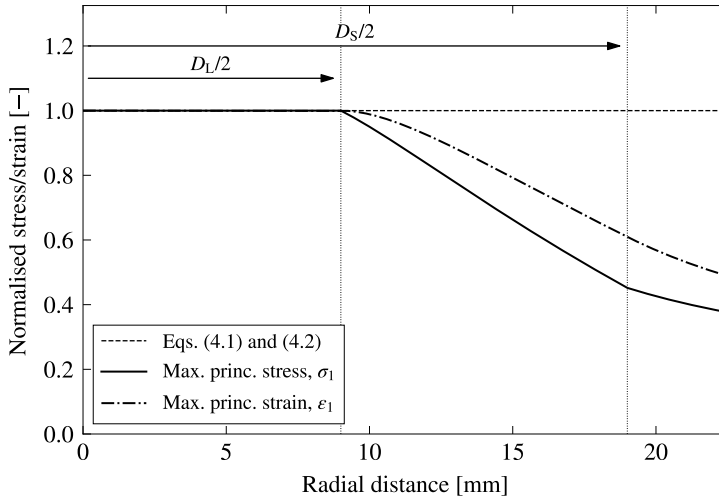


**Fig. 4.5** Numerically determined rotationally symmetric distribution of the maximum principal stress and strain (normalised with Eqs. (4.1) and (4.2)) in a glass sample loaded in the ring-on-ring test configuration.

Overall, the individual strength measurements (cf. Paper III) show that samples with edge failures had remarkable lower tensile strengths compared to samples with surface failures, as was expected. The samples that failed outside the load ring resulted in strengths comparable to those that failed within, thus being a sound supplement. Furthermore, the samples with enhanced edges by etching (cf. Sec. 4.2.2) did not show altered surface strengths, as they spread across the existing scatter in the results without significant jumps. Thus, it is concluded that the etching procedure successfully modified only the edges of the samples, which increased the likelihood of surface failure in the ring-on-ring test.

A summary of the equibiaxial flexural surface strength characterisation of the soda-lime-silica glass is provided in Table 4.1 on the basis of the valid categorised samples, i.e. edge failures have been excluded. The experimental results show a significant scatter in the measured surface strengths, which is usual for glass due to the characteristic differences in surface flaws (see e.g. SWAB et al. 2014; MEYLAND et al. 2019). At the quasi-static loading rate the standard deviation is between 18 % and 34 % of the means, and between 25 % and 35 % at the dynamic loading rate. Since the glass surfaces were kept as-received, the observed variations reflect the characteristic differences in the critical surface flaws. Furthermore, nearly identical averaged strain rates were achieved between the residual stress groups, enabling a direct comparison within the tested rates. The two dependencies, residual stress and strain rate, are further discussed below.

#### Residual Stress Dependency

The bending strength of thermally tempered glass can be determined as the sum of the intrinsic glass strength,  $\sigma_i$ , governed by the nature of surface flaws and the residual com-

**Table 4.1** Summary of the equibiaxial flexural surface strength characterisation of the soda-lime-silica glass tested at two loading rates, a quasi-static and a dynamic. Results for the five residual stress groups RS1 to RS5 include the number of samples ( $N$ , valid/total tested), and the mean of the strain rate ( $\dot{\epsilon}$ ) and the failure stress ( $\sigma_f$ ). In parentheses, the standard deviation to each value is given.

	Quasi-static loading			Dynamic loading		
	$N$ [-]	$\dot{\epsilon}$ [s <sup>-1</sup> ]	$\sigma_f$ [MPa]	$N$ [-]	$\dot{\epsilon}$ [s <sup>-1</sup> ]	$\sigma_f$ [MPa]
RS1	16/30	$2.2 \cdot 10^{-5}$ ( $\pm 0.1 \cdot 10^{-5}$ )	173 ( $\pm 30.7$ )	16/32	45 ( $\pm 8.7$ )	324 ( $\pm 109$ )
RS2	19/30	$2.2 \cdot 10^{-5}$ ( $\pm 0.3 \cdot 10^{-5}$ )	210 ( $\pm 67.7$ )	17/32	47 ( $\pm 5.3$ )	364 ( $\pm 91$ )
RS3	22/30	$2.2 \cdot 10^{-5}$ ( $\pm 0.2 \cdot 10^{-5}$ )	240 ( $\pm 81.2$ )	19/32	49 ( $\pm 7.9$ )	387 ( $\pm 113$ )
RS4	24/30	$2.3 \cdot 10^{-5}$ ( $\pm 0.2 \cdot 10^{-5}$ )	232 ( $\pm 57.0$ )	16/37	47 ( $\pm 9.5$ )	381 ( $\pm 133$ )
RS5	15/30	$2.3 \cdot 10^{-5}$ ( $\pm 0.2 \cdot 10^{-5}$ )	240 ( $\pm 49.0$ )	16/32	51 ( $\pm 3.8$ )	433 ( $\pm 115$ )

pressive surface stress,  $\sigma_c$ , a definition similar to what is found in the European glass code CEN/TS 19100-1:2021 (cf. Eq. (2.22)). Thus, a simplified linear relationship exists between the measured apparent tensile strengths,  $\sigma_f$ , and the residual compressive surface stresses, expressed as (RODICHEV et al. 2007):

$$\sigma_f = \sigma_i + k\sigma_c \quad (4.3)$$

where  $k$  is an empirical constant that determines the strength increase with increasing residual stresses, i.e. the slope  $\Delta\sigma_f/\Delta\sigma_c$ . Ideally, it should take the value one. The measured mean failure stress of each residual stress group is shown in Fig. 4.6 as a function of the mean residual compressive surface stress. The error bars are the standard deviations, and the shadowed blue boxes represent a 95 % confidence interval. Although the standard deviations are too large to prove a statistically significant difference between all group means and the range of compressive surface stresses investigated is relatively narrow, a trend is noticeable at both loading rates.

Lines of best fit through the means determine slopes of 1.4 and 1.7 for the quasi-statically and dynamically tested glass, respectively, which are larger than the expected 1.0, for comparison also drawn in Fig. 4.6. Both the fitted and the expected lines cross the 95 % confidence intervals. The observed deviations to one can be explained by the narrow range of tested residual compressive surface stresses between 40 MPa and 53 MPa, in which minor variations in the mean strengths more significantly impacted the slope, i.e. the strength increase. For comparison, strength data reported by SCHIAVONATO et al. (2005) also resulted in an increased slope as high as  $k = 1.21$ . However, the deviation to the expected slope of 1.0 is believed to be less pronounced because the investigated glass had compressive surface stresses spanning from 40 MPa to 140 MPa, a range 7.7 times larger than the present one. Nevertheless, it is shown that strength increases with residual compressive surface stress at both loading rates.

#### 4. High Strain Rate Characterisation of Glass Mechanical Properties

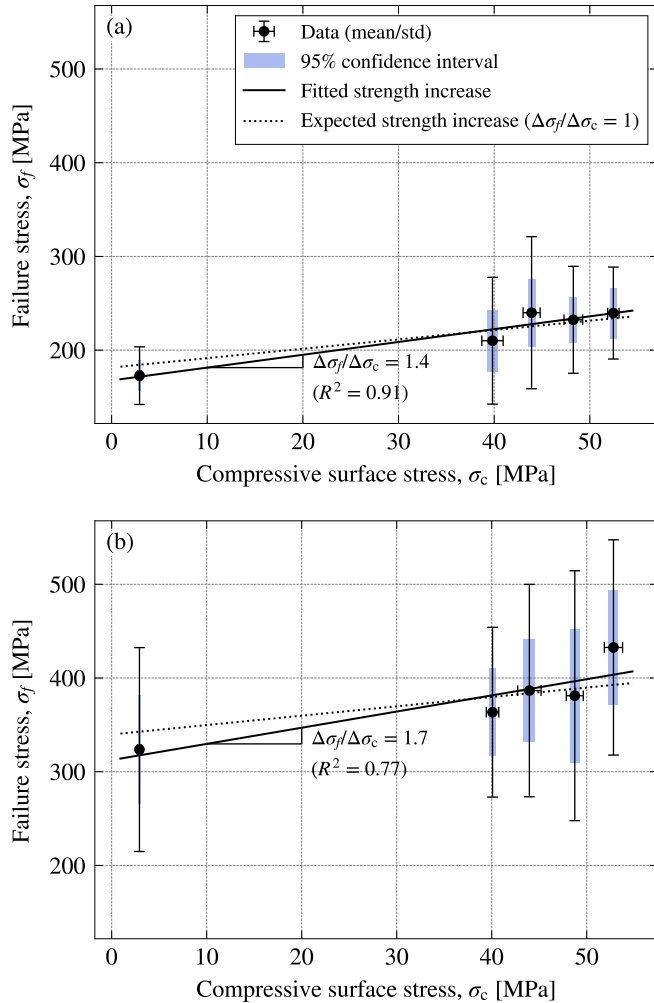


**Fig. 4.6** The measured failure stress,  $\sigma_f$ , of the soda-lime-silica glass as a function of the residual compressive surface stress,  $\sigma_c$ , for the five residual stress groups RS1 to RS5: (a) quasi-static loading and (b) dynamic loading.

#### Strain Rate Dependency

The analytical derivation applicable to describe the loading rate dependence of the glass sample's flexural surface strength is given in Sec. 2.1.4 by Eq. (2.19) for a constant loading rate. The double-logarithmic linear relationship is used to compare the measured strengths for the five residual stress groups. The strengths are normalised as in Fig. 2.8 according to Paper I (MEYLAND et al. 2021a), and plotted in Fig. 4.7 as a function of strain rate.

A significant strain rate dependency is evident for all five residual stress groups investigated. With respect to  $\sigma_f/\sigma_0 = 1$ , increases in strength between 60% and 86% were measured for an average strain rate of  $48 \text{ s}^{-1}$ . However, there is no significant indication that the different residual stress levels affected the loading rate dependency of the glass

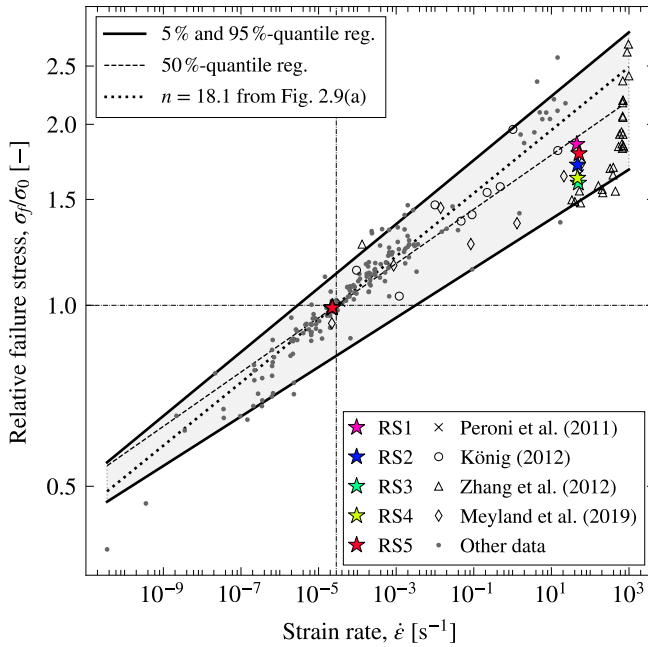


**Fig. 4.7** The relative failure stress,  $\sigma_f/\sigma_0$ , of the soda-lime-silica glass in the five residual stress groups as a function of strain rate. For comparison, data from the most recent research is shown together with 'other data' that remain from Fig. 2.9(a). The quantile regressions include all data shown. (adapted from Paper III)

strength. RS1 display the highest strength enhancement and RS3 the lowest, while the remaining three residual stress groups are in between. A dependency was not expected by the relationship given by Eq. (4.3). Once compressive surface stresses are cancelled out by bending tensile stresses, glass failure is essentially governed by the intrinsic glass strength controlled by the presence of surface flaws. Since the surface conditions of all samples were comparable due to identical handling, similar strain rate sensitivities were observed. The difference between the residual stress groups is thus more likely to be considered as scatter rather than a cause of changing residual stresses. As concluded by the other studies reviewed in Sec. 2.2, the observed glass strength's sensitivity to loading rate is explained by the decrease or even absence of sub-critical crack growth effects (cf. Sec. 2.1.1).

Also, Fig. 4.7 includes data from the most recent research related to the high strain rate characterisation of soda-lime-silica glass (PERONI et al. 2011; KÖNIG 2012; ZHANG et al. 2012; MEYLAND et al. 2019) and remaining 'other data' from Fig. 2.9(a), which enable a direct comparison with the present study due to similar test environments. Furthermore, 5%, 50%, and 95% quantile regression lines have been plotted based on all data shown. Overall, a good agreement with the previous studies is seen at the high strain rate. While the range defined by RS2, RS4, and RS5 is consistent with tensile strengths reported by PERONI et al. and MEYLAND et al., the data from KÖNIG and ZHANG et al. show higher and lower strengths, respectively, with the lower coinciding with the 5% quantile regression. The sudden increase in strength measured by ZHANG et al. at higher strain rates is debatable because the plotted data are individual measurements and not mean values as for the other

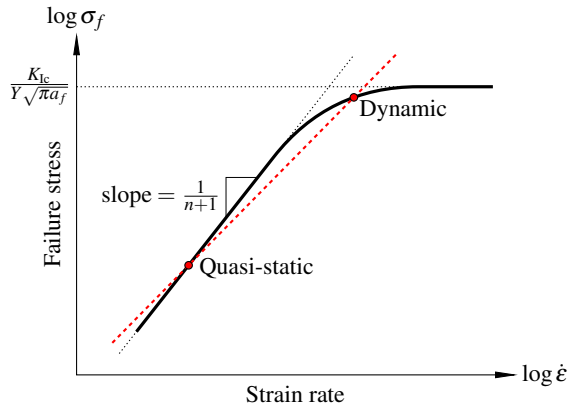


**Fig. 4.8** A schematic of the interpretation of obtained strength data. The shown limit is the inert strength according to Eq. (2.10).

studies included.

Looking at the general trend of all data in Fig. 4.7, represented by the shown dynamic fatigue regression line for the crack growth parameter  $n = 18.1$  after Fig. 2.9(a), the measured mean surface strengths of the residual stress groups RS1 to RS5 tend to deflect. This might indicate a beginning plateauing in the observed strength increase, which aligns with the assertion that glass strength approaches an upper limit, the inert strength, for very short load duration, i.e. for  $\dot{\epsilon} \rightarrow \infty$ .

The interpretation of the obtained strengths is schematically shown in Fig. 4.8. The black curve represents the glass' dynamic fatigue behaviour, including the inert strength limit, and the red dashed line demonstrates a linear fit through the two data points obtained for each of the five residual stress groups, with a lower slope. The lower slopes of each residual stress group result in  $n$ -values 22% to 66% higher than the 18.1 used in Fig. 4.7. Assuming that  $n = 18.1$  represents the investigated glass in the low to intermediate range of strain rates, i.e. the linear dynamic fatigue behaviour, the increases of  $n$  according to Fig. 4.8 suggest that a limit is approaching at the high strain rate tested due to inhibited sub-critical crack growth. The investigation conducted by NIE et al. (2010) on borosilicate glass shows similar behaviour at a stress rate of  $5 \cdot 10^6 \text{ MPa s}^{-1}$  ( $\sim 60 \text{ s}^{-1}$ ), comparable to the present study. However, additional tests at intermediate and higher strain rates are necessary to map the transition into the inert strength limit more significantly. These have not been achieved due to limited time in the project.

#### 4.4 Deflection Measurements with Stereo-DIC

The performed deflection measurements on the glass samples tested dynamically with the modified SHPB is detailed in the following. A non-contact optical measuring technique was employed by the use of high-speed cameras and Stereo Digital Image Correlation (Stereo-DIC), as described in Sec. 3.4. In the SHPB experiments, time-synchronised image pairs with two different views of a speckled glass sample (cf. Fig. 3.16(a)) were captured at 200,000 fps and an exposure time of  $0.6 \mu\text{s}$ . The ensuing image correlation was performed in the commercial software GOM Correlate Professional 2019 with analysis

DIC software	GOM Correlate Professional 2019
Facet size	$15 \times 15$ pixels <sup>2</sup>
Point distance	10 pixels
Intersection deviation	0.3 pixels
Interpolation	Bi-cubic
Calibration deviation	0.018 pixels
Scale deviation	0.0006 mm
Camera angle	20.2°
Measuring volume	$35 \times 35 \times 20$ mm <sup>3</sup>
Image scale	7.3 pixels/mm

**Table 4.2** Stereo-DIC analysis parameters.

parameters as listed in Table 4.2.

From the correlated images, meshed surfaces of about 480 points could be constructed at which the deflections of the dynamically tested glass samples were evaluated. Examples can be found in both Paper II and Paper III. Since the data acquisition system was configured to acquire strains measured in the bar/tube system synchronised with images captured by the high-speed cameras, the measured sample deflections could be related to the applied force determined from the support ring side. However, the distance from the glass sample to the strain gauge on the transmission tube required a time shift of 150  $\mu$ s (determined in Sec. 3.4), corresponding to a shift of 30 images, to match the series of image pairs with the related force history.

A representative force history from an experiment on a glass sample in RS4 and the different load stages for which matching image pairs were captured is shown in Fig. 4.9. Depending on the peak force, 60-70 image pairs could be used for the deflection measurements, with a sufficient number of images defining the unloaded state of the glass sample and a high temporal resolution up to fracture. Based on the force history in Fig. 4.9, a corresponding full-field deflection measurement,  $\Delta\delta$ , is exemplified in Fig. 4.10 for load stage 56 ( $F = 6.69$  kN), which has been determined relative to load stage 1 at which the deflection was set to 0.0 mm. The contour plot shows a deflection state that is nearly rotationally symmetrical with the maximum deflection in the sample centre, which implies pure bending loading of the glass in the experiments with the modified SHPB. This observation supports the conclusion drawn from the images in Fig. 4.4.

Additional measurements have been extracted along the section shown in Fig. 4.10 for the load stages 40, 44, 48 and 52 to quantify the undergone deflection of the sample further. In Fig. 4.11, these are compared to an analytical plate bending solution of the ring-on-ring test derived from a standard solution given by TIMOSHENKO and WOJNOSKY-KRIEGER (1959) for a concentrically loaded, simply supported circular plate (see derivation in Paper II, Appendix A). The shown analytical plate bending is estimated with  $E = 70$  GPa,  $\nu = 0.23$ ,  $h = 3.11$  mm, and  $D = 45$  mm. First of all, it is to be noted that the Stereo-DIC measurement with the high-speed cameras remarkably captured the glass sample deflection in the magnitude of 100 microns and shows an increase with increasing load. Furthermore, the measured deflection curves are in good agreement with the analytical plate bending so-

#### 4. High Strain Rate Characterisation of Glass Mechanical Properties

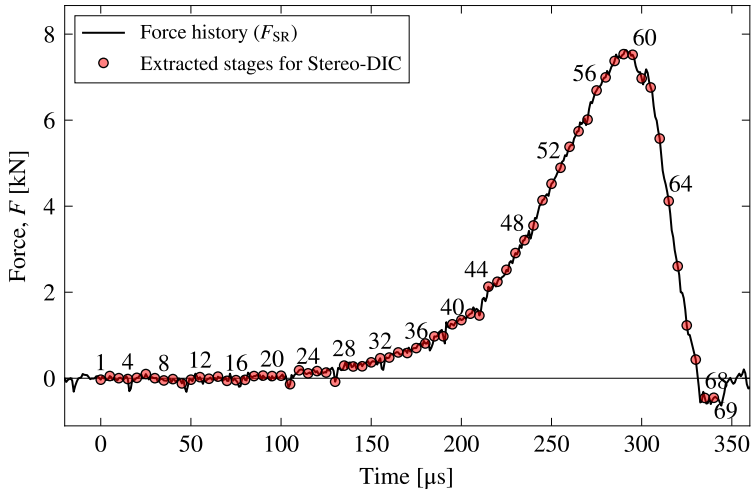


**Fig. 4.9** A force history from an experiment on a glass sample in RS4 determined for the support ring side ( $F_{SR}$ , cf. Eq. (3.5)), and the load stages at which matching image pairs were extracted for Stereo-DIC.

lution, indicating that the material stiffness (Young’s modulus) seems not to be affected by the rapid loading. The minor noise in the measurements is likely due to image noise, which is usually caused by the camera sensors, the interpolation algorithm employed in the digital image correlation, and the structure of the speckle pattern (GAO et al. 2016). Also, the deflection curves demonstrate that a major part of the sample surface could be measured in the modified SHPB, providing sufficient details to characterise the glass’ bending behaviour at the rapid loading. However, because glass is a linear elastic, brittle material,

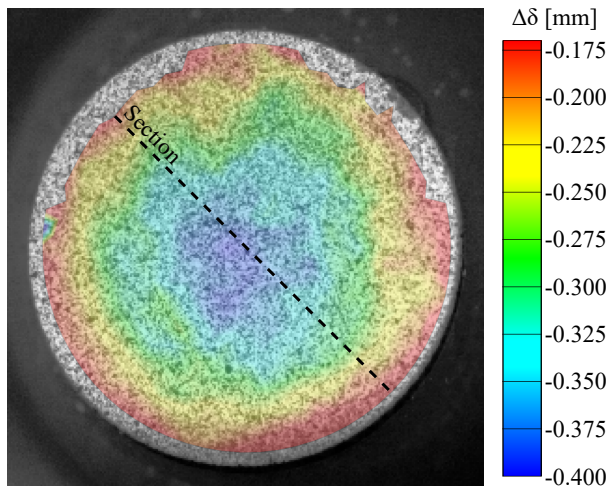


**Fig. 4.10** A full-field deflection measurement with Stereo-DIC on the glass sample that relates to the force history in Fig. 4.9 at load stage 56.

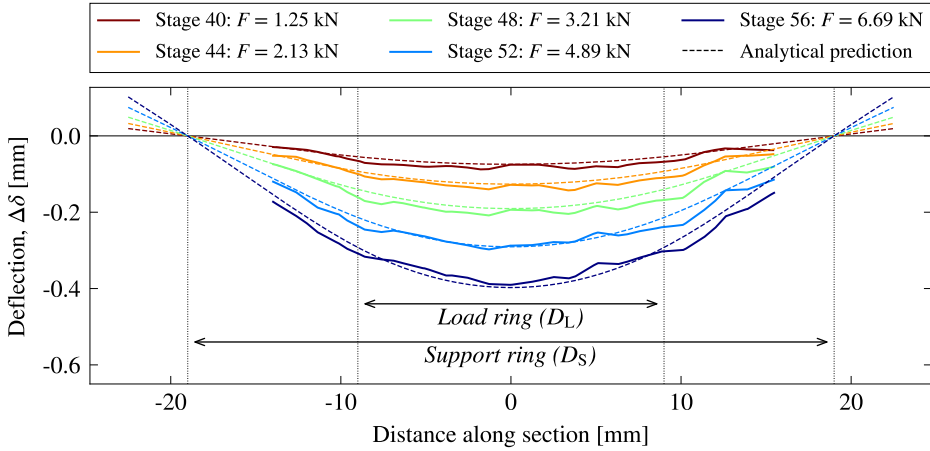


**Fig. 4.11** Glass sample deflections measured with Stereo-DIC along the section in Fig. 4.10 for five load stages, which relate to the force history in Fig. 4.9, compared to the analytical plate bending solution for a linear elastic material.

not capable of redistributing stresses, details about crack formations cannot be measured optically with Stereo-DIC, as it can be done for, e.g. quasi-brittle materials like concrete showing a softening-phase after maximum stress (see e.g. GEHRI et al. 2020). Once cracks have grown, discontinuities are present in the digital image correlation, challenging the analysis of the glass' post-fracture behaviour.

## 4.5 Material Stiffness (Young's Modulus)

The sample deflection in the employed ring-on-ring test configuration is well-captured by an analytical plate bending solution, as discovered in the previous section. Hence, the non-contact optical Stereo-DIC measurements provide details about the glass' Young's modulus. Following the plate bending solution derived in Paper II, Appendix A, the material stiffness,  $E$ , relates to the plate bending by the following expression:

$$E = \frac{F}{\delta} \frac{3(1-\nu^2)}{8\pi h^3} (D_L^2 + 4r^2) \left[ \ln \frac{D_L^2}{D_S^2} + \frac{D_S^2 - D_L^2}{D_L^2 + 4r^2} \right] \quad (4.4)$$

$$\left( 1 + \frac{(D_S^2 - 4r^2)(1-\nu)}{2(1+\nu)D^2} \right) \quad \text{for} \quad 0 \leq r \leq \frac{D_L}{2}$$

where  $\delta$  is the measured deflection at a distance  $r$  from the common central axis of the ring-on-ring test configuration, occurring from the applied force,  $F$ . From Eq. (4.4) it is evident that the ratio  $F/\delta$ , which is measured experimentally, is proportional to  $E$ .

In Paper III, the investigation of the glass' Young's modulus was conducted on two sam-

#### 4. High Strain Rate Characterisation of Glass Mechanical Properties

samples per residual stress group, resulting in ten measurements. For each of the tested samples, force-deflection curves were determined at ten arbitrary chosen points within the load ring diameter from the Stereo-DIC full-field measurement, to estimate a well-defined mean of the material stiffness. The ten resulting force-deflection curves up to the peak force are exemplified in Fig. 4.12 for a glass sample of group RS4. Expectedly, the glass shows a linear material response. Therefore, the slope of each curve,  $\Delta F/\Delta\delta$ , was determined from a linear regression using the least squares method. With the slope and the exact distance,  $r$ , to the point in the full-field deflection measurement, an estimate for  $E$  was determined from Eq. (4.4). The ten measurements' mean per tested sample in each residual stress group is plotted in Fig. 4.13. The error bars are the standard deviation.

The stiffness investigation of the glass at an average strain rate of  $46 \text{ s}^{-1}$  ( $\pm 8.5 \text{ s}^{-1}$ ) shows minor variations in the estimated Young's modulus across residual stress groups, with no indication of being significantly affected by the residual stresses themselves. The standard deviation within and the variation between the samples are most likely caused by the image

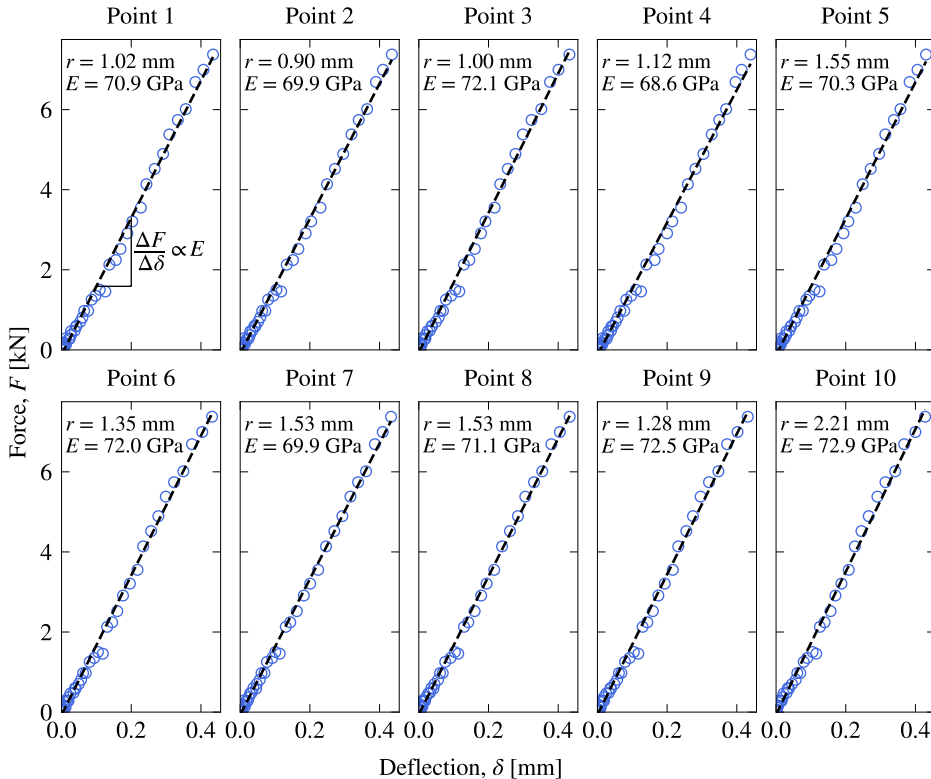


**Fig. 4.12** Force-deflection curves (up to the peak force) for the ten points extracted from a Stereo-DIC full-field deflection measurement on a glass sample of group RS4. The slope of each curve is proportional to Young's modulus,  $E$ , determined with Eq. (4.4).

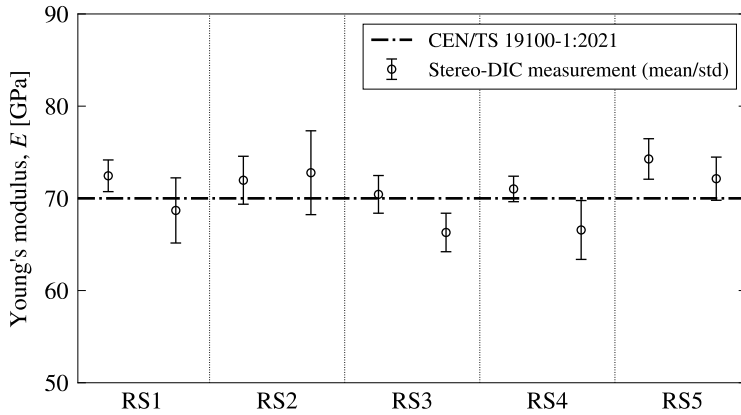


**Fig. 4.13** Young's modulus,  $E$ , of the glass in the five residual stress groups (RS1 to RS5) determined from the high strain rate experiments ( $\dot{\epsilon} = 46\text{ s}^{-1} \pm 8.5\text{ s}^{-1}$ ) with the modified SHPB using Stereo-DIC deflection measurements. The rate-independent value given in CEN/TS 19100-1:2021 is shown for comparison. (from Paper III)

noise in the Stereo-DIC measurements, as mentioned in Sec. 4.4. However, calculating the overall mean results in  $E = 70.7\text{ GPa} (\pm 2.7\text{ GPa})$ , which agrees well with the 70 GPa in the European glass code CEN/TS 19100-1:2021; also plotted in Fig. 4.13. No deflection measurements were performed on the samples tested quasi-statically. Therefore, Young's modulus in the European Standard serves as the only reference for quasi-static loading. With that in mind, the glass' Young's modulus seems insensitive to loading rate, which aligns with the findings reported in Paper I (MEYLAND et al. 2021a). Additional Stereo-DIC results, similar to Figs. 4.9, 4.10 and 4.11, which relate to the investigation of the glass' Young's modulus, are provided in Appendix B.

#### 4. High Strain Rate Characterisation of Glass Mechanical Properties

# Simulation of Monolithic Glass Fracture Under Blast Loading

This chapter includes the project's numerical phases, which have not been devised into a scientific publication yet. Therefore, a detailed presentation and discussions of the conducted work are given here. The numerical modelling of the monolithic glass fracture under blast loading is divided into three parts. First, a brief introduction is given to numerical modelling and failure formulations applicable to brittle materials (Sec. 5.1). Then, the development of a material damage model based on the element deletion technique within the explicit FEM framework is presented (Sec. 5.2), which includes a rate-dependent strength formulation based on theory discussed in Chapter 2. Lastly, the application of the model is validated against experimental data from full-scale blast tests found in the literature, which also demonstrates the application of the damage model on larger scale (Sec. 5.3).

## 5.1 Numerical Modelling

The following briefly introduces the numerical modelling. The first part provides basics about the explicit Finite Element Method (FEM) used for the simulations presented in this chapter, and the second looks into different developed modelling techniques to simulate failure of brittle materials.

### 5.1.1 Explicit Finite Element Method

Computational modelling has become a significant practice for engineers enabling the analysis of complex structures spanning from the micro to the macro scale. For problems in civil engineering, the implicit Finite Element Method has proven to be a versatile tool with a broad range of applications. However, considering non-linear problems such as high-speed dynamic events like short-duration blast waves, the analysis with the implicit method can become rather time-consuming due to its more comprehensive formulation, at times also with non-converging solutions. In such cases, an explicit time integration is often better suited and therefore shown to be widely used to analyse extreme loading problems. The present work used the commercial software ABAQUS/Explicit 2021 to perform the simulations. To understand better the advantages of the used explicit procedure above the implicit in ABAQUS, a brief comparison is provided hereinafter based on the software manual (DASSAULT SYSTÈMES 2021).

For both time integration methods, equilibrium is determined from Newton's second law where the system inertia given as the mass matrix,  $\mathbf{M}$ , times the nodal accelerations,  $\ddot{\mathbf{u}}$ , equals the net nodal forces, i.e. the difference between the externally applied forces,  $\mathbf{P}$ ,

and the internal element forces,  $\mathbf{I}$ :

$$\mathbf{M}\ddot{\mathbf{u}} = \mathbf{P} - \mathbf{I} \quad (5.1)$$

In both procedures, the equations of motion by Eq. (5.1) are solved for the given state of the nodes, i.e. displacements, velocities and accelerations. The difference between the two procedures is found in the integration method. The implicit procedure uses an automated incrementation based on the full Newton iterative solution method, where at each iteration and time increment, a set of linear equations is solved by a direct solution method to obtain the given state. In contrast, the explicit procedure in ABAQUS uses a diagonal (or lumped) mass matrix that allows for a central difference rule to integrate the equations of motion explicitly through time, where the given state of each node is obtained directly by its mass and the net force acting on it. Since highly dynamic events need to be evaluated by very small time increments to capture the dynamic response accurately, the implicit procedure by its formulation becomes computational costly and even more if the system of linear equations is large. Typically, the explicit procedure requires many increments in the order of 10,000 to 1,000,000. Fortunately, the computational cost per increment is smaller by far compared to the implicit procedure as there are no simultaneous equations to solve, which explains its preferred choice regarding dynamic simulations.

While the implicit scheme in ABAQUS is unconditionally stable, the explicit comes with a conditional stability. A conservative simple estimate of the stability limit,  $\Delta t_{\text{stable}}$ , which a time increment may not exceed to secure a stable explicit time integration, can be determined element-wise as follows:

$$\Delta t_{\text{stable}} \approx \frac{L_{\min}}{C_{\ell}} \quad (5.2)$$

where  $L_{\min}$  is the size of the smallest element in a mesh, and  $C_{\ell}$  is the longitudinal wave speed of the material represented by the element (see e.g. MEYERS 1994). However, in ABAQUS, the time incrementation is automated with no required user intervention. An elaborate description of time-dependent integration methods can be found in WRIGGERS (2008, pp. 205-254).

Furthermore, the explicit procedure not only allows for inexpensive time integration but also, due to the decoupling of the individual equations, enables a partition of the problem into smaller parts that can be computed simultaneously using, for instance, high-performance computing. Also, it comes with a great advantage in modelling material degradation and failure, where the implicit method often leads to severe convergence difficulties.

### 5.1.2 Modelling Techniques for Brittle Failure

Modelling the failure of solid materials has been a research interest for decades. Several approaches have been developed to simulate crack initiation and formation in brittle materials numerically. In general, the modelling challenges lie within the combination of the material behaviour both prior and after the fractured stage, where a transition from

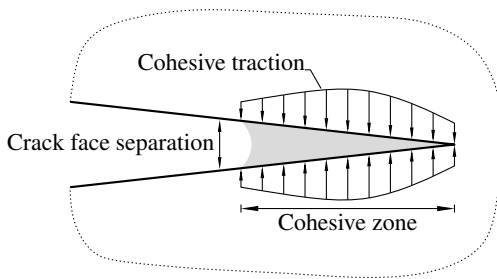


**Fig. 5.1** The cohesive zone interpretation close to a crack tip.

continuity to discontinuity happens. The commonly used numerical techniques can be classified into continuum and discontinuum based methods, depending on the underlying theory adopted.

To the continuum-based methods count, e.g. the Finite Element Method (FEM) and the Extended Finite Element Method (XFEM), which is an extension to FEM allowing dynamic crack growth problems to be solved with no or very little re-meshing (BELYTSCHKO et al. 2007; NISTOR et al. 2008). However, in XFEM, cracks typically have to be distant from each other because an enriched element can capture only a single crack. This hinders the simulation of multiple crack branches and intersections, which is typically seen in the dynamic fracture of glass (PARK and CHEN 2012). More promising are the cohesive zone elements developed within the FEM framework where cracks are allowed to form and propagate along element boundaries following a cohesive Traction-Separation Law (see e.g. XU and NEEDLEMAN 1994; CAMACHO and ORTIZ 1996). The basic idea of the cohesive zone approach is to describe fracture as a gradual process of separation that is resisted by traction in a small region of material close to a tip of a growing crack (see Fig. 5.1), thereby seeking to model accumulated damage as an effective behaviour of the fracture process zone only. A detailed overview of advances in the cohesive zone modelling of dynamic fracture can be found in SEAGRAVES and RADOVITZKY (2009). Another approach that has been adopted using FEM, is node splitting, in which a crack, after having reached a failure criteria, is formed by new nodes and free element faces (NURHUDA et al. 2012; OSNES et al. 2019). A less comprehensive approach to the simulation of crack formations is the element deletion technique (or killing elements), where an element is removed from the model upon reaching a criterion. The implementation is shown to be rather simple, whilst any fracture criterion or damage model can be coupled with it as demonstrated in MEYLAND and NIELSEN (2020). Examples of such models are the Hillerborg model (HILLERBORG et al. 1976) or the Johnson-Holmquist (JH-2) ceramic model intended for brittle materials subjected to large strains, high strain rates and high pressure, e.g. ballistic impact (JOHNSON and HOLMQUIST 1994; HOLMQUIST et al. 1995). Due to its flexible and straightforward implementation, numerous studies have adopted the element deletion technique for the dynamic fracture simulation of large-sized, thin-walled glass panes (ZHANG et al. 2013; ZHANG et al. 2015a; PELFRENE et al. 2016; ALTER et al. 2017; CHEN et al. 2019; ZHOU et al. 2019). However, a significant drawback is the method's inherent mesh dependency. Due to a fixed mesh, crack formations are determined solely by the discretisation. This also holds for the cohesive zone modelling and the node splitting

technique. Furthermore, the mesh dependency is also shown to be significant in predicting the state at a crack tip, where a too coarse mesh (the case in many engineering problems) cannot capture gradients near the tip leading to an overestimation of the fracture energy (UNOSSON et al. 2006).

To the discontinuum-based methods belong among others the Discrete Element Method (DEM) and the hybrid Combined Finite-Discrete Element Method (FEM/DEM) (WANG et al. 2017). In the DEM, a continuum is represented by particles in which discontinuities from crack formations are formulated by simple block contact and bond laws making the implementation of empirical constitutive laws unnecessary. In FEM/DEM the advantages of FEM and DEM are combined (see e.g. MUNJIZA et al. 1995). For instance, fracture of laminated glass could be simulated using DEM to represent the brittle behaviour of glass, while FEM is better suited to model the hyper-elastic behaviour of the PVB interlayer (see e.g. XU and ZANG 2014). In WANG et al. (2017), a comparative study is reported on the modelling of the dynamic fracture of a glass beam subjected to low-velocity hard body impact. The study compared the application of FEM, XFEM, DEM, and FEM/DEM, with the latter approach yielding the most satisfactory performance.

Despite the numerous approaches presented to model dynamic glass fracture, many of them are still challenging to apply in general engineering practice. This is owed to their complexity in the adopted theories, the input parameters being difficult to determine for glass, or their exorbitantly high computational efforts to solve the numerical problem. Although the element deletion technique is not optimal for the simulation of the detailed state around a crack tip, it is at present one of the few methods practically applicable to simulate multiple cracks in large-sized, thin-walled glass structures (PELFRÉNE et al. 2016). Furthermore, taking its simplicity into account, the technique is capable of predicting global quantities such as displacements and loads reliably (PELFRÉNE 2016).

The present work aims at simulating the dynamic fracture and the fragmentation process of thin-walled monolithic glass panes, as typically installed in buildings, subjected to blast loading by adopting simple approaches that are practicable in general engineering practice. Therefore, the implementation of an element deletion technique with a rate-dependent strength evaluation will be outlined and discussed in the next section.

### **5.2 Rate-dependent Progressive Damage Model for Dynamic Glass Fracture**

Several aspects need to be considered in designing a damage model for dynamic glass fracture using the element deletion technique. In this regard, PELFRÉNE (2016) performed a comprehensive investigation of different model formulations, which included the Hillerborg model directly available in ABAQUS, and two self-implemented models, with and without a damage phase. In common for all three models is a smeared crack definition (see Fig. 5.2) introduced by HILLERBORG et al. (1976) for concrete using the cohesive zone concept, in which cracks are not modelled explicitly, but their effect is ‘smeared’ over an element in terms of an elastic stiffness reduction until a complete loss is reached and the element gets deleted.

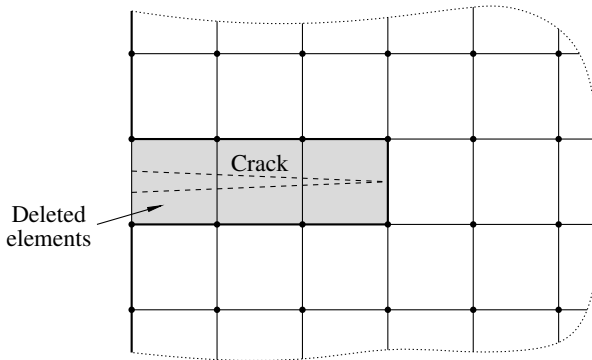


**Fig. 5.2** FE-representation of the smeared crack definition.

A strong mesh dependency was found for the Hillerborg model in predicting fracture energy and crack formations. The model without a damage phase resulted in a faster crack growth with severe stress oscillations in neighbouring intact elements due to the missing softening, which caused an elastic spring back. Such stress wave reflections may cause spurious element failure away from original crack paths as reported by SONG et al. (2008). These shortcomings were successfully bypassed by the third model investigated, which has a linear varying damage phase together with a maximum damage rate to simulate crack velocities more realistically. Also, the formulation was designed to be more independent of element size. However, none of the three models accounted for a loading rate dependency in the glass strength, as discussed in Chapter 2 and experimentally discovered in Chapter 4. Only a fixed strength value could be given as an input parameter. A rate dependency in the glass strength was accounted for in the damage model developed by ALTER et al. (2017), which was designed for the simulation of head impact tests on windscreens, showing promising results.

The objective of the hereinafter presented damage model for the dynamic fracture simulation of large-sized, thin-walled glass panes is to predict global quantities such as the load-bearing capacity and the post-fracture response for, e.g. hazard evaluations according to the International Standard ISO 16933. The following requirements were specified for the model using the element deletion technique:

- The loading rate may vary in large-sized glass structures subjected to blast loading. Therefore, the brittle fracture should be evaluated upon a criterion considering a loading rate dependency of the glass strength.
- The crack growth should happen fast. However, the instabilities mentioned above in terms of stress oscillations should be reduced with a damage phase of specific duration after crack initiation using a monotonously decreasing element stiffness.
- The constitutive behaviour of the glass after crack initiation should be independent of the element size as much as possible.

Since such material failure model is not readily available in ABAQUS/Explicit, a VUMAT user subroutine was written in FORTRAN, which allows the definition of customised me-

chanical constitutive material behaviours for the explicit time integration. In a simulation, it is called for blocks of material calculation points for which the user subroutine defines the material behaviour.

### 5.2.1 User Subroutine Implementation

The intended material model for the simulation of dynamic glass fracture can be divided into three parts: (1) the linear elastic material response prior to crack initiation, (2) the crack initiation itself (a strength model) and (3) the progressive damage phase after crack initiation. However, in the implementation, it is necessary to consider the convention of stresses/strains used in the VUMAT user subroutine. An overview of the stress components stored as vectors is provided in Table 5.1 for both shell and plane stress elements (2D case) and 3D solid elements (3D case). Important to note here is that the shear strain is stored as tensor shear strain, i.e.  $\epsilon_{12} = \frac{1}{2}\gamma_{12}$ . Since the simulation is aimed at large-sized glass panes, the meshing with 3D solid elements would require a large number of elements both in thickness and surface to capture bending stresses sufficiently. Hence, the formulation of the material damage model is made for shell elements, i.e. the 2D case in Table 5.1, to reduce the computational time. In the following, the underlying theories and assumptions for the three parts defining the damage model are outlined. The FORTRAN code of the VUMAT implementation can be found in Appendix C, Sec. C.3.

**Table 5.1** Order of direct and shear stress components used in the VUMAT user subroutine (DASSAULT SYSTÈMES 2021).

Component	2D Case	3D Case
1	$\sigma_{11}$	$\sigma_{11}$
2	$\sigma_{22}$	$\sigma_{22}$
3	$\sigma_{33}$	$\sigma_{33}$
4	$\sigma_{12}$	$\sigma_{12}$
5		$\sigma_{23}$
6		$\sigma_{31}$

#### Linear Elastic Material Response

Glass is generally known as an isotropic linear elastic material. Therefore, Hooke’s law for isotropic materials is used to describe its response until crack initiation. On tensor notation, the interrelationship between stresses and strains can be written as follows:

$$\boldsymbol{\sigma} = 2\mu\boldsymbol{\epsilon} + \lambda\text{tr}(\boldsymbol{\epsilon})\mathbf{I} \tag{5.3}$$

where  $\boldsymbol{\sigma}$  and  $\boldsymbol{\epsilon}$  are symmetric stress and strain tensors,  $\mathbf{I}$  is a second-order identity tensor, and ‘tr’ is a trace operator. The appertaining Lamé parameters,  $\lambda$  and  $\mu$ , are given as:

$$\lambda = \frac{E\nu}{(1+\nu)(1-2\nu)}, \quad \mu = \frac{E}{2(1+\nu)} \tag{5.4}$$

Here,  $E$  and  $\nu$  are the glass’ Young’s modulus and Poisson’s ratio, respectively. Further, Eq. (5.3) can be rewritten on incremental form using index notation to suit the explicit

time integration scheme in ABAQUS, in which a new strain increment,  $\Delta\varepsilon_{ij}$ , is passed to the VUMAT for each time increment,  $\Delta t$ :

$$\tilde{\sigma}_{ij}|_{(t+\Delta t)} = \tilde{\sigma}_{ij}|_{(t)} + \underbrace{2\mu\Delta\varepsilon_{ij} + \lambda\delta_{ij}\left(\sum_{k=1}^3\Delta\varepsilon_{kk}\right)}_{\Delta\sigma_{ij}(\Delta t)} \quad (5.5)$$

where  $\tilde{\sigma}_{ij}$  denotes the stress tensor in the undamaged state,  $\varepsilon_{ij}$  the strain tensor, and  $\delta_{ij}$  the Kronecker delta. However, in the case of shell elements, the thickness strain increment, i.e.  $\Delta\varepsilon_{33}$ , must be defined explicitly in the user subroutine. Within the formulation of an isotropic linear elastic material,  $\Delta\varepsilon_{33}$  can be directly computed from the state of plane stress in which  $\sigma_{33} = 0$  (a reasonable assumption for thin plates), yielding the following expression (see e.g. KANG and ZHONG-CI 1996):

$$\Delta\varepsilon_{33} = -\frac{\nu}{1-\nu} \sum_{k=1}^2 \Delta\varepsilon_{kk} \quad (5.6)$$

Additionally, a transverse shear stiffness must be defined for shell elements when the material response is defined by a VUMAT. Details are provided in Appendix C, Sec. C.1.

#### Crack Initiation (A Strength Model)

Glass failure is, due to the material's brittle nature, often predicted by the maximum normal stress theory, according to the inequality given by Eq. (2.1). This criterion is adopted in the progressive damage model to determine crack initiation (the onset of the damage phase), using a rate-dependent tensile strength, as discussed in Chapter 2 and Chapter 4.

In the VUMAT, the applied strain rate,  $\dot{\varepsilon}$ , used for the strength evaluation is determined incremental-wise by dividing the change in maximum principal strain,  $\Delta\varepsilon_1$ , with the appertaining time increment,  $\Delta t$ :

$$\dot{\varepsilon} = \frac{\Delta\varepsilon_1}{\Delta t} \quad (5.7)$$

The rate-induced enhancement of the tensile strength is then based on the normalised dynamic fatigue curve shown in Fig. 2.9(a), which is found by curve fitting data reviewed in Paper I (MEYLAND et al. 2021a) for the test environment air (25 to 67% RH); an environment that might well be expected for glass installed in buildings. Since it is unrealistic to think of the glass strength decreasing or increasing continuously for loading rates approaching zero and infinity (cf. Sec. 2.1.4), the proposed limits in Fig. 2.9(a) are inherited in the strength model. However, within strain rates typically associated with blast loading (see Fig. 1.7), only the upper limit becomes crucial in the dynamic glass fracture simulation. In between these limits, the strength varies with strain rate using the normalisation relationship given by Eq. (2.21), in which, due to the assumption of identical cracks that are loaded in identical conditions, only the rate dependency of the glass strength dominates.

## 5. Simulation of Monolithic Glass Fracture Under Blast Loading

Hence, no considerations regarding crack sizes and their distribution must be made in the proposed model. As a piece-wise function, the implemented strength model is defined as follows:

$$\frac{\sigma_f}{\sigma_0} = \begin{cases} 0.65 & \text{for } \dot{\epsilon} < \dot{\epsilon}_{th} \\ \left(\frac{\dot{\epsilon}}{\dot{\epsilon}_0}\right)^{1/(n+1)} & \text{for } \dot{\epsilon}_{th} \leq \dot{\epsilon} \leq \dot{\epsilon}_{in} \\ 2.30 & \text{for } \dot{\epsilon} > \dot{\epsilon}_{in} \end{cases} \quad (5.8)$$

Here, the apparent tensile strength,  $\sigma_f$ , is determined relative to a quasi-static reference tensile strength,  $\sigma_0$ , representative for a strain rate  $\dot{\epsilon}_0 = 2.86 \cdot 10^{-5} \text{ s}^{-1}$  (equivalent to  $\dot{\sigma} = 2.0 \text{ MPa s}^{-1}$  for  $E = 70 \text{ GPa}$ ), which conveniently is chosen to match the normalisation performed in Fig. 2.9(a). Also, the choice of  $\dot{\epsilon}_0$  fits well with the quasi-static loading rate prescribed by the European Standards for strength testing glass (EN 1288-2:2001; EN 1288-3:2001; EN 1288-5:2001). In a double-logarithmic plot, the strength between the set limits varies linearly with a slope equal to  $1/(n+1)$ , where  $n$  is the sub-critical crack growth parameter. Conservatively, it can be taken as 16, which is reasonable for structural glass design (see e.g. HALDIMANN et al. 2008), or any other relevant value can be chosen as for example 18.1 from Fig. 2.9(a). Furthermore, the strain rates defining the transition into the threshold and inert strength limits,  $\dot{\epsilon}_{th}$  and  $\dot{\epsilon}_{in}$ , correspond to:

$$\dot{\epsilon}_{th} = \dot{\epsilon}_0 \cdot 0.65^{n+1} \quad , \quad \dot{\epsilon}_{in} = \dot{\epsilon}_0 \cdot 2.30^{n+1} \quad (5.9)$$

A schematic representation of the strength model is shown in Fig. 5.3. In a simulation, the model requires  $\sigma_0$  and  $n$  as input parameters; the other are preset.

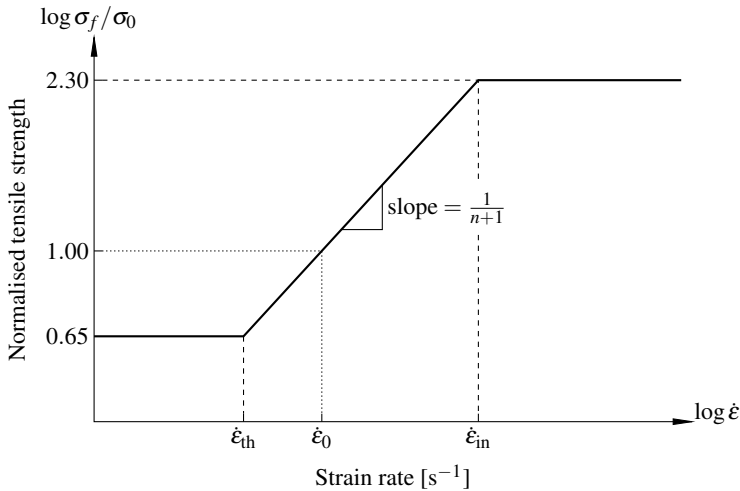


**Fig. 5.3** The implemented glass strength model shown as a relative tensile strength as a function of strain rate ( $\dot{\epsilon}_0 = 2.86 \cdot 10^{-5} \text{ s}^{-1}$ ).

### Progressive Damage Phase

After crack initiation is detected, the progressive damage phase is entered. The degradation in stiffness and thereby stresses is described by a cohesive Traction-Separation Law (TSL) in a smeared crack formulation. The chosen TSL follows a linear relationship between the crack opening stress normal to the crack (Mode I crack opening),  $\sigma_{\perp}$ , which according to Eq. (2.1) equates to  $\sigma_1$ , and the relative crack opening displacement<sup>1</sup>,  $\Delta w_c$ . This is an often assumed behaviour in brittle cracking simulations (see e.g. HILLERBORG et al. 1976; CAMACHO and ORTIZ 1996). Delaying the damage in that way helps control the damage rate whilst securing that the evolution of damage is not instantaneous at possible stress variations, thereby providing the demanded stability in the simulation of crack growth.

As described in Sec. 2.1.3, glass fracture may be determined by a fracture energy,  $G_{Ic}$ , which defines the energy required to create two new surfaces by cracking. The fracture energy can be directly related to the fracture toughness of glass,  $K_{Ic}$  (cf. Eq. (2.9) for a stationary crack). Both are constants that are well-defined for glass. Once crack growth is initiated according to Eq. (2.1), the elastic element stiffness reduces gradually with increasing crack opening,  $\Delta w_c$ , as shown in Fig. 5.4, until the work performed on the element matches  $G_{Ic}$ , i.e. until a complete loss in stiffness is reached. At that point, ABAQUS/Explicit deletes the element from the visualisation, and passes zero stresses and strain increments to the material point for the subsequent time increments in the analysis. However, if a crack is not fully developed, compressive stresses can still be carried by the element. The damage phase is then halted until tensile stresses, now following the dashed line with reduced stiffness in Fig. 5.4, cause the crack to grow again.

In the model,  $G_{Ic}$  is defined as the difference between the total work performed on the element and the elastic strain energy prior to crack initiation. Mathematically, the fracture energy can be expressed as the area of the triangle shown in Fig. 5.4:

$$G_{Ic} = \int_{\Delta u_0}^{\Delta u_f} \sigma_{\perp} d\Delta u = \frac{1}{2} \sigma_f (\Delta u_f - \Delta u_0) = \frac{1}{2} \sigma_f \Delta w_{cf} \quad (5.10)$$

where, in function of the relative nodal displacement,  $\Delta u$ ,  $\Delta u_0$  defines the relative displacement at which crack growth is initiated, and  $\Delta u_f$  the point where a crack is considered fully developed, i.e. complete loss in stiffness. Furthermore, in function of the relative crack opening width,  $\Delta w_c$ , a fully developed crack is determined at  $\Delta w_{cf}$ . Due to the included loading rate dependency in the tensile strength determination, these values may vary as the strain rate varies, as illustrated in Fig. 5.4. In other words, for a fixed element size and a constant  $G_{Ic}$ ,  $\Delta w_c$  decreases with increasing strain rate. Since the strain rate may also change in the damage phase, jumps can arise in the stiffness reduction. To avoid this, the tensile strength,  $\sigma_f$ , is fixed once it is exceeded by the maximum principal stress,  $\sigma_1$ , which is considered a reasonable assumption as long as crack growth happens fast.

In a smeared crack formulation where cracks are not modelled explicitly, it is more con-

<sup>1</sup>In fracture mechanics also known as Crack Mouth Opening Displacement (CMOD).

## 5. Simulation of Monolithic Glass Fracture Under Blast Loading

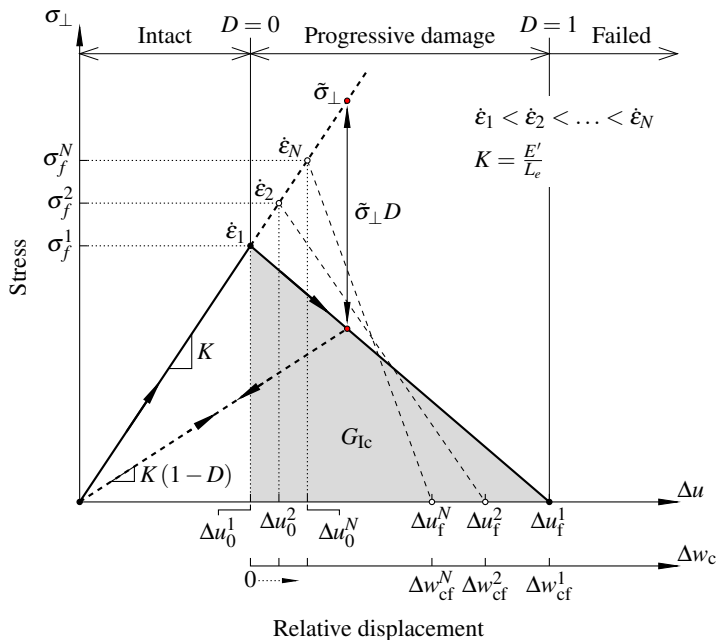


**Fig. 5.4** Crack opening stress as a function of relative nodal displacement,  $\Delta u$ , and relative crack opening displacement,  $\Delta w_c$ . The shown damage phase is governed by the rate-dependent strength model in Eq. (5.8).

venient in the VUMAT to characterise the crack opening by strains since no discontinuities are present until elements are removed. Fig. 5.4 defines an initial stiffness,  $K$ , which is expressed as:

$$K = \frac{E'}{L_e} = \frac{\sigma_f}{\Delta u_0} \quad (5.11)$$

where  $E'$  is the element stiffness in principal direction (normal to the crack), i.e.  $\sigma_1/\varepsilon_1$ , and  $L_e$  is the characteristic element length. Utilising Eq. (5.11) in combination with Eq. (5.10),  $\Delta u_0$  and  $\Delta u_f$  can be translated into strains as follows:

$$\varepsilon_0 = \frac{\Delta u_0}{L_e} = \frac{\sigma_f}{E'} \quad , \quad \varepsilon_f = \frac{\Delta u_f}{L_e} = \varepsilon_0 + \frac{2G_{1c}}{\sigma_f L_e} \quad (5.12)$$

Eq. (5.12) directly implies that the inequality  $(\varepsilon_f - \varepsilon_0) > 0$  is satisfied for any choice of  $L_e > 0$ . Hence, no element size dependency is embodied in the damage model concerning the correct prediction of the fracture energy,  $G_{1c}$ .

After the principal strain,  $\varepsilon_1$ , exceeds  $\varepsilon_0$ , the element starts to accumulate damage according to the damage evolution law given by Eq. (5.13), until  $\varepsilon_f$  is reached at which

the damage scalar,  $D$ , takes the value one and the material point is flagged zero, telling ABAQUS/Explicit to delete the element from the simulation:

$$D(\varepsilon_1) = \begin{cases} 0 & \text{for } \varepsilon_1 < \varepsilon_0 \\ \frac{\varepsilon_f(\varepsilon_1 - \varepsilon_0)}{\varepsilon_1(\varepsilon_f - \varepsilon_0)} & \text{for } \varepsilon_0 \leq \varepsilon_1 \leq \varepsilon_f \\ 1 & \text{for } \varepsilon_1 > \varepsilon_f \end{cases} \quad (5.13)$$

Here, a non-linear damage evolution is chosen to provide a linear degradation of the stiffness and the resulting stresses, thereby permitting the determination of  $G_{Ic}$  using the area of a triangle. In addition, the damage is defined as irreversible, i.e. the damage scalar is not allowed to decrease for again decreasing crack opening displacements. Lastly, the undamaged stresses,  $\tilde{\sigma}_{ij}$ , determined by Eq. (5.5) are subjected to the damage scalar to degrade them accordingly as shown in Fig. 5.4:

$$\sigma_{ij}|_{(t+\Delta t)} = (1 - D) \langle \tilde{\sigma}_{ij}|_{(t+\Delta t)} \rangle_+ - \langle \tilde{\sigma}_{ij}|_{(t+\Delta t)} \rangle_- \quad (5.14)$$

All stress components are reduced equally. Thus, a directional dependency of the crack in the damage phase is not considered, leaving the crack growth to be driven solely by the maximum principal stress/strain. To distinguish between tension and compression loading, Macaulay brackets,  $\langle \cdot \rangle$ , are used in Eq. (5.14).

A flowchart of the VUMAT implementation is provided in Appendix C, Sec. C.2. Summing up, the material damage model requires the following five input parameters to define the dynamic glass fracture:

1. the Young's modulus,  $E$ ,
2. the Poisson's ratio,  $\nu$ ,
3. a reference tensile strength,  $\sigma_0$ , representative for quasi-static loading, i.e.  $\dot{\varepsilon}_0 = 2.86 \cdot 10^{-5} \text{ s}^{-1}$ ,
4. the sub-critical crack growth parameter,  $n$ , to define the glass' dynamic fatigue behaviour, and
5. the fracture energy,  $G_{Ic}$ .

These are physical material properties that are well-defined for glass, independent of the element size. Hereinafter, the damage model is demonstrated and evaluated for a unit shell element.

### 5.2.2 Unit Element Test

The characteristics of the developed rate-dependent material damage model for ABAQUS/Explicit are evaluated for a unit shell element with dimensions as shown in Fig. 5.5. First, a single element is tested (Fig. 5.5(b)), followed by a three-element test (Fig. 5.5(c)) to investigate the effect of the damage phase on the elastic spring back of surrounding elements

5. Simulation of Monolithic Glass Fracture Under Blast Loading

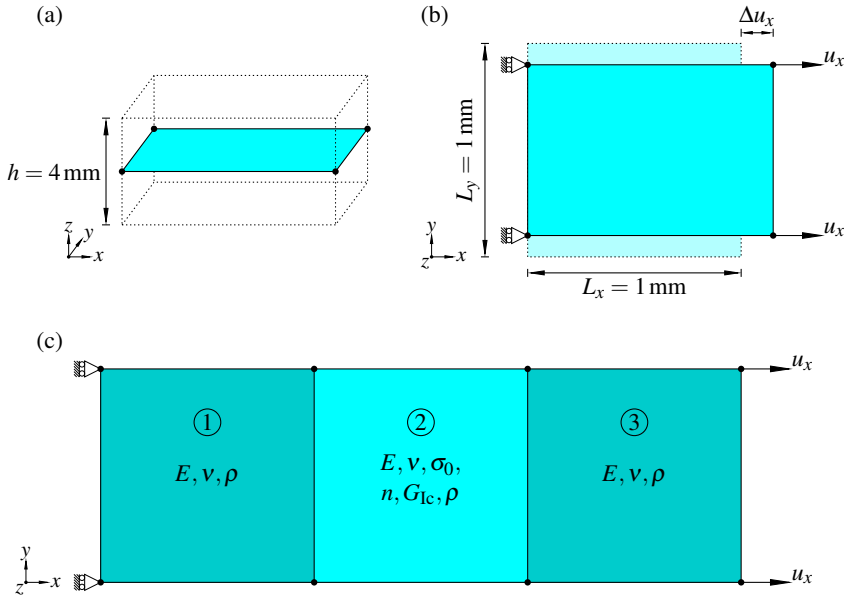


**Fig. 5.5** A unit shell element with the chosen dimensions (not in scale) and the applied boundary conditions: (a) the shell thickness, (b) the single unit element, and (c) three unit elements assembled in a row where the damage model is assigned to the central element.

that have not undergone damage. Both tests simulate the effect of a crack growing normal to the applied uniaxial tensile loading. To emphasise the included rate-dependency in the damage model, simulations were performed at four different constant strain rates: 1,  $10^1$ ,  $10^2$  and  $10^3 \text{ s}^{-1}$ . For that, a 4-node general-purpose shell element with reduced integration (S4R in ABAQUS) was chosen, having material properties assigned according to Table 5.2, which are typical values for glass.

The results for the single unit shell element strained uni-axially at four different rates are shown in Fig. 5.6 as the evolution of tensile stress as a function of the relative nodal displacement. It is demonstrated that the tensile strength increases expectedly with strain rate following the relationship given in Eq. (5.8). Data for the two highest rates simulated coincides with identical damage phases because the applied strain rates caused the tensile

**Table 5.2** Material properties assigned to the unit shell element.

Property, Symbol	Value and unit
Young's modulus, $E$	70.0 GPa
Poisson's ratio, $\nu$	0.23
Reference tensile strength, $\sigma_0$	45.0 MPa
Sub-critical crack growth parameter, $n$	16.0
Fracture energy, $G_{Ic}$	$8.0 \text{ J m}^{-2}$
Density, $\rho$	$2500 \text{ kg m}^{-3}$

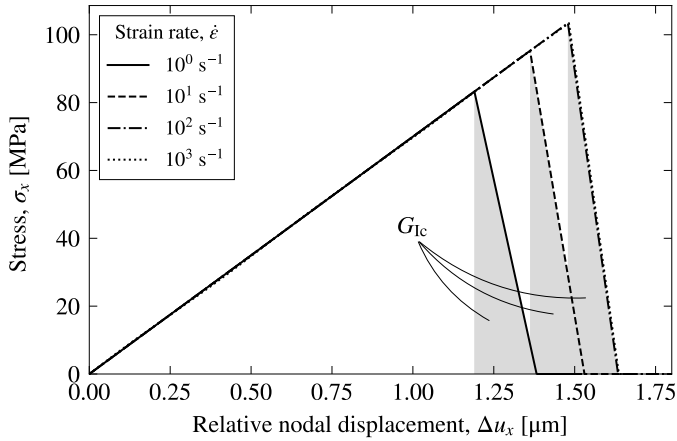


**Fig. 5.6** Crack opening stress as a function of relative nodal displacement for the unit shell element.

strength to reach the limit at  $\sigma_f/\sigma_0 = 2.30$ , which according to Eq. (5.9) with properties listed in Table 5.2 is expected to happen at rates above  $4 \cdot 10^1 \text{ s}^{-1}$ . Also, the damage model show to perform well regarding the prediction of the fracture energy. The triangular areas beneath the damage phases amount to the set value of  $G_{Ic}$ . Moreover, it is seen that the slope of the damage becomes steeper with increasing tensile strength as a direct consequence of a constant chosen fracture energy (also sketched in Fig. 5.4), meaning that damage occurs faster at higher loading rates. Whilst being independent of element size in calculating  $G_{Ic}$ , the damage model in its current implementation is dependent on the element size when predicting crack velocities. This dependency is evident from the following expression derived to estimate a crack velocity,  $v$ , defined as the time,  $\Delta t$ , it takes a crack to develop fully through an element of length  $L_e$ , assuming a constant strain rate throughout the damage phase:

$$v = \frac{L_e}{\Delta t} = \frac{L_e \dot{\epsilon}}{\epsilon_f - \epsilon_0} = \frac{L_e^2 \sigma_f \dot{\epsilon}}{2G_{Ic}} \quad (5.15)$$

Here,  $L_e$  enters into the equation with a power of two, thus being a dominant factor in the prediction of  $v$ . For example, achieving crack velocities correctly between  $1500$  and  $2500 \text{ m s}^{-1}$  (a range typically expected for dynamic glass fracture (OVEREND et al. 2007b)) at a strain rate of  $10^1 \text{ s}^{-1}$  with properties given in Table 5.2, an element size of  $5$  to  $6.5 \text{ mm}$  would be needed, which seems feasible. However, as strain rate may vary in a blast loaded glass structure,  $L_e$  can scale quickly when aiming a constant crack velocity. Therefore, the damage model should be used with caution in this regard.

The delayed damage is further investigated on three unit shell elements assembled in a row that are subjected to uniaxial loading with the central element having assigned the damage model; see Fig. 5.5(c). The outer elements only determine the elastic response. This setup enables the evaluation of the earlier discussed elastic spring back of neighbouring

## 5. Simulation of Monolithic Glass Fracture Under Blast Loading

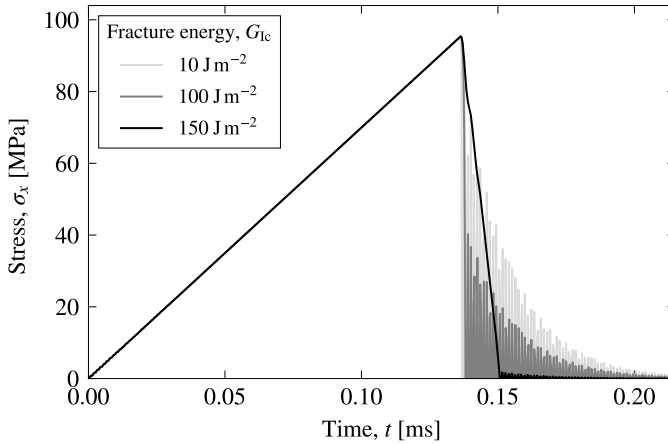


**Fig. 5.7** Stress normal to the crack growth direction as a function of time for the first shell element (damage model not applied) in the three-element test, uni-axially strained at  $\dot{\epsilon} = 10^1 \text{ s}^{-1}$ .

elements that have not undergone damage. Although the boundary conditions are not entirely equivalent to what is found in a larger discretisation of a structure, where more than one element surrounds a developed crack, this three-element test can still showcase the effect of the delayed damage on the elastic spring back.

The rate at which damage evolves in the model can be directly linked to the applied strain rate. Hence, the duration of the damage phase can be determined from Eq. (5.12), as in Eq. (5.15), which at constant strain rate varies with  $G_{Ic}$  and  $L_e$ . Therefore, the spring back is simulated for three different fracture energies, 10, 100 and  $150 \text{ J m}^{-2}$ , while the element length and the applied strain rate are kept constant with 1 mm and  $10^1 \text{ s}^{-1}$ , respectively. All other required model input parameters are defined according to Table 5.2. The effect of the delayed cracking, i.e. the progressive damage phase in Fig. 5.4, on the spring back of surrounding elements, is shown in Fig. 5.7. For the first shell element, having no damage model assigned, the stress normal to the crack growth direction is plotted as a function of time for the three fracture energies.

From Fig. 5.7 it is evident that the magnitude of  $G_{Ic}$  has a significant effect on the elastic spring back of the neighbouring elements. The lowest fracture energy of  $10 \text{ J m}^{-2}$  with the shortest damage phase results in the most severe oscillations after a complete loss in stiffness is reached in the central element. An improvement is observed for a fracture energy increased with a factor of ten. However, it still causes oscillations of significant amplitudes. Another increase to  $150 \text{ J m}^{-2}$ , having the longest damage phase of the three investigated, show the most significant damping effect on the spring back as oscillations are negligibly small upon failure of the central element. When considering glass, its fracture energy for a stationary crack typically ranges in the order of magnitude around  $10 \text{ J m}^{-2}$  (see Table 2.1), which for most engineering problems with the present damage model would result in an abrupt damage evolution due to the often coarser mesh used. To improve stability in terms

of damping out eventual aroused crack-induced stress oscillations, one can reduce the element size according to Eq. (5.12), thereby favourably extending the damage phase without the need to modify the fracture energy. However, this comes with the cost of increased computational efforts.

### 5.3 Damage Model Validation on Full-scale Blast Test Data

The developed rate-dependent progressive damage model for dynamic glass fracture is validated in simulations of full-scale blast tests on monolithic window glass found in the literature. Typically, such test setups consist of a test window (a glass pane mounted into a frame) that is installed in a (concrete) test cubicle, as illustrated in Fig. 5.8(a). A certain distance apart from the window, the stand-off distance, an explosive is placed on or close to the ground, thereby at detonation producing a hemispherical pressure wave loading the window destructively with a pressure-time history as schematically shown in Fig. 1.10. Similar arrangement was used by SPILLER et al. (2016) and JOHNS and CLUBLEY (2015), both reporting on the blast performance of monolithic glazing. The main parameters of these experiments that are considered in the validating simulations are summarised in Table 5.3. That is, the glass plate dimensions, and parameters characterising the blast tests such as stand-off distance,  $R$ , charge weight (TNT-equivalent),  $W$ , and scaled distance (see also Eq. (1.2)),  $Z$ .

From the numbers in Table 5.3 it should be noted that both the surface area of the tested glass panes as well as the blast wave characteristics based on the values for  $Z$  are almost identical. However, the reported research objectives of these blast tests are different; there-

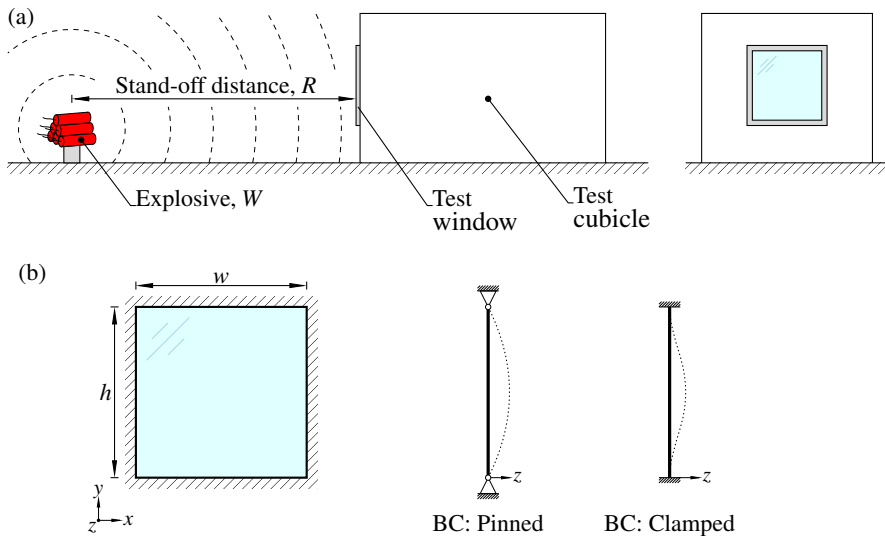


**Fig. 5.8** A sketch of the considered blast test setups in (a), and the boundary conditions (BC) of the glass pane applied to the ABAQUS/Explicit simulations of the blast tests in (b).

## 5. Simulation of Monolithic Glass Fracture Under Blast Loading

**Table 5.3** The blast test parameters from the literature.

	Glass plate dimensions <sup>‡</sup>		Blast test data		
	$t_{\text{nom}}$ [mm]	$w \times h$ [mm <sup>2</sup> ]	$R$ [m]	$W$ [kg]	$Z$ [m kg <sup>-1/3</sup> ]
Test A*	12	894 × 894	20.00	51.25	5.38
Test B-1 <sup>†</sup>	4	870 × 870	19.50	41.00	5.66
Test B-2 <sup>†</sup>	8	870 × 870	19.50	41.00	5.66

\* Data from SPILLER et al. (2016).

<sup>†</sup> Data from JOHNS and CLUBLEY (2015).

<sup>‡</sup> The exposed glass area of the window.

fore, named Test A and Test B in the following. While SPILLER et al. (2016) investigated the response of 12 mm-thick annealed window glass up to fracture (Test A), JOHNS and CLUBLEY (2015) made detailed investigations on the post-fracture response of 4 mm- and 8 mm-thick monolithic glazing panels (Test B-1 and B-2), measuring displacement and velocity of flying glass shards. Thus, various glass performance measures for blast loading are provided, against which the damage model can be validated.

As with any other problem to model with the Finite Element Method (FEM), it is vital to consider boundary conditions and material properties that reflect any given case as closely as possible. Beginning with the boundary conditions, the blast tests to simulate are reduced to the exposed area of the glass panes, i.e. the direct interaction with a window frame and the underlying supporting structure is disregarded as only glass performance is of interest. As the clamping stiffness of the test window frames is unknown, two types of supports can be taken into consideration for the glass pane: (i) a pinned support, being the least stiff solution, allowing for rotations of the glass pane's edges, and (ii) a clamped support preventing the edges from rotating (see Fig. 5.8(b)). However, typically, a frame only sustains a small fraction of a glass pane's edge, making it difficult to think of a fully clamped support. Therefore, the pinned solution is expected to model the problem most precisely. Both boundary conditions will be looked at in the validation of the damage model as they can be considered a lower and upper bound.

In the definition of the glass' physical and mechanical material properties, values according to the European Standard CEN/TS 19100-1:2021 are chosen:  $E = 70.0 \text{ GPa}$ ,  $\nu = 0.23$ , and  $\rho = 2500 \text{ kg m}^{-3}$ . The other parameters governing the cracking in the material model are  $\sigma_0$ ,  $n$ , and  $G_{\text{Ic}}$ . Since glass strength is not a material constant, the reference tensile strength,  $\sigma_0$ , is varied in the simulations of the blast tests. The sub-critical crack growth parameter is chosen according to Fig. 2.9(a), i.e.  $n = 18.1$ . Further, the fracture energy of the glass is assumed not to vary with strain rate. Hence, a constant value is determined from Eq. (2.9) (for plane stress) using  $K_{\text{Ic}} = 0.75 \text{ MPa m}^{1/2}$ , resulting in  $G_{\text{Ic}} = 8.0 \text{ J m}^{-2}$  for a stationary crack.

The models of the three glass panes in Table 5.3 consider the full pane size. The discretisation is performed using 4-node general-purpose shell elements (S4 in ABAQUS) with seven integration points through the thickness. As some mesh dependency in the damage phase

of the model was identified in Sec. 5.2.2, a structured mesh with homogeneous element sizes is chosen, resulting in identical cracking behaviour throughout the mesh. In ABAQUS, the blast pressure loading is modelled as an incident wave interaction using the built-in CONWEP model, which takes the TNT-equivalent charge mass and the type of blast loading, i.e. surface or air blast, as input. These properties are then assigned to a reference point defining the location of the explosive. For Test A, no height is reported in which the explosive was placed, while for Test B, the glass panes were oriented normal to the explosive. Therefore, in the simulations, the blast source is placed 0.5 m below the pane centre for Test A, which was estimated from the images reported, and in the height of the centre of the panes for Test B, both with the stand-off distance and charge weight given in Table 5.3. Fig. 5.9 compares the simulated time histories of the reflected pressure acting on the glass panes resulting from a hemispherical blast wave definition (surface blast) with the measurements reported in SPILLER et al. (2016) and JOHNS and CLUBLEY (2015). Overall, a good agreement is seen between experiment and simulation, indicating that the CONWEP model in ABAQUS/Explicit reliably predicts blast wave characteristics, both the positive and the negative phase of the pressure-time profile, and the peak positive reflected pressure,  $p_r$ . The discrepancy between the predicted and the measured impulse values are in SPILLER et al. (2016) explained by a sudden venting into the test cubicle allowed by the fracture of the window glass. It is assumed that this was also the case for Test B-1 and B-2, although nothing is reported about it. Since the fluid medium (in this case air) is not captured by the FEM formulation, such changes cannot be simulated.

### 5.3.1 Pre-fracture Response (Test A)

The prediction of the pre-fracture response of monolithic glazing to blast loads, i.e. the deflection up to fracture and the resulting load-bearing capacity, using the developed damage model, is validated on blast test data reported by SPILLER et al. (2016). For the simulations, the squared glass pane with dimensions as in Table 5.3 is discretised using  $150 \times 150$  elements, resulting in a uniform element size of approx. 6 mm and converged deflection results (see Appendix D). The thickness of the shell elements is set according to the reported nominal thickness of 12 mm. In addition to the blast tests, SPILLER et al. (2016) also investigated the quasi-static strength of small-scale samples of the same glass as the windows without reporting the exact loading rate, determining a mean strength of 80.3 MPa ( $\pm 13$  MPa). To reflect the scatter in the strength data, the simulations are performed for reference tensile strengths  $\sigma_0 = [70, 80, 90]$  MPa, assuming that the loading rate of the reported strength tests matches the model's reference of  $\dot{\epsilon} = 2.86 \cdot 10^{-5} \text{ s}^{-1}$  ( $\approx 2.0 \text{ MPa s}^{-1}$ ).

The first task in the prediction is to identify when the glass pane fractured. This point is assumed to be reached when the glass can no longer carry loads. Therefore, from the simulations, the total lateral reaction forces ( $\Sigma R_z$ , normal to the glass pane) were extracted as a function of time for the three values of  $\sigma_0$  and both boundary conditions shown in Fig. 5.8(b). The results are given in Fig. 5.10(a) and (b) for the pinned and clamped edge support, respectively. The pane with the pinned edge shows a significant drop in the reaction force after a maximum is reached at different times depending on the reference tensile strength used in the simulation (marked by red dots in the figure), determining the

5. Simulation of Monolithic Glass Fracture Under Blast Loading

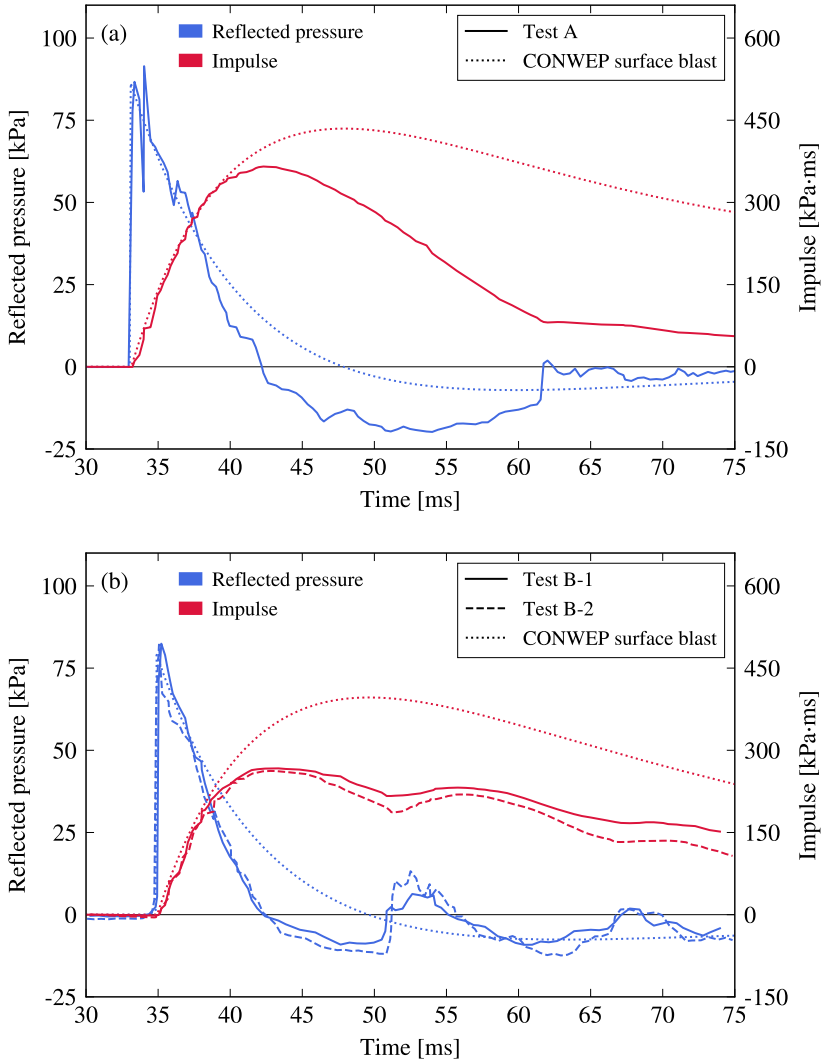


**Fig. 5.9** In the literature reported measurements on the reflected pressure and impulse from blast tests on monolithic window glass compared to the CONWEP surface blast in ABAQUS/Explicit. Blast test data in (a) from SPILLER et al. (2016) (Test A), and in (b) from JOHNS and CLUBLEY (2015) (Test B-1 and B-2).

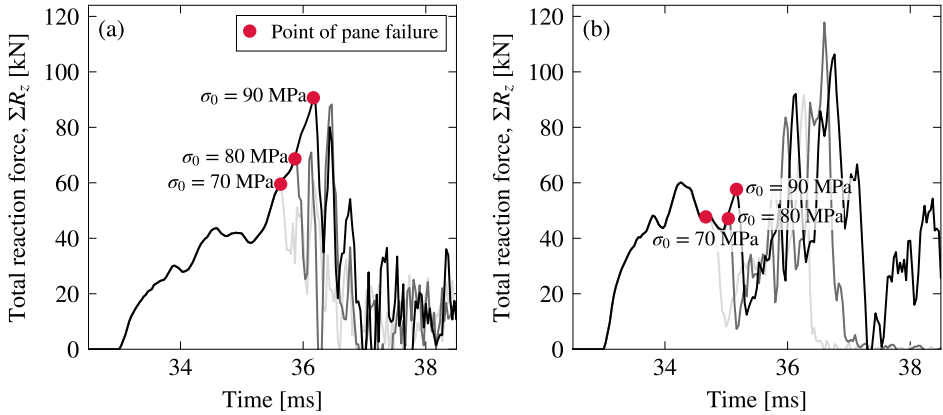


**Fig. 5.10** The sum of the lateral reaction forces ( $\Sigma R_z$ ) of the glass pane as a function of time for the three reference tensile strengths simulated, and the estimated points of pane failure: (a) pinned edge support and (b) clamped edge support.

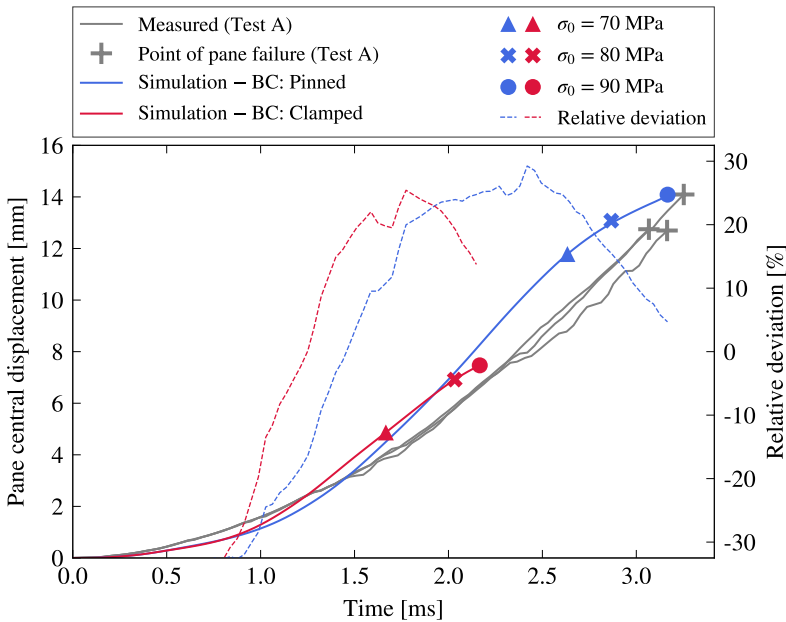


**Fig. 5.11** The numerically determined central displacement of the glass pane as a function of time for the two boundary conditions, i.e. pinned and clamped, compared to measurements from SPILLER et al. (2016) (Test A), and the estimated points of pane failure for the three reference tensile strengths.

point at which the glass has lost its load-carrying capacity. Almost similar behaviour can be observed for the pane simulated with the clamped edge. However, after the indicated initial sudden partial loss in load-carrying capacity caused by some cracks that developed along the pane's edge due to the clamping, further load is carried by the corners until the pane centre fractures completely. This is seen as the second drop that reaches zero. In the further analysis, the initial loss in load-bearing capacity defines the point of pane failure. The oscillations after the identified pane failure seen in Fig. 5.10(a) are caused by some elements that, after fracture, still adhere to the pane support and vibrate. A note to add here is that the time at which the reaction forces reaches zero, at around 37 ms, matches the time at which the predicted impulse values in Fig. 5.9(a) start to deviate from the measurements, supporting the explanation of venting given by SPILLER et al. (2016). Furthermore, the data in Fig. 5.10(a) demonstrate that the material damage model can predict an increase in a glass structure's load-carrying capacity with increasing tensile strength, which by its formulation also was expected.

With the identified points of pane failure, the pane central displacement is plotted in Fig. 5.11 as a function of time relative to the arrival time of the blast wave front,  $t_a$ , for both support conditions, and further compared to measurements from SPILLER et al. (2016). It is seen that the simulations for both supports over-predict the displacements up to 30% compared to the measured values, while still having similar courses. An overprediction is also observed in some of the simulations reported by SPILLER et al. (2016) with no further explanations given. The clamped edge support results in a too early pane failure, which can be attributed to the increased stiffness introduced by the clamping. For the pane with the pinned edge support, the damage model show to perform well in determining both the peak central displacement and time at failure, as the results for  $\sigma_0$  between 80 and 90 MPa are close to the measurements from the blast test in which the glass had similar quasi-static strengths. This good agreement further indicates that the glass strengths determined by the damage model at the high loading rate induced by the blast wave must have been similar to those present in the experiments. Hence, it is demonstrated that the chosen input parameters sufficiently define the rate-dependency in the developed material damage model. However, a parameter to vary could be the sub-critical crack growth parameter,  $n$ . For instance, changing it to 16, typically used in the design of load-bearing glass members, will cause the strength to enhance faster with increasing strain rate following Eq. (5.8). This results in a slight extension of the time-to-failure, delaying the initiation of the damage phase according to Fig. 5.4.

### 5.3.2 Post-fracture Response (Test B)

The damage model's capability to predict the post-fracture response of monolithic glazing subjected to blast loading is validated on blast test data reported by JOHNS and CLUBLEY (2015). The squared glass panes with dimensions as in Table 5.3, cf. Test B-1 and B-2, are discretised with a structured mesh, again securing homogeneous element sizes. However, since the post-fracture response is more a matter of fragment sizes and their acceleration than the material's constitutive behaviour in the deformation of the glass pane up to fracture, the mesh is assumed to have a significant impact due to the inherent mesh depen-

dency in the element deletion technique. Therefore, three different mesh configurations are investigated with the size in number of elements along the edges of  $N_{el} = 100 \times 100$ ,  $150 \times 150$ , and  $200 \times 200$ , resulting in element sizes of 8.7, 5.8 and 4.4 mm, respectively, with converged deformations/stresses up to fracture (see Appendix D). No detailed quasi-static strength data for the glass is reported by JOHNS and CLUBLEY (2015). Thus,  $\sigma_0$  is determined iteratively until the best fit to measurements is obtained for each of the three mesh configurations. In terms of the pane's edge support, only the pinned boundary condition is applied, as it previously for Test A was shown to fit better the experimental data.

The simulated post-fracture responses of the 4 mm and 8 mm monolithic glazing, subjected to the pressure-time profile given in Fig. 5.9(b), are shown in Figs. 5.12 and 5.13, respectively. The results are the peak leading fragment displacement and velocity as a function of time. Furthermore, these values are compared to measurements reported in JOHNS and CLUBLEY (2015). From the figure legends, it is evident that there exist some mesh size dependency in the iterative process of determining  $\sigma_0$ . For the 4 mm glazing, strength values between 175 MPa and 200 MPa result in the best fit, while values between 117.5 MPa and 125 MPa are found for the 8 mm glazing. These are strength values that are representative for glass (see e.g. SWAB et al. 2014), although they seem somewhat high compared to what is reported in SPILLER et al. (2016) for Test A. With a properly chosen value for  $\sigma_0$ , only minor differences are seen between the three mesh configurations investigated. Furthermore, simulations and experiments are seen to be in good agreement with a maximum difference of 20 % over the majority of time investigated. However, no resistance from air nor gravity was included in the simulations, which, if it would have been, would cause a deceleration of the flying fragments. In that case, a better match between simulations and measurements from the blast tests could be presumed where most considerable deviations are seen, i.e. at the sudden drops in measurements. That is, after 20 ms in Fig. 5.12 and after 30 ms in Fig. 5.13. At pane failure, where the blast wave is still acting on the glass, it seems reasonable to disregard these counteracting forces. In a longer simulation, where the blast wave at some point is less dominant, these physical properties need to be included to better capture the glass' post-fracture response.

Potential sources of error include the crack formation through the element deletion technique and resulting fragment sizes. A comparison of the different obtained fracture patterns from the simulations with the three mesh configurations is provided in Fig. 5.14 for both glazing thicknesses. It is seen that the fractured panes mainly consist of horizontally and vertically growing cracks with some symmetry, which directly stems from the choice of using a structured mesh. Apart from that, some physically valid characteristics can still be identified, which is that cracks tend to seek direction towards the pane corners as a direct consequence of plate bending. Comparing the three mesh configurations reveals no significant difference in fracture patterns. Furthermore, they have in common that large-sized glass pieces are produced by fragmenting, which could explain some of the observed differences between simulations and experiments. Of course, this is not expected cracking behaviour for glass under such load conditions. However, the focus of the developed material damage model was not to capture realistically looking fracture patterns, which

5. Simulation of Monolithic Glass Fracture Under Blast Loading

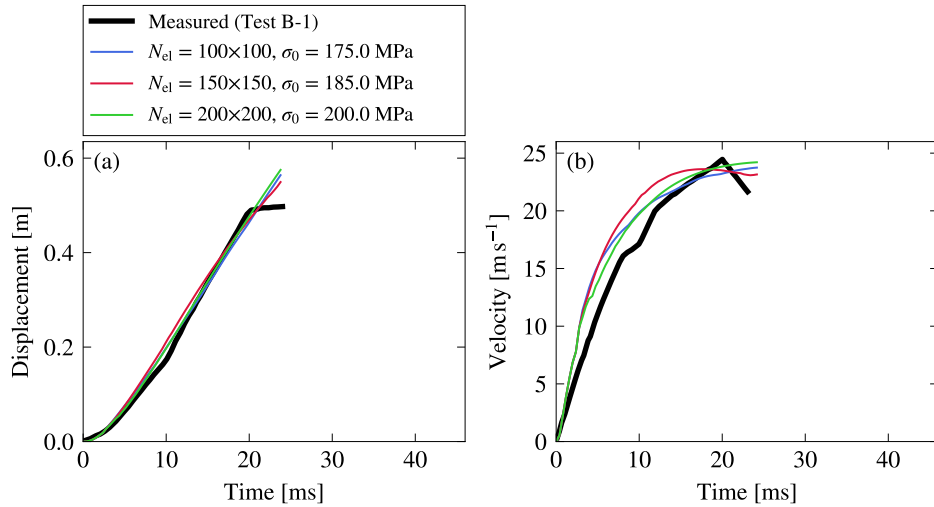


**Fig. 5.12** Simulated post-fracture response, shown as the peak leading fragment displacement in (a) and velocity in (b) as a function of time, for the 4 mm monolithic glazing (Test B-1) compared to measurements from JOHNS and CLUBLEY (2015). Results are provided for different mesh sizes and reference tensile strengths that resulted in the best fit.

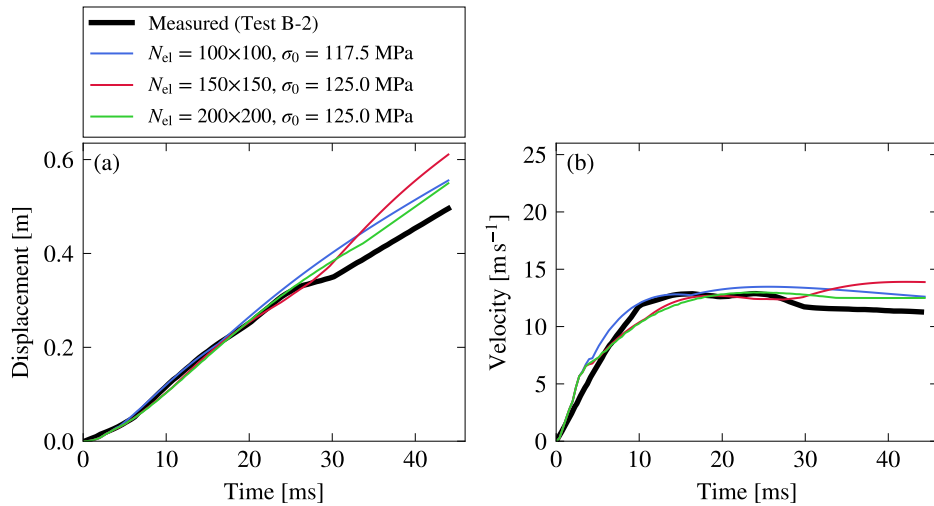


**Fig. 5.13** Simulated post-fracture response, shown as the peak leading fragment displacement in (a) and velocity in (b) as a function of time, for the 8 mm monolithic glazing (Test B-2) compared to measurements from JOHNS and CLUBLEY (2015). Results are provided for different mesh sizes and reference tensile strengths that resulted in the best fit.

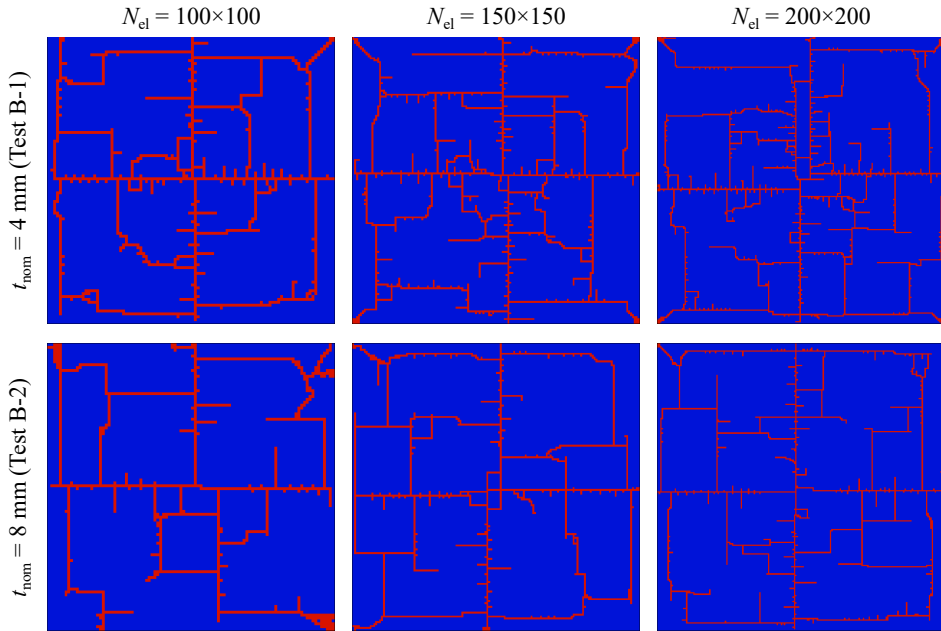


**Fig. 5.14** Fracture patterns for the three mesh configurations obtained from the simulations of Test B-1 and B-2 in the final time step.

definitely would require more advanced techniques and increased computational efforts, but rather to predict global quantities, such as load-bearing capacity and the glass response after fracture by adopting simple approaches that are practicable in general engineering practice. An improvement for future investigations, however, could be to apply an unstructured mesh with uniform element sizes as suggested by PELFRENE et al. (2016) to obtain more natural crack paths.

Lastly, the post-fracture response prediction using the damage model is further validated by comparing linear approximations of 2D deflected panel shapes with high-speed images by JOHNS and CLUBLEY (2015). The comparison is performed for the 8 mm monolithic glazing panel with  $N_{el} = 200 \times 200$  at different times relative to the arrival time of the blast wave front,  $t_a$ . The images to compare are shown in Fig. 5.15 together with the linear approximations of the panel shape. Overall, the dynamic glass fracture simulation captures similar characteristics as the experiment where the angle of the upper and lower pane,  $\alpha$ , increases with time. However, it becomes visible once more that the simulated fragmentation deviates from reality. The damage model results in too large fragment sizes, disturbing the continuity in the displacement shape. Because the glass pane in the blast test fragmented into smaller glass shards, the shapes captured by the high-speed images show more continuity. A direct comparison of the different approximated angles is provided in Table 5.4. Here, only  $\alpha_3$ ,  $\alpha_5$ , and  $\alpha_7$  compare well with the experimental data. The remaining angles show deviations between 35 % and 63 %.

5. Simulation of Monolithic Glass Fracture Under Blast Loading

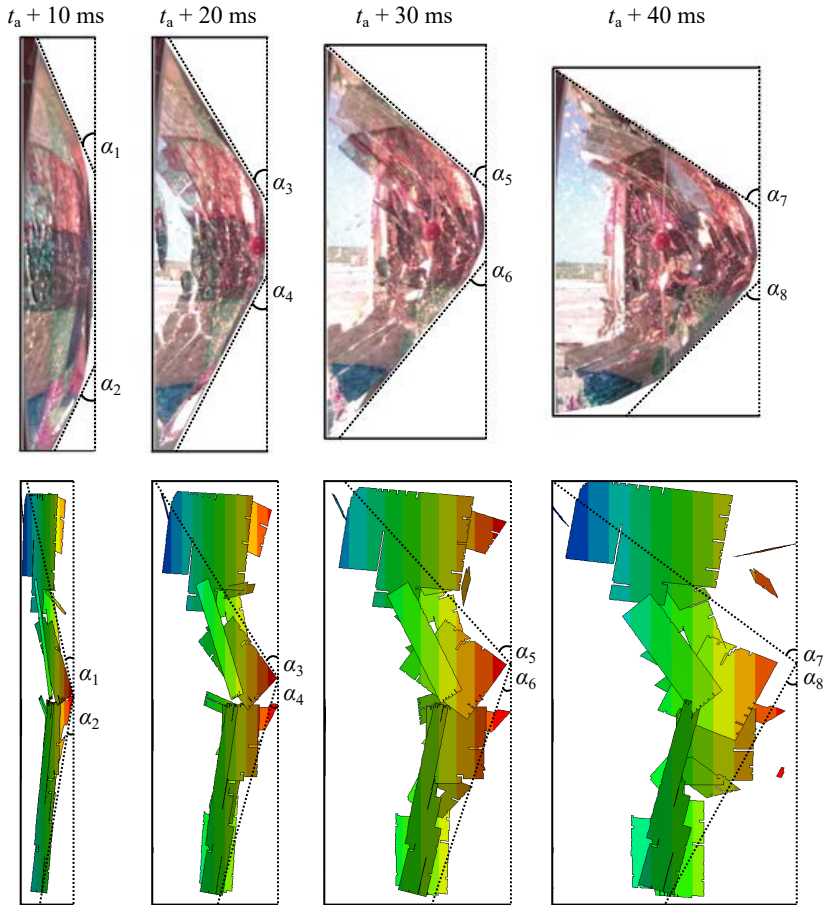


**Fig. 5.15** The 8 mm monolithic glazing panel post-fracture displacement shape for different times, captured with high-speed cameras in the blast test (upper row) and obtained from a simulation with the material damage model using  $N_{el} = 200 \times 200$  (lower row). (Upper row images are reused from JOHNS and CLUBLEY (2015) with permission of ICE Publishing; permission conveyed through Copyright Clearance Center, Inc.)

**Table 5.4** Comparison of upper and lower panel angle,  $\alpha$ , for the 8 mm monolithic glazing (Test B-2) shown in Fig. 5.15.

	$\alpha_1$	$\alpha_2$	$\alpha_3$	$\alpha_4$	$\alpha_5$	$\alpha_6$	$\alpha_7$	$\alpha_8$
Experiment*	24°	25°	34°	29°	48°	40°	54°	44°
Simulation	12°	9°	32°	15°	42°	18°	53°	29°
Difference	49 %	63 %	6 %	49 %	12 %	55 %	1 %	35 %

\* Data from JOHNS and CLUBLEY (2015).

### 5.3.3 Concluding Remarks

The rate-dependent progressive damage model in Sec. 5.2 has been validated in simulations of full-scale blast experiments found in the literature. These reports on two types of glass performance investigations: (1) the response to blast loading up to fracture (SPILLER et al. 2016), and (2) the post-fracture response (JOHNS and CLUBLEY 2015). Given the simple approaches adopted for the crack simulation, both cases were predicted well using the damage model, although with minor differences to the reported measurements from the blast tests. While the simulated crack growth and resulting fracture patterns cannot be compared to the physical cracking behaviour of glass, the prediction of global quantities such as load-bearing capacity and displacement/velocity histories of flying glass prove to be sufficiently captured by the model. However, a parameter that should be chosen carefully is the tensile strength defined by  $\sigma_0$ , which, due to the nature of glass, cannot be considered a material constant (cf. Sec. 2.1).

## 5. Simulation of Monolithic Glass Fracture Under Blast Loading

## Conclusions and Future Work

*Structural Engineering is “the art of moulding materials we do not really understand into shapes we cannot really analyze, so as to withstand forces we cannot really assess, in such a way that the public does not really suspect.”*

– Dr. E. H. BROWN (1967)

### 6.1 Conclusions

This thesis contributes to an improved understanding of the mechanical properties of glass used in construction, focusing on tensile strength and stiffness at loading rates relevant for blast loading. In the context of the threats, such as terror, faced by our society, this is a load scenario buildings are increasingly exposed to. Furthermore, the work presented contributes to the computer-aided engineering, supporting the design of blast resilient glazing.

A comprehensive literature review based on 57 publications that report on the dynamic fatigue behaviour of soda-lime-silica glass was conducted, revealing a significant strain rate dependency of the glass' tensile strength, which increases with increasing strain rate (linearly on a log-log scale). The lowest and highest rates reported determine a strength reduction of about 60 % and an increase of about 175 %, respectively, relative to a strength ( $\sigma_0$ ) interpolated at a strain rate of  $2.86 \cdot 10^{-5} \text{ s}^{-1}$  ( $\approx 2.0 \text{ MPa s}^{-1}$  for  $E = 70 \text{ GPa}$ ). From the reviewed dynamic fatigue tests, which were divided into the test environments air (25-67 % RH) and water (liquid or 100 % RH), the sub-critical crack growth parameter  $n$  was determined to be 18.1 and 16.5, respectively, confirming a decrease in  $n$  for increasing water content. Most of the data were measured at moderate strain rates, and only a limited amount of data were found to characterise glass at high strain rates relevant to blast loading. Nevertheless, possible strength limits were suggested because the data exhibited a beginning asymptotic behaviour at the very low and very high rates. For  $\dot{\epsilon} \rightarrow 0$ , a limit at  $\sigma_{f,d}/\sigma_0 = 0.65$ , and for  $\dot{\epsilon} \rightarrow \infty$ , a limit at  $\sigma_{f,d}/\sigma_0 = 2.30$  were estimated for the glass tested in air. Only a lower limit at 0.65 could be estimated from the data that characterise glass in water. However, much more testing is needed to determine well-defined limits and rule out the disagreements observed at the high strain rates relevant to blast loading. Lastly, from the reviewed glass strengths, it could be concluded that these agree with most of the load duration factors specified by several national and international Standards and that they support extrapolations into shorter load duration than currently provided by the Standards. Engineers routinely use these Standards for structural glass design.

## 6. Conclusions and Future Work

To expand on the limited knowledge about the glass' behaviour at high strain rates, a novel and successful design of a modified Split-Hopkinson Pressure Bar (SHPB) was developed to test flat glass samples dynamically in a ring-on-ring bend test configuration. The modifications to the standard SHPB design enabled high-speed cameras for fracture assessment and non-contact optical deflection measurements with Stereo Digital Image Correlation (Stereo-DIC) by transforming the transmission bar into a tube having the incident bar going through. With the load ring mounted to the incident bar and the support ring, with a conical trough-going hole, to the transmission tube, a significant part of a sample's tensile surface (around 54 %) were made visible. However, two challenges important to consider in future designs were identified: (1) the modifications caused some noise in the measured incident bar signal, and (2) signals began to overlap in the rear part of the reflected pulse, which did not disturb the reported strengths but could have been prevented by using a longer incident bar.

Using the modified SHPB and a universal testing machine, 315 soda-lime-silica glass samples, annealed and thermally tempered with as-received surfaces, were tested at two strain rates: a quasi-static in average at  $2.2 \cdot 10^{-5} \text{ s}^{-1}$  ( $\propto 2.0 \text{ MPa s}^{-1}$ ) and a dynamic in average at  $48 \text{ s}^{-1}$  ( $\propto 4.3 \cdot 10^6 \text{ MPa s}^{-1}$ ). As expected, the glass' surface strength increased with increasing compressive surface stress at both strain rates tested. For the quasi-statically tested glass, a slope of 1.4, and for the dynamically tested glass, a slope of 1.7 was found. Also, the residual stresses did not show to significantly influence the strain rate dependency of the glass strength. Each tested state of residual compressive surface stress (including the almost zero-state in the annealed float glass) significantly enhanced with increasing strain rate at similar trends. Thus, strength increases between 60 % and 86 % were found, which agree with comparable data found in the literature. From the performed Stereo-DIC deflection measurements with high-speed cameras, the glass' Young's modulus was found not to be dependent on strain rate, therefore concluding that the 70 GPa as provided by the European glass code CEN/TS 19100-1:2021 also applies to high strain rate loading.

Based on the glass characteristics at high strain rates obtained through the literature review and the conducted experimental characterisation, a rate-dependent progressive damage model was developed to simulate monolithic glass fracture under blast loading with shell elements in the commercial FEM software ABAQUS/Explicit. The focus was on a simple implementation, the element deletion technique, which is considered practicable for general engineering practice. The damage model was successfully tested on a unit shell element and further validated on full-scale blast experiments on monolithic glazing found in the literature. The validation showed that the damage model could reliably predict global quantities such as a glass pane's resistance to blast loading and its post-fracture response. However, realistic crack growth and fracture patterns were not achieved due to the inherent mesh dependency in the element deletion technique and the use of a structured mesh. A model input parameter that should be chosen carefully is the glass' tensile strength, which is not a material constant due to the nature of glass.

## 6.2 Future Work

Recommendations for future work within the areas of research covered by the thesis are given below:

- In the present investigation of the effect of residual stresses on the glass strength's strain rate dependency, only a narrow range of residual compressive surface stresses (40 MPa to 53 MPa) were included because the small sample geometry made it difficult to reach higher stresses with the commercial thermal tempering. Thus, an alternative way of tempering small glass samples to introduce higher residual stresses would be required to extend the investigation to include fully tempered glass.
- The measured glass strengths show a typical large scatter due to the as-received surface condition. This was not changed to capture the actual characteristic differences in surface flaws. Conducting a thorough investigation of the effect of different surface qualities on the loading rate sensitivity at high strain rates could provide necessary data to determine the resistance to blast loading of, e.g. aged and weathered glass (see e.g. DATSIU and OVEREND 2017). Also, well-controlled surface conditions can reduce the scatter significantly (see e.g. NIE et al. 2010; MEYLAND et al. 2019).
- To a large extent, laminated glass is used for blast mitigating glazing designs. In the present thesis, only the high strain rate properties of monolithic glass were investigated because the properties of interlayer materials, such as PVB, are well-described in the literature (see e.g. PELFRENE 2016). Conducting dynamic tests on small laminated glass samples in the modified SHPB could probably determine the high strain rate characteristics of the sandwich-structure, i.e. the interaction between the glass and the interlayer material in bending. However, this would require changes in the design of the modified SHPB, as the samples become much stiffer than the single monolithic glass samples investigated in this thesis.
- The glass strengths reported are determined at two strain rates. More tests at intermediate and even higher strain rates could provide data to determine the sub-critical crack growth parameter  $n$  and more accurately show when a possible strength limit is reached.
- A rate-dependent progressive damage model for glass was developed and validated against data from full-scale blast experiments on monolithic glazing found in the literature. Further research interests could be directed towards the simulation of laminated glass by applying the developed damage model for glass with models validated for the PVB-interlayer from the literature.
- In the sense of computer-aided engineering, the developed rate-dependent damage model for glass could be applied in a design case. Such a case could include predicting a glass pane's resistance to blast loading and the dimensioning of, e.g. the underlying load-bearing structure and possible energy-absorbing brackets, typically applied to further mitigate the effect of an explosion.

## 6. Conclusions and Future Work

# Bibliography

## Literature

- ABEN, H. and GUILLEMET, C. (1993). *Photoelasticity of Glass*. Berlin, Heidelberg: Springer. ISBN: 978-3-642-50073-2. DOI: 10.1007/978-3-642-50071-8.
- ALTER, C., KOLLING, S., and SCHNEIDER, J. (2017). An enhanced non-local failure criterion for laminated glass under low velocity impact. *International Journal of Impact Engineering* **109**, pp. 342–353. DOI: 10.1016/j.ijimpeng.2017.07.014.
- ANDERSON, T. L. (2017). *Fracture Mechanics: Fundamentals and Applications*. 4th ed. Boca Raton, FL, USA: CRC Press, Taylor & Francis Group. ISBN: 978-1-4987-2813-3.
- ANGELIDES, S. C., TALBOT, J. P., and OVEREND, M. (2022). The influence of fracture pattern on the residual resistance of laminated glass at high strain-rates: an experimental investigation of the post-fracture bending moment capacity based on time-temperature mapping of interlayer yield stress. *Glass Structures & Engineering*. DOI: 10.1007/s40940-022-00168-y.
- ANGELIDES, S., TALBOT, J., and OVEREND, M. (2021). High strain-rate effects from blast loads on laminated glass: An experimental investigation of the post-fracture bending moment capacity based on time-temperature mapping of interlayer yield stress. *Construction and Building Materials* **273**. DOI: 10.1016/j.conbuildmat.2020.121658.
- ANGELIDES, S. C. and TALBOT, J. P. (2021). Blast response of laminated glass panels: a critical review of analysis and design methods. *Proceedings of the Institution of Civil Engineers – Structures and Buildings*, pp. 1–33. DOI: 10.1680/jstbu.20.00248.
- ANGELIDES, S. C., TALBOT, J. P., and OVEREND, M. (2019). The effects of high strain-rate and in-plane restraint on quasi-statically loaded laminated glass: a theoretical study with applications to blast enhancement. *Glass Structures & Engineering* **4**(3), pp. 403–420. DOI: 10.1007/s40940-019-00107-4.
- ANTON, J. (2015). *Scattered Light Polariscopes SCALP*. Instruction Manual (Ver. 5.8.2). Tallinn: GlasStress Ltd.
- ARMSTRONG, R. W. and WALLEY, S. M. (2008). High strain rate properties of metals and alloys. *International Materials Reviews* **53**(3), pp. 105–128. DOI: 10.1179/174328008X277795.
- BAKER, W., COX, P., WESTINE, P., KULESZ, J., and STREHLOW, R. (1983). *Explosion Hazards and Evaluation*. Amsterdam: Elsevier Science B.V. ISBN: 978-0-444-42094-7.
- BELYTSCHKO, T., SONG, J.-H., WANG, H., and GRACIE, R. (2007). On Applications of XFEM to Dynamic Fracture and Dislocations. In: *IUTAM Symposium on Discretization Methods for Evolving Discontinuities*. Ed. by COMBESCURE, A., BORST, R. D., and BELYTSCHKO, T. Dordrecht: Springer, pp. 155–170. ISBN: 978-1-4020-6529-3. DOI: 10.1007/978-1-4020-6530-9\_9.
- BERMBACH, T., TEICH, M., and GEBBEKEN, N. (2016). Experimental investigation of energy dissipation mechanisms in laminated safety glass for combined blast-temperature loading scenarios. *Glass Structures & Engineering* **1**(1), pp. 331–350. DOI: 10.1007/s40940-016-0029-y.

## Bibliography

- BISCHOFF, P. H. and PERRY, S. H. (1991). Compressive behaviour of concrete at high strain rates. *Materials and Structures* **24**(6), pp. 425–450. DOI: 10.1007/BF02472016.
- BØRVIK, T., HANSEN, A., LANGSETH, M., and OLOVSSON, L. (2009). Response of structures to planar blast loads – A finite element engineering approach. *Computers & Structures* **87**(9-10), pp. 507–520. DOI: 10.1016/j.compstruc.2009.02.005.
- BROWN, E. H. (1967). *Structural Analysis Volume 1*. Longmans.
- CAMACHO, G. and ORTIZ, M. (1996). Computational modelling of impact damage in brittle materials. *International Journal of Solids and Structures* **33**(20-22), pp. 2899–2938. DOI: 10.1016/0020-7683(95)00255-3.
- CHANDAN, H. C., BRADT, R. C., and RINDONE, G. E. (1978). Dynamic Fatigue of Float Glass. *Journal of the American Ceramic Society* **61**(5-6), pp. 207–210. DOI: 10.1111/j.1151-2916.1978.tb09280.x.
- CHARLES, R. J. (1958). Dynamic fatigue of glass. *Journal of Applied Physics* **29**(12), pp. 1657–1662. DOI: 10.1063/1.1723019.
- CHARLES, R. and HILLIG, W. (1962). The kinetics of glass failure by stress corrosion. In: *Symposium sur la resistance due verre et les moyens de l'ameliorer*. Charleroi, Belgium.
- CHEN, S., CHEN, X., LI, G.-Q., and LU, Y. (2019). Development of Pressure-Impulse Diagrams for Framed PVB-Laminated Glass Windows. *Journal of Structural Engineering* **145**(3), p. 04018263. DOI: 10.1061/(ASCE)ST.1943-541X.0002258.
- CHEN, W. and SONG, B. (2011). *Split Hopkinson (Kolsky) Bar*. Mechanical Engineering Series. Boston, MA: Springer US. ISBN: 978-1-4419-7981-0. DOI: 10.1007/978-1-4419-7982-7.
- CHENG, M., CHEN, W., and SRIDHAR, K. R. (2002). Experimental Method for a Dynamic Biaxial Flexural Strength Test of Thin Ceramic Substrates. *Journal of the American Ceramic Society* **85**(5), pp. 1203–1209. DOI: 10.1111/j.1151-2916.2002.tb00246.x.
- CHOPINET, M.-H. (2019). The History of Glass. In: *Springer Handbook of Glass*. Ed. by MUSGRAVES, J. D., HU, J., and CALVEZ, L. Cham: Springer, pp. 1–47. DOI: 10.1007/978-3-319-93728-1\_1.
- CHREE, C. (1889). The equations of an isotropic elastic solid in polar and cylindrical co-ordinates. *Transactions of the Cambridge Philosophical Society* **14**, pp. 250–369.
- CORMIE, D., MAYS, G., and SMITH, P. (2019). *Blast Effects on Buildings*. 3rd ed. Westminster, London: ICE Publishing. ISBN: 978-0-7277-6147-7. DOI: 10.1680/beob.61477.
- CULF, C. J. (1957). Fracture of Glass Under Various Liquids and Gases. *Journal of the Society of Glass Technology* **41**(199), pp. 157–167.
- DAS ADHIKARY, S. (2016). Review of Glazing and Glazing Systems under Blast Loading. *Practice Periodical on Structural Design and Construction* **21**(1), pp. 1–10. DOI: 10.1061/(ASCE)SC.1943-5576.0000264.
- DATSIU, K. C. and OVEREND, M. (2017). The strength of aged glass. *Glass Structures & Engineering* **2**(2), pp. 105–120. DOI: 10.1007/s40940-017-0045-6.
- DAVIES, R. M. (1948). A Critical Study of the Hopkinson Pressure Bar. *Philosophical Transactions of the Royal Society A: Mathematical, Physical and Engineering Sciences* **240**(821), pp. 375–457. DOI: 10.1098/rsta.1948.0001.
- DEL LINZ, P., HOOPER, P., ARORA, H., SMITH, D., PASCOE, L., CORMIE, D., BLACKMAN, B., and DEAR, J. (2015). Reaction forces of laminated glass windows subject to blast loads. *Composite Structures* **131**, pp. 193–206. DOI: 10.1016/j.compstruc.2015.04.050.

- DEL LINZ, P., LIANG, X., HOOPER, P., WANG, L., and DEAR, J. (2016). An analytical solution for pre-crack behaviour of laminated glass under blast loading. *Composite Structures* **144**, pp. 156–164. DOI: 10.1016/j.compstruct.2016.02.058.
- DEL LINZ, P., HOOPER, P. A., ARORA, H., WANG, Y., SMITH, D., BLACKMAN, B. R., and DEAR, J. P. (2017). Delamination properties of laminated glass windows subject to blast loading. *International Journal of Impact Engineering* **105**, pp. 39–53. DOI: 10.1016/j.ijimpeng.2016.05.015.
- DELLIEU, L., LEYBROS, P., and JEANFILS, J. (2018). Are laminated security glazing standards still adapted to the current demand? In: *Challenging Glass 6: Conference on Architectural and Structural Applications of Glass, CGC 2018*. Ed. by LOUTER, C., BOS, F., BELIS, J., VEER, F., and NUSSE, R. TU Delft Open. ISBN: 978-94-6366-044-0. DOI: 10.7480/cgc.6.2198.
- DEWEY, J. M. (2018). The Friedlander Equations. In: *Blast Effects. Shock Wave and High Pressure Phenomena*. Ed. by SOCHET, I. Cham, Switzerland: Springer. Chap. 3, pp. 37–55. ISBN: 978-3-319-70829-4. DOI: 10.1007/978-3-319-70831-7\_3.
- ERIKSEN, R. N. W. (2014). High Strain Rate Characterisation of Composite Materials. DCAMM Special Report No. S179. Ph.D. Thesis. Department of Mechanical Engineering, Technical University of Denmark.
- EVANS, A. G. (1974). Slow crack growth in brittle materials under dynamic loading conditions. *International Journal of Fracture* **10**(2), pp. 251–259. DOI: 10.1007/BF00113930.
- EVANS, A. G. and JOHNSON, H. (1975). The fracture stress and its dependence on slow crack growth. *Journal of Materials Science* **10**(2), pp. 214–222. DOI: 10.1007/BF00540345.
- EVANS, A. G. and WIEDERHORN, S. M. (1974). Proof testing of ceramic materials – an analytical basis for failure prediction. *International Journal of Fracture* **10**(3), pp. 379–392. DOI: 10.1007/BF00035499.
- FÖRCH, M. (2019). *Analysis of Glass Panels Subjected to Blast Load*. Vol. 1. Fassadensysteme und Gebäudehüllen. Berlin, Heidelberg: Springer. ISBN: 978-3-662-59086-7. DOI: 10.1007/978-3-662-59087-4.
- FORQUIN, P. (2017). Brittle materials at high-loading rates: an open area of research. *Philosophical Transactions of the Royal Society A: Mathematical, Physical and Engineering Sciences* **375**(2085). DOI: 10.1098/rsta.2016.0436.
- FREW, D. J., FORRESTAL, M. J., and CHEN, W. (2001). A split hopkinson pressure bar technique to determine compressive stress-strain data for rock materials. *Experimental Mechanics* **41**(1), pp. 40–46. DOI: 10.1007/BF02323102.
- FREW, D. J., FORRESTAL, M. J., and CHEN, W. (2002). Pulse shaping techniques for testing brittle materials with a split hopkinson pressure bar. *Experimental Mechanics* **42**(1), pp. 93–106. DOI: 10.1007/BF02411056.
- GAO, Z., XU, X., SU, Y., and ZHANG, Q. (2016). Experimental analysis of image noise and interpolation bias in digital image correlation. *Optics and Lasers in Engineering* **81**, pp. 46–53. DOI: 10.1016/j.optlaseng.2016.01.002.
- GEHRI, N., MATA-FALCÓN, J., and KAUFMANN, W. (2020). Automated crack detection and measurement based on digital image correlation. *Construction and Building Materials* **256**, p. 119383. DOI: 10.1016/j.conbuildmat.2020.119383.
- GEHRKE, E., ULLNER, C., and HÄHNERT, M. (1987). Correlation between multistage crack growth and time-dependent strength in commercial silicate glasses - Part 1. Influence of ambient media and types of initial cracks. *Glastechnische Berichte* **60**(8), pp. 268–278.

## Bibliography

- GEHRKE, E., ULLNER, C., and HÄHNERT, M. (1990). Effect of corrosive media on crack growth of model glasses and commercial silicate glasses. *Glastechnische Berichte* **63**(9), pp. 255–265.
- GHOSH, S. B., JONES, F. R., and HAND, R. J. (2010). A novel indentation based method to determine the threshold stress intensity factor for sub-critical crack growth in glass. *Glass Technology: European Journal of Glass Science and Technology Part A* **51**(4), pp. 156–160.
- GRAFF, K. F. (1975). *Wave Motion in Elastic Solids*. Dover Publications.
- GRENET, L. (1899). Mechanical strength of glass. *Bull. Soc. Encour. Ind. Nat.* **5**(4), pp. 838–848.
- GRIFFITH, A. A. (1920). The phenomena of rupture and flow in solids. *Philosophical Transactions of the Royal Society of London. Series A, Containing Papers of a Mathematical or Physical Character* **221**, pp. 163–198. DOI: 10.1098/rsta.1921.0006.
- GURNEY, C. and PEARSON, S. (1949). The Effect of the Surrounding Atmosphere on the Delayed Fracture of Glass. *Proceedings of the Physical Society. Section B* **62**(8), pp. 469–476. DOI: 10.1088/0370-1301/62/8/301.
- GY, R. (2003). Stress corrosion of silicate glass: A review. *Journal of Non-Crystalline Solids* **316**(1), pp. 1–11. DOI: 10.1016/S0022-3093(02)01931-2.
- HALDIMANN, M. (2006). Fracture strength of structural glass elements – Analytical and Numerical Modelling, Testing and Design. Ph.D. Thesis. École Polytechnique Fédérale de Lausanne (EPFL). DOI: 10.5075/EPFL-THESIS-3671.
- HALDIMANN, M., LUIBLE, A., and OVEREND, M. (2008). *Structural Use of Glass*. Zürich, Switzerland: International Association for Bridge and Structural Engineering (IABSE). ISBN: 978-3-85748-119-2.
- HENTZ, S., DONZÉ, F. V., and DAUDEVILLE, L. (2004). Discrete element modelling of concrete submitted to dynamic loading at high strain rates. *Computers & Structures* **82**(29-30), pp. 2509–2524. DOI: 10.1016/j.compstruc.2004.05.016.
- HIDALLANA-GAMAGE, H., THAMBIRATNAM, D., and PERERA, N. (2014). Failure analysis of laminated glass panels subjected to blast loads. *Engineering Failure Analysis* **36**, pp. 14–29. DOI: 10.1016/j.engfailanal.2013.09.018.
- HILLERBORG, A., MODÉER, M., and PETERSSON, P.-E. (1976). Analysis of crack formation and crack growth in concrete by means of fracture mechanics and finite elements. *Cement and Concrete Research* **6**(6), pp. 773–781. DOI: 10.1016/0008-8846(76)90007-7.
- HOLMQUIST, T. J., JOHNSON, G. R., GRADY, D. E., LOPATIN, C. M., and HERTEL, E. S. (1995). High strain rate properties and constitutive modeling of glass. In: *15th International Symposium on Ballistics*. Jerusalem.
- HOOPER, P., SUKHRAM, R., BLACKMAN, B., and DEAR, J. (2012). On the blast resistance of laminated glass. *International Journal of Solids and Structures* **49**(6), pp. 899–918. DOI: 10.1016/j.ijsolstr.2011.12.008.
- HOPKINSON, B. (1914). A Method of Measuring the Pressure Produced in the Detonation of High Explosives or by the Impact of Bullets. *Philosophical Transactions of the Royal Society of London. Series A, Containing Papers of a Mathematical or Physical Character* **213**, pp. 437–456.
- HOPKINSON, J. (1872). On the rupture of iron wire by a blow. *Proc. Literary and Philosophical Society of Manchester* **1**, pp. 40–45.
- INAGAKI, M., URASHIMA, K., TOYOMASU, S., GOTO, Y., and SAKAI, M. (1985). Work of Fracture and Crack Healing in Glass. *Journal of the American Ceramic Society* **68**(12), pp. 704–706. DOI: 10.1111/j.1151-2916.1985.tb10129.x.

- IRWIN, G. R. (1956). Onset of fast crack propagation in high strength steel and aluminum alloys. *Naval Research Laboratory*.
- IRWIN, G. R. (1957). Analysis of stresses and strains near the end of a crack traversing a plate. *Journal of Applied Mechanics* **24**(3), pp. 361–364.
- JOHAR, S. (1982). *Dynamic fatigue of flat glass, phase III: Final report*. Technical Report. Mississauga, Canada: Department of Metals, Glass and Ceramics. DOI: 10.4224/20326324.
- JOHNS, R. V. and CLUBLEY, S. K. (2015). Post-fracture response of blast-loaded monolithic glass. *Proceedings of the Institution of Civil Engineers: Structures and Buildings* **168**(7), pp. 469–478. DOI: 10.1680/stbu.13.00099.
- JOHNSON, G. R. and HOLMQUIST, T. J. (1994). An improved computational constitutive model for brittle materials. In: *AIP Conference Proceedings*. Vol. 309. AIP, pp. 981–984. DOI: 10.1063/1.46199.
- KALTHOFF, J. F. (2000). Modes of dynamic shear failure in solids. *International Journal of Fracture* **101**(1-2), pp. 1–31. DOI: 10.1023/a:1007647800529.
- KANG, F. and ZHONG-CI, S. (1996). *Mathematical Theory of Elastic Structures*. Berlin, Heidelberg: Springer. ISBN: 978-3-662-03288-6. DOI: 10.1007/978-3-662-03286-2.
- KOCER, C. and COLLINS, R. E. (2001). Measurement of Very Slow Crack Growth in Glass. *Journal of the American Ceramic Society* **84**(11), pp. 2585–2593. DOI: 10.1111/j.1151-2916.2001.tb01058.x.
- KOLSKY, H. (1949). An Investigation of the Mechanical Properties of Materials at very High Rates of Loading. *Proceedings of the Physical Society. Section B* **62**(11), pp. 676–700. DOI: 10.1088/0370-1301/62/11/302.
- KÖNIG, C. (2012). Dehnratenabhängigkeit mechanischer Werkstoffkennwerte von Kalk-Natronsilicatglas. Ph.D. Thesis. Fakultät Architektur, Bauingenieurwesen und Umweltwissenschaften, Technische Universität Carolo-Wilhelmina zu Braunschweig. ISBN: 978-3-8472-3523-1.
- KROHN, M. H., HELLMANN, J. R., SHELLEMAN, D. L., PANTANO, C. G., and SAKOSKE, G. E. (2004). Biaxial Flexure Strength and Dynamic Fatigue of Soda-Lime-Silica Float Glass. *Journal of the American Ceramic Society* **85**(7), pp. 1777–1782. DOI: 10.1111/j.1151-2916.2002.tb00352.x.
- KUNTSCHKE, J. K. (2015). Mechanisches Verhalten von Verbundglas unter zeitabhängiger Belastung und Explosionsbeanspruchung. Ph.D. Thesis. Institut für Statik und Konstruktion, Technische Universität Darmstadt. ISBN: 978-3-662-48830-0. DOI: 10.1007/978-3-662-48831-7.
- LANDON, J. W. and QUINNEY, H. (1923). Experiments with the Hopkinson Pressure Bar. *Proceedings of the Royal Society of London. Series A, Containing Papers of a Mathematical and Physical Character* **103**(723), pp. 622–643. DOI: 10.1098/rspa.1923.0084.
- LARCHER, M., ARRIGONI, M., BEDON, C., DOORMAAL, J. C. A. M. VAN, HABERACKER, C., HÜSKEN, G., MILLON, O., SAARENHEIMO, A., SOLOMOS, G., THAMIE, L., VALSAMOS, G., WILLIAMS, A., and STOLZ, A. (2016). Design of Blast-Loaded Glazing Windows and Facades: A Review of Essential Requirements towards Standardization. *Advances in Civil Engineering* **2016**, pp. 1–14. DOI: 10.1155/2016/2604232.
- LARCHER, M., SOLOMOS, G., CASADEI, F., and GEBBEKEN, N. (2012). Experimental and numerical investigations of laminated glass subjected to blast loading. *International Journal of Impact Engineering* **39**(1), pp. 42–50. DOI: 10.1016/j.ijimpeng.2011.09.006.
- LIFSHITZ, J. and LEBER, H. (1994). Data processing in the split Hopkinson pressure bar tests. *International Journal of Impact Engineering* **15**(6), pp. 723–733. DOI: 10.1016/0734-743X(94)90011-9.

## Bibliography

- LINGER, K. R. and HOLLOWAY, D. G. (1968). The fracture energy of glass. *Philosophical Magazine* **18**(156), pp. 1269–1280. DOI: 10.1080/14786436808227756.
- MCSPORRAN, N. (2014). Properties and performance of vacuum insulated glazing. *Journal of Green Building* **9**(1), pp. 60–74. DOI: 10.3992/1943-4618-9.1.60.
- MECHOLSKY, J. J., RICE, R. W., and FREIMAN, S. W. (1974). Prediction of Fracture Energy and Flaw Size in Glasses from Measurements of Mirror Size. *Journal of the American Ceramic Society* **57**(10), pp. 440–443. DOI: 10.1111/j.1151-2916.1974.tb11377.x.
- MENČÍK, J. (1992). *Strength and fracture of glass and ceramics*. New York: Elsevier Science Publishing Company, Inc. ISBN: 0-444-98685-5.
- MEYERS, M. A. (1994). *Dynamic Behavior of Materials*. Wiley. ISBN: 9780471582625. DOI: 10.1002/9780470172278.
- MEYLAND, M. J., BØNDING, C. K. T., ERIKSEN, R. N. W., and NIELSEN, J. H. (2019). An experimental investigation of the flexural strength of soda–lime–silica glass at high loading rates. *Glass Structures & Engineering* **4**(2), pp. 175–183. DOI: 10.1007/s40940-018-0089-2.
- MEYLAND, M. J., NIELSEN, J. H., and KOCER, C. (2021a). Tensile behaviour of soda-lime-silica glass and the significance of load duration – A literature review. *Journal of Building Engineering* **44**, p. 102966. DOI: 10.1016/j.jobe.2021.102966.
- MEYLAND, M. J. and NIELSEN, J. H. (2020). Ongoing Research into the Failure of Glass at High Strain-Rates. In: *Challenging Glass 7: Conference on Architectural and Structural Applications of Glass, CGC 7*. Ed. by BELIS, J., BOS, F., and LOUWER, C. TU Delft Open. ISBN: 978-94-6366-296-3. DOI: 10.7480/cgc.7.4428.
- MEYLAND, M. J., NIELSEN, J. H., and KOCER, C. (2021b). Datasets: Tensile behaviour of soda-lime-silica glass and the significance of load duration – A literature review. *DTU Data, Technical University of Denmark*. DOI: 10.11583/DTU.13655525.
- MICHALSKE, T. A. and FREIMAN, S. W. (1983). A Molecular Mechanism for Stress Corrosion in Vitreous Silica. *Journal of the American Ceramic Society* **66**(4), pp. 284–288. DOI: 10.1111/j.1151-2916.1983.tb15715.x.
- MORISON, C. (2007). The resistance of laminated glass to blast pressure loading and the coefficients for single degree of freedom analysis of laminated glass. Ph.D. Thesis. Engineering Systems Department, Cranfield University.
- MUNJIZA, A., OWEN, D., and BICANIC, N. (1995). A combined finite-discrete element method in transient dynamics of fracturing solids. *Engineering Computations* **12**(2), pp. 145–174. DOI: 10.1108/02644409510799532.
- MUNZ, D. and FETT, T. (1999). *Ceramics: Mechanical Properties, Failure Behaviour, Materials Selection*. Springer Series in Materials Science. Berlin, Heidelberg: Springer. ISBN: 978-3-642-63580-9. DOI: 10.1007/978-3-642-58407-7.
- NAGHDABADI, R., ASHRAFI, M. J., and ARGHAVANI, J. (2012). Experimental and numerical investigation of pulse-shaped split Hopkinson pressure bar test. *Materials Science and Engineering A* **539**, pp. 285–293. DOI: 10.1016/j.msea.2012.01.095.
- NEMAT-NASSER, S., ISAACS, J. B., and STARRETT, J. E. (1991). Hopkinson techniques for dynamic recovery experiments. *Proceedings of the Royal Society of London. Series A: Mathematical and Physical Sciences* **435**(1894), pp. 371–391. DOI: 10.1098/rspa.1991.0150.

- NEMAT-NASSER, S. (2000). Introduction to High Strain Rate Testing. In: *Mechanical Testing and Evaluation*. Ed. by KUHN, H. and MEDLIN, D. Vol. 8. ASM International, pp. 427–428. DOI: 10.31399/asm.hb.v08.a0003293.
- NIE, X. and CHEN, W. (2013). High-Rate Progressive Failure of Borosilicate Glass under Mechanical Confinement at High Temperatures. *Experimental Mechanics* **53**(1), pp. 67–75. DOI: 10.1007/s11340-012-9635-z.
- NIE, X. and CHEN, W. W. (2012). Dynamic Equibiaxial Flexural Strength of Borosilicate Glass at High Temperatures. *Experimental Mechanics* **52**(2), pp. 135–143. DOI: 10.1007/s11340-011-9549-1.
- NIE, X., CHEN, W. W., SUN, X., and TEMPLETON, D. W. (2007). Dynamic Failure of Borosilicate Glass Under Compression/Shear Loading Experiments. *Journal of the American Ceramic Society* **90**(8), pp. 2556–2562. DOI: 10.1111/j.1551-2916.2007.01819.x.
- NIE, X., CHEN, W. W., and TEMPLETON, D. W. (2010). Dynamic Ring-on-Ring Equibiaxial Flexural Strength of Borosilicate Glass. *International Journal of Applied Ceramic Technology* **7**(5), pp. 616–624. DOI: 10.1111/j.1744-7402.2010.02508.x.
- NIE, X., CHEN, W. W., WERESZCZAK, A. A., and TEMPLETON, D. W. (2009). Effect of Loading Rate and Surface Conditions on the Flexural Strength of Borosilicate Glass. *Journal of the American Ceramic Society* **92**(6), pp. 1287–1295. DOI: 10.1111/j.1551-2916.2009.03019.x.
- NIELSEN, J. H. and BJARRUM, M. (2017). Deformations and strain energy in fragments of tempered glass: experimental and numerical investigation. *Glass Structures & Engineering* **2**(2), pp. 133–146. DOI: 10.1007/s40940-017-0043-8.
- NIELSEN, J. H., OLESEN, J. F., and STANG, H. (2010). Characterization of the Residual Stress State in Commercially Fully Toughened Glass. *Journal of Materials in Civil Engineering* **22**(2), pp. 179–185. DOI: 10.1061/(ASCE)0899-1561(2010)22:2(179).
- NIELSEN, J. H., THIELE, K., SCHNEIDER, J., and MEYLAND, M. J. (2021). Compressive zone depth of thermally tempered glass. *Construction and Building Materials* **310**. DOI: 10.1016/j.conbuildmat.2021.125238.
- NISTOR, I., PANTALÉ, O., and CAPERAA, S. (2008). Numerical implementation of the eXtended Finite Element Method for dynamic crack analysis. *Advances in Engineering Software* **39**(7), pp. 573–587. DOI: 10.1016/j.advengsoft.2007.06.003.
- NORVILLE, H. S., HARVILL, N., CONRATH, E. J., SHARIAT, S., and MALLONEE, S. (1999). Glass-Related Injuries in Oklahoma City Bombing. *Journal of Performance of Constructed Facilities* **13**(2), pp. 50–56. DOI: 10.1061/(ASCE)0887-3828(1999)13:2(50).
- NURHUDA, I., LAM, N. T. K., JIANG, H., and GAD, E. F. (2012). Simulation of crack propagation in glass panels using finite element analysis. *Australian Journal of Structural Engineering* **12**(3), pp. 225–236. DOI: 10.7158/S11-108.2012.12.3.
- OSNES, K., HOLMEN, J. K., HOPPERSTAD, O. S., and BØRVIK, T. (2019). Fracture and fragmentation of blast-loaded laminated glass: An experimental and numerical study. *International Journal of Impact Engineering* **132**(7491), p. 103334. DOI: 10.1016/j.ijimpeng.2019.103334.
- OVEREND, M., PARKE, G. A., and BUHAGIAR, D. (2007a). Predicting Failure in Glass—A General Crack Growth Model. *Journal of Structural Engineering* **133**(8), pp. 1146–1155. DOI: 10.1061/(ASCE)0733-9445(2007)133:8(1146).
- OVEREND, M. and ZAMMIT, K. (2012). A computer algorithm for determining the tensile strength of float glass. *Engineering Structures* **45**, pp. 68–77. DOI: 10.1016/j.engstruct.2012.05.039.

## Bibliography

- OVEREND, M., DE GAETANO, S., and HALDIMANN, M. (2007b). Diagnostic Interpretation of Glass Failure. *Structural Engineering International* **17**(2), pp. 151–158. DOI: 10.2749/101686607780680790.
- PARK, H. and CHEN, W. (2012). Crack Branching in Glass Interface Driven by Dynamic Loading. In: *Fractography of Glasses and Ceramics VI: Ceramic Transactions, Volume 230*. Ed. by VARNER, J. R. and WIGHTMAN, M. Hoboken, New Jersey: John Wiley & Sons, pp. 95–99. DOI: 10.1002/9781118433010.ch6.
- PAVELCHEK, E. K. and DOREMUS, R. H. (1974). Fracture strength of soda-lime glass after etching. *Journal of Materials Science* **9**(11), pp. 1803–1808. DOI: 10.1007/BF00541749.
- PELFRENE, J., KUNTSCHKE, J., VAN DAM, S., VAN PAEPEGEM, W., and SCHNEIDER, J. (2016). Critical assessment of the post-breakage performance of blast loaded laminated glazing: Experiments and simulations. *International Journal of Impact Engineering* **88**, pp. 61–71. DOI: 10.1016/j.ijimpeng.2015.09.008.
- PELFRENE, J. (2016). Numerical Analysis of the Post-Fracture Response of Laminated Glass under Impact and Blast Loading. Ph.D. Thesis. Department of Materials Science and Technology, Ghent University, Belgium. ISBN: 978-90-85789-27-7.
- PERONI, M., SOLOMOS, G., PIZZINATO, V., and LARCHER, M. (2011). Experimental Investigation of High Strain-Rate Behaviour of Glass. *Applied Mechanics and Materials* **82**, pp. 63–68. DOI: 10.4028/www.scientific.net/AMM.82.63.
- PETZOLD, A., MARUSCH, H., and SCHRAMM, B. (1990). *Der Baustoff Glas: Grundlagen, Eigenschaften, Erzeugnisse, Glasbauelemente, Anwendungen*. 3rd ed. Schorndorf, Germany: Verlag Karl Hofmann. ISBN: 3-7780-1181-2.
- PFAENDER, H. G. (1996). *Schott Guide to Glass*. 2nd ed. Dordrecht: Springer Science+Business Media, B.V. ISBN: 978-94-010-4230-7. DOI: 10.1007/978-94-011-0517-0.
- POCHHAMMER, L. (1876). Ueber die Fortpflanzungsgeschwindigkeiten kleiner Schwingungen in einem unbegrenzten isotropen Kreiscylinder. *Journal für die reine und angewandte Mathematik* **81**, pp. 324–336. DOI: 10.1515/crll.1876.81.324.
- POLOÇOŞER, T., KASAL, B., and STÖCKEL, F. (2017). State-of-the-art: intermediate and high strain rate testing of solid wood. *Wood Science and Technology* **51**(6), pp. 1479–1534. DOI: 10.1007/s00226-017-0925-6.
- POURMOGHADDAM, N., KRAUS, M. A., SCHNEIDER, J., and SIEBERT, G. (2018). Relationship between strain energy and fracture pattern morphology of thermally tempered glass for the prediction of the 2D macro-scale fragmentation of glass. *Glass Structures & Engineering*. DOI: 10.1007/s40940-018-00091-1.
- POURMOGHADDAM, N. and SCHNEIDER, J. (2019). Determination of the engine power for quenching of glass by forced convection: simplified model and experimental validation of residual stress levels. *Glass Structures & Engineering* **4**(1), pp. 117–125. DOI: 10.1007/s40940-018-0078-5.
- RASMUSSEN, S. C. (2012). *How Glass Changed the World: The History and Chemistry of Glass from Antiquity to the 13th Century*. Springer Briefs in Molecular Science. Berlin, Heidelberg: Springer. ISBN: 978-3-642-28182-2. DOI: 10.1007/978-3-642-28183-9.
- RAVICHANDRAN, G. and SUBHASH, G. (1994). Critical Appraisal of Limiting Strain Rates for Compression Testing of Ceramics in a Split Hopkinson Pressure Bar. *Journal of the American Ceramic Society* **77**(1), pp. 263–267. DOI: 10.1111/j.1151-2916.1994.tb06987.x.

- RIEDEL, H., MOKDAD, S., SCHULZ, I., KOCER, C., ROSENDAHL, P. L., SCHNEIDER, J., KRAUS, M. A., and DRASS, M. (2022). Automated quality control of vacuum insulated glazing by convolutional neural network image classification. *Automation in Construction* **135**(December 2021). DOI: 10.1016/j.autcon.2022.104144.
- ROBERTSON, R. (1921). Some properties of explosives. *Journal of the Chemical Society, Transactions* **119**, pp. 1–29. DOI: 10.1039/CT9211900001.
- RODICHEV, Y., MASLOV, V., NETYCHUK, A., BODUNOV, V., and YEVPLOV, Y. (2007). Bending strength and fracture of glass materials under the different loading conditions. In: *Glass Performance Days 2007*. Tampere, Finland, pp. 615–618.
- ROSSMANITH, H. P. (1982). The method of caustics for static plane elasticity problems. *Journal of Elasticity* **12**(2), pp. 193–200. DOI: 10.1007/BF00042215.
- RUDICK, M. M. and NORVILLE, H. S. (2000). Glass-Related Injuries in Oklahoma City Bombing. *Journal of Performance of Constructed Facilities* **14**(4), pp. 167–167. DOI: 10.1061/(ASCE)0887-3828(2000)14:4(167).
- SAMUEL, A. and WEIR, J. (1999). *Introduction to Engineering Design*. Elsevier Butterworth-Heinemann. ISBN: 978-0-7506-4282-8. DOI: 10.1016/B978-0-7506-4282-8.X5000-3.
- SCHIAVONATO, M., MOGNATO, E., and REDNER, A. S. (2005). Stress Measurement, Fragmentation and Mechanical Strength. In: *Glass Processing Days 2005*. Tampere, Finland, pp. 92–95.
- SCHITTICH, C., STAIB, G., BALKOW, D., SCHULER, M., and SOBEK, W. (2007). *Glass Construction Manual*. Ed. by LENZEN, S. 2. Edition. Basel, Switzerland: Birkhäuser Verlag AG. ISBN: 978-3-7643-8122-6. DOI: 10.11129/detail.9783034615549.
- SCHNEIDER, J., KUNTSCHKE, J., SCHULA, S., SCHNEIDER, F., and WÖRNER, J.-D. (2016). *Glasbau: Grundlagen, Berechnung, Konstruktion*. Berlin, Heidelberg: Springer. ISBN: 978-3-540-28476-5. DOI: 10.1007/978-3-540-68927-0.
- SEAGRAVES, A. and RADOVITZKY, R. (2009). Advances in Cohesive Zone Modeling of Dynamic Fracture. In: *Dynamic Failure of Materials and Structures*. Ed. by SHUKLA, A., RAVICHANDRAN, G., and RAJAPAKSE, Y. D. Boston, MA: Springer US, pp. 349–405. ISBN: 978-1-4419-0445-4. DOI: 10.1007/978-1-4419-0446-1\_12.
- SGLAVO, V. M. and BERTOLDI, M. (2006). Vickers Indentation: A Powerful Tool for the Analysis of Fatigue Behavior on Glass. In: *Indentation Techniques in Ceramic Materials Characterization*. Ed. by SOLOMAH, A. Vol. 156, pp. 13–22. DOI: 10.1002/9781118407042.ch2.
- SGLAVO, V. M. and GREEN, D. J. (1996). Threshold stress intensity factor in soda-lime silicate glass by interrupted static fatigue test. *Journal of the European Ceramic Society* **16**(6), pp. 645–651. DOI: 10.1016/0955-2219(95)00176-X.
- SHARON, E. and FINEBERG, J. (1999). Confirming the continuum theory of dynamic brittle fracture for fast cracks. *Nature* **397**(6717), pp. 333–335. DOI: 10.1038/16891.
- SHUKLA, A., RAVICHANDRAN, G., and RAJAPAKSE, Y. D., eds. (2010). *Dynamic Failure of Materials and Structures*. 1st ed. Boston, MA: Springer. ISBN: 978-1-4419-0445-4. DOI: 10.1007/978-1-4419-0446-1.
- SIMMONS, C. J. and FREIMAN, S. (1981). Effect of Corrosion Processes on Subcritical Crack Growth in Glass. *Journal of the American Ceramic Society* **64**(11), pp. 683–686. DOI: 10.1111/j.1151-2916.1981.tb15870.x.
- SMITH, D. (2001). Glazing for Injury Alleviation Under Blast Loading – United Kingdom Practice. In: *Glass Processing Days*, pp. 335–340.

## Bibliography

- SMITH, P. D. and ROSE, T. A. (2006). Blast wave propagation in city streets—an overview. *Progress in Structural Engineering and Materials* **8**(1), pp. 16–28. DOI: 10.1002/pse.209.
- SMITH, R. L., MECHOLSKY, J. J., and FREIMAN, S. W. (2009). Estimation of fracture energy from the work of fracture and fracture surface area: I. Stable crack growth. *International Journal of Fracture* **156**(1), pp. 97–102. DOI: 10.1007/s10704-009-9350-7.
- SNIJDER, B. H. (2004). Structural Glass and Glass Structures: An Introduction. *Structural Engineering International* **14**(2), pp. 72–72. DOI: 10.2749/101686604777964071.
- SONG, J. H., WANG, H., and BELYTSCHKO, T. (2008). A comparative study on finite element methods for dynamic fracture. *Computational Mechanics* **42**(2), pp. 239–250. DOI: 10.1007/s00466-007-0210-x.
- SPILLER, K., PACKER, J. A., SEICA, M. V., and YANKELEVSKY, D. Z. (2016). Prediction of annealed glass window response to blast loading. *International Journal of Impact Engineering* **88**, pp. 189–200. DOI: 10.1016/j.ijimpeng.2015.10.010.
- STEIN, M., DRAPER, P., and HELLYER, R. (2019). City of Glass: Recent Advancements in Glass Structures in New York City. *Structural Engineering International* **29**(1), pp. 101–111. DOI: 10.1080/10168664.2018.1519365.
- SUBHASH, G. and RAVICHANDRAN, G. (2000). Split-Hopkinson Pressure Bar Testing of Ceramics. In: *Mechanical Testing and Evaluation*. Ed. by KUHN, H. and MEDLIN, D. Vol. 8. ASM International, pp. 497–504. DOI: 10.31399/asm.hb.v08.a0003299.
- SUKKARIEH, G., LAHOUD, C., GHORAYEB, R., ABI KARAM, M., SUCCARIEH, Y., SALEH, M., and JALKH, A. (2021). Characteristics of open eye injuries in the Beirut Port explosion. *Injury* **52**(9), pp. 2601–2605. DOI: 10.1016/j.injury.2021.07.031.
- SUTTON, M. A., ORTEU, J.-J., and SCHREIER, H. (2009). *Image Correlation for Shape, Motion and Deformation Measurements*. Boston, MA: Springer US. ISBN: 978-0-387-78746-6. DOI: 10.1007/978-0-387-78747-3.
- SWAB, J. J., PATEL, P. J., TRAN, X., GILDE, L., LUOTO, E., GAVIOLA, M. H., GOTT, A., PAULSON, B., and KILCZEWSKI, S. (2014). Equibiaxial Flexure Strength of Glass: Influence of Glass Plate Size and Equibiaxial Ring Ratio. *International Journal of Applied Glass Science* **5**(4), pp. 384–392. DOI: 10.1111/ijag.12094.
- TIMOSHENKO, S. and WOJNOWSKY-KRIEGER, S. (1959). *Theory of plates and shells*. 2nd ed. McGraw-Hill. ISBN: 0-07-085820-9.
- TSUJI, K. (2018). *The Micro-World Observed by Ultra High-Speed Cameras*. Cham: Springer International Publishing AG. ISBN: 978-3-319-61490-8. DOI: 10.1007/978-3-319-61491-5.
- TYAS, A. and WATSON, A. J. (2001). An investigation of frequency domain dispersion correction of pressure bar signals. *International Journal of Impact Engineering* **25**(1), pp. 87–101. DOI: 10.1016/S0734-743X(00)00025-7.
- UNOSSON, M., OLOVSSON, L., and SIMONSSON, K. (2006). Failure modelling in finite element analyses: Element erosion with crack-tip enhancement. *Finite Elements in Analysis and Design* **42**(4), pp. 283–297. DOI: 10.1016/j.finel.2005.07.001.
- WACHTMAN, J. B., CANNON, W. R., and MATTHEWSON, M. J. (2009). *Mechanical Properties of Ceramics*. 2nd ed. John Wiley & Sons. ISBN: 978-0-471-73581-6.
- WAN, K. T., LATHABAI, S., and LAWN, B. R. (1990). Crack velocity functions and thresholds in brittle solids. *Journal of the European Ceramic Society* **6**(4), pp. 259–268. DOI: 10.1016/0955-2219(90)90053-1.

- WANG, X. ER, YANG, J., LIU, Q. FENG, ZHANG, Y. MEI, and ZHAO, C. (2017). A comparative study of numerical modelling techniques for the fracture of brittle materials with specific reference to glass. *Engineering Structures* **152**, pp. 493–505. DOI: 10.1016/j.engstruct.2017.08.050.
- WIEDERHORN, S. M. (1966). Fracture Surface Energy of Soda-Lime Glass. In: *The Role of Grain Boundaries and Surfaces in Ceramics*. Ed. by KRIEGER, W. and PALMOUR, H. Boston, MA: Springer US. Chap. 27, pp. 503–528. DOI: 10.1007/978-1-4899-6311-6\_27.
- WIEDERHORN, S. M. (1967). Influence of Water Vapor on Crack Propagation in Soda-Lime Glass. *Journal of the American Ceramic Society* **50**(8), pp. 407–414. DOI: 10.1111/j.1151-2916.1967.tb15145.x.
- WIEDERHORN, S. M. (1969). Fracture Surface Energy of Glass. *Journal of the American Ceramic Society* **52**(2), pp. 99–105. DOI: 10.1111/j.1151-2916.1969.tb13350.x.
- WIEDERHORN, S. M. and BOLZ, L. H. (1970). Stress Corrosion and Static Fatigue of Glass. *Journal of the American Ceramic Society* **53**(10), pp. 543–548. DOI: 10.1111/j.1151-2916.1970.tb15962.x.
- WRIGGERS, P. (2008). *Nonlinear Finite Element Methods*. Berlin, Heidelberg: Springer. ISBN: 978-3-540-71000-4. DOI: 10.1007/978-3-540-71001-1.
- XU, W. and ZANG, M. (2014). Four-point combined DE/FE algorithm for brittle fracture analysis of laminated glass. *International Journal of Solids and Structures* **51**(10), pp. 1890–1900. DOI: 10.1016/j.ijsolstr.2014.01.026.
- XU, X.-P. and NEEDLEMAN, A. (1994). Numerical simulations of fast crack growth in brittle solids. *Journal of the Mechanics and Physics of Solids* **42**(9), pp. 1397–1434. DOI: 10.1016/0022-5096(94)90003-5.
- YUAN, Y., TAN, P., and LI, Y. (2017). Dynamic structural response of laminated glass panels to blast loading. *Composite Structures* **182**(August), pp. 579–589. DOI: 10.1016/j.compstruct.2017.09.028.
- ZHANG, Q. B. and ZHAO, J. (2014). A Review of Dynamic Experimental Techniques and Mechanical Behaviour of Rock Materials. *Rock Mechanics and Rock Engineering* **47**(4), pp. 1411–1478. DOI: 10.1007/s00603-013-0463-y.
- ZHANG, X. and BEDON, C. (2017). Vulnerability and Protection of Glass Windows and Facades under Blast: Experiments, Methods and Current Trends. *International Journal of Structural Glass and Advanced Materials Research* **1**(2), pp. 10–23. DOI: 10.3844/sgamrsp.2017.10.23.
- ZHANG, X. and HAO, H. (2015). Experimental and numerical study of boundary and anchorage effect on laminated glass windows under blast loading. *Engineering Structures* **90**, pp. 96–116. DOI: 10.1016/j.engstruct.2015.02.022.
- ZHANG, X. and HAO, H. (2016). The response of glass window systems to blast loadings: An overview. *International Journal of Protective Structures* **7**(1), pp. 123–154. DOI: 10.1177/2041419615626061.
- ZHANG, X., HAO, H., and MA, G. (2013). Parametric study of laminated glass window response to blast loads. *Engineering Structures* **56**, pp. 1707–1717. DOI: 10.1016/j.engstruct.2013.08.007.
- ZHANG, X., HAO, H., and MA, G. (2015a). Dynamic material model of annealed soda-lime glass. *International Journal of Impact Engineering* **77**, pp. 108–119. DOI: 10.1016/j.ijimpeng.2014.11.016.
- ZHANG, X., HAO, H., and WANG, Z. (2015b). Experimental study of laminated glass window responses under impulsive and blast loading. *International Journal of Impact Engineering* **78**, pp. 1–19. DOI: 10.1016/j.ijimpeng.2014.11.020.

## Bibliography

- ZHANG, X., ZOU, Y., HAO, H., LI, X., MA, G., and LIU, K. (2012). Laboratory Test on Dynamic Material Properties of Annealed Float Glass. *International Journal of Protective Structures* 3(4), pp. 407–430. DOI: 10.1260/2041-4196.3.4.407.
- ZHOU, X. Q., WANG, M. Y., and LI, L. X. (2019). Dynamic damage assessment of float glass under blast loading. *Advances in Structural Engineering*. DOI: 10.1177/1369433219845691.
- ZONGZHE, J., JUNARONG, M., and XIAORUI, L. (1986). Dynamic Fracture Toughness and Strength of Glass. *XIV International Congress on Glass - Collected Papers* 2, pp. 78–83.

## Standards and Technical Guidelines

- AS 1288 (2006). *Glass in buildings – Selection and installation*. National Standard. Sydney, NSW 2001, Australia: Standards Australia.
- ASTM C1499-15 (2015). *Standard Test Method for Monotonic Equibiaxial Flexural Strength of Advanced Ceramics at Ambient Temperature*. International Standard. West Conshohocken, PA: ASTM International. DOI: 10.1520/C1499-15.
- ASTM E1300-16 (2016). *Standard practice for determining load resistance of glass in buildings*. International Standard. West Conshohocken, PA: ASTM International. DOI: 10.1520/E1300-16.2.
- ASTM F2248-19 (2019). *Standard Practice for Specifying an Equivalent 3-Second Duration Design Loading for Blast Resistant Glazing Fabricated with Laminated Glass*. Standard. West Conshohocken, PA: ASTM International. DOI: 10.1520/F2248-19.
- CEN/TS 19100-1 (2021). *Design for glass structures – Part 1: Basis of design and materials*. European Standard. Brussels: European Committee for Standardization (CEN).
- CNR-DT 210 (2013). *Istruzioni per la Progettazione, l'Esecuzione ed il Controllo di Costruzioni con Elementi Strutturali di Vetro*. National Standard. Rome, Italy: Commissione di studio per la predisposizione e l'analisi di norme tecniche relative alle costruzioni (CNR).
- DIN 18008-1 (2010). *Glas im Bauwesen – Bemessungs- und Konstruktionsregeln – Teil 1: Begriffe und allgemeine Grundlagen*. National Standard. Berlin: Normenausschuss Bauwesen (NABau) im DIN.
- DIN 18008-4 (2013). *Glas im Bauwesen – Bemessungs- und Konstruktionsregeln – Teil 4: Zusatzanforderungen an absturzsichernde Verglasungen*. National Standard. Berlin: Normenausschuss Bauwesen (NABau) im DIN.
- EN 1288-1 (2001). *Glass in building – Determination of the bending strength of glass – Part 1: Fundamentals of testing glass*. European Standard. Brussels: European Committee for Standardization (CEN).
- EN 1288-2 (2001). *Glass in building – Determination of the bending strength of glass – Part 2: Coaxial double ring test on flat specimens with large test surface areas*. European Standard. Brussels: European Committee for Standardization (CEN).
- EN 1288-3 (2001). *Glass in building – Determination of the bending strength of glass – Part 3: Test with specimen supported at two points (four point bending)*. European Standard. Brussels: European Committee for Standardization (CEN).
- EN 1288-5 (2001). *Glass in building – Determination of the bending strength of glass – Part 5: Coaxial double ring test on flat specimens with small test surface areas*. European Standard. Brussels: European Committee for Standardization (CEN).

- EN 13123-1 (2001). *Windows and doors and shutters – Explosion resistance – Requirements and classification – Part 1: Shock tube*. European Standard. Brussels: European Committee for Standardization (CEN).
- EN 13123-2 (2004). *Windows, doors and shutters – Explosion resistance – Requirements and classification – Part 2: Range test*. European Standard. Brussels: European Committee for Standardization (CEN).
- EN 13124-1 (2001). *Windows, doors and shutter – Explosion resistance – Test method – Part 1: Shock tube*. European Standard. Brussels: European Committee for Standardization (CEN).
- EN 13124-2 (2004). *Windows, doors and shutters – Explosion resistance – Test method – Part 2: Range test*. European Standard. Brussels: European Committee for Standardization (CEN).
- EN 13541 (2001). *Glass in building – Security glazing – Testing and classification of resistance against explosion pressure*. European Standard. Brussels: European Committee for Standardization (CEN).
- EN 1652 (1998). *Copper and copper alloys – Plate, sheet, strip and circles for general purposes*. European Standard. Brussels: European Committee for Standardization (CEN).
- EN 16612 (2019). *Glass in building – Determination of the lateral load resistance of glass panes by calculation*. European Standard. Brussels: European Committee for Standardization (CEN).
- EN 1863-1 (2012). *Glass in building – Heat strengthened soda lime silicate glass – Part 1 : Definition and description*. European Standard. Brussels: European Committee for Standardization (CEN).
- EN 1990 (2002). *Eurocode – Basis of structural design*. European Standard. Brussels: European Committee for Standardization (CEN).
- EN 572-1 (2012). *Glass in building – Basic soda lime silicate glass products – Part 1: Definitions and general physical and mechanical properties*. European Standard. Brussels: European Committee for Standardization (CEN).
- EN12150-1 (2015). *Glass in building – Thermally toughened soda lime silicate safety glass – Part 1 : Definition and description*. European Standard. Brussels: European Committee for Standardization (CEN).
- ISO 16933 (2007). *Glass in building – Explosion-resistant security glazing – Test and classification for arena air-blast loading*. International Standard. Vernier, Geneva Switzerland: International Organization for Standardization.
- ISO 16934 (2007). *Glass in building – Explosion-resistant security glazing – Test and classification by shock-tube loading*. International Standard. Vernier, Geneva Switzerland: International Organization for Standardization.
- ISO 20657 (2017). *Glass in building – Heat soaked tempered soda lime silicate safety glass*. International Standard. Vernier, Geneva, Switzerland: International Organization for Standardization.
- ISO 22509 (2020). *Glass in building – Heat strengthened soda lime silicate glass*. International Standard. Vernier, Geneva, Switzerland: International Organization for Standardization.
- NEN 2608 (2014). *Glass in building – Requirements and determination method*. National Standard. Delft: Nederlands Normalisatie-instituut.
- ÖNORM B 3716-1 (2016). *Glas im Bauwesen – Konstruktiver Glasbau – Teil 1: Grundlagen*. National Standard. Wien, Austria: Austrian Standards Institute.
- UFC 3-340-02 (2008). *Structures To Resist The Effects Of Accidental Explosions*. Manual. Washington, DC: U.S. Department of Defense.

## Miscellaneous

- CTA (2021). *Assessment of the Terrorist threat to Denmark 2021*. Report. Søborg, Denmark: Danish Security and Intelligence Service (PET), Centre for Terror Analysis (CTA).
- DASSAULT SYSTÈMES (2021). *SIMULIA User Assistance 2021* → *Abaqus*. Online User Manual.
- DBI (2021). *RAMT (Risiko Arkitektur Mennesker Terror) – A digital platform for counter-terrorism measures for buildings and urban spaces*. URL: <https://www.terrorsikring.nu>. Online; accessed 10-01-2022. The Danish Institute of Fire and Security Technology, Hvidovre, Denmark.
- EIS (2022). *Resource Specifications* → *SHY-039-Instron-8872*. URL: <https://eis.dtu.dk/Assets/Details.aspx?id=442>. Online; accessed 29-03-2022. DTU Equipment Information System.
- EUROPOL (2021). *European Union Terrorism Situation and Trend report 2021*, pp. 1–98. ISBN: 978-92-95220-26-3. DOI: 10.2813/677724.
- FORSVARSBYGG (2016). *Sikringshåndboka: Håndbok i sikring av eiendom, bygg og anlegg mot terror, sabotasje, spionasje og annen kriminalitet*. 1st ed. Oslo.
- GLASS FOR EUROPE (2022). *Flat glass key features / Key data*. URL: <https://glassforeurope.com/>. Online; accessed 12-03-2022. Glass for Europe, Brussels, Belgium.
- HYDE, D. W. (1991). *CONWEP: Conventional weapons effects program*. US Army Engineer Waterways Experiment Station, USA.
- IPCC (2022). *Climate Change 2022: Impacts, Adaptation, and Vulnerability*. Ed. by PÖRTNER, H.-O., ROBERTS, D., TIGNOR, M., POLOCZANSKA, E., MINTENBECK, K., ALEGRÍA, A., CRAIG, M., LANGSDORF, S., LÖSCHKE, S., MÖLLER, V., OKEM, A., and RAMA, B. Contribution of Working Group II to the Sixth Assessment Report of the Intergovernmental Panel on Climate Change. Cambridge University Press.
- IYOg (2022). *The UN International Year Of Glass 2022*. URL: <https://www.iyog2022.org/>. Online; accessed 12-03-2022.
- KIRK, A., WATSON, C., TORPEY, P., and LEVETT, C. (2020). *Visual guide: how explosion caused mass casualties and devastation across Beirut*. URL: <https://www.theguardian.com/world/2020/aug/05/visual-guide-how-explosion-caused-mass-casualties-and-devastation-across-beirut>. Online; accessed 18-03-2022.
- START (2019). *Global Terrorism Database (GTD)*. URL: <https://www.start.umd.edu/gtd/>. Online; accessed 07-01-2022. National Consortium for the Study of Terrorism and Responses to Terrorism, University of Maryland, USA.
- WIKIPEDIA (2022). *2011 Norway attacks* — *Wikipedia, The Free Encyclopedia*. URL: [https://en.wikipedia.org/w/index.php?title=2011\\_Norway\\_attacks&oldid=1077522946](https://en.wikipedia.org/w/index.php?title=2011_Norway_attacks&oldid=1077522946). Online; accessed 18-03-2022.

# Appendices



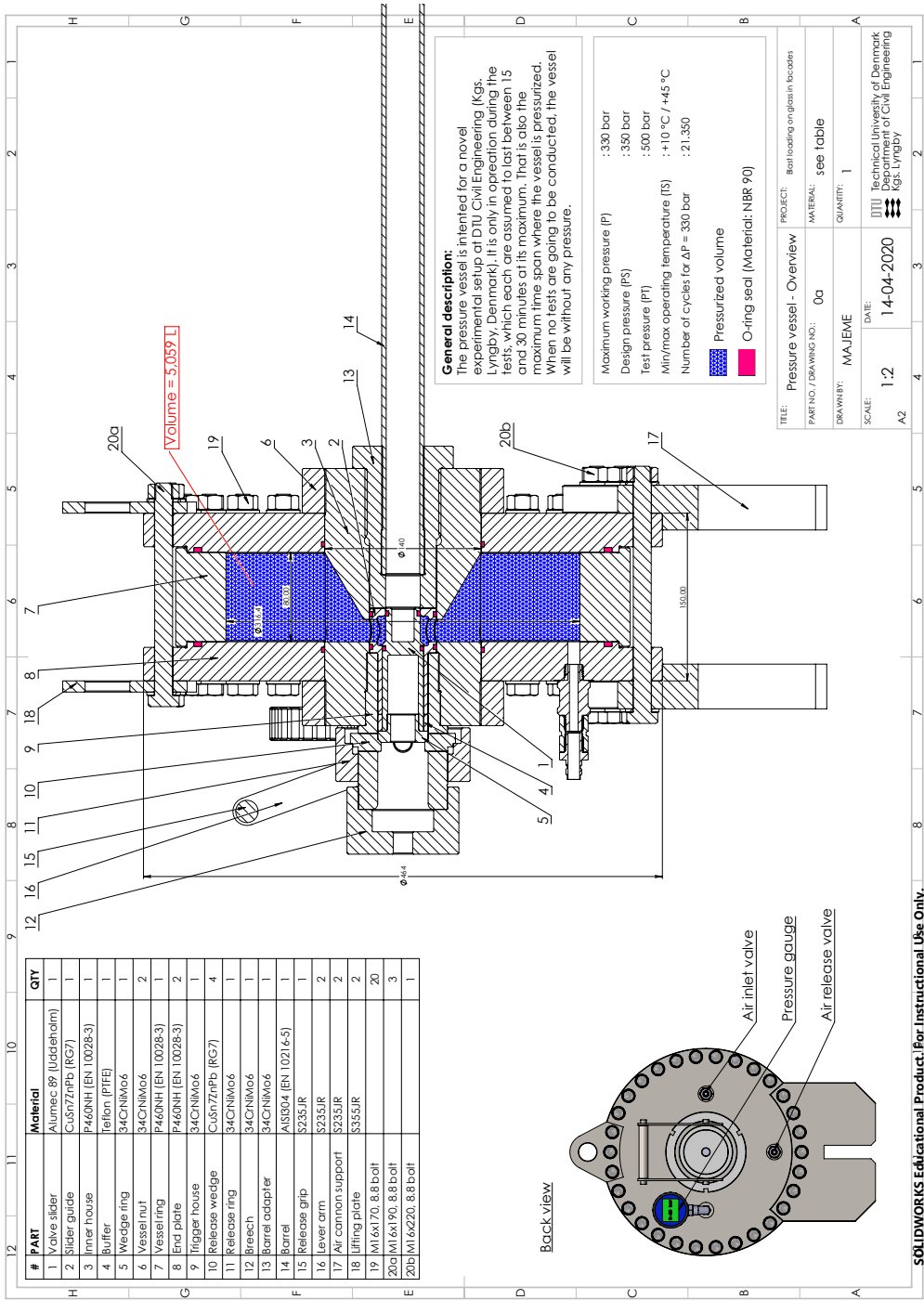
## Additional Experimental Details

This appendix contains additional experimental details related to Chapter 3 and Paper II. In Sec. A.1, a selection of technical drawings of the modified Split-Hopkinson Pressure Bar (SHPB) are provided. The procedure used to shunt-calibrate the Wheatstone bridges for the strain measurements is outlined in Sec. A.2. An overview of the individual measurements related to the elastic wave speed of the bar/tube material reported in Sec. 3.3.2 is provided in Sec. A.3. Lastly, in Sec. A.4, results from the pulse shaper experiments are summarised.

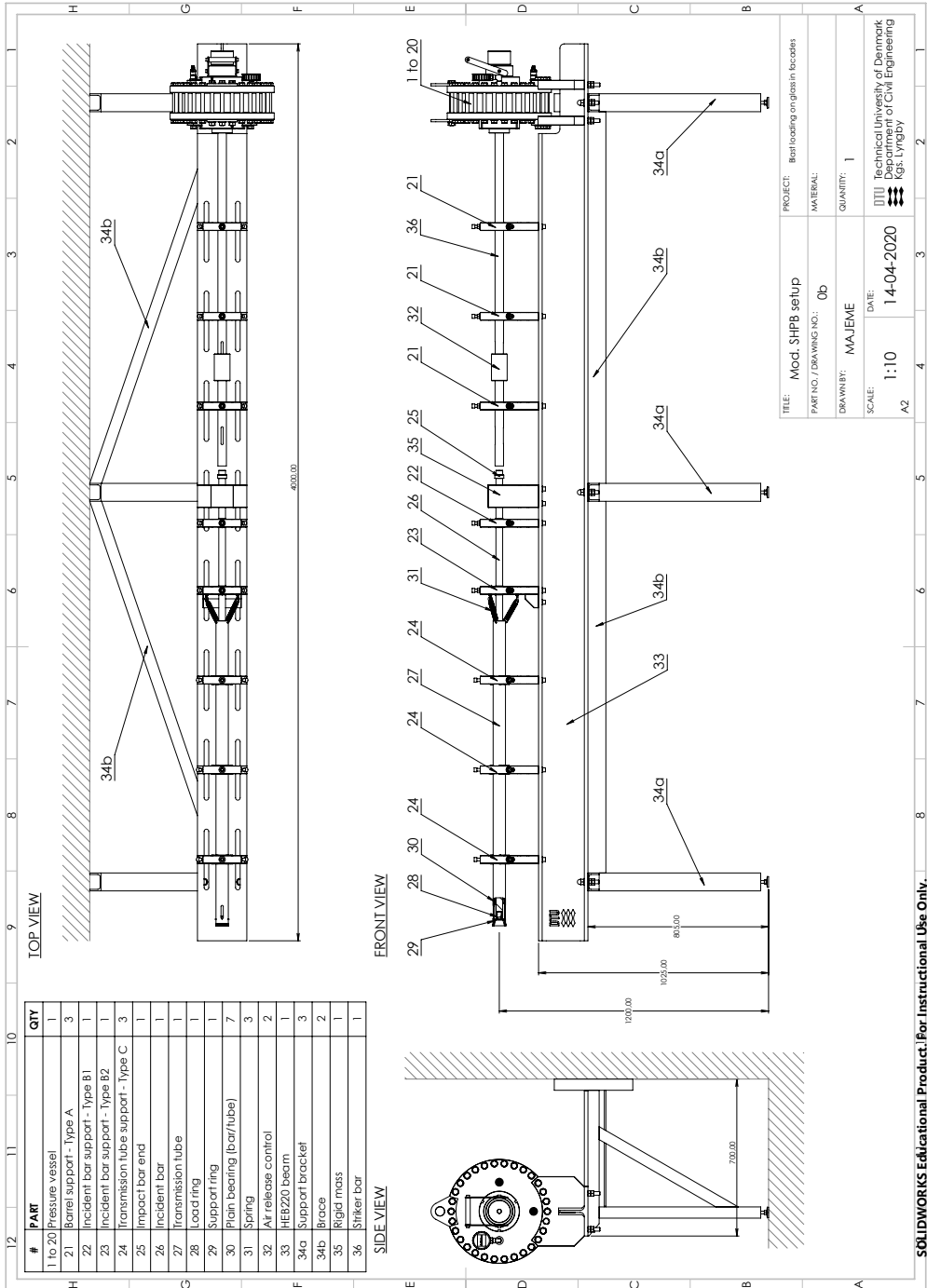
### A.1 Technical Drawings of the Modified SHPB Setup

*Go to the next page* →

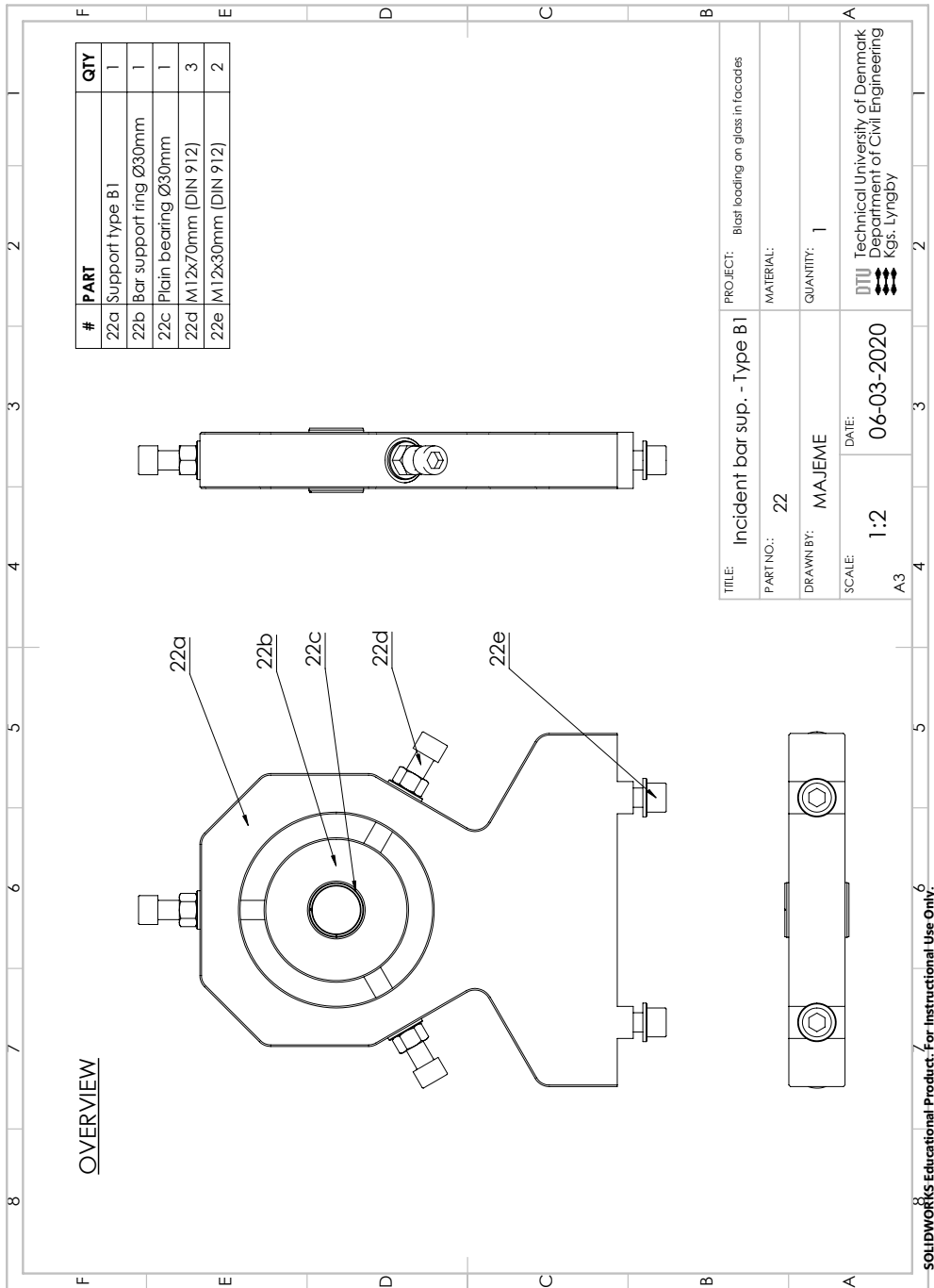
Appendix A. Additional Experimental Details



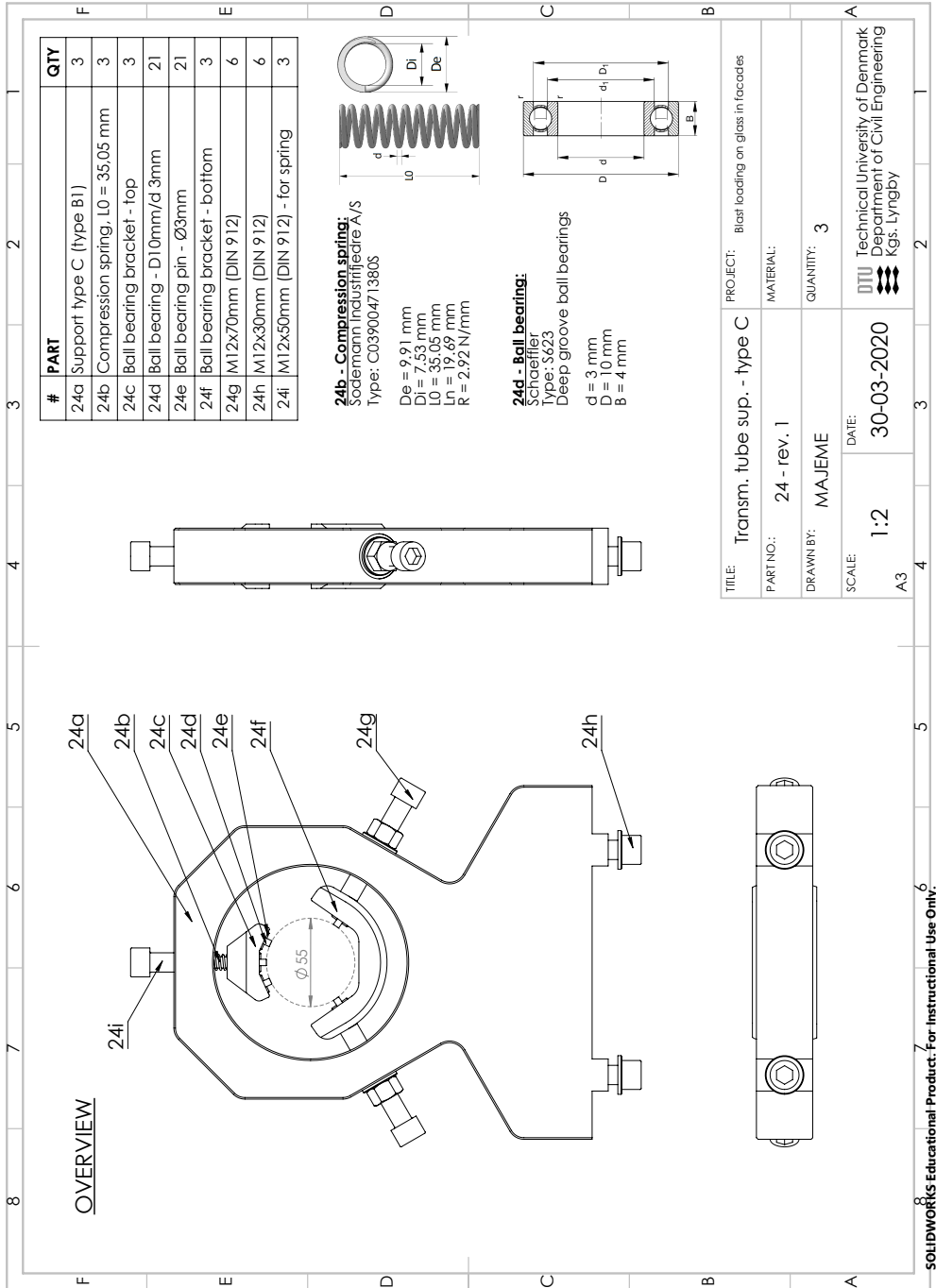
A.1. Technical Drawings of the Modified SHPB Setup

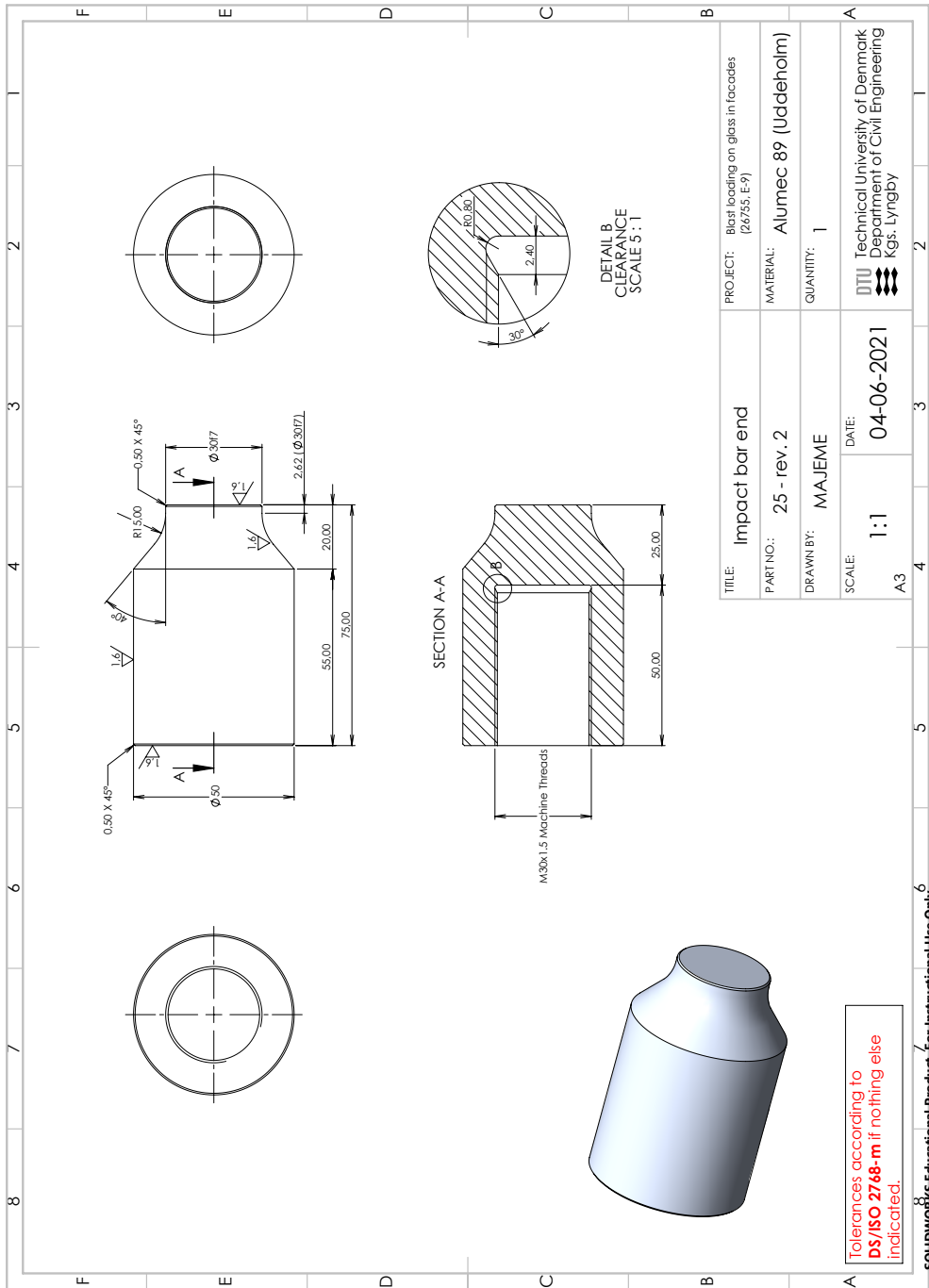


Appendix A. Additional Experimental Details



A.1. Technical Drawings of the Modified SHPB Setup

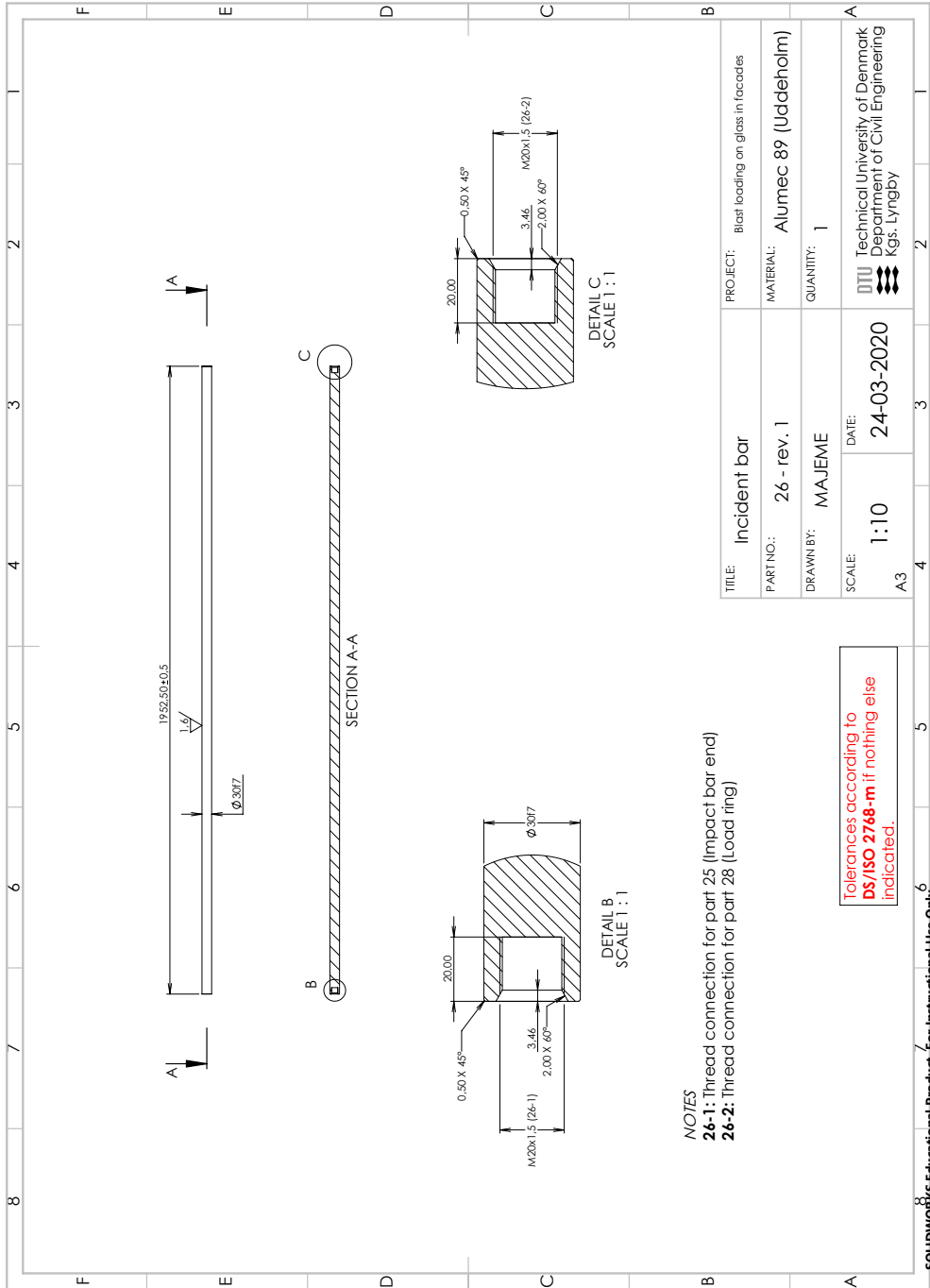


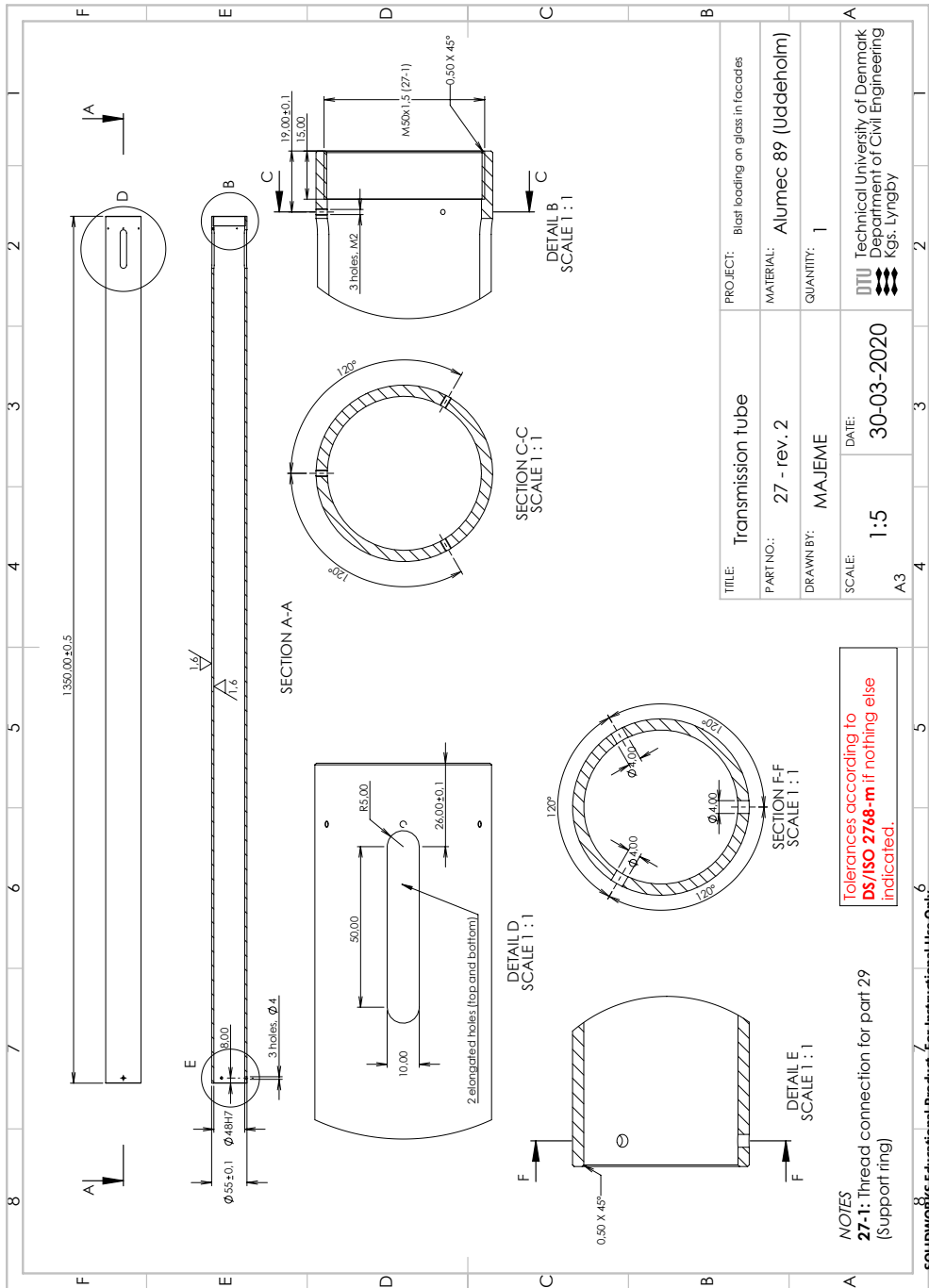


Tolerances according to  
**DS/ISO 2768-m** if nothing else  
indicated.

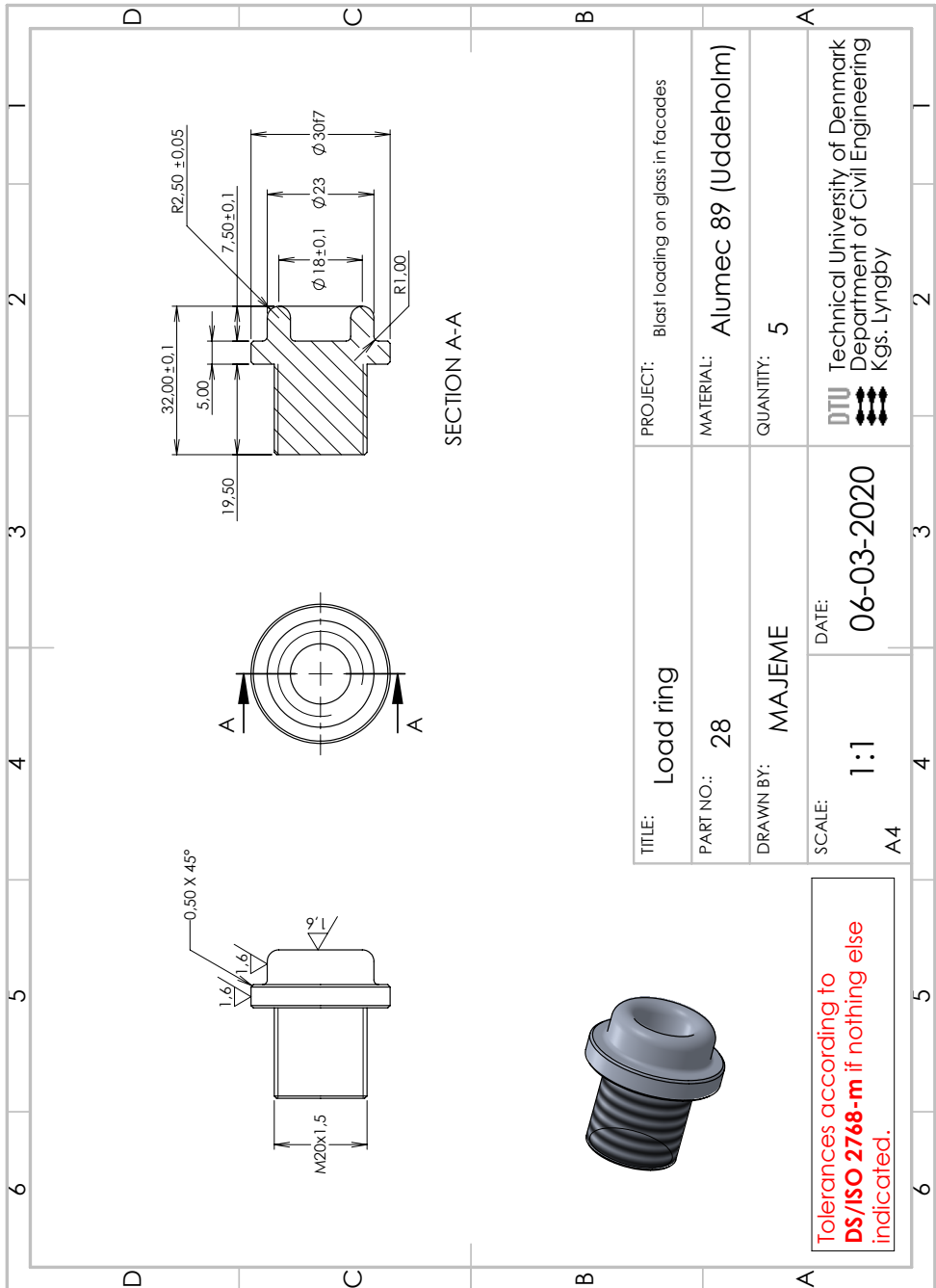
SOLIDWORKS Educational Product. For Instructional Use Only.

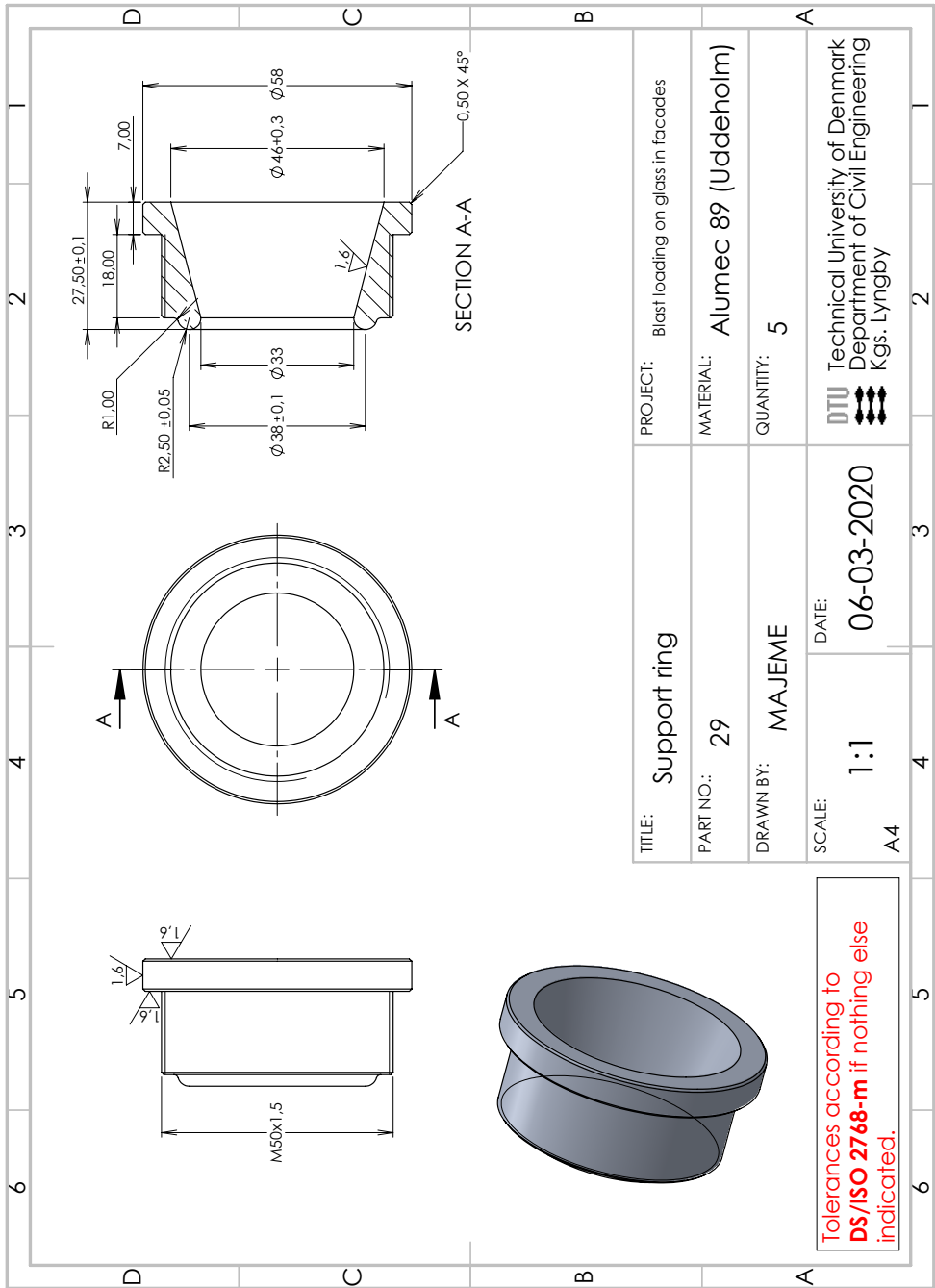
# A.1. Technical Drawings of the Modified SHPB Setup



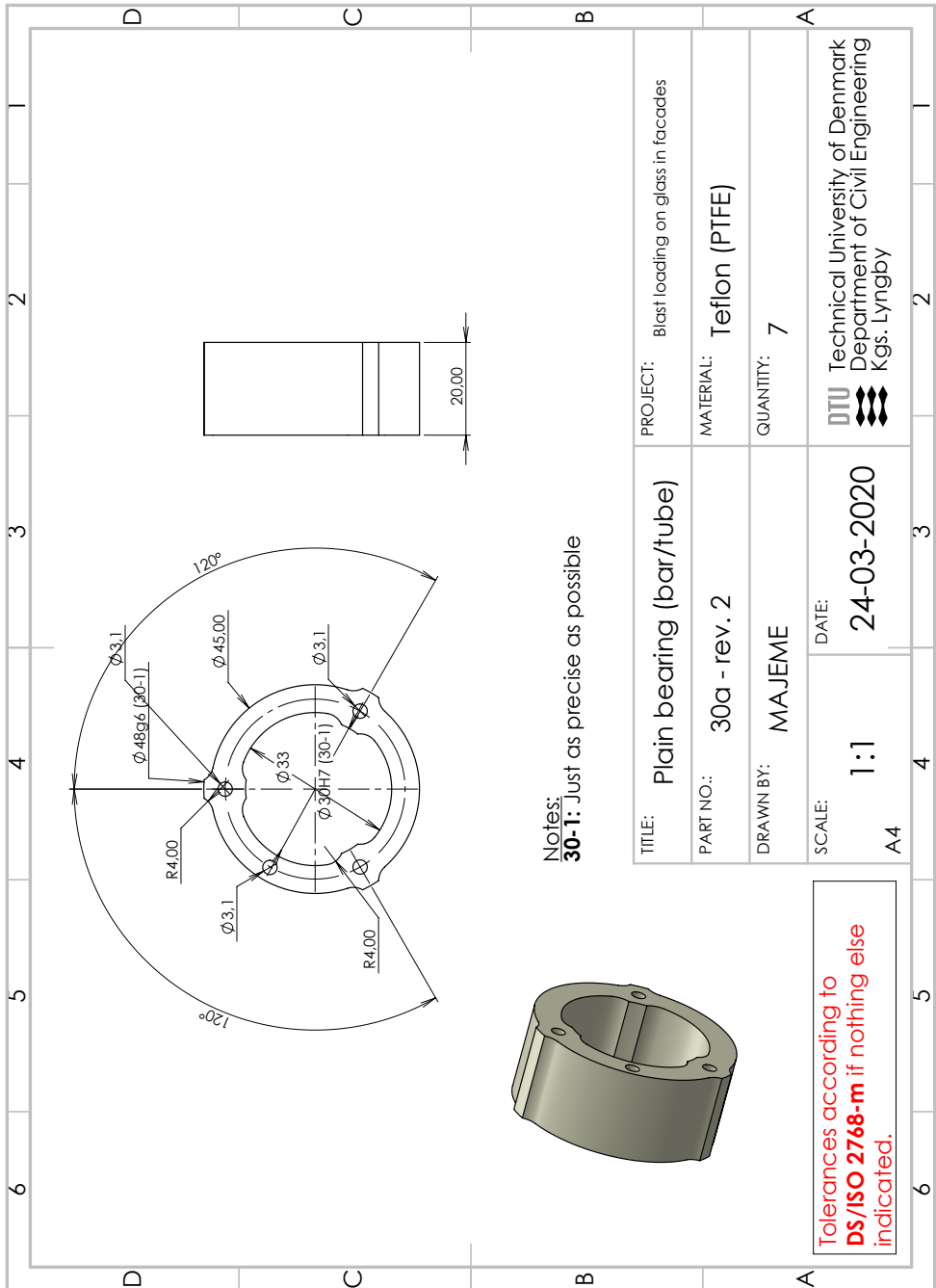


A.1. Technical Drawings of the Modified SHPB Setup





A.1. Technical Drawings of the Modified SHPB Setup



## A.2 Shunt Calibration of a Wheatstone Bridge

The signals measured with strain gauges as described in Chapter 3 are pre-amplified using a high-speed transducer amplifier from FYLDE (FE-H379-TA). The amplification is controlled with a coarse gain switch having three gain values, i.e. 10 (1 V), 100 (100 mV), and 1000 (10 mV), that is set together with a fine gain control (a dial) to develop full scale ( $\pm 10$  V) at the direct output. Since the fine gain control cannot be set precisely, a shunt calibration is performed for each Wheatstone bridge using a factory-fitted calibration resistance  $R_{\text{cal}} = 350 \text{ k}\Omega$  to get a more exact value of the dialled gain. The procedure is outlined with an example below.

Assume a maximum strain of  $\epsilon_{\text{max}} = 950 \cdot 10^{-6}$  that is expected to be measured in an experiment, then the expected maximum output voltage (unconditioned),  $U_{A,\text{max}}$ , is found from the following relationship:

$$U_{A,\text{max}} = \frac{1}{4} \cdot \epsilon_{\text{max}} \cdot k \cdot B \cdot U_E = 6.0 \text{ mV} \quad (\text{A.1})$$

where  $k$  is a dimensionless gauge factor provided by the manufacturer of the strain gauges ( $= 2.11 \pm 1.0\%$ ),  $B$  is a bridge factor that is dependent on the Wheatstone bridge configuration and in this setup equals 2 (a half-bridge compensating for superimposed bending forces), and  $U_E$  is the bridge excitation voltage that was set to 6.0 V.

Following the handbook of the pre-amplifier device,  $U_{A,\text{max}} = 6.0 \text{ mV}$  will require a coarse gain of  $G_{V,\text{coarse}} = 10 \text{ mV}$  and a fine gain of  $G_{V,\text{fine}} = 600/1000$  to scale the signal to full output (10 V). With these settings, a bridge output signal,  $\partial v$ , is simulated by a shunt calibration, and the magnitude is determined as follows:

$$\partial v = \frac{R_d/2}{R_{\text{cal}} + R_d/2} \cdot \frac{U_E}{2} = 0.5142 \text{ mV} \quad (\text{A.2})$$

where  $R_d$  is the resistance of the applied strain gauges ( $= 120 \Omega \pm 0.35\%$ ). Further, this signal gets amplified, and the resulting target output,  $\hat{U}_{A,\text{target}}$ , for the above gain settings is found from the ratio between the bridge output signal and the expected unconditioned maximum output voltage:

$$\hat{U}_{A,\text{target}} = 10 \text{ V} \cdot \frac{\partial v}{U_{A,\text{max}}} = 0.8570 \text{ V} \quad (\text{A.3})$$

This value is compared to the actual output,  $\hat{U}_{A,\text{actual}}$ , which is determined as the average of a performed measurement of a shunt calibrated output signal (amplified),  $\hat{U}_A$ :

$$\hat{U}_{A,\text{actual}} = \frac{\sum_{i=1}^n \hat{U}_{A,i}}{n} \quad (\text{A.4})$$

In Fig. A.1, a performed shunt calibration for the gain settings reported here is exemplified. A minor deviation is seen between the target and the actual output signal, meaning that the

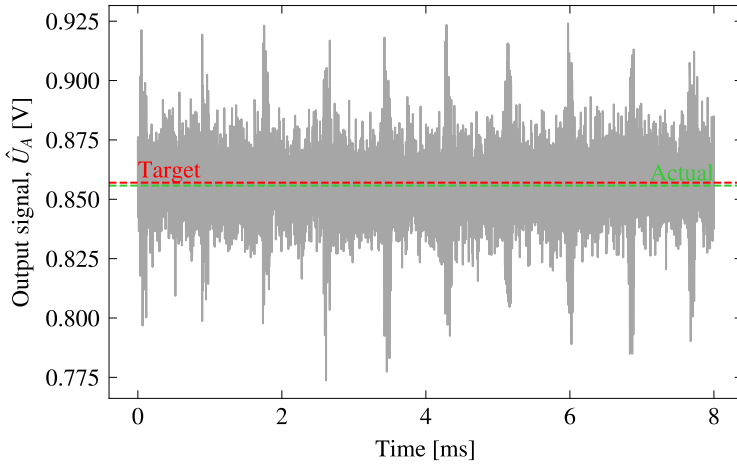


**Fig. A.1** Example measurement of a performed shunt calibration.

actual fine gain setting slightly deviates from the set 600/1000. Hence, a corrected fine gain is determined from the following expression using  $\hat{U}_{A,\text{actual}} = 0.8558 \text{ V}$  found from the data shown in Fig. A.1:

$$G_{V,\text{fine,cor}} = \frac{\partial v}{\hat{U}_{A,\text{actual}} \cdot G_{V,\text{coarse}}} \cdot 10^4 / 1000 = 600.87 / 1000 \quad (\text{A.5})$$

Each time a bridge needed a shunt calibration, e.g. when the gain was adjusted, the above procedure was repeated five times and the average determined the corrected fine gain value.

### A.3 Elastic Wave Speed Data of the Bar/Tube Material

The elastic wave speed of the high-strength aluminium allow used for the bar/tube system in the modified SHPB is reported in Sec. 3.3.2. The value is determined from ten calibration experiments with the 500 mm-long striker bar, which directly impacted the incident bar, i.e. no pulse shaping. For the determination of  $C_0$ , a method utilising the longitudinal resonance phenomena of the incident bar was employed (GRAFF 1975). Considering a cylindrical bar of length  $\ell$ , allowed to move freely at both ends, the natural frequencies in units Hertz,  $f_n$ , is found from the following relationship:

$$f_n = \frac{nC_0}{2\ell} \quad (n = 0, 1, 2, \dots) \quad (\text{A.6})$$

Since the incident bar is not purely cylindrical, an effective bar length of 2.0857 m is reported in Paper II, which is determined from a FEM model. This is the length of a pure cylindrical bar that approximately matches the natural frequencies of the actual incident bar geometry. Each of the ten measured incident bar signals was converted into the fre-

quency domain using a Fourier transformation from which the first natural frequency,  $f_1$ , was extracted; exemplified in Paper II. Finally, Eq. (A.6) allowed the calculation of  $C_0$ . The ten measurements are summarised in Table A.1.

**Table A.1** Summary of the individual measurements conducted to determine the elastic wave speed of the high-strength aluminium alloy used for the bar/tube system in the modified SHPB.

Test No.	First natural frequency $f_1$ [Hz]	Elastic wave speed $C_0$ [ $\text{m s}^{-1}$ ]
1	1219.3	5086.1
2	1220.7	5092.1
3	1220.0	5089.1
4	1218.6	5083.1
5	1218.6	5083.1
6	1220.7	5092.1
7	1219.3	5086.1
8	1219.3	5086.1
9	1218.6	5083.1
10	1218.6	5083.1
$\bar{x}$	1219.4	5086.4
$s_x$	0.8113	3.3841
95 % CI	(1218.7, 1220.0)	(5083.9, 5089.0)

$\bar{x}$  = sample mean;  $s_x$  = sample standard deviation; CI = Confidence Interval

## A.4 Pulse Shaper Data

Pulse shaper data provided in Fig. 3.9 are listed in Table A.2. The initial thickness,  $h_0$ , and the initial cross-sectional area,  $a_0$ , of the pulse shaper were measured using a digital vernier calliper before each test. After testing, the final thickness,  $h(t_{\text{end}})$ , was measured and the final cross-sectional area,  $a(t_{\text{end}})$ , was determined considering mass conservation, i.e.  $h_0 a_0 = h(t) a(t)$ .

**Table A.2** Post-test pulse shaper data for annealed Cu-DHP (CW024A – R240, cf. EN 1652:1998) copper.

Test No.	$v_{\text{st}}$ [ $\text{m s}^{-1}$ ]	$L_{\text{st}}$ [mm]	Before testing		After testing		$\varepsilon_p$ [–]	$\sigma_p$ [MPa]
			$h_0$ [mm]	$a_0$ [ $\text{mm}^2$ ]	$h(t_{\text{end}})$ [mm]	$a(t_{\text{end}})$ [ $\text{mm}^2$ ]		
1	40.67	250	1.01	178.60	0.43	419.51	0.574	496.4
2	39.46	250	1.04	125.28	0.35	372.27	0.663	551.3
3	39.47	250	1.04	80.12	0.26	320.47	0.750	639.4
4	39.36	250	2.08	178.37	0.94	394.69	0.548	486.4
5	39.38	250	2.04	123.90	0.73	346.24	0.642	567.9

*Continued on next page...*

**Table A.2** Post-test pulse shaper data for annealed Cu-DHP (CW024A – R240, cf. EN 1652:1998) copper. (*Continued*)

Test No.	$v_{st}$ [m s <sup>-1</sup> ]	$L_{st}$ [mm]	Before testing		After testing		$\varepsilon_p$ [–]	$\sigma_p$ [MPa]
			$h_0$ [mm]	$a_0$ [mm <sup>2</sup> ]	$h(t_{end})$ [mm]	$a(t_{end})$ [mm <sup>2</sup> ]		
6	38.95	250	2.06	79.64	0.51	321.70	0.748	614.4
7	40.93	250	2.04	45.48	0.39	237.92	0.809	864.0
8	40.11	250	3.10	179.55	1.47	378.65	0.526	435.6
9	40.87	250	3.10	125.68	1.14	341.77	0.632	508.2
10	38.92	250	3.10	81.07	0.95	264.55	0.694	633.9
11	39.22	250	3.10	46.32	0.65	220.93	0.790	807.1
12	39.00	250	4.09	179.55	2.23	329.32	0.455	453.0
13	40.31	250	4.09	126.08	1.69	305.13	0.587	489.3
14	39.22	250	4.08	80.75	1.24	265.71	0.696	556.8
15	40.46	250	4.08	46.32	0.81	233.34	0.801	736.8
16	39.23	250	5.08	179.55	2.74	332.89	0.461	411.8
17	39.21	250	5.08	125.88	2.24	285.48	0.559	459.4
18	40.51	250	5.06	80.44	1.64	248.17	0.676	578.0
19	40.65	250	5.07	45.96	1.02	228.47	0.799	715.2
20	23.77	500	5.07	179.55	3.38	269.33	0.333	407.1
21	22.85	500	5.07	179.55	3.45	263.87	0.320	392.9
22	21.75	500	4.04	179.55	2.81	258.15	0.304	403.7
23	22.19	500	4.04	179.55	2.73	265.71	0.324	406.6
24	21.37	500	5.07	125.68	3.02	210.99	0.404	412.0
25	21.64	500	5.06	125.48	2.97	213.79	0.413	410.8
26	20.77	500	5.07	125.68	3.10	205.55	0.389	407.8
27	16.67	500	5.06	179.55	3.93	231.18	0.233	329.7
28	38.54	250	2.05	79.33	0.55	295.67	0.732	646.4
29	38.56	250	2.05	79.33	0.56	290.39	0.727	658.3
30	6.41	500	1.02	45.60	0.67	69.43	0.343	444.0
31	6.75	500	1.00	45.60	0.64	71.26	0.360	422.8
32	3.82	500	1.00	20.43	0.62	32.95	0.380	462.9
33	6.30	500	1.01	20.43	0.42	49.12	0.584	557.4
34	6.32	500	1.00	80.12	0.81	98.91	0.190	325.7
35	6.05	500	1.01	10.18	0.27	38.08	0.733	727.0
36	6.01	500	1.01	13.20	0.33	40.41	0.673	659.3
37	6.04	500	1.01	7.50	0.22	34.43	0.782	801.9
38	6.20	500	1.00	10.18	0.24	42.41	0.760	658.0
39	7.81	500	1.01	20.43	0.32	64.48	0.683	587.7
40	7.87	500	1.00	13.20	0.24	55.01	0.760	698.8
41	7.17	500	1.00	13.20	0.25	52.81	0.750	636.4
42	6.80	500	1.00	13.14	0.27	48.66	0.730	681.4
43	6.30	500	1.00	10.18	0.24	42.41	0.760	680.1
44	6.02	500	1.00	10.18	0.25	40.72	0.750	678.4



## Stereo-DIC Results

This appendix contains additional results related to the non-contact optical full-field deflection measurements with Stereo-DIC, which constitute the basis for the determination of the glass' Young's modulus, as reported in Chapter 4, Sec. 4.5. For each of the two samples in the five residual stress groups (see Table B.1), the following pages include a load history and the load stages for which Stereo-DIC deflection measurements were performed, a full-field deflection measurements for a chosen load stage, and additional measured deflections along a section for five load stages. Results for sample RS4/B465 are excluded here because they already are included in Chapter 4 (Figs. 4.9, 4.10 and 4.11). Table B.1 is a summary of the conducted experiments, which include the residual compressive surface stress of the samples, the applied strain rate, the failure stress and the measured Young's modulus.

**Table B.1** Additional results related to deflection measurements with Stereo-DIC, which are reported in Chapter 4. The table include the residual compressive surface stress ( $\sigma_c$ ), the applied strain rate ( $\dot{\epsilon}$ ), the obtained failure stress ( $\sigma_f$ ), and the measured Young's modulus ( $E$ ) (mean and standard deviation) for each of the two samples in the five residual stress groups.

Group	Sample ID	$\sigma_c$ [MPa]	$\dot{\epsilon}$ [s <sup>-1</sup> ]	$\sigma_f$ [MPa]	$E$ [GPa]	Remarks
RS1	A096	2.9	49.3	456.4	72.4 ( $\pm 1.7$ )	
	A097	2.9	44.3	282.4	68.7 ( $\pm 3.5$ )	
RS2	B317	40.1	46.6	359.1	72.0 ( $\pm 2.6$ )	
	B318	39.8	40.5	260.0	72.8 ( $\pm 4.5$ )	
RS3	B151	44.6	53.4	387.6	70.4 ( $\pm 2.0$ )	
	B153	44.4	25.0	122.0	66.3 ( $\pm 2.1$ )	
RS4	B465	47.9	50.4	421.1	71.0 ( $\pm 1.4$ )	<i>Figs. included in Ch. 4</i>
	B466	49.2	40.0	201.3	66.6 ( $\pm 3.2$ )	
RS5	B602	52.0	55.8	394.1	74.3 ( $\pm 2.2$ )	
	B605	54.6	52.2	525.5	72.1 ( $\pm 2.3$ )	

## Sample RS1/A096

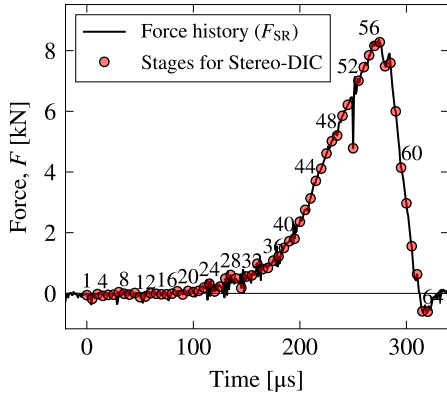


**Fig. B.1** RS1/A096: Force history + load stages.

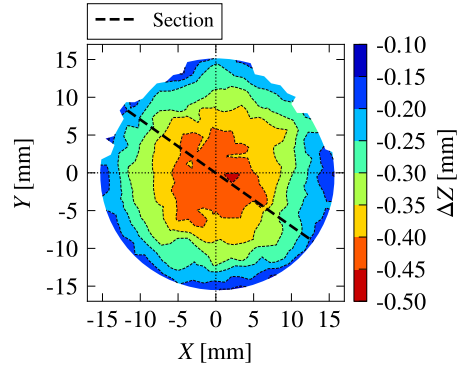


**Fig. B.2** RS1/A096: Full-field deflection at load stage 53 ( $F = 7.46$  kN).

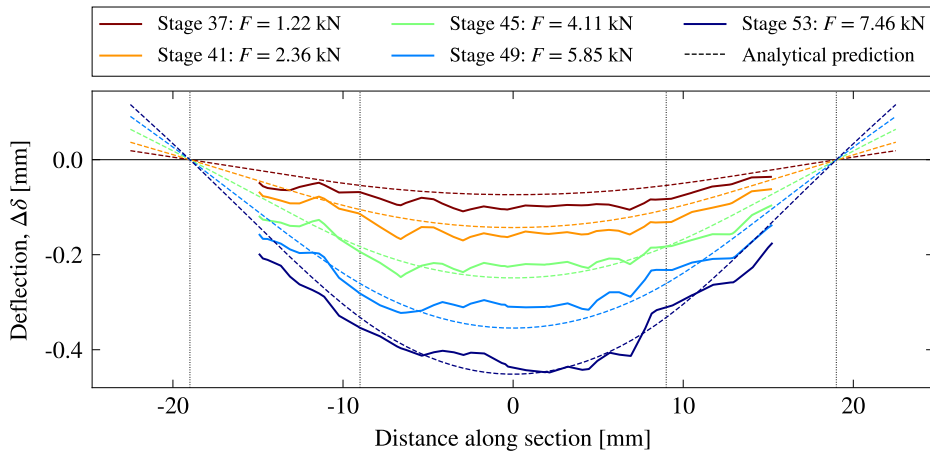


**Fig. B.3** RS1/A096: Glass sample deflection along the section in Fig. B.2 for five load stages related to Fig. B.1, compared to analytical plate bending.

## Sample RS1/A097

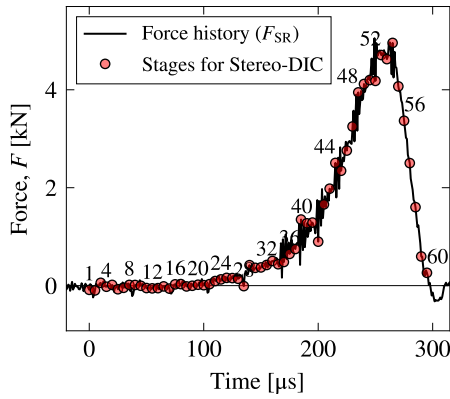


**Fig. B.4** RS1/A097: Force history + load stages.

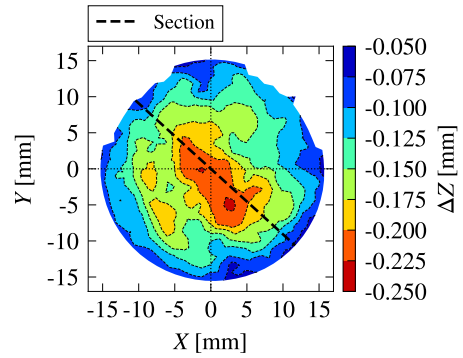


**Fig. B.5** RS1/A097: Full-field deflection at load stage 48 ( $F = 3.95$  kN).

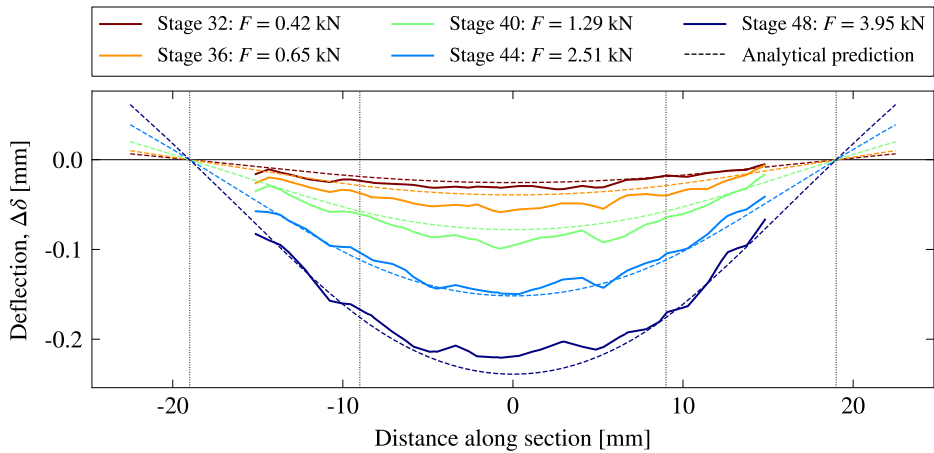


**Fig. B.6** RS1/A097: Glass sample deflection along the section in Fig. B.5 for five load stages related to Fig. B.4, compared to analytical plate bending.

### Sample RS2/B317

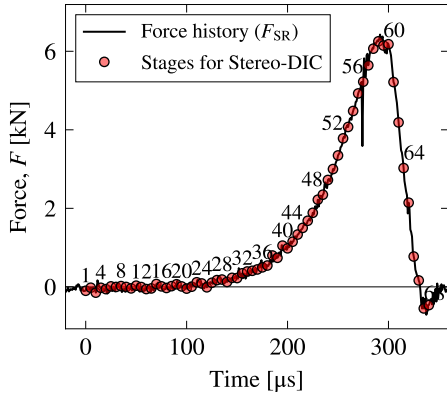


**Fig. B.7** RS2/B317: Force history + load stages.

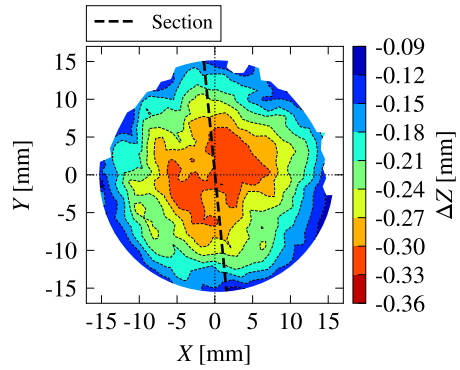


**Fig. B.8** RS2/B317: Full-field deflection at load stage 56 ( $F = 5.22$  kN).

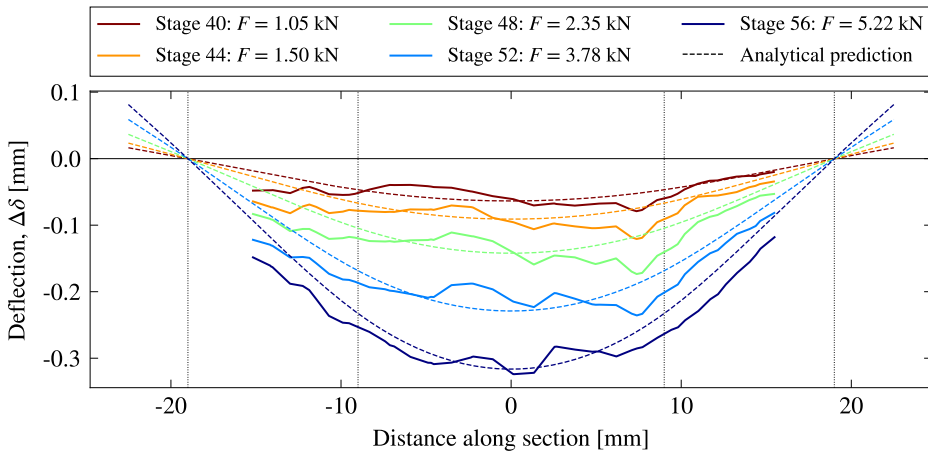


**Fig. B.9** RS2/B317: Glass sample deflection along the section in Fig. B.8 for five load stages related to Fig. B.7, compared to analytical plate bending.

## Sample RS2/B318

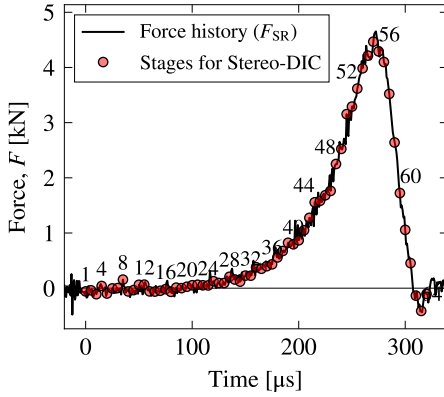


**Fig. B.10** RS2/B318: Force history + load stages.

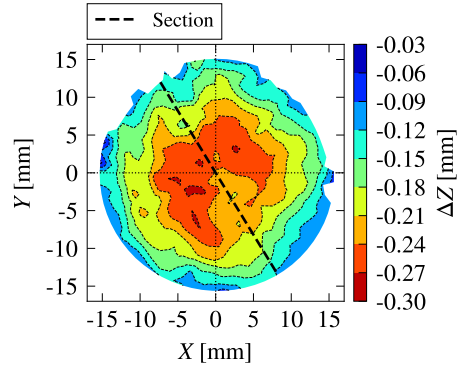


**Fig. B.11** RS2/B318: Full-field deflection at load stage 54 ( $F = 4.21$  kN).

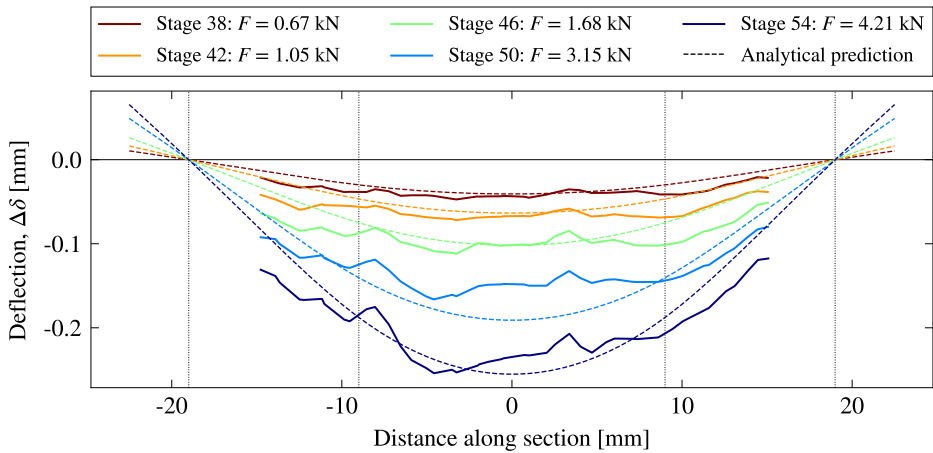


**Fig. B.12** RS2/B318: Glass sample deflection along the section in Fig. B.11 for five load stages related to Fig. B.10, compared to analytical plate bending.

### Sample RS3/B151

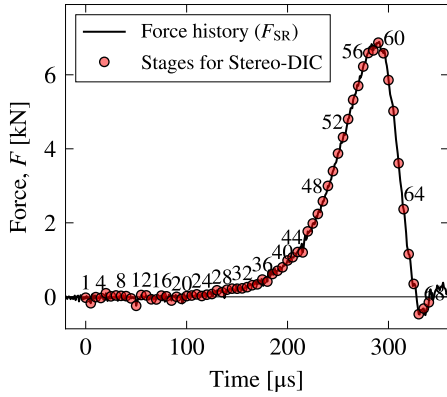


**Fig. B.13** RS3/B151: Force history + load stages.

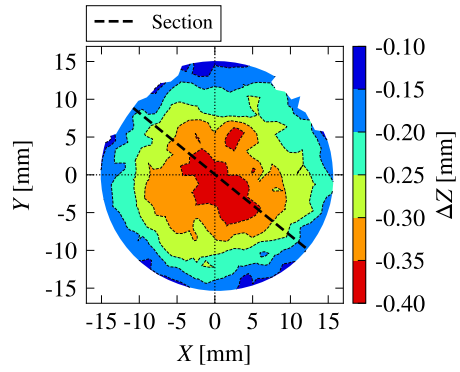


**Fig. B.14** RS3/B151: Full-field deflection at load stage 56 ( $F = 6.22$  kN).

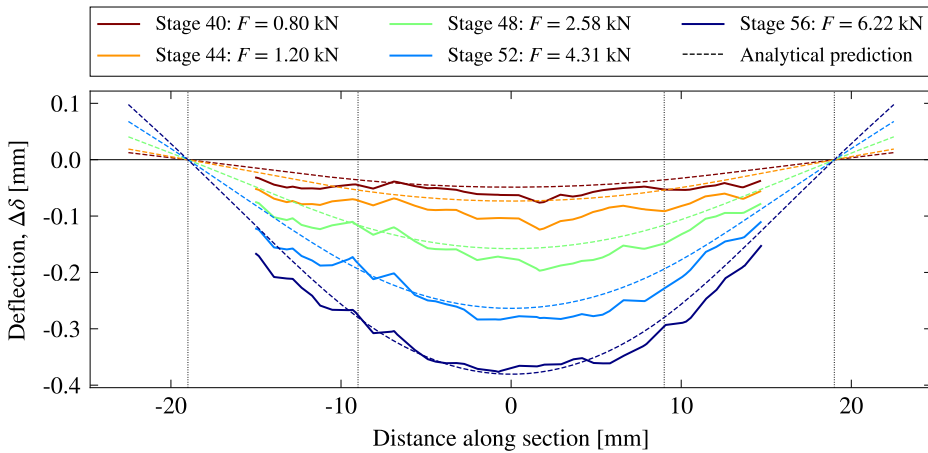


**Fig. B.15** RS3/B151: Glass sample deflection along the section in Fig. B.14 for five load stages related to Fig. B.13, compared to analytical plate bending.

## Sample RS3/B153

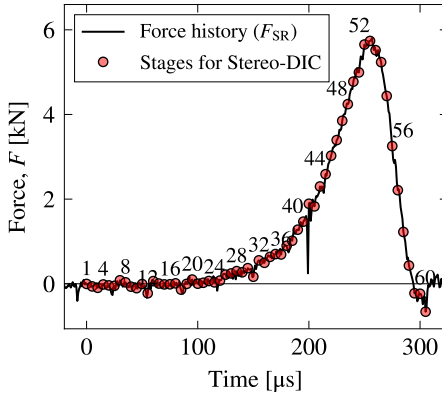


**Fig. B.16** RS3/B153: Force history + load stages.

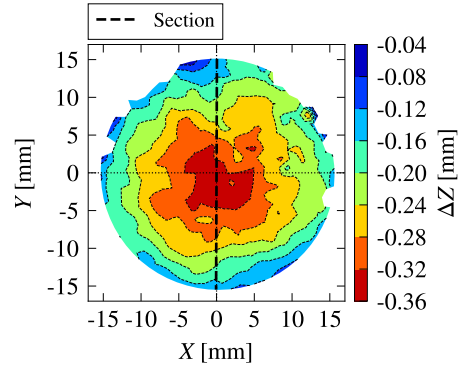


**Fig. B.17** RS3/B153: Full-field deflection at load stage 50 ( $F = 5.00$  kN).

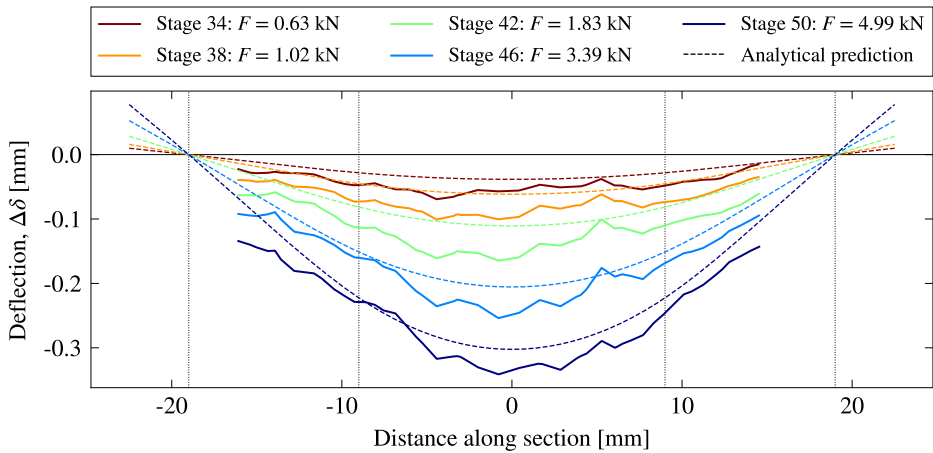


**Fig. B.18** RS3/B153: Glass sample deflection along the section in Fig. B.17 for five load stages related to Fig. B.16, compared to analytical plate bending.

### Sample RS4/B466

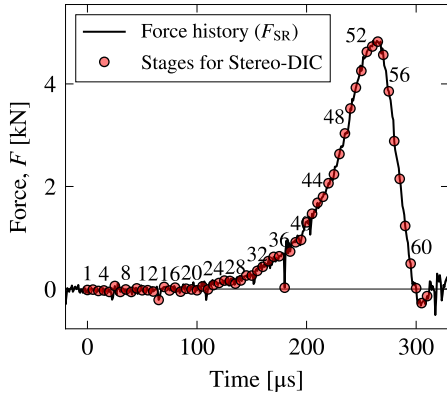


**Fig. B.19** RS4/B466: Force history + load stages.

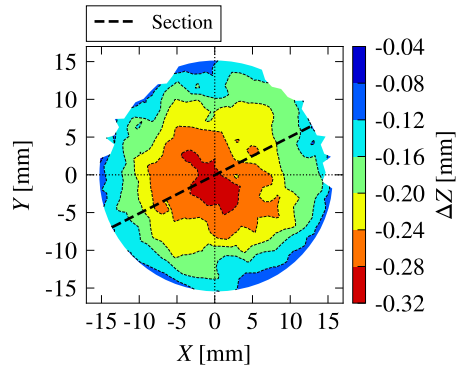


**Fig. B.20** RS4/B466: Full-field deflection at load stage 52 ( $F = 4.62$  kN).

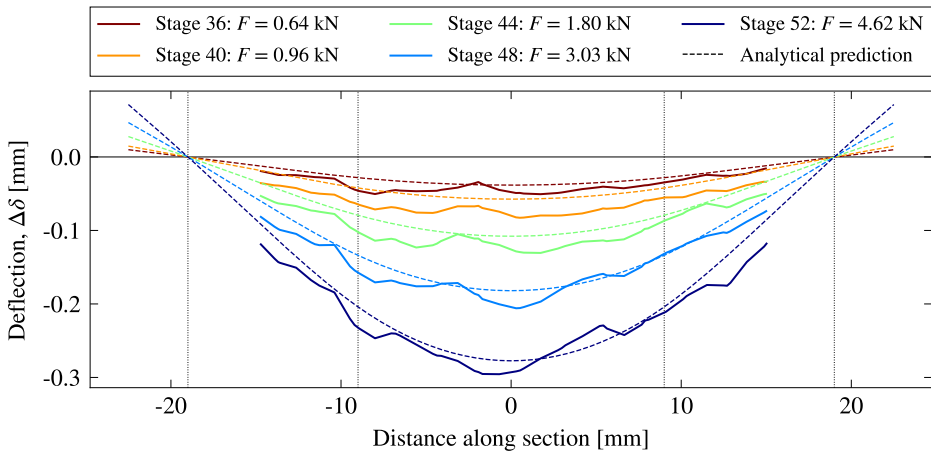


**Fig. B.21** RS4/B466: Glass sample deflection along the section in Fig. B.20 for five load stages related to Fig. B.19, compared to analytical plate bending.

## Sample RS5/B602

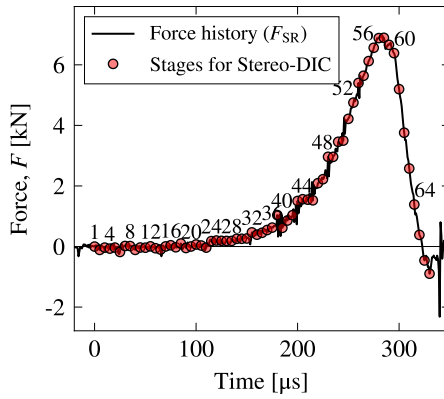


**Fig. B.22** RS5/B602: Force history + load stages.

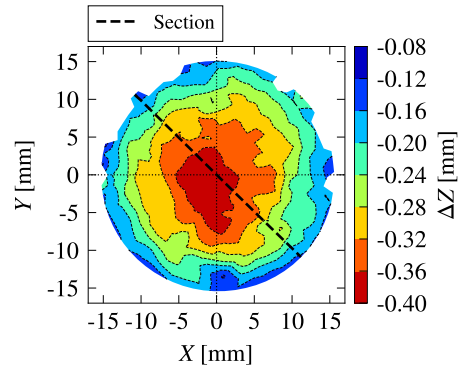


**Fig. B.23** RS5/B602: Full-field deflection at load stage 56 ( $F = 6.56$  kN).

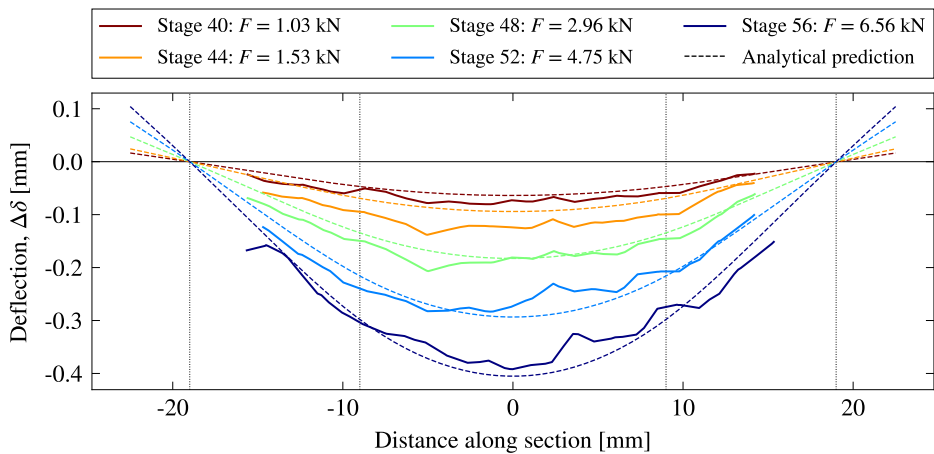


**Fig. B.24** RS5/B602: Glass sample deflection along the section in Fig. B.23 for five load stages related to Fig. B.22, compared to analytical plate bending.

### Sample RS5/B605

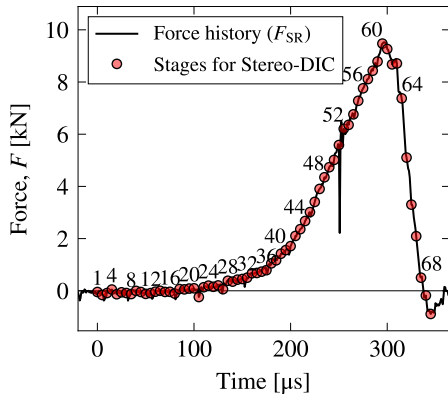


**Fig. B.25** RS5/B605: Force history + load stages.

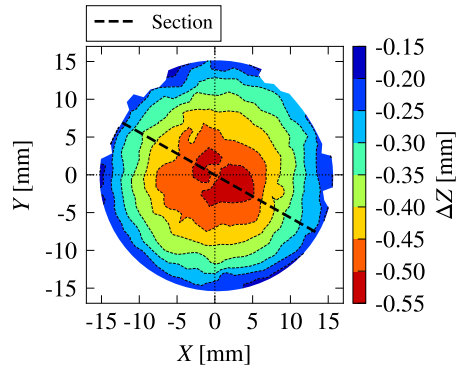


**Fig. B.26** RS5/B605: Full-field deflection at load stage 58 ( $F = 8.43$  kN).

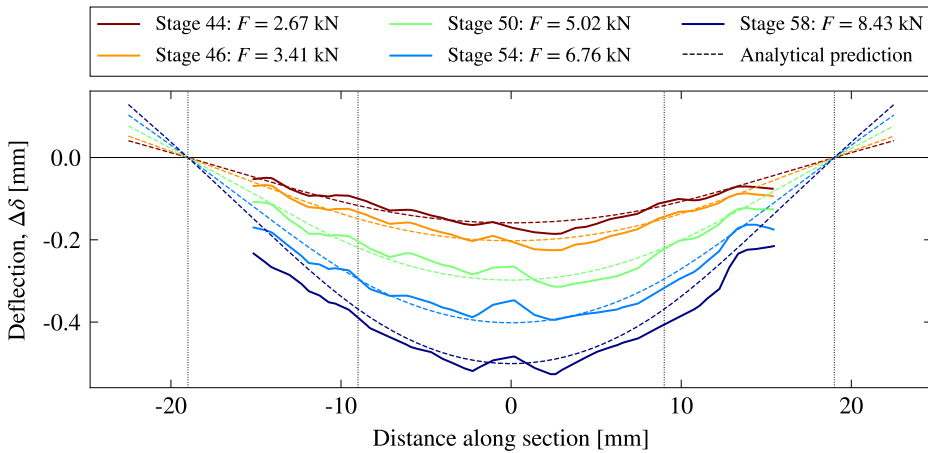


**Fig. B.27** RS5/B605: Glass sample deflection along the section in Fig. B.26 for five load stages related to Fig. B.25, compared to analytical plate bending.

## User Subroutine for ABAQUS/Explicit

This appendix contains additional information on the developed rate-dependent progressive damage model for dynamic glass fracture implemented as a VUMAT user subroutine for ABAQUS/Explicit, as presented in Chapter 5. Sec. C.1 describes two options in ABAQUS to define the transverse shear stiffness of a shell element for which the damage model is defined. A flowchart of the VUMAT implementation of the damage model is provided in Sec. C.2 and the related source code written in FORTRAN is given in Sec. C.3.

### C.1 Shell Elements

When the VUMAT is used to define the material response of shell elements, ABAQUS/Explicit is not capable of calculating a default value for the transverse shear stiffness of the element. Therefore, one must define explicitly either the material transverse shear modulus or the element's transverse shear stiffness in accordance with DASSAULT SYSTÈMES (2021).

#### Option 1: Defining the Elastic Transverse Shear Modulus

ABAQUS allows the specification of the initial elastic transverse shear modulus for computing the transverse shear stiffness of shells. It can be defined either isotropic, orthotropic, or anisotropic. A direct input in ABAQUS/CAE is not supported. Therefore, the following lines need to be added to the input file (\*.inp) after \*Material:

- Isotropic:

$$\begin{Bmatrix} \sigma_{13} \\ \sigma_{23} \end{Bmatrix} = \begin{bmatrix} G & 0 \\ 0 & G \end{bmatrix} \begin{Bmatrix} \gamma_{13} \\ \gamma_{23} \end{Bmatrix} \quad (\text{C.1})$$

```
1 *Transverse shear, type=isotropic
2 G,
```

- Orthotropic:

$$\begin{Bmatrix} \sigma_{13} \\ \sigma_{23} \end{Bmatrix} = \begin{bmatrix} G_{13} & 0 \\ 0 & G_{23} \end{bmatrix} \begin{Bmatrix} \gamma_{13} \\ \gamma_{23} \end{Bmatrix} \quad (\text{C.2})$$

```

1 *Transverse shear, type=orthotropic
2 G12, G13, G23,

```

- Anisotropic:

$$\begin{Bmatrix} \sigma_{13} \\ \sigma_{23} \end{Bmatrix} = \begin{bmatrix} D_{1313} & D_{1323} \\ D_{1323} & D_{2323} \end{bmatrix} \begin{Bmatrix} \gamma_{13} \\ \gamma_{23} \end{Bmatrix} \quad (\text{C.3})$$

```

1 *Transverse shear, type=anisotropic
2 D1212, D1313, D2323, D1323,

```

## Option 2: Defining the Transverse Shear Stiffness

A shell element's transverse shear stiffness can be directly defined in ABAQUS/CAE at: **Sections**→**Shell**→**Advanced**→**Transverse Shear Stiffness**. In ABAQUS, the transverse shear stiffness of the section of a shear flexible shell element is defined as follows (DASSAULT SYSTÈMES 2021):

$$\bar{K}_{\alpha\beta}^{ts} = f_p K_{\alpha\beta}^{ts} \quad (\text{C.4})$$

where  $\bar{K}_{\alpha\beta}^{ts}$  are the components of the section shear stiffness,  $f_p$  is a dimensionless factor controlling that the shear stiffness is not becoming too large in thin shells, and  $K_{\alpha\beta}^{ts}$  is the actual shear stiffness of the section (a required user-defined input when a VUMAT defines the material behaviour of the section).

The transverse shear stiffness is to be specified as an initial, linear elastic stiffness of the shell in response to pure transverse shear strains. For a homogeneous shell representing an *isotropic linear elastic material*, the transverse shear stiffness can be computed by the following expressions:

$$K_{11}^{ts} = \frac{5}{6}Gt \quad , \quad K_{22}^{ts} = K_{11}^{ts} \quad , \quad K_{12}^{ts} = 0 \quad (\text{C.5})$$

where  $G$  is the material's shear modulus, and  $t$  is the thickness of the shell. Is the shell representing an *orthotropic linear elastic material*, where the strong material direction aligns with the element's local 1-direction, then the transverse shear stiffness can take the following values:

$$K_{11}^{ts} = \frac{5}{6}G_{13}t \quad , \quad K_{22}^{ts} = \frac{5}{6}G_{23}t \quad , \quad K_{12}^{ts} = 0 \quad (\text{C.6})$$

In both transverse shear stiffness definitions, the number  $5/6$  is a shear correction coefficient that results from matching the transverse shear energy to that for a 3D structure in pure bending.

### C.2 VUMAT Flowchart

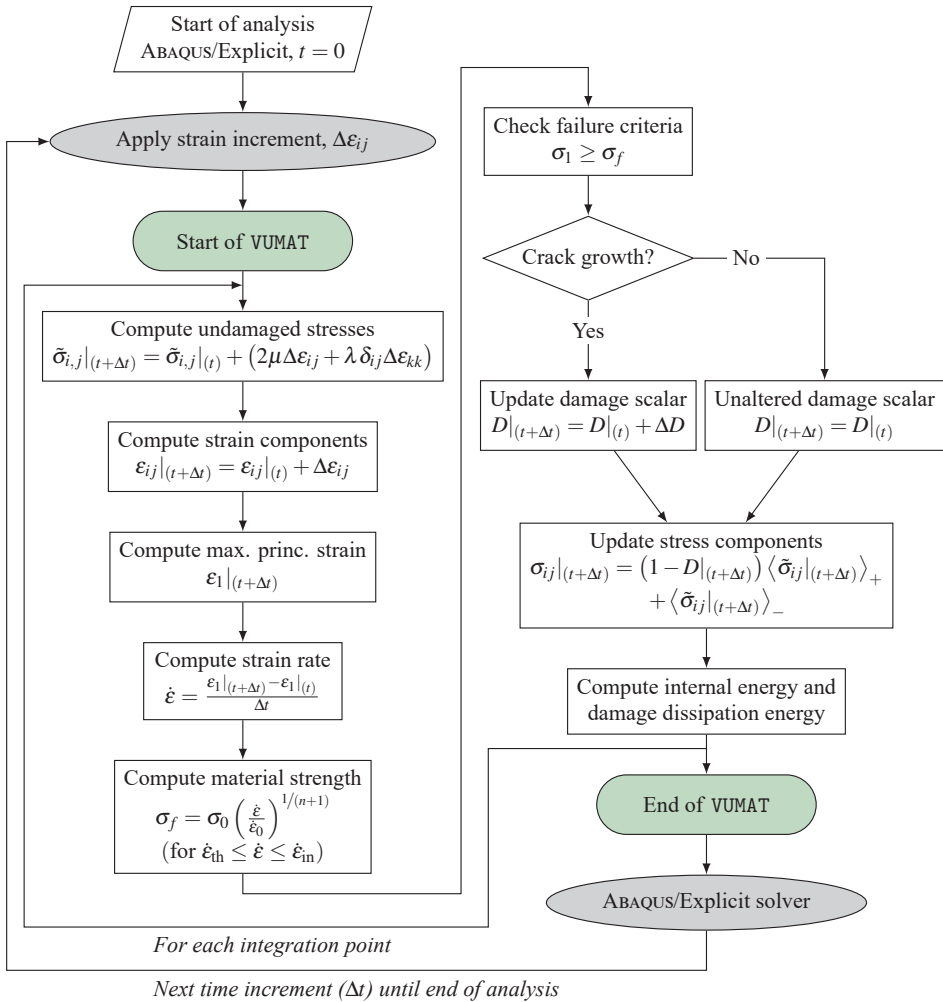


**Fig. C.1** Flowchart of the VUMAT implementation of the rate-dependent progressive damage model for dynamic glass fracture, as presented in Chapter 5.

### C.3 VUMAT Code

```

1 C %%%%%%%%%%%%%%%%%%%%%%%%%%%%%%%%%%%%%%%%%%%%%%%%%%%%%%%%%%%%%%%%%%%%%%%%%%
2 C VUMAT for ABAQUS/Explicit:
3 C Isotropic isothermal elastic material behaviour combined with a
4 C progressive damage model that is based on a rate-dependent material
5 C strength, SIGF, and a fracture energy, G1c.
6 C -----
7 C Tested element type: S4R, S4
8 C -----
9 C Copyright (C) 2021 by Martin J. Meyland. All rights reserved.
10 C DTU Civil Engineering, Kgs. Lyngby | Ramboll Denmark A/S, Copenhagen
11 C E-Mail: majeme@byg.dtu.dk / MJME@ramboll.dk
12 C %%%%%%%%%%%%%%%%%%%%%%%%%%%%%%%%%%%%%%%%%%%%%%%%%%%%%%%%%%%%%%%%%%%%%%%%%%
13 C
14 C -----
15 C >> START OF VUMAT <<
16 C -----
17 SUBROUTINE VUMAT(
18 C *****
19 C *** Read only (unmodifiable)variables ***
20 C *****
21 1 NBLOCK, NDIR, NSHR, NSTATEV, NFIELDV, NPROPS, LANNEAL,
22 2 STEPTIME, TOTALTIME, DT, CMNAME, COORDMP, CHARLENGTH,
23 3 PROPS, DENSITY, STRAININC, RELSPININC,
24 4 TEMPOLD, STRETCHOLD, DEFGRADOLD, FIELDOLD,
25 5 STRESSOLD, STATEOLD, ENERINTERNOLD, ENERINELASOLD,
26 6 TEMPNEW, STRETCHNEW, DEFGRADNEW, FIELDNEW,
27 C *****
28 C *** Write only (modifiable) variables ***
29 C *****
30 7 STRESSNEW, STATENEW, ENERINTERNNEW, ENERINELASNEW )
31 C
32 INCLUDE 'VABA_PARAM.INC'
33 C
34 DIMENSION PROPS(NPROPS), DENSITY(NBLOCK), COORDMP(NBLOCK),
35 1 CHARLENGTH(NBLOCK), STRAININC(NBLOCK, NDIR+NSHR),
36 2 RELSPININC(NBLOCK, NSHR), TEMPOLD(NBLOCK),
37 3 STRETCHOLD(NBLOCK, NDIR+NSHR),DEFGRADOLD(NBLOCK, NDIR+NSHR+NSHR),
38 4 FIELDOLD(NBLOCK, NFIELDV), STRESSOLD(NBLOCK, NDIR+NSHR),
39 5 STATEOLD(NBLOCK, NSTATEV), ENERINTERNOLD(NBLOCK),
40 6 ENERINELASOLD(NBLOCK), TEMPNEW(NBLOCK),
41 7 STRETCHNEW(NBLOCK, NDIR+NSHR),DEFGRADNEW(NBLOCK, NDIR+NSHR+NSHR),
42 8 FIELDNEW(NBLOCK, NFIELDV), STRESSNEW(NBLOCK, NDIR+NSHR),
43 9 STATENEW(NBLOCK, NSTATEV), ENERINTERNNEW(NBLOCK),
44 1 ENERINELASNEW(NBLOCK), EIGVAL(NBLOCK, 3)
45 C
46 CHARACTER*80 CMNAME
47 C
48 PARAMETER( ZERO = 0.DO, ONE = 1.DO, TWO = 2.DO, THREE = 3.DO,
49 1 THIRD = 1.DO/3.DO, HALF = .5DO, TWO_THIRDS = 2.DO/3.DO,
50 2 THREE_HALFS = 1.5DO, FOUR_THIRDS = 4.DO/3.DO,
51 3 PI = 4.DO*DATAN(1.DO) )
52 C
53 C *****

```

```

54 C *** Description of used VUMAT variables ***
55 C *****
56 C   NPROPS           - user-specified number of user-defined
57 C                   material properties
58 C   NBLOCK          - number of material points to be processed in this
59 C                   call to VUMAT
60 C   NDIR             - number of direct components in a symmetric tensor
61 C                   (direct stress)
62 C   NSHR             - number of indirect components in a symmetric
63 C                   tensor (shear stress)
64 C   STRAININC        - strain increment tensor at each material point
65 C   STRESSOLD         - stress tensor at each material point
66 C   STRETCHOLD       - stretch tensor, U, at each material point at the
67 C                   beginning of the increment
68 C   ENERINTERNOLD    - Internal energy per unit mass
69 C   ENERINELASOLD    - Dissipated inelastic energy unit mass
70 C
71 C *****
72 C *** Used state variables are stored as ***
73 C *****
74 C   STATE(*, 1) = material point status
75 C   STATE(*, 2) = max princ. strain
76 C   STATE(*, 3) = max princ. strain rate
77 C   STATE(*, 4) = rate dependent material strength (SIGF)
78 C   STATE(*, 5) = element stiffness in max. principal direction
79 C   STATE(*, 6) = 'flag' to identify first time EPS0 is reached
80 C   STATE(*, 7) = damage scalar (D)
81 C   STATE(*, 8) = strain at highest obtained damage scalar
82 C
83 C   Undamaged stress components:
84 C   STATE(*, 9) = SIG11
85 C   STATE(*,10) = SIG22
86 C   STATE(*,11) = SIG33
87 C   STATE(*,12) = SIG12
88 C
89 C   Strain components:
90 C   STATE(*,13) = EPS11
91 C   STATE(*,14) = EPS22
92 C   STATE(*,15) = EPS33
93 C   STATE(*,16) = EPS12
94 C
95 C *****
96 C *** Declare precision of real variables ***
97 C *****
98 C   DOUBLE PRECISION EO, XNU, SIGO, EPSDOTO, N, GIC,
99 C   1 TWOMU, ALAMBDA, TRACE, STRESSPOWER, ENERSTRAIN,
100 C   2 EPS11, EPS22, EPS33, EPS12, EPS23, EPS31,
101 C   3 I1, I2, I3, PHI, PHICONST,
102 C   4 EPS1, EPS2, EPS3, MAXPRINCSTRAIN, MINPRINCSTRAIN,
103 C   5 MAXPRINCSTRESSOLD, E,
104 C   6 EPSOLD, EPSNEW, EPSDOT, EPSO, LELEM, EPSF, SIGF,
105 C   7 FSCALE, DELTAD, D, VC
106 C
107 C *****
108 C *** Mechanical Constants (User Material) ***

```

## Appendix C. User Subroutine for ABAQUS/Explicit

```

109 C *****
110     EO      = PROPS(1) ! Young's modulus
111     XNU     = PROPS(2) ! Poisson's ratio
112     SIGO    = PROPS(3) ! Reference material strength
113     N       = PROPS(4) ! Sub-critical crack growth parameter
114     GIC     = PROPS(5) ! Fracture energy (Mode I)
115 C
116 C     Lamé material parameters:
117     TWOMU   = EO / ( ONE + XNU )
118     ALAMBDA = EO * XNU / ( ( ONE - TWO * XNU ) * ( ONE + XNU ) )
119 C
120 C -----
121 C     Call utility routine for calculating principal stress values
122 C     using the stresses from the previous time increment:
123 C     CALL VSPRINC(NBLOCK, STRESSOLD, EIGVAL, NDIR, NSHR)
124 C
125 C -----
126 C     DO K = 1, NBLOCK ! Iteration through block of material points
127 C
128 C *****
129 C ***     Definition of the thickness strain increment,          ***
130 C ***     i.e. STRAININC(*,3)                                   ***
131 C *****
132     STRAININC(K,3) = - ( XNU / ( 1 - XNU ) )
133     1 *           ( STRAININC(K,1) + STRAININC(K,2) )
134
135 C *****
136 C ***     Undamaged stress components                          ***
137 C ***     (isotropic linear elastic material)                  ***
138 C *****
139     TRACE = STRAININC(K,1) + STRAININC(K,2) + STRAININC(K,3)
140 C
141     STATENEW(K, 9) = STATEOLD(K, 9) + ALAMBDA * TRACE
142     1 +           TWOMU * STRAININC(K,1)
143     STATENEW(K,10) = STATEOLD(K,10) + ALAMBDA * TRACE
144     1 +           TWOMU * STRAININC(K,2)
145     STATENEW(K,11) = STATEOLD(K,11) + ALAMBDA * TRACE
146     1 +           TWOMU * STRAININC(K,3)
147     STATENEW(K,12) = STATEOLD(K,12)
148     1 +           TWOMU * STRAININC(K,4)
149 C
150 C *****
151 C ***     Strain and strain-rate - EPS, EPSDOT                 ***
152 C *****
153 C     Obtain total strains:
154     STATENEW(K,13) = STATEOLD(K,13) + STRAININC(K,1) ! EPS11
155     STATENEW(K,14) = STATEOLD(K,14) + STRAININC(K,2) ! EPS22
156     STATENEW(K,15) = STATEOLD(K,15) + STRAININC(K,3) ! EPS33
157     STATENEW(K,16) = STATEOLD(K,16) + STRAININC(K,4) ! EPS12
158 C
159     EPS11 = STATENEW(K,13)
160     EPS22 = STATENEW(K,14)
161     EPS33 = STATENEW(K,15)
162     EPS12 = STATENEW(K,16)
163     EPS23 = ZERO

```

```

164     EPS31 = ZERO
165 C
166 C Determine strain invariants - I1, I2, I3:
167 I1 = EPS11 + EPS22 + EPS33
168 C
169     I2 = EPS11 * EPS22 + EPS22 * EPS33 + EPS33 * EPS11
170     1 - EPS12**TWO
171     2 - EPS23**TWO
172     3 - EPS31**TWO
173 C
174     I3 = EPS11 * EPS22 * EPS33
175     1 - EPS11 * EPS23**TWO
176     2 - EPS22 * EPS31**TWO
177     3 - EPS33 * EPS12**TWO
178     4 + TWO * EPS12 * EPS23 * EPS31
179 C
180     PHICONST = ( TWO * I1**THREE - 9.DO * I1 * I2 + 27.DO * I3 ) /
181     1 ( TWO * ( I1**TWO - THREE * I2 )** ( THREE_HALFS ) )
182 C
183 C --> check if PHICONST is within the range [-1, 1]:
184 IF ( PHICONST .GT. ONE ) THEN
185     PHICONST = ONE
186 ELSE IF ( PHICONST .LT. -ONE ) THEN
187     PHICONST = - ONE
188 END IF
189 C
190     PHI = THIRD * ACOS( PHICONST )
191 C
192 C Calculate principal strains:
193     EPS1 = THIRD * I1
194     1 + TWO_THIRDS * ( SQRT( I1**TWO - THREE * I2 ) )
195     2 * COS( PHI )
196 C
197     EPS2 = THIRD * I1
198     1 + TWO_THIRDS * ( SQRT( I1**TWO - THREE * I2 ) )
199     2 * COS( PHI - TWO_THIRDS * PI )
200 C
201     EPS3 = THIRD * I1
202     1 + TWO_THIRDS * ( SQRT( I1**TWO - THREE * I2 ) )
203     2 * COS( PHI - FOUR_THIRDS * PI )
204 C
205 C Obtain max and min princ. strain:
206     MAXPRINCSTRAIN = MAX( EPS1, EPS2, EPS3 )
207     MINPRINCSTRAIN = MIN( EPS1, EPS2, EPS3 )
208 C
209 C Strains used for crack evaluation:
210     STATENEW(K,2) = MAXPRINCSTRAIN
211     EPSNEW = STATENEW(K,2)
212     EPSOLD = STATEOLD(K,2)
213 C
214 C Strain rate for the material strength:
215     STATENEW(K,3) = ( EPSNEW - EPSOLD ) / DT
216 C
217     EPSDOT = STATENEW(K,3)
218 C

```

Appendix C. User Subroutine for ABAQUS/Explicit

```

219 C *****
220 C *** Rate-dependent material strength - SIGF ***
221 C *****
222 C Normalisation according to Meyland et al. (2021):
223 C EPSDOTO = 2.86D-05 ! [s^-1] reference strain rate
224 C
225 C Define lower and upper strength limit:
226 C SIGFMIN = SIGO * 0.65D0 ! lower limit of material strength
227 C ! (i.e. threshold strength)
228 C
229 C SIGFMAX = SIGO * 2.30D0 ! upper limit of material strength
230 C ! (i.e. inert strength)
231 C
232 C Calculate material strength:
233 C IF ( STEPTIME .EQ. ZERO ) THEN
234 C STATENEW(K,4) = SIGO
235 C ELSE IF ( EPSDOT .GT. ZERO ) THEN
236 C STATENEW(K,4) = SIGO
237 C 1 * ( EPSDOT / EPSDOTO )** ( ONE / ( N + ONE ) )
238 C ELSE IF ( EPSDOT .LE. ZERO ) THEN
239 C STATENEW(K,4) = STATEOLD(K,4)
240 C END IF
241 C
242 C Limit check:
243 C IF ( STATENEW(K,4) .LT. SIGFMIN ) STATENEW(K,4) = SIGFMIN
244 C IF ( STATENEW(K,4) .GT. SIGFMAX ) STATENEW(K,4) = SIGFMAX
245 C
246 C SIGF = STATENEW(K,4)
247 C
248 C *****
249 C *** Stiffness in terms of max princ. stress/strain - E' ***
250 C *** - used to determine the onset of damage ***
251 C *****
252 C Calculation of max. princ. stress from previous
253 C time increment:
254 C MAXPRINCSTRESSOLD = MAX(EIGVAL(K,1), EIGVAL(K,2), EIGVAL(K,3))
255 C
256 C Stiffness:
257 C IF ( STEPTIME .EQ. ZERO .OR. STEPTIME .EQ. DT ) THEN
258 C STATENEW(K,5) = EO
259 C ELSE
260 C STATENEW(K,5) = MAXPRINCSTRESSOLD / EPSOLD
261 C END IF
262 C
263 C E = STATENEW(K,5)
264 C
265 C *****
266 C *** Crack opening strain at damage initiation - EPSO ***
267 C *****
268 C *** - A flag, STATE(*, 6), is used to identify the first time ***
269 C *** EPSO is reached. At this point EPSO and SIGF are kept ***
270 C *** fixed for the further analysis, i.e. no rate dependence ***
271 C *** in the damage phase. ***
272 C *****
273 C IF ( STATEOLD(K,6) .EQ. ZERO ) THEN

```

```

274         EPSO = SIGF / E
275         IF ( EPSNEW .GE. EPSO ) THEN
276             STATENEW(K,6) = ONE
277         ELSE
278             STATENEW(K,6) = ZERO
279         END IF
280     ELSE IF ( STATEOLD(K,6) .EQ. ONE ) THEN
281         STATENEW(K,4) = STATEOLD(K,4) ! update: SIGF
282         STATENEW(K,5) = STATEOLD(K,5) ! update: E'
283         STATENEW(K,6) = STATEOLD(K,6) ! update: 'flag'
284         SIGF = STATENEW(K,4)
285         E = STATENEW(K,5)
286         EPSO = SIGF / E
287     END IF
288 C
289 C *****
290 C ***      Crack opening strain at failure - EPSF      ***
291 C *****
292         LELEM = CHARLENGTH(K) ! characteristic element length
293         EPSF = EPSO + TWO * GIC / (SIGF * LELEM)
294 C
295 C *****
296 C ***      Determination of the damage scalar - D      ***
297 C *****
298         IF ( STEPTIME .EQ. ZERO ) THEN
299             DELTAD = ZERO
300         ELSE IF ( EPSNEW .GE. EPSO .AND. EPSNEW .LE. EPSF ) THEN
301             DELTAD = MAX( ZERO ,
302                 1         (EPSF * (EPSNEW - EPSO)) / (EPSNEW * (EPSF - EPSO))
303                 2         - (EPSF * (EPSOLD - EPSO)) / (EPSOLD * (EPSF - EPSO))
304                 3         )
305         ELSE
306             DELTAD = ZERO
307         END IF
308 C
309 C      Controls the damage scalar in case a not fully developed
310 C      crack closes again (i.e. compression load):
311         IF ( EPSNEW .GT. STATEOLD(K,8) .AND.
312             1         MAXPRINCSTRAIN .GT. ABS( MINPRINCSTRAIN ) ) THEN
313             STATENEW(K,8) = EPSNEW
314             STATENEW(K,7) = STATEOLD(K,7) + DELTAD
315             IF ( STATENEW(K,7) .GE. ONE .OR. EPSNEW .GE. EPSF ) THEN
316                 STATENEW(K,7) = ONE
317             END IF
318         ELSE
319             STATENEW(K,8) = STATEOLD(K,8)
320             STATENEW(K,7) = STATEOLD(K,7)
321         END IF
322 C
323         D = STATENEW(K,7)
324 C
325 C *****
326 C ***      Fracture criterion/Material point status      ***
327 C ***      - i.e element deletion control      ***
328 C *****

```

Appendix C. User Subroutine for ABAQUS/Explicit

```

329     IF ( EPSNEW .GE. EPSF .AND.
330     1     MAXPRINCSTRAIN .GT. ABS( MINPRINCSTRAIN ) ) THEN
331         STATENEW(K,1) = ZERO ! MP status (fractured)
332     ELSE
333         STATENEW(K,1) = ONE ! MP status (not fractured)
334     END IF
335 C
336 C *****
337 C *** Updating stresses with damage scalar (Macaulay brackets) ***
338 C *****
339     IF ( STEPTIME .EQ. ZERO .OR.
340     1     MAXPRINCSTRAIN .LT. ABS( MINPRINCSTRAIN ) ) THEN
341         STRESSNEW(K,1) = STATENEW(K, 9)
342         STRESSNEW(K,2) = STATENEW(K,10)
343         STRESSNEW(K,3) = STATENEW(K,11)
344         STRESSNEW(K,4) = STATENEW(K,12)
345     ELSE IF ( MAXPRINCSTRAIN .GT. ABS( MINPRINCSTRAIN ) ) THEN
346         STRESSNEW(K,1) = STATENEW(K, 9) * ( ONE - D )
347         STRESSNEW(K,2) = STATENEW(K,10) * ( ONE - D )
348         STRESSNEW(K,3) = STATENEW(K,11) * ( ONE - D )
349         STRESSNEW(K,4) = STATENEW(K,12) * ( ONE - D )
350     END IF
351 C
352 C *****
353 C *** >>> ENERGIES <<< ***
354 C *****
355 C *** Specific internal energy ***
356 C *****
357 C STRESSPOWER - strain energy density function (W)
358     STRESSPOWER = HALF * (
359     1     ( STRESSOLD(K,1) + STRESSNEW(K,1) ) * STRAININC(K,1)
360     2     + ( STRESSOLD(K,2) + STRESSNEW(K,2) ) * STRAININC(K,2)
361     3     + ( STRESSOLD(K,3) + STRESSNEW(K,3) ) * STRAININC(K,3) )
362     4     + ( STRESSOLD(K,4) + STRESSNEW(K,4) ) * STRAININC(K,4)
363 C
364     ENERINTERNNEW(K) = ENERINTERNOLD(K)
365     1     + STRESSPOWER / DENSITY(K)
366 C
367 C *****
368 C *** Damage dissipation ***
369 C *** --> output is written to 'plastic' dissipation: ALLPD ***
370 C *** --> Damage dissipation = Work - Strain energy ***
371 C *****
372     ENERSTRAIN = HALF * (
373     1     STRESSNEW(K,1) * ( STRETCHNEW(K,1) - ONE )
374     2     + STRESSNEW(K,2) * ( STRETCHNEW(K,2) - ONE )
375     3     + STRESSNEW(K,3) * ( STRETCHNEW(K,3) - ONE ) )
376     4     + STRESSNEW(K,4) * STRETCHNEW(K,4)
377 C
378     ENERINELASNEW(K) = ENERINTERNNEW(K)
379     1     - ENERSTRAIN / DENSITY(K)
380 C
381 C -----
382     END DO
383 C

```

```
384     RETURN
385     END SUBROUTINE
386 C -----
387 C                               >> END OF VUMAT <<
388 C -----
389 C
390 C USED REFERENCES:
391 C -----
392 C Meyland, M.J., Nielsen, J.H., Kocer, C. (2021). Tensile behaviour
393 C   of soda-lime-silica glass and the significance of load duration -
394 C   A literature review. J. Build. Eng. 44, 102966 (2021).
395 C   doi: https://doi.org/10.1016/j.jobbe.2021.102966
```

**Listing C.1** VUMAT code for shell elements defining the rate-dependent progressive damage model for dynamic glass fracture, as presented in Chapter 5.



## Mesh Convergence Analysis

This appendix contains mesh convergence analyses related to the simulations in Chapter 5, Sec. 5.3, which were performed to determine the element size ( $L_e$ ) that was required to obtain consistent results in the pane central displacement and the maximum principal stress in the pane centre before fracture. In total, three different cases were simulated (Test A, Test B-1 and Test B-2, cf. Table 5.3) and for each case a convergence analysis is provided hereinafter.

*Go to the next page* →

## Test A

Test A relates to the simulation of the blast test performed and reported by SPILLER et al. (2016). Figs. D.1 and D.2 are the results of the mesh convergence analysis for a 12 mm monolithic glass pane with a quasi-static strength  $\sigma_0 = 80$  MPa subjected to the pressure-time history shown in Fig. 5.9(a).

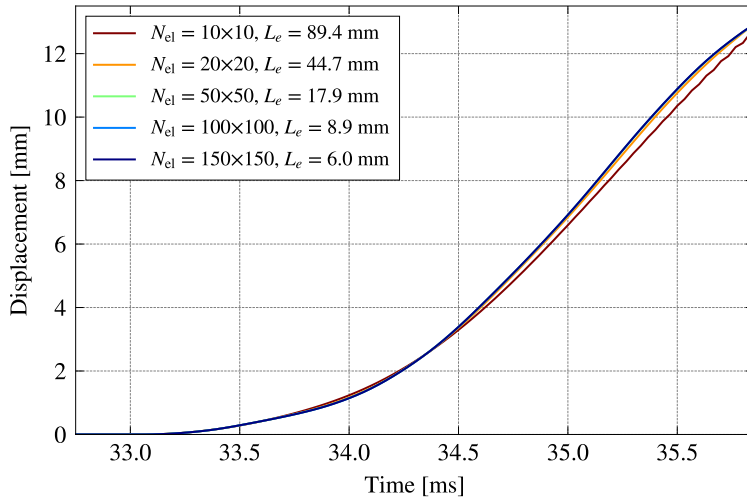


**Fig. D.1** Test A: Pane central displacement as a function of time.

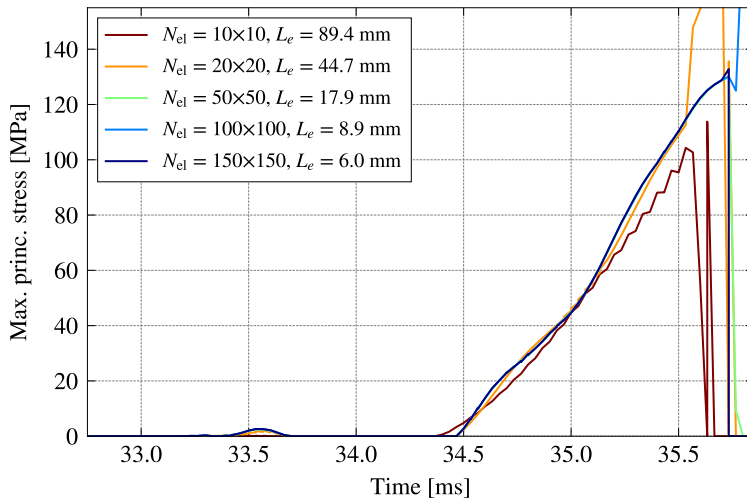


**Fig. D.2** Test A: Maximum principal stress in the pane centre as a function of time.

### Test B-1

Test B-1 relates to the simulation of the blast test performed and reported by JOHNS and CLUBLEY (2015). Figs. D.3 and D.4 are the results of the mesh convergence analysis for a 4 mm monolithic glass pane with a quasi-static strength  $\sigma_0 = 175$  MPa subjected to the pressure-time history shown in Fig. 5.9(b).

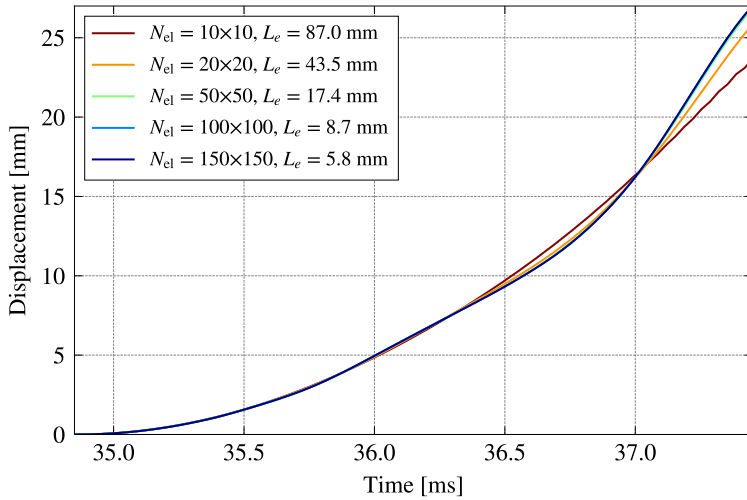


**Fig. D.3** Test B-1: Pane central displacement as a function of time.

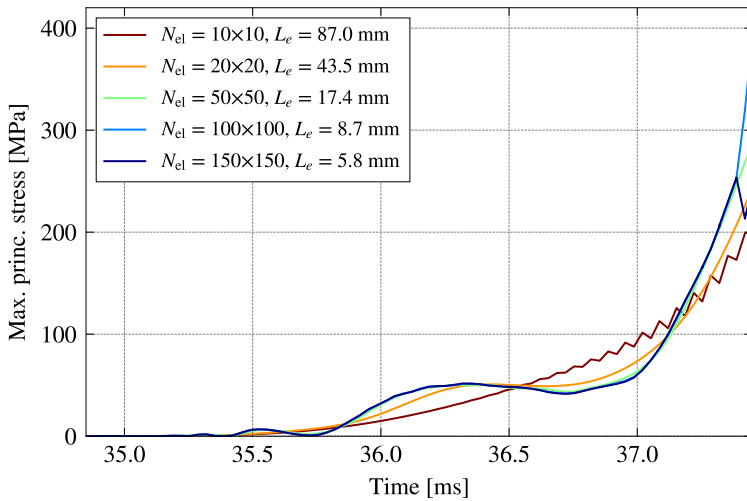


**Fig. D.4** Test B-1: Maximum principal stress in the pane centre as a function of time.

### Test B-2

Test B-2 relates to the simulation of the blast test performed and reported by JOHNS and CLUBLEY (2015). Figs. D.5 and D.6 are the results of the mesh convergence analysis for a 8 mm monolithic glass pane with a quasi-static strength  $\sigma_0 = 125$  MPa subjected to the pressure-time history shown in Fig. 5.9(b).

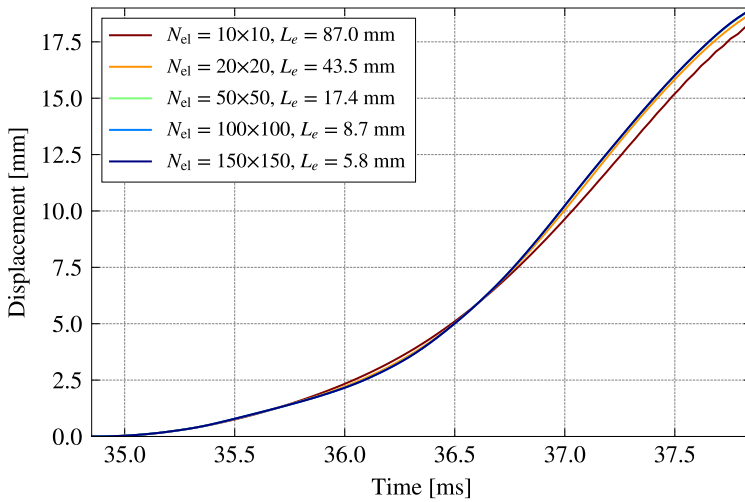


**Fig. D.5** Test B-2: Pane central displacement as a function of time.

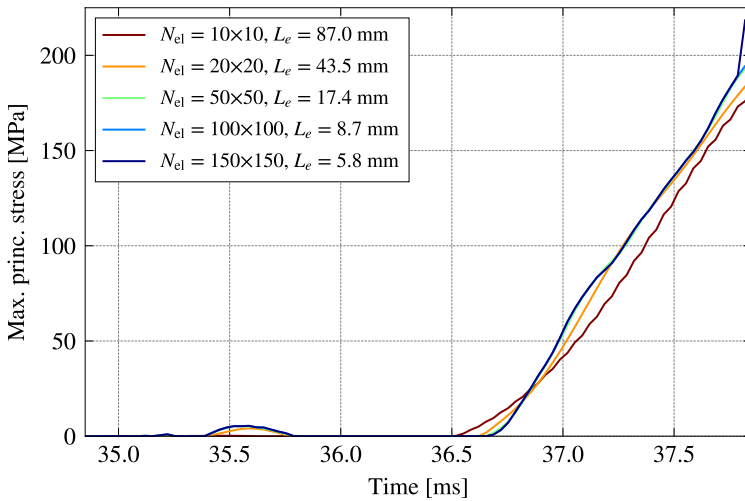


**Fig. D.6** Test B-2: Maximum principal stress in the pane centre as a function of time.

# Part II

## Scientific Papers



**Tensile behaviour of soda-lime-silica glass and the significance of load duration – A literature review**

MEYLAND, M. J., NIELSEN, J. H., and KOCER, C.

Published in: *Journal of Building Engineering* (2021)

DOI: 10.1016/j.jobe.2021.102966





# Tensile behaviour of soda-lime-silica glass and the significance of load duration – A literature review

Martin J. Meyland<sup>a,b,\*</sup>, Jens H. Nielsen<sup>a</sup>, Cenk Kocer<sup>c</sup>

<sup>a</sup> Technical University of Denmark, Department of Civil Engineering, Brovej, Building 118, 2800, Kgs. Lyngby, Denmark

<sup>b</sup> Ramboll Denmark A/S, Structures & Facade Engineering, Hannemanns Allé 53, 2300 Copenhagen S, Denmark

<sup>c</sup> The University of Sydney, School of Physics, NSW, 2006, Sydney, Australia

## ARTICLE INFO

### Keywords:

Float glass  
Time-dependent strength  
Static fatigue  
Dynamic fatigue  
Loading rate  
Experimental material characterisation

## ABSTRACT

Soda-lime-silica glass is a widely used material in society today and its strength over various loading times is of major engineering concern. This paper reviews studies from the published literature, which report on the time-dependent tensile behaviour of soda-lime-silica glass. Furthermore, current normative definitions are reviewed and compared to the literature concerned with time-dependent glass strength.

In general, there exists two common applied test methods to characterise glass: (1) the static fatigue test, a constant applied stress over time, and (2) the dynamic fatigue test, a constant applied stress rate. After a thorough search of the available scientific and engineering publications, 92 articles were found to have studied glass using these two test methods. In the tests the typical setups employed to apply load on a glass specimen were the three-point and four-point-bending, and axisymmetric bending configurations. From these tests the load duration and loading rate effects on the strength of glass were investigated. For comparison purposes, all data found were normalised with respect to a reference strength, which for static fatigue is a '60-second' strength, and for dynamic fatigue is a strength corresponding to a stress rate of  $2.0 \text{ MPa s}^{-1}$ . This means that the time-dependent effect on strength are highlighted and the governing crack properties and size effects are not included.

The review supports the general observations that the tensile strength of soda-lime-silica glass is strongly affected by the load duration. The static fatigue tests generally show that strength decreases with increasing load duration. Furthermore, the dynamic fatigue tests show that glass strength increases with loading rate, equivalent to a decreasing load duration. However, a significant lack of data is present at the very short and long loading times, making it difficult to draw a final conclusion at the extreme ends of the load duration and loading rate tests. Additionally, the experiments demonstrate that glass tested in air is less susceptible to static and dynamic fatigue as compared to water immersion, or in air at high relative humidity. However, for the Young's modulus, there are a limited number of studies in the literature and these studies do not highlight a conclusive outcome regarding the sensitivity on loading rates. The fatigue data also support well the load duration dependence given in the various Standards for the design of glass structures, with a few exceptions.

## 1. Introduction

In civilian infrastructure, soda-lime-silica glass is used in a wide range of applications, such as windshields, load-bearing glass beams, residential windows, large glass plates covering whole building facades, and many more. To ensure improved performance, these applications are typically based on post-processed flat glass (also denoted 'float' or 'annealed' glass) either in the form of laminated glass, tempered glass, or a combination of both. Depending on the application, the glass is exposed to different load history during its lifetime, which can be a

period of stress as long as several years to as low as a few microseconds. Therefore, it is important that a detailed level of knowledge about the material dependent constitutive relation and the failure criteria has been developed over a wide range of strain rates (see Fig. 1). This is essential for the design of glass structures that will have a well-defined service lifetime.

Examples of the typical long/short term loads found to act on glass structures are, snow loads [1–4], wind loads [5–11], seismic loads [12–18], wind-born debris impact [19–24], ballistic (hail and bullets) impact [25–31], and blast loads (accidental and man-made) [32–58]. In

\* Corresponding author. Technical University of Denmark, Department of Civil Engineering, Brovej, Building 118, 2800, Kgs. Lyngby, Denmark.  
E-mail addresses: [majeme@byg.dtu.dk](mailto:majeme@byg.dtu.dk), [mjme@ramboll.dk](mailto:mjme@ramboll.dk) (M.J. Meyland), [jhn@byg.dtu.dk](mailto:jhn@byg.dtu.dk) (J.H. Nielsen), [cenk.kocer@sydney.edu.au](mailto:cenk.kocer@sydney.edu.au) (C. Kocer).

<https://doi.org/10.1016/j.job.2021.102966>

Received 14 February 2021; Received in revised form 2 July 2021; Accepted 8 July 2021

Available online 22 July 2021

2352-7102/© 2021 The Authors. Published by Elsevier Ltd. This is an open access article under the CC BY license (<http://creativecommons.org/licenses/by/4.0/>).

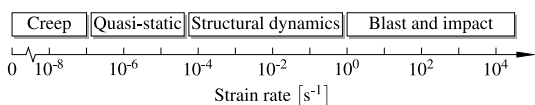


Fig. 1. Strain rates associated with different types of loading.

In all cases, the load duration as well as the rate of loading affects the static and dynamic glass strength significantly. The rate-of-loading effect also impacts other structural materials used by civil engineers, see e.g. Refs. [59–61]. Nevertheless, the affect on strength is only significant when the duration or rate-of-loading changes by more than one order of magnitude.

In the past, research on glass strength focused on long-term behaviour (static to quasi-static loading) and the effects of sub-critical crack growth (described in Sec. 2), showing that the strength of glass is being sensitive to the applied load duration. Even though glass is generally acknowledged to exhibit a higher dynamic strength, the available data, however, is quite limited for higher loading rates relevant to impact and blast loading events [49,53,55,62,63]. In general, this is attributed to the fact that dynamic load experiments are much more complicated to perform and interpret, because several parameters such as the measurement equipment, specimen geometry, and stress-wave propagation effects, must be given careful consideration.

To provide a broad overview of the time-dependent tensile behaviour of soda-lime-silica glass, it is the aim of this paper to review all available literature (to the best of the authors' knowledge) concerning experimental investigations on the mechanical material properties, such as strength and stiffness, over a wide range of load duration and rate of loading. No limits are set on the magnitude of the load duration and rate of loading to be considered. Furthermore a brief overview of applied experimental techniques is presented. In closing, a direct comparison is made between the collected strength data and various available Standards defining the load duration dependence on glass strength.

2. Fundamental aspects of time- and rate-dependent failure

Typically, glass is a linear elastic, isotropic material that exhibits brittle failure. Before post-processing, such as chemical treatments or thermal/chemical tempering, glass strength is essentially governed by the surface flaws (or surface cracks) located on the tensile loaded surface. The compressive strength of glass is much higher, and usually not important in structural applications; therefore, not considered in this paper. As with many other brittle materials, glass will fail instantaneously after reaching a critical value for the stress intensity at the tip of one surface crack. However, because of the characteristic differences in surface flaws, glass strength is not considered to be a material constant, and the size of the glass element, the load history (intensity and duration), the residual stress, and the environmental conditions, also affect significantly the ultimate strength exhibited. Moreover, glass has a unique characteristic where its atomic structure reacts with moisture from the environment [64–66]. As a result, sub-critical crack growth<sup>1</sup> effects are observed under normal environmental conditions where a level of humidity is present and surface flaws grow under a constant tensile load (see e.g. Refs. [67–69]). This is directly related to the phenomenon of long-term loads leading to a distinct reduction in strength. The first observation of static fatigue was published in 1899 by the

<sup>1</sup> Other terms are used as well, such as 'slow crack growth', 'delayed failure', 'static fatigue', and 'environmental fatigue'. The term 'stress corrosion' mostly refers to the chemical process.

French scientist Grenet [70], who also explained the unexpected fracture of filled champagne bottles by the delayed failure of glass<sup>2</sup>.

Taking into account the effect of load duration on glass strength requires a known corrosive crack behaviour, characterised through the crack velocity,  $v$ , and the stress intensity factor for mode I loading,  $K_I$ . Extensive studies have looked at the effect of different environmental conditions [72–84], and within the construction industry water appears to be decisive. A schematic representation of the relationship between  $v$  and  $K_I$  is given in Fig. 2 with four essential regions highlighted:

- 0 In region 0, no measurable sub-critical crack growth effects occur below  $K_{th}$ . For soda-lime-silica glass this value can range from 0.14 to 0.28 MPa m<sup>1/2</sup> in water [79,83,85–90] and from 0.37 to 0.39 MPa m<sup>1/2</sup> in air (50% RH) [86,88], at crack velocities as low as 10<sup>-14</sup> m/s.
- I In region I, the crack velocity is essentially governed by the molecular mechanisms of stress corrosion at the crack tip. The crack growth rate thus depends on the applied stress intensity and relative humidity. A measure of how reactive water molecules are within the glass lattice, is characterised by the slope of the curve. For region I, the fracture behaviour in water at 25 °C can be characterised with a minimum crack velocity of around 10<sup>-10</sup> m/s [74]. While in very dry air (0.017% RH) a maximum crack velocity of 10<sup>-7</sup> m/s is observed, the maximum crack velocity in saturated air (100% RH) increases to 10<sup>-4</sup> m/s [73].
- II In region II, sub-critical crack growth is still influenced by the chemical reactivity of the surrounding environment, but is independent of the stress intensity. As the crack velocity is directly proportional to relative humidity, a plateau is formed in the  $v(K_I)$ -curve. The constant crack velocity range narrows as relative hu-

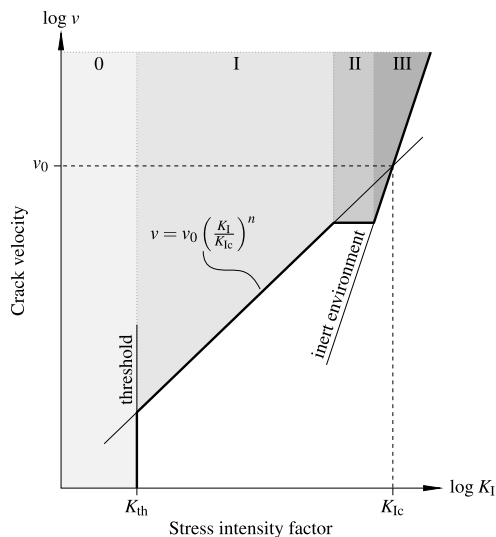


Fig. 2. Schematic representation of a typical  $v(K_I)$ -curve seen for soda-lime-silica glass.

<sup>2</sup> Partial English translation provided by Preston [71].

midity increases, which emerges from the findings of Wiederhorn [73].

III In region III, the  $v(K_I)$ -curve increases rapidly approaching the limit for an inert environment. At this point, it is no longer possible for the surrounding reactive environment to follow the crack tip, thus resulting in an environment independent crack velocity between  $10^{-3}$  m/s and 1 m/s. After reaching the fracture toughness of the glass,  $K_{Ic}$ , crack growth becomes unstable leading to failure of the glass element. For soda-lime-silica glass  $K_{Ic}$  is estimated to be between 0.72 and 0.82 MPa m<sup>1/2</sup> at room temperature [91].

In general, the determination of the design lifetime of a glass element is based on region I, while the contribution from region II and III can be neglected for quasi-static loads. A good approximation of sub-critical crack growth in region I is described by the following empirical power law<sup>3</sup> originally proposed by Evans and Wiederhorn [92]:

$$v = \frac{da}{dt} = v_0 \left( \frac{K_I}{K_{Ic}} \right)^n \quad (1)$$

where  $v_0$ , on a logarithmic scale, represents the ordinate of  $K_{Ic}$  and the exponent  $n$  defines the slope of the curve. When the value of the crack growth parameter  $n$  is high, it indicates that the chemical reactivity at the crack tip is reduced due to a decrease in humidity, resulting in slower crack growth. The opposite is true when  $n$  is low. The well-established theory of linear elastic fracture mechanics (LEFM) defines the stress intensity factor,  $K_I$ , with respect to a geometry (correction) factor  $Y$  (0.637 for half penny shaped cracks and 1.12 for edge cracks in semi-infinite plates) and a crack (or flaw) depth,  $a$  (see e.g. Ref. [93]):

$$K_I = \sigma \cdot Y \sqrt{\pi a} \quad (2)$$

where  $\sigma$  is the stress acting normal to the crack plane. Inserting Eq. (2) into Eq. (1) and assuming the ordinary differential equation to be valid over the full range of  $K_I$  with a constant  $n$ , the method of variable separation yields:

$$\int_0^{t_f} \sigma^n(t) dt = \frac{2 K_{Ic}^n}{(n-2) a_i^{(n-2)/2} \cdot v_0 (Y \sqrt{\pi})^n} \quad (3)$$

With a given stress history,  $\sigma(t)$ , and neglecting the crack growth threshold,  $K_{th}$ , this equation can be used to estimate the time-to-failure of a crack (or flaw) with an initial depth,  $a_i$ .

### 2.1. Crack resistance at constant stress

For a constant applied stress, i.e.  $\sigma(t) = \sigma_{f,s}$  as shown in Fig. 3a, a static crack resistance for any given load duration is found by inserting the stress history into Eq. (3):

$$\sigma_{f,s} = \alpha \cdot t_{f,s}^{-1/n} \quad (4)$$

where

$$\alpha = \left[ \frac{(n-2) a_i^{(n-2)/2} \cdot v_0 (Y \sqrt{\pi})^n}{2 K_{Ic}^n} \right]^{-1/n}$$

with  $t_{f,s}$  being the time to failure or lifetime of a given initial crack exposed to  $\sigma_{f,s}$ .

It follows from Eq. (4) that for two identical cracks ( $a_i$ ,  $Y$ ) found on two identically sized glass elements, index 1 and 2, for identical conditions ( $v_0$ ,  $n$ ,  $K_{Ic}$ ), the interrelationship between the constant applied stresses and lifetimes can be expressed as:

<sup>3</sup> In some literature the exponential function  $v = v_0 \cdot e^{\gamma K_I}$  is proposed to model the  $v$ - $K_I$  relationship (see e.g. Refs. [72,74,75,83]).

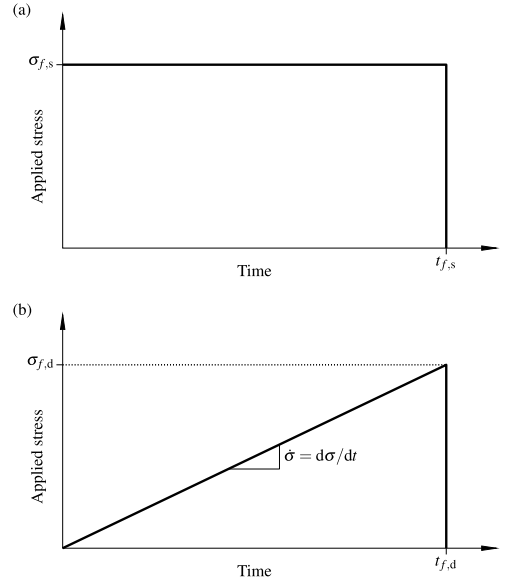


Fig. 3. Applied stress as a function of time: (a) constant stress and (b) constant stress rate. ( $t_{f,s}$ ,  $t_{f,d}$  = time to failure,  $\sigma_{f,s}$  = statically applied stress,  $\sigma_{f,d}$  = dynamic fracture strength,  $\dot{\sigma}$  = stress rate).

$$\frac{\sigma_{f,s,2}}{\sigma_{f,s,1}} = \left( \frac{t_{f,s,1}}{t_{f,s,2}} \right)^{1/n} \quad (5)$$

This result can be used to determine  $n$ , since it is independent of  $v_0$ .

### 2.2. Crack resistance at constant stress rate

In the case of a constant stress rate,  $\dot{\sigma}$ , commonly used for strength testing glass, the applied stress increases linearly with time as illustrated in Fig. 3b:

$$\dot{\sigma} = \frac{d\sigma}{dt} = \text{const.} \Rightarrow \sigma(t) = \dot{\sigma} \cdot t \quad (6)$$

Similar to  $\sigma_{f,s}$ , a dynamic crack resistance,  $\sigma_{f,d}$ , can then be found by inserting Eq. (6) into Eq. (3):

$$\sigma_{f,d} = \beta \cdot \dot{\sigma}^{1/(n+1)} \quad (7)$$

where

$$\beta = [\alpha^n \cdot (n+1)]^{1/(n+1)}$$

Here, the constant  $\beta$  is defined such that it depends on  $\alpha$  from tests with constant applied stress (see Eq. (4)). By doing so, one could use data from constant stress rate tests to describe crack growth in cases with constant applied stresses. The reverse approach is also possible when data from tests with constant applied stresses is available and an estimate of crack growth at constant stress rate is needed. However, both approaches implies that cracks and conditions must be identical to be able to perform the conversion.

The use of Eq. (7) was first suggested by Charles in 1958 [94] to describe rate dependent crack growth at constant temperature in his dynamic load experiments on glass. For low stress rates, it is sufficient to

only consider the contribution from region I. However, for dynamic events over short times, such as impact loads and blast waves, region II and III seem to affect the design lifetime significantly according to Kuntsche [95].

Also, Eq. (7) can be used to describe the interrelationship dependence between two identical cracks ( $a_i, Y$ ) found on two identically sized glass elements, index 1 and 2, in identical conditions ( $v_0, n, K_{IC}$ ) loaded at constant stress rates  $\dot{\sigma}_1$  and  $\dot{\sigma}_2$ :

$$\frac{\sigma_{f,d,2}}{\sigma_{f,d,1}} = \left(\frac{\dot{\sigma}_2}{\dot{\sigma}_1}\right)^{1/(n+1)} \quad (8)$$

Since Eq. (8) also is independent of  $v_0$ , it is commonly used to determine  $n$  from experiments, by plotting the failure stress as a function of the stress rate on a logarithmic scale, resulting in a slope of  $1/(n + 1)$ . However, this is only valid in limited cases in which flaws, conditions, and  $v_0$  are identical during all tests. According to Haldimann et al. [96],  $v_0$  can be strongly stress rate dependent, which is why this method should be used with caution.

It has been shown that the  $v(K_I)$ -curves, as illustrated in Fig. 2, successfully describe the variations observed in time-to-failure at constant applied tensile stress. Expanding on this, these curves can be used to examine the characteristics of dynamic failure at a constant stress rate; this was first reported by Evans in 1974 [85] and later reexamined by Evans and Johnson [97] and Chandan et al. [98]. These authors suggest that by integrating over the 4-regions of the sub-critical crack growth velocity curve, a new curve is obtained where fracture strength is a function of stress rate (the corresponding four regions are now A, B, B' and C), as depicted in Fig. 4.

At low stress rates, region A, glass strength begins to increase from a minimum value,  $\sigma_0$ . For an increasing stress rate, region B, there exists a simple logarithmic relationship between  $\sigma_{f,d}$  and  $\dot{\sigma}$ , which is identical to that derived by Charles [94] (see Eq. (7)). At still higher stress rates, region B', strength varies in a non-trivial manner with stress rate. Lastly, at the highest stress rate, region C, strength is independent of stress rate due to the absence of sub-critical crack growth effects.

Evans and Johnson [97] described the transition between the different regions analytically and presented strength data at stress rates ranging from  $2 \cdot 10^{-4}$  to  $3 \cdot 10^1$  MPa  $s^{-1}$ . However, their results did not

provide any conclusive evidence of distinctly different regions. A few years later, Chandan et al. expanded on this work to try and characterise the two higher regions, B' and C, using stress rates between  $5 \cdot 10^{-1}$  and  $2 \cdot 10^6$  MPa  $s^{-1}$ . However, the work was unsuccessful because the measured strength data would fit region B only and no evidence was found of the two higher regions, confirming the general agreement on the applicability of Eq. (7).

As shown, the fracture resistance of glass, for a surface crack (or flaw) loaded at either constant stress or constant stress rate, can in both cases be described by an empirical power law, in which the stress intensity at the crack tip is given by LEMF. In either load case, the load duration, or time to failure, is a fundamental parameter governing the fracture resistance of a glass element. For constant applied loads, the load duration is a common measure when investigating material characteristics, whereas it is the rate of loading that is of more importance when considering a constant loading rate. However, the constant loading rate is inversely proportional to the load duration, allowing a direct comparison between these two types of load configurations. The following sections present, and discuss, the study undertaken to understand better the behaviour of soda-lime-silica glass to tensile loads, using the two load configurations. First, the focus of this work is on the various applied experimental techniques, followed by a discussion of the material characteristics measured.

### 3. Experimental techniques

A variety of experimental techniques have been employed by researchers to investigate the mechanical properties of glass for various load conditions, using strain rates typically expected in practice. The typical strain rates found in engineering applications, range from creep loading ( $<10^{-6} s^{-1}$ ), through the quasi-static case of around  $10^{-6} s^{-1}$ – $10^{-5} s^{-1}$  to an intermediate range ( $\approx 10^{-4} s^{-1}$ – $1 s^{-1}$ ) covering structural dynamics imposed by wind and seismic loading, to even higher levels ( $>1 s^{-1}$ ) that include debris impact and blast loads, as shown in Fig. 1. Other relevant load conditions that have been used are constant loads, e.g. similar to snow load or dead-weight, also considered as static loads, where strength is dependent on load duration, rather than the loading rate.

In general, two different test methods can be identified, which are used to study the mechanical properties of glass:

1. *Static fatigue test* ( $\sigma = \text{const.}$ ) – used to investigate failure that would occur over time when a constant stress is applied, see Fig. 3a. This method is used to measure the sub-critical crack growth effects that result in delayed fracture. The advantage of such tests is that the test conditions are representative of typical scenarios of long-term loading. However, a disadvantage is that they can be extremely time-consuming.
2. *Dynamic fatigue test* ( $\dot{\sigma} = \text{const.}$ ) – used to investigate fracture that would occur at a constant stress/strain rate, see Fig. 3b. This is a common method used to investigate the rate-dependent tensile strength, and often used to identify the crack growth parameter,  $n$ , using Eq. (8).

Tensile strength is a critical parameter when designing load carrying glass structures. To study it by means of the above mentioned methods, several experimental setups have been employed to test materials on an engineering scale; the most common are the three-point and four-point bend test, and the axisymmetric bending (coaxial double ring tests). The load configurations and resulting stress distributions are illustrated in Fig. 5.

However, other, albeit rather rare techniques have also been reported, such as uniaxial tension and diametral compression tests. For the direct investigation of sub-critical crack growth effects in glass, the double cantilever beam test is a widely used technique. A brief introduction to each technique is provided below. Local characterisation of a

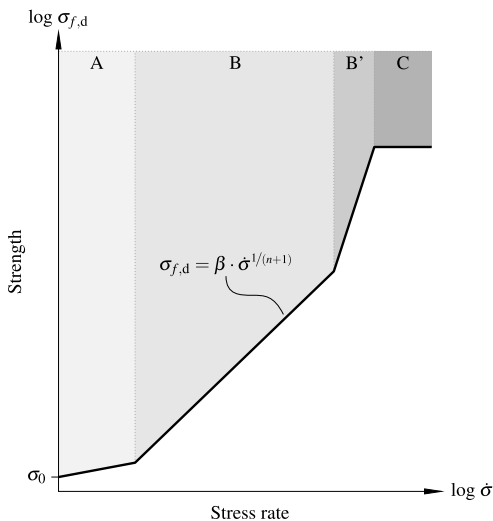


Fig. 4. An illustration of the stress rate dependence on strength, predicted from the 4-region sub-critical crack growth curve as given in Fig. 2 (after Refs. [85, 97,98]).

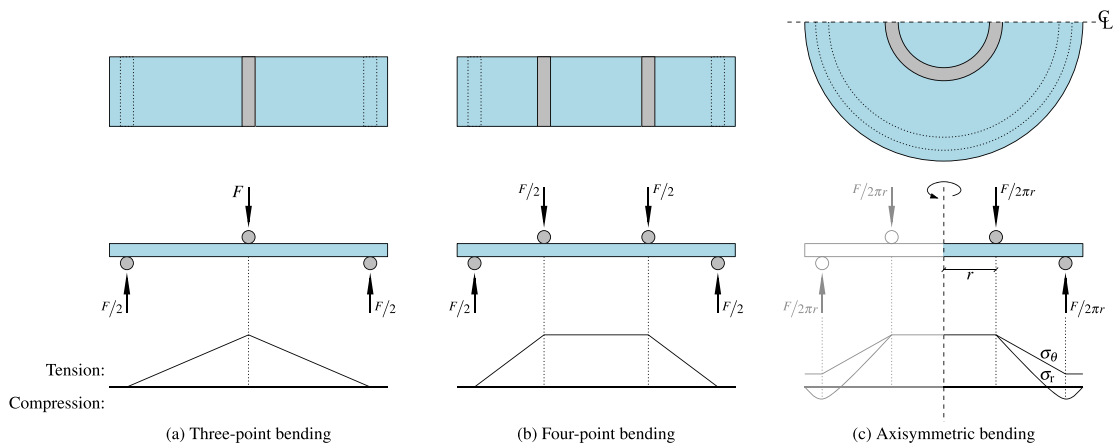


Fig. 5. An illustration of the load configuration (top and side view) and resulting stress distribution for three well-known methods used to measure the strength of glass.

material can also be carried out by e.g. indentation techniques such as the Vickers indentation; however, these methods are not within the scope of this review paper.

**Three-point bending:** The glass sample is loaded at three points as shown in Fig. 5a. The load points are typically placed symmetrically over the test sample. In order to minimise membrane stresses, two of the applied forces (typically the reaction points) are roller contacts, allowing for horizontal movement. The setup introduces a linearly varying tensile stress on the bottom surface between the two roller supports, with a maximum value below the central load point, as shown in Fig. 5a. In this configuration, the probability of finding a critical favourably located flaw, in the relatively small area of highest tensile stress, is low. It is, therefore, important to locate the origin of fracture in order to precisely determine the strength of the test sample. Furthermore, the distribution of stress can complicate the statistical analysis of the data.

**Four-point bending:** This configuration is similar to the previous test with the difference that there are four contact points as shown in Fig. 5b. Again the contact points are typically placed symmetrically and three of the applied forces are rolling contacts (free horizontal movement) in order to minimise membrane stresses. An advantage over the three-point bend test is the relatively larger area of maximum tensile stress as shown in Fig. 5b. However, both the three- and four-point bend tests produce undesirable high tensile stresses at the sample edges. Since there is a higher probability of finding a critical favourable flaw at the edge of the sample as compared to surface areas far from the edge (a consequence of glass cutting and handling), it can be challenging to determine the true surface strength of the glass specimen using these two bend test methods.

**Axisymmetric bending:** In order to minimise undesirable edge effects, the axisymmetric bend configuration can be employed. Such tests are usually carried out in a ring-on-ring test setup where two concentric rings sandwich a flat sample: a support ring on which a sample of glass is placed and then loaded using a smaller load ring. The circular geometry gives rise to rotationally symmetric stresses, where the maximum surface stress is nearly uniformly distributed within the area of the load ring. This is similar to the four-point bend test, but with the exception that this configuration reduces significantly the stress at the specimen edges, resulting in strength data directly related to the surface, see Fig. 5c. However, due to non-linear effects, the acceptable specimen size in the test is limited; to overcome the limit more complicated test setups have been suggested as in EN 1288-2 [99].

**Other loading techniques:** Although it is often more convenient to test glass in bending due to the relatively simple support and load configuration, some researchers have used alternative techniques to study the tensile behaviour of glass. One of them is the uniaxial tensile test, which is a direct and fundamental technique used to characterise the pure tensile behaviour of a solid. However, for the test the tensile grips to the sample must be chosen carefully since large stress concentrations at the grip point would be highly undesirable. This may explain the infrequent reporting of direct tensile tests. There is also the diametral compression test. It is used for indirect measurements of the tensile strength of brittle materials, such as rock like materials and concrete. By placing a cylindrical specimen in diametral compression, as shown in Fig. 6, a broad region of tensile stress is produced, with a narrow region of compressive stress produced at the ends of the sample, where the load is applied. The maximum tensile stress is located at the centre of the sample. Unfortunately, this method tends to overestimate tensile strength [100], and together with a load configuration that is far from the typical bending induced tensile stresses, it explains why this method is seldom used. Another, frequently reported test is the double cantilever beam technique (DCB). However, its intention is not to determine the strength of a material, but rather to characterise crack growth in the pure mode I opening configuration. By applying a constant tensile load

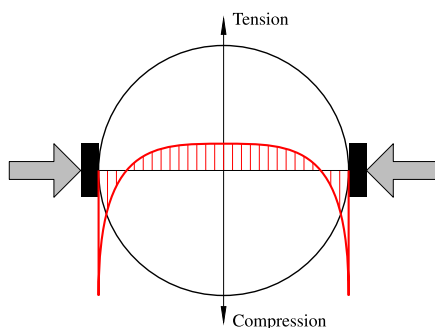


Fig. 6. Typical stress distribution along the loading axis of a cylindrical sample in a diametral compression test (after Refs. [101,102]).

perpendicular to a crack surface of known dimensions, in a predefined sample geometry (see Fig. 8), the crack velocity is measured where the stress intensity at the crack tip can be calculated for any measurable length of the crack. There are several other methods used to measure stable and unstable crack growth data over quite a wide range of crack velocities. In this paper the reviewed articles have only used the DCB method and as such it is the only method presented.

The discussion above provides a brief outline of the more common load configurations. It is, however, more complete to also consider the implications of how the load is actually applied to a glass specimen; that is, what are the implications of static and dynamic loads.

### 3.1. Static fatigue tests

In general, static fatigue data is gathered by measuring the time-to-failure of a number of samples at different constant applied stresses, as shown in Fig. 3a. A summary of the failure times achieved in the published works is shown in Fig. 7, while the detail of a review of the tests can be found in Appendix A, Table A.1.

It is relatively straight forward to implement a test on glass using a constant load configuration. Grenet [70] in 1899 was one of the first to report performing such a load test. He used a bucket filled with water, hung from the centre of a glass plate, which was supported along two of its four edges (three-point bending), to study time dependent failure. Since then, the use of ‘dead-weight’ loads has been extensive; in most cases, the weight is applied by either filling containers with e.g. sand [103] or weights, attached to a lever arm that applies the load to a specimen in a three- or four-point bend test configuration [104–109].

This simple static configuration allows users to perform measurements over weeks to months (see e.g. Ref. [110]). However, failure over

shorter periods is only possible for much higher loads. Typically, this then produces undesirable inertial effects, which places a lower limit on the static load duration. This explains why the majority of published data summarised in Fig. 7 are at failure times above 1 s. Baker and Preston [103] and, Mould and Southwick [105] have both reported measurements below this limit using an apparatus constructed from a loudspeaker, which is capable of applying loads without inertia effects. Thereby reaching static fatigue failure times as low as approx. 2.5 ms.

Even though simple ‘dead-weight’ load configurations have proven to be highly useful, since the 1980s a new class of ‘universal testing machines’ have been developed. Using integrated systems with efficient mechanical actuators and computer software, these testing machines have greatly improved the study of the static fatigue process [111–114]. This allowed highly controllable load duration in the range of 4 s to almost 1 d.

#### 3.1.1. Crack velocity measurements

Since it is common practice to measure crack velocities at constant applied load, the study of crack growth can be considered as a subgroup of static fatigue tests. Therefore it is included in this review. From the literature reviewed here, it is found that the double cantilever beam technique is employed in most work. In this technique a glass specimen with an initial edge crack of known dimensions is prepared and loaded at constant load perpendicular to the crack surfaces, as shown in Fig. 8. In this specimen/load configuration the stress intensity of the crack is well defined, Eq. (2), and therefore, can be calculated at each point the velocity of the crack is measured, resulting in a  $v(K_I)$ -curve and an estimate of the sub-critical crack growth parameters,  $K_{Ic}$ ,  $v_0$ , and  $n$ , defined in Eq. (1) (also see Fig. 2).

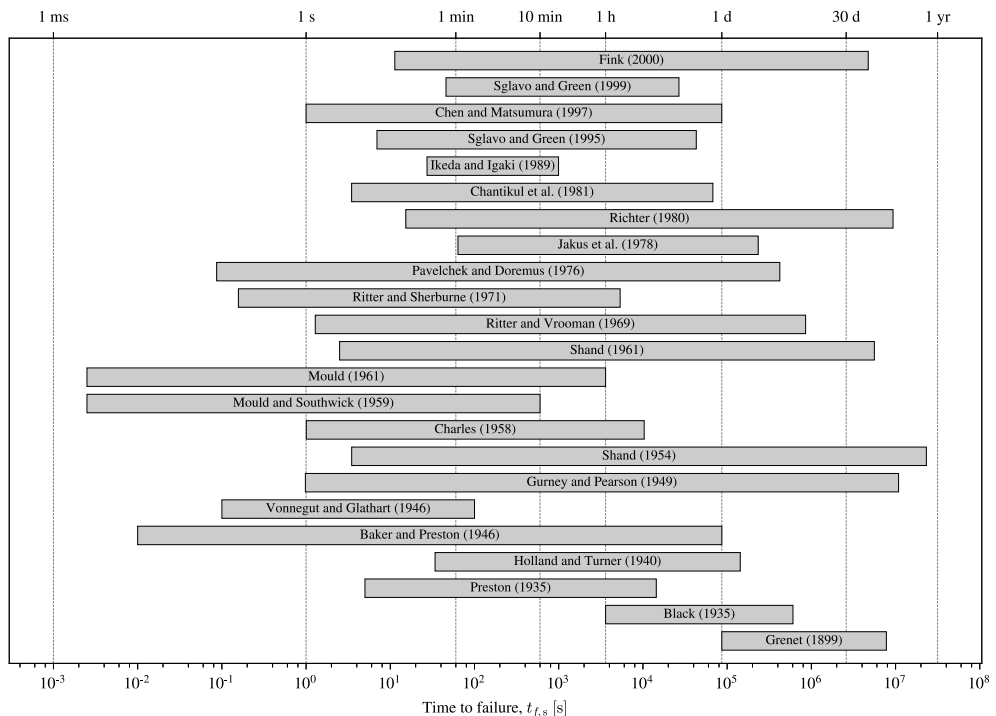


Fig. 7. The failure times reported in the published static fatigue tests. See also Table A.1.

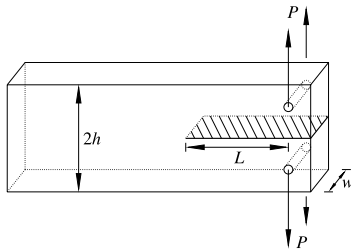


Fig. 8. An illustration of the double cantilever beam configuration. Cross-hatched area marks the crack surface (after Ref. [74]).

### 3.1.2. Definition of relative applied stress

The static fatigue data of soda-lime-silica glass reviewed here are reported for failure loads presented as either an applied mass (lb. or kg) or an applied stress (psi or MPa). In the following assessment and discussion, all reviewed data are converted to a relative applied stress by normalising with respect to a '60-second' strength,  $\sigma_{60}(t_0 = 60 \text{ s})$ , using the relationship defined in Eq. (5). Therefore, the crack growth constant  $\alpha$  vanishes, and only the relative glass strength is highlighted, without showing absolute strength values for the various specimen sizes provided in Table A.1.

### 3.2. Dynamic fatigue tests

All the reported dynamic fatigue data are measurements of the failure load of a number of samples at different constant loading rates. The detail of the experiments in these previous tests are given in Appendix A, Table A.2, while Fig. 9 is a summary of the range of loading rates achieved, which also indicates the strain rates that can be expected for the different experimental techniques. However, it should be noted that the strain rate not only depends on the experimental technique but also on the specimen geometry under investigation.

Typically, universal testing machines are used to strength test glass in the quasi-static load regime at constant stress rates near  $2 \text{ MPa s}^{-1}$  (see e.g. Refs. [99,115,116]), corresponding to strain rates of around  $10^{-5} \text{ s}^{-1}$  at a Young's modulus of  $70 \text{ GPa}$ . The summary of data in Fig. 9 highlights this point since most of the published works before 2010 are for lower strain rates from  $10^{-9} \text{ s}^{-1}$  to about  $10^{-3} \text{ s}^{-1}$ . By using fast valves and gas reservoirs, to pressurise an oil reservoir (pneumatic-hydraulic system), higher strain rates as high as  $10^1 \text{ s}^{-1}$  have been reported [117–119]. However, it is difficult to implement a direct feedback control system for constant strain rates over a short duration, which is why the strain rate depends more on the relationship between machine and specimen stiffness. Strain rates at about  $10^1 \text{ s}^{-1}$  were also reported by Chandan et al., in 1978 [98]. The authors used a pendulum impact machine to test Charpy sized glass specimens in three-point bending – this setup is traditionally used to measure the impact resistance of many other materials. Pal and Pennington [120] employed a drop test setup, releasing weights between 44 and 84 kg, from drop heights of 1.5–3.0 m, resulting in impact velocities of about 5–7 m/s. They undertook dynamic impact tests of rectangular glass plates, of dimensions  $812.8 \times 685.8 \times 2.2 \text{ mm}^3$ , which were simply supported along all four edges. Since the samples were large in area and thin, the measured strain rates (around  $10^{-5} \text{ s}^{-1}$ ) were quite low.

Much higher impact velocities, and thus, higher strain rates, can be achieved when using a gas gun driven test setup, such as a split Hopkinson pressure bar (see e.g. Ref. [121]), in which more recently strain rates up to  $10^2 \text{ s}^{-1}$ – $10^3 \text{ s}^{-1}$  have been reported in a split tensile test configuration [101,102]. To the authors' best knowledge, these are the highest strain rates reported when characterising the tensile behaviour of soda-lime-silica glass.

In addition, other, less conventional dynamic fatigue load tests have been reported in the literature reviewed here. To these tests belong the investigations conducted by Borchard in 1937 [122], who studied the effect of loading rate on the strength of 1/2-L glass bottles. The author performed his measurements by pressurising the internal volume of the bottle at a constant rate until glass failure, where lower strain rates from about  $10^{-9}$  to  $10^{-6} \text{ s}^{-1}$  were obtained. One order of magnitude higher strain rates were reported by Thompson and Cousins in 1949 [123] using explosive charges (black powder) placed inside a box, to which a glass pane of size  $355.6 \times 482.6 \times 2.3/3.1 \text{ mm}^3$  was mounted, where the glass was constrained along its four edges to the box. In the 1980s, similar boundary conditions were reported in the test setups employed by Johar [124,125] and Pal and Pennington [120] to investigate large sized window glass panes at low strain rates, from about  $10^{-11}$  to  $10^{-7} \text{ s}^{-1}$ . An air chamber on one side of the constrained glass pane was pressurised by moving a plunger, until failure of the glass.

### 3.2.1. Definition of loading rate and relative strength

In the literature reviewed here the dynamic fatigue data in each publication are presented differently. That is, the loading rate has been related to the applied mass, the stress rate (slope of the stress-time curve as in Fig. 3b), strain rate, and/or at some cases with respect to the rate of travel of a piston actuator. In the following discussion of the data, no distinction is made between the different methods used to measure the loading rate. Here, the reported data have been converted to strain rate, using a Young's modulus of  $E = 70 \text{ GPa}$  (unless otherwise stated) for comparison purposes:

$$\dot{\epsilon} = \frac{\dot{\sigma}}{E} \quad (9)$$

In the case of axisymmetric bending, Poisson's effects are present, which are accounted for by the following expression, using a Poisson's ratio of  $\nu = 0.23$ :

$$\dot{\epsilon} = \frac{\dot{\sigma}}{E} (1 - \nu) \quad (10)$$

Moreover, crack properties (as defined by  $\beta$  in Eq. (7)) and specimen size effects, have been made dimensionless using Eq. (8) by normalising dynamic strength with respect to a static strength,  $\sigma_{s0}$ , interpolated or extrapolated at a strain rate of  $\dot{\epsilon}_0 = 2.86 \cdot 10^{-5} \text{ s}^{-1}$  ( $\alpha\dot{\sigma} = 2.0 \text{ MPa s}^{-1}$  for  $E = 70 \text{ GPa}$ ), which means that only the rate dependence of the glass strength dominates and other effects are removed.

## 4. Investigated material characteristics

Over a century numerous tests have been carried out to investigate the behaviour of glass under various test conditions. Whether the tests were looking at crack growth or strength, glass specimens were either subjected to a number of constant loads or constant loading rates, using experimental techniques as discussed in the previous sections. Therefore, the published data of these tests provide information about load duration effects and the effect of test environment.

This section reviews the results from past investigations that looked into the tensile behaviour of soda-lime-silica glass. All the data presented satisfy the inclusion (search) criteria defined in Appendix B, and no limits were set with respect to the acceptable loading rate. These data are available in digital format in the online repository *DTU Data* [126]. Results from static fatigue tests have confirmed, generally, that increasing the applied load decreases the time to failure. Similar behaviour applies to the dynamic fatigue data, where the strength increases when the loading rate is increased (i.e. decreasing load duration). In both cases, the data follow well a linear line of best fit when using a log-log plot.

In the following sections, the test results are subdivided into the two categories of static and dynamic fatigue. Furthermore, all of the compiled strength data (from the literature review) are compared to the

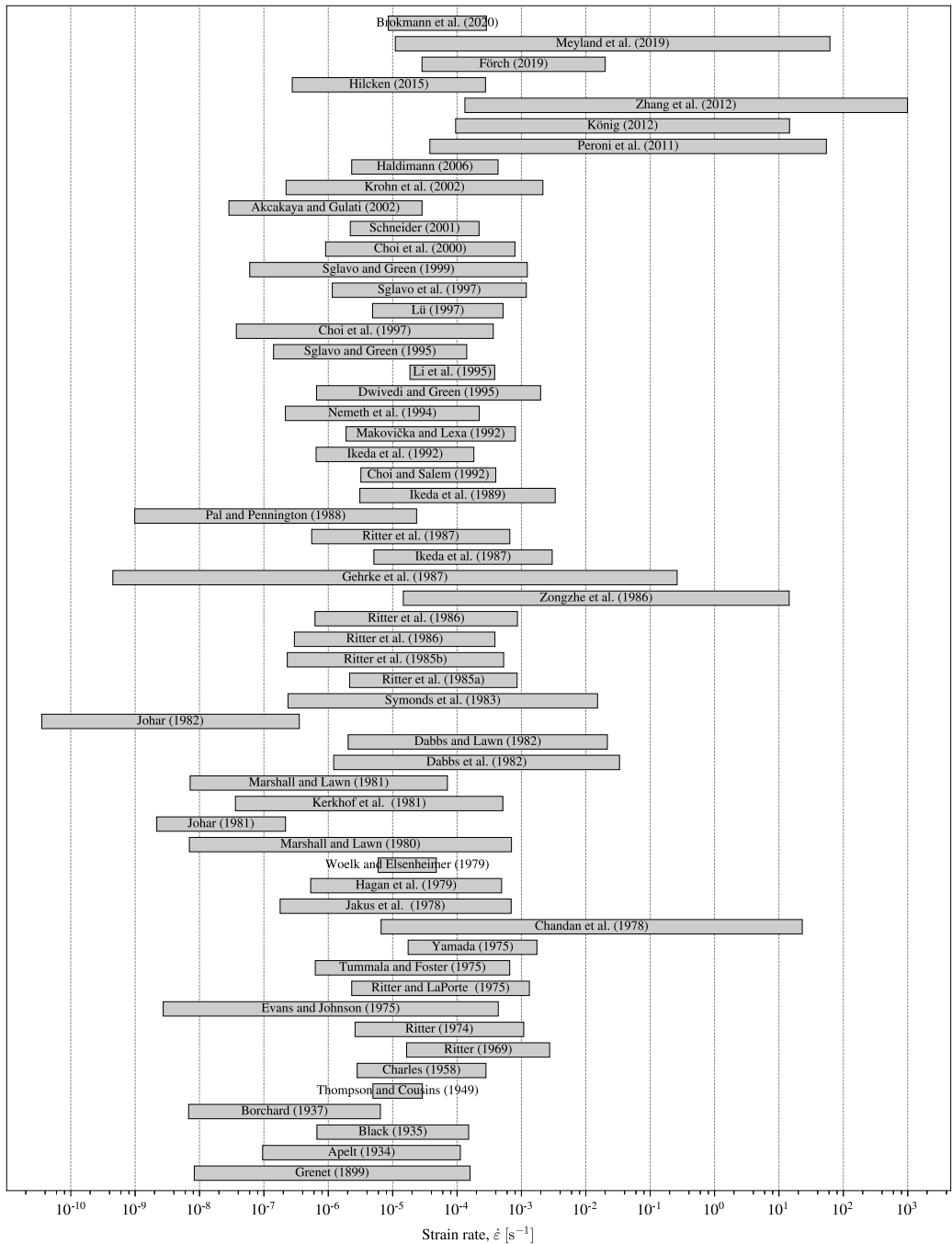


Fig. 9. Range of experimental loading rates reported in the published dynamic fatigue tests. See also Table A.2.

existing definition of glass strength as typically accepted in the Standards. A few of the reviewed works are highlighted here since they provide further detail to explain the connection between loading rate and Young’s modulus.

4.1. Load duration effects on strength (static fatigue)

4.1.1. Static fatigue data

The static fatigue data (constant stress) is presented in Fig. 10, as a plot of strength (normalised to a ‘60-second’ strength,  $\sigma_{t_0}$ , as explained in Sec. 3.1.2) as a function of time to failure. A summary of the key parameters related to test condition, applied minimum and maximum stress, and sub-critical crack growth parameters, are given in Appendix A, Table A.3. A common outcome from all the data reviewed, is that the glass strength decreases when the load duration increases, which is a result that is not dependent on test method and/or specimen geometry. This relationship can be described using a power law as defined by Eq. (4), where the time to failure is related to Eq. (1), which defines crack growth through the crack tip stress intensity factor,  $K_I$ , Eq. (2).

Failure times span from 2.5 ms (Mould and Southwick [105]) to 270 d (Shand [110]), resulting in a strength increase of about 100% and a reduction of about 50%, respectively, with respect to  $\sigma_{t_0}$ . However, a greater number of strength data exists for load duration between 1 s and 1 d, which highlights typical results of experiments; for a very short duration, inertia effects must be considered, and for a very long duration space and patience are needed.

For times lower and higher than  $t_0 = 60$  s, it is clear that the data in Fig. 10 diverges from the general trend seen. However, most of divergent data should not be treated as a scatter. In this plot the test results

obtained for different test conditions show deviations, because of the sub-critical crack growth effect, which is highly dependent on environmental conditions, such as temperature and humidity (see Sec. 2). This results in a change of the log-log linear slope.

The results which exhibit the most significant divergence from the trend are those obtained by Gurney and Pearson [127], who investigated the static fatigue behaviour of soda-lime-silica glass in air and vacuum. In the case of the latter  $n$ -values where higher, between 40 to around 135 (see Table A.3), confirming that the crack growth rate strongly depends on the environment. This dependence has been validated further, by investigations that have varied humidity in the surrounding air, up to liquid water, which showed that  $n$ , between 14.1 and 20.3, decreases with increasing water content [106,108,128–132]. In predicting the design lifetime of a glass element, a constant value of  $n = 16$  is a reasonable and conservative choice [96].

Other, more extreme, variations in test conditions have been used by Vonnegut and Glathart [133], who studied the effect of temperature on the strength and fatigue of scratched soda-lime-silica glass rods, between  $-190$  °C and  $520$  °C. They found a very strong dependence on temperature, and between  $100$  °C and  $200$  °C, the strength was at a minimum and the fatigue process dominated. When the temperature was outside this range, lower or higher, the effect of delayed failure was less, which was explained by a low reaction activity at the lower temperatures and evaporation of water at the higher temperatures. Complete control of the surrounding atmosphere is extremely difficult. Therefore, in 1958 Charles [129] performed additional experiments at temperatures between  $-170$  °C and  $242$  °C, where a constant atmosphere of saturated water vapour was used in the tests above  $0$  °C, and below  $0$  °C the atmosphere was adjusted from saturated water vapour to low humidity air. Similar to Vonnegut and Glathart, the strongest delayed

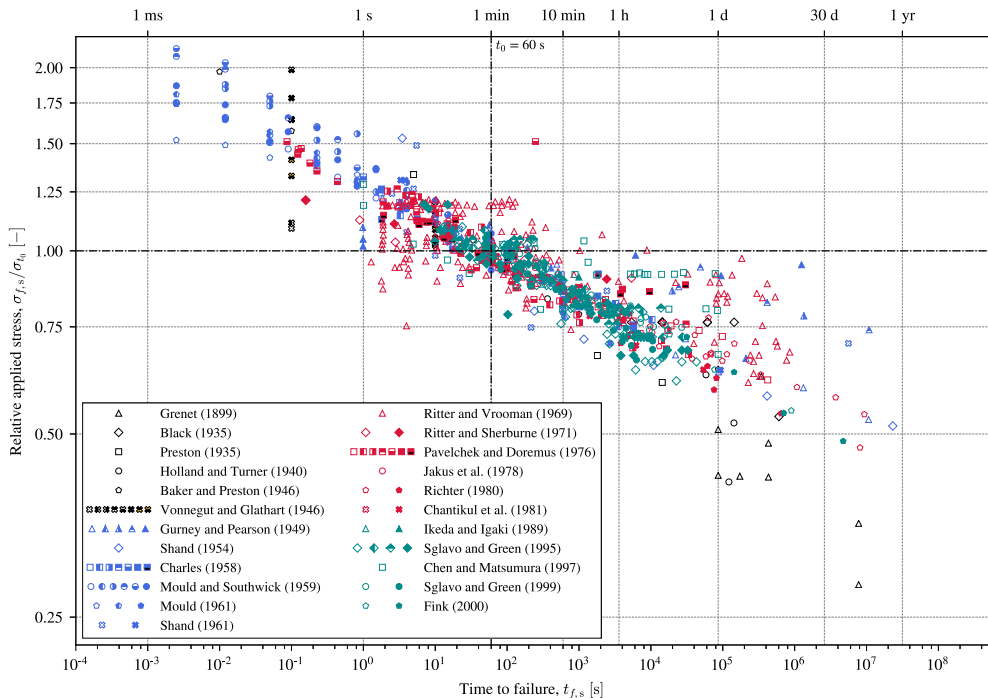


Fig. 10. A re-plot of the reviewed static fatigue data of soda-lime-silica glass, as the relative applied stress (see Sec. 3.1.2) as a function of time to failure.

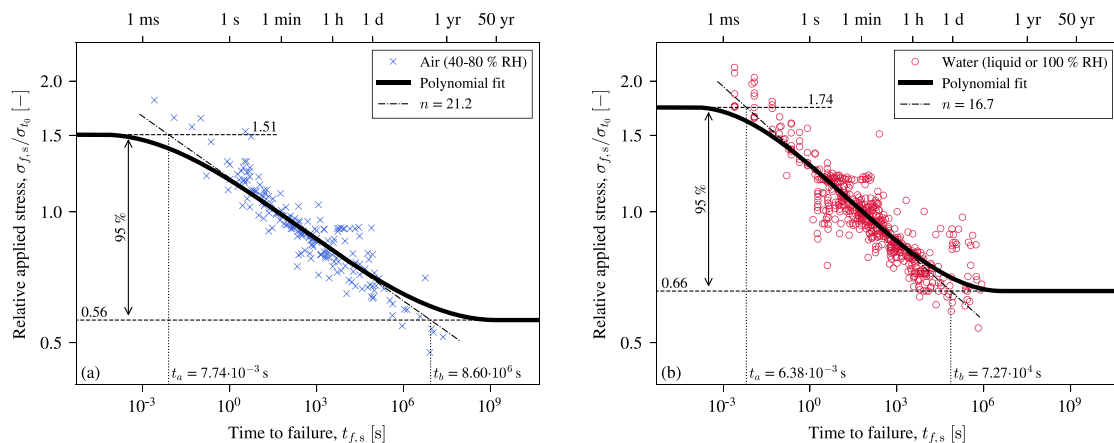


Fig. 11. The static fatigue data from Fig. 10, divided into the test environments (a) air (40–80% RH) and (b) water (liquid or 100% RH), are fitted to a cubic function, applying the strength model proposed by Overend and Zammit [136].

failure effect together with lowest strength was found at a temperature around 150 °C, while the effect was weaker for higher temperatures, also indicated by an increased  $n$ -value in Table A.3.

In addition to environmental conditions, the strength of glass also strongly depends on the surface condition of the glass. The effect of removing surface scratches on glass rods, using an acid solution, has been studied by Ritter and Vrooman [134] and Ritter and Sherburne [107], both concluding that acid-etched glass is less susceptible to static fatigue, where for  $n$  an increased value between 31.0 and 37.6 was found. The opposite effect was investigated extensively by Mould and Southwick [105], who tested microscope slides under controlled ambient conditions with six different surface abrasions produced by grit blasting and emery cloth. These tests resulted in the same general fatigue behaviour, however, with differences in slope. Taking a closer look at the data, it is clear that the abrasions produced from the emery cloth are more susceptible to static fatigue than those produced from grit blasting.

Other studies looking into glass strength and surface condition effects have been conducted by Shand [135], Chantikul et al. [111], and Sglavo and Green [113,114], all of these works introduced local surface cracks either in the form of cleaved cracks or through Vickers indentation. The procedure of crack formation can introduce a residual stress field around the crack, which in all studies has been removed by annealing the glass at 520 to 540 °C. Both as-received and annealed conditions have been tested and compared. While Shand showed that the annealed specimens with cleaved cracks exhibit shorter lifetimes compared to the as-received specimens, the other authors have reported an opposite behaviour for specimens with Vickers indentation cracks. However, no explanation for the effect of annealing was given for the data from the investigation with cleaved cracks. For the Vickers indented specimens, the increase in lifetime after the annealing process is assumed to be caused by the removal of the indentation residual stress field.

The works summarised in Fig. 10 are in agreement about the general static fatigue behaviour of soda-lime-silica glass. Nevertheless, from the summary the influence of environmental conditions is not apparent. To

Table 1

Estimation of initial crack length range from static fatigue tests using the strength model proposed by Overend and Zammit [136].

Test condition	$n$	$a_i^{min}$	$a_i^{max}$
Air (40–80% RH)	21.2	38.1 $\mu\text{m}$	0.45 mm
Water (liquid or 100% RH)	16.7	173.7 $\mu\text{m}$	1.41 mm

highlight these environmental effects, Fig. 11 are two plots which divide the relevant data from Fig. 10 into test environments (around room temperature) important for the construction industry: (a) air (40–80% RH) and (b) water (liquid or 100% RH). To estimate the sub-critical crack growth parameter  $n$ , the extreme data points have been excluded by only considering values within the interval from the 2.5<sup>th</sup> to the 97.5<sup>th</sup> percentile, i.e. the interval of values containing the central 95% of the data. Since these data points are based on different sample sizes, the method of weighted least squares (WLS) is used for the linear regression with  $\sqrt{N}$  as the weight factor, where  $N$  is the sample size provided in the digital datasets [126] (e.g.  $N = 1$  for data points representing single measurements). Thus, for both test environments (water content) the value for  $n$  listed in Table 1 is determined from the resulting slope  $1/n$  according to Eq. (5). As expected, soda-lime-silica glass is less susceptible to static fatigue in humid air than in water, which is also indicated by a lower gradient of the curve in Fig. 11a. This can be explained by the fact that in humid air, less water molecules react with the atomic structure of glass, as compared to a water environment (liquid or 100% RH), resulting in a slower crack growth and thus a longer life time. The values of  $n$  further confirm that the most accepted value of  $n = 16$  is a reasonable and conservative estimate for the design of float glass used in buildings.

According to the model proposed by Overend and Zammit [136] to determine the tensile strength of float glass, it is unlikely that the strength will continue to increase or decrease constantly for a load

duration approaching zero or infinity, respectively. For very short duration tests the strength will approach the inert strength of glass and for a very long duration the threshold strength becomes the limiting factor, as also seen from the  $v(K_I)$ -curve in Fig. 2. This leads to a strength interval, which can be expressed as:

$$\frac{K_{th}}{Y\sqrt{\pi a_{th}}} \leq \sigma_{f,s} \leq \frac{K_{Ic}}{Y\sqrt{\pi a_f}} \quad (11)$$

where  $a_{th}$  and  $a_f$  are the threshold crack size and the critical crack size, respectively. The 2.5<sup>th</sup> and 97.5<sup>th</sup> percentile values are used to establish the two asymptotes shown in Fig. 11. In the literature review it was found that in most studies the inert strength of glass is unknown. Therefore, the data here are normalised with respect to a ‘60-second’ strength,  $\sigma_{t_0}$ , see Sec. 3.1.2. For glass tested in air, 40–80% RH, the relative strength is estimated to approach the asymptotes at 0.56 and 1.51. These values are in line with the asymptotes determined by Overend and Zammit [136] for several initial crack sizes. Similar good agreement to the results from Overend and Zammit is found for the glass tested in water where the estimated asymptotes are located at 0.66 and 1.74.

Additional information can be drawn from Fig. 11 by applying the strength model proposed by Overend and Zammit [136]. For example, on the glass there is a distribution of surface flaws, which vary in length. An estimate of the minimum and maximum initial length of the flaws,  $a_i^{min}$  and  $a_i^{max}$ , respectively, can be calculated using Eqs. (12) and (13). The times  $t_a$  and  $t_b$  are the intersection points between the asymptotes and the linear regression curve, as labelled in Fig. 11.

$$a_i^{min} = \frac{t_a}{2} (n - 2) v_0 \quad (12)$$

$$a_i^{max} = \frac{t_b}{2} (n - 2) v_0 \left( \frac{K_{th}}{K_{Ic}} \right)^n \quad (13)$$

The calculated minimum and maximum initial surface crack length are given in Table 1, and for both test environments they are determined by assuming a sub-critical crack growth limit  $K_{th} = 0.25 \text{ MPa m}^{1/2}$  [137] and a fracture toughness  $K_{Ic} = 0.75 \text{ MPa m}^{1/2}$  [96]. However, a distinction is made between the crack velocities applied. For the glass tested in air  $v_0 = 6 \text{ mm/s}$ , which can be considered a conservative estimate for in-service conditions of float glass in buildings, and for the glass tested in water  $v_0 = 30 \text{ mm/s}$  is representative [96].

The minimum to maximum length ranges from micrometres to millimetres. Furthermore, it appears from the values given in Table 1 that for some of the glass specimens tested in water the initial crack length might have been larger compared to those tested in moist air. Nevertheless, the estimated crack length range, for both test environments, is comparable in magnitude and an overlap is present in the millimetre range. According to Petzold et al. [138] these dimensions correspond to micro-cracks from processing, up to visible flaws typically arising from handling and ageing. Relating these crack origins to the glass samples from the studies, i.e. with respect to handling and surface treatment, the magnitude of the estimated initial crack lengths appear reasonable. Hence, the values given in Table 1 provide a suitable basis for the determination of the design lifetime of a glass element using Eq. (4).

#### 4.1.2. Crack velocity data

Crack velocity data can also be used to describe the static fatigue behaviour of soda-lime-silica glass (see e.g. Wiederhorn and Bolz [74]). Although, published crack velocity experiments do not provide direct strength measurements, the data from region I in  $v(K_I)$ -curves can be used to estimate the sub-critical crack growth parameters  $n$  and  $v_0$  (see Sec. 2). A summary of the parameters determined from the literature is

**Table 2**

Summary of sub-critical crack growth parameters<sup>a</sup>,  $n$  and  $v_0$ , from crack velocity tests on soda-lime-silica glass divided into the test environments (a) air and (b) water. An averaged value of each parameter is provided at the bottom of the table.

(a) Test environment: air			
Reference	Test cond.	$n$	$v_0$
		[–]	[mm/s]
Wiederhorn [72]	Moist air	22.3	–
Wiederhorn [73]	30% RH	22.7	1.8
Kerkhof et al. [78]	50% RH	18.1	2.4
Gehrke et al. [82]	50% RH	16.7	0.9
Ullner [84]	Air	19.6	2.5
Dwivedi and Green [139]	64–78% RH	20.4	0.3
<i>Average</i>		<i>20.0</i>	<i>1.6</i>
(b) Test environment: water			
Reference	Test cond.	$n$	$v_0$
		[–]	[mm/s]
Wiederhorn [72]	Water	17.1	–
Wiederhorn [73]	Water	17.9	4.3
Wiederhorn [73]	100% RH	21.0	3.8
Wiederhorn and Bolz [74]	Water	17.2	35.3
Wiederhorn and Johnson [75]	Water	16.9	6.8
Freiman [76]	Water	15.6	6.6
Kerkhof et al. [78]	Water	16.0	50.2
Simmons and Freiman [79]	Water	17.9	12.7
Wiederhorn et al. [80]	Water	17.4	9.7
Gehrke et al. [82]	Water	15.5	3.1
Gehrke et al. [83]	Water	19.0	1.8
Singh and Shetye [140]	Water	11.8	2.5
Ullner [84]	Water	18.4	14.9
<i>Average</i>		<i>17.0</i>	<i>12.6</i>

<sup>a</sup> Determined from  $v(K_I)$ -curves using the relationship given by Eq. (1) and assuming a fracture toughness of  $K_{Ic} = 0.75 \text{ MPa m}^{1/2}$ .

provided in Table 2. It is clear that the average value of  $n$  is slightly larger for glass tested in moist air as compared to water immersion, which agrees well with the static fatigue data. Furthermore, the listed values for  $v_0$  confirm that this parameter is also affected by water content in the environment, as an increase is seen for most of the investigations conducted in water. This behaviour has already been accounted for in the estimate of the initial crack lengths conducted in the previous subsection, using conservative values proposed in the literature, see Sec. 4.1.1.

Based on the relationship given in Eq. (5), which assumes identical cracks for identical conditions, a static fatigue curve from crack velocity experiments can be estimated using  $n$  only and neglecting the asymptotes defined by the inert and threshold strengths:

$$\frac{\sigma_{f,s}}{\sigma_{t_0}} = \left( \frac{t_{f,s}}{t_0} \right)^{-1/n} \quad (14)$$

with  $\sigma_{t_0}$  being the strength at a load duration of  $t_0 = 60 \text{ s}$ . For each of the studies listed in Table 2 a static fatigue curve was estimated and compared to the static fatigue data from Fig. 11. The comparison is shown in Fig. 12 divided into the test environments (a) air and (b) water.

The estimated static fatigue curves in air are in good agreement with static fatigue data obtained in the same test environment. Variations in slopes are seen, however, they are within the scatter of static fatigue data. Thus, the  $n$ -values from crack velocity experiments in air provides a good estimate for the static fatigue behaviour of soda-lime-silica for a

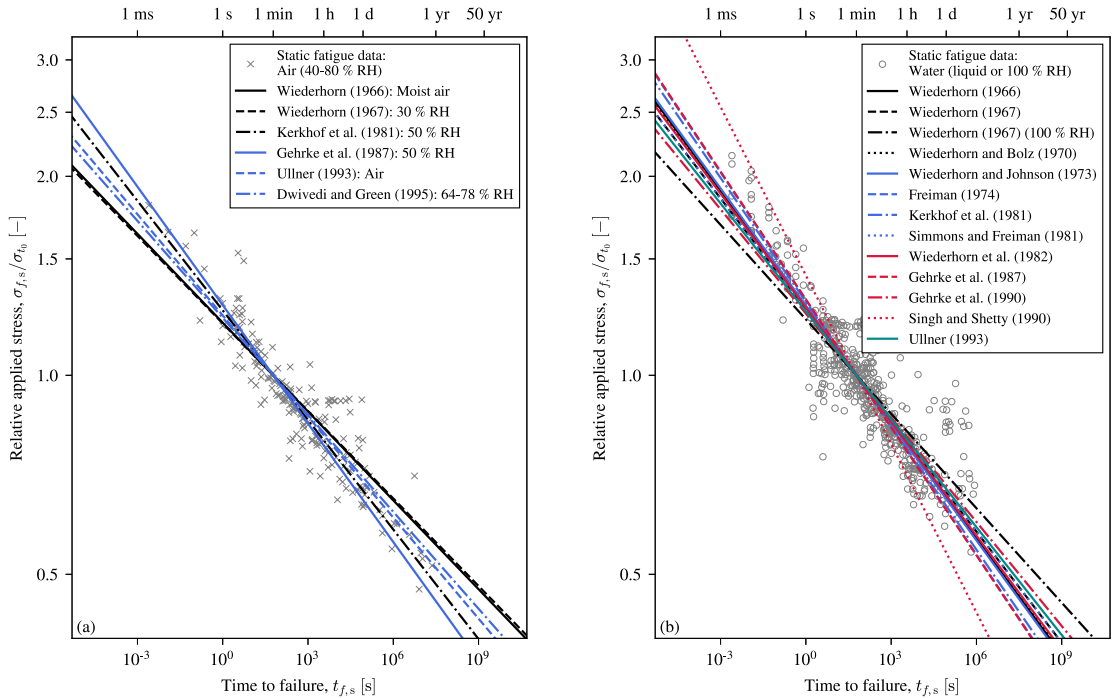


Fig. 12. Static fatigue curves estimated from crack velocity experiments listed in Table 2, and compared to static fatigue data from Fig. 11. The comparison is divided into the test environments (a) air and (b) water.

load duration where a constant decrease in strength can be assumed.

A good agreement between estimated curves and static fatigue data is seen for the experiments conducted in water as well. Although, it seems like the estimates based on data from Wiederhorn [73] (for 100% RH) and Gehrke et al. [83] underestimate the strength for a shorter load duration than 1 s, the variation in slope is still within scatter seen in the static fatigue data. The largest deviation seen, however, is the estimate determined from data published by Singh and Shetty [140], which results in  $n = 11.8$ . The increase in slope is most likely related to the experimental setup where crack velocities were obtained from cylindrical specimens in a diametral compression test.

#### 4.2. Loading rate effects on strength (dynamic fatigue)

A large number of dynamic fatigue tests (constant stress rate) have been carried out on soda-lime-silica glass. All the data found in the literature are presented in Fig. 13, where the tensile strength is normalised to a strength,  $\sigma_{i0}$ , interpolated or extrapolated at  $\dot{\epsilon}_0 = 2.86 \cdot 10^{-5} \text{ s}^{-1}$  ( $\approx 2.0 \text{ MPa s}^{-1}$  for  $E = 70 \text{ GPa}$ ), as explained in Sec. 3.2.1. Table A.4 in Appendix A is a summary of the key parameters, such as test condition, minimum and maximum failure stress, and the sub-critical crack growth parameters  $n$  and  $v_0$ , from the literature reviewed in this work.

Fig. 13 clearly shows that strength increases with increasing strain rate, i.e. decreasing load duration, which is similar to the behaviour seen in static fatigue tests. Most of the studies have been carried out at strain rates between  $10^{-7} \text{ s}^{-1}$  and  $10^{-3} \text{ s}^{-1}$  (quasi-static range of loading

according to Fig. 1), where the data are in quite good agreement. The strain rate range of the data in Fig. 13 is quite typical because most research facilities have access to equipment suitable for quasi-static loading, i.e. universal testing machines. When looking at the lowest and highest strain rates in the plot, there are fewer data points because special equipment would be needed. It is also clear that at the extremes of strain rate, the data exhibits a strong divergence from the general trend of the dynamic fatigue curve. Since no distinction has been made here between tests conducted under different conditions, the effect of sub-critical crack growth is again an explanation for the strong divergence in the data. However, at the very high strain rates, the experimental execution also becomes more complex, which is an additional cause of scatter.

Strain rates that have been achieved in experiments range from  $3.5 \cdot 10^{-11} \text{ s}^{-1}$  (Johar [125]) to  $9.9 \cdot 10^2 \text{ s}^{-1}$  (Zhang et al. [102]), resulting in a strength reduction of about 60% and an increase of about 175% with respect to the reference strength,  $\sigma_{i0}$ , defined in Sec. 3.2.1. Many of the publications found were conducted to study the sub-critical crack growth parameter  $n$  under various conditions and moderate strain rates. In recent years, however, the demand for high strain rate properties of glass has increased, due to an increased threat of blast load scenarios from terror attacks. It has been shown that glass is the cause of many injuries in such terror attacks [141–143]. This recent interest has highlighted that the number of existing published test results are small, for the high strain rate regime, which further increases the demand for such data.

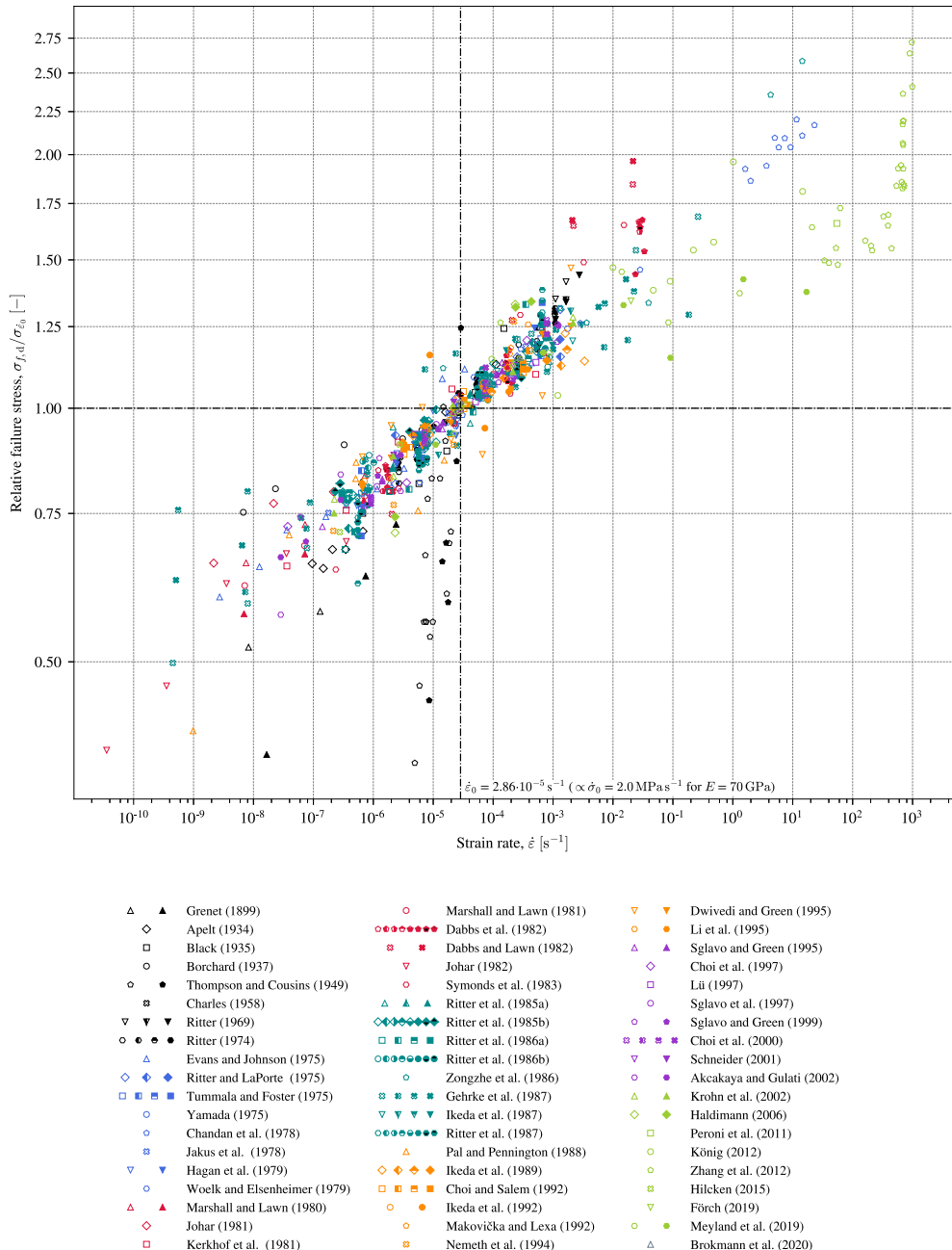


Fig. 13. A re-plot of the reviewed dynamic fatigue data of soda-lime-silica glass, as the relative failure stress (see Sec. 3.2.1) as a function of strain rate.

It is interesting to note that the data from Thompson and Cousins [123] diverge strongly from the general trend of the dynamic fatigue behaviour. The significantly steeper curve can be attributed to the experimental setup, where thin window glass panes (see Table A.2) clamped along all four edges were tested in bending, in an explosion test

box. Similar thin glass panes (that is, glass thickness is much less than the width and length of the pane) were tested in bending at ambient conditions by Johar [124,125] and Pal and Pennington [120], resulting in *n*-values between 13.4 and 22.6. Comparable values for the crack growth parameter have also been obtained by many other investigators

listed in Table A.4, who have tested soda-lime-silica glass in either air or water at moderate temperatures. This also becomes evident from Fig. 13 where the majority of test results are located in a narrow band.

Apart from varying the water content in the test environment, some also included the effect of temperature. The earliest studies found, are from 1935, where Mengelkoch [144] tested glass at two loading rates for temperatures between  $-190\text{ }^{\circ}\text{C}$  and  $545\text{ }^{\circ}\text{C}$ . The strength reduced to a minimum at  $140\text{ }^{\circ}\text{C}$  and began to increase steadily at higher temperatures. At the same time, Mengelkoch also showed that the strength decreased with loading rate. Later on, in the same year, Eichler [145] conducted experiments with 3–4 different loading rates at  $400\text{ }^{\circ}\text{C}$  and  $445\text{ }^{\circ}\text{C}$ , concluding the opposite behaviour at high temperatures, namely that the strength increases with decreasing loading rate. However, these two studies have not been included in Fig. 13, because the significant difference in testing temperature compared to the other works makes a direct comparison meaningless. Other results on the effect of temperature, between  $5\text{ }^{\circ}\text{C}$  and  $85\text{ }^{\circ}\text{C}$ , are reported by Ritter et al. [146,147]. Soda-lime-silica specimens with indented and abraded surfaces and two different treatments, annealing and ageing, have been tested. No significant variation in the dynamic fatigue behaviour as a function of temperature was observed since the slope of the data remains nearly unchanged.

Also in dynamic fatigue tests the effect of surface scratches and other mechanical impacts that damages the surface has been subject to a number of studies. It is well-known that the more severe a glass is damaged, the lower its resistance to tensile stresses becomes. But how do these cracks or even the absence of them impact the dynamic fatigue behaviour of soda-lime-silica glass remains an open question. This was investigated by Ritter [148] and Ritter and LaPorte [149] where abraded and acid-etched specimens were tested in air and water, respectively, resulting in slightly larger  $n$ -values for the acid-etched glass, see Table A.4. When deriving characteristic fatigue parameters from experiments with constant loading rates, Gehrke et al. [82] included different surface treatments in these studies: emery paper, Vickers indentation, and powder jets. While the general fatigue behaviour with reference to  $n$  was almost unchanged, the behaviour was significantly affected by the different initial crack size at low stressing rates. Here, both Vickers indentation and powder jet surface damage showed reduced fatigue behaviour with an increase in the fatigue limit. The application of identical grinding at different angles to the stress direction has been studied by Choi et al. [150], where it has been shown that the dynamic fatigue behaviour is unaffected by the orientation of grinding. Also, well-controlled surface scratches have been applied in a

number of dynamic fatigue studies to limit the scatter of the test results and thus improve the precision of the measurements [118,119,151].

A more in-depth studied surface crack is the Vickers indentation, which due to the indentation method produces residual stresses around the crack [113,114,139,152–158]. Based on found publications, it can be concluded in summary that the dynamic fatigue behaviour investigated in air and water is comparable to other surface treatments tested in similar conditions. However, it is important to consider the residual stresses introduced around the crack, in the determination of failure stresses, as it has been shown that the strength level is significantly lower than found for specimens that have been annealed after indentation [114,152]. For more details about the characteristics of post and sub threshold indentation flaws, which constitutes a significant part of the mentioned studies about Vickers indentations, the reader is referred to the cited publications, as it is beyond the scope of this review paper.

Only a few high strain rate publications (above  $1\text{ s}^{-1}$ ) on soda-lime-silica glass were found. While publications from Chandan et al. [98], Zongzhe et al. [159], and König [117] show an almost linear dynamic fatigue behaviour that clearly is in line with data found at lower strain rates. The other studies in the high strain rate regime tend to deflect from the general trend. The highest rates of strain were reached by Zhang et al. [102], who investigated cylindrical glass specimens in diametral compression applying a split Hopkinson pressure bar test setup. Based on their findings, shown as individual data points in Fig. 13, two dynamic increase functions (DIF) have been proposed within the ranges (1)  $10^{-5}\text{ s}^{-1} \leq \dot{\epsilon} \leq 3.5 \cdot 10^2\text{ s}^{-1}$ , and (2)  $3.5 \cdot 10^2\text{ s}^{-1} \leq \dot{\epsilon}$ . It is the only study found where a sudden increase in strength is observed. However, this behaviour is found at strain rates that were higher than what other researchers have reported. With similar experiments at only two strain rates, a quasi-static one at around  $3.8 \cdot 10^{-5}\text{ s}^{-1}$  and a dynamic one at around  $5.5 \cdot 10^1\text{ s}^{-1}$ , Peroni et al. [101] also confirmed a strain rate sensitivity for the glass strength, but with an indication of an approaching limit with respect to all other data shown. A similar tendency is seen from the dynamic fatigue curves provided by Meyland et al. [119], where a servo-hydraulic high-speed testing machine was used to test circular specimens with two different surface treatments in axisymmetric bending. An explanation given for the observed increase in strength, is the decrease (or even absence) of sub-critical crack growth effects at high loading rates. Comparing the obtained  $n$ -values (see Table A.4) between Peroni et al. and Meyland et al., one will observe substantial higher numbers in relation to the other studies reported. As an increased value for  $n$  demonstrates reduced fatigue behaviour, this might further indicate that the data approaches a limit.

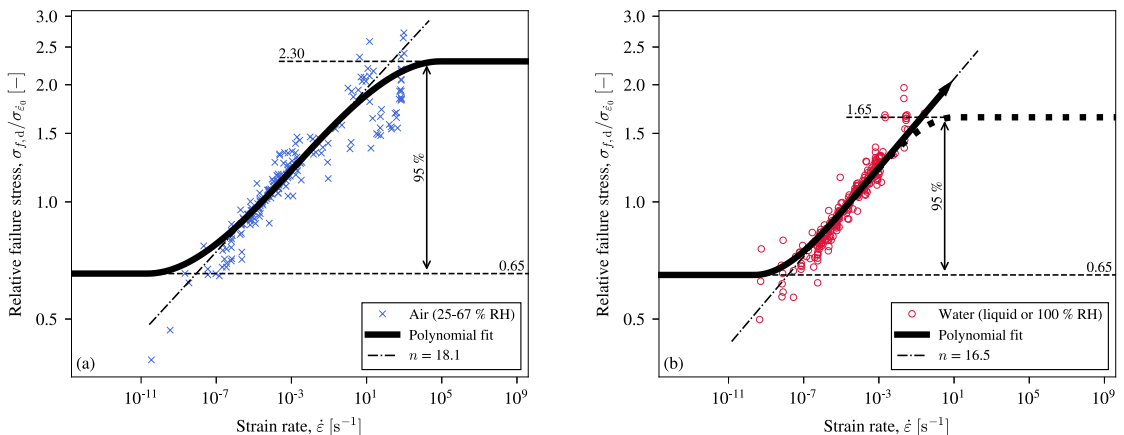


Fig. 14. The dynamic fatigue data from Fig. 13, divided into the test environments (a) air (25–67% RH) and (b) water (liquid or 100% RH), are fitted to a cubic function. Due to an observed lack of data at high strain rates in (b), the arrow indicates that a limit possibly is not reached.

As mentioned above, no special attention is given to the test environment for data shown in Fig. 13. While a strain rate sensitivity is clearly seen for the strength of soda-lime-silica glass, the effect of water in the surrounding test medium, which controls the sub-critical crack growth, is less prevailing. Therefore, the same approach as used for the static fatigue data is applied, where in Fig. 14 relevant data from Fig. 13 are divided into the test environments (around room temperature): (a) air (25–67% RH) and (b) water (liquid or 100% RH). Based on data ranging between the 2.5<sup>th</sup> and 97.5<sup>th</sup> percentile, the sub-critical crack growth parameter  $n$  is once more determined by means of WLS using the weight  $\sqrt{N}$ , where  $N$  (given in the digital datasets [126]) is the number of tests that is representative for each data point. From the resulting slope  $1/(n + 1)$ ,  $n = 18.1$  is found for the glass tested in air. As expected, a slightly lower value of 16.5 is obtained for the glass tested in water, which agrees well with the typical value of  $n = 16$  that is recommended for the design of glass elements for buildings.

It is unrealistic to think of the glass strength decreasing continuously for loading rates approaching zero, as also shown by Gehrke et al. [82]. At very low loading rates it is therefore reasonable to assume static load conditions, by which the lower limit can be defined by the threshold strength as in Eq. (11). An upper limit at very high loading rates, as suggested by the Refs. [85,97,98], has not been well validated, although a small indication of it seems to be present in Fig. 13. Above a certain loading rate, however, it must be assumed that sub-critical crack growth effects are negligible because very rapid loading limits the rate at which water can migrate to the crack tip, resulting in an inert environment. Thus, the inert glass strength theoretically becomes the limiting measure for loading rates approaching infinity.

An estimate of these limits, for both test environments, is given by applying the previously mentioned percentiles, as shown in Fig. 14. The lower limits of the strength are found to be identical with a value of 0.65 and are very close to the limits estimated from the static fatigue data in Sec. 4.1.1. The upper limit for the glass tested in air is 2.30, which means that the strength increases by up to 130% as compared to the reference

strength,  $\sigma_{i0}$ . However, the value of 1.65 for the glass tested in water seems in comparison to be quite low. This can be explained by the lack of data seen at the high strain rates, where it is difficult to test glass in a water environment. In Fig. 14b, a dotted line is used to indicate that the upper limit possibly is not reached, along with an arrow on the solid curve indicating that the strength could increase further at higher strain rates. It is obvious that for both test environments more tests are needed in the high strain rate regime; first, in air to rule out the disagreement in dynamic fatigue curves, and then, in water to actually measure well-defined data. Also the low strain rate range needs further attention to obtain a more conclusive threshold strength limit.

Here no estimate of the initial crack length range is determined, as was provided for the static fatigue data. To make such a determination would require additional assumptions concerning the load duration needed for Eqs. (12) and (13), which again would add further undesirable uncertainty to the range estimate.

### 4.3. Normative definition of the interrelationship between load duration and glass strength

Structural engineers are usually bound by Standards to maintain sufficient safety when designing building structures. A variety of normative definitions do exist that define the interrelationship between the load duration and glass strength. This section of the paper reviews the most current Standards that were available to the authors.

International Standards specifying the load resistance of annealed glass include the European Standards, EN 16612 [160] and the final draft of a new Eurocode 10 for the design of glass structures FprCEN/TS 19100-1 [161], the American Standard, ASTM E1300-16 [162], and the Australian Standard, AS 1288-2006 [163]. However, there are also a number of national Standards, such as the German Standards, DIN 18008-1 [164] and DIN 18008-4 [165], the Netherlands Standard, NEN 2608 [166], the Austrian Standard, ÖNORM B 3716-1 [167], and the Italian Standard, CNR-DT 210 [168]. Common for all is a load duration factor, often denoted as  $k_{mod}$ . This factor is used in the defined design

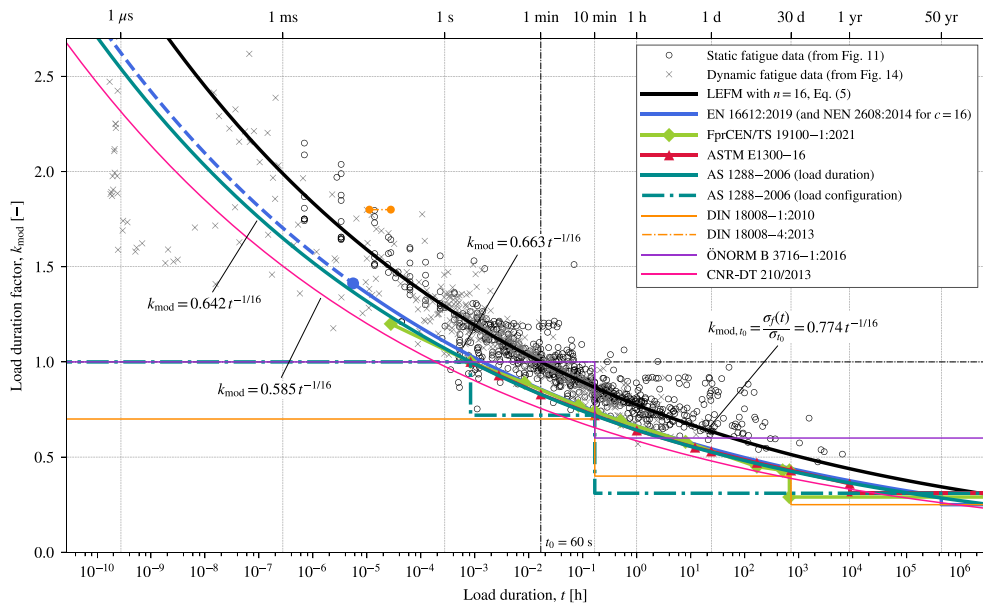


Fig. 15. Load duration factor,  $k_{mod}$ , as defined by different Standards for annealed glass, compared to static and dynamic fatigue data from Fig. 11 and Fig. 14 as well as an analytical solution based on LEFM.

equations to scale the fracture resistance of the base material with respect to a predefined duration. Such a factor can be expressed as the strength relative to the inert strength of the glass; however, determining the inert strength experimentally is challenging [136]. Instead it is more convenient to define the load duration factor with respect to a reference strength,  $\sigma_{t_0}$ , for a given load duration that usually is  $t_0 = 1$  s, 3 s or 60 s [96].

Fig. 15 is a plot of the factor  $k_{mod}$  as function of load duration in hours. The data is static and dynamic fatigue data from Fig. 11 and Fig. 14, and from the calculations defined in the Standards. In addition, the analytical solution based on the empirical power law together with the theory of linear elastic fracture mechanics (LEFM) using  $n = 16$  is given (see Eq. (5)). Strain rates in the dynamic fatigue data are converted to a load duration by assuming a constant loading rate as depicted in Fig. 3b. Both experimental data and the analytical solution are normalised with respect to a '60-second' strength, which is the less conservative strength normalisation relative to the Standards.

A fairly good agreement is obtained between the experimental data and the empirical power law for  $n = 16$ , again confirming that this choice is reasonable in the design of glass structures in buildings. Furthermore, the comparison in Fig. 15 shows that there are two approaches used to define the load duration dependence:

1. An expression dependent on the load duration, that is defined by a continuous function. This function is an empirical power law and describes sub-critical crack growth in glass, and
2. a more conservative approach where fixed values for given types of load configurations (long-term, medium-term, and short-term) are defined, i.e. a step function.

The Standards based on the continuous function approach, i.e. EN 16612, ASTM E1300-16, AS 1288–2006, NEN 2608, and CNR-DT 210, all use the crack growth exponent  $n = 16$ . No value for  $n$  is to be found in FprCEN/TS 19100-1, but the individual  $k_{mod}$  values nearly overlap with the function defined by EN 16612 and are defined for load duration down to 100 ms (impact loading). For even shorter load duration, e.g. blast loading, it is defined that  $k_{mod}$  can be taken from a transparent and reproducible assessment. However, there are differences in Fig. 15 because of the choice of  $t_0$ . The smaller the reference load duration is, the more conservative is the estimate of load resistance. In CNR-DT 210  $t_0 = 0.67$  s forms the basis, whereas both AS 1288–2006 and ASTM E1300-16 uses 3 s. Although, the American Standard follows the empirical power law, the maximum value that the load duration factor can take is 1.0. For a shorter duration, e.g. relevant for blast loads, an equivalent 3-second duration design load is to be determined according to ASTM F2248-19 [169]; however, only valid for laminated glass. The longest reference duration of 5 s is found in EN 16612 and NEN 2608. The European Standard is the only one that sets an upper limit of 20 ms, which is an exceptional load duration (relates to, for example, blast loads), resulting in a  $k_{mod}$  factor greater than one. For ordinary load cases, this factor must be between 0.25 and 1.0. Regardless of the choice of  $t_0$ , the data from the literature and the Standards are in good agreement down to around 1 ms. In many cases glass must withstand a permanent constant load (e.g. atmospheric pressure in Vacuum Insulated Glass, glass wall load-bearing elements in buildings, etc.). The Standards provide the range in load duration to determine the lifetime to failure of the glass in such cases, often seen up to 50 yr. Nevertheless, it is important to note that in this work, looking through all of the reviewed literature, no experimental data supporting the extrapolations provided in the Standards was found.

When only the type of loading is known, and not the exact duration of applied load, the Australian Standard provides predefined values for short-term ( $\leq 3$  s), medium-term ( $>3$  s and  $\leq 10$  min), and long-term ( $>10$  min) load duration, where the point at which the Standards step change occurs coincides with the curve used when the load duration is exactly known. By doing so, the load duration factors are typically lower

than the values obtained from experiments, which means that failure in glass can be determined with greater certainty. In particular, this applies to load duration below 3 s, where the load duration factor is always equal to 1.0. There is even greater certainty in the process described in the German Standard, DIN 18008-1, where  $k_{mod}$  takes the maximum value of 0.70 for short-term loading, e.g. wind loads. Medium-term and permanent load duration are given the values 0.40 and 0.25, respectively. However, no specific load duration range is specified for these types of load configurations. The ones shown in Fig. 15 are defined according to Schula [170]. More extreme load cases are covered by DIN 18008-4, which is intended for the design of barrier glazing. Here, a  $k_{mod} = 1.8$  is specified for soft body impact loading on float glass, typically having a load duration between 40 ms and 100 ms [171], as in Fig. 15. This is the only definition in the German Standards for glass that accounts for the strain rate sensitivity previously discussed. In comparison to the values obtained from experiments, the certainty in DIN 18008-4 is less. However, the data in Fig. 15 does not include soft-body impact, which might demonstrate a higher level of certainty for that specific load case. Lastly, the Austrian Standard, ÖNORM B 3716-1, also specifies fixed load duration factors, using a value of 1.0 for short-term duration, 0.6 for both the medium-term and long-term duration, leading to a less flexible estimate of crack growth effects in glass. Using the same load duration as for DIN 18008-1, an overestimate of the  $k_{mod}$  factor is obtained for a load duration above 1 min, and this means that for a very short duration, high level of certainty is again ensured. In conclusion, Fig. 15 shows that all the Standards, except for the Austrian Standard, are in good agreement when considering the long-term behaviour ( $>1$  yr) of float glass.

#### 4.3.1. Simplified strength determination using the load duration factor

Some variation in the definition of the load duration factor  $k_{mod}$  is seen between the international and national Standards reviewed. To emphasise the impact of this variation on the design of glass members, a simple example is provided here. In general, the design strength of glass is not only dependent on load duration. However, for simplicity, all other factors that need to be accounted for in the different Standards are disregarded. Taking into account the characteristic bending strength of soda-lime-silica glass  $f_k = 45.0$  MPa (cf. EN 572-1 [172]), a simplified design strength,  $\sigma_f$ , is found from the following relationship:

$$k_{mod} = \frac{\sigma_f}{f_k} \tag{15}$$

Due to larger variations observed in the dynamic load range in Fig. 15, the data given in Table 3 is based on a load duration  $t = 100$  ms. The American Standard ASTM E1300-16 is excluded from the comparison, as the chosen load duration is out of the defined range. In that case, ASTM F2248-19 is to be used in conjunction with ASTM E1300-16, but this would require detailed knowledge of the blast scenario that is to be

**Table 3**

A simplified design strength ( $\sigma_f$ ) calculation with  $k_{mod}$  at a fixed load duration  $t = 100$  ms as defined by the various Standards and the analytical solution that are compared in Fig. 15.  $f_k = 45.0$  MPa is used with Eq. (15). The Standards listed in the top are based on the continuous function approach for  $k_{mod}$ , while the ones below define a step function.

Standard	$k_{mod}(100 \text{ ms})$ [–]	$\sigma_f$ [MPa]
EN 16612:2019	1.28	57.6
FprCEN/TS 19100-1:2021	1.20	54.0
AS 1288–2006 (load duration)	1.24	55.8
CNR-DT 210/2013	1.13	50.8
LEFM with $n = 16$ , Eq. (5)	1.49	67.1
AS 1288–2006 (load configuration)	1.00	45.0
ÖNORM B 3716-1:2016	1.00	45.0
DIN 18008-1:2010	0.70	31.5
DIN 18008-4:2013	1.80	81.0

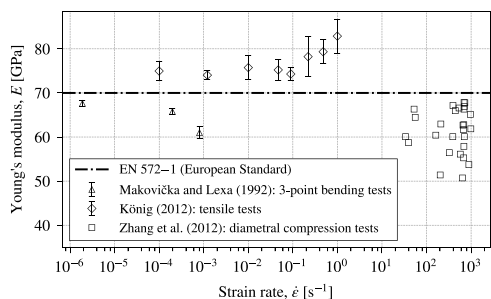


**Fig. 16.** The Young's modulus of soda-lime-silica glass determined from experiments performed at different strain rates. Note that the number of available tests is limited and carried out using different experimental techniques.

designed for and is therefore not done.

Minor variations are seen in the simplified design strengths found by the Standards using a continuous function of  $k_{\text{mod}}$  that is related to the empirical power law described in Sec. 2. With the same approach, the analytical solution based on LEFM with  $n = 16$ , representing the individual data points from the reviewed static and dynamic fatigue tests, results in a larger  $\sigma_f$ . However, this deviation is related to the choice of  $t_0 = 60$  s. The lowest values for the simplified design strength are found by the Standards that define a step function for the load duration factor. This is a rather conservative approach, which does not properly take into account the measured time-dependencies as they are shown in Fig. 11 and Fig. 14. The German Standard DIN 18008-4, accounting for soft body impacts, determines the highest value of  $\sigma_f$  however,  $k_{\text{mod}}$  is only valid over a very short load duration.

#### 4.4. Loading rate effects on the Young's modulus

There are few publications that report the Young's modulus of soda-lime-silica glass at various loading rates. The authors have reviewed three publications: Makovička and Lexa [34], performed glass tests in three-point bending, König [117], used a universal high-speed testing machine on 'dog-bone' shaped specimens, and Zhang et al. [102], performed diametral compression tests on cylindrical specimens in a split Hopkinson pressure bar setup. The data from these works are summarised in Fig. 16.

Data from Makovička and Lexa, and König, are presented as averaged values, and the error bars are the standard deviation. However, the results from Zhang et al. are not averaged because the strain rate much more varied. A slight increase in Young's modulus is observed from the data in König during the three highest obtained strain rates. The data from Makovička and Lexa, on the other hand, exhibit a decrease in stiffness with increasing strain rate. No clear tendency is visible in the scatter in the data from Zhang et al., as the individual data points are clustered around 60 GPa at strain rates between  $10^1 \text{ s}^{-1}$  and  $10^3 \text{ s}^{-1}$ . This disagreement in these three results could be attributed to the different experimental techniques employed. Generally, the Young's modulus of glass is not found to be sensitive to the rate of loading, as also stated by Mainstone [173]. The European Standard EN 572-1 [172] defines a rate insensitive modulus of elasticity of 70 GPa for soda-lime-silica glass, which for comparison purposes also is shown in Fig. 16.

## 5. Conclusion

In this work an extensive literature review, based on 92 publications dating back to 1899, has been presented. The data from these publications were reviewed in detail to compile a summary of current state-of-

the-art understanding of the time-dependent tensile behaviour of soda-lime-silica glass, a material used routinely in civilian infrastructure. In general, it is concluded that glass can be characterised using two test methods: (1) the static fatigue test, constant applied stress, and (2) the dynamic fatigue test, constant stress rate. From these tests the interrelationship between the load duration and the strength of the glass specimen can be readily defined for in-service glass components. It was found that most researchers prefer using the three- and four-point bending, and axisymmetric bending configurations, when testing glass. In static fatigue tests data with load duration between 2.5 ms and 270 d were produced. The dynamic fatigue tests were performed using a universal testing machine and more advanced test machines, such as a split Hopkinson pressure bar, at strain rates between  $3.5 \cdot 10^{-11} \text{ s}^{-1}$  and  $9.9 \cdot 10^2 \text{ s}^{-1}$ .

The static fatigue tests on soda-lime-silica glass are, in general, sensitive to the load duration. On a double-logarithmic scale, a linear decrease in strength was confirmed for increasing load duration. With respect to a '60-second' strength, an increase of about 100% and a reduction of about 50% has been achieved. Furthermore, the sub-critical crack growth parameter  $n$  indicates that glass tested in air (40–80% RH,  $n = 21.2$ ) is less susceptible to static fatigue as compared to tests in water (liquid or 100% RH,  $n = 16.7$ ). Crack velocity experiments, also considered as static fatigue tests, have further confirmed that the crack growth parameter  $v_0$  is affected by the amount of water in the surrounding environment.

Similarly, the dynamic fatigue tests are, in general, sensitive to the loading rate, where glass strength increases with loading rate (linearly on a log-log scale), i.e. decreasing load duration. At the lowest and highest rates, a strength reduction of about 60% and an increase of about 175% have been obtained, respectively; this is calculated with respect to a strength corresponding to a strain rate of  $2.86 \cdot 10^{-5} \text{ s}^{-1}$  ( $\approx 2.0 \text{ MPa s}^{-1}$  for  $E = 70 \text{ GPa}$ ). These dynamic fatigue tests confirmed that  $n$  decreases with an increasing water content; from the literature  $n = 18.1$  for air (25–67% RH) and  $n = 16.5$  for water (liquid or 100% RH).

In the reviewed works many results were obtained at moderate load duration and loading rates. Only a few studies also attempted to measure beyond the current strength limits. Estimates for possibly reached strength limits (asymptotes) were determined using the central 95% data range. Static fatigue data obtained in air and water yielded lower and upper relative strength limits at 0.56 and 1.51, and 0.66 and 1.74, respectively. Dynamic fatigue data obtained in air resulted in limits at 0.65 and 2.30, while it was only possible to estimate a lower limit at 0.65 for the data obtained in water. However, much more testing is needed to address properly the limits; especially at the high loading rates relevant to blast and impact events. Furthermore, it was shown that glass strength data, both from static and dynamic fatigue tests, agree with most of the load duration factors specified in several international and national Standards. These Standards are routinely used by civil engineers to design glass structures that use soda-lime-silica glass. Lastly, the three studies which report Young's modulus data for soda-lime-silica glass, did not find a significant loading rate effect.

#### Declaration of competing interest

The authors declare that they have no known competing financial interests or personal relationships that could have appeared to influence the work reported in this paper.

#### Acknowledgements

The first author gratefully acknowledges the financial support provided by the Innovation Fund Denmark (IFD) [grant No. 8053-00088B], Rambøll Fonden [grant No. 2018-51], and the Danish engineering consultancy Rambøll Denmark A/S, Private & Public Buildings East.

## Appendix A. Experimental details and results

Tables A.1 and A.2 in the following provide the detail of the static and dynamic fatigue tests reviewed: specimen geometry, surface treatment, load configuration, and load application. Moreover, Tables A.3 and A.4 summarises the key numbers from the various tests: test condition, minimum and maximum failure stress, and parameters defining the sub-critical crack growth ( $n$  and  $v_0$ ).

**Table A.1**

A detailed summary of the reviewed static fatigue tests reported on soda-lime-silica glass.

Year	Reference	Specimen	Treatment	Load configuration	Load application
1899	Grenet [70]	Ø4.5 mm (in average), glass rods	Untreated	3-point bending	Dead-weight (water)
1935	Black [104]	254.0 × 50.8 × 2.8 mm <sup>3</sup> , glass plates	Untreated	3-point bending	Dead-weight cantilevered bending device (water)
1935	Preston [71]	406.4 × 50.8 × 6.4 mm <sup>3</sup> , glass plates	Polished	3-point bending	Dead-weight
1940	Holland and Turner [176]	100 × 8 × 0.265–0.285 mm <sup>3</sup> , glass samples	Ground and polished edges	3-point bending	Dead-weight (lead shot)
1946	Baker and Preston [128]	Ø5.6 mm × 152.4 mm, annealed glass rods	As-received	3-point bending	Dead-weight (sand); dynamic loudspeaker
1946	Vonnegut and Glathart [133]	Ø5.6 mm × 152.4 mm, glass rods	Abraded	3-point bending	Dynamic loudspeaker
1949	Gurney and Pearson [127]	Ø6.4 mm × 76.2 mm, glass rods	Untreated	4-point bending	–
1954	Shand <sup>a</sup> [110]	Ø6.4 mm, annealed glass rods	–	Bending	–
1958	Charles [129]	Ø2.5 mm × 101.6 mm, glass rods	Abraded	4-point bending	Dead-weight
1959	Mould and Southwick [105]	76.2 × 25.4 × 1 mm <sup>3</sup> , annealed microscope slides	Various abrasions	3-point bending	Dead-weight cantilevered bending device; electromagnetic loader
1961	Mould [106]	76.2 × 25.4 × 1 mm <sup>3</sup> , annealed microscope slides	Abraded	3-point bending	Dead-weight cantilevered bending device; electromagnetic loader
1961	Shand [135]	114.3 × 19.1 × 2.4 mm <sup>3</sup> , glass strips	Cleaved cracks; as-received and re-annealed	4-point bending	Screw traverse testing machine
1969	Ritter and Vrooman [134]	Ø3 mm × 165.1 mm, glass rods	Acid-etched	4-point bending	Dead-weight cantilevered bending device
1971	Ritter and Sherburne [107]	Ø3 mm × 152.4 mm, annealed glass rods	Acid-etched	4-point bending	Dead-weight cantilevered bending device
1976	Pavelchek and Doremus [108]	Ø3 mm × 50 mm, glass rods	Abraded	4-point bending	Dead-weight cantilevered bending device
1978	Jakus et al. [130]	–	–	–	–
1980	Richter [131]	–	One side notched ( $a_i = 1.2\text{--}3.5$ mm)	Uniaxial tensile test	Dead-weight
1981	Chantikul et al. [111]	Ø50 mm × 3 mm, glass discs	Vickers indentation (5 N)	Axisymmetric bending	Universal testing machine
1989	Ikeda and Igaki [112]	Ø21 mm × 2.8 mm, glass discs	Indented-induced flaw	Diametral compression and axisymmetric bending	Universal testing machine
1995	Sglavo and Green [113]	63.5 × 6.4 × 2.4 mm <sup>3</sup> , annealed glass bars	Vickers indentation (9.8 N)	4-point bending	Universal testing machine
1997	Chen and Matsumura [109]	60 × 10 × 5 mm <sup>3</sup> , glass bars	Scratched	3-point bending	Dead-weight cantilevered bending device
1999	Sglavo and Green [114]	50 × 5 × 2 mm <sup>3</sup> , annealed glass bars	Vickers indentation (9.8 N)	4-point bending	Universal testing machine
2000	Fink [132]	1000 × 360 × 4 mm <sup>3</sup> , glass plates	Corundum treatment	4-point bending	Dead-weight

<sup>a</sup> Original work published by Phillips in 1937 [175].

**Table A.2**

A detailed summary of the reviewed dynamic fatigue tests reported on soda-lime-silica glass.

Year	Reference	Specimen	Treatment	Load configuration	Load application
1899	Grenet [70]	24.5 × 2.5 mm <sup>2</sup> and Ø4.8 mm (cross-sectional areas in average), glass plates and rods	–	3-point bending	Bucket filled with water
1934	Apelt [177]	Glass rods, $A_s = 1.31\text{--}1.48$ mm <sup>2</sup>	Natural fire polishing	Uniaxial tensile test	Tearing apparatus
1935	Black [104]	254.0 × 50.8 × 2.8 mm <sup>3</sup> , glass plates	Untreated	3-point bending	Lever arm loaded with water
1937	Borchard [122]	1/2-L glass bottles (225 g), 3.5 mm thick	–	Pressure test	Pressure testing unit with water
1949	Thompson and Cousins [123]	2.3/3.1 × 355.6 × 482.6 mm <sup>3</sup> , glass panes	–	Plate bending test	Explosion test box
1958	Charles [94]	Ø2.54 mm × 101.6 mm, glass rods	Abraded	4-point bending	Bending device
1969	Ritter [148]	Ø3 mm × 101.6 mm, annealed glass rods	Abraded and acid-etched	4-point bending	Universal testing machine
1974	Ritter [178]	Ø3 mm × 127 mm, annealed glass rods	Abraded, different surface coatings	4-point bending	Universal testing machine
1975	Evans and Johnson [97]	–	Abraded	4-point bending	–

(continued on next page)

Table A.2 (continued)

Year	Reference	Specimen	Treatment	Load configuration	Load application
1975	Ritter and LaPorte [149]	Ø6 mm × 101.6 mm, annealed glass rods	Abraded	4-point bending	Universal testing machine
1975	Tummala and Foster [179]	50.8 × 3.18 × 3.18 mm <sup>3</sup> , glass bars	As-received and annealed	3-point bending	Universal testing machine
1975	Yamada [180]	Ø6.4 mm × 88.9 mm, glass rods	As-received	4-point bending	Screw-driven mechanical tester
1978	Chandan et al. [98]	10 × 10 × 55 mm <sup>3</sup> (standard Charpy size), float glass bars	Ground	3-point bending	Universal testing machine and pendulum impact machine
1978	Jakus et al. [130].	–	–	–	–
1979	Hagan et al. [181]	5 × 10 × 130 mm <sup>3</sup> , annealed glass bars	Vickers indentation (2–20 N)	4-point bending	–
1979	Woelk and Eisenheimer [182]	1100 × 360 mm <sup>2</sup> , glass plates with various thicknesses	As-delivered and different abrasions	4-point bending	–
1980	Marshall and Lawn [152]	Ø50 mm × 3 mm, float glass discs	Vickers indentation (5 N); as-indented and annealed	Axisymmetric bending	Universal testing machine
1981	Johar [124]	2440 × 1525 × 6 mm <sup>3</sup> , float glass panels	Untreated	Plate bending test	Hydraulically driven piston
1981	Kerkhof et al. [78]	100 × 100 × 5 mm <sup>3</sup> , squared float glass plates	60 mm long and 0.1 mm deep scratch	Axisymmetric bending	Universal testing machine
1981	Marshall and Lawn [183]	Ø50 mm × 3 mm, float glass discs	Abraded	Axisymmetric bending	Universal testing machine
1982	Dabbs et al. [153]	Ø5 mm × 215 mm, annealed glass rods	Acid-etched and Vickers indentation (0.05–10 N)	4-point bending	Universal testing machine
1982	Dabbs and Lawn [154]	Ø5 mm × 215 mm, annealed glass rods	Acid-etched and Vickers indentation (0.15 and 0.25 N)	4-point bending	Universal testing machine
1982	Johar [125]	2440 × 1525 × 6 mm <sup>3</sup> , float glass panels	Untreated	Plate bending test	Hydraulically driven piston
1983	Symonds et al. [184]	50 × 10 × 3 mm, annealed glass bars	Indentation line flaws ( $P = 5$ N)	4-point bending	–
1985a	Ritter et al. [185].	75 × 25 × 1.0 mm <sup>3</sup> , annealed microscope slides	Ground edges	4-point bending	Universal testing machine
1985b	Ritter et al. [146]	57 × 57 × 3 mm <sup>3</sup> , squared glass plates	Vickers indentation (10 N); aged and annealed	Axisymmetric bending	Universal testing machine
1986a	Ritter et al. [155]	75 × 50 × 1 mm <sup>3</sup> , annealed microscope slides	Acid-etched and Vickers indentation (0.2 N)	Axisymmetric bending	Universal testing machine
1986b	Ritter et al. [147]	75 × 50 × 1 mm <sup>3</sup> , microscope slides	Abraded in air; aged and annealed	Ball-on-ring bending test	Universal testing machine
1986b	Zongzhe et al. [159]	100 × 20 × 5 mm, glass samples	Vickers indentation	3-point bending	–
1987	Gehrke et al. [82]	Ø5 mm, round glass bars	Abraded with emery paper	3-point bending	Electronically controlled testing machine
1987	Ikeda et al. [186]	40 × 20 × 2.7 mm <sup>3</sup> and Ø38 mm × 2.8 mm, glass plates and discs	Vickers indentation	4-point bending and axisymmetric bending	Universal testing machine
1987	Ritter et al. [156]	75 × 50 × 1 mm <sup>3</sup> , annealed microscope slides	Acid-etched and Vickers indentation (0.15, 0.25, and 0.35 N)	Axisymmetric bending	Universal testing machine
1988	Pal and Pennington [120]	812.8 × 685.8 × 2.2 mm <sup>3</sup> , glass plates	–	Plate bending test	Universal testing machine and drop test facility
1989	Ikeda et al. [187]	40 × 20 × 2.7 mm <sup>3</sup> and Ø38 mm × 2.8 mm, glass plates and discs	Vickers indentation	4-point bending and axisymmetric bending	Universal testing machine
1992	Choi and Salem [157]	75 × 25 × 1 mm <sup>3</sup> , annealed microscope slides	Vickers indentation (19.6 N)	4-point bending	Universal testing machine
1992	Ikeda et al. [188]	Ø21 mm × 2.8 mm, glass discs	Knoop indentation	Diametral compression	–
1992	Makovička and Lexa [34]	Glass beam samples	–	Bending	–
1994	Nemeth et al. [189]	50 × 50 × 1.5 mm <sup>3</sup> , squared glass plates	–	Axisymmetric bending	–
1995	Dwivedi and Green [139]	60 × 7 × 2.2 mm <sup>3</sup> , annealed glass bars	Natural flaws and Vickers indentation (9.8 N)	4-point bending	Universal testing machine
1995	Li et al. [190]	Ø3 mm × 60 mm, heat treated glass rods	Abraded	4-point bending	Universal testing machine
1995	Sglavo and Green [113]	63.5 × 6.4 × 2.4 mm <sup>3</sup> , annealed glass bars	Vickers indentation (9.8 N)	4-point bending	Universal testing machine
1997	Choi et al. [191]	Ø51 mm × 3 mm, glass discs	–	Axisymmetric bending	–
1997	Lü [192]	90 × 20 × 5 mm, glass specimens	Unnotched	3-point bending	Universal testing machine
1997	Sglavo et al. [158]	50 × 5 × 2 mm <sup>3</sup> , glass bars	Vickers indentation (9.8 N); as-indented	4-point bending	Universal testing machine
1999	Sglavo and Green [114]	50 × 5 × 2 mm <sup>3</sup> , glass bars	Vickers indentation (9.8 N); as-indented and annealed	4-point bending	Universal testing machine
2000	Choi et al. [150]	48 × 8 × 5 mm <sup>3</sup> , float glass specimens	Ground surface at different angles (0, 30, 60 and 90°)	4-point bending	Universal testing machine
2001	Schneider [171]	300 × 300 × 10 mm <sup>3</sup> , drilled float glass plates	Untreated	Axisymmetric bending	–
2002	Akçakaya and Gulati [193]	100 × 20 × 3 mm <sup>3</sup> , float glass specimens	Ground and V-belt edge finish	4-point vertical bending	Universal testing machine
2002	Krohn et al. [151]	76.3 × 76.3 × 3.89 mm <sup>3</sup> , squared glass plates	Vickers indentation (300 N)	Axisymmetric bending	Universal testing machine
2006	Haldimann [137]	200 × 200 × 6 mm <sup>3</sup> , squared glass plates	As-received	Axisymmetric bending	Universal testing machine
2011	Peroni et al. [101]	Ø9 mm × 5 mm/10 mm, glass cylinders	Surface ground	Diametral compression	Universal testing machine and SHPB test setup
2012	König [117]	$t = 8$ mm, dog-bone glass specimens	Untreated	Uniaxial tensile test	Universal high-speed testing machine

(continued on next page)

Table A.2 (continued)

Year	Reference	Specimen	Treatment	Load configuration	Load application
2012	Zhang et al. [102]	∅15 mm × 15 mm, glass cylinders	Surface ground	Diametral compression	Universal testing machine and SHPB test setup
2015	Hilcken [194]	250 × 250 × 6 mm <sup>3</sup> , squared glass plates	Pre-damaged	Axisymmetric bending	Universal testing machine
2019	Förch [118]	1000 × 360 × 4 mm <sup>3</sup> , float glass plates	Corundum treatment	4-point bending	High-speed testing machine (up to 1 m/s)
2019	Meyland et al. [119]	∅45 mm × 3 mm, float glass discs	As-received and pre-damaged	Axisymmetric bending	High-speed testing machine (up to 5 m/s)
2020	Brokmann et al. [195]	∅80 mm × 1.8 mm, annealed glass discs	Vickers indentation (9.8 N)	Axisymmetric bending	Universal testing machine

Table A.3

Summary of key numbers of the reviewed soda-lime-silica glass static fatigue tests.

Year	Reference	Test condition	Applied stress [MPa]		SCG <sup>d</sup> parameters	
			$\sigma_{f,s}^{min}$	$\sigma_{f,s}^{max}$	$n [-]$	$v_0 [mm/s]$
1899	Grenet [70]	–	19.5	43.0	10.8 <sup>b</sup>	–
1935	Black [104]	–	24.2	34.6	–	–
1935	Preston [71]	–	37.4	82.0	10.0 <sup>b</sup>	–
1940	Holland and Turner [176]	–	26.2	87.3	11.3 <sup>b</sup>	–
1946	Baker and Preston [128]	23.9 °C, water	44.5	137.2	14.1 <sup>b</sup>	–
1946	Vonnegut and Glathart [133]	–190 °C	91.3	99.8	76.5 <sup>b</sup>	–
		–80 °C	74.0	82.9	60.8 <sup>b</sup>	–
		20 °C	39.2	69.0	12.5 <sup>b</sup>	–
		110 °C	32.1	54.8	12.9 <sup>b</sup>	–
		200 °C	29.3	58.3	9.7 <sup>b</sup>	–
		300 °C	34.4	61.5	11.5 <sup>b</sup>	–
		420 °C	50.1	70.6	19.4 <sup>b</sup>	–
		520 °C	67.2	82.4	–	–
1949	Gurney and Pearson [127]	Atmospheric pressure, no prior vacuum treatment	41.7	96.5	18.1 <sup>b</sup>	–
		Atmospheric pressure, after prior vacuum heat treatment	52.0	86.2	18.3 <sup>b</sup>	–
		Vacuum < 10 <sup>-5</sup> mmHg, after prior vacuum treatment at room temp.	69.1	96.5	40.8 <sup>b</sup>	–
		Vacuum 10 <sup>-1</sup> mmHg, after prior vacuum heat treatment	89.5	126.8	46.1 <sup>b</sup>	–
		Vacuum <10 <sup>-5</sup> mmHg, after prior vacuum heat treatment	117.0	134.4	134.7 <sup>b</sup>	–
1954	Shand <sup>c</sup> [110]	–	34.9	103.6	15.9 <sup>b</sup>	–
1958	Charles [129]	22 °C, 50% RH	55.9	77.9	17.4 <sup>b</sup>	–
		–50 °C, 100% RH and air	87.0	128.8	20.5 <sup>b</sup>	–
		–10 °C, 100% RH and air	59.3	96.3	15.3 <sup>b</sup>	–
		22 °C, 100% RH	43.7	75.8	16.2 <sup>b</sup>	–
		50 °C, 100% RH	39.0	68.6	15.4 <sup>b</sup>	–
		150 °C, 100% RH	33.2	55.5	16.8 <sup>b</sup>	–
		200 °C, 100% RH	43.5	53.5	35.4 <sup>b</sup>	–
1959	Mould and Southwick [105]	23 °C, distilled water (abr. (a): severe)	39.2	69.3	17.5 <sup>b</sup>	–
		23 °C, distilled water (abr. (b): mild)	33.0	66.9	17.1 <sup>b</sup>	–
		23 °C, distilled water (abr. (c): 150 grit)	42.0	96.0	12.9 <sup>b</sup>	–
		23 °C, distilled water (abr. (d): 600 grit)	26.2	67.2	12.8 <sup>b</sup>	–
		23 °C, distilled water (abr. (e): 320 grit)	21.9	57.0	12.5 <sup>b</sup>	–
		23 °C, distilled water (abr. (f): 150 grit)	19.7	46.5	14.9 <sup>b</sup>	–
1961	Mould [106]	0.5% RH	35.2	66.3	20.3 <sup>b</sup>	–
		43% RH	31.0	74.7	16.4 <sup>b</sup>	–
		Liquid water	31.2	66.9	17.5 <sup>b</sup>	–
1961	Shand [135]	Room temp., controlled humidity (as-received)	43.0	91.0	23.5 <sup>b</sup>	–
		Room temp., controlled humidity (re-annealed)	28.1	57.6	14.2 <sup>b</sup>	–
1969	Ritter and Vrooman [134]	26.7 °C, 100% RH	884.5	1767.8	31.0	–
1971	Ritter and Sherburne [107]	23.3 °C, 50% RH	1385.4	1859.5	37.6 <sup>b</sup>	–
		23.3 °C, 100% RH	1176.4	1587.3	31.1 <sup>b</sup>	–
1976	Pavelchek and Doremus [108]	21-25 °C, 50% RH (aged 24 h - pkg. I)	42.4	81.6	19.5 <sup>b</sup>	–
		21-25 °C, 50% RH (aged 24 h - pkg. II)	42.2	75.5	14.1 <sup>b</sup>	–
		21-25 °C, 100% RH (aged 24 h)	36.3	67.9	14.7 <sup>b</sup>	–
		21-25 °C, 50% RH	49.1	81.9	17.4 <sup>b</sup>	–
		21-25 °C, 100% RH	38.9	70.6	14.6 <sup>b</sup>	–
		21-25 °C, 50% RH (heated 400 °C)	77.9	106.7	24.1 <sup>b</sup>	–
		21-25 °C, 50% RH (heated 500 °C)	79.6	107.1	28.5 <sup>b</sup>	–
1978	Jakus et al. [130]	Room temperature, water	38.7	59.6	18.1	–
1980	Richter <sup>d</sup> [131]	40–60% RH	–	–	18.1	–
		Water	–	–	15.0	–
1981	Chantikul et al. [111]	Distilled water (annealed)	36.7	64.1	18.4 <sup>b</sup>	–
		Distilled water (as-indent)	23.8	44.9	13.9 <sup>b</sup>	–
1989	Ikedo and Igaki [112]	(Diametral compression)	66.8	76.9	13.3	–

(continued on next page)

Table A.3 (continued)

Year	Reference	Test condition	Applied stress [MPa]		SCG <sup>a</sup> parameters	
			$\sigma_{f,s}^{\min}$	$\sigma_{f,s}^{\max}$	$n$ [-]	$v_0$ [mm/s]
1995	Sglavo and Green [113]	(Axisymmetric bending)	70.7	81.6	26.3	-
		Water (indented in air)	20.9	37.6	-	-
		Water (indented in air, annealed)	34.4	51.5	16.1	1.6
		Water (indented in water)	20.6	36.5	-	-
		Water (indented in water, annealed)	28.5	44.6	18.2	9.5
1997	Chen and Matsumura [109]	Air with 40–80% RH	31.4	59.6	36.2 <sup>b</sup>	-
1999	Sglavo and Green [114]	Deionized water (annealed)	31.8	43.3	18.7 <sup>b</sup>	-
		Deionized water (as-indented)	21.6	34.6	14.0 <sup>b</sup>	-
2000	Fink [132]	23 °C, 60% RH	15.0	30.0	16.4	-
		0-38 °C, 28–96% RH (field test)	13.5	30.0	15.6	-

<sup>a</sup> SCG = sub-critical crack growth.

<sup>b</sup> Estimated by means of least squares fit using Eq (5).

<sup>c</sup> Original work published by Phillips in 1937 [175].

<sup>d</sup> Based on published  $K_{Ic}$ -data, a relative strength ( $K_I$  divided by  $K_{Ic}$ ) is estimated using  $K_{Ic} = 0.75 \text{ MPa m}^{1/2}$ .

Table A.4

Summary of key numbers of the reviewed soda-lime-silica glass dynamic fatigue tests.

Year	Reference	Test condition	Failure stress [MPa]		SCG <sup>a</sup> parameters			
			$\sigma_{f,d}^{\min}$	$\sigma_{f,d}^{\max}$	$n$ [-]	$v_0$ [mm/s]		
1899	Grenet [70]	Glass plates at unk. conditions	28.9	78.4	11.2 <sup>b</sup>	-		
1934	Apelt [177]	Glass rods at unk. conditions	33.0	83.4	6.9 <sup>b</sup>	-		
		Room temperature	73.6	128.5	11.3 <sup>b</sup>	-		
1935	Black [104]	-	44.8	74.2	10.1 <sup>b</sup>	-		
1937	Borchard [122]	10 °C	2.4	3.0	30.6 <sup>b</sup>	-		
1949	Thompson and Cousins [123]	Single strength glass at unk. cond.	$6.2 \cdot 10^{-3}$	$3.1 \cdot 10^{-2}$	-	-		
		Double strength glass at unk. cond.	$1.7 \cdot 10^{-2}$	$5.0 \cdot 10^{-2}$	-	-		
1958	Charles [94]	25 °C, water vapour	75.2	97.3	16.0	-		
1969	Ritter [148]	Room temp., air (abraded)	86.6	114.0	11.9	-		
		Room temp., wet (abraded)	78.2	99.5	13.4	-		
		Room temp., air and wet (acid-etched)	1311.4	1963.6	13.0	-		
		Room temp., wet (coating: none)	57.1	88.6	13.0–16.0	-		
1974	Ritter [178]	Room temp., wet (coating: acrylic)	63.3	102.0	12.0	-		
		Room temp., wet (coating: silicone)	70.5	107.4	14.4	-		
		Room temp., wet (coating: epoxy)	82.9	121.4	16.9	-		
		1% RH	51.1	96.9	16.5 <sup>b</sup>	-		
1975	Evans and Johnson [97] Ritter and LaPorte [149]	6 N NaOH (abraded)	72.2	99.7	19.5	-		
		Distilled H <sub>2</sub> O (abraded)	60.3	97.1	13.0	-		
		6 N HCl (abraded)	46.3	57.4	25.1	-		
		6 N NaOH (acid-polished)	-	-	19.3	-		
		Distilled H <sub>2</sub> O (acid-polished)	-	-	16.9	-		
		6 N HCl (acid-polished)	-	-	17.8	-		
		1975	Tummala and Foster [179]	Room temp., air (as-rec., atm. side)	92.1	126.1	22.0	-
				Room temp., air (as-rec., float side)	77.8	118.6	17.0	-
Room temp., air (annealed, atm. side)	70.3			133.1	10.0	-		
Room temp., air (annealed, float side)	77.3			126.2	13.3	-		
1975	Yamada [180]	20 °C, 50% RH	77.3	99.8	17.1 <sup>b</sup>	-		
1978	Chandan et al. [98]	Ambient, 41–67% RH	45.3	107.5	17.2	-		
1978	Jakus et al. [130]	Room temperature, water	50.2	79.1	17.9	-		
1979	Hagan et al. [181]	Water	56.1	87.1	15.9 <sup>b</sup>	-		
		Silicone oil	75.7	110.0	13.5 <sup>b</sup>	-		
1979	Woelk and Eisenheimer <sup>b</sup> [182]	-	-	-	-			
1980	Marshall and Lawn [152]	Water (annealed glass)	44.2	78.6	17.9	2.4		
		Water (as-indented glass)	28.6	62.0	13.7	55.0		
1981	Johar [124]	20-25 °C, 28–55% RH	$5.4 \cdot 10^{-3}$	$6.6 \cdot 10^{-3}$	22.6 <sup>b</sup>	-		
1981	Kerkhof et al. [78]	20 °C, 50% RH	15.4	26.0	16.0 <sup>b</sup>	-		
1981	Marshall and Lawn [183]	Water	38.6	67.3	15.7	-		
1982	Dabbs et al. [153]	Distilled water	34.5	251.9	14.0 (18.4) <sup>c</sup>	31.6		
1982	Dabbs and Lawn [154]	Distilled water	233.7	638.1	9.0	-		
1982	Johar [125]	16-24 °C, 26–57% RH	$3.6 \cdot 10^{-3}$	$6.3 \cdot 10^{-3}$	14.3 <sup>b</sup>	-		
1985a	Ritter et al. [185]	Room temp., dist. water (surface) <sup>f</sup>	87.0	104.0	17.7	10.7		
		Room temp., dist. water (edge) <sup>f</sup>	64.9	93.1	15.5	0.5		
		Room temp., dist. water (overall) <sup>f</sup>	62.0	88.1	16.8	1.8		
		5 °C, dist. water (indented, annealed)	45.8	67.9	15.7 <sup>b</sup>	-		
1985b	Ritter et al. [146]	25 °C, dist. water (indented, annealed)	36.4	60.6	13.3 <sup>b</sup>	-		
		55 °C, dist. water (indented, annealed)	32.8	49.6	16.5 <sup>b</sup>	-		

(continued on next page)

Table A.4 (continued)

Year	Reference	Test condition	Failure stress [MPa]		SCG <sup>2</sup> parameters	
			$\sigma_{f,d}^{min}$	$\sigma_{f,d}^{max}$	$n [-]$	$v_0$ [mm/s]
		85 °C, dist. water (indented, annealed)	26.6	40.1	15.3 <sup>b</sup>	–
		5 °C, dist. water (indented, aged)	35.5	50.0	19.9 <sup>b</sup>	–
		25 °C, dist. water (indented, aged)	32.1	45.6	19.2 <sup>b</sup>	–
		55 °C, dist. water (indented, aged)	25.7	34.3	21.3 <sup>b</sup>	–
		85 °C, dist. water (indented, aged)	21.3	29.7	21.1 <sup>b</sup>	–
1986a	Ritter et al. [155]	25 °C, dist. water (subthreshold flaws)	62.6	111.0	10.5 (13.7) <sup>c</sup>	–
		85 °C, dist. water (subthreshold flaws)	56.3	104.9	–	–
		25 °C, dist. water (postthreshold flaws)	40.2	58.0	14.4 (18.8) <sup>c</sup>	–
		85 °C, dist. water (postthreshold flaws)	25.9	36.6	–	–
1986b	Ritter et al. [147]	5 °C, dist. water (abraded, annealed)	86.3	109.9	24.7 <sup>b</sup>	–
		25 °C, dist. water (abraded, annealed)	79.5	107.5	21.1 <sup>b</sup>	18.0
		55 °C, dist. water (abraded, annealed)	76.9	102.9	22.9 <sup>b</sup>	–
		85 °C, dist. water (abraded, annealed)	75.5	103.2	20.2 <sup>b</sup>	–
		5 °C, dist. water (abraded, aged)	63.1	95.0	15.3 <sup>b</sup>	–
		25 °C, dist. water (abraded, aged)	55.5	92.6	12.6 <sup>b</sup>	5.3
		55 °C, dist. water (abraded, aged)	49.0	84.2	11.5 <sup>b</sup>	–
		85 °C, dist. water (abraded, aged)	50.3	82.3	11.8 <sup>b</sup>	–
1986	Zongzhe et al. [159]	Ordinary temp.	104.0	240.8	14.2 <sup>c</sup>	–
1987	Gehrke et al.* [82]	Water (emery paper)	–	–	14.8/15.7	–
		Water (Vickers indentation)	–	–	15.0	–
		Water (powder jets)	–	–	16.3	–
		Nonane (emery paper)	–	–	–	–
1987	Ikeda et al. [186]	Air (axisymmetric bending)	46.7	63.4	18.5 <sup>b</sup>	–
		Air (4-point bending)	43.1	63.9	16.3 <sup>b</sup>	–
		Water (axisymmetric bending)	41.6	54.7	16.6 <sup>b</sup>	–
		Water (4-point bending)	39.9	50.0	21.1 <sup>b</sup>	–
1987	Ritter et al. [156]	25 °C, dist. water (low strength, subthreshold, $P = 0.25$ N)	69.7	111.1	13.4 <sup>d</sup>	–
		25 °C, dist. water (low strength, subthreshold, $P = 0.35$ N)	59.6	103.3	11.5 <sup>d</sup>	–
		25 °C, dist. water (low strength, postthreshold, $P = 0.15$ N)	69.9	124.0	11.4 <sup>d</sup>	–
		25 °C, dist. water (low strength, postthreshold, $P = 0.25$ N)	64.0	112.1	11.5 <sup>d</sup>	–
		25 °C, dist. water (low strength, postthreshold, $P = 0.35$ N)	60.2	101.9	12.3 <sup>d</sup>	–
		25 °C, dist. water (high strength, subthreshold, $P = 0.15$ N)	190.2	424.3	8.1 <sup>d</sup>	–
		25 °C, dist. water (high strength, subthreshold, $P = 0.25$ N)	171.6	326.4	10.1 <sup>d</sup>	–
		25 °C, dist. water (high strength, subthreshold, $P = 0.35$ N)	122.5	218.1	12.7 <sup>d</sup>	–
1988	Pal and Pennington [120]	–	$7.2 \cdot 10^{-3}$	$1.8 \cdot 10^{-2}$	13.4 <sup>b</sup>	–
1989	Ikeda et al. [187]	Air (axisymmetric bending)	65.2	82.5	19.0	–
		Air (4-point bending)	65.1	85.9	22.3	–
		Water (axisymmetric bending)	63.0	78.9	22.3	–
		Water (4-point bending)	60.6	71.9	27.8	–
1992	Choi and Salem [157]	Room temperature, alcohol	42.0	52.5	20.2 (26.3) <sup>d</sup>	2.2
		Room temperature, air	39.8	51.8	16.2 (20.9) <sup>d</sup>	16.2
		Room temperature, acetone	38.1	47.8	19.3 (25.1) <sup>d</sup>	24.0
		Room temperature, distilled water	35.6	44.3	20.1 (26.1) <sup>d</sup>	97.7
1992	Ikeda et al. [188]	Air (diametral compression)	26.7	34.2	18.4	–
		Water (diametral compression)	24.1	34.3	31.2	–
1992	Makovička and Lexa [34]	–	35.1	64.6	13.4 <sup>b</sup>	–
1994	Nemeth et al. [189]	Room temp., distilled water	163.6	289.9	11.3 <sup>b</sup>	–
1995	Dwivedi and Green [139]	Room temp., air (natural flaws)	96.1	160.9	21.8	2.6
		Room temp., air (Indentation flaws)	40.9	63.6	16.1 (21.1) <sup>c</sup>	2.4
1995	Li et al. [190]	Room temp., 25–30% RH ( $T_f = 470$ °C)	52.3	67.9	11.0	–
		Room temp., 25–30% RH ( $T_f = 530$ °C)	68.2	75.8	28.0	–
1995	Sglavo and Green [113]	Deionized water (indented in air)	32.4	50.8	14.3 (18.8) <sup>c</sup>	14.3
		Deionized water (indented in water)	33.4	45.1	14.3 (18.7) <sup>c</sup>	11.7
1997	Choi et al. [191]	Room temp., distilled water	46.5	251.9	16.4	–
1997	Lü [192]	–	56.0	68.2	25.0	–
1997	Sglavo et al. [158]	Deionized water	34.5	56.3	13.7 (18.0) <sup>c</sup>	19.0
1999	Sglavo and Green [114]	Deionized water (annealed)	37.8	62.6	15.2 (19.9) <sup>c</sup>	6.4
		Deionized water (as-indentated)	27.8	53.9	15.3 (20.1) <sup>c</sup>	28.8
2000	Choi et al. [150]	Ambient temp., water (grind angle 0°)	61.8	100.9	13.4	–
		Ambient temp., water (grind angle 30°)	59.2	95.5	13.3	–
		Ambient temp., water (grind angle 60°)	41.2	66.3	13.2	–
		Ambient temp., water (grind angle 90°)	40.3	64.1	13.4	–
2001	Schneider [171]	20 °C, 40–60% RH (group A)	51.3	66.2	16.9	–
		20 °C, 40–60% RH (group B)	68.4	84.0	21.2	–
2002	Akcakaya and Gulati [193]	Room temp., 100% RH (V-belt)	29.5	44.0	16.2	–
		Room temp., 100% RH (ground)	30.6	53.5	13.5	–
2002	Krohn et al. [151]	Room temp., air (air side)	49.8	91.5	21.7	–
		Room temp., air (tin side)	50.4	88.9	21.6	–
2006	Haldimann [137]	23.4–23.8 °C, 51.4–54.7% RH (ambient)	55.3	103.2	2.5 <sup>b</sup>	–
		23.2–23.9 °C, 51.7–54.7% RH (dry/coated)	85.1	153.4	7.6	–
2011	Peroni et al. [101]	Air at ambient conditions	47.3	98.1	27.4 <sup>b</sup>	–
2012	König [117]	Air at ambient conditions	105.4	199.6	19.7 <sup>b</sup>	–
2012	Zhang et al. [102]	Air at ambient conditions	18.2	41.5	–	–
2015	Hilcken [194]	22.7 °C, 50% RH	30.7	49.3	14.2	2.2

(continued on next page)

Table A.4 (continued)

Year	Reference	Test condition	Failure stress [MPa]		SCG <sup>a</sup> parameters	
			$\sigma_{f,d}^{\min}$	$\sigma_{f,d}^{\max}$	$n$ [-]	$v_0$ [mm/s]
2019	Förch [118]	20-21 °C, 40% RH	35.8	48.0	17.9	–
2019	Meyland et al. [119]	22 °C, 30% RH (as-received)	169.0	313.0	26.4 <sup>b</sup>	–
		22 °C, 30% RH (pre-damaged)	56.0	88.0	34.6 <sup>b</sup>	–
2020	Brokmann et al. [195]	25 °C, 50% RH	64.1	80.6	14.8	10.5

<sup>a</sup> SCG = sub-critical crack growth.

<sup>b</sup> Estimated by means of least squares fit using Eq. (8).

<sup>c</sup> True fatigue parameter in parenthesis obtained by  $n' = 0.763 n$ , where  $n'$  is denoted the apparent fatigue parameter.

<sup>d</sup> True fatigue parameter in parenthesis obtained by  $n' = 0.75 n + 0.5$ , where  $n'$  is denoted the apparent fatigue parameter.

<sup>e</sup> True fatigue parameter in parenthesis obtained by  $n' = (3n - 2)/4$ , where  $n'$  is denoted the apparent fatigue parameter.

<sup>f</sup> Averaged results determined by eight different laboratories.

<sup>g</sup> Only relative strength data are reported.

<sup>h</sup> Only the increase in strength as function of loading rate is reported and no absolute strength data are available.

<sup>i</sup> Apparent fatigue constant,  $n'$ .

## Appendix B. Literature search and data collection

The Technical University of Denmark internal web search engine *DTU Findit*<sup>4</sup> was used to perform the initial literature search; the data from the literature is discussed in Sec. 3 and 4. Keywords chosen to be relevant for the search are given in Table B.1.

Table B.1

Relevant keywords grouped into subject category used to find the literature that is discussed in Sec. 3 and 4. The symbol \* is used to perform the multiple character wildcard search.

Main material	glass
Material subgroup	silica, lime, soda lime, soda lime silica, float, annealed, commercial
Time dependency	static fatigue, stress corrosion, sub-critical crack growth, dynamic fatigue, strain rate, stress rate, loading rate
Research objective	strength, failure stress, failure time, crack velocity, stress intensity, stress concentration, properties
Not included	nano*, strengthening, sand, fibre*, fiber*, coat*, compo*, rock*, alloy, metallic glass, alum*, polym*

A combination of all keywords using the search engine specific operators AND, OR and NOT resulted in 164 hits, of which 25 scientific publications met the criteria to be included in the literature review. The criteria was that the published work focus on the tensile behaviour of soda-lime-silica glass, where data has been obtained from experiments as either static or dynamic fatigue, or crack velocity measurements. No limits were used in either the year of publication or the language. Based on the reference lists of previously found literature and studies on the topic already known to the authors, additional relevant publications were considered in the review, resulting in the following total number of publications reviewed in this paper:

- Static fatigue data → 23 publications
- Crack velocity data → 12 publications
- Dynamic fatigue data → 57 publications

In several publications the data of interest were not presented in a table and only provided in the publication as a plot. In these cases data from the plots were extracted using the freeware software *WebPlotDigitizer* (ver. 4.3) [174]. Therefore, data from all the publications were gathered as independent values that could be further tabulated and analysed in this work.

## References

- [1] R.A. Behr, J.E. Minor, H.S. Norville, Structural behavior of architectural laminated glass, *J. Struct. Eng.* 119 (1) (1993) 202–222, [https://doi.org/10.1061/\(ASCE\)0733-9445\(1993\)119:1\(202\)](https://doi.org/10.1061/(ASCE)0733-9445(1993)119:1(202)).
- [2] J.E. Minor, H.S. Norville, Design of window glass for lateral pressures, *J. Architect. Eng.* 12 (3) (2006) 116–121, [https://doi.org/10.1061/\(ASCE\)1076-0431\(2006\)12:3\(116\)](https://doi.org/10.1061/(ASCE)1076-0431(2006)12:3(116)).
- [3] R. Davies, N. Vigener, Architectural glass to resist snow loads, 9781845693695, in: R.A. Behr (Ed.), *Archit. Glas. To Resist Seism. Extrem. Clim. Events*, Elsevier, 2009, pp. 96–146, <https://doi.org/10.1533/9781845696856.96>.
- [4] M. Badalassi, L. Biolzi, G. Royer-Carfigni, W. Salvatore, Safety factors for the structural design of glass, *Construct. Build. Mater.* 55 (2014) 114–127, <https://doi.org/10.1016/j.conbuildmat.2014.01.005>.
- [5] C. Kameswara Rao, Safety of glass panels against wind loads, *Eng. Struct.* 6 (3) (1984) 232–234, [https://doi.org/10.1016/0141-0296\(84\)90050-6](https://doi.org/10.1016/0141-0296(84)90050-6).
- [6] D.A. Reed, E. Simiu, Wind loading and strength of cladding glass, *J. Struct. Eng.* 110 (4) (1984) 715–729, [https://doi.org/10.1061/\(ASCE\)0733-9445\(1984\)110:4\(715\)](https://doi.org/10.1061/(ASCE)0733-9445(1984)110:4(715)).
- [7] I. Calderone, W. Melbourne, The behaviour of glass under wind loading, *J. Wind Eng. Ind. Aerod.* 48 (1) (1993) 81–94, [https://doi.org/10.1016/0167-6105\(93\)90282-5](https://doi.org/10.1016/0167-6105(93)90282-5).
- [8] I.J. Calderone, W.H. Melbourne, The equivalent wind load for design of glass in buildings, in: A. Larsen, G. Larose, F. Livesey (Eds.), *Wind Eng. Into 21st Century*, A.A. Balkema Publishers, Rotterdam, Netherland, 1999, pp. 1111–1115, 1–3.
- [9] C. Barry, Architectural glass to resist wind pressures, 9781845693695, in: R. A. Behr (Ed.), *Archit. Glas. To Resist Seism. Extrem. Clim. Events*, Elsevier, 2009, pp. 169–192, <https://doi.org/10.1533/9781845696856.169>.
- [10] T. Henriksen, S.O. Hansen, Design of glass for high, short duration wind loads, in: F. Bos, C. Louter, F. Veer (Eds.), *Challenging Glas. 2 - Conf. Archit. Struct. Appl. Glas. CGC 2010*, May, TU Delft Open, 2010, pp. 629–637.
- [11] E. Gavanski, G.A. Kopp, Glass breakage tests under fluctuating wind loads, *J. Architect. Eng.* 17 (1) (2011) 34–41, [https://doi.org/10.1061/\(ASCE\)AE.1943-5568.0000028](https://doi.org/10.1061/(ASCE)AE.1943-5568.0000028).
- [12] C. Pantelides, K. Truman, R. Behr, A. Belarbi, Development of a loading history for seismic testing of architectural glass in a shop-front wall system, *Eng. Struct.* 18 (12) (1996) 917–935, [https://doi.org/10.1016/0141-0296\(95\)00224-3](https://doi.org/10.1016/0141-0296(95)00224-3).

<sup>4</sup> Data processed and indexed for DTU Findit are sourced from providers listed here: <https://findit.dtu.dk/en/about/providers> (retrieved: 28-01-2021).

- [13] R.A. Behr, Seismic performance of architectural glass in mid-rise curtain wall, *J. Architect. Eng.* 4 (3) (1998) 94–98, [https://doi.org/10.1061/\(ASCE\)1076-0431\(1998\)4:3\(94\)](https://doi.org/10.1061/(ASCE)1076-0431(1998)4:3(94)).
- [14] T.J. Renick, R.A. Behr, Seismic performance of architectural glass in mid-rise curtain wall, *J. Architect. Eng.* 5 (3) (1999) 105–106, [https://doi.org/10.1061/\(ASCE\)1076-0431\(1999\)5:3\(105\)](https://doi.org/10.1061/(ASCE)1076-0431(1999)5:3(105)).
- [15] R.A. Behr, Closure to “seismic performance of architectural glass in mid-rise curtain wall” by Richard A. Behr, *J. Architect. Eng.* 5 (3) (1999), [https://doi.org/10.1061/\(ASCE\)1076-0431\(1999\)5:3\(106\)](https://doi.org/10.1061/(ASCE)1076-0431(1999)5:3(106)), 106–106.
- [16] A.M. Memari, R.A. Behr, P.A. Kremer, Seismic behavior of curtain walls containing insulating glass units, *J. Architect. Eng.* 9 (2) (2003) 70–85, [https://doi.org/10.1061/\(ASCE\)1076-0431\(2003\)9:2\(70\)](https://doi.org/10.1061/(ASCE)1076-0431(2003)9:2(70)).
- [17] R.A. Behr, Design of architectural glazing to resist earthquakes, *J. Architect. Eng.* 12 (3) (2006) 122–128, [https://doi.org/10.1061/\(ASCE\)1076-0431\(2006\)12:3\(122\)](https://doi.org/10.1061/(ASCE)1076-0431(2006)12:3(122)).
- [18] B. Huang, S. Chen, W. Lu, K.M. Mosalam, Seismic demand and experimental evaluation of the nonstructural building curtain wall: a review, *Soil Dynam. Earthq. Eng.* 100 (May) (2017) 16–33, <https://doi.org/10.1016/j.soildyn.2017.05.025>.
- [19] W.L. Beason, G.E. Meyers, R.W. James, Hurricane related window glass damage in Houston, *J. Struct. Eng.* 110 (12) (1984) 2843–2857, [https://doi.org/10.1061/\(ASCE\)0733-9445\(1984\)110:12\(2843\)](https://doi.org/10.1061/(ASCE)0733-9445(1984)110:12(2843)).
- [20] K.C. Mehta, Wind induced damage observations and their implications for design practice, *Eng. Struct.* 6 (4) (1984) 242–247, [https://doi.org/10.1016/0141-0296\(84\)90019-1](https://doi.org/10.1016/0141-0296(84)90019-1).
- [21] R.A. Behr, P.A. Kremer, Performance of laminated glass units under simulated windborne debris impacts, *J. Architect. Eng.* 2 (3) (1996) 95–99, [https://doi.org/10.1061/\(ASCE\)1076-0431\(1996\)2:3\(95\)](https://doi.org/10.1061/(ASCE)1076-0431(1996)2:3(95)).
- [22] D. Hattis, Architectural glass to resist wind-borne debris impacts, in: R.A. Behr (Ed.), *Archit. Glas. To Resist Seism. Extrem. Clim. Events*, Elsevier, 2009, ISBN 9781845693695, pp. 193–216, <https://doi.org/10.1533/9781845696856.193>.
- [23] F.J. Masters, K.R. Gurley, N. Shah, G. Fernandez, The vulnerability of residential window glass to lightweight windborne debris, *Eng. Struct.* 32 (4) (2010) 911–921, <https://doi.org/10.1016/j.engstruct.2009.12.016>.
- [24] X. Zhang, H. Hao, G. Ma, Laboratory test and numerical simulation of laminated glass window vulnerability to debris impact, *Int. J. Impact Eng.* 55 (2013) 49–62, <https://doi.org/10.1016/j.ijimpeng.2013.01.002>.
- [25] F. Flocker, L. Dharani, Stresses in laminated glass subject to low velocity impact, *Eng. Struct.* 19 (10) (1997) 851–856, [https://doi.org/10.1016/S0141-0296\(97\)00162-4](https://doi.org/10.1016/S0141-0296(97)00162-4).
- [26] R.A. Behr, P.A. Kremer, L.R. Dharani, F.S. Ji, N.D. Kaiser, Dynamic strains in architectural laminated glass subjected to low velocity impacts from small projectiles, *J. Mater. Sci.* 34 (23) (1999) 5749–5756, <https://doi.org/10.1023/A:1004702100357>.
- [27] S.M. Walley, Historical review of high strain rate and shock properties of ceramics relevant to their application in armour, *Adv Appl Ceram* 109 (8) (2010) 446–466, <https://doi.org/10.1179/174367609X422180>.
- [28] X. Nie, W.W. Chen, Impact strength of glass for armor applications, in: J.J. Swab, S. Widjaja, D. Singh (Eds.), *Adv. Ceram. Armor VII*, Chap. 19, John Wiley & Sons, Ltd, 2011, pp. 215–226, <https://doi.org/10.1002/9781118095256.ch19>.
- [29] T.G. Talladay, D.W. Templeton, Glass armor - an overview, *Int. J. Appl. Glass Sci.* 5 (4) (2014) 331–333, <https://doi.org/10.1111/jjag.12096>.
- [30] S.M. Walley, An introduction to the properties of glass in ballistic applications, *Strain* 50 (6) (2014) 470–500, <https://doi.org/10.1111/str.12075>.
- [31] K. Osnes, S. Dey, O.S. Hopperstad, T. Borvik, On the dynamic response of laminated glass exposed to impact before blast loading, *Exp. Mech.* 59 (7) (2019) 1033–1046, <https://doi.org/10.1007/s11340-019-00496-1>.
- [32] E.M. Pugh, R.v. Heine-Geldern, S. Foner, E.C. Mutschler, Glass cracking caused by high explosives, *J. Appl. Phys.* 23 (1) (1952) 48–53, <https://doi.org/10.1063/1.1701977>.
- [33] R.J. Harris, M.R. Marshall, D.J. Moppett, Response of glass windows to explosion pressures, *Inst Chem Eng Symp Ser* 49 (1977) 83–97.
- [34] D. Makovička, P. Lexa, Dynamic response of window glass plates under explosion overpressure, in: P. Bulson (Ed.), *Struct. Under Shock Impact II*, Computational Mechanics Publications Ltd, Southampton, 1992, pp. 381–392.
- [35] D. Makovička, Shockwave load of window glass plate structure and hypothesis of its failure, in: N. Jones, D.G. Talasidis, C.A. Brebbia, G.D. Manolis (Eds.), *Struct. Under Shock Impact V*, Computational Mechanics Inc, 1998, pp. 43–52.
- [36] T. Krauthammer, A. Altenberger, Negative phase blast effects on glass panels, *Int. J. Impact Eng.* 24 (1) (2000) 1–17.
- [37] L. Dharani, J. Wei, F. Ji, Failure analysis of laminated architectural glass panels subjected to blast loading, in: N. Jones, C. Brebbia, A. Rajendran (Eds.), *Struct. Under Shock Impact VII*, WIT Press, Southampton, UK, 2002, pp. 37–46.
- [38] L.R. Dharani, J. Wei, Dynamic response of laminated glass under blast loading: effect of negative phase, in: N. Jones, C. Brebbia (Eds.), *Struct. Under Shock Impact VIII*, vol. 15, WIT Press, Southampton, UK, 2004, pp. 181–190.
- [39] K.A. Marchand, E.J. Conrath, D.J. Stevens, S.B. Meyer, Blast induced glass hazards: a comparison of design approaches and recent research, in: N. Jones, C. A. Brebbia (Eds.), *Struct. Under Shock Impact IX*, WIT Press, Southampton, UK, 2006, pp. 259–268, <https://doi.org/10.2495/SU060261>.
- [40] J. Wei, M.S. Shetty, L.R. Dharani, Failure analysis of architectural glazing subjected to blast loading, *Eng. Fail. Anal.* 13 (7) (2006) 1029–1043, <https://doi.org/10.1016/j.engfailanal.2005.07.010>.
- [41] J. Wei, M.S. Shetty, L.R. Dharani, Stress characteristics of a laminated architectural glazing subjected to blast loading, *Comput. Struct.* 84 (10–11) (2006) 699–707, <https://doi.org/10.1016/j.compstruct.2005.11.007>.
- [42] P. Kumar, A. Shukla, Blast loading response of glass panels, in: T. Proulx (Ed.), *Conf. Proc. Soc. Exp. Mech. Ser. 177*, vol. 6, Springer, New York, NY, 2011, pp. 131–132, [https://doi.org/10.1007/978-1-4419-9792-0\\_21](https://doi.org/10.1007/978-1-4419-9792-0_21).
- [43] M. Larcher, M. Teich, N. Gebbeken, G. Solomos, F. Casadei, G.A. Falcon, et al., Simulation of laminated glass loaded by air blast waves, *Appl. Mech. Mater.* 82 (2011) 69–74, <https://doi.org/10.4028/www.scientific.net/AMM.82.69>.
- [44] M.V. Seica, M. Krynski, M. Walker, J.A. Packer, Analysis of dynamic response of architectural glazing subject to blast loading, *J. Architect. Eng.* 17 (2) (2011) 59–74, [https://doi.org/10.1061/\(ASCE\)AE.1943-5568.0000035](https://doi.org/10.1061/(ASCE)AE.1943-5568.0000035).
- [45] P. Hooper, R. Sukhrum, B. Blackman, J. Dear, On the blast resistance of laminated glass, *Int. J. Struct. Struct. Anal.* 49 (6) (2012) 899–918, <https://doi.org/10.1016/j.ijstruct.2011.12.008>.
- [46] X. Zhang, H. Hao, G. Ma, Parametric study of laminated glass window response to blast loads, *Eng. Struct.* 56 (2013) 1707–1717, <https://doi.org/10.1016/j.engstruct.2013.08.007>.
- [47] X. Zhang, H. Hao, Experimental and numerical study of boundary and anchorage effect on laminated glass windows under blast loading, *Eng. Struct.* 90 (2015) 96–116, <https://doi.org/10.1016/j.engstruct.2015.02.022>.
- [48] X. Zhang, H. Hao, Z. Wang, Experimental study of laminated glass window responses under impulsive and blast loading, *Int. J. Impact Eng.* 78 (2015) 1–19, <https://doi.org/10.1016/j.ijimpeng.2014.11.020>.
- [49] M. Larcher, M. Arrigoni, C. Bedon, J.C.A.M. van Doormaal, C. Haberacker, G. Hüskens, et al., Design of blast-loaded glazing windows and facades: a review of essential requirements towards standardization, *Adv. Civ. Eng.* 2016 (2016) 1–14, <https://doi.org/10.1155/2016/2604232>.
- [50] D. Makovička, D. Makovička Jr., Failure of window glass plate under blast load, *Appl. Mech. Mater.* 821 (2016) 248–253, <https://doi.org/10.4028/www.scientific.net/AMM.821.248>.
- [51] J. Pelfrene, J. Kuntsche, S. Van Dam, W. Van Paeppegem, J. Schneider, Critical assessment of the post-breakage performance of blast loaded laminated glazing: experiments and simulations, *Int. J. Impact Eng.* 88 (2016) 61–71, <https://doi.org/10.1016/j.ijimpeng.2015.09.008>.
- [52] K. Spiller, J.A. Packer, M.V. Seica, D.Z. Yankelevsky, Prediction of annealed glass window response to blast loading, *Int. J. Impact Eng.* 88 (2016) 189–200, <https://doi.org/10.1016/j.ijimpeng.2015.10.010>.
- [53] X. Zhang, H. Hao, The response of glass window systems to blast loadings: an overview, *Int. J. Prot. Struct.* 7 (1) (2016) 123–154, <https://doi.org/10.1177/2041419615626061>.
- [54] P. Del Linz, P.A. Hooper, H. Arora, Y. Wang, D. Smith, B.R. Blackman, et al., Delamination properties of laminated glass windows subject to blast loading, *Int. J. Impact Eng.* 105 (2017) 39–53, <https://doi.org/10.1016/j.ijimpeng.2016.05.015>.
- [55] X. Zhang, C. Bedon, Vulnerability and protection of glass windows and facades under blast: experiments, methods and current trends, *Int. J. Struct. Glas. Adv. Mater. Res* 1 (2) (2017) 10–23, <https://doi.org/10.1084/sgamrsp.2017.10.23>.
- [56] M.A. Samieian, D. Cormie, D. Smith, W. Whaley, B.R. Blackman, J.P. Dear, et al., Prediction of blast response in laminated glass, *June 2018*, *Eng. Struct.* 188 (2019) 650–664, <https://doi.org/10.1016/j.engstruct.2019.01.008>.
- [57] M.V. Seica, J.A. Packer, D.Z. Yankelevsky, Blast and impact loading effects on glass and steel elements and materials, *November 2018*, *Thin-Walled Struct.* 134 (2019) 384–394, <https://doi.org/10.1016/j.tws.2018.07.048>.
- [58] X.Q. Zhou, M.Y. Wang, L.X. Li, Dynamic damage assessment of float glass under blast loading, *Adv. Struct. Eng.* (2019), <https://doi.org/10.1177/1369433219845691>.
- [59] P.H. Bischoff, S.H. Perry, Compressive behaviour of concrete at high strain rates, *Mater. Struct.* 24 (6) (1991) 425–450, <https://doi.org/10.1007/BF02472016>.
- [60] R.W. Armstrong, S.M. Walley, High strain rate properties of metals and alloys, *Int. Mater. Rev.* 53 (3) (2008) 105–128, <https://doi.org/10.1179/174328008X277795>.
- [61] Q.B. Zhang, J. Zhao, A review of dynamic experimental techniques and mechanical behaviour of rock materials, *Rock Mech. Rock Eng.* 47 (4) (2014) 1411–1478, <https://doi.org/10.1007/s00603-013-0463-y>.
- [62] J. Pelfrene, Numerical Analysis of the Post-Fracture Response of Laminated Glass under Impact and Blast Loading, ph.d., Ghent University, 2016.
- [63] P. Forquin, Brittle materials at high-loading rates: an open area of research, *Philos Trans R Soc A Math Phys Eng Sci* 375 (2085) (2017) 20160436, <https://doi.org/10.1098/rsta.2016.0436>.
- [64] S.M. Budd, The mechanisms of chemical reaction between silicate glass and attacking agents – Part 1: electrophilic and nucleophilic mechanisms of attack, *Phys. Chem. Glasses* 2 (4) (1961) 111–114.
- [65] T.A. Michalske, S.W. Freiman, A molecular interpretation of stress corrosion in silica, *Nature* 295 (5849) (1982) 511–512, <https://doi.org/10.1038/295511a0>.
- [66] T.A. Michalske, S.W. Freiman, A molecular mechanism for stress corrosion in vitreous silica, *J. Am. Ceram. Soc.* 66 (4) (1983) 284–288, <https://doi.org/10.1111/j.1151-2916.1983.tb15715.x>.
- [67] R. Gy, Stress corrosion of silicate glass: a review, *J. Non-Cryst. Solids* 316 (1) (2003) 1–11, [https://doi.org/10.1016/S0022-3093\(02\)01931-2](https://doi.org/10.1016/S0022-3093(02)01931-2).
- [68] S.W. Freiman, S.M. Wiederhorn, J.J. Mecholsky Jr., Environmentally enhanced fracture of glass: a historical perspective, *J. Am. Ceram. Soc.* 92 (7) (2009) 1371–1382, <https://doi.org/10.1111/j.1551-2916.2009.03097.x>.
- [69] S. Freiman, The fracture of glass: past, present, and future, *Int. J. Appl. Glass Sci.* 3 (2) (2012) 89–106, <https://doi.org/10.1111/j.2041-1294.2012.00091.x>.
- [70] L. Grenet, Mechanical strength of glass, *Bull Soc Encour Ind Nat* 5 (4) (1899) 838–848.
- [71] F.W. Preston, The time factor in the testing of glassware, *J. Am. Ceram. Soc.* 18 (1–12) (1935) 220–224, <https://doi.org/10.1111/j.1151-2916.1935.tb19384.x>.

- [72] S.M. Wiederhorn, Fracture surface energy of soda-lime glass, in: *Role Grain Boundaries Surfaces Ceram.*, vol. 52, Springer US, Boston, MA, 1966, pp. 503–528, <https://doi.org/10.1007/978-1-4899-6311-6-27>.
- [73] S.M. Wiederhorn, Influence of water vapor on crack propagation in soda-lime glass, *J. Am. Ceram. Soc.* 50 (8) (1967) 407–414, <https://doi.org/10.1111/j.1151-2916.1967.tb15145.x>.
- [74] S.M. Wiederhorn, L.H. Bolz, Stress corrosion and static fatigue of glass, *J. Am. Ceram. Soc.* 53 (10) (1970) 543–548, <https://doi.org/10.1111/j.1151-2916.1970.tb15962.x>.
- [75] S.M. Wiederhorn, H. Johnson, Effect of electrolyte pH on crack propagation in glass, *J. Am. Ceram. Soc.* 56 (4) (1973) 192–197, <https://doi.org/10.1111/j.1151-2916.1973.tb12454.x>.
- [76] S.W. Freiman, Effect of alcohols on crack propagation in glass, *J. Am. Ceram. Soc.* 57 (8) (1974) 350–353, <https://doi.org/10.1111/j.1151-2916.1974.tb10920.x>.
- [77] S.M. Wiederhorn, E.R. Fuller, R. Thomson, Micromechanisms of crack growth ceramics and glasses in corrosive environments, *Met. Sci.* 14 (8–9) (1980) 450–458, <https://doi.org/10.1111/j.1151-2916.1980.14.8.9.450>.
- [78] F. Kerkhof, H. Richter, D. Stahn, Festigkeit von Glas zur Abhängigkeit von Belastungsdauer und -verlauf, *Glastech. Ber.* 54 (8) (1981) 265–277.
- [79] C.J. Simmons, S. Freiman, Effect of corrosion processes on subcritical crack growth in glass, *J. Am. Ceram. Soc.* 64 (11) (1981) 683–686, <https://doi.org/10.1111/j.1151-2916.1981.tb15870.x>.
- [80] S.M. Wiederhorn, S.W. Freiman, E.R. Fuller, C.J. Simmons, Effects of water and other dielectrics on crack growth, *J. Mater. Sci.* 17 (12) (1982) 3460–3478, <https://doi.org/10.1007/BF00752191>.
- [81] S.W. Freiman, G.S. White, E.R. Fuller, Environmentally enhanced crack growth in soda-lime glass, *J. Am. Ceram. Soc.* 68 (3) (1985) 108–112, <https://doi.org/10.1111/j.1151-2916.1985.tb09646.x>.
- [82] E. Gehrke, C. Ullner, M. Hähnert, Correlation between multistage crack growth and time-dependent strength in commercial silicate glasses - Part 1. Influence of ambient media and types of initial cracks, *Glastech. Ber.* 60 (8) (1987) 268–278.
- [83] E. Gehrke, C. Ullner, M. Hähnert, Effect of corrosive media on crack growth of model glasses and commercial silicate glasses, *Glastech. Ber.* 63 (9) (1990) 255–265.
- [84] C. Ullner, Forschungsvorhaben-Nr. 43 D: Untersuchungen zum Festigkeitsverhalten und zur Rißalterung von Glas unter dem Einfluß korrosiver Umgebungsbedingungen, *Tech. Rep., Bundesanstalt für Materialforschung und -prüfung, Berlin, 1993*.
- [85] A.G. Evans, Slow crack growth in brittle materials under dynamic loading conditions, *Int. J. Fract.* 10 (2) (1974) 251–259, <https://doi.org/10.1007/BF00113930>.
- [86] K.T. Wan, S. Lathabai, B.R. Lawn, Crack velocity functions and thresholds in brittle solids, *J. Eur. Ceram. Soc.* 6 (4) (1990) 259–268, [https://doi.org/10.1016/0955-2219\(90\)90053-1](https://doi.org/10.1016/0955-2219(90)90053-1).
- [87] V.M. Sglavo, D.J. Green, Threshold stress intensity factor in soda-lime silicate glass by interrupted static fatigue test, *J. Eur. Ceram. Soc.* 16 (6) (1996) 645–651, [https://doi.org/10.1016/0955-2219\(96\)00176-X](https://doi.org/10.1016/0955-2219(96)00176-X).
- [88] C. Kocer, R.E. Collins, Measurement of very slow crack growth in glass, *J. Am. Ceram. Soc.* 84 (11) (2001) 2585–2593, <https://doi.org/10.1111/j.1151-2916.2001.tb01058.x>.
- [89] V.M. Sglavo, M. Bertoldi, Vickers indentation: a powerful tool for the analysis of fatigue behavior on glass, *Ceram. Trans.* 156 (2012) 13–22, <https://doi.org/10.1002/9781118407042.ch2>.
- [90] S.B. Ghosh, F.R. Jones, R.J. Hand, A novel indentation based method to determine the threshold stress intensity factor for sub-critical crack growth in glass,  *Glas Technol Eur J Glas Sci Technol Part A 51 (4) (2010) 156–160*.
- [91] J. Menčík, Strength and Fracture of Glass and Ceramics, Elsevier Science Publishing Company, Inc., New York, 1992, 0-444-98685-5.
- [92] A.G. Evans, S.M. Wiederhorn, Proof testing of ceramic materials - an analytical basis for failure prediction, *Int. J. Fract.* 10 (3) (1974) 379–392, <https://doi.org/10.1007/BF00035499>.
- [93] T.L. Anderson, Fracture Mechanics - Fundamentals and Applications, fourth ed., CRC Press, Boca Raton, USA, 2017 <https://doi.org/10.1201/9781315370293>, 9781315370293.
- [94] R.J. Charles, Dynamic fatigue of glass, *J. Appl. Phys.* 29 (12) (1958) 1657–1662, <https://doi.org/10.1063/1.1723019>.
- [95] J.K. Kuntze, Mechanisches Verhalten von Verbundglas unter zeitabhängiger Belastung und Explosionsbeanspruchung, ph.D., Technische Universität Darmstadt, 2015, <https://doi.org/10.1007/978-3-662-48831-7>.
- [96] M. Haldimann, A. Läubli, M. Overend, Structural Use of Glass, International Association for Bridge and Structural Engineering, Zürich, Switzerland, 2008, ISBN 978-3-85748-119-2.
- [97] A.G. Evans, H. Johnson, The fracture stress and its dependence on slow crack growth, *J. Mater. Sci.* 10 (2) (1975) 214–222, <https://doi.org/10.1007/BF00540345>.
- [98] H.C. Chandan, R.C. Bradt, G.E. Rindone, Dynamic fatigue of float glass, *J. Am. Ceram. Soc.* 61 (5–6) (1978) 207–210, <https://doi.org/10.1111/j.1151-2916.1978.tb09280.x>.
- [99] EN 1288-2, Glass in Building - Determination of the Bending Strength of Glass - Part 2: Coaxial Double Ring Test on Flat Specimens with Large Test Surface Area, European Committee for Standardization (CEN), Brussels, Belgium, 2000.
- [100] D. Li, L.N.Y. Wong, The Brazilian disc test for rock mechanics applications: review and new insights, *Rock Mech. Rock Eng.* 46 (2) (2013) 269–287, <https://doi.org/10.1007/s00603-012-0257-7>.
- [101] M. Peroni, G. Solomos, V. Pizzinato, M. Larcher, Experimental investigation of high strain-rate behaviour of glass, *Appl. Mech. Mater.* 82 (2011) 63–68, <https://doi.org/10.4028/www.scientific.net/AMM.82.63>.
- [102] X. Zhang, Y. Zou, H. Hao, X. Li, G. Ma, K. Liu, Laboratory test on dynamic material properties of annealed float glass, *Int J Prot Struct* 3 (4) (2012) 407–430, <https://doi.org/10.1260/2041-4196.3.4.407>.
- [103] T.C. Baker, F.W. Preston, Wide range static strength testing apparatus for glass rods, *J. Appl. Phys.* 17 (3) (1946) 162–170, <https://doi.org/10.1063/1.1707701>.
- [104] L.V. Blak, Effect of the rate of loading on the breaking strength of glass, *Bull Am Ceram Soc* 15 (8) (1935) 274–275.
- [105] R.E. Mould, R.D. Southwick, Strength and static fatigue of abraded glass under controlled ambient conditions: I, general concepts and apparatus, *J. Am. Ceram. Soc.* 42 (11) (1959) 542–547, <https://doi.org/10.1111/j.1151-2916.1959.tb13571.x>.
- [106] R.E. Mould, Strength and static fatigue of abraded glass under controlled ambient conditions: IV, effect of surrounding medium, *J. Am. Ceram. Soc.* 44 (10) (1961) 481–491, <https://doi.org/10.1111/j.1151-2916.1961.tb13710.x>.
- [107] J.E. Ritter, C.L. Sherburne, Dynamic and static fatigue of silicate glasses, *J. Am. Ceram. Soc.* 54 (12) (1971) 601–605, <https://doi.org/10.1111/j.1151-2916.1971.tb16013.x>.
- [108] E. Pavelchek, R. Doremus, Static fatigue in glass — a reappraisal, *J. Non-Cryst. Solids* 20 (3) (1976) 305–321, [https://doi.org/10.1016/0022-3093\(76\)90115-0](https://doi.org/10.1016/0022-3093(76)90115-0).
- [109] X. Chen, M. Matsumura, Effect of preloading on the strength of soda-lime glass, *J. Test. Eval.* 25 (3) (1997) 354–357, <https://doi.org/10.1520/JTE11350J>.
- [110] E.B. Shand, Experimental study of fracture of glass: I, the fracture process, *J. Am. Ceram. Soc.* 37 (2) (1954) 52–59, <https://doi.org/10.1111/j.1151-2916.1954.tb14005.x>.
- [111] P. Chantikul, B.R. Lawn, D.B. Marshall, Micromechanics of flaw growth in static fatigue: influence of residual contact stresses, *J. Am. Ceram. Soc.* 64 (6) (1981) 322–325, <https://doi.org/10.1111/j.1151-2916.1981.tb10295.x>.
- [112] K. Ikeda, H. Igaki, Static fatigue test by diametral compression in soda-lime glass disk specimen, *Trans Japan Soc Mech Eng Ser A* 55 (511) (1989) 555–559, <https://doi.org/10.1299/kikaa.55.555>.
- [113] V. Sglavo, D. Green, Influence of indentation crack configuration on strength and fatigue behaviour of soda-lime silicate glass, *Acta Metall. Mater.* 43 (3) (1995) 965–972, [https://doi.org/10.1016/0956-7151\(94\)00335-F](https://doi.org/10.1016/0956-7151(94)00335-F).
- [114] V.M. Sglavo, D.J. Green, Indentation fatigue testing of soda-lime silicate glass, *J. Mater. Sci.* 34 (3) (1999) 579–585, <https://doi.org/10.1023/A:1004507131588>.
- [115] EN 1288-3, Glass in Building - Determination of the Bending Strength of Glass - Part 3: Test with Specimen Supported at Two Points (Four Point Bending), European Committee for Standardization (CEN), Brussels, Belgium, 2000.
- [116] EN 1288-5, Glass in Building - Determination of the Bending Strength of Glass - Part 5: Coaxial Double Ring Test on Flat Specimens with Small Test Surface Areas, European Committee for Standardization (CEN), Brussels, Belgium, 2000.
- [117] C. König, Dehnratenabhängigkeit mechanischer Werkstoffkennwerte von Kalk-Natronsilicatglas, Ph.D., Technische Universität Carolo-Wilhelmina zu Braunschweig, 2012.
- [118] M. Förch, Analysis of Glass Panels Subjected to Blast Load; vol. 1 of *Fassadensysteme und Gebäudehüllen*, Springer Berlin Heidelberg, Berlin, Heidelberg, 2019, [https://doi.org/10.1007/978-3-662-59087-4\\_978-3-662-59086-7](https://doi.org/10.1007/978-3-662-59087-4_978-3-662-59086-7).
- [119] M.J. Meyland, C.K.T. Bonding, R.N.W. Eriksen, J.H. Nielsen, An experimental investigation of the flexural strength of soda-lime-silica glass at high loading rates, *Glas Struct Eng* 4 (2) (2019) 175–183, <https://doi.org/10.1007/s40940-018-0089-2>.
- [120] H.S. Pal, W. Pennington, Strength of window glass plates subjected to rapid loading, *Texas Civ Eng* 58 (4) (1988) 11–16.
- [121] W. Chen, B. Song, Split Hopkinson (Kolsky) Bar, Mechanical Engineering Series, Springer US, Boston, MA, 2011, [https://doi.org/10.1007/978-1-4419-7982-7\\_978-1-4419-7981-0](https://doi.org/10.1007/978-1-4419-7982-7_978-1-4419-7981-0).
- [122] K.H. Borchard, Einfluß der Belastungsgeschwindigkeit und der Gestalt der Belastungskurve auf den Meßwert der Festigkeit von Glashohlgefäßen, *Glastech. Ber.* 15 (3) (1937) 99–105.
- [123] N.J. Thompson, E.W. Cousins, Explosion tests on glass windows; effect on glass breakage of varying rate of pressure application, *J. Am. Ceram. Soc.* 32 (10) (1949) 313–315, <https://doi.org/10.1111/j.1151-2916.1949.tb18903.x>.
- [124] S. Johar, Dynamic Fatigue of Flat Glass, Phase II: Final Report, Technical Report; Department of Glass and Ceramics, Mississauga, Canada, 1981, <https://doi.org/10.4224/20328096>.
- [125] S. Johar, Dynamic Fatigue of Flat Glass, Phase III: Final Report, Technical Report, Department of Metals, Glass and Ceramics; Mississauga, Canada, 1982, <https://doi.org/10.4224/20326324>.
- [126] M.J. Meyland, J.H. Nielsen, C. Kocer, Datasets: Tensile Behaviour of Soda-Lime-Silica Glass and the Significance of Load Duration - A Literature Review, Technical University of Denmark, DTU Data, 2021, <https://doi.org/10.11583/DTU.13655525>.
- [127] C. Gurney, S. Pearson, The effect of the surrounding atmosphere on the delayed fracture of glass, *Proc. Phys. Soc. B* 62 (8) (1949) 469–476, <https://doi.org/10.1088/0370-1301/62/8/301>.
- [128] T.C. Baker, F.W. Preston, Fatigue of glass under static loads, *J. Appl. Phys.* 17 (3) (1946) 170–178, <https://doi.org/10.1063/1.1707702>.
- [129] R.J. Charles, Static fatigue of glass. II, *J. Appl. Phys.* 29 (11) (1958) 1554–1560, <https://doi.org/10.1063/1.1722992>.

- [130] K. Jakus, D.C. Coyne, J.E. Ritter, Analysis of fatigue data for lifetime predictions for ceramic materials, *J. Mater. Sci.* 13 (10) (1978) 2071–2080, <https://doi.org/10.1007/BF00541660>.
- [131] H. Richter, Langsame Ribausbreitung und Lebensdauerbestimmung. Vergleich zwischen Rechnung und Experiment, *Ber. Dtsch. Keram. Ges.* 57 (1) (1980) 10–12.
- [132] A. Fink, Ein Beitrag zum Einsatz von Floatglas als dauerhaft tragender Konstruktionswerkstoff im Bauwesen, ph.d., Technische Universität Darmstadt, 2000.
- [133] B. Vonnegut, J.L. Glathart, The effect of temperature on the strength and fatigue of glass rods, *J. Appl. Phys.* 17 (12) (1946) 1082–1085, <https://doi.org/10.1063/1.1707679>.
- [134] J.E. Ritter, D.L. Vrooman, *Static Fatigue of Acid-Etched, Soda-Lime-Silica Glass Rods*, University of Massachusetts, Amherst, Massachusetts, 1969. Technical Report.
- [135] E.B. Shand, Correlation of strength of glass with fracture flaws of measured size, *J. Am. Ceram. Soc.* 44 (9) (1961) 451–455, <https://doi.org/10.1111/j.1151-2916.1961.tb13754.x>.
- [136] M. Overend, K. Zammit, A computer algorithm for determining the tensile strength of float glass, *Eng. Struct.* 45 (2012) 68–77, <https://doi.org/10.1016/j.engstruct.2012.05.039>.
- [137] M. Haldimann, *Fracture Strength of Structural Glass Elements - Analytical and Numerical Modelling, Testing and Design*, ph.d.; EPFL, 2006.
- [138] A. Petzold, H. Marusch, B. Schramm, *Der Baustoff Glas: Grundlagen, Eigenschaften, Erzeugnisse, Glasbauelemente, Anwendungen*, 3. ed., Verlag Karl Hofmann, Schorndorf, Germany, 1990, 3-7780-1181-2.
- [139] P.J. Dwidwi, D.J. Green, Determination of subcritical crack growth parameters by in situ observation of indentation cracks, *J. Am. Ceram. Soc.* 78 (8) (1995) 2122–2128, <https://doi.org/10.1111/j.1151-2916.1995.tb08624.x>.
- [140] D. Singh, D.K. Shetty, Subcritical crack growth in soda-lime glass in combined mode I and mode II loading, *J. Am. Ceram. Soc.* 73 (12) (1990) 3597–3606, <https://doi.org/10.1111/j.1151-2916.1990.tb04264.x>.
- [141] H.S. Norville, N. Harvill, E.J. Conrath, S. Shariat, S. Mallonee, Glass-related injuries in Oklahoma city bombing, *J. Perform. Constr. Facil.* 13 (2) (1999) 50–56, [https://doi.org/10.1061/\(ASCE\)0887-3828\(1999\)13:2\(50\)](https://doi.org/10.1061/(ASCE)0887-3828(1999)13:2(50)).
- [142] M.M. Rudick, H.S. Norville, Glass-related injuries in Oklahoma city bombing, *J. Perform. Constr. Facil.* 14 (4) (2000), [https://doi.org/10.1061/\(ASCE\)0887-3828\(2000\)14:4\(167\)](https://doi.org/10.1061/(ASCE)0887-3828(2000)14:4(167)), 167–167.
- [143] D. Smith, *Glazing for injury alleviation under blast loading - United Kingdom practice*, in: *Glas. Process. Days*, 2001, pp. 335–340.
- [144] K. Mengelkoch, Temperaturabhängigkeit der Zerreißeigenschaft von Glasstäben, *Z. Phys.* 97 (1–2) (1935) 46–63, <https://doi.org/10.1007/BF01331634>.
- [145] M. Eichler, Reißverfestigung an glasstäben, *Z. Phys.* 98 (3–4) (1935) 280–282, <https://doi.org/10.1007/BF01336913>.
- [146] J.E. Ritter, M. Vicedomine, K. Breder, K. Jakus, Dynamic fatigue of indented, soda-lime glass as a function of temperature, *J. Mater. Sci.* 20 (8) (1985) 2868–2872, <https://doi.org/10.1007/BF00535050>.
- [147] J.E. Ritter, G.S. Glaesemann, K. Jakus, P. Rampono, *Dynamic fatigue of soda-lime glass as a function of temperature*, *Phys. Chem. Glasses* 27 (2) (1986) 65–70.
- [148] J.E. Ritter, *Dynamic fatigue of soda-lime-silica glass*, *J. Appl. Phys.* 40 (1) (1969) 340–344, <https://doi.org/10.1063/1.1657056>.
- [149] J.E. Ritter, R.P. LaPorte, Effect of test environment on stress-corrosion susceptibility of glass, *J. Am. Ceram. Soc.* 58 (7–8) (1975) 265–267, <https://doi.org/10.1111/j.1151-2916.1975.tb11471.x>.
- [150] S.R. Choi, F.A. Holland, N.N. Nemeth, D.C. Butler, Machining damage and slow crack growth/reliability analysis of glass specimens, *Ceram. Eng. Sci. Proc.* 21 (3) (2000) 259–270.
- [151] M.H. Krohn, J.R. Hellmann, D.L. Shelleman, C.G. Pantano, G.E. Sakoske, Biaxial flexure strength and dynamic fatigue of soda-lime-silica float glass, *J. Am. Ceram. Soc.* 85 (7) (2002) 1777–1782, <https://doi.org/10.1111/j.1151-2916.2002.tb00352.x>.
- [152] D.B. Marshall, B.R. Lawn, Flaw characteristics in dynamic fatigue: the influence of residual contact stresses, *J. Am. Ceram. Soc.* 63 (9–10) (1980) 532–536, <https://doi.org/10.1111/j.1151-2916.1980.tb10759.x>.
- [153] T.P. Dabbs, B.R. Lawn, P.L. Kelly, A dynamic fatigue study of soda-lime silicate and borosilicate glasses using small scale indentation flaws, *Phys. Chem. Glasses* 23 (2) (1982) 58–66.
- [154] T.P. Dabbs, B.R. Lawn, Fatigue of high-strength soda-lime glass: a constant stressing rate study using subthreshold indentation flaws, *Phys. Chem. Glasses* 23 (4) (1982) 93–97.
- [155] J.E. Ritter, C.A. Ray, K. Jakus, *Dynamic fatigue of soda-lime glass with subthreshold flaws*, *Phys. Chem. Glasses* 27 (5) (1986) 210–214.
- [156] J.E. Ritter, P. Shi, K. Jakus, *Fatigue failure of sub threshold flaws in soda-lime glass*, *Phys. Chem. Glasses* 28 (3) (1987) 121–126.
- [157] S.R. Choi, J.A. Salem, Slow crack growth of indent cracks in glass with and without applied stress, *Mater Sci Eng A* 149 (2) (1992) 259–264, [https://doi.org/10.1016/0921-5093\(92\)90387-G](https://doi.org/10.1016/0921-5093(92)90387-G).
- [158] V.M. Sglavo, M. Gadotti, T. Micheletti, Cyclic loading behaviour of soda-lime silicate glass using indentation cracks, *Fatig. Fract. Eng. Mater. Struct.* 20 (8) (1997) 1225–1234, <https://doi.org/10.1111/j.1460-2695.1997.tb00326.x>.
- [159] J. Zongzhe, M. Junarong, L. Xiaorui, Dynamic fracture toughness and strength of glass, *XIV Int Congr Glas - Collect Pap 2* (1986) 78–83.
- [160] EN 16612, *Glass in Building - Determination of the Lateral Load Resistance of Glass Panes by Calculation*, European Committee for Standardization (CEN), Brussels, Belgium, 2019.
- [161] FprCEN/TS 19100-1, *Design of Glass Structures - Part 1: Basis of Design and Materials*, European Committee for Standardization (CEN), Brussels, Belgium, 2021.
- [162] ASTM E1300-16, *Standard Practice for Determining Load Resistance of Glass in Buildings*, ASTM International, West Conshohocken, PA, USA, 2016, <https://doi.org/10.1520/E1300-16.2>.
- [163] AS 1288-2006, *Glass in Buildings - Selection and Installation*, Standards Australia, Sydney, NSW 2001, Australia, 2006.
- [164] DIN 18008-1, *Glas im Bauwesen - Bemessungs- und Konstruktionsregeln - Teil 1: Begriffe und allgemeine Grundlagen*, Normenausschuss Bauwesen (NABau) im DIN, Berlin, Germany, 2010.
- [165] DIN 18008-4, *Glas im Bauwesen - Bemessungs- und Konstruktionsregeln - Teil 4: Zusatzanforderungen an absturzsichernde Verglasungen*, Normenausschuss Bauwesen (NABau) im DIN, Berlin, Germany, 2013.
- [166] NEN 2608, *Glass in Building - Requirements and Determination Method*, Nederlands Normalisatie-instituut, Delft, Netherlands, 2014.
- [167] ONORM B 3716-1, *Glas im Bauwesen - Konstruktiver Glasbau - Teil 1: Grundlagen*, Austrian Standards Institute, Wien, Austria, 2016.
- [168] CNR-DT 210, *Istruzioni per la Progettazione, l'Esecuzione ed il Controllo di Costruzioni con Elementi Strutturali di Vetro*, Commissione di studio per la predisposizione e l'analisi di norme tecniche relative alle costruzioni (CNR), Italy, Rome, 2013.
- [169] ASTM F2248-19, *Standard Practice for Specifying an Equivalent 3-Second Duration Design Loading for Blast Resistant Glazing Fabricated with Laminated Glass*, ASTM International, West Conshohocken, PA, USA, 2019, <https://doi.org/10.1520/F2248-19>.
- [170] S. Schula, *Charakterisierung der Kratzanfälligkeit von Gläsern im Bauwesen*, Springer Berlin Heidelberg, Berlin, Heidelberg, 2015, <https://doi.org/10.1007/978-3-662-47782-3>.
- [171] J. Schneider, *Festigkeit und Bemessung punktgeladener Gläser und stoßbeanspruchter Gläser*, ph.d., Technische Universität Darmstadt, 2001.
- [172] EN 572-1, *Glass in Building - Basic Soda Lime Silicate Glass Products - Part 1: Definitions and General Physical and Mechanical Properties*, European Committee for Standardization (CEN), Brussels, Belgium, 2012.
- [173] R.J. Mainstone, Properties of materials at high rates of straining or loading, *Mater. Construcción* 8 (2) (1975) 102–116, <https://doi.org/10.1007/BF02476328>.
- [174] A. Rohatgi, *WebPlotDigitizer*, Pacifica, California, USA; Pacifica, California, USA, 2020. URL, Version 4.3. <https://automeris.io/WebPlotDigitizer>.
- [175] C.J. Phillips, *Mechanical strength of glass*, Tech. Rep., Research Laboratory, Corning Glass Works, 1937.
- [176] A.J. Holland, W.E.S. Turner, The effect of sustained loading on the breaking strength of sheet glass, *J Soc Glas Technol* 24 (101) (1940) 46–57.
- [177] G. Apelt, Einfluß von Belastungsgeschwindigkeit und Verdrehungsverformung auf die Zerreißeigenschaft von Glasstäben, *Z. Phys.* 91 (5–6) (1934) 336–343, <https://doi.org/10.1007/BF01342552>.
- [178] J.E. Ritter, Effect of polymeric coatings on strength of soda-lime glass, in: R. Bradt, D. Hasselmann, F. Lange (Eds.), *Fract. Mech. Ceram.*, Springer US, Boston, MA, 1974, pp. 735–747, [https://doi.org/10.1007/978-1-4615-7014-1\\_18](https://doi.org/10.1007/978-1-4615-7014-1_18).
- [179] R.R. Tummala, B.J. Foster, Strength and dynamic fatigue of float glass surfaces, *J. Am. Ceram. Soc.* 58 (3–4) (1975), <https://doi.org/10.1111/j.1151-2916.1975.tb19593.x>, 156–156.
- [180] H. Yamada, Strength degradation of soda-lime-silica glass during dynamic loading, *J. Am. Ceram. Soc.* 58 (5–6) (1975) 197–200, <https://doi.org/10.1111/j.1151-2916.1975.tb11443.x>.
- [181] J.T. Hagan, M.V. Swain, J.E. Field, Fracture-strength studies on annealed and tempered glasses under dynamic conditions, *Philos. Mag.* A 39 (6) (1979) 743–756, <https://doi.org/10.1080/01418617908239304>.
- [182] H. Woelk, K. Eelsenheimer, *Biegebruchspannung von Floatglas und thermisch vorgespanntem Floatglas*, *Glastech. Ber.* 52 (1) (1979) 14–24.
- [183] D.B. Marshall, B.R. Lawn, Residual stresses in dynamic fatigue of abraded glass, *J. Am. Ceram. Soc.* 64 (1) (1981), <https://doi.org/10.1111/j.1151-2916.1981.tb09535.x>, C-6–C-7.
- [184] B.L. Symonds, R.F. Cook, B.R. Lawn, Dynamic fatigue of brittle materials containing indentation line flaws, *J. Mater. Sci.* 18 (5) (1983) 1306–1314, <https://doi.org/10.1007/BF01111947>.
- [185] J.E. Ritter, T.H. Service, C. Guillemet, Strength and fatigue parameters for soda-lime glass, *Glas Technol.* 26 (6) (1985) 273–278.
- [186] K. Ikeda, H. Igaki, K. Tagashira, Equibiaxial tensile strength of soda-lime glass in a water environment, *Trans Japan Soc Mech Eng Ser A* 53 (495) (1987) 2085–2089, <https://doi.org/10.1299/kikaia.53.2085>.
- [187] K. Ikeda, H. Igaki, K. Tagashira, Effect of environment and polyaxial stress states on subcritical crack growth in soda-lime glass. Examination based on constant stressing rate technique, *Trans Japan Soc Mech Eng Ser A* 55 (509) (1989) 129–133, <https://doi.org/10.1299/kikaia.55.129>.
- [188] K. Ikeda, T. Suzuki, Y. Tanigawa, H. Igaki, Effect of biaxial stress states on dynamic fatigue of soda-lime glass: an examination by diametral-compression, in: M. Jono, T. Inoue (Eds.), *Mech. Behav. Mater. VI*, Pergamon Press plc, Kyoto, Japan, 1992, pp. 497–502, <https://doi.org/10.1016/b978-0-08-037890-9.50332-x>.
- [189] N.N. Nemeth, L.M. Powers, L.A. Janosik, J.P. Gyekenyesi, Time-dependent reliability analysis of monolithic ceramic components using the cares/life integrated design program, in: C.R. Brinkman, S.F. Duffy (Eds.), *Life Predict. Methodol. Data Ceram. Mater. ASTM STP 1201*, American Society for Testing and Materials, Philadelphia, 1994, pp. 390–408.

- [190] H. Li, A. Agarwal, M. Tomozawa, Effect of fictive temperature on dynamic fatigue behavior of silica and soda-lime glasses, *J. Am. Ceram. Soc.* 78 (5) (1995) 1393–1396, <https://doi.org/10.1111/j.1151-2916.1995.tb08502.x>.
- [191] S.R. Choi, J.A. Salem, F.A. Holland, Estimation of slow crack growth parameters constant stress-rate test data of advanced ceramics and glass by the individual data and arithmetic mean methods. Tech. Rep. February, NASA Lewis Research Center, Cleveland, OH United States, 1997.
- [192] B.T. Lü, Fatigue strength prediction of soda-lime glass, *Theor. Appl. Fract. Mech.* 27 (2) (1997) 107–114, [https://doi.org/10.1016/S0167-8442\(97\)00012-8](https://doi.org/10.1016/S0167-8442(97)00012-8).
- [193] R. Akcakaya, S.T. Gulati, Effect of edge finish of float glass products on their strength and fatigue behaviour, *Glass Technol.* 43 (3) (2002) 95–96.
- [194] J. Hilcken, Zyklische Ermüdung von thermisch entspanntem und thermisch vorgespanntem Kalk-Natron-Silikatglas, ph.d., Technische Universität Darmstadt, Berlin, Heidelberg, 2015, <https://doi.org/10.1007/978-3-662-48353-4>.
- [195] C. Brokmann, S. Kolling, J. Schneider, Subcritical crack growth parameters in glass as a function of environmental conditions, *Glas Struct Eng* (2020), <https://doi.org/10.1007/s40940-020-00134-6>.



**A modified split-Hopkinson pressure bar setup enabling  
stereo digital image correlation measurements for flexural  
testing**

MEYLAND, M. J., ERIKSEN, R. N. W., and NIELSEN, J. H.

Submitted to: *International Journal of Impact Engineering* (2021)

DOI: 10.13140/RG.2.2.30301.33760



# A modified split-Hopkinson pressure bar setup enabling stereo digital image correlation measurements for flexural testing

Martin J. Meyland<sup>a,b,\*</sup>, Rasmus N. W. Eriksen<sup>c</sup>, Jens H. Nielsen<sup>a</sup>

<sup>a</sup>Technical University of Denmark, Department of Civil Engineering, Brovej, Building 118, 2800 Kgs. Lyngby, Denmark

<sup>b</sup>Ramboll Denmark A/S, Structures & Facade Engineering, Hannemanns Allé 53, 2300 Copenhagen S, Denmark

<sup>c</sup>IDTCE ApS, Amsterdamvej 25, 2300 Copenhagen S, Denmark

---

## Abstract

A novel experimental setup for dynamic material characterisation that combines a ring-on-ring test configuration for equibiaxial flexural testing with a modification of the well-known split-Hopkinson pressure bar (SHPB) is presented. The design is generic, but in the present paper intended for and validated by experiments on flat circular glass samples at high strain rates. The novel modification allows an unobstructed view of a significant part of the sample's tensile surface that is made possible by replacing the conventional transmission bar with a tube through which the incident bar passes. This modification enables the application of high-speed cameras for assessing the fracture together with stereo digital image correlation (stereo-DIC) for non-contact out-of-plane displacement measurements and, at the same time, reduces the total length of the setup compared to the original design. An FE-model of the bar/tube system was generated to characterise the setup better. From that, information on strain gauge locations was extracted. Two similar experiments on glass show that the required dynamic force equilibrium could be established and that the application of high-speed cameras work as intended. Lastly, promising results were achieved from the pilot stereo-DIC measurements, indicating pure bending deflections of the sample in line with theory.

**Keywords:** Brittle material characterisation, High-speed imaging, High strain rates, Ring-on-ring test, Soda-lime-silica glass

---

## 1. Introduction

Characterising engineering materials at high strain rates is essential to sufficiently design structural components that are exposed to extreme loading such as extreme weather, impacts, or blast loads. Most materials used in civilian infrastructures, such as steel, concrete, rock, wood, and glass, exhibits a strain rate sensitivity [1–5]. Usually, these materials are tested in conventional testing machines at quasi-static strain rates below  $1 \text{ s}^{-1}$ . Higher strain rates require different test methods, which often differ from the conventional ones by not having a closed-loop feedback control system of the loading conditions. The first steps into such methods have been pioneered by John Hopkinson [6] and his son, Bertram Hopkinson [7, 8], the inventor of the pressure-bar method. Further developments were made by Robertson [9], Landon and Quinney [10], and Davies [11], leading to the design of the well-known split-Hopkinson pressure bar (SHPB) devised originally by Kolsky [12]; therefore, in literature also named 'Kolsky bar'. The basic concept of the SHPB setup involves a material sample sandwiched between an input and output bar, also denominated incident and transmission bar, respectively (see Fig. 1(a)). Typically, a gas gun accelerates a striker bar that impacts the incident bar, initiating a

stress wave travelling towards the sample and loading it at high strain rates. Part of the wave reflects at the incident bar/sample interface, whereas the rest transmits through the sample into the transmission bar. A measurement of the material's stress-strain response, often ranging between  $50 \text{ s}^{-1}$  and  $10^4 \text{ s}^{-1}$  depending on the sample size [13], is provided by analysing the recorded strains in the bars.

Despite being often used in urban areas and in the automotive industry, a rarely investigated material in the range of high strain rates is soda-lime-silica glass [5, 14–18]. Recent studies going above  $1 \text{ s}^{-1}$  are reported by Peroni et al. [19], König [20], Zhang et al. [21], and Meyland et al. [22]. König (uniaxial tension) and Meyland et al. (axisymmetric bending) employed a servo-hydraulic high-speed test rig with limitations at the higher loading rates. Peroni et al. and Zhang et al. investigated the strain rate sensitivity of cylindrical glass samples in diametral compression (split tensile test) and regular compression using a traditional SHPB design, similar to what is shown in Fig. 1(a). However, when considering an explosion shock wave acting laterally on a thin glass pane, e.g. installed in a building envelope, the stress state is different. In such a case, the loading is of a more global character that introduces bending stresses to the material.

Various test configurations arranged in an SHPB setup to investigate the flexural strength of other ceramics are reported. A modified piston-on-three-ball test configuration was employed by Cheng et al. [23] to test thin glass substrates dynamically. Borosilicate glass was the subject of a series of investigations in

---

\*Corresponding author.

Email addresses: majeme@byg.dtu.dk; mjme@ramboll.dk (Martin J. Meyland), rwe@idtce.com (Rasmus N. W. Eriksen), jhn@byg.dtu.dk (Jens H. Nielsen)

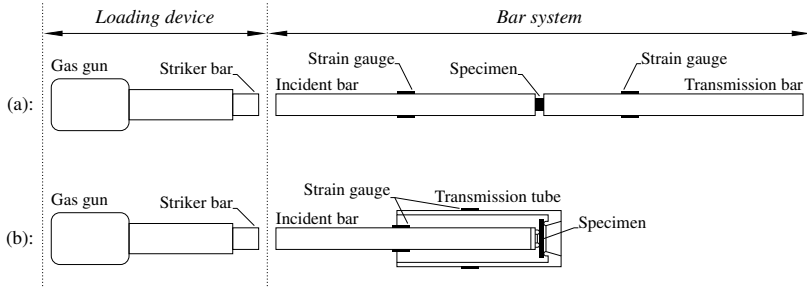


Figure 1: A sketch of the basic concept of a traditional split-Hopkinson pressure bar setup (SHPB) in (a) compared to the modified design presented in this paper in (b).

which rectangular samples were tested in a four-point bending fixture, and circular samples in a ring-on-ring test configuration [24–26]. Based on the findings reported, the ring-on-ring test configuration is preferable as it minimises stressing of edges having significant strength reducing flaws, e.g. due to cutting, and thus more reliable provide a measure of the surface strength.

The application of high-speed cameras and the technique of digital image correlation (DIC) for non-contact optical displacement/strain measurements has become general practice within the field of dynamic material characterisation [27]. It enables the researcher to explore features, such as fracture/failure processes and displacement/strain fields that are otherwise impossible to assess. However, applying such technology to a bend test configuration arranged in a traditional SHPB design is not feasible since the sample surfaces are hidden by the bars and are not visible for the cameras.

This paper presents and validates the design of a novel experimental setup, following the concept illustrated in Fig. 1(b), that combines well-established SHPB techniques with a ring-on-ring test configuration and provides the possibility of using high-speed cameras. The setup design is to be considered generic, but in the following, the validation is based on the dynamic material characterisation of glass. First, the principles and characteristics of the experimental setup are described and analysed; see Sec. 2. Then, all experimental procedures and necessary calibrations are outlined in Sec. 3. Lastly, in Sec. 4, results from initial tests are presented and discussed, serving as a proof of concept.

## 2. Design of the Experimental Setup

Typically, an SHPB setup is a build-up of three main parts: (i) a loading device, (ii) a bar system consisting of an incident and a transmission bar, and (iii) a data acquisition system [28]. In this regard, little has been changed in the modified SHPB setup presented hereinafter; see comparison in Fig. 1. To accommodate the design requisites stated in Sec. 1, only the design of the bar system has been rethought. A free view on the sample’s tensile surface was established by replacing the traditional transmission bar with a tube having the incident bar going through, as shown in Fig. 2. The ring-on-ring test configuration is placed at the end furthest away from the loading device with the load

ring mounted to the incident bar and the support ring to the transmission tube, see Fig. 3(a). The resulting stress state in a loaded sample in tangential-, radial-, and principal stresses,  $\sigma_\theta$ ,  $\sigma_r$ , and  $\sigma_1$ , respectively, is sketched in Fig. 3(b). A conical hole through the support ring exposes the sample’s tensile surface. This transformation not only provides an unobstructed view of the sample but also significantly reduces the total length of the setup compared to a traditional SHPB design (see Fig. 1).

As apparent from Fig. 2, all setup parts are arranged on top of a 4.0 m long HEB220 steel beam, which also defines the total length of the setup. The barrel has a length of 1.6 m including the threaded connection going inside the air tank. In extension of the muzzle, the incident bar with a length of 1.99 m (measured from impact end to tip of load ring) and a diameter of 30 mm is placed, which goes through the transmission tube with a length of 1.35 m. Inside the tube, the bar is held axially in place by in-house fabricated, low friction PTFE (polytetrafluoroethylene) bearings. The tube is manufactured with an outer and inner diameter of 55 mm and 48 mm, respectively, resulting in a wall thickness of 3.5 mm. The loading of the incident bar is done with a striker bar of the same diameter as the incident bar. The length of the striker bar controls the duration of the imposed stress wave.

Usually, high-strength steel is used for the bars in an SHPB. However, as flat glass tested in bending is expected to exhibit significantly lower strengths than other materials tested in pure compression, a high-strength aluminium alloy, Alumec 89<sup>®</sup> (a 7000 series alloy), is chosen for the bar/tube system. Due to the lower stiffness (approx. three times lower than steel), a higher strain response is to be measured.

The same aluminium alloy is chosen for the interchangeable load ring and support ring. The ring dimensions are determined according to the international Standard ASTM C1499-15 [29]. Both rings have a tip radius of 2.5 mm, and their respective contact diameters are 18 mm and 38 mm, as specified in Fig. 3(a). With the chosen support ring dimensions, an area of 855 mm<sup>2</sup> (53.8% of the samples total surface area) with a free sample surface is ensured that can be captured by high-speed cameras through the conical hole. The current ring-on-ring test configuration is designed for samples with dimensions  $\varnothing 45 \text{ mm} \times 3 \text{ mm} \pm 1 \text{ mm}$ , securing that high strain rates in the

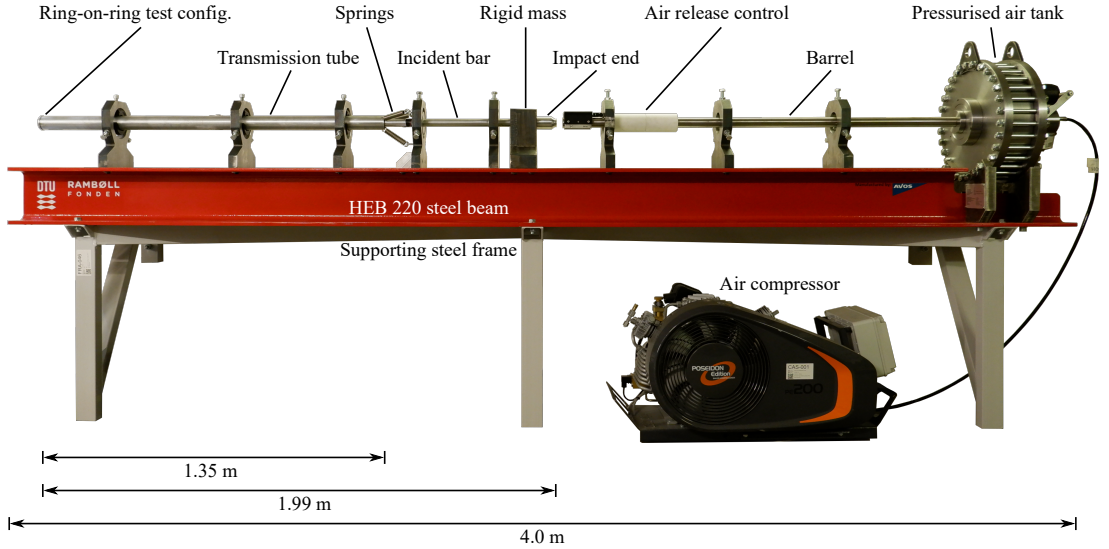


Figure 2: A photo of the novel experimental setup with the main parts highlighted. For more details on the ring-on-ring test configuration, see Fig. 3(a).

material can be achieved due to the short span relative to the sample thickness (i.e. high flexural rigidity).

For safety precautions, a rigid steel mass is placed between the barrel and the transmission tube that retains the incident bar after loading. This is done via an impact end with an enlarged diameter that cannot pass through the hole in the rigid mass. An elastomer buffer of polyurethane (PUR, soft shore hardness 70A) is inserted to reduce contact stresses at the impact. The transmission tube is retained by springs connected to a bar/tube support located next to it. After testing, a sample is replaced either via the slotted holes in the proximity of the ring-on-ring test configuration, also visible in Fig. 3(a), or by detaching the support ring.

### 2.1. Setup characteristics determined from an FE-model

The here presented SHPB setup has been subjected to several modifications to enable an unobstructed view of the sample that is to be investigated in a bend test configuration. To determine the setup characteristics in terms of how strains are propagating axially, a solid FE-model of the bar/tube system was established in ABAQUS/Explicit® 2020. The model was comprised of four parts: (i) the striker bar, (ii) the incident bar, (iii) the transmission tube, and (iv) the glass sample. Linear elastic isotropic material properties were assigned according to Table 1, and fracture of the glass sample was disregarded.

The computational time of the explicit FE-model was reduced by utilising symmetry boundary conditions in the  $xy$ - and  $xz$ -plane, as depicted in Fig. 4. The bars, tube, and glass sample were discretised with linear eight-node displacement elements (C3D8 in ABAQUS). A global element size of 3 mm was set for the bars and tube, whereas 1 mm was used for the glass sample. Node paths of interest extending along the whole length

Table 1: Material properties for the explicit FE-model of the experimental setup.

Property	Symbol	Unit	Alumec 89*	Glass†
Young's modulus	$E$	GPa	71.5	70.0
Poisson's ratio	$\nu$	—	0.33	0.23
Density	$\rho$	$\text{kg m}^{-3}$	2830	2500
Elastic wave speed‡	$C_0$	$\text{m s}^{-1}$	5026	5292

\* Data-sheet values

† Soda-lime-silica glass according to the European Standard EN 572-1 [30]

‡ See Eq. (2)

of the incident bar and the transmission tube are also highlighted in Fig. 4; however, only shown around the ring-on-ring test configuration. The chosen direction of the paths follows the stress wave propagation, i.e. in the incident bar, compressive waves travel towards the glass sample, while in the transmission tube, tensile waves travel towards the impact end.

In addition to the assigned symmetry boundary conditions, the movement of the transmission tube in the  $x$ -direction was limited by a spring support similar to what is shown in Fig. 2. The other parts, that is the striker bar, the incident bar and the glass sample, were allowed to move freely in the horizontal direction. The general contact formulation with zero friction was chosen for the interaction between the striker bar and the incident bar, and the rings and the glass sample. When the striker bar impacts the incident bar, the duration of the loading,  $T$ , is dependent on the striker bar length,  $L_{st}$ , according to:

$$T = \frac{2L_{st}}{C_0} \quad (1)$$

Here,  $C_0$  denotes the elastic wave speed in a cylindrical bar

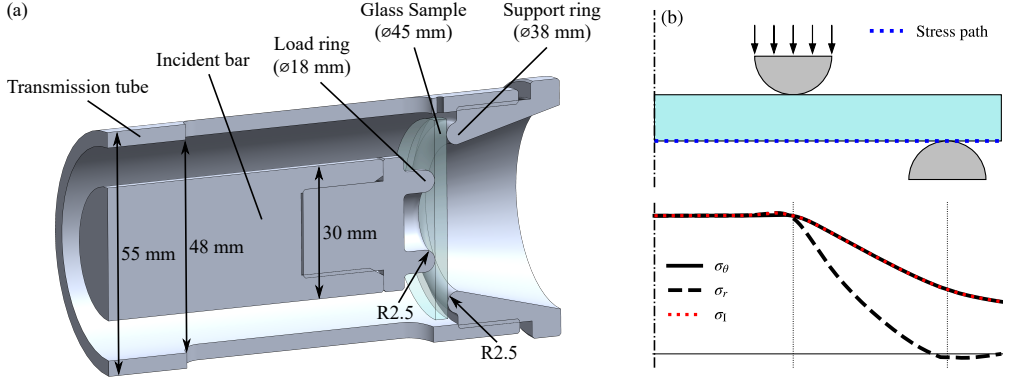


Figure 3: Detailed cut view on the ring-on-ring test configuration located at the furthest end of the setup and mounted to the bar/tube system (see also Fig. 2) in (a), and the resulting equibiaxial stress state ( $\sigma_\theta$  is the tangential stress,  $\sigma_r$  is the radial stress,  $\sigma_I$  is the first principal stress) on the tensile side of the sample during loading in (b).

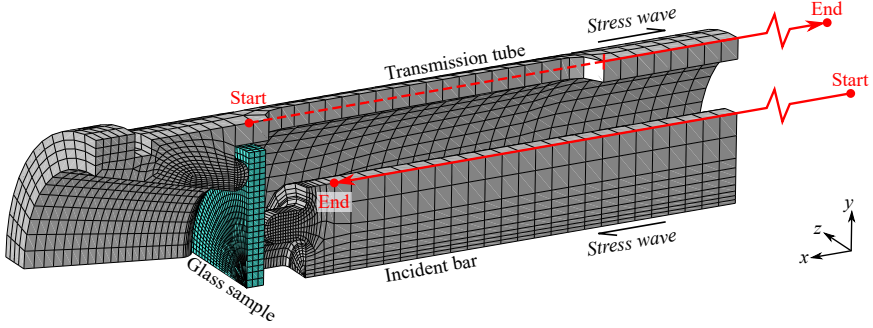


Figure 4: A cutout of the meshed model of the bar/tube system. Symmetry is utilised in the  $xy$ - and  $xz$ -plane. Node paths of interest are highlighted with red lines.

determined from Young's modulus,  $E$ , and the material density,  $\rho$ :

$$C_0 = \sqrt{\frac{E}{\rho}} \quad (2)$$

Due to identical material and cross-sectional properties for the striker and incident bar, the length of the impact generated incident pulse will be twice the length of the striker bar [31]. Moreover, the stress (or strain) amplitude of the incident pulse,  $\sigma_I$  (or  $\varepsilon_I$ ), is varying with the striker bar velocity,  $v_{st}$ , only:

$$\sigma_I = \frac{1}{2} \rho C_0 v_{st} \quad (3a)$$

or

$$\varepsilon_I = \frac{\sigma_I}{E} = \frac{1}{2} \frac{v_{st}}{C_0} \quad (3b)$$

The numerical model used for characterising the setup simulates a striker bar of the length 500 mm that directly impacts the incident bar with a velocity of  $6.0 \text{ m s}^{-1}$ . According to Eq. (1) and Eq. (3a), such impact produces an incident pulse with  $T =$

$0.199 \text{ ms}$  and  $\sigma_I = 42.7 \text{ MPa}$  that travels towards the sample. Part of the pulse is reflected back at the interface between the incident bar and the sample, whereas the rest is transmitted through the sample to the transmission tube. Consequently, there can be identified three pulses in the propagating strains, as highlighted in Fig. 5(a) and (b):

1. the incident pulse,  $\varepsilon_i$
2. the reflected pulse,  $\varepsilon_r$ , and
3. the transmitted pulse,  $\varepsilon_t$ .

From the simulation, the peak strain of each pulse is extracted along the node paths shown in Fig. 4, and the data is plotted in Fig. 5(c) and (d).

As can be seen, the peak of the incident pulse becomes steady almost from the very beginning on, but decreases in the vicinity of the sample due to the interaction. A similar course is seen in the reflected pulse that is on the way back to the impact end. The pulse that is transmitted to the tube is significantly impacted by the slotted holes used for sample replacement, but becomes constant right after at around 0.3 m (measured from the samples tensile surface, as shown in Fig. 4). At the other tube end, a

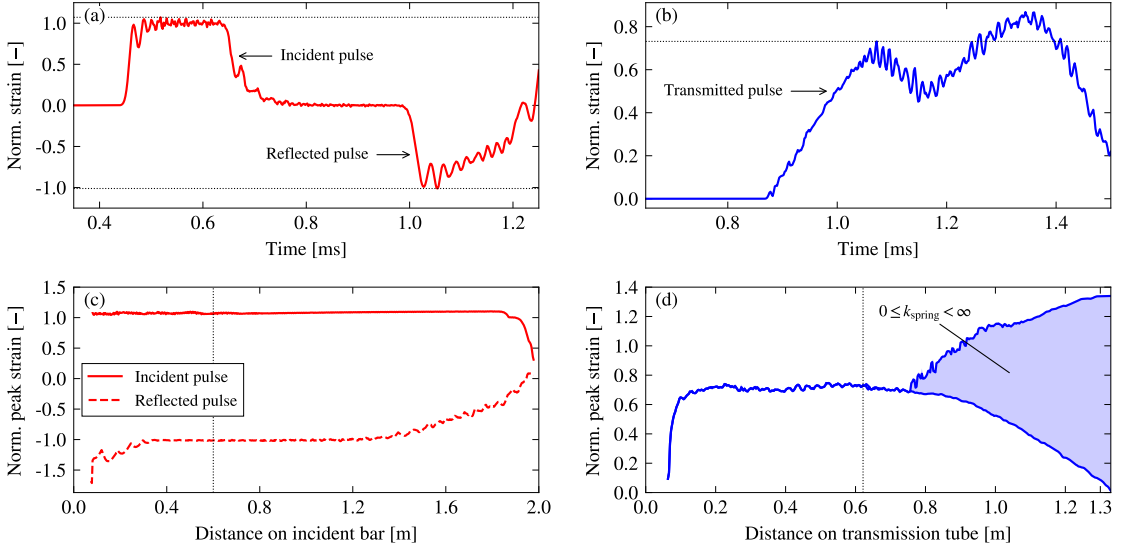


Figure 5: For  $L_{st} = 500\text{ mm}$  and  $v_{st} = 6.0\text{ m s}^{-1}$  numerically determined axial strains (normalised using Eq. (3b)) as function of time in the incident bar and the transmission tube exemplified in (a) and (b), respectively, for the locations highlighted with vertical dotted lines drawn in (c) and (d). For each location on the node paths shown in Fig. 4, the peak surface strain determined as shown by the horizontal dotted lines in (a) and (b) is plotted as function of the longitudinal coordinate along the incident bar and the transmission tube in (c) and (d), respectively. Additionally, in (d) the influence of the spring stiffness is investigated in the range  $0 \leq k_{spring} < \infty$ .

rise and decrease is seen depending on the spring stiffness. The interaction with a rigid boundary, i.e.  $k_{spring} = \infty$ , amplifies the wave with a factor of 2, whereas a free surface, i.e.  $k_{spring} = 0$ , nullifies the wave [31]. In the present SHPB setup, a signal somewhere in between is to be expected.

Taking into account the observed irregularities in the numerically determined strain pulses, reliable strain measurements in an experiment using a 500 mm striker bar can be performed between 0.4 m and 1.3 m on the incident bar measured from the impact end, and between 0.2 m and 0.75 m on the transmission tube measured from the tensile surface of the glass sample. For shorter striker bars, the range will be increased. This information is used for the strain gauge instrumentation, which is subject to the following section.

### 3. Experimental Procedures

This section presents and discusses the applied experimental procedures necessary for characterising the flexural properties of circular flat glass samples at high strain rates. An overview of the setup with the instrumentation of the applied measuring equipment is provided in Fig. 6. The figure highlights the measurement of the exit velocity of the striker bar, the location of strain gauges and the appertaining signals, and the placement of high-speed cameras for fracture assessment and DIC.

The data measured was acquired through a multifunction I/O device (National Instruments USB-6356 (BNC)) controlled via LabVIEW NXG 5.0. In the software, the data acquisition has

been customised using graphical programming to fit the experimental needs, such as rapid data storage, correct triggering, and combining strain gauge measurements with the measurement of the striker bar velocity.

#### 3.1. Exit velocity of the striker bar

For validation of obtained test results, the exit velocity of the striker bar is a key measure, see Eq. (3a) or (3b). In the experiments, the velocity was determined from two photogates<sup>1</sup> placed at the end of the barrel that measured the time it took the striker bar to travel a distance of  $\ell_{ph} = 50\text{ mm}$ , as depicted in Fig. 6. These photogates were connected to the counter of the multifunction I/O device, and the 'two-edge separation' task in LabVIEW was used for the timing between two rising edges that were exerted by the striker bar while passing the two light beams. The measurement was verified with a high-speed camera placed perpendicular to the barrel's muzzle capturing the exit velocity of the striker bar.

#### 3.2. Strain measurements

The strength characterisation of the flat glass samples is based on the stress waves propagating in the incident bar and the transmission tube, respectively. These are associated with strains that were recorded by means of  $120\ \Omega$  ( $\pm 0.35\%$ ) strain gauges<sup>2</sup> glued to the bar and tube surfaces. A diagonal Wheatstone half

<sup>1</sup> Applied component: OMRON photomicrosensor EE-SX461-P11

<sup>2</sup> Applied component: HBM 6/120 LY43

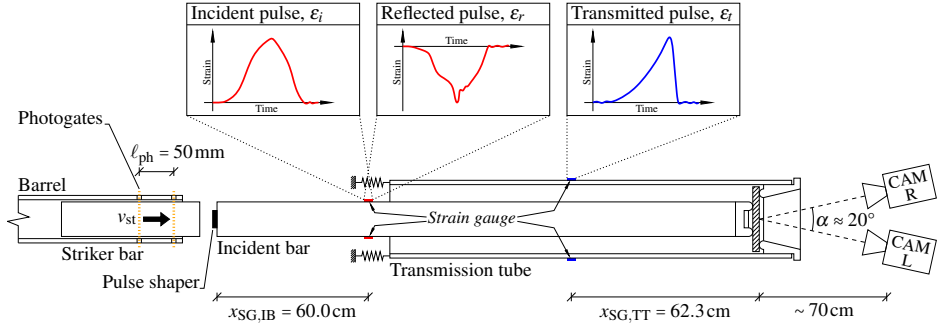


Figure 6: A schematic of the setup showing the strain gauge instrumentation and the associated strain signals generated by the impact of the striker bar. Additionally, the location of the high-speed cameras (CAM L and CAM R) in a stereo setup is shown.

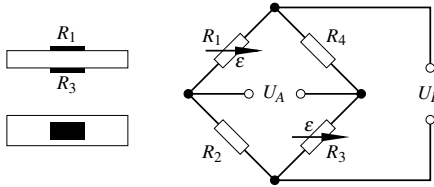


Figure 7: The applied Wheatstone bridge circuit: a diagonal half bridge compensating for superimposed bending forces.  $R_1, R_3$  = active  $120 \Omega$  strain gauges on the bar and the tube;  $R_2, R_4$  = fixed  $120 \Omega$  resistors. (after Ref. [32])

bridge circuit, as depicted in Fig. 7, was chosen for the axial strain measurements. By connecting the active strain gauges to the opposite legs of the bridge, a compensation of potentially superimposed bending forces can be achieved. Additionally, the application of two active strain gauges doubles the signal, reducing noise in the measurements.

The chosen strain gauge locations are based on the numerical findings presented in Sec. 2.1 and are shown in Fig. 6. On the incident bar, the strain gauges (two of a kind placed towards each other according to Fig. 7) were located  $x_{SG,IB} = 60.0$  cm from the impact end to maximise the time between the incident pulse and the reflected pulse and thereby avoiding overlapping of these signals. The strain gauges on the transmission tube were placed  $x_{SG,TT} = 62.3$  cm away from the tensile surface of the glass sample. As the strain gauges on the incident bar were relatively close to the impact end, part of the reflected pulse was overlapped by a reverse travelling stress pulse. However, this did not influence the part of the signal corresponding to the interaction with the glass sample, as discussed later.

For the data acquisition, the output signals from the two bridges,  $U_A$ , were conditioned with a high-speed transducer amplifier (FYLDE FE-H379-TA) connected to the multifunction I/O device. To secure correct measurements, the setup was shunt calibrated<sup>3</sup> using a factory-fitted calibration resistance of  $350 \text{ k}\Omega$ . During the tests, each bridge output signal (in Volt) was sampled

<sup>3</sup>Simulation of a bridge output signal by shunting one arm of a bridge by a resistor of known size.

at a rate of  $1.25 \text{ MHz}$ , which is 12.5 times faster than the minimum recommended by Chen and Song [28]. Subsequently, the acquired data were post-processed with the following expression to obtain the desired effective strains,  $\epsilon$ :

$$\epsilon = \frac{1}{B} \cdot \frac{4}{k} \cdot \frac{U_A}{U_E} \quad (4)$$

Here,  $B$  denotes the bridge factor that is dependent on the Wheatstone bridge configuration and in the present setup equals 2. Further,  $k$  designates a dimensionless gauge factor that is provided by the manufacturer of the strain gauges ( $= 2.11 \pm 1.0\%$ ), and  $U_E$  is the bridge excitation voltage that in the experiments was set constant to  $6.0 \text{ V}$ . The bridge output voltage,  $U_A$ , is the acquired signal in its unconditioned form, i.e. the amplification has been negated.

### 3.3. Setup calibration

#### 3.3.1. Bar/tube material properties

The post-processing of the data acquired from the SHPB experiments requires that Young's modulus and the density of the bar/tube material are known to calculate the elastic wave speed. The numbers provided in Table 1 are taken from a data sheet and do not necessarily represent the correct values applicable for the post-processing. Any error that evolves in one of these quantities is directly found in the determined stresses and strains. Lifshitz and Leber [33], for example, shows that an error in the determination of the elastic wave speed of just 1% significantly changes the shape of the dynamic stress-strain curve. Hence, the properties of the applied high-strength aluminium alloy need to be determined carefully from calibration experiments with the modified SHPB setup.

First the material density,  $\rho$ , is determined from the two striker bars at hand using their respective dimensions and weight. The average of both calculated densities, equalling  $2823.5 \text{ kg m}^{-3}$  and  $2823.8 \text{ kg m}^{-3}$ , is given in Table 2.

Next, the elastic wave speed,  $C_0$ , is found. In [28] a procedure is described that requires the determination of the time interval between the incident and reflected pulses. However, the reading of the times is mainly dependent on the experimenters' judgement and thus often associated with some errors. Therefore,

Table 2: The experimentally calibrated material properties of the high-strength aluminium alloy used for the bars and the tube.

Density, $\rho$ [kg m <sup>-3</sup> ]	Elastic wave speed, $C_0$ [ms <sup>-1</sup> ]	Young's modulus, $E$ [GPa]
2823.6	5086.4	73.051

an alternative method utilising the longitudinal resonance phenomena of the incident bar is employed [34]. Considering a cylindrical bar of length  $\ell$ , allowed to move freely at both ends, the natural frequencies in units Hertz,  $f_n$ , can be determined from:

$$f_n = \frac{\omega_n}{2\pi} = \frac{nC_0}{2\ell} \quad (n = 0, 1, 2, \dots) \quad (5)$$

where  $\omega_n$  are the natural frequencies of the cylindrical bar in units radian. From the natural frequencies and the lengths of a bar, the material's elastic wave speed can be determined using Eq. (5).

The natural frequencies of the incident bar are found experimentally. In total, ten experiments have been conducted, where the 500 mm striker bar was launched on the incident bar with a velocity of around 3.8 m s<sup>-1</sup>. A representative signal from one of these tests is shown in Fig. 8(a) with a present overlap starting in the rear portion of the reflected pulse, as indicated by the vertical dashed line. The overlap is caused by the short distance between the off-centred strain gauges and the impact end, but has no further influence on the determination of  $C_0$ . For the extraction of the natural frequencies, each signal has been converted into the frequency domain using a Fourier transformation, as exemplified in Fig. 8(b). Here, each peak defines a natural frequency of the bar, and the first and highest corresponds to the first natural frequency, i.e.  $f_1$ , that is used to calculate the elastic wave speed with Eq. (5). The equation also requires the length of the incident bar to be known. However, as the cross-section of the bar is varying due to the mounted impact end and load ring, the bar can not be considered purely cylindrical anymore; hence the actual length may not match the measured natural frequencies. Therefore, a characteristic bar length was found from an explicit FE-model of the experiment in which  $C_0$  is known and was set to the value given in Table 1. Only the interaction between the striker bar and the incident bar was modelled and axisymmetric conditions were applied using the four-node axisymmetric displacement element with reduced integration (CAX4R in ABAQUS). Element sizes and contact properties were chosen according to the FE-model described in Sec. 2.1. The strains were read at the same location as measured in the experiments and the data is plotted in Fig. 8(c) together with the appertaining Fourier transformation in (d). With the first natural frequency  $f_{1,num} = 1205.0$  Hz and  $C_0$  from Table 1, a characteristic bar length  $\bar{\ell} = 2.0857$  m results from Eq. (5), which is used to determine the elastic wave speed from the experiments. The average of  $C_0$  from the ten experiments carried out is given in Table 2, with a 95 % confidence interval of  $\pm 2.55$  m s<sup>-1</sup>.

Finally, the Young's modulus,  $E$ , can be determined from the relationship given in Eq. (2), and the result is also found in

Table 2.

### 3.3.2. Alignment of the bar/tube system

A good bar/tube system alignment is a prerequisite to obtaining reliable and precise measurements for material characterisation. It is checked by looking at the shape of the incident pulse. If the alignment between the striker and the incident bar is good, the incident pulse will have an analytically predictable trapezoidal profile with a clean baseline. Contrary, if a good alignment is not established, the incident pulse will be distorted and thus disturbing the measurements; see examples in Chen and Song [28].

An unshaped incident pulse from an experiment with the 500 mm striker bar impacting the incident bar at  $v_{st} = 6.13$  m s<sup>-1</sup> is seen in Fig. 9 and compared to the analytical expression given by Eq. (3b). Additionally, an incident pulse predicted by the previously mentioned axisymmetric FE-model with material properties as in Table 2 is shown, as it can be considered perfectly aligned and thus provides a good check of the actual alignment. Here, the numerical incident pulse was fitted to the experimental by introducing an imperfection in the form of a small gap of 0.11 mm between the parts representing the impact end and the incident bar. Furthermore, the material stiffness was reduced around the tie constraint established between the two parts to represent the stiffness of the threaded connection that was tightened by hand only.

The incident pulse has a clear baseline without any distortion that furthermore coincides with Eq. (3b). Also, the data agree satisfactory with the prediction from the FE-model. Hence, a good alignment between the striker and the incident bar can be concluded. Since the transmission tube cannot be put in direct contact with the incident bar, as is the case for a transmission bar in a traditional SHPB design, the alignment between them is challenging to verify. Therefore, it is assumed that the precision of the PTFE bearings used to hold the bar axially in place inside the tube is sufficient to pass on the good alignment established between the striker and the incident bar.

### 3.4. Pulse shaping

In conventional SHPB experiments, the shape of the incident pulse is trapezoidal with high-frequency oscillations in the plateau, as also evident from Fig. 9. However, when testing brittle materials like glass, and especially in bending, this pulse needs to be controlled carefully to obtain a constant strain rate and to eliminate these high-frequency components that otherwise may cause the flat sample to vibrate. Usually, this is done with a thin, ductile metal disc, also called a 'pulse shaper', placed on the impact end. Such disc can vary in thickness, diameter, and material properties to obtain the desired pulse shape. As glass undergoes small elastic strains up to fracture (without following plastic deformation), a slow ramp pulse is aimed at that corresponds to the material response [35]. Thereby the desired constant strain rate can be achieved whilst securing that enough time is available to build up a dynamic force equilibrium.

It is a commonly seen practise to use copper for the pulse shaper [21, 24, 25, 36–38]. Since the material has been shown

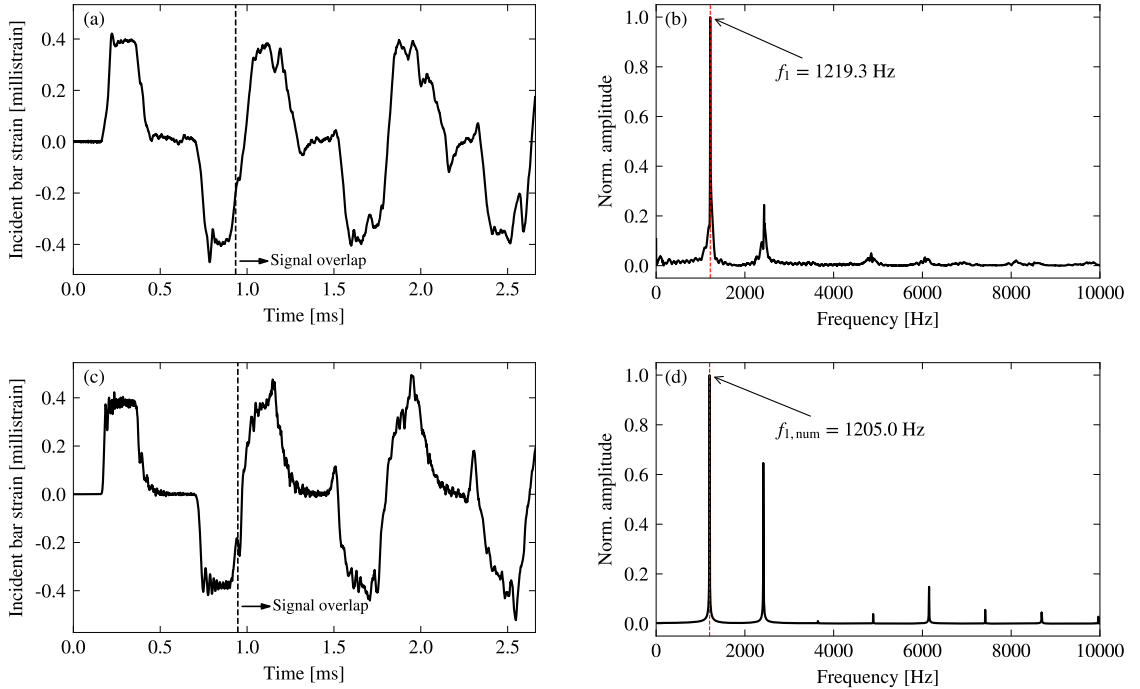


Figure 8: A set of incident bar signals and corresponding Fourier transformations employed to determine the elastic wave speed,  $C_0$ , of the bar/tube material: (a) and (b) are data from a representative experiment with a 500 mm striker bar launched at approx.  $3.8 \text{ m s}^{-1}$ , whereas (c) and (d) are numerically (FEM) generated data for similar conditions as in the experiments.

to perform well, it was also employed in this work to shape the incident pulse. A commercial available Cu-DHP copper was chosen, and the final pulse shaper geometry was determined from the procedure described in Frew et al. [37] resulting in a  $\varnothing 3.6 \text{ mm} \times 1.0 \text{ mm}$  disc. The as-received pulse shapers were heated for approx. 2 h at  $500 \text{ }^\circ\text{C}$  to obtain annealed conditions.

### 3.5. High-speed cameras

The modified SHPB setup, as described in Sec. 2, allows an unobstructed view of the tensile surface of the glass sample. Hence, the use of high-speed cameras and DIC measurements is obvious for the assessment of fracture processes and displacements/strains. For that, two Phantom v2512 ultrahigh-speed cameras equipped with 100 mm macro lenses were placed 70 cm apart from the glass sample with an angle of approx.  $20^\circ$  to each other; see Fig. 6. The right camera (CAM R) was set as 'master' whereas the left (CAM L) was the 'slave'. An optimal image resolution, capturing sufficient details, was found at  $256 \times 256 \text{ pixels}^2$ , resulting in a maximum frame rate of 200,000 fps for each camera. In experiments where DIC measurements has been deselected, the acquisition rate was doubled by delaying CAM L with  $2.5 \mu\text{s}$  (alternating image acquisition), which is otherwise only possible by reducing the image resolution. During testing, sufficient lightening was secured with a single white LED lamp (MultiLED LT, GS Vitec). Further details about the

application of the cameras related to DIC is provided along with the results presented and discussed in Sec. 4.2.

## 4. Results and discussion

The results presented here are only intended as proof of concept and are not considered complete for the investigation of the glass strength. In total, data from two similar experiments are provided. One is used to showcase the determination of a sample's flexural strength and the fracture assessment, whereas the other demonstrates the application of stereo-DIC measurements.

### 4.1. Determination of the flexural strength

The determination of a sample's equibiaxial flexural strength is based on the three pulses identified in the strains propagating in the bar and the tube generated from the impact of the striker bar: the incident pulse,  $\epsilon_i$ , the reflected pulse,  $\epsilon_r$ , and the transmitted pulse,  $\epsilon_t$ . Fig. 10(a) shows the measured signals from an experiment on a 3.1 mm-thick glass sample where the 500 mm-long striker bar was launched at  $v_{st} \approx 6.0 \text{ m s}^{-1}$ . Here, the incident pulse is shaped with a copper disc, as explained in Sec. 3.4, ensuring a nearly constant loading rate up to fracture. Essential in such an experiment is achieving a dynamic stress/force equilibrium at the sample's surfaces to characterise

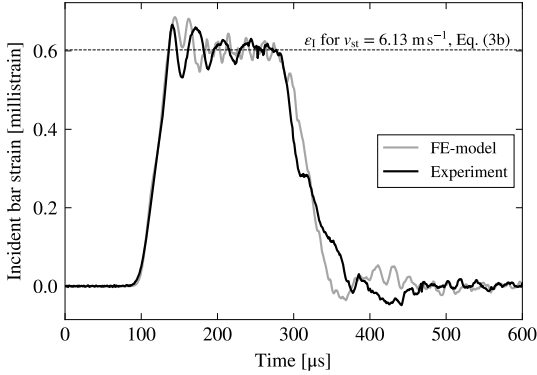


Figure 9: An unshaped incident pulse from an experiment with the 500 mm striker bar launched at  $v_{st} = 6.13 \text{ m s}^{-1}$  compared to Eq. (3b) and results from an FE-model.

the material. Assuming that the measured surface strains propagate uniformly over the entire cross-section of the bar and the tube, the resulting forces at the loading side,  $F_{LR}$ , and supporting side,  $F_{SR}$ , can be determined as follows:

$$F_{LR} = EA_{IB} (\varepsilon_i + \varepsilon_r) \quad (6a)$$

$$F_{SR} = EA_{TT} \varepsilon_t \quad (6b)$$

where  $E$  is the Young's modulus of the bar/tube material (see Table 2), and  $A_{IB}$  and  $A_{TT}$  are the cross-sectional areas of the incident bar and the transmission tube, respectively.

The resulting force histories are compared in Fig. 10(b). An overall good agreement is seen between the two curves  $F_{LR}$  and  $F_{SR}$ , indicating a dynamic force equilibrium, i.e.  $F_{LR} \cong F_{SR}$ . However, some minor oscillations are present in the force history for the loading side. As they do not appear on the supporting side, they are likely to have been caused by stress wave reflections in the load ring section, which did not influence the loading of the sample but only the reflected pulse. This was confirmed by a strain measurement performed directly on a glass sample, not indicating any oscillations in the loading. Further, comparing the signal amplitudes of the incident and reflected pulse in Fig. 10(a), one sees that these are similar magnitudes indicating a weak sample that resulted in a low force amplitude relative to the incident pulse. As the loading of the sample is determined by adding together the incident and reflected pulse (with opposite signs), possible signal noise caused by the modifications in the incident bar might have been amplified due to the weak sample explaining the observed oscillations.

Returning to Fig. 10(b) and looking at the peak forces, the ratio of the force difference between the sample's surfaces to the mean force within the sample is calculated to be 2%, which is below the threshold of 5% required to determine dynamic force equilibrium [39]. Also, it becomes evident that the signal overlap in the rear part of the reflected pulse, as indicated in

(a), does not influence the force determination as it happens after the sample has failed. However, if a longer ramp pulse is required for a different test condition, such as investigating another material or sample geometry, the overlap might disturb the measurements. In that case, an extended incident bar is to be used to increase the distance to the strain gauges from both ends of the bar.

As soon as dynamic force equilibrium is established and a failure load is recorded, the equibiaxial flexural strength of the sample can be calculated using plate bending theory [40]:

$$\sigma_f = \frac{3F}{2\pi h^2} \left[ (1-\nu) \frac{D_S^2 - D_L^2}{2D^2} + (1+\nu) \ln \frac{D_S}{D_L} \right] \quad (7)$$

where  $F$  is the recorded peak load,  $h$  is the sample thickness,  $D_S$  is the contact diameter of the support ring,  $D_L$  is the contact diameter of the load ring,  $D$  is the sample diameter, and  $\nu$  is Poisson's ratio of the sample material. However, Eq. (7) assumes that the failure originates within the load ring where maximum stresses are present. If the failure occurs outside, the test must be rejected, or strength is determined from an FE-model using the exact failure origin location and the principal stress distribution as shown in Fig. 3(b). Hence, in each experiment, the fracture is assessed through high-speed images, as exemplified in Fig. 11(a)-(f) where the time elapsed between each image equals  $2.5 \mu\text{s}$ . In this example, it is clearly seen from Fig. 11(b) that failure originates within the load ring (the black dot/shadow also referred to as *caustics*, see e.g. Refs. [41, 42]) and from there develops into a radial fracture pattern, certainly indicating a bending-induced failure.

In dynamic material characterisation, strength is usually associated with a loading rate [5]. An estimate of it using the method of least squares is drawn in Fig. 10(b) where the determined slope,  $\dot{F}$ , is based on  $F_{SR}$  ranging between  $0.4 \cdot \max(F_{SR})$  and  $\max(F_{SR})$ . The linear fit results in  $R^2 = 0.98$ , indicating that a constant loading rate could be assured in the major part of the loading.

#### 4.2. Deflection measurements with stereo digital image correlation (stereo-DIC)

In addition to the fracture assessment, the unhindered view on the sample's tensile surface surrounded by the support ring was used in a second experiment to further detail the glass's bending behaviour during the rapid loading by applying stereo-DIC. Prior testing, the sample was spray painted with white (grounding) and black (speckles) chalk painting to create a unique surface. During testing, images of the sample were captured with two synchronised high-speed cameras, as described in Sec. 3.5, each equipped with a 100 mm macro lens. All the DIC hardware parameters are summarised in Table 3. The correlation of the images was performed with the software GOM Correlate Professional 2019, and the related analysis parameters are listed in Table 4.

In total, 63 images have been extracted for the analysis of the sample's out-of-plane displacement. The signals from the strain gauges on the incident bar and the transmission tube were

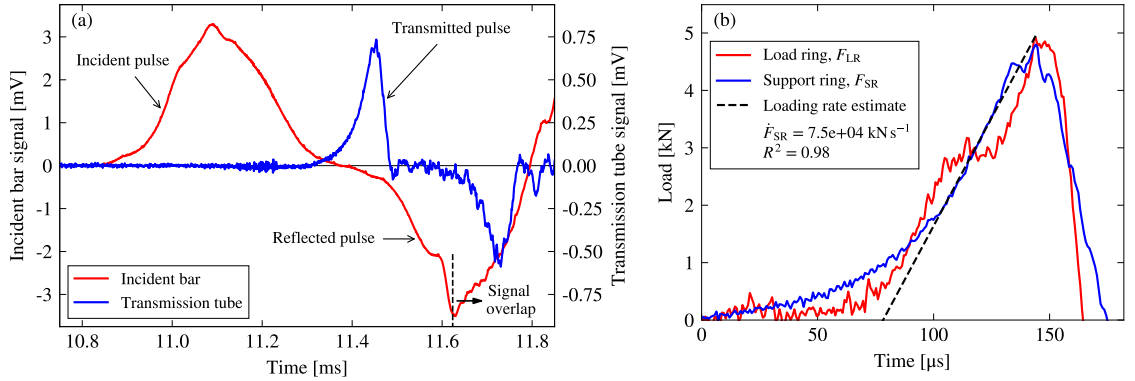


Figure 10: Recorded signals (unconditioned) on the incident bar and the transmission tube from an experiment on a 3.1 mm-thick glass sample where  $v_{st} \approx 6.0 \text{ m s}^{-1}$  (a) and the appertaining dynamic force equilibrium check with a loading rate estimate (b).

Table 3: DIC hardware parameters.

Camera	Phantom v2512 (ultrahigh-speed camera)
Image resolution	$256 \times 256 \text{ pixels}^2$
Lens	Carl Zeiss 100mm f/2 Makro-Planar T* 2/100
Aperture	f/2.0
Field-of-view (FOV)	$35 \times 35 \text{ mm}^2$
Image scale	7.3 pixels/mm
Image acquisition rate	200,000 fps
Exposure time	0.6 μs
Stand-off distance	~70 cm
Patterning technique	White (grounding) and black (speckles) chalk spray painting
Pattern feature size (approx.)	3-4 pixels

Table 4: DIC analysis parameters.

DIC software	GOM Correlate Professional 2019
Facet size	$15 \times 15 \text{ pixels}^2$
Point distance	10 pixels
Intersection deviation	0.3 pixels
Interpolation	Bi-cubic
Calibration deviation	0.020 pixels
Scale deviation	0.0006 mm
Camera angle	$20.094^\circ$

recorded synchronised with the image acquisition to relate measured deflections with the applied load more reliably. However, these signals were recorded before and after the sample fractured; hence a time shift is present between the acquired images and the force histories. Therefore, an additional experiment with a sample equipped with a centrally placed strain gauge was conducted to determine when the glass gets loaded relative to the signals measured on the bar and the tube. From that, a shift of 305 μs was found between the incident bar signal and the glass, whereas it is 150 μs for the transmission tube signal. Since it previously is shown that some minor oscillations were present in the force history on the loading side, only the recorded force history on the supporting side,  $F_{SR}$ , is used in the following analysis knowing that a dynamic force equilibrium was established. The force history for the showcased DIC measurement is plotted in Fig. 12. With the determined time shift of 150 μs, corresponding to a shift of 30 images, the acquired images have been matched to the different load stages indicated by the red markers in the figure. Out of the 63 images, around 30 images

define the loading of the sample up to the peak load, inferring a sufficient high temporal resolution in the DIC measurement.

Deflection measurements were performed on a surface constructed of 486 points at which data were extracted. The surface is plotted in Fig. 13(a) together with the approximate load ring location. A section going through the surface centre, drawn by the red line, was also used for data extraction and analysis. An example of a full-field out-of-plane displacement measurement,  $dZ$ , is provided in Fig. 13(b), showing the deflection state at load stage 52 (just before the peak load), i.e.  $F = 5.172 \text{ kN}$  according to Fig. 12, relative to stage 1 where  $dZ$  was set to 0.0 mm. The contour plot clearly shows that the sample was subjected to an equibiaxial symmetrical bending with a peak deflection located at the centre that is found to equal  $-0.300 \text{ mm}$ .

To further quantify the sample's undergone deflection, measurements for additional load stages (36, 40, 44 and 48) have been extracted along the chosen section that goes through 50 points on the surface. The measurements are shown in Fig. 14 together with load stage 52, and compared with an analytical plate bending solution using  $h = 3.1 \text{ mm}$ ,  $E = 70 \text{ GPa}$ , and  $\nu = 0.23$ ; see derivation in Appendix A.

As expected, the deflection increases with load. Also, a good agreement is seen between the measurements and the analytical predictions that, in this regard, assume rate insensitive material properties. The minor irregularities observed are likely due to image noise, which is usually caused by the camera sensors,

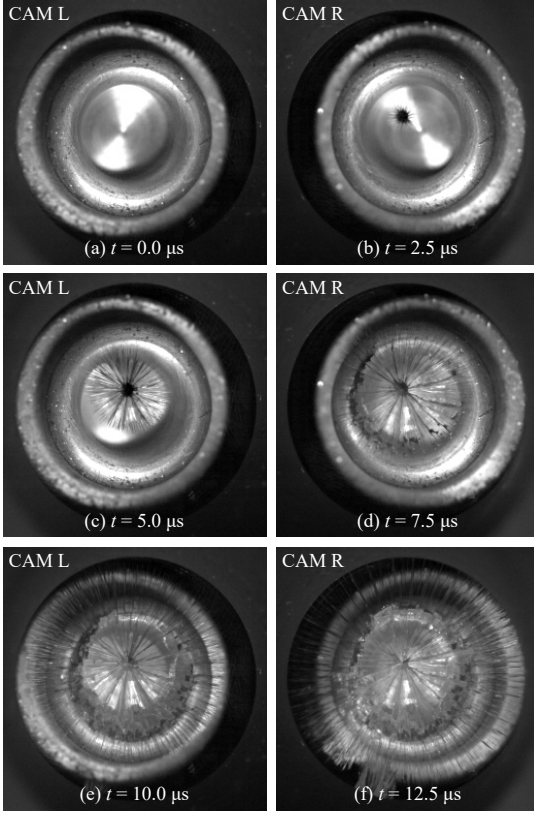


Figure 11: A series of high-speed recordings (from the same experiment as in Fig. 10) capturing the fracture process of a glass sample loaded dynamically in the ring-on-ring test configuration. On the images, the load ring is visible. The times stated indicate the intervals between the individual images. ( $2\times$  Phantom v2512 high-speed cameras, image acquisition rate 200,000 fps with a 2.5  $\mu$ s frame delay on CAM L, exposure time 0.6  $\mu$ s, resolution  $256 \times 256$  pixels $^2$ )

the interpolation algorithm employed in the digital image correlation, and the structure of the speckle pattern [43]. However, these are not disturbing the overall outcome of the stereo-DIC measurement that has delivered satisfactory results. Since glass is considered linear elastic and brittle and therefore incapable of redistributing stresses, capturing information regarding crack formations with DIC is very limited. Hence, the most reliable data determining, e.g. the material stiffness, are acquired on the loading path up to fracture.

## 5. Conclusions

A successful design of a modified split-Hopkinson pressure bar was presented. The modifications enabled the application of high-speed cameras for fracture assessment and stereo digital image correlation (stereo-DIC) measurements in an equibiaxial flexural test configuration. A significant part of a sample's tensile surface (around 54 %) were made visible by converting

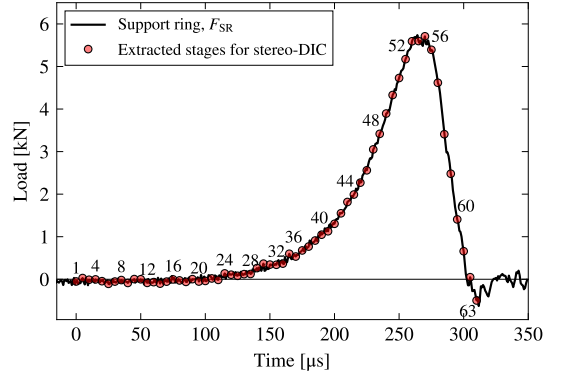


Figure 12: Recorded force history on the supporting side,  $F_{SR}$ , and the load stages at which images for the stereo-DIC were extracted.

the traditional transmission bar into a tube through which the incident bar passes. The load ring was mounted to the incident bar and the support ring with a conical through-going hole to the transmission tube.

The novel design was verified by two identical experiments where glass samples with the dimensions  $\varnothing 45$  mm  $\times$  3.1 mm were tested at high loading rates (approx.  $7.5 \cdot 10^4$  kN s $^{-1}$ ). The first experiment concluded that a dynamic force equilibrium could be established using a properly designed copper disc as a pulse shaper. Here, the ratio of the peak force difference between the sample's surfaces to the mean peak force within the sample was found to equal 2%. Furthermore, this experiment successfully demonstrated the usage of two Phantom v2512 high-speed cameras for fracture assessment.

However, based on the data presented, two significant challenges with the modified SHPB setup were identified that are important to consider in future designs. One was a present noise in the incident bar signal explained by the modifications in the bar, which due to the weak glass sample (low force amplitude) got amplified when adding together the incident and reflected pulse. The other was an overlapping signal in the rear part of the reflected pulse, which did not disturb the measurements presented here, but can be prevented by extending the incident bar for other test conditions.

The second experiment demonstrated with success the application of stereo-DIC for non-contact out-of-plane displacement measurements using GOM Correlate Professional 2019. With an image acquisition rate of 200,000 fps detailed information about the sample's deflection could be measured every 5  $\mu$ s up to fracture. Also, the measured out-of-plane displacements for five chosen load stages agreed satisfactory with an analytical plate bending solution, in which rate insensitive material properties were assumed.

## CRediT authorship contribution statement

**Martin J. Meyland:** Conceptualization, Methodology, Validation, Formal analysis, Investigation, Resources, Writing –

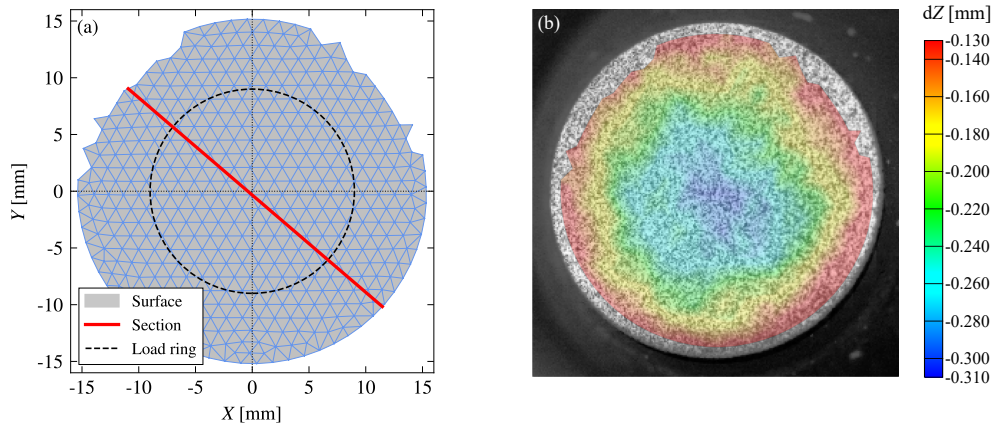


Figure 13: In (a), the surface component and a section through it created by the stereo-DIC using images of the speckled glass sample. In (b), an example of a full-field out-of-plane displacement measurement corresponding to load stage 52 (see Fig. 12).

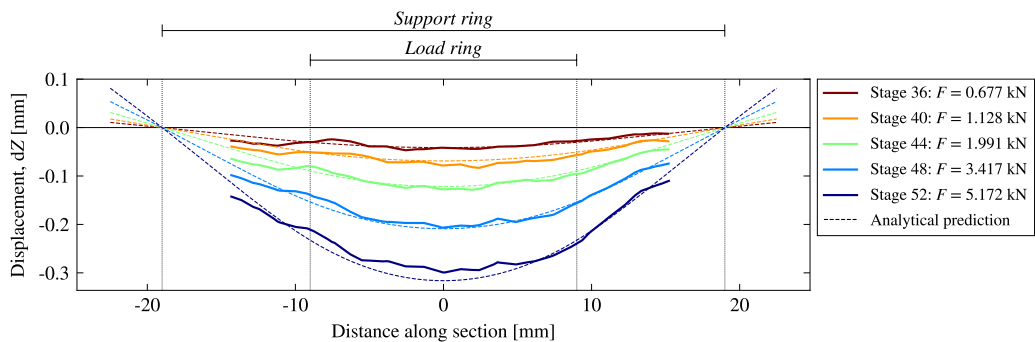


Figure 14: Out-of-plane displacements, measured with stereo-DIC, along the section shown in Fig. 13(a) for five different load stages compared with an analytical prediction.

Original Draft, Writing – Review & Editing, Visualization, Project administration, Funding acquisition. **Rasmus N. W. Eriksen:** Methodology, Writing – Review & Editing, Supervision. **Jens H. Nielsen:** Conceptualization, Methodology, Writing – Review & Editing, Supervision, Project administration, Funding acquisition.

Private & Public Buildings East. Also, the authors are truly grateful for the funding of the experimental setup received by Rambøll Fonden [grant No. 2019-090], the laboratories at DTU Civil Engineering, and the manufacturer of the setup AVOS A/S by Anders Vølund, Kalundborg, Denmark.

### Declaration of competing interest

The authors declare that they have no known competing financial interests or personal relationships that could have appeared to influence the work reported in this paper.

### Acknowledgements

The first author gratefully acknowledges funding for his PhD project provided by the Innovation Fund Denmark (IFD) [grant No. 8053-00088B], Rambøll Fonden [grant No. 2018-51], and the Danish engineering consultancy Rambøll Denmark A/S,

## Appendix A. Analytical plate bending deflection in a ring-on-ring test

The analytical derivation of the symmetrical bending of a circular plate describing the ring-on-ring test is presented hereinafter. It is based on the standard solution for a concentrically loaded, simply supported circular plate derived by Timoshenko and Woinowsky-Krieger [40]. The plate boundary conditions we are looking for are sketched in Fig. A.1(a), where the supports are moved toward the centre resulting in an overhanging plate edge. Here, the radius to the applied load,  $F$ , is denoted  $b_1$  and the radius to the support  $b_2$ . The plate itself has a radius of  $a$ .

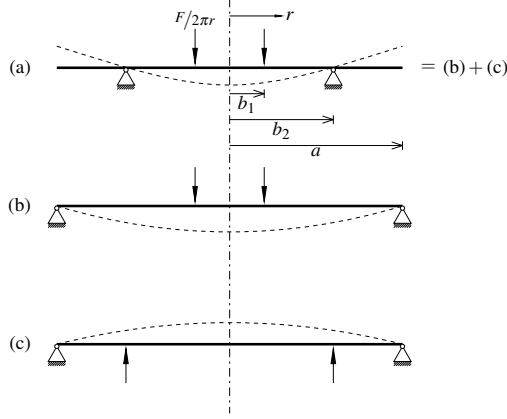


Figure A.1: Schematic representation of the symmetrical bending of a circular plate: (a) plate bending as in the ring-on-ring test, and (b) + (c) plate bending configurations that combined results in (a) and for each of which there exists a standard solution.

Assuming a linear elastic material and small deflections, a solution can be found using the principles of superposition, where the deflection of the 'standard' plate in Fig. A.1(b) is added to the deflection of another 'standard' plate as in (c). Thereby the reaction forces at the plate edges are cancelled out, and only forces as in Fig. A.1(a) are governing. To nullify the deflection at the supports in (a), the deflection at  $r = b_2$  resulting from the superposition of (b) and (c) must be subtracted. The final derived plate deflection,  $\delta(r)$ , describing the ring-on-ring test is given by Eq. (A.1):

$$\delta(r) = \frac{3F(1-\nu^2)}{2\pi E h^3} \begin{cases} (b_1^2 + r^2) \left[ \ln \frac{b_1}{b_2} + \frac{b_2^2 - b_1^2}{b_1^2 + r^2} \left( 1 + \frac{(b_2^2 - r^2)(1-\nu)}{2(1+\nu)a^2} \right) \right] & \text{for } 0 \leq r \leq b_1 \\ (b_1^2 + r^2) \left[ \ln \frac{r}{b_2} + \frac{b_2^2 - r^2}{b_1^2 + r^2} \left( 1 + \frac{(b_2^2 - b_1^2)(1-\nu)}{2(1+\nu)a^2} \right) \right] & \text{for } b_1 < r \leq b_2 \\ (b_2^2 - b_1^2) \left[ \ln \frac{b_2}{r} + \frac{(b_2^2 - r^2)(1-\nu)}{2(1+\nu)a^2} \right] & \text{for } b_2 < r \leq a \end{cases} \quad (\text{A.1})$$

where  $h$  is the plate thickness, and  $E$  and  $\nu$  are Young's modulus and Poisson's ratio of the plate material, respectively.

## References

- [1] Armstrong, R.W., Walley, S.M.. High strain rate properties of metals and alloys. *Int Mater Rev* 2008;53(3):105–128. doi:10.1179/174328008X277795.
- [2] Bischoff, P.H., Perry, S.H.. Compressive behaviour of concrete at high strain rates. *Mater Struct* 1991;24(6):425–450. doi:10.1007/BF02472016.
- [3] Zhang, Q.B., Zhao, J.. A Review of Dynamic Experimental Techniques and Mechanical Behaviour of Rock Materials. *Rock Mech Rock Eng* 2014;47(4):1411–1478. doi:10.1007/s00603-013-0463-y.
- [4] Polocoser, T., Kasal, B., Stöckel, F.. State-of-the-art: intermediate and high strain rate testing of solid wood. *Wood Sci Technol* 2017;51(6):1479–1534. doi:10.1007/s00226-017-0925-6.
- [5] Meyland, M.J., Nielsen, J.H., Kocer, C.. Tensile behaviour of soda-lime-silica glass and the significance of load duration – A literature review. *J Build Eng* 2021;44(December):102966. doi:10.1016/j.jobe.2021.102966.
- [6] Hopkinson, J.. On the rupture of iron wire by a blow. *Proc Lit Philos Soc Manchester* 1872;1:40–45.
- [7] Hopkinson, B.. The effects of momentary stresses in metals. *Proc R Soc London* 1905;74(497):498–506.
- [8] Hopkinson, B.. A Method of Measuring the Pressure Produced in the Detonation of High Explosives or by the Impact of Bullets. *Philos Trans R Soc London Ser A, Contain Pap a Math or Phys Character* 1914;213:437–456.
- [9] Robertson, R.. Some properties of explosives. *J Chem Soc Trans* 1921;119:1–29. doi:10.1039/CT9211900001.
- [10] Landon, J.W., Quinney, H.. Experiments with the Hopkinson Pressure Bar. *Proc R Soc London* 1923;103(723):622–643. doi:10.1098/rspa.1923.0084.
- [11] Davies, R.M.. A Critical Study of the Hopkinson Pressure Bar. *Philos Trans R Soc A Math Phys Eng Sci* 1948;240(821):375–457. doi:10.1098/rsta.1948.0001.
- [12] Kolsky, H.. An Investigation of the Mechanical Properties of Materials at very High Rates of Loading. *Proc Phys Soc Sect B* 1949;62(11):676–700. doi:10.1088/0370-1301/62/11/302.
- [13] Nemat-Nasser, S.. Introduction to High Strain Rate Testing. In: Kuhn, H., Medlin, D., editors. *Mechanical Testing and Evaluation*; vol. 8. ASM International; 2000. p. 427–428. doi:10.31399/asm.bb.v08.a0003293.
- [14] Larcher, M., Arrigoni, M., Bedon, C., van Doormaal, J.C.A.M., Habacker, C., Hüsken, G., et al. Design of Blast-Loaded Glazing Windows and Facades: A Review of Essential Requirements towards Standardization. *Adv Civ Eng* 2016;2016:1–14. doi:10.1155/2016/2604232.
- [15] Zhang, X., Hao, H.. The response of glass window systems to blast loadings: An overview. *Int J Prot Struct* 2016;7(1):123–154. doi:10.1177/2041419615626061.
- [16] Pelfrene, J.. Numerical Analysis of the Post-Fracture Response of Laminated Glass under Impact and Blast Loading. PhD Thesis; Ghent University, Belgium; 2016.
- [17] Forquin, P.. Brittle materials at high-loading rates: an open area of research. *Philos Trans R Soc A Math Phys Eng Sci* 2017;375(2085):20160436. doi:10.1098/rsta.2016.0436.
- [18] Zhang, X., Bedon, C.. Vulnerability and Protection of Glass Windows and Facades under Blast: Experiments, Methods and Current Trends. *Int J Struct Glas Adv Mater Res* 2017;1(2):10–23. doi:10.3844/sgamrsp.2017.10.23.
- [19] Peroni, M., Solomos, G., Pizzinato, V., Larcher, M.. Experimental Investigation of High Strain-Rate Behaviour of Glass. *Appl Mech Mater* 2011;82:63–68. doi:10.4028/www.scientific.net/AMM.82.63.
- [20] König, C.. Dehnratenabhängigkeit mechanischer Werkstoffkennwerte von Kalk-Natronsilicatglas. PhD Thesis; Technischen Universität Carolo-Wilhelmina zu Braunschweig, Germany; 2012.
- [21] Zhang, X., Zou, Y., Hao, H., Li, X., Ma, G., Liu, K.. Laboratory Test on Dynamic Material Properties of Annealed Float Glass. *Int J Prot Struct* 2012;3(4):407–430. doi:10.1260/2041-4196.3.4.407.
- [22] Meyland, M.J., Bønding, C.K.T., Eriksen, R.N.W., Nielsen, J.H.. An experimental investigation of the flexural strength of soda-lime-silica glass at high loading rates. *Glas Struct Eng* 2019;4(2):175–183. doi:10.1007/s40940-018-0089-2.
- [23] Cheng, M., Chen, W., Sridhar, K.R.. Experimental Method for a Dynamic Biaxial Flexural Strength Test of Thin Ceramic Substrates. *J Am Ceram Soc* 2002;85(5):1203–1209. doi:10.1111/j.1151-2916.2002.tb00246.x.
- [24] Nie, X., Chen, W.W., Wereszczak, A.A., Templeton, D.W.. Effect of Loading Rate and Surface Conditions on the Flexural Strength of Borosilicate Glass. *J Am Ceram Soc* 2009;92(6):1287–1295. doi:10.1111/j.1551-2916.2009.03019.x. 1204. 3107.
- [25] Nie, X., Chen, W.W., Templeton, D.W.. Dynamic ring-on-ring equibiaxial flexural strength of borosilicate glass. *Int J Appl Ceram Technol* 2010;7(5):616–624. doi:10.1111/j.1744-7402.2010.02508.x.
- [26] Nie, X., Chen, W.W.. Dynamic Equibiaxial Flexural Strength of Borosilicate Glass at High Temperatures. *Exp Mech* 2012;52(2):135–143. doi:10.1007/s11340-011-9549-1.
- [27] Hild, F., Bouterf, A., Forquin, P., Roux, S.. On the Use of Digital Image Correlation for the Analysis of the Dynamic Behavior of Materials. In: Tsuji, K., editor. *The Micro-World Observed by Ultra High-Speed Cameras*. Cham: Springer International Publishing; 2018. p. 185–206. doi:10.1007/978-3-319-61491-5.8.
- [28] Chen, W., Song, B.. Split Hopkinson (Kolsky) Bar. *Mechanical Engineering Series*; Boston, MA: Springer US; 2011. ISBN 978-1-4419-7981-0. doi:10.1007/978-1-4419-7982-7.
- [29] ASTM C1499-15.. Standard Test Method for Monotonic Equibiaxial Flexural Strength of Advanced Ceramics at Ambient Temperature. West Conshohocken, PA: ASTM International; 2015. doi:10.1520/C1499-15.
- [30] EN 572-1:2012.. Glass in building – Basic soda lime silicate glass products – Part 1: Definitions and general physical and mechanical properties. European Standard; European Committee for Standardization (CEN); Brussels; 2012.
- [31] Meyers, M.A.. *Dynamic Behavior of Materials*. Wiley; 1994. doi:10.1002/9780470172278.
- [32] Hoffmann, K.. Applying the Wheatstone Bridge Circuit. Technical note; Hottinger Baldwin Messtechnik GmbH (HBM); Darmstadt, Germany; 2005.
- [33] Lifshitz, J., Leber, H.. Data processing in the split Hopkinson pressure bar tests. *Int J Impact Eng* 1994;15(6):723–733. doi:10.1016/0734-743X(94)90011-9.
- [34] Graff, K.F.. *Wave Motion in Elastic Solids*. Dover Publications; 1975.
- [35] Subhash, G., Ravichandran, G.. Split-Hopkinson Pressure Bar Testing of Ceramics. In: Kuhn, H., Medlin, D., editors. *Mechanical Testing and Evaluation*; vol. 8. ASM International; 2000. p. 497–504. doi:10.31399/asm.bb.v08.a0003299.
- [36] Frew, D.J., Forrestal, M.J., Chen, W.. A split hopkinson pressure bar technique to determine compressive stress-strain data for rock materials. *Exp Mech* 2001;41(1):40–46. doi:10.1007/BF02323102.
- [37] Frew, D.J., Forrestal, M.J., Chen, W.. Pulse shaping techniques for testing brittle materials with a split hopkinson pressure bar. *Exp Mech* 2002;42(1):93–106. doi:10.1007/BF02411056.
- [38] Nie, X., Chen, W.W., Sun, X., Templeton, D.W.. Dynamic Failure of Borosilicate Glass Under Compression/Shear Loading Experiments. *J Am Ceram Soc* 2007;90(8):2556–2562. doi:10.1111/j.1551-2916.2007.01819.x.
- [39] Ravichandran, G., Subhash, G.. Critical Appraisal of Limiting Strain Rates for Compression Testing of Ceramics in a Split Hopkinson Pressure Bar. *J Am Ceram Soc* 1994;77(1):263–267. doi:10.1111/j.1151-2916.1994.tb06987.x.
- [40] Timoshenko, S., Woinowsky-Krieger, S.. *Theory of plates and shells*. New York: McGraw-Hill; 2 ed.; 1959.
- [41] Rossmannith, H.P.. The method of caustics for static plane elasticity problems. *J Elast* 1982;12(2):193–200. doi:10.1007/BF00042215.
- [42] Kalthoff, J.F.. Modes of dynamic shear failure in solids. *Int J Fract* 2000;101(1-2):1–31. doi:10.1023/a:1007647800529.
- [43] Gao, Z., Xu, X., Su, Y., Zhang, Q.. Experimental analysis of image noise and interpolation bias in digital image correlation. *Opt Lasers Eng* 2016;81:46–53. doi:10.1016/j.optlaseng.2016.01.002.

**High strain rate characterisation of soda-lime-silica glass and  
the effect of residual stresses**

MEYLAND, M. J., and NIELSEN, J. H.

Accepted for publication in: *Glass Structures & Engineering* (2022)

DOI: 10.21203/rs.3.rs-1317618/v1



# High strain rate characterisation of soda-lime-silica glass and the effect of residual stresses

Martin J. Meyland · Jens H. Nielsen

Received: 24 March 2022 / Accepted: / Published online:

**Abstract** A ring-on-ring test configuration for the equibiaxial flexural testing of flat samples was integrated into a novel modified split-Hopkinson pressure bar (SHPB) setup. The established modifications enabled high-speed cameras for fracture assessment and non-contact optical deflection measurements using stereo digital image correlation (stereo-DIC). In the present paper, this setup was utilised to characterise the flexural surface strength and stiffness (Young's modulus) of circular, as-received soda-lime-silica glass samples at high strain rates. The effect of residual stresses was also studied by including thermally tempered glass samples divided into four residual stress groups. Despite the frequent application of glass products in the built environment, often post-processed into tempered or laminated glass, these investigations are still rare and thus highly demanded when designing for extreme events such as extreme weather, ballistic impacts, or blast loads. A total of 315 samples were tested at a quasi-static and a dynamic loading rate ranging from  $2.0 \text{ MPas}^{-1}$  to  $4.3 \cdot 10^6 \text{ MPas}^{-1}$ . It was found that the flexural strength of the glass across residual stress groups was strongly dependent on the applied dynamic loading rate, while the residual stresses themselves showed no significant effect on the loading rate dependence. At the dynamic loading, the strength increased between 60 and 86 %. Within the two tested loading rates, strength increased expectedly with compressive surface stress. From the stereo-DIC deflection

measurements, no change in Young's modulus with loading rate was observed.

**Keywords** Float glass · Thermally tempered glass · Flexural strength and stiffness · Dynamic material characterisation · Digital image correlation · Split-Hopkinson pressure bar

## 1 Introduction

Soda-lime-silica glass (SLSG) is a linear elastic, brittle material that exhibits time-dependent strength characteristics. Essentially, the strength is governed by surface defects that grow with time when loaded in tension as a consequence of sub-critical crack growth effects (Freiman et al. 2009). Because of the characteristic differences in surface defects, glass strength is not a pure material constant.

Frequently used in the built environment, glass is mainly considered an architectural feature that provides occupants with daylight and views while protecting against the weather. Also, the material has, due to its transparent nature, gained an increasing interest in the design of load-bearing structures (see e.g. Snijder 2004; Stein et al. 2019). Mostly being included in the outer envelope of a building, it has to resist several externally imposed loads; at times also of a more extreme character in the form of extreme weather, ballistic impacts, or blast loads (accidental and man-made). All with a considerably shorter load duration than the usual design static load assumptions.

Not considering such load cases in the glass design might have disastrous consequences. For instance, in the unfortunate event of an explosion, such as the Oklahoma City Bombing in 1995 (USA) and the Beirut Port explosion in 2020 (Lebanon), it has been shown that numerous injuries and often deaths can be attributed to flying or falling glass shards (Norville et al. 1999; Rudick and Norville 2000; Kirk et al.

---

M.J. Meyland (✉) · J.H. Nielsen  
Technical University of Denmark, Department of Civil and Mechanical Engineering, Brovej, Building 118, 2800 Kgs. Lyngby, Denmark  
E-mail: majeme@byg.dtu.dk

M.J. Meyland  
Ramboll Denmark A/S, Structures & Facade Engineering, Hannemanns Allé 53, 2300 Copenhagen S, Denmark  
E-mail: mjme@ramboll.dk

J.H. Nielsen  
E-mail: jhn@byg.dtu.dk

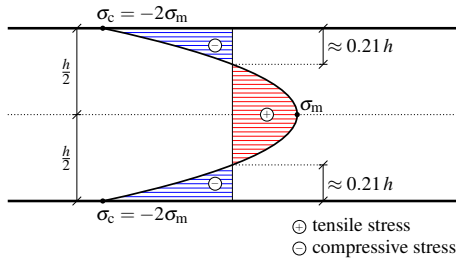


**Fig. 1** Symmetric parabolic distribution of residual stresses across the thickness of thermally tempered glass ( $\sigma_c$  is the surface stress;  $\sigma_m$  is the mid-plane stress;  $h$  is the glass thickness).

2020; Sukkariet al. 2021). Therefore, mitigating an explosion's effects is crucial. It can be partly met by improving performance of the monolithic glass. For that, several techniques exist to post-process float glass (standard flat glass, also known as 'annealed' glass), which commonly includes thermal treatment (tempering) and/or lamination.

The tempering process, which includes heating and subsequently quenching, strengthens the float glass by introducing a residual stress state with compressive stresses near the surfaces, balanced by tensile stresses in the core. Far from edges, the stress distribution can be assumed to follow a symmetrical parabola, as shown in Fig. 1. The depth of the compressive zone is both analytically and experimentally found to be reasonably good approximated by 21 % of the glass thickness (Nielsen et al. 2021). Failure of thermally tempered glass may be initiated as soon as the compressive surface stress that prevents flaws from opening (i.e. negating the time-dependency) is exceeded, allowing them to grow until the equilibrated residual stress state is disturbed sufficiently. The tempering also causes the glass to fail more safely by fragmenting in small dice due to higher amounts of strain energy release (see e.g. Nielsen et al. 2009; Nielsen and Bjarrum 2017; Pourmoghaddam et al. 2018). Further improvements, in terms of energy absorption and level of protection, can be achieved with lamination that bonds two or more glass panes together by a ductile, transparent plastic interlayer (usually polyvinyl butyral – PVB). In case of glass fracture, the interlayer can deform further, absorbing energy whilst glass fragments adhere to its surface.

The scientific literature has reported numerous studies of laminated glass under blast loading (Hooper et al. 2012; Larcher et al. 2012; Zhang et al. 2013, 2015; Kuntsche 2015; Pelfrene et al. 2016; Del Linz et al. 2017; Angelides et al. 2019; Osnes et al. 2019; Angelides et al. 2022). However, the focus was on the interlayer material and the composite interactions in the post-fracture response, while the glass characteristics were less considered at these high strain rates.

In predicting glass failure, strength is an essential parameter to assess. A recent review paper by Meyland et al. (2021c)

demonstrates a decisive strain rate sensitivity in the tensile strength of float glass and remarks a lack of data at the high strain rates, e.g. relevant for blast loading. The few experimental studies observing enhanced strength characteristics at strain rates above  $1 \text{ s}^{-1}$  ( $\approx 7 \cdot 10^4 \text{ MPas}^{-1}$ ) were performed by Peroni et al. (2011), König (2012), Zhang et al. (2012), and Meyland et al. (2019). While Peroni et al. and Zhang et al. performed diametral compression tests on cylindrical specimens in a split-Hopkinson pressure bar (SHPB) setup, König and Meyland et al. employed a high-speed universal testing machine to study flat glass in pure tension and equibiaxial bending, respectively. Also, limited data is found to report how the residual stress state in thermally tempered glass affects the tensile strength when loaded at high strain rates (König 2012; Kuntsche 2015; Förch 2019). Furthermore, little has been undertaken to investigate the stiffness of soda-lime-silica glass at various loading rates. The available data indicate that no strain rate sensitivity is present (Meyland et al. 2021c).

The flexural mechanical properties of soda-lime-silica glass, that is, surface tensile strength and stiffness, at high strain rates remains an open research topic and thus is the focus of the present paper. Both annealed and also thermally tempered glass were studied to include the effect of residual stresses. In the experiments, as-received circular flat glass samples were loaded in a small ring-on-ring test configuration arranged in a modified SHPB setup for the high strain rate tests. The modifications enabled the application of high-speed cameras for fracture assessment and non-contact out-of-plane displacement measurements using stereo digital image correlation (stereo-DIC). For tests at moderate strain rates (quasi-static loading), a universal testing machine was used with the same ring-on-ring test configuration.

## 2 Experimental details

### 2.1 Glass samples

For this study, circular annealed float glass samples of soda-lime-silica were produced with a nominal thickness of  $3 \text{ mm} \pm 0.2 \text{ mm}$  and a diameter of  $45 \text{ mm} \pm 0.5 \text{ mm}$ . After the cut-out of the samples, the manufacturer seamed the edges to remove sharp burrs and secure safe handling of them. The surfaces remained unmachined, and thus in the following, the term *as-received* will be used. Furthermore, UV light was utilised to identify and mark each sample's air-side, securing that strength tests were performed for identical surface conditions, the air-side.

The chemical elemental composition of the glass was checked using a scanning electron microscope (SEM) together with energy-dispersive X-ray spectroscopy (EDS). As expected, Table 1 shows that the measured composition (in

**Table 1** The chemical elemental composition (in oxide wt%) for the soda-lime-silica glass measured using a scanning electron microscope (SEM) together with an energy-dispersive X-ray spectroscopy (EDS) compared to the values prescribed by the European Standard EN 572-1 (2012).

[Oxide %]	SiO <sub>2</sub>	CaO	Na <sub>2</sub> O	MgO	Al <sub>2</sub> O <sub>3</sub>	Others
SEM/EDS	74.0	8.5	12.8	4.0	0.5	0.2
EN 572-1	69-74	5-14	10-16	0-6	0-3	0-5

oxide wt%) is according to the European Standard EN 572-1 (2012).

Some of the received samples were thermally tempered to include the effect of residual stresses in the high strain rate investigations. In the tempering process, the samples' tin-side was in contact with the rollers, leaving the air-side to the air. The manufacturer used a fixture with point-contacts on the glass surface that enabled the small samples to pass through the tempering process. Following the linear relationship between the mid-plane tensile stress and the cooling rate in the quenching (engine power in %), as reported by Pourmoghaddam and Schneider (2019), the tempered glass samples were ordered in four different quench levels to obtain a great variability in the study: 25 %, 50 %, 75 %, and 100 %. The achieved residual compressive surface stresses are reported in more detail in Sec. 2.1.1.

The dimensions of all samples were recorded using a digital vernier calliper. All diameters were in agreement with the ordered specifications. The measured thicknesses varied between 3.08 mm and 3.14 mm with a mean of 3.11 mm, without any influence of the tempering process being apparent. Further, the measured range show that the float glass producer utilised the upper bound of the allowable tolerance to the nominal thickness prescribed by the European Standard EN 572-2 (2012), which is opposite to what is reported by Schneider (2001). In the evaluation of experimental results presented in Sec. 3, the actual thickness of each sample is used.

### 2.1.1 Measurement of the compressive surface stress

The SCALP-05, a Scattered Light Polaroscope from Glas-Stress Ltd., Tallinn, Estonia, was used to measure the residual compressive surface stress,  $\sigma_c$ , in the glass samples. In short, the principle of the SCALP is to measure the retardation of an inclined laser beam sent through the thickness of the glass. Due to the material's photoelastic effect, the retardation of the laser beam varies with strains and thereby stresses in the plane perpendicular to the direction of the beam. A cubic function is often used to fit the retardation profile, and by differentiation, stresses are obtained following a parabolic function as sketched in Fig. 1. For more details, the reader may refer to Aben and Guillemet (1993) and Anton (2015).

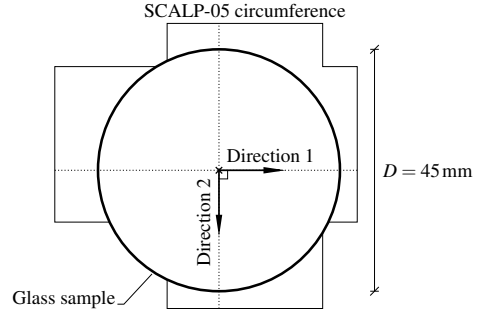


**Fig. 2** A sketch of the two directions, perpendicular to each other, used to measure the residual compressive surface stresses in the centre of the glass samples with the SCALP-05.

Using the SCALP, the derivative of the measured retardation of the laser beam,  $\delta$ , includes two stress components,  $\sigma_x$  and  $\sigma_y$  (Anton 2015):

$$\frac{1}{C} \frac{d\delta(\eta)}{d\eta} = \sigma_x - \sigma_y \cos^2 \alpha \quad (1)$$

Here,  $C$  denotes the photoelastic constant,  $\eta$  is the coordinate along the laser beam, and  $\alpha$  is the beam inclination, which in the used SCALP-05 is 72°. Performing a measurement far away from edges, one may assume an equibiaxial stress field, i.e.  $\sigma_x = \sigma_y = \sigma$ , for which Eq. (1) reduces to the following:

$$\frac{1}{C} \frac{d\delta(\eta)}{d\eta} = \sigma \sin^2 \alpha \quad (2)$$

However, since it was presumed that the thermal tempering of the small glass samples did not result in a stress field that was perfectly equibiaxial, two orthogonal measurements were required to obtain  $\sigma_x$  and  $\sigma_y$  from Eq. (1). These were chosen to originate from the sample centre on the air-side, as illustrated in Fig. 2. This provided the most accurate measurement of the surface stress due to the crossing of the laser beams at surface level. The rotation of the sample was chosen arbitrarily due to the circular geometry.

Denoting the two measurements  $\sigma_\eta$  and  $\sigma_\xi$ , a stress separation is performed by equating Eq. (2) with Eq. (1) for each of the two measurements considering orthogonality. Consequently, two analogous equations are found, which can be solved for  $\sigma_x$  and  $\sigma_y$ , resulting in:

$$\sigma_x = \frac{\sigma_\eta + \sigma_\xi \cos^2 \alpha}{1 + \cos^2 \alpha}, \quad \sigma_y = \frac{\sigma_\xi + \sigma_\eta \cos^2 \alpha}{1 + \cos^2 \alpha} \quad (3)$$

For the surface stress measurements, a photoelastic constant  $C = 3.01 \text{ TPa}^{-1}$  was used as found by Nielsen et al. (2010). To secure a good optical contact between the SCALP and the glass sample, an immersion liquid with a refractive index similar to glass was applied between the interfaces. A measurement was repeated five times in both directions, and

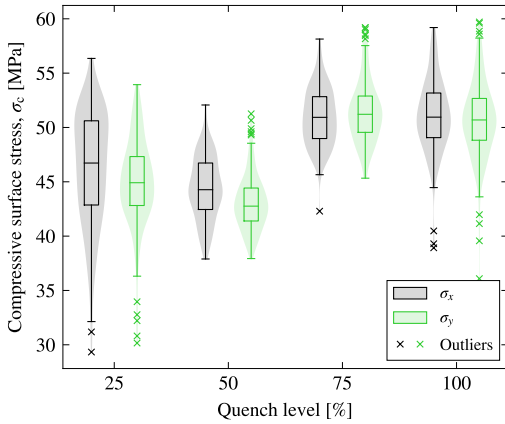


**Fig. 3** Box-plot and the distribution of the samples' measured residual compressive surface stresses for the four quench levels after stress separation with Eq. (3).

the mean was used for the stress separation with Eq. (3). The results for  $\sigma_x$  and  $\sigma_y$  measured on each glass sample's air-side (720 samples in total) are shown as box-plots in Fig. 3, together with the distribution of the data.

The measured residual compressive surface stresses vary between 30 MPa and 60 MPa. These values are lower than what is typically expected for fully tempered glass, which according to ISO 20657 (2017), should be a minimum 80 MPa. For heat-strengthened glass the values should be between 25 MPa and 52 MPa according to ISO 22509 (2020), which is covered mostly by the measured range. Furthermore, a large scatter is seen in the results for each quench level. The reason is difficult to outline since details about the tempering process other than the fixture to hold the samples were unknown to the authors. Nevertheless, some increase in compressive surface stress with quench level is evident, however, not with a linear variation as expected. From the data presented in Fig. 3, increasing the quench level from 25 % to 50 % did not have had a significant enhancing impact on the compressive surface stress. At 75 % a more significant jump is seen, and quenching with 100 % did not enhance further. The unusual tempering behaviour is presumably caused by the small sample geometry that made uniform tempering challenging. Furthermore, comparing  $\sigma_x$  and  $\sigma_y$  in the different quench levels, only a slight variation in surface stresses within a sample is present. Hence, the determination of principal stresses using a third measurement in an angle of 45° to the two other directions was not considered necessary since shear stresses in the glass samples are negligible.

The investigation of the effect of residual stresses at high strain rate loading demands less variation in the compressive surface stress, and therefore another grouping than the

**Table 2** Statistical evaluation of the minimum measured compressive surface stresses, i.e.  $\min(\sigma_x, \sigma_y)$ , in the five residual stress groups. ( $N$  is the number of samples measured; min is the minimum value; max is the maximum value;  $\bar{x}$  is the sample mean;  $s_x$  is the sample standard deviation)

	$N$	min	max	$\bar{x}$	$s_x$
	[–]	[MPa]	[MPa]	[MPa]	[MPa]
RS1	10	2.7	3.2	2.9	0.21
RS2	86	37.9	41.2	39.9	0.91
RS3	177	42.4	45.8	43.9	1.01
RS4	189	46.9	50.3	48.7	0.98
RS5	81	51.4	54.6	52.7	0.87

quench level was chosen. A minor variation was secured by dividing the thermally tempered glasses into four residual stress (RS) groups, namely RS2 to RS5, using evenly spaced intervals (linear variation between groups). The samples were selected across quench levels based on the minimum measured compressive surface stresses, i.e.  $\min(\sigma_x, \sigma_y)$ . The intervals were chosen to fall within  $\sigma_c \pm 1.7$  MPa where  $\sigma_c = [39.5, 44.0, 48.6, 53.1]$  MPa, which maximised the number of samples in each group. The residual stress group RS1 contained the annealed float glass samples. A statistical evaluation of the compressive surface stresses in each residual stress group is provided in Table 2. Data for RS1 are based on measurements on ten float glass samples; more samples support the later investigations. Usually, when designing float glass, it is considered not to have residual stresses. However, the relatively slow cooling in the annealing part of the float glass production leaves a small amount of residual stress, as shown here.

### 2.1.2 Etching

The objective of the present study is to investigate the surface tensile strength of glass. However, testing at the high loading rate caused a more significant number of samples to fail at the edge (a cause for rejection, as discussed in Sec. 3.1) compared to those tested in the universal testing machine at a moderate rate. This behaviour may be explained by the rate-induced strength enhancement, which caused higher loads at which the failure mechanisms began to compete between surface and edge flaws. Therefore, a technique was sought to enhance only the edge quality of some samples. This reduced the total number of tests required to achieve the desired minimum number of valid samples.

Since surface defects govern glass strength, an enhancing effect can be achieved by smoothening or completely removing them. This can be done by etching (see e.g. Kolli et al. 2009; Nielsen et al. 2019). In this study, an etching procedure was developed that only modified the edges without changing the as-received condition of the sample surfaces.

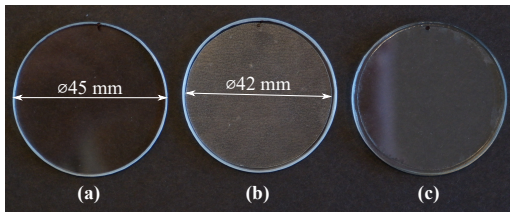


**Fig. 4** Image series of a glass sample demonstrating the sample preparation for the etching procedure: (a) the cleaned as-received glass sample, (b) an adhesive foil with a diameter of 42 mm is applied to both sample surfaces, and (c) the sample after an etching time of 30 min where a clear rim from the etching is visible.

Prior to the etching, the samples were prepared by first cleaning the surfaces and then covering them centrally using an adhesive foil with a diameter of 42 mm, only leaving approximately 1.5 mm around the edge uncovered; see Fig. 4(a) and (b). Subsequently, the prepared samples were immersed for 30 min in a 15-wt%  $\text{NH}_4\text{HF}_2$  aqueous acid solution (ammonium hydrogen fluoride). The etching produced a clear rim of removed glass (approx.  $60\ \mu\text{m}$  depth) on both sides of the samples surrounding the adhesive foil that were removed afterwards; see Fig. 4(c). From the microscope images in Fig. 5, the enhancing effect becomes more visible. Before etching, in (a), the sample edge contained small, sharp defects due to the sanding. Those have been removed or significantly blunted in (b), resulting in a strengthened edge. Thereby the rate of edge failures was reduced from 57 % to 26 %.

## 2.2 Strength test

In a previous study (Meyland et al. 2019), the flexural strength of soda-lime-silica glass was investigated using a high-speed universal testing machine. However, some limitations arose at the very high loading rates. The used load cell started ringing at some point, making reliable measurements difficult.

The present study accommodated these challenges by employing a modified SHPB setup, a well-established experimental practice for dynamic material characterisation (Chen and Song 2011). The modifications included a ring-on-ring test configuration for equibiaxial flexural loading of circular flat glass samples. This load configuration was chosen to minimise stressing of the sample's edge where more severe defects are located due to cutting, causing reduced strengths. With maximum stresses in the sample centre, the likelihood of edge failures was reduced, providing a more reliable measure of the surface tensile strength. The integration of a ring-on-ring test configuration was inspired by Nie et al. (2010) who investigated borosilicate glass at high loading rates. Here, a flat sample was sandwiched between an incident bar and a transmission bar (the original SHPB design), hiding a significant part of the sample's surfaces.

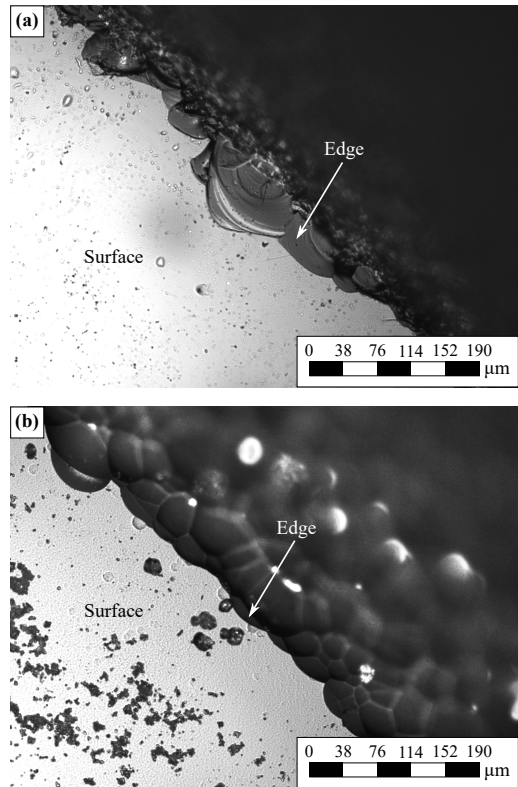


**Fig. 5** The effect of etching the sample edge with  $\text{NH}_4\text{HF}_2$  after 30 min (the microscope images are not taken at the same location): (a) before etching, and (b) after etching.

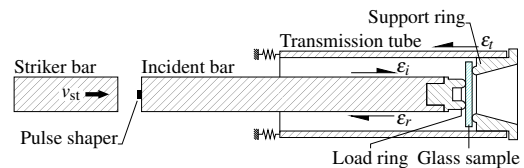


**Fig. 6** A schematic representation (cut-view) of the modified split-Hopkinson pressure bar setup employed in the present study and reported in detail in Meyland et al. (2021a).

However, when testing materials at high loading rates, the application of high-speed cameras is of interest, which in the original SHPB design is limited. Therefore, the novel SHPB setup was subjected to further modifications to ensure an unobstructed view of the sample's tensile surface by replacing the transmission bar with a tube through which the incident bar passes; see illustration in Fig. 6. All design details and the experimental techniques are reported in detail in Meyland et al. (2021a). A short outline is given here.

The introduced ring-on-ring test configuration is a pair of concentric rings that were designed according to the international Standard ASTM C1499-15 (2015). The load ring was mounted to the incident bar, and the support ring with a conical through-going hole to the transmission tube, exposing approx. 54 % of a glass sample's tensile surface. Both rings were produced with a tip radius of 2.5 mm, and their respective contact diameters were 18 mm and 38 mm. The incident bar was produced with a diameter of 30 mm and the transmission tube with an external diameter of 55 mm having a wall-thickness of 3.5 mm. All setup parts, that is, the bar, the tube, and the rings, were made of a high-strength aluminium alloy. The material properties were carefully calibrated and can be taken from Meyland et al. (2021a).

In an experiment, a 500 mm-long striker bar, with the same diameter as the incident bar, was accelerated to approx.  $6.0 \text{ ms}^{-1}$  before impacting the incident bar. A stress wave was thereby initiated that travelled towards the sample, loading it at high strain rates. Part of the wave reflected at the load ring/sample interface, whereas the rest transmitted through the sample into the tube. Consequently, three strain pulses could be identified. These are indicated by the arrows in Fig. 6 and shown as recorded strain signals in Fig. 7, measured with strain gauges attached to the bar/tube surfaces:

1. the incident pulse,  $\varepsilon_i$
2. the reflected pulse,  $\varepsilon_r$ , and
3. the transmitted pulse,  $\varepsilon_t$ .

Here, a 1 mm-thick and 3.6 mm in diameter annealed copper disc pulse shaper placed between the striker and incident bar (see Fig. 6) was used to shape the incident pulse into the desired ramp pulse. In that way, a constant stress rate of approx.  $4.3 \cdot 10^6 \text{ MPas}^{-1}$  was secured on average, providing sufficient time to build up a required dynamic force equi-

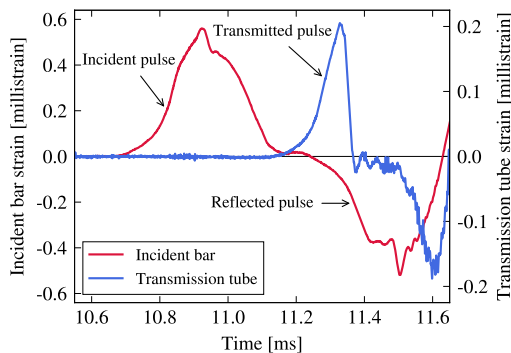


**Fig. 7** Example of recorded strain signals on the incident bar and the transmission tube from an experiment with the 500 mm-long striker bar launched at  $v_{st} \approx 6.0 \text{ ms}^{-1}$ .

librium between the load ring and support ring, as will be discussed later.

The experiments at moderate strain rates, i.e. quasi-static loading at a rate of  $2.0 \text{ MPas}^{-1}$ , were performed using a universal testing machine (Instron 8872,  $\pm 25 \text{ kN}$ ). A fixture was built to hold the same pair of concentric rings as included in the modified SHPB setup. The desired loading rate was achieved by setting the crosshead speed to approx.  $0.18 \text{ mm min}^{-1}$ . All samples were equipped with an adhesive foil on the compressive surface to retain the fractured glass in the quasi-static experiments for later assessment.

The temperature of the test environment was  $23.4 \text{ }^\circ\text{C}$  ( $\pm 0.4 \text{ }^\circ\text{C}$ ), with a relative humidity of 43.4 % ( $\pm 5.2 \text{ }%$ ).

### 2.3 High-speed imaging and non-contact deflection measurements

The design of the modified SHPB setup enabled the application of two Phantom v2512 high-speed cameras, providing additional details about the glass behaviour under high strain rate loading. The cameras equipped with 100 mm macro lenses were placed 70 cm apart from the ring-on-ring test configuration with a mutual angle of approx.  $20^\circ$  (see Fig. 8). With an image resolution of  $256 \times 256 \text{ pixels}^2$ , sufficient details were captured at a frame rate of 200,000 fps.

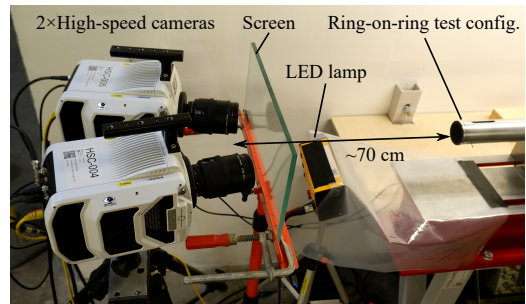


**Fig. 8** An image of the two Phantom v2512 high-speed cameras placed in a stereo setup in front of the ring-on-ring test configuration in the modified SHPB setup.

Since it was not an option in the high strain rate experiments to use adhesive foil to retain the fragmented glass samples, the fracture was assessed through high-speed images. The cameras were set to acquire images alternately by delaying one camera by  $2.5 \text{ } \mu\text{s}$ , resulting in a doubled frame rate without reducing the image resolution. From images, the failure origin was identified, necessary to determine a sample's fracture strength as further discussed in Sec. 3.1. The observed locations of failure origin could be categorised as follows for both the quasi-static and dynamic loading:

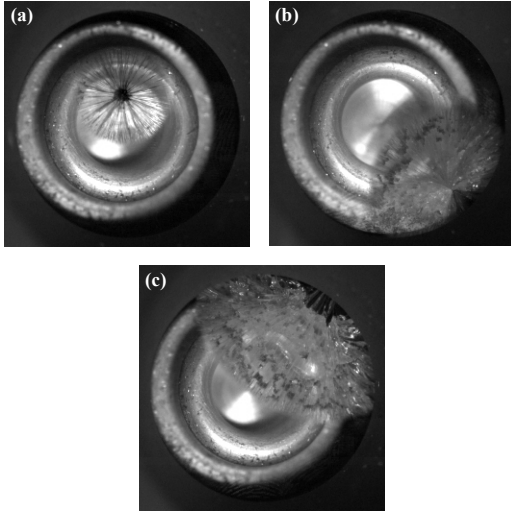


**Fig. 9** Examples of the three observed locations of failure origin captured by the use of high-speed cameras at 200,000 fps (on the images the load ring is visible): (a) within the load ring, (b) outside the load ring on the surface, and (c) edge.

- (a) within the load ring,
- (b) outside the load ring on the surface, and
- (c) edge.

Examples for each location are shown in Fig. 9(a)-(c). In (a), the failure originates within the load ring, seen as a black dot/shadow, and from there develops into a radial fracture pattern indicating a pure bending induced failure. Similar appears in (b), however, with an origin outside the load ring but still on the surface. A non-radial fracture pattern is evident in (c), where the failure originates from the sample's edge outside the support ring (not visible on the image).

Also, some samples were subjected to deflection measurements using stereo digital image correlation (stereo-DIC) with the software GOM Correlate Pro 2019. It is a non-contact measuring technique that required a unique surface on the glass, which due to its transparency, did not come naturally. Therefore, chalk spray paint was used to create a white ground with black speckles on a sample's tensile surface, having a pattern feature size of approx. 3 to 4 pixels. After a thorough calibration of the two now synchronised cameras, image pairs of the speckled sample surface were captured during the dynamic testing using an exposure time of 0.6  $\mu$ s. Further, the image acquisition was synchronised with the strain measurements in the modified SHPB setup. The subsequent analysis of the various image series was performed with parameters as listed in Table 3.

In the experiments, the strain gauges on the incident bar and the transmission tube were placed with a distance to the glass sample, which caused a time shift between the captured

**Table 3** Stereo-DIC analysis parameters.

DIC software	GOM Correlate Pro 2019
Facet size	$15 \times 15$ pixels <sup>2</sup>
Point distance	10 pixels
Intersection deviation	0.3 pixels
Interpolation	Bi-cubic
Calibration deviation	0.018 pixels
Scale deviation	0.0006 mm
Camera angle	20.2°
Measuring volume	$35 \times 35 \times 20$ mm <sup>3</sup>

sample deflection and the associated recorded force histories. In Meyland et al. (2021a), the time shift was experimentally found to equal 305  $\mu$ s between the incident bar and the glass sample, whereas it was 150  $\mu$ s for the transmission tube.

### 3 Results and discussions

The high strain rate characterisation of soda-lime-silica glass comprises an investigation of the material's flexural strength and stiffness (Young's modulus), including the effect of residual stresses. The achieved results are detailed and discussed in the following.

#### 3.1 Equibiaxial flexural strength

Equibiaxial flexural strength tests were conducted on glass samples in the five residual stress groups at two stress rates, that is, a quasi-static at 2.0 MPa s<sup>-1</sup>, and a dynamic at  $4.3 \cdot 10^6$  MPa s<sup>-1</sup>. At quasi-static loading, the applied load was directly recorded with a load cell in the universal testing machine, whereas the dynamically applied load in the modified SHPB setup was determined from strains measured on the incident bar and the transmission tube surfaces. With the three pulses identified in the strain measurements, see Fig. 7, and assuming that the strains propagated uniformly over the entire cross-section of the bar and the tube, the resulting force histories on the load ring side,  $F_{LR}$ , and support ring side,  $F_{SR}$ , can be determined as follows:

$$F_{LR} = EA_{IB} (\epsilon_i + \epsilon_r) \quad (4a)$$

and

$$F_{SR} = EA_{TT} \epsilon_t \quad (4b)$$

where  $E$  is Young's modulus of the bar/tube material, which in Meyland et al. (2021a) was found to 73.1 GPa, and  $A_{IB}$  and  $A_{TT}$  are the cross-sectional areas of the incident bar and the transmission tube, respectively.

Examples of force histories acquired at a quasi-static and a dynamic loading rate from tests on float glass samples

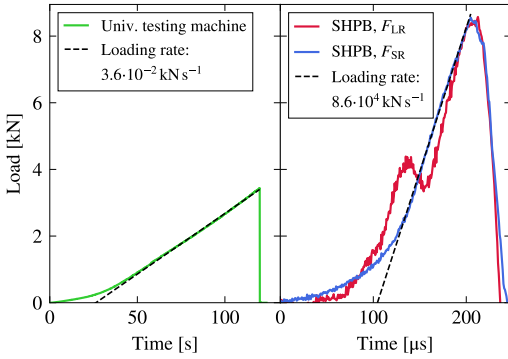


**Fig. 10** Examples of force histories achieved in the strength characterisation of annealed float glass samples (RS1). A quasi-static loading path is shown on the left, and on the right, a dynamic. In both, the loading rate estimation is exemplified.

(RS1) are given in Fig. 10. Linear loading up to fracture is evident in both, implying a constant loading rate estimated by linear regression with the least squares method. Further, the high strain rate experiments determined two force histories held against each other to check the required dynamic force equilibrium, which successfully is shown here. However, on the loading side minor oscillations are seen in the force history,  $F_{LR}$ , which presumably were caused by stress wave reflections in the ring-on-ring test configuration but did not influence the loading of the glass sample (further discussed in Meyland et al. 2021a). Since equilibrium was established in all tests, the force history on the support ring side, the most undisturbed signal, was used to determine the fracture strength of the samples.

Failure of brittle materials is often predicted by the Rankine criterion, defining that failure occurs when the maximum principal stress (principal tensile stress),  $\sigma_1$ , at any point reaches a value equal to or larger than the materials apparent tensile strength,  $\sigma_f$  (see e.g. Samuel and Weir 1999):

$$\sigma_1 \geq \sigma_f \quad (5)$$

For the glass sample, the maximum principal stresses within the load ring of the ring-on-ring test configuration, which are constant, can be determined analytically from plate bending theory (Timoshenko and Woinowsky-Krieger 1959):

$$\sigma_1 = \frac{3F}{2\pi h^2} \left[ (1-\nu) \frac{D_S^2 - D_L^2}{2D^2} + (1+\nu) \ln \frac{D_S}{D_L} \right] \quad (6)$$

Here,  $F$  is the applied load,  $h$  is the glass sample thickness,  $D$  is the sample diameter,  $D_L$  is the load ring diameter,  $D_S$  is the support ring diameter, and  $\nu$  is the Poisson's ratio of glass (0.23 according to CEN/TS 19100-1 (2021), assuming a rate-insensitivity). With the maximum applied load, i.e.

the failure load, Eq. (6) determines according to Eq. (5) the failure stress,  $\sigma_f$ , of a sample, and using a loading rate for  $F$  gives a stress rate,  $\dot{\sigma}$ . Maximum principal strains within the load ring can further be determined using the following relationship valid due to a rotationally symmetrical stress distribution:

$$\varepsilon_1 = \frac{\sigma_1}{E_g} (1-\nu) \quad (7)$$

where  $E_g$  is the glass' Young's modulus, equalling 70 GPa according to CEN/TS 19100-1 (2021) and assumed to be rate-insensitive as reported in Sec. 3.2. Eq. (7) also determines a strain rate,  $\dot{\varepsilon}$ , in principal direction by inserting a stress rate for  $\sigma_1$ .

The application of Eqs. (6) and (7) requires that failure of a sample originates within the load ring, and usually, those that fail outside are considered not valid. In the present study, all edge failures were excluded since the aim was to investigate the glass' surface tensile strength. Samples that failed between the load ring and the edge were still included as they could measure the surface tensile strength using the exact location of the failure origin, which was estimated from the fractured samples. Based on the location, failure stress and also strain rate was reduced according to the rotationally symmetric stress/strain distributions given in Fig. 11. These were determined from an axisymmetric FE-model in ABAQUS/Standard 2021 using 3-node quadratic shell elements (SAX2), and normalised with Eqs. (6) and (7), respectively. The difference seen after the load ring between the distributions of the maximum principal stresses and strains is due to the material's Poisson's ratio.

The flexural strength of the soda-lime-silica glass was determined for the samples' air-side. In each residual stress group, 30 samples were tested at each loading rate, and a

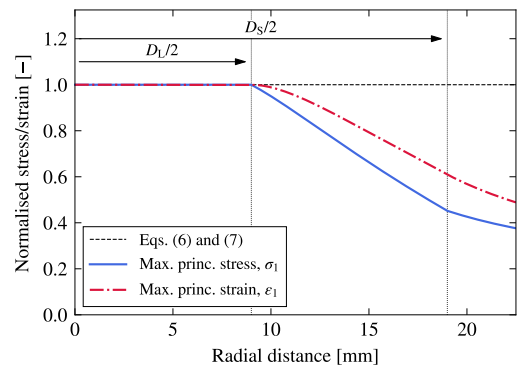


**Fig. 11** Rotationally symmetric distribution of maximum principal stresses and strains (numerically determined and normalised with Eqs. (6) and (7)) in a glass sample loaded in the ring-on-ring test configuration.

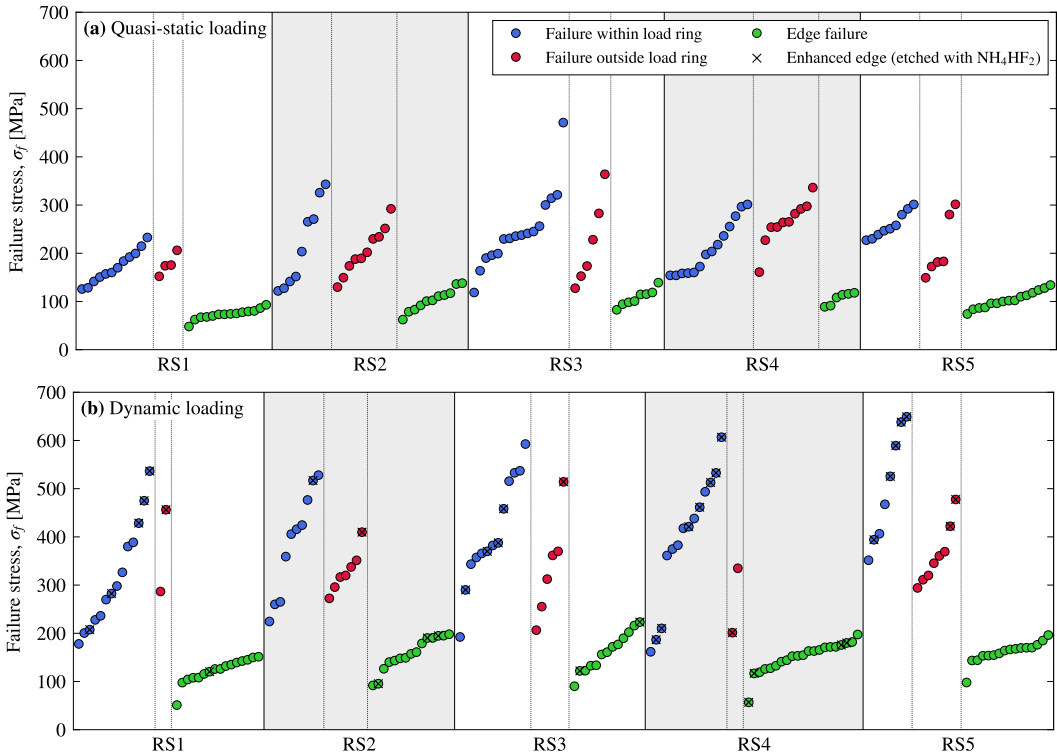


**Fig. 12** The individual measured failure stresses of the tested samples in the five residual stress groups, categorised in the three identified locations of failure origin: (a) quasi-static loading and (b) dynamic loading.

minimum of 15 valid samples (surface failure either within or outside the load ring) was the set goal in this study. These numbers are comparable and slightly higher than what other similar studies have reported (e.g. Nie et al. 2010; Peroni et al. 2011; König 2012). However, at dynamic loading this goal was not met for RS4, which is why the number of samples was increased with five. Furthermore, additional two samples from the stereo-DIC measurements were added to each residual stress group, and some samples' edges were enhanced using an acid solution to increase the success rate at dynamic loading, as described in Sec. 2.1.2. The individual measured failure stresses, categorised in the three identified locations of failure origin, are summarised in Fig. 12(a) and (b) for both loading rates. The samples with enhanced edges are marked with a cross.

Expectedly, remarkable lower strengths are seen for the samples that failed at the edge compared to those that failed on the surface. Some samples also failed at the edge when loaded at high strain rates despite having enhanced edges. However, the chance of edge failure was reduced, increasing the number of valid samples. Furthermore, the individ-

ual strength measurements reveal that samples with a failure origin outside the load ring are a sound supplement to those that failed within because obtained failure stresses have comparable magnitudes within the different residual stress groups. Also, enhancing the edge strength of some samples in the dynamic tests did not alter the measured surface tensile strengths. The obtained strength data are spread across the existing scatter with no significant jump. Since the edge strength was enhanced, more samples failed on the surface, some at higher stresses. Those could not have been measured without an enhancement, as the applied load probably would have caused an edge failure instead.

A complete summary of the equibiaxial flexural strength characterisation of soda-lime-silica glass, based on samples categorised as valid, is provided in Table 4. The stress and strain rates only show a minor variation between residual stress groups. Hence nearly identical loading conditions can be concluded, making a direct comparison within the two loading rates possible. Furthermore, flexural strength is observed to be affected by compressive surface stress and loading rate, however, with a significant scattering, as also seen

**Table 4** Summary of the equibiaxial flexural surface strength characterisation of soda-lime-silica glass tested at two loading rates, a quasi-static and a dynamic. Data for the five residual stress groups RS1 to RS5 include the number of samples ( $N$ , valid/total tested) and the means of the stress rate ( $\dot{\sigma}$ ), strain rate ( $\dot{\epsilon}$ ), and failure stress ( $\sigma_f$ ). In parentheses, the standard deviation to each value is given.

	Quasi-static loading				Dynamic loading			
	$N$ [-]	$\dot{\sigma}$ [MPas <sup>-1</sup> ]	$\dot{\epsilon}$ [s <sup>-1</sup> ]	$\sigma_f$ [MPa]	$N$ [-]	$\dot{\sigma}$ [MPas <sup>-1</sup> ]	$\dot{\epsilon}$ [s <sup>-1</sup> ]	$\sigma_f$ [MPa]
RS1	16/30	2.0 (±0.2)	2.2 · 10 <sup>-5</sup> (±0.1 · 10 <sup>-5</sup> )	173 (±30.7)	16/32	4.1 · 10 <sup>6</sup> (±0.8 · 10 <sup>6</sup> )	45 (±8.7)	324 (±109)
RS2	19/30	1.9 (±0.3)	2.2 · 10 <sup>-5</sup> (±0.3 · 10 <sup>-5</sup> )	210 (±67.7)	17/32	4.1 · 10 <sup>6</sup> (±0.6 · 10 <sup>6</sup> )	47 (±5.3)	364 (± 91)
RS3	22/30	2.0 (±0.3)	2.2 · 10 <sup>-5</sup> (±0.2 · 10 <sup>-5</sup> )	240 (±81.2)	19/32	4.4 · 10 <sup>6</sup> (±0.8 · 10 <sup>6</sup> )	49 (±7.9)	387 (±113)
RS4	24/30	2.1 (±0.2)	2.3 · 10 <sup>-5</sup> (±0.2 · 10 <sup>-5</sup> )	232 (±57.0)	16/37	4.2 · 10 <sup>6</sup> (±0.9 · 10 <sup>6</sup> )	47 (±9.5)	381 (±133)
RS5	15/30	2.0 (±0.2)	2.3 · 10 <sup>-5</sup> (±0.2 · 10 <sup>-5</sup> )	240 (±49.0)	16/32	4.5 · 10 <sup>6</sup> (±0.4 · 10 <sup>6</sup> )	51 (±3.8)	433 (±115)

from Fig. 12. At quasi-static loading, the standard deviation ranges from 18 to 34 % of the mean values, and from 25 to 35 % at dynamic loading. These ranges are similar to what is reported by Swab et al. (2014) and Meyland et al. (2019) for as-received soda-lime-silica glass, thus considered reasonable. Since the scattering of the strength results reflects the variation of flaw sizes present on the tested glass surfaces, a reduction could have been achieved by applying a well-controlled, uniform surface condition. Either by introducing flaws of known size, or removing the present processing/handling flaws by etching (Nie et al. 2010; Meyland et al. 2019). However, the surface condition was kept as-received in this study not to modify the actual glass strength.

As evident from the above, this study considered two parameters that significantly affected the flexural strength of the tested glass, namely residual stress and loading rate. Beginning with the residual stresses, a simplified linear relationship between the apparent equibiaxial flexural strength,  $\sigma_f$ , and the compressive surface stress,  $\sigma_c$ , can be expressed as (Rodichev et al. 2007):

$$\sigma_f = \sigma_i + k\sigma_c \quad (8)$$

where  $\sigma_i$  is the glass' intrinsic material strength, and  $k$  is an empirical constant ( $k \cong 1$ ) determining how strength increases with residual stresses, which also can be written as  $\Delta\sigma_f/\Delta\sigma_c$ . In Fig. 13, the mean failure stress of each residual stress group is plotted against the mean compressive surface stress. The error bars are the standard deviations, and the blue shadowed boxes the 95 % confidence intervals. Despite observing somewhat large standard deviations, as already discussed, and having investigated a small range of compressive surface stresses, a strength increase is evident at both tested loading rates. A line of best fit through the means of the data indicates that the slope, i.e.  $\Delta\sigma_f/\Delta\sigma_c$ , for the glass tested quasi-statically is 1.4, and 1.7 for the glass tested dynamically. For comparison, the expected slope of 1, fitted to the data points, is also drawn in Fig. 13(a) and (b). Both the fitted and expected line go through the shown 95 % confidence intervals. The deviation to the expected strength increase

might be because only tempered glass samples with residual stresses spanning over a narrow range between 40 and 53 MPa were tested, and within each residual stress group a large scattering was present, by which fluctuations between the residual stress groups had a more significant impact on the overall strength increase. For example, strength data reported in Schiavonato et al. (2005) also show an increased slope (as high as  $k = 1.21$ ), but with a less pronounced deviation to 1 because the glass was tested with compressive surface stresses from 40 MPa up to 140 MPa. With glass sample dimensions employed in this study, it was challenging going this high in compressive surface stress using the conventional tempering process (see Sec. 2.1.1). Nevertheless, the studied compressive surface stresses could still be shown to affect the glass strength expectedly, both at quasi-static and dynamic loading.

Next, looking at the loading rate dependency of the flexural strength, the following relationship derived from the theory of sub-critical crack growth exists (see e.g. Meyland et al. 2021c):

$$\sigma_f = \beta \dot{\sigma}^{1/(n+1)} \quad (9)$$

where  $\beta$  and  $n$  are sub-critical crack growth parameters that depend on the flaw characteristics and test environment, and in a log-log plot the exponent  $1/(n+1)$  is the slope of the data. Usually, a constant value of  $n = 16$  is a reasonable and conservative assumption for structural design (see e.g. Haldimann et al. 2008). The variable  $\beta$  varies much more; hence, no fixed value can be given.

The double-logarithmic linear relationship provided by Eq. (9) is used to compare results given in Table 4 for the five residual stress groups. Obtained failure stresses are normalised with respect to a stress,  $\sigma_0$ , interpolated at  $\dot{\epsilon}_0 = 2.86 \cdot 10^{-5} \text{ s}^{-1}$  ( $= \dot{\sigma}_0/E_g$  for  $\dot{\sigma}_0 = 2.0 \text{ MPas}^{-1}$ ), similar to Meyland et al. (2021c). The normalised data are presented in Fig. 14 and compared with the most recent investigations on soda-lime-silica glass at high strain rates (mentioned in Sec. 1) together with 'other data' from Meyland et al. (2021b).

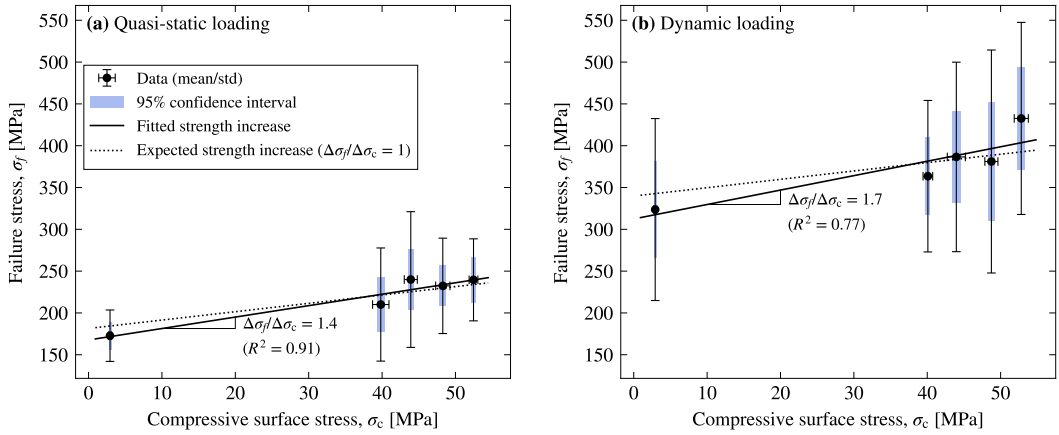


**Fig. 13** The measured failure stress,  $\sigma_f$ , of the soda-lime-silica glass as a function of the compressive surface stress,  $\sigma_c$ , for the five residual stress groups RS1 to RS5: (a) quasi-static loading and (b) dynamic loading.

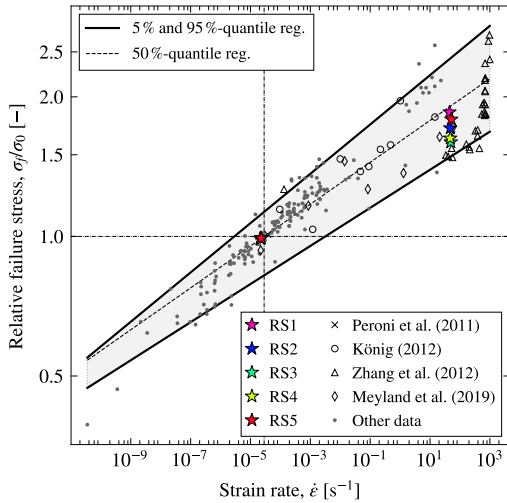


**Fig. 14** The relative failure stress,  $\sigma_f/\sigma_0$ , of the soda-lime-silica glass as a function of strain rate,  $\dot{\epsilon}$ . Additionally, data from the most recent investigations and ‘other data’ from Meyland et al. (2021b) for similar test environments, that is, air with a relative humidity between 25 and 67%, are included. The quantile regressions include all data shown.

A significant loading rate dependency can be ascertained for all five residual stress groups. With respect to  $\sigma_f/\sigma_0 = 1$ , strength increases from 60 to 86% are determined at an average strain rate of  $48 \text{ s}^{-1}$ . However, the residual stresses do not show any significant effect on the loading rate dependence of the glass strength, since samples in RS1 have the highest and samples in RS3 the lowest strength increase, with the other

groups (RS2, RS4 and RS5) in between. No dependency was expected either as the compressive surface stresses are superimposed to the glass’ intrinsic material strength. After tensile stresses due to bending loading nullify the compressive surface stresses, glass failure is essentially governed by the nature of surface flaws, which must be assumed to have been comparable on all samples tested. Thus, similar behaviour in strength increase with loading rate between the tested residual stress groups is shown here. The observed strength increase at these high strain rates can be explained by decreased or even cancelled sub-critical crack growth effects. It is a unique effect for glass where its atomic structure (silica bonds) at a crack tip reacts with moisture from the environment. Combined with constant or slow tensile loading, it causes cracks to grow steadily, leading to a degradation of the fracture strength with time (Freiman et al. 2009). At rapid loading, however, time for the reaction at a crack tip is shortened or even not existing for water molecules to reach a crack tip, thus delaying or inhibiting the occurrence of crack growth, leading to the observed strength increase.

Comparing the measurements with data from recent studies (Peroni et al. 2011; König 2012; Zhang et al. 2012; Meyland et al. 2019), a good agreement is seen at the tested high strain rate. All strength data are clustered within a narrow range of strain rates with data from Zhang et al. showing the lowest strength increase that furthermore coincides with the plotted 5%-quantile regression. Including the ‘other data’ from Meyland et al. (2021b) in the comparison, data from the present study seem to deviate from the general trend, indicating a beginning levelling in the observed strength increases. Such behaviour aligns with the assertion that the effect of sub-critical crack growth is inhibited at very rapid loading, which at some point will result in a rate-independent strength,

i.e. the inert strength of glass. However, the ensuing sudden increase reported by Zhang et al. is debatable, as the plotted data are individual measurements and not mean values as for the other studies.

A further indication of a beginning levelling in the determined strength increases can be found from the slopes of the data, represented by  $n$  that results from Eq. (9). Usually, soda-lime-silica glass is conservatively assumed to be well represented by  $n = 16$ . As an extra reference, the slope of the 50 %-quantile regression line in Fig. 14 results in  $n = 21.2$ , and data for the five residual stress groups determine  $n$ -values between 22 and 30 as they are located below the quantile regression. When  $n$  is high, the chemical reactivity at the crack tip is reduced. Since the obtained values for  $n$  are significantly higher than 16, it indicates that the strengths measured at the high strain rate result in lower slopes than the linear trend of the other data shown in Fig. 14. This suggests that a limit is approaching at which sub-critical crack growth effects are inhibited.

### 3.2 Young's modulus

Results reported in Meyland et al. (2021a) show that the glass sample deflection in the employed ring-on-ring test configuration is well-described by an analytical plate bending solution, derived from a standard solution given in Timoshenko and Woinowsky-Krieger (1959). Hence, the performed non-contact deflection measurements with stereo-DIC provide the determination of Young's modulus,  $E_g$ , using a load-displacement curve and the following analytical expression:

$$E_g = \frac{F}{u} \frac{3(1-\nu^2)}{8\pi h^3} (D_L^2 + 4r^2) \left[ \ln \frac{D_L^2}{D_S^2} + \frac{D_S^2 - D_L^2}{D_L^2 + 4r^2} \left( 1 + \frac{(D_S^2 - 4r^2)(1-\nu)}{2(1+\nu)D^2} \right) \right] \quad (10)$$

for  $0 \leq r \leq \frac{D_L}{2}$

where  $u$  is the deflection at a distance  $r$  (within the load ring) from the common central axis of the ring-on-ring test configuration, resulting from the applied load,  $F$ .

The stiffness investigation was conducted on two samples in each residual stress group, resulting in ten measurements. From the digital image correlation in the software, GOM Correlate Pro 2019, a meshed surface, as exemplified in Fig. 15(a) together with the approximate location of the load ring, was constructed of about 480 points at which the glass sample deflection could be evaluated. A contour plot of a full-field deflection measurement is shown in Fig. 15(b) for a load stage corresponding to 5.9 kN, from which clearly

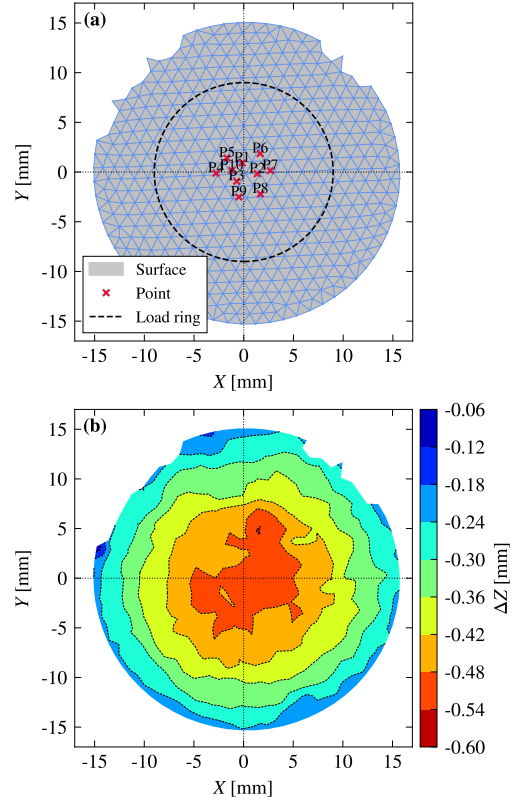


**Fig. 15** Results from a stereo-DIC measurement. In (a), a surface component created by the stereo digital image correlation technique and the ten points at which deflection measurements were extracted, and in (b), for the same surface, a contour plot of a full-field deflection measurement,  $\Delta Z$ , for a load stage corresponding to 5.9 kN.

can be seen that the sample was subjected to an equibiaxial bending at the high strain rate loading. As minor noise was present in the measurements (more in Meyland et al. 2021a), deflection histories were extracted at ten arbitrary chosen points, also highlighted in Fig. 15(a), on each of the ten surfaces in the proximity of the sample centre. After dynamic force equilibrium was checked, the force histories recorded on the support ring side (see example of  $F_{SR}$  in Fig. 10) were matched to the measured deflections by applying the time shift of  $150 \mu s$ , corresponding to a shift of 30 images.

A resulting load-deflection curve is plotted in Fig. 16. As expected, the glass shows a linear material response up to the peak load. Thus, a linear regression was performed using the least squares method, providing a measure of Young's modulus as it is proportional to the regression slope,  $\Delta F / \Delta u$ . With the slope and the exact distance  $r$ , at which the deflection was

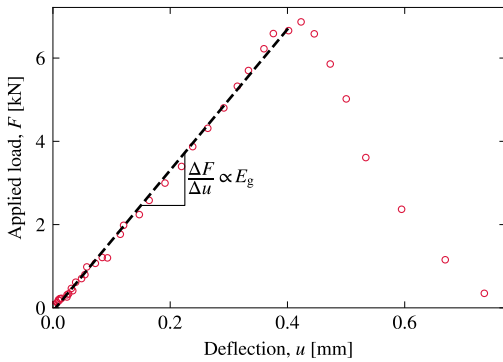


**Fig. 16** A load-deflection curve determined by the stereo-DIC measurements exemplified by point 5 from the surface in Fig. 15(a).

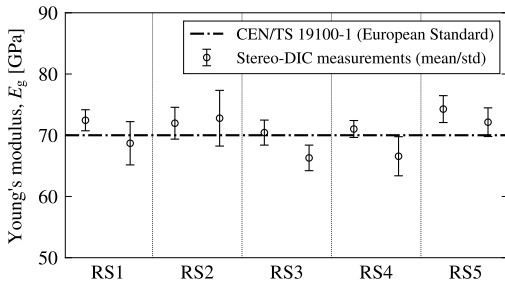


**Fig. 17** Young's modulus,  $E_g$ , of the glass in the five residual stress groups (RS1 to RS5) determined from the high strain rate experiments using stereo-DIC deflection measurements. For comparison, the value given in CEN/TS 19100-1 (2021) is also shown.

extracted on the DIC-generated surface, an estimate for the glass' Young's modulus was determined using Eq. (10). The mean of the ten extracted points per tested sample in each residual stress group is plotted in Fig. 17 with error bars as the standard deviation.

The estimated Young's modulus of the soda-lime-silica glass at high strain rates show minor variations across the residual stress groups, with no indication of being affected by the residual stresses themselves. Both the standard deviation within and the variation between the samples are most likely a result of the noise in the stereo-DIC measurements. However, taking the overall mean, determined as 70.7 GPa ( $\pm 2.7$  GPa), it is in good agreement with the 70 GPa defined in the European Standard CEN/TS 19100-1 (2021), also plotted in Fig. 17. Thus, Young's modulus seems not to be loading rate dependent, which also agrees with the findings in Meyland et al. (2021c).

## 4 Conclusions

A ring-on-ring test configuration for equibiaxial flexural loading of small circular flat soda-lime-silica glass samples was successfully integrated into a modified split-Hopkinson pressure bar setup. The modifications in the setup enabled an unobstructed view of a sample's tensile surface, making the application of high-speed cameras possible for fracture assessment and non-contact optical deflection measurements using the technique of stereo digital image correlation (stereo-DIC). Together with a universal testing machine, the glass characteristics, such as strength and stiffness, were investigated on samples with as-received surfaces at two loading rates: a quasi-static at  $2.0 \text{ MPa s}^{-1}$ , and a dynamic at  $4.3 \cdot 10^6 \text{ MPa s}^{-1}$ . The effect of residual stresses in thermally tempered glass was also considered in the investigations.

The flexural surface strength investigation showed two dependencies. As expected, the strength increased with compressive surface stress within the two tested loading rates. The glass tested at quasi-static loading showed to increase with a slope of 1.4, whereas the dynamic loading caused a slightly different slope of 1.7. Also, it was shown that the residual compressive surface stress itself did not significantly influence the loading rate dependence of the glass strength. Each tested residual stress group revealed a significant strength increase with loading rate at similar trends. Thus, strength enhancements between 60 and 86 % were found, which furthermore agree with other comparable data found in the literature.

Lastly, the performed stereo-DIC deflection measurements determined the stiffness of the glass (Young's modulus) using analytical plate bending theory. The dynamic experiments across the five residual stress groups could not show any loading rate dependency. Hence, it is concluded that the 70 GPa specified in the European glass code CEN/TS 19100-1 (2021) also applies to high strain rate loading.

**Acknowledgements** This work is funded by the Innovation Fund Denmark (IFD) [grant No. 8053-00088B], Rambøll Fonden [grant No. 2018-51], and the Danish engineering consultancy Rambøll Denmark A/S. The authors acknowledge Søren P. Kristensen and Hans Exner from Rambøll Denmark A/S for their interest and support given throughout this project. Furthermore, Prof. Jakob B. Wagner and his team from DTU CEN (Center for Electron Nanoscopy) are acknowledged for helping with the SEM/EDS analysis, which detected the studied glass samples' chemical elemental composition.

**Conflict of interest** The authors declare that they have no known competing financial interests or personal relationships that could have appeared to influence the work reported in this paper.

**Data availability** The data that support the findings of this study are openly available (licensed under CC BY-SA 4.0, <https://creativecommons.org/licenses/by-sa/4.0/>) in the data repository DTU Data, a figshare platform, at <https://doi.org/10.11583/DTU.17694692>.

## References

- Aben, H. and Guillemet, C. (1993). *Photoelasticity of Glass*. Springer Berlin Heidelberg, Berlin, Heidelberg. doi: [10.1007/978-3-642-50071-8](https://doi.org/10.1007/978-3-642-50071-8).
- Angelides, S. C., Talbot, J. P., and Overend, M. (2019). The effects of high strain-rate and in-plane restraint on quasi-statically loaded laminated glass: a theoretical study with applications to blast enhancement. *Glas. Struct. Eng.* doi: [10.1007/s40940-019-00107-4](https://doi.org/10.1007/s40940-019-00107-4).
- Angelides, S. C., Talbot, J. P., and Overend, M. (2022). The influence of fracture pattern on the residual resistance of laminated glass at high strain-rates: an experimental investigation of the post-fracture bending moment capacity based on time-temperature mapping of interlayer yield stress. *Glas. Struct. Eng.* doi: [10.1007/s40940-022-00168-y](https://doi.org/10.1007/s40940-022-00168-y).
- Anton, J. (2015). Scattered Light Polariscopes SCALP. Instruction Manual (Ver. 5.8.2), GlasStress Ltd., Tallinn, Estonia.
- ASTM C1499-15 (2015). *Standard Test Method for Monotonic Equibiaxial Flexural Strength of Advanced Ceramics at Ambient Temperature*. ASTM International, West Conshohocken, PA. doi: [10.1520/C1499-15](https://doi.org/10.1520/C1499-15).
- CEN/TS 19100-1 (2021). Design for glass structures – Part 1: Basis of design and materials. European Standard, European Committee for Standardization (CEN), Brussels.
- Chen, W. and Song, B. (2011). *Split Hopkinson (Kolsky) Bar*. Mechanical Engineering Series. Springer US, Boston, MA. doi: [10.1007/978-1-4419-7982-7](https://doi.org/10.1007/978-1-4419-7982-7).
- Del Linz, P., Hooper, P. A., Arora, H., Wang, Y., Smith, D., Blackman, B. R., and Dear, J. P. (2017). Delamination properties of laminated glass windows subject to blast loading. *Int. J. Impact Eng.*, 105:39–53. doi: [10.1016/j.ijimpeng.2016.05.015](https://doi.org/10.1016/j.ijimpeng.2016.05.015).
- EN 572-1 (2012). Glass in building – Basic soda lime silicate glass products – Part 1: Definitions and general physical and mechanical properties. European Standard, European Committee for Standardization (CEN), Brussels.
- EN 572-2 (2012). Glass in building – Basic soda lime silicate glass products – Part 2: Float glass. European Standard, European Committee for Standardization (CEN), Brussels.
- Förch, M. (2019). *Analysis of Glass Panels Subjected to Blast Load*. PhD thesis, HafenCity University Hamburg, Hamburg, Germany. doi: [10.1007/978-3-662-59087-4](https://doi.org/10.1007/978-3-662-59087-4).
- Freiman, S. W., Wiederhorn, S. M., and Mecholsky, Jr., J. J. (2009). Environmentally Enhanced Fracture of Glass: A Historical Perspective. *J. Am. Ceram. Soc.*, 92(7):1371–1382. doi: [10.1111/j.1551-2916.2009.03097.x](https://doi.org/10.1111/j.1551-2916.2009.03097.x).
- Haldimann, M., Luible, A., and Overend, M. (2008). *Structural Use of Glass*. International Association for Bridge and Structural Engineering, Zürich, Switzerland.
- Hooper, P., Sukhran, R., Blackman, B., and Dear, J. (2012). On the blast resistance of laminated glass. *Int. J. Solids Struct.*, 49(6):899–918. doi: [10.1016/j.ijsolstr.2011.12.008](https://doi.org/10.1016/j.ijsolstr.2011.12.008).
- ISO 20657 (2017). Glass in building – Heat soaked tempered soda lime silicate safety glass. International Standard, International Organization for Standardization, Vernier, Geneva, Switzerland.
- ISO 22509 (2020). Glass in building – Heat strengthened soda lime silicate glass. International Standard, International Organization for Standardization, Vernier, Geneva, Switzerland.
- Kirk, A., Watson, C., Torpey, P., and Levett, C. (2020). Visual guide: how explosion caused mass casualties and devastation across Beirut. url: <https://www.theguardian.com/world/2020/aug/05/visual-guide-how-explosion-caused-mass-casualties-and-devastation-across-beirut>. Online; accessed 18-03-2022.
- Kolli, M., Hamidouche, M., Bouaouadja, N., and Fantozzi, G. (2009). HF etching effect on sandblasted soda-lime glass properties. *J. Eur. Ceram. Soc.*, 29(13):2697–2704. doi: [10.1016/j.jeurceramsoc.2009.03.020](https://doi.org/10.1016/j.jeurceramsoc.2009.03.020).
- König, C. (2012). *Dehnratenabhängigkeit mechanischer Werkstoffkennwerte von Kalk-Natronsilicatglas*. PhD thesis, Technische Universität Carolo-Wilhelmina zu Braunschweig, Germany. doi: [10.24355/dbbs.084-201204230927-0](https://doi.org/10.24355/dbbs.084-201204230927-0).
- Kuntsche, J. K. (2015). *Mechanisches Verhalten von Verbundglas unter zeitabhängiger Belastung und Explosionsbeanspruchung*. PhD thesis, Institut für Statik und Konstruktion, Technische Universität Darmstadt, Germany. doi: [10.1007/978-3-662-48831-7](https://doi.org/10.1007/978-3-662-48831-7).
- Larcher, M., Solomos, G., Casadei, F., and Gebbeken, N. (2012). Experimental and numerical investigations of laminated glass subjected to blast loading. *Int. J. Impact Eng.*, 39(1):42–50. doi: [10.1016/j.ijimpeng.2011.09.006](https://doi.org/10.1016/j.ijimpeng.2011.09.006).
- Meyland, M. J., Bønding, C. K. T., Eriksen, R. N. W., and Nielsen, J. H. (2019). An experimental investigation of the flexural strength of soda-lime-silica glass at high loading rates. *Glas. Struct. Eng.*, 4(2):175–183. doi: [10.1007/s40940-018-0089-2](https://doi.org/10.1007/s40940-018-0089-2).
- Meyland, M. J., Eriksen, R. N. W., and Nielsen, J. H. (2021a). A modified split-Hopkinson pressure bar setup enabling stereo digital image correlation measurements for flexural testing. doi: [10.13140/RG.2.2.30301.33760](https://doi.org/10.13140/RG.2.2.30301.33760). Preprint (not peer reviewed).
- Meyland, M. J., Nielsen, J. H., and Kocer, C. (2021b). Datasets: Tensile behaviour of soda-lime-silica glass and the significance of load duration – A literature review. DTU Data, Technical University of Denmark. doi: [10.11583/DTU.13655525](https://doi.org/10.11583/DTU.13655525).
- Meyland, M. J., Nielsen, J. H., and Kocer, C. (2021c). Tensile behaviour of soda-lime-silica glass and the significance of load duration – A literature review. *J. Build. Eng.*, 44(December):102966. doi: [10.1016/j.jobte.2021.102966](https://doi.org/10.1016/j.jobte.2021.102966).
- Nie, X., Chen, W. W., and Templeton, D. W. (2010). Dynamic Ring-on-Ring Equibiaxial Flexural Strength of Borosilicate Glass. *Int. J. Appl. Ceram. Technol.*, 7(5):616–624. doi: [10.1111/j.1744-7402.2010.02508.x](https://doi.org/10.1111/j.1744-7402.2010.02508.x).
- Nielsen, J. H. and Bjarrum, M. (2017). Deformations and strain energy in fragments of tempered glass: experimental and numerical investigation. *Glas. Struct. Eng.*, 2(2):133–146. doi: [10.1007/s40940-017-0043-8](https://doi.org/10.1007/s40940-017-0043-8).
- Nielsen, J. H., Meyland, M. J., Thorup, B. E., Zugravu, A., and Olesen, J. F. (2019). Investigating the strength effects of drilling in tempered glass. *Glas. Struct. Eng.*, 4(2):243–256. doi: [10.1007/s40940-019-00095-5](https://doi.org/10.1007/s40940-019-00095-5).
- Nielsen, J. H., Olesen, J. F., and Stang, H. (2009). The Fracture Process of Tempered Soda-Lime-Silica Glass. *Exp. Mech.*, 49(6):855–870. doi: [10.1007/s11340-008-9200-y](https://doi.org/10.1007/s11340-008-9200-y).
- Nielsen, J. H., Olesen, J. F., and Stang, H. (2010). Characterization of the Residual Stress State in Commercially Fully Toughened Glass. *J. Mater. Civ. Eng.*, 22(2):179–185. doi: [10.1061/\(asce\)0899-1561\(2010\)22:2\(179\)](https://doi.org/10.1061/(asce)0899-1561(2010)22:2(179)).
- Nielsen, J. H., Thiele, K., Schneider, J., and Meyland, M. J. (2021). Compressive zone depth of thermally tempered glass. *Constr. Build. Mater.*, 310. doi: [10.1016/j.conbuildmat.2021.125238](https://doi.org/10.1016/j.conbuildmat.2021.125238).
- Norville, H. S., Harvill, N., Conrath, E. J., Shariat, S., and Mallonee, S. (1999). Glass-Related Injuries in Oklahoma City Bombing. *J. Perform. Constr. Facil.*, 13(2):50–56. doi: [10.1061/\(ASCE\)0887-3828\(1999\)13:2\(50\)](https://doi.org/10.1061/(ASCE)0887-3828(1999)13:2(50)).
- Osnes, K., Holmen, J. K., Hopperstad, O. S., and Børvik, T. (2019). Fracture and fragmentation of blast-loaded laminated glass: An experimental and numerical study. *Int. J. Impact Eng.*, 132(7491):103334. doi: [10.1016/j.ijimpeng.2019.103334](https://doi.org/10.1016/j.ijimpeng.2019.103334).
- Pellreine, J., Kuntsche, J., Van Dam, S., Van Paeppegem, W., and Schneider, J. (2016). Critical assessment of the post-breakage performance of blast loaded laminated glazing: Experiments and simulations. *Int. J. Impact Eng.*, 88:61–71. doi: [10.1016/j.ijimpeng.2015.09.008](https://doi.org/10.1016/j.ijimpeng.2015.09.008).
- Peroni, M., Solomos, G., Pizzinato, V., and Larcher, M. (2011). Experimental Investigation of High Strain-Rate Behaviour of Glass. *Appl. Mech. Mater.*, 82:63–68. doi: [10.4028/www.scientific.net/AMM.82.63](https://doi.org/10.4028/www.scientific.net/AMM.82.63).

- Pourmoghaddam, N., Kraus, M. A., Schneider, J., and Siebert, G. (2018). Relationship between strain energy and fracture pattern morphology of thermally tempered glass for the prediction of the 2D macro-scale fragmentation of glass. *Glas. Struct. Eng.* doi: [10.1007/s40940-018-00091-1](https://doi.org/10.1007/s40940-018-00091-1).
- Pourmoghaddam, N. and Schneider, J. (2019). Determination of the engine power for quenching of glass by forced convection: simplified model and experimental validation of residual stress levels. *Glas. Struct. Eng.*, 4(1):117–125. doi: [10.1007/s40940-018-0078-5](https://doi.org/10.1007/s40940-018-0078-5).
- Rodichev, Y., Maslov, V., Netychuk, A., Bodunov, V., and Yevplov, Y. (2007). Bending strength and fracture of glass materials under the different loading conditions. In *Glass Performance Days 2007*, pages 615–618, Tampere, Finland.
- Rudick, M. M. and Norville, H. S. (2000). Discussion and Closure to "Glass-Related Injuries in Oklahoma City Bombing". *J. Perform. Constr. Facil.*, 14(4):167–167. doi: [10.1061/\(ASCE\)0887-3828\(2000\)14:4\(167\)](https://doi.org/10.1061/(ASCE)0887-3828(2000)14:4(167)).
- Samuel, A. and Weir, J. (1999). *Introduction to Engineering Design*. Elsevier Butterworth-Heinemann. doi: [10.1016/B978-0-7506-4282-8.X5000-3](https://doi.org/10.1016/B978-0-7506-4282-8.X5000-3).
- Schiavonato, M., Mognato, E., and Redner, A. S. (2005). Stress Measurement, Fragmentation and Mechanical Strength. In *Glass Processing Days 2005*, pages 92–95, Tampere, Finland.
- Schneider, J. (2001). *Festigkeit und Bemessung punktgelagerter Gläser und stoßbeanspruchter Gläser*. PhD thesis, Fachbereich Bauingenieurwesen und Geodäsie, Technische Universität Darmstadt, Germany.
- Snijder, B. H. H. (2004). Structural Glass and Glass Structures: An Introduction. *Struct. Eng. Int.*, 14(2):72–72. doi: [10.2749/10168660477964071](https://doi.org/10.2749/10168660477964071).
- Stein, M., Draper, P., and Hellyer, R. (2019). City of Glass: Recent Advancements in Glass Structures in New York City. *Struct. Eng. Int.*, 29(1):101–111. doi: [10.1080/10168664.2018.1519365](https://doi.org/10.1080/10168664.2018.1519365).
- Sukkarieh, G., Lahoud, C., Ghorayeb, R., Abi Karam, M., Succarieh, Y., Saleh, M., and Jalkh, A. (2021). Characteristics of open eye injuries in the Beirut Port explosion. *Injury*, 52(9):2601–2605. doi: [10.1016/j.injury.2021.07.031](https://doi.org/10.1016/j.injury.2021.07.031).
- Swab, J. J., Patel, P. J., Tran, X., Gilde, L., Luoto, E., Gaviola, M. H., Gott, A., Paulson, B., and Kilczewski, S. (2014). Equibiaxial Flexure Strength of Glass: Influence of Glass Plate Size and Equibiaxial Ring Ratio. *Int. J. Appl. Glas. Sci.*, 5(4):384–392. doi: [10.1111/ijag.12094](https://doi.org/10.1111/ijag.12094).
- Timoshenko, S. and Woinowsky-Krieger, S. (1959). *Theory of plates and shells*. McGraw-Hill, 2. edition.
- Zhang, X., Hao, H., and Ma, G. (2013). Parametric study of laminated glass window response to blast loads. *Eng. Struct.*, 56:1707–1717. doi: [10.1016/j.engstruct.2013.08.007](https://doi.org/10.1016/j.engstruct.2013.08.007).
- Zhang, X., Hao, H., and Wang, Z. (2015). Experimental study of laminated glass window responses under impulsive and blast loading. *Int. J. Impact Eng.*, 78:1–19. doi: [10.1016/j.ijimpeng.2014.11.020](https://doi.org/10.1016/j.ijimpeng.2014.11.020).
- Zhang, X., Zou, Y., Hao, H., Li, X., Ma, G., and Liu, K. (2012). Laboratory Test on Dynamic Material Properties of Annealed Float Glass. *Int. J. Prot. Struct.*, 3(4):407–430. doi: [10.1260/2041-4196.3.4.407](https://doi.org/10.1260/2041-4196.3.4.407).

Limited data characterise glass for short duration loads, typical of blast loading. The present Ph.D. thesis focuses on the high strain rate characterisation of monolithic soda-lime-silica glass and the further application for computer-aided engineering. Because high strain rate testing of materials is not a standard laboratory discipline, a novel test setup based on the well-known principles of a Split-Hopkinson Pressure Bar (SHPB) is developed and constructed to test flat, circular samples in bending dynamically. The novel design enables high-speed cameras for fracture assessment and non-contact optical deflection measurements using the Stereo Digital Image Correlation (Stereo-DIC) technique. Based on the obtained material characteristics, a material damage model for computer simulations of blast-loaded glass panes, as typically installed in building facades, is developed for use in commercial finite element software like Abaqus.

**DTU Civil and Mechanical Engineering**  
Technical University of Denmark

Brovej, Bld. 118  
DK-2800 Kgs. Lyngby  
Denmark  
Phone (+45) 4525 1960

[www.byg.dtu.dk](http://www.byg.dtu.dk)

March 2022

ISBN: 978-87-7877-569-6